DISSERTATION

Submitted to the

Combined Faculty of Natural Sciences and Mathematics

Heidelberg University, Germany

for the degree of

Doctor of Natural Sciences (Dr. rer. nat.)

Presented by

Jessica Matthias (M.Sc.)

Oral examination: December 6, 2019

STED Nanoscopy to Illuminate New Avenues in Cancer Research

–

From Live Cell Staining and Direct Imaging
to Decisive Preclinical Insights for Diagnosis and Therapy

Examiners: Prof. Dr. Joachim Spatz

Prof. Dr. Stefan W. Hell

ABSTRACT

Molecular imaging is established as an indispensable tool in various areas of cancer research, ranging from basic cancer biology and preclinical research to clinical trials and medical practice. In particular, the field of fluorescence imaging has experienced exceptional progress during the last three decades with the development of various *in vivo* technologies. Within this field, fluorescence microscopy is primarily of experimental use since it is especially qualified for addressing the fundamental questions of molecular oncology. As stimulated emission depletion (STED) nanoscopy combines the highest spatial and temporal resolutions with live specimen compatibility, it is best-suited for real-time investigations of the differences in the molecular machineries of malignant and normal cells to eventually translate the acquired knowledge into increased diagnostic and therapeutic efficacy.

This thesis presents the application of STED nanoscopy to two acute topics in cancer research of direct or indirect clinical interest. The first project has investigated the structure of telomeres, the ends of the linear eukaryotic chromosomes, in intact human cells at the nanoscale. To protect genome integrity, a telomere can mask the chromosome end by folding back and sequestering its single-stranded 3'-overhang in an upstream part of the double-stranded DNA repeat region. The formed t-loop structure has so far only been visualized by electron microscopy and fluorescence nanoscopy with cross-linked mammalian telomeric DNA after disruption of cell nuclei and spreading. For the first time, this work demonstrates the existence of t-loops within their endogenous nuclear environment in intact human cells. The identification of further telomere conformations has laid the groundwork for distinguishing cancerous cells that use different telomere maintenance mechanisms based on their individual telomere populations by a combined STED nanoscopy and deep learning approach. The population difference was essentially attributed to the promyelocytic leukemia (PML) protein that significantly perturbs the organization of a subpopulation of telomeres towards an open conformation in cancer cells that employ a telomerase-independent, alternative telomere lengthening mechanism. Elucidating the nanoscale topology of telomeres and associated proteins within the nucleus has provided new insight into telomere structure-function relationships relevant for understanding the deregulation of telomere maintenance in cancer cells.

After understanding the molecular foundations, this newly gained knowledge can be exploited to develop novel or refined diagnostic and treatment strategies. The second project has characterized the intracellular distribution of recently developed prostate cancer tracers. These novel prostate-specific membrane antigen (PSMA) inhibitors have revolutionized the treatment regimen of prostate cancer by enabling targeted imaging and therapy approaches. However, the exact internalization mechanism and the subcellular fate of these tracers have remained elusive. By combining STED nanoscopy with a newly developed non-standard live cell staining protocol, this work confirmed cell surface clustering of the targeted membrane antigen upon PSMA inhibitor binding, subsequent clathrin-dependent endocytosis and endosomal trafficking of the antigen-inhibitor complex. PSMA inhibitors accumulate in prostate cancer cells at clinically relevant time points, but strikingly and in contrast to the targeted antigen itself, they eventually distribute homogenously in the cytosol. This project has revealed the subcellular fate of PSMA/PSMA inhibitor complexes for the first time and provides crucial knowledge for the future application of these tracers including the development of new strategies in the field of prostate cancer diagnostics and therapeutics.

Relying on the photostability and biocompatibility of the applied fluorophores, the performance of live cell STED nanoscopy in the field of cancer research is boosted by the development of improved fluorophores. The third project in this thesis introduces a biocompatible, small molecule near-infrared dye suitable for live cell STED imaging. By the application of a halogen dance rearrangement, a dihalogenated fluorinatable pyridinyl rhodamine could be synthesized at high yield. The option of subsequent radiolabeling combined with excellent optical properties and a non-toxic profile renders this dye an appropriate candidate for medical and bioimaging applications. Providing an intrinsic and highly specific mitochondrial targeting ability, the radiolabeled analogue is suggested as a vehicle for multimodal (positron emission tomography and optical imaging) medical imaging of mitochondria for cancer diagnosis and therapeutic approaches in patients and biopsy tissue.

The absence of cytotoxicity is not only a crucial prerequisite for clinically used fluorophores. To guarantee the generation of meaningful data mirroring biological reality, the absence of cytotoxicity is likewise a decisive property of dyes applied in live cell STED nanoscopy. The fourth project in this thesis proposes a universal approach for cytotoxicity testing based on characterizing the influence of the compound of interest on the proliferation behavior of human cell lines using digital holographic cytometry. By applying this approach to recently developed live cell STED compatible dyes, pronounced cytotoxic effects could be excluded. Looking more closely, some of the tested dyes slightly altered cell proliferation, so this project provides guidance on the right choice of dye for the least invasive live cell STED experiments.

Ultimately, live cell STED data should be exploited to extract as much biological information as possible. However, some information might be partially hidden by image degradation due the dynamics of living samples and the deliberate choice of rather conservative imaging parameters in order to preserve sample viability. The fifth project in this thesis presents a novel image restoration method in a Bayesian framework that simultaneously performs deconvolution, denoising as well as super-resolution, to restore images suffering from noise with mixed Poisson-Gaussian statistics. Established deconvolution or denoising methods that consider only one type of noise generally do not perform well on images degraded significantly by mixed noise. The newly introduced method was validated with live cell STED telomere data proving that the method can compete with state-of-the-art approaches.

Taken together, this thesis demonstrates the value of an integrated approach for STED nanoscopy imaging studies. A coordinated workflow including sample preparation, image acquisition and data analysis provided a reliable platform for deriving meaningful conclusions for current questions in the field of cancer research. Moreover, this thesis emphasizes the strength of iteratively adapting the individual components in the operational chain and it particularly points towards those components that, if further improved, optimize the significance of the final results rendering live cell STED nanoscopy even more powerful.

ZUSAMMENFASSUNG

Die molekulare Bildgebung hat sich als unverzichtbares Instrument zahlreicher Felder der onkologischen Forschung etabliert und erfährt insbesondere Anwendung in der Grundlagenforschung, in der präklinischen Forschung, in klinischen Studien sowie in der Diagnostik und Therapie. In den letzten drei Jahrzehnten wurden im Speziellen auf dem Gebiet der Fluoreszenzbildgebung mit der Entwicklung verschiedener *In-vivo*-Varianten außergewöhnliche Fortschritte gemacht. Als Teilgebiet ist die Fluoreszenzmikroskopie in erster Linie ein experimentelles Mittel, welches einen direkten Zugang zu den zentralen Fragestellungen der molekularen Onkologie eröffnet. Die *Stimulated Emission Depletion* (STED) Nanoskopie bietet herausragende räumliche und zeitliche Auflösung bei gleichzeitiger Eignung für die Bildgebung lebender Proben. Folglich erlaubt sie die Echtzeituntersuchung von Unterschieden in der molekularen Maschinerie entarteter und gesunder Zellen und generiert hierbei Wissen, welches schließlich in einer verbesserten diagnostischen und therapeutischen Wirksamkeit mündet.

Diese Dissertation präsentiert die Anwendung der STED-Nanoskopie auf zwei hochaktuelle wissenschaftliche Thematiken der Krebsforschung von direktem sowie indirektem klinischen Interesse. Das erste Projekt widmete sich der Strukturcharakterisierung von Telomeren in intakten menschlichen Zellen auf molekularer Ebene. Telomere, die Enden der linearen eukaryotischen Chromosomen, dienen dem Schutz der Genomintegrität. Sie können das jeweilige Chromosomenende maskieren, indem sie eine schleifenartige Struktur ausbilden, welche durch den Einschub des einzelsträngigen 3'-Überhangs in einen stromaufwärts gelegenen Abschnitt der doppelsträngigen repetitiven Telomere-DNA Sequenz stabilisiert wird. Bisher untersucht wurde diese T-Loop-Struktur ausschließlich mittels Elektronenmikroskopie und optischer Nanoskopie anhand von Telomer-DNA, die aus Säugetierzellkernen isoliert, chemisch quervernetzt und auf einer Oberfläche präpariert wurde. Die vorliegende Arbeit dokumentiert zum ersten Mal die Existenz von T-Loops in endogenem Kontext in intakten menschlichen Zellen. Die Identifizierung weiterer Telomerkonformationen lieferte die Grundlage für die Unterscheidung von Krebszellen, die verschiedene Telomererhaltungsmechanismen verwenden. Ein kombinierter Ansatz aus STED-Nanoskopie und Tiefenlernen (*Deep Learning*) konnte charakteristische Gegensätze in den individuellen Telomerpopulationen quantifizieren. Diese Gegensätze wurden im Wesentlichen auf das Promyelozytenleukämie (PML) Protein zurückgeführt, welches eine offenere DNA-Konformation für eine Subpopulation von Telomeren in Krebszellen begünstigt, die einen Telomerase-unabhängigen, alternativen Telomerverlängerungsmechanismus verwenden. Die Aufklärung der molekularen Topologie von Telomeren und assoziierten Proteinen im Zellkern ermöglichte neue Einblicke in die Struktur-Funktions-Zusammenhänge von Telomeren, die für das Verständnis der Deregulierung der Telomererhaltung in Krebszellen relevant sind.

Nachdem die molekularen Grundlagen verstanden wurden, kann das neu gewonnene Wissen zur Entwicklung neuartiger sowie verfeinerter Diagnose- und Behandlungsansätze eingesetzt werden. In diesem Sinne beschäftigte sich das zweite Projekt mit der Charakterisierung der intrazellulären Verteilung kürzlich entwickelter Prostatakrebs-*Tracer*. Diese neuartigen Inhibitoren des Prostata-spezifischen Membranantigens (PSMA) haben die Behandlung des Prostatakarzinoms revolutioniert, indem sie zielgerichtete Ansätze für bildgebende Diagnostik und Therapie ermöglichen. Der genaue Internalisierungsmechanismus sowie der subzelluläre Verbleib dieser *Tracer* sind bisher allerdings

noch nicht bekannt gewesen. Die Kombination von STED-Nanoskopie mit einem in dieser Arbeit neu entwickelten atypischen Protokoll zur Anfärbung lebender Zellen konnte bestätigen, dass PSMA-Inhibitoren die Aggregation (*Clustering*) des gebundenen Membranantigens induzieren und dass der Antigen-Inhibitor-Komplex nach anschließender Clathrin-abhängiger Endozytose den endosomalen Transportweg durchläuft. PSMA-Inhibitoren reichern sich innerhalb des klinisch relevanten Zeitrahmens in Prostatakrebszellen an und zeigen bemerkenswerterweise, im Gegensatz zum Membranantigen, final eine homogene zytosolische Verteilung. Dieses Projekt hat erstmalig den subzellulären Verbleib von PSMA/PSMA-Inhibitor-Komplexen aufgeklärt und liefert entscheidende Erkenntnisse für die zukünftige Anwendung der untersuchten *Tracer*, einschließlich der Entwicklung neuer Strategien auf dem Gebiet der Diagnostik und Therapie von Prostatakrebs.

Die Leistungsfähigkeit der Lebendzell-STED-Bildgebung in der onkologischen Forschung hängt maßgeblich von der Photostabilität und Biokompatibilität der verwendeten Fluorophore ab und wird daher durch die Entwicklung verbesserter Fluorophore weiter gesteigert. Das dritte Projekt dieser Dissertation stellt einen nicht-toxischen, niedermolekularen Nah-Infrarot-Farbstoff vor, welcher für die STED-Bildgebung lebender Zellen geeignet ist. Durch Anwendung einer Halogentanz-Umlagerung konnte ein dihalogeniertes, fluorierbares Pyridinylrhodamin mit hoher Ausbeute synthetisiert werden. Die optionale Radiomarkierung, hervorragende optische Eigenschaften sowie die Biokompatibilität qualifizieren diesen Farbstoff für die medizinische und biologische Bildgebung. Aufgrund seiner intrinsischen, hochspezifischen Affinität zu Mitochondrien, kann das radiomarkierte Analogon voraussichtlich in der multimodalen medizinischen Bildgebung (Positronen-Emissions-Tomographie und optische Bildgebung) von Mitochondrien in Krebspatienten sowie in der Pathologie für diagnostische und therapeutische Ansätze eingesetzt werden.

Die Abwesenheit von Zytotoxizität ist nicht nur für klinisch angewandte Fluorophore eine unerlässliche Voraussetzung. Sie ist ebenfalls eine entscheidende Eigenschaft von Farbstoffen, die in der Lebendzell-STED-Bildgebung eingesetzt werden. Je weniger diese Farbstoffe das biologische System stören, umso getreuer spiegeln die Daten die biologische Realität wider. Das vierte Projekt dieser Dissertation schlägt einen universellen Ansatz für einen Zytotoxizitätstest vor, der mittels digitaler holographischer Zytometrie den Einfluss der zu untersuchenden Verbindung auf das Proliferationsverhalten menschlicher Zelllinien charakterisiert. Durch diesen Ansatz konnten für kürzlich entwickelte lebendzell-STED-kompatible Farbstoffe ausgeprägte zytotoxische Effekte ausgeschlossen werden. Da einige der getesteten Farbstoffe die Zellproliferation leicht beeinflussten, bieten die vorliegenden Ergebnisse eine Unterstützung bei der geeigneten Farbstoffwahl, um minimal-invasive Lebendzell-STED-Experimente zu gewährleisten.

Im finalen Schritt der Datenanalyse sollten aus Lebendzell-STED-Daten so viele biologische Informationen wie möglich extrahiert werden. Die gezielte Wahl konservativer Bildgebungsparameter zum Schutz der Lebensfähigkeit der Proben sowie deren Dynamik führen zu Kompromissen in der Bildqualität. Hierdurch können gewisse biologische Informationen teilweise verborgen bleiben. In dem fünften Projekt dieser Dissertation wird eine neuartige Bildwiederherstellungsmethode (*image restoration*) mit einem Bayes‘schen Ansatz vorgestellt, die gleichzeitig Entfaltung, Rauschentfernung sowie Auflösungssteigerung (*super-resolution*) erlaubt und Bilder mit gemischter Poisson-Gauß'scher Rauschstatistik wiederherstellt. Etablierte Entfaltungs- sowie Entrauschungsverfahren, die nur eine Art von Rauschen berücksichtigen, führen bei Bildern, die durch signifikantes Mischrauschen

beeinträchtigt werden, in der Regel nicht zu zufriedenstellenden Ergebnissen. Dass die neu eingeführte Methode mit aktuellen Bildverarbeitungsansätzen konkurrieren kann, wurde mittels Anwendung auf Lebendzell-STED-Telomerdaten nachgewiesen.

Zusammenfassend demonstriert diese Dissertation den Stellenwert eines integrierten Ansatzes für STED-nanoskopische Studien. Eine koordinierte Vorgehensweise von der Probenvorbereitung über die Bildaufnahme bis zur Datenanalyse lieferte eine zuverlässige Grundlage, auf der in aktuellen Fragen der onkologischen Forschung aussagekräftige Rückschlüsse gezogen werden konnten. Diese Arbeit unterstreicht die Bedeutung einer iterativen Anpassung der einzelnen Schritte und motiviert gezielte Verbesserungsansätze, um die Signifikanz der Endergebnisse zu optimieren und die Leistungsfähigkeit von Lebendzell-STED-Bildgebung weiter zu steigern.

ACKNOWLEDGEMENTS

I am proud to present this work and grateful for the support and assistance that have carried me through my dissertation projects. First and foremost, I acknowledge Prof. Dr. Stefan W. Hell for offering me the opportunity to complete my PhD in his department `Optical Nanoscopy´ at the Max Planck Institute for Medical Research and for being my doctoral supervisor. Thank you for inspiring me on many different levels. I deeply appreciate your trust and the freedom you have granted me to pursue my scientific vision and to unite a PhD and a competitive dancing career.

I acknowledge Prof. Dr. Joachim Spatz for being my first supervisor, first examiner and part of my thesis advisory committee (TAC). Thank you for your creative contributions during our TAC meetings. Your ideas have encouraged me to consider my research from new perspectives and have stimulated valuable `out of the box´ approaches.

I acknowledge Prof. Dr. Karsten Rippe for being part of my thesis advisory committee and for closely collaborating on fascinating telomere research. Thank you for introducing me to the biological questions that have guided me through my PhD work. I am grateful for your scientific advice and for all our profound discussions shaping the project and kindling my motivation.

I acknowledge Prof. Dr. Klaus Kopka for being part of my thesis advisory committee and for extensively supporting two fruitful collaborations with his group. Thank you for your contagious enthusiasm towards these projects and for contributing with your expertise.

I acknowledge the Helmholtz International Graduate School for Cancer Research for financially supporting my PhD work through a stipend.

I acknowledge Dr. Ann-Christin Eder, previously Baranski for the close collaboration on the subcellular fate of novel prostate cancer-specific radiotracers. Thank you for introducing me to radiopharmaceutical research and for being scientifically creative with me. I am grateful for the focused and smooth exchange of expertise.

I acknowledge Dr. Inn Chung for the collaboration on telomere biology. Thank you for initially fueling the project and supporting me with excellent biological advice and helpful discussions.

I acknowledge Prof. Dr. Karl Rohr and Roman Spilger for the close collaboration on the analysis of telomere STED data. Thank you for implementing all my desired analysis strategies in code. Your contribution allowed for the extraction of quantitative conclusions.

I acknowledge Dr. Carsten Kramer for the close collaboration on the novel mitochondrial STED probe. Thank you for the short but intense project boosted by your remarkable scientific ambition and chemical expertise.

I acknowledge Dr. Jan Seikowski and Dr. Vladimir Belov for the dye conjugation of the PNA probes, Dr. Francesca Bottanelli for kindly providing the plasmid SNAP-CLC and Caroline Bauer for support with plasmid cloning.

My special gratitude goes to my colleagues and our group leader. Thank you for creating a pleasant workplace filled with a relaxed yet productive work atmosphere. I appreciate our team spirit and the

interdisciplinary exchange of knowledge that stimulates the conceptualization of innovative ideas. I enjoy being part of our vibrant group.

In particular, I acknowledge our group leader Dr. Johann Engelhardt for extensive support with optics and data analysis strategies. Thank you for your inexhaustible willingness to discuss all aspects of science. Your advice and serenity have guided me throughout my research.

I acknowledge Dr. Rifka Vlijm for profound support with Monte Carlo simulations generating synthetic telomere STED data. Thank you for sharing the last years with me, mentoring, inspiring and pushing me. I am deeply grateful for our numerous discussions and your critical and honest feedback on my research and beyond.

I acknowledge Dr. Mariano Bossi for support with spectroscopic analyses. Thank you for fascinating me even more for photophysics. Your pragmatic attitude has provided me with the necessary ease.

I acknowledge Dr. Elisa D'Este, Dr. Jade Cottam Jones and Dr. Steffen Sahl for valuable discussions on science and science-related topics. Thank you for sharing your expertise, scientific experience and personal opinion. I profoundly appreciate your steady and reliable support.

I acknowledge Dr. Alexey Butkevich and Dr. Vladimir Belov for generously providing live cell STED compatible organic dyes. Your dyes made the difference!

I acknowledge Jasmine Hubrich for extensive practical assistance in the lab. Thank you for establishing and maintaining a lab organization that enables an efficient research workflow. I am deeply grateful for your honest scientific and personal interest.

I acknowledge my former colleagues Dr. Janina Hanne, Dr. Jonas Marquard and Dr. Fabian Bergermann for introducing me to graduate student life. Thank you for giving me the easiest start possible into our group. I truly appreciate your company during our shared time.

My deepest gratitude goes to my friends, my brother, my partner and my parents for supporting me throughout my academic career. I am thankful for your encouragement, understanding, patience and love. Your confidence in my abilities has steadily pushed me forward. When necessary, you have provided a protected environment that has allowed me to focus all my time and energy into this work.

With love and gratitude, I dedicate this thesis to my parents.

TABLE OF CONTENTS

PREFACE

During the course of the 20th century, fluorescence microscopy has established itself as an essential method in life sciences. Its diverse implementations provide minimally invasive tools for three dimensional and real-time analysis of structures, processes and dynamics in living cells and organisms, with exceptionally high selectivity and sensitivity. Creativity in photophysics paired with profound knowledge in optics have joined in a universal concept for breaking the diffraction limit of far-field fluorescence microscopy [1].

Rapid technical developments during the turn of the century have led to a set of realizations that extend the field of application of far-field fluorescence microscopy from the sub-micrometer range down to even the single-digit nanometer regime [2-6]. At that time, alternative methods like electron microscopy (EM) or atomic force microscopy (AFM) had already provided resolutions in the single-nanometer digit range, but these techniques still lack the ease of specificity that fluorescence microscopy fundamentally offers. Moreover, convincing live cell EM studies remain to be reported and live cell AFM is limited to observations on the cell surface [7-11].

Similarly, two of the key players yielding the highest resolutions in the field of fluorescence nanoscopy – stimulated emission depletion microscopy (STED) [12] and stochastic optical reconstruction microscopy (STORM) [13] – were also limited to fixed samples for a long time. Since the major advantage of fluorescence microscopy in life sciences is its *in cellulo* and *in vivo* applicability, a strong demand for live cell compatibility of these two methods arose.

True live cell nanoscopy relies on a technique that combines high temporal resolution with physiological imaging conditions. The crucial point was the lack of adequate organic dyes providing the required photophysical properties while still maintaining cell membrane permeability. In the 1990s, the genetic fusion of the green fluorescent protein (GFP) [14] and its variants to proteins of interest had become the method of choice for live cell imaging [15-17]. And indeed, adaptations of both nanoscopy methods using fluorescent proteins (FPs) were realized.

Photoactivated localization microscopy (PALM) [18] – a STORM related single molecule localization microscopy (SMLM) technique – makes use of genetically encoded fusion constructs of photoconvertible or photoactivatable FPs, but suffers from lengthy acquisition times resulting in motion blur [6, 19]. Reversible saturable/switchable optical linear fluorescence transitions (RESOLFT) microscopy [20] – a STED-related deterministic, coordinate-targeted nanoscopy method – employs reversibly photoswitchable FPs, but its resolution does not meet that of STED or STORM.

Unfortunately, no member of the diverse GFP family [21, 22] truly fulfills the photophysical requirements for STED yet. Indeed, the technology of self-labeling protein tags like SNAP-tag [23, 24] and HaloTag [25] or small molecule binders such as jasplakinolide (F-actin) [26], taxol (polymerized tubulin) [27] or triphenylphosphane (mitochondria) [28] has already allowed live cell labeling. However, it was their combination with newly developed, STED compatible, non-toxic, cell membrane permeable carbopyronine and rhodamine dyes [29-33] that paved the way for proper multicolor live STED imaging. In principle, variants of these rhodamine dyes [34-36] also enable live cell STORM. However, there have only been a few proofs of concept since the imaging buffers required to

guarantee their photophysical properties are generally not live cell compatible and, additionally, data acquisition with STORM is rather slow [37-43].

The thesis presented here achieves live cell STED nanoscopy in two different fashions in the field of cancer research with direct and indirect clinical interest in close collaboration with the German Cancer Research Center (DKFZ) in Heidelberg (Germany) and the University Medical Center Freiburg (Germany).

PART I of this thesis provides the methodological foundation of common aspects shared by all projects included in this work. It covers theoretical basics and practical expertise of fluorescence nanoscopy and in particular of STED microscopy applications in the field of biomedical research. Furthermore, PART I includes common materials and methods that are relevant for all projects.

PART II presents work on human telomere conformations and their implication on genome integrity and telomere maintenance in cancer. Staining and imaging DNA (deoxyribonucleic acid) and associated proteins without affecting cellular health is not trivial. Together with the DKFZ Division of Chromatin Networks, we have developed a new robust staining protocol for novel live cell STED compatible dyes in the cell's most delicate environment – the nucleus. This protocol literally sheds light on living cells' telomeres – long established as the key to aging and cancer [44, 45]. This work deepens the fundamental understanding of their structure-function relationship in two different aspects.

As a first step and in combination with elaborate fixed staining methods, we have visualized human t-loop structures in intact cells for the first time. Biological controls and Monte Carlo simulations of synthetic STED data support the validity of the actual STED data and exclude false positive results through imaging and staining artefacts. In collaboration with the DKFZ Division of Biomedical Computer Vision, a neural network classification approach has been established to quantify t-loops and additional telomere conformations. In the second step, this project has characterized and quantified visual hallmarks of the rare telomere maintenance mechanism `alternative lengthening of telomeres´ (ALT) [46, 47]. It is the first to distinguish ALT-positive and ALT-negative cancer cell lines based on conformational differences in their telomere populations via a joint approach of STED nanoscopy and deep learning.

PART III reports work on the biological characterization of novel dual-modality radiotracers specifically targeting prostate cancer and is of direct clinical interest. Together with the DKFZ Division of Radiopharmaceutical Chemistry and the Department of Nuclear Medicine at the University Medical Center Freiburg, we have developed a set of innovative live cell staining protocols to investigate the subcellular fate of dual-labeled tracers for non-invasive diagnosis and fluorescence-guided surgery of prostate cancer. The bimodality allows the pre-surgical detection of lesions by positron emission tomography (PET) as well as the intraoperative distinction between tumor and healthy tissue during resection. For the detailed intracellular characterization, STED compatible derivatives of clinically relevant dual-labeled tracers [48] based on the PET tracer PSMA-11 [49] were synthesized and applied in combination with immunofluorescence staining of the targeted membrane protein. Even though staining with antibodies normally requires chemical fixation of cells, our newly developed antibody staining protocols have enabled the live investigation of antigen-tracer colocalization and substantiate clathrin-mediated uptake, lysosomal antigen recycling, antigen clustering and cytosolic tracer distribution in living cells. Along with complemental biodistribution and small-animal PET imaging

studies, the results provide valuable knowledge for the design and development of new diagnostic and therapeutic approaches for prostate cancer.

PART IV addresses different aspects of live cell STED nanoscopy and comprises various smaller projects, preliminary results and conceptual ideas directly relating to the challenges faced during live cell imaging. In collaboration with the DKFZ Division of Radiopharmaceutical Chemistry, we have introduced a novel live cell STED compatible mitochondrial probe based on the popular silicon rhodamine dye [30]. Together with the DKFZ Division of Biomedical Computer Vision, we have proposed a novel method for image restoration of noise-degraded images. This part finally presents a cytotoxicity study of recently published live cell STED compatible dyes that were applied in PART II [29, 32].

In conclusion, PART V emphasizes the common strengths and shared challenges of the different projects. It further encourages the imaging community to agree on a concordant handling of phototoxicity in live cell imaging. Taken together, this work demonstrates that live cell STED nanoscopy is feasible using state-of-the-art labeling and staining procedures spiced with scientific intuition and creativity. Combined in a coordinated workflow with sophisticated fixed and live cell sample preparation methods, elaborate imaging schemes, rigorous controls and extended data analysis, STED nanoscopy has provided valuable insights into two different areas of cancer research.

I – FOUNDATIONS:

FLUORESCENCE NANOSCOPY IN BIOLOGY

Which processes preserve the cell's homeostasis and how does a cell dynamically react to environmental cues disturbing this steady state? Life science research aims at answering these questions both on the molecular scale and inside living organisms. To comprehensively investigate these biological and biochemical processes, a multiparametric approach is required that addresses structural as well as spatio-temporal details. However, the relevant timescale and spatial scale span several orders of magnitude (Figure I-1) [50].

For example, conformational changes of and biochemical reactions within molecules occur in less than milliseconds [50]. Small molecules like adenosine triphosphate (ATP, radius approx. 0.7 nm) – the universal energy currency of life – diffuse through the cell's volume at millisecond timescales with cell volumes ranging from μm^3 for bacterial up to mm^3 for mammalian cells (BioNumbers ID (BNID) 106978, 105906, 114924) [51]. In comparison, the diffusion of clustered receptors in the cell membrane (thickness approx. 10 nm) is slowed down by one order of magnitude to less than 1 μm^2/sec (BNID 100787, 114189) [51]. The ribosome (diameter approx. 30 nm) synthesizes an average-sized, nascent protein in seconds, whereas complex multilayered cellular processes last from minutes to hours (BNID 100483, 113762) [50, 51]. For instance, eukaryotic deoxyribonucleic acid (DNA, diameter approx. 2 nm) is replicated with a speed of approximately 2-3 kb/min resulting in around 8 h of replication for the entire human genome (BNID 104136, 111770, 105243, 108484 – 108486, 113435) [51].

Within the diverse field of advanced imaging technologies, different methods are highly specialized in one or the other spatio-temporal direction. At the lower end of the spatial resolution spectrum, positron emission tomography (PET), magnetic resonance imaging (MRI) and optical coherence tomography (OCT) offer real-time, live imaging of intact organisms with resolutions in the mm to µm range [52-54]. At the upper end, electron microscopy (EM) [55] and scanning probe microscopy (SPM) resolve biological structures at near-atomic scale. However, EM imaging conditions are not compatible with any form of true live cell imaging. In contrast, SPM techniques like atomic force microscopy (AFM) [56, 57], scanning tunneling microscopy (STM) [58] or near-field scanning optical microscopy (NSOM)

[59, 60] offer millisecond temporal resolutions but with an inevitable, technological restriction to surface studies [61-63].

Fluorescence microscopy lies in the intermediate range of the spatio-temporal resolution spectrum uniting the experimental demands of life science research with the smallest tradeoffs. In combination with its target specificity, imaging flexibility and easy sample preparation techniques, far-field optical microscopy has for many years been the major contributor to microscopy-based investigations in this field. It allows the study of biomolecular interactions, structure-function relationships and complex, dynamic processes at the (sub)cellular level to connect molecular to cellular behavior and bridge the gap between genetics, developmental biology, biochemistry and pathology [64, 65].

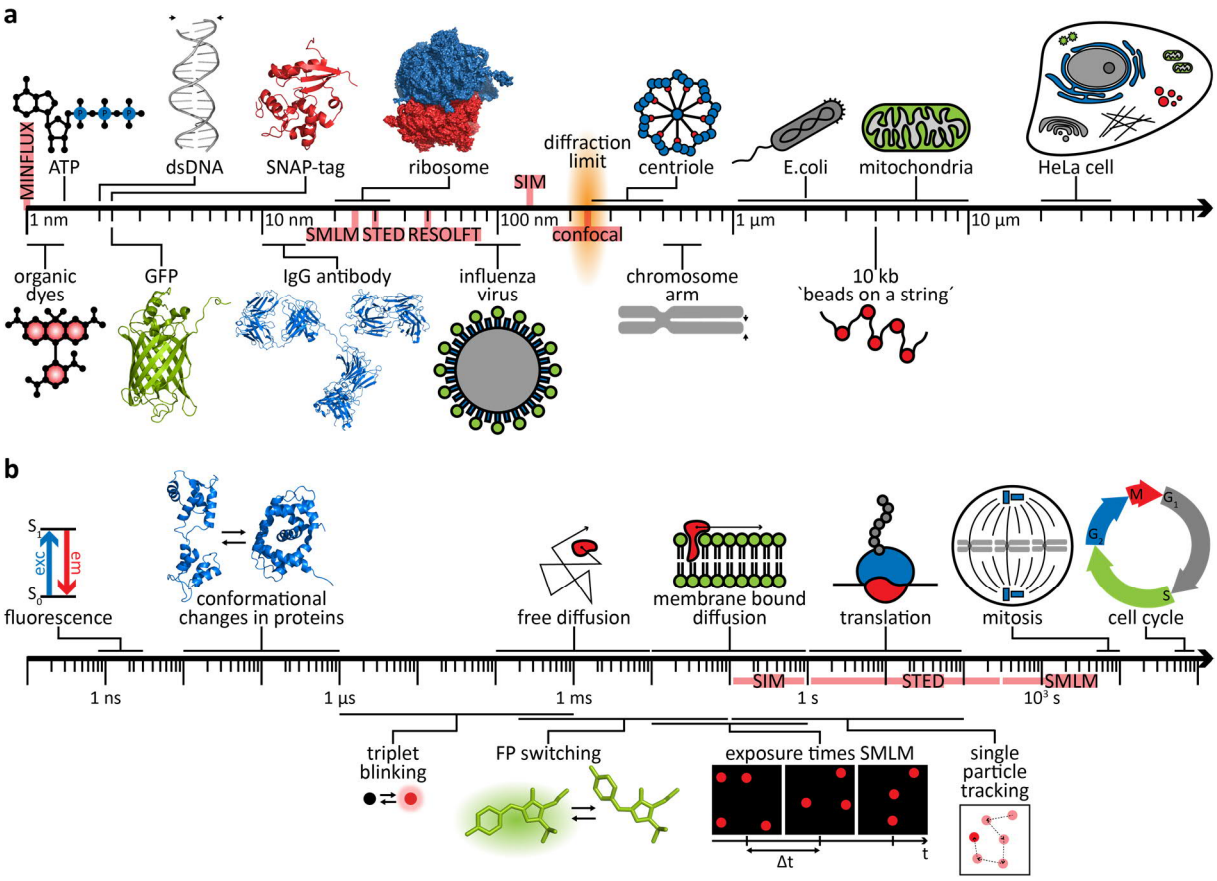

Figure I-1. The spatial and temporal scales of biology and selected fluorescence imaging modalities used in life sciences.

(**a**) Representative examples of biomolecules, macromolecular complexes and assemblies, cell organelles and cells sorted by their increasing dimensions. The routine effective resolution levels of important fluorescence microscopy and nanoscopy techniques obtained with biological samples are shown in red. (**b**) Representative examples of the kinetics of important biological processes and of photophysical, photochemical and technical processes involved in fluorescence microscopy imaging. The range of acquisition speeds of important fluorescence microscopy and nanoscopy techniques is given in red. The acquisition speed of confocal microscopy is comparable to that of STED nanoscopy. As point-scanning methods, the acquisition speed of confocal and STED imaging essentially depends on the size of the field of view. The acquisition speed of MINFLUX is comparable to that of SMLM. The crystal structures were obtained from the Protein Data Bank (PDB) [GFP 5DTY, GFP chromophore 5DTY and 5DTX, double-stranded DNA (dsDNA) 1W0U, SNAP-tag 3KZY, IgG antibody 1IGT, ribosome 2WDK and 2WDL, conformational change in calmodulin 1CFD and 1SY9]. For abbreviations, refer to Definition of Abbreviations.

Historically, insight has traditionally been gained through either ensemble measurements and end-point assays on whole cell populations or via *in vitro* interaction studies on purified proteins. Yet, the former approach veils heterogeneity, stochasticity and the complex single molecule behavior by providing only the sample mean; the latter strategy neglects most environmental and physiologically

relevant influences. Only native conditions ensure undisturbed processes are witnessed and hence biologically meaningful conclusions are inferred. By combining both, specific single molecule sensitivity and physiological experimental conditions, fluorescence microscopy has developed into one of the most powerful tools to study the individual molecular players involved in the processes of interest [2-6].

A picture is worth a thousand words. All imaging-based methods share the benefit of generating visual results qualifying them as rather intuitive techniques. Especially fluorescence microscopy – in its basic concept – is one of the most direct approaches, since the researcher sees what the researcher gets. Beyond pure visualization, various fluorescence methods also allow for quantitative measurements [66-72]. In both cases, selective labeling techniques for proteins, lipids and nucleic acids guarantee high biomolecular specificity during the imaging process. Major developments in the field of fluorescent labeling comprising both fluorophores and targeting strategies has strongly contributed and will continue to contribute strongly to the progress in fluorescence microscopy [64, 73-75].

On the other side of the coin is the necessity of controls proving that the structure or process of interest remains unaffected by the labeling procedure and by the label itself. With such proof, fluorescence microscopy shows high biological system compatibility enabling the least-invasive access to the interior of a cell, which is essentially transparent to light. Fluorescence provides contrast, single molecule sensitivity and selectivity, but is also a potential source of phototoxicity. If prevented, fluorescence microscopy allows the recording of four-dimensional (4D) data of living cells, tissues and even whole organisms in real-time with high spatial resolution covering a large field of view (FOV) over a long period of time. However, all these parameters are interdependent and tweaking one to the extreme is only possible at the expense of all the others. While most of these parameters are technically limited, the spatial resolution barrier was assumed to be fundamental for many years.

I.1 SURVEY OF THE FIELD

I.1.1 Spatial Resolution and Diffraction in Optical Imaging

Commonly, fluorescence microscopy operates in the far-field and uses lenses to discriminate features by focusing light. Hence, its resolution is determined by the focusing strength of the optics and governed by diffraction due to the wave nature of electromagnetic radiation. Even with optimal focusing of an infinitely small point-like light source through a lens, constructive interference of light waves in one defined spot in space creates a finite-sized intensity pattern $I(x, y, z)$ in the image plane, referred to as the point spread function (PSF). The PSF is the fundamental unit in the image formation process and its full width half maximum (FWHM) defines the microscope's resolution in real space. The final image is a convolution of the real image and the PSF of the system. The PSF's Fourier transform is the optical transfer function (OTF) specifying the spatial frequencies contained in the final image.

As early as 1835, Airy explained the blurring effect of diffraction on images of point like structures [76]. His description of the main interference maximum (Airy disk) and its surrounding higher-order diffraction rings (Airy pattern) allows for an intuitive formulation of the Rayleigh criterion for resolution stated by Lord Rayleigh in 1874. The criterion is met as soon as the main lobe maximum of the intensity

pattern of one point source coincides with the first minimum of the intensity pattern of a second point source (Figure I-2) [77]. However, Abbe in 1873 [78] and Helmholtz in 1874 [79] were the first to explicitly connect diffraction with resolution in lens-based optical microscopy. Their theoretical analyses led to the classical resolution limit

in lateral dimension $$\Delta r = \frac{\lambda}{2n \sin \alpha} \quad \textbf{(I-1)}$$

in axial dimension $$\Delta z = \frac{2\lambda}{n^2 \sin^2 \alpha} \quad \textbf{(I-2)}$$

with Δr being the lateral resolution, Δz the axial resolution, λ the wavelength of light, $NA = n \sin \alpha$ the numerical aperture comprising n the refractive index of the medium the objective is working in and α the one-half angular aperture of the objective.

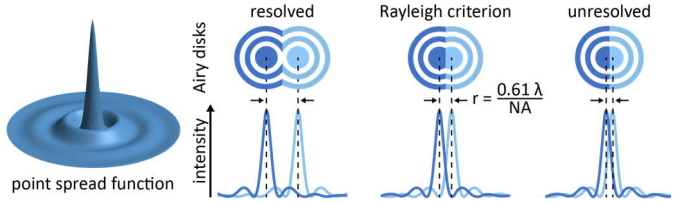

Figure I-2. Illustration of the Rayleigh criterion.

According to Rayleigh, two closely spaced point sources can be resolved if their Airy disks are separated by more than the distance at which the principal maximum of one Airy disk coincides with the first minimum of the second Airy disk.

For more than a century, science was stuck considering the resolution barrier imposed by diffraction as impenetrable. Obtaining a spatial resolution in the nanometer range was thought to be impossible because the resolution barrier was only seen from the perspective of the microscope's limited passband of spatial frequencies. According to general conviction, lens-based optical microscopy had fundamentally reached its limit with resolutions of approximately 200 nm laterally and approximately 500 nm axially [80].

At first glance, near-field optics seemed to be the only way to circumvent the diffraction limit because it avoids conventional lenses and thereby free wave propagation by mechanically confining the excitation spot. In near-field scanning optical microscopy (NSOM), the light is focused to the subwavelength sized aperture of a sharp tip creating a near-field spot with a size on the order of the tip, which is scanned over the sample. Hence, NSOM is limited to the surface of cells and to structures directly underneath the cell membrane [60, 81-85].

However, to keep its advantage of being minimally invasive while providing access to the entire cell, fluorescence microscopy must be applied in the far-field. Thus, attempts to modify the focal spot size in far-field optics started in the mid-20th century with concepts such as confocal [86-88] and nonlinear approaches like multiphoton microscopy [89, 90]. In the 1990s, various elaborate techniques pushed the resolution to the very limits of optics by perfecting focusing, complex imaging schemes and post-processing. 4Pi [12, 91, 92] and I^{5}M [93-95] microscopy improve the axial resolution three to seven-fold. Both techniques expand the illumination and/or detection wave front by increasing the aperture angle of the system α through the usage of two objectives for the respective light path: the more spherical the wave front, the more isotropic the resolution. Classical, interference-based, linear structured illumination microscopy (SIM) in two and three dimensions (2D and 3D) improves the lateral and axial resolution two-fold. Widefield illumination with a sinusoidally modulated pattern that is

shifted or rotated several times during image acquisition generates Moiré fringes. This extends the observable region in reciprocal (frequency) space making high spatial frequencies accessible, which – via Fourier transformation – increases the resolution in real space [59, 96-101]. Through the use of multi-pixel detectors, SIM (single or multiple) point-scanning approaches avoid the loss of high frequency information, which in classical confocal systems are rejected at the pinhole [102-106]. However, post-processing always bears the danger of potential artefacts [107-116].

I.1.2 Fluorescence Nanoscopy

To truly cross the diffraction barrier in far-field fluorescence microscopy, a paradigm shift towards an alternative perspective was necessary. The key was the reformulation of the resolution problem knowing full well that the physical phenomenon of diffraction will always hold true. It cannot be eliminated *per se* and governs both excitation and detection. Instead, it is rather the quasi-simultaneous emission of all emitters that are collectively excited by the excitation PSF $I_{exc}(x, y, z)$ – be it widefield or confocal – that renders the separation of individual fluorophores virtually impossible (Figure I-3). Analogously to the illumination, the propagation of emitted photons is governed by a similar function $I_{em}(x, y, z)$, veiling the exact coordinate of the respective emitter of individual photons, irrespective of detection by a camera (widefield) or by a point detector (beam-scanning system). As a consequence, all fluorophores in closer proximity than the diffraction limit are not separable.

Figure I-3. Essence of the resolution problem in fluorescence microscopy.

In classical diffraction-limited fluorescence microcopy, the fluorophores are collectively excited and emit quasi-simultaneously. Thus, emitters spaced by less than the diffraction limit cannot be individually distinguished.

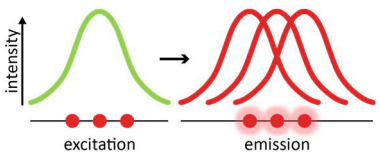

It is not diffraction itself that has to be challenged, but rather discrimination of individual markers within a densely packed accumulation smaller than $\lambda/2NA$. If these markers differ spectrally, single fluorophore separation is easily realized by the implementation of different filters [117-119]. Thus, the key to success is confinement of molecular states rather than confinement of light.

All nanoscopy methods transiently prepare neighboring fluorescent markers in different photophysical states rendering them discernable. Usually, transitions between a signal-giving, fluorescent ON state (A) and a dark, non-fluorescent OFF state (B) are exploited to make them emit time-sequentially from areas that are much smaller than the diffraction limit [120, 121]. None of these states necessarily need to be fluorescent [122]. A series of different photophysical states qualify for the implementation of this focal ON-OFF switch. However, the shorter the lifetimes of these states are, the harder the readout becomes. Virtual states are the extreme example; their transient nature makes them essentially non-observable [1, 123, 124].

Introducing a focal switch neutralizes the limiting effect of diffraction. The determination of the molecular coordinate with arbitrary precision is not hindered if the next emitters reside at a distance

larger than $\lambda/2NA$ [125, 126]. Although this concept in no way refutes the physics work of the 19th century, the vision of diffraction-unlimited fluorescence imaging was confronted with a lot of skepticism in the beginning. Teaming up of chemistry and optics has proven to be the solution to the diffraction problem in far-field fluorescence microscopy. Fluorescent markers are no longer seen as simple reporters for image generation, but as active components in image formation [1, 127].

With the advent and evolution of fluorescence nanoscopy, scientific research has gained access to new fields in biology, chemistry, (bio)physical and (bio)medical research. The new level of unprecedented detail is literally changing views in cellular and molecular biology. Finally, mapping the spatial organization and the interactions of all molecules in a cell becomes possible. While being one of the most momentous developments in these fields nowadays, fluorescence nanoscopy also introduces new challenges. However, due to their non-fundamental nature and to the fast pace of progress, none of these problems are expected to persist.

The challenges faced are not only technical but multi-faceted, involving specimen characteristics, dye choice, labeling method, sample preparation, imaging conditions, aberration correction, post-processing and data analysis. Considering these issues thoroughly is more critical with fluorescence nanoscopy than with diffraction-limited fluorescence microscopy, since potential artefacts are more easily exposed by the increased sensitivity and resolution. Whereas certain fixation artefacts might be hidden by diffraction blur in conventional fluorescence microscopy, they are disclosed at nanoscopic resolutions [128]. Parameters like spatial resolution, temporal resolution, signal-to-noise ratio (SNR), FOV, observation time and cell viability are interdependent and competing (Figure I-4).

While high irradiation intensities are likely to compromise cell health during live cell imaging, they are commonly required for high spatial resolutions. Spatial resolution in general is limited by the photostability of the dye. The photostability of the dye also sets an upper bound for following individual molecules over a certain period, whereas the photon flux of the dye sets a lower bound on the observation of molecular dynamics. It affects minimum exposure times and scanning speed, thus limiting the observation rate.

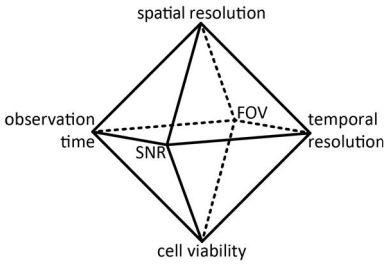

Figure I-4. Interdependent imaging parameters of fluorescence microcopy.

Extension of the `triangle/pyramid of frustration´ commonly encountered in live cell fluorescence imaging. The effective image resolution, the temporal resolution, the observation time, the SNR, the FOV and the sample health are interdependent. No single parameter can be changed without affecting the others. For live cell imaging, cell viability should be awarded the highest priority but is clearly irrelevant in fixed cell imaging.

The acquisition speed differs amongst the various nanoscopy methods and applications, but they are all *per se* slower than regular epifluorescence microscopy due to the time-sequential readout of the diffraction-limited zone. To avoid motion blur during live cell imaging, the time to acquire an image must be faster than the time in which the structure of interest moves one measure of resolution [129]. Just as the temporal resolution is subjected to the Nyquist-Shannon sampling theorem [130, 131], so is the spatial resolution of an image. Consequently, the image resolution cannot be better than double

the distance between neighboring emitters [132-134]. Thus, a high labeling density is very important to infer the true topological structure of the target and it is essential for quantitative imaging. In this context, it is important to point out that the resolving power of the imaging technique itself, the resolution in its true optical meaning, is independent of the fluorescence labeling (refer to also I.1.6.2). To distinguish thoroughly in the following, the term `image resolution´ is used when describing the effective resolution obtained in the final fluorescence image; the term `biological resolution´ is used when discussing the effects of labeling on the effective image resolution.

The label itself can hamper complete labeling due to steric hindrance. In contrast to diffraction-limited approaches, the label size participates significantly in fluorescence nanoscopy. Conventional fluorescence microscopy only knows sterical problems concerning protein folding and interactions with genetic labels. Fluorescence nanoscopy, however, is also confronted with a `steric resolution limit´, since its spatial resolution lies in the range of conventional label sizes. Depending on the labeling method, the fluorophore is placed at a certain distance to its target. Nanoscopic imaging records the position of the emitter, which is in no case identical with the position of the molecule of interest. The more precise the determination of the emitter's coordinates and the larger the label size, the greater the recorded mismatch to the coordinates of the target of interest [135]. Thus, progress in (bio)chemistry is desperately desired to live up to the current state in optics.

I.1.2.1 Coordinate-Targeted Approach

The field of fluorescence nanoscopy, in the literature also commonly referred to as super-resolution microscopy, distinguishes two main approaches, albeit conceptually identical, to truly cross the diffraction limit. They differ in the nature of emitter readout being either deterministic or stochastic.

The deterministic, coordinate-targeted approach is generalized under the acronym RESOLFT (reversible saturable/switchable optical linear (fluorescence) transitions). It pools various techniques that exploit reversible, saturable or photoswitchable transitions A↔B (Figure I-5a) [123]. All of them are based on point-scanning acquisition and confocal detection targeting defined positions r_i in space. By initiating the transition A→B, the population of A (e.g. emissive state) is prevented everywhere in the sample except for one (several) particular spot(s) of sub-diffraction size at the coordinate(s) r_i. The forced transition to B is applied via a light-intensity distribution $I(r,t)$ providing ideally an intensity zero (or several up to many) around r_i where no switching happens, leaving the fluorophores in their initial state A at $r_i \pm \Delta r/2$ with $\Delta r \ll \lambda/2NA$. Signal (e.g. fluorescence) is only detected from this (these) specific region(s) (Figure I-5b). The saturation intensity $I_s(r,t)$ sets a certain threshold for outperforming all competing A→B transitions (e.g. spontaneous fluorescence) everywhere except at r_i. Scanning of r_i across the sample sequentially detects neighboring features and determines their coordinates through the position of the zero.

Without the need for post-processing, a super-resolved image is created with the lateral resolution Δr

$$\Delta r \approx \frac{\lambda}{2n \sin\alpha \sqrt{1 + b\frac{I}{I_s}}} \qquad \textbf{(I-3)}$$

with the factor $b > 0$ determining the actual shape of the zero (e.g. zero spot, zero line) [136]. In either case, the intensity distribution around the zero r_i can be parabolically approximated leading to the square root factor in the denominator of equation (I-3).

To double the resolution, $I(r,t)$ must be quadrupled. Routinely, the RESOLFT approach reaches effective lateral image resolutions between 20 to 50 nm in biological samples [137-147]. Practically limiting is the SNR [148], but in ideal cases and under certain conditions, lateral resolutions of $\Delta r < 10$ nm can be achieved [149, 150]. Additional improvement of Δz is possible in selected 3D implementations (for further details, refer to I.1.3).

The RESOLFT approach is an ensemble-based imaging scheme and thus relies on state population probabilities. In the majority of biological samples, more than one emitter resides within Δr. Hence, several fluorophores are recorded simultaneously. By varying $I(r,t)$, the resolution Δr and therefore the number of emitters within the intensity zero can be tuned to the biological question of interest. In principle, strongly increasing $I(r,t)$ should eventually lead to a single molecule within the zero. Theoretically, infinite resolution is attainable with $I \gg I_s$ and thus $I/I_s \to \infty$ expanding the OTF with an infinite frequency passband [12, 120, 123, 143]. Assuming this extreme, the orbitals of a single molecule within the zero will experience different strengths of the electric field. Therefore, the photophysical transition becomes a function of the orbital structure and the dipole approximation will no longer hold. Consequently, the spatial distribution of intensity cannot be ignored with respect to the molecules' size [127].

The first theoretical RESOLFT proposal introduced the game changing rationale of diffraction-unlimited microscopy in the form of stimulated emission depletion (STED) nanoscopy in 1994 [12, 137, 141, 151, 152]. Only five years later, STED was practically demonstrated for the first time [153]. It was followed by ground state depletion (GSD) nanoscopy, theoretically introduced in 1995 [154] and technically realized in 2007 [142]. While STED involves the electronic ground state S_0 (B) and the first electronically excited state S_1 (A) (refer to I.1.3), GSD exploits the metastable, dark triplet state T_1 (B) as counterpart to the singlet system (S_0/S_1) (A). Since $I_s(r,t)$ scales inversely with the lifetimes of the involved states, the intensity $I(r,t)$ used in GSD to operate the focal switch is markedly lower (~100 kW/cm^2 *vs.* ~10 MW/cm^2) [1].

Introduced at the beginning of this century, saturated patterned excitation microscopy (SPEM) [155] and saturated structured illumination microscopy (SSIM) [144] parallelize the RESOLFT principle in one possible implementation. As nonlinear variants of SIM, the techniques use saturated excitation to deplete S_0 (A) and populate S_1 (B). This inverse RESOLFT scheme records `negative data´ exemplifying that the ON state does not necessarily need to be a fluorescent one as the coordinates are defined solely by the zero position.

Around the same time, RESOLFT nanoscopy based on photochromism was theoretically proposed [121]. Photoswitchable fluorescent proteins (psFPs) [20, 120, 121, 123, 145, 147] or photoswitchable organic dyes [146, 156] offer metastable fluorescent and non-fluorescent states that differ in their molecular configuration (e.g. *cis-trans* isomerization). Optical transitions in these bistable molecular systems demand dramatically lower switching intensities $I(r,t)$ (~10 W/cm^2) compared to STED due to the longevity of the involved states [121, 123].

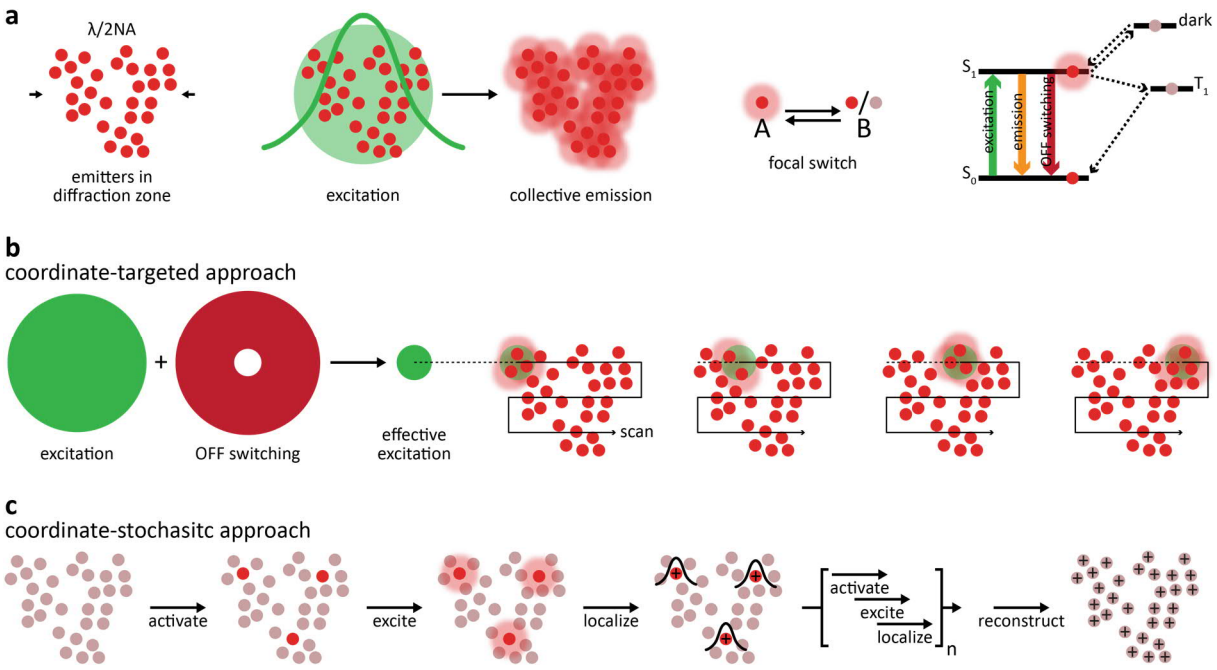

Figure I-5. Data acquisition schemes of the coordinate-targeted and coordinate-stochastic nanoscopy approaches.

(**a**) All emitters residing within a diffraction-limited spot are simultaneously excited by a regularly focused excitation beam and thus emit collectively. The implementation of a focal switch that exploits a photophysical transition between A (ON state) and B (OFF state) allows distinguishing of subsets of/individual emitters within the collective by time-sequential readout. (**b**) In the coordinate-targeted approach, the initially established state A (e.g. emissive state) is prevented everywhere in the sample except for the intensity zero position(s) of the light intensity distribution that initiates the transition A→B. Thereby, the presence of A is restricted to one (several) subdiffraction-sized spot(s) (e.g. effective excitation). Time-sequential readout is realized by deliberately scanning the intensity zero position(s) across the sample. (**c**) In the coordinate-stochastic approach, time-sequential readout is achieved by preventing the presence of A (emissive state) everywhere except from single emitters stochastically distributed in the sample (separated by at least one unit of diffraction limit $\lambda/2NA$). The emitters are localized with sub-diffraction accuracy by centroid fitting of their individual photon distributions. The repetition of the imaging scheme allows finally for the reconstruction of the super-resolved image.

I.1.2.2 Coordinate-Stochastic Approach

The stochastic approach, generally referred to as single molecule localization microscopy (SMLM), differs from the RESOLFT approach not by concept but only by implementation. Likewise, it exploits the transition between two distinct photophysical states and uses photon distributions to infer precisely the molecules' positions in space. In RESOLFT, the coordinate information is defined by the intensity pattern of the depletion beam, whereas, in SMLM, this information derives from the PSF of a single molecule. A priori dealing with single molecules is the main advantage of SMLM compared to the ensemble based RESOLFT approach. Yet, in both cases, the number of photons matters. RESOLFT builds on a sufficient number of photons provided by the depletion laser, whereas SMLM relies on a sufficient number of photons obtained from each single emitter. In the latter case, dye stability and photobleaching limit the number of photons whereas for RESOLFT, the laser supplies a virtually infinite number of photons directly injecting the coordinates into the system.

The SMLM approach prevents the occupation of a certain photophysical state A (emissive state) everywhere except for single emitters stochastically distributed in the sample and separated by at least one unit of diffraction limit. Thus, their signals are recorded as distinct diffraction spots on a camera.

During the acquisition of one frame, the molecules are repeatedly excited (A→A*) providing N detected photons per single diffraction-limited fluorescence spot. These data allow the emitters' localization with sub-diffraction accuracy by centroid fitting providing their positions with precision σ in coordinate space [118, 125, 126]. Switching the registered molecules to their OFF state enables the repetition of the imaging procedure and reconstruction finally yields the super-resolved image (Figure I-5c). Since all molecules are originally in their OFF state B, no initial OFF switching event is needed and one single switching cycle B→A→B' per emitter is commonly enough. The probability for ON switching must correlate inversely with the fluorophore density to avoid ON switching of two molecules within a diffraction-limited spot [18].

The number of collected photons N per ON switching event strongly governs the precision of localization σ and therefore the spatial resolution Δr. Neglecting background, Δr is given by:

$$\Delta r \approx \frac{\lambda}{2n \sin \alpha \sqrt{N}} \qquad \textbf{(I-4)}$$

However, the switching properties and the orientation of the fluorophore's dipole also directly affect the spatial resolution attained [39, 40, 157]. As events with poor photon output are excluded from the image formation process, this post-processing procedure additionally influences Δr. Routinely, SMLM reaches an effective lateral image resolution of ~20 nm in biological samples [18, 158, 159]. Under optimized conditions, lateral resolutions $\Delta r < 10$ nm can be obtained [160].

As a widefield technique, its SNR benefits from total internal reflection fluorescence (TIRF) [161] or highly inclined and laminated optical sheet (HILO) illumination [162]. However, the out-of-focus blur can be exploited to extend SMLM imaging to 3D introducing astigmatic [163] or helical [164] optical distortions or bi-plane detection [165]. For both 2D and 3D SMLM imaging, data collection and image assembly are more challenging than technical implementation [166]. Complex post-processing is necessary and is always accompanied by the danger of introducing artefacts due to false localizations [167].

How to precisely determine single molecule coordinates has already been known for many decades [125, 126]. Yet, it was no earlier than 1995 that single molecule localization has been suggested to provide nanoscale resolution in combination with sequential readout through photoswitching [118] and to enable theoretically `infinite´ resolution with $N \rightarrow \infty$ [168].

The first demonstrations of the SMLM approach were realized in 2006. (Fluorescence) photoactivated localization microscopy ((F)PALM) traditionally employs photoactivatable or photoconvertible fluorescent proteins (paFPs, pcFPs) [18, 169], but photoactivatable organic dyes are equally applicable [159, 170]. In both cases, OFF switching after emitter detection is done by deliberate photobleaching (B'≠B). Stochastic optical reconstruction microscopy (STORM) [13, 158] traditionally uses tandem dye pairs with an activator dye reversibly enhancing the activation rate of a reporter dye, a photoswitchable organic fluorophore [171]. In contrast to (F)PALM, the OFF state of the reporter is identical to its initial state (B' = B).

Nowadays, most SMLM applications exploit the blinking of fluorophores under illumination with excitation light in well-defined redox buffer conditions. Although all fluorophores blink, not all fluorophores are suitable for these SMLM techniques as certain switching kinetics are required [172].

In ground state depletion with individual molecular return (GSDIM) [173-175], also called direct STORM (dSTORM) [176], the electronic ground state S_0 (A) is depleted and all molecules are forced into long-lived triplet or radical states (B). Spontaneous return (B→A) either happens with back-pumping in dSTORM or without optical activation in GSDIM.

Transient stochastic ON switching can also be implemented via specific molecular interactions as realized in point accumulation for imaging in nanoscale topography (PAINT) [177] and its variants [178-182] or in (fluctuation-assisted) binding-activated localization microscopy ((f)BALM) [183, 184]. The reversible binding to the structure of interest equals the ON state while the unbound population constitutes the OFF state.

I.1.2.3 Pooling Forces

Pioneering, launching and driving the `super-resolution revolution´ was recognized with the Nobel Prize in chemistry in 2014. Yet, that is not the end of the story. Both approaches, coordinate-targeted and stochastic, have substantially crossed the diffraction-barrier but "there's [still] plenty of room at the bottom" [185]. Smartly combining their advantages in a new concept will eventually push the resolution to its ultimate extreme. Single molecule localization with minimal emission fluxes (MINFLUX) elegantly circumvents the limitations enforced by the finite photon budget. It alleviates the photon demand on both, the excitation (high in RESOLFT) and the detection side (high in SMLM). Conceptually different from the established approaches and without any constraints on wavelength or NA, MINFLUX probes the emitters with an excitation light intensity minimum after stochastic ON-OFF switching instead of reading out the fluorophores' information via high light intensities [186-188].

As the `super-resolution revolution´ progresses, various creative combinations of the methods pushing and crossing the diffraction limit have been developed (e.g. PA NL-SIM, ExSTED, ROSE, …) [140, 189-209]. Fusing these methods bundles the individual strengths of each but indeed also compounds complexity and accumulates the individual disadvantages. These hybrid techniques focus on one (or a few) of the crucial imaging parameters namely spatial resolution, temporal resolution, SNR, FOV, 3D imaging, observation time and cell viability.

Every technique – classic or hybrid – has its own niche due to an individual combination of advantages and disadvantages. The biological question of interest should guide the choice of method. Although, fluorescence nanoscopy is still young and rapidly evolving, it has already had a prominent impact in life sciences. Serving the tools to unravel long-standing secrets, fluorescence nanoscopy can revisit and refine existing biological models that are either incomplete or simplified due to the limited resolution at the time of data acquisition [6]. Motivations in method development drastically diverge, but the ultimate goal is the combination of quantitative multicolor imaging at the single molecule level in tissues and whole organisms in real-time to enable the dynamic mapping of true molecular colocalization patterns. As instrumentation, sample preparation and fluorophore properties are equally critical, fluorescence nanoscopy continues to benefit from both technical and (bio)chemical advancements [2].

I.1.3 STED Nanoscopy

It was not much more than 20 years ago that the principle of STED nanoscopy was proposed and still less than 20 years ago that it was realized. Yet, already more than 600 publications deal with the technique in one fashion or another. More than 90% of these studies have been published in the last ten years, but only approximately 15% involve live cell STED imaging. A combination of complexity and high cost of the first implementations, along with skepticism regarding long-term live cell imaging, due to the high laser intensities potentially photodamaging the sample, slowed down the broad adoption in the beginning [210, 211].

I.1.3.1 Photophysics

STED nanoscopy was the first modality of the RESOLFT approach to be proposed and realized (for details on the basic RESOLFT principle, refer to I.1.2.1). Its focal switch exploits the transition between S_1 (A) and S_0 (B) induced via stimulated emission. During stimulated emission an incoming photon matching the emitters emission spectrum forces an electronically excited energy state (here S_1) to de-excite (basically) instantaneously via the emission of a second photon having the same phase, frequency, polarization and direction as the stimulating photon. In contrast, spontaneous emission occurs stochastically during the lifetime of the excited state (here S_1). The emitted photon has a random phase and is angularly distributed according to the dipole radiation pattern. One of the key strengths of STED nanoscopy is the universality of its focal switch. In contrast to other nanoscopy methods requiring designated emitters, STED imaging works in principle with any fluorescent molecule.

In a standard 2D STED implementation as illustrated in Figure I-6, the excitation beam is Gaussian-shaped and overlaid with the red-shifted, donut-shaped STED beam confining the effective excitation and its spontaneous emission to the intensity zero of the donut. Shaping of the still diffraction-limited STED beam is achieved either by phase and/or by polarization engineering. For lateral resolution enhancements, vortex phase plates are mostly used. Axial resolution enhancements are generally attained via annular phase plates. Their combination enables 3D STED. Other beam shaping options include segmented wave plates and liquid crystal spatial light modulators (SLM). The narrow spectral band width of the STED laser ensures a high quality intensity zero [211], but aberrations potentially fill up the donut's center impairing the attainable resolution. For a resolution < 30 nm, the intensity zero must be < 2% of the STED laser intensity I at the donut crest.

The wavelength of the STED beam lies in the far-red part of the fluorophore's emission spectrum and represents a compromise between the cross section σ_{STED} for stimulated emission from S_1 to S_0 being as large as possible and the probability of re-excitation from S_0 to S_1 being as low as possible. As all photons coming from stimulated emission and from the STED beam have the same wavelength, they can be filtered out efficiently before detection. For an actual resolution improvement, the STED rate must outperform the spontaneous emission rate from S_1 with $k_{fl} \approx 10^9\,s^{-1}$. This narrow temporal window in combination with small optical cross sections for STED in the range of $\sigma_{STED} \approx 10^{-17}\,cm^2$ require high STED laser intensities as $I_s \equiv k_{fl}\sigma_{STED}{}^{-1}$. The saturation intensity I_s typically ranges

between 1-10 MW/cm^2. The depletion probability scales with $e^{-(I/I_S)}$ and the STED laser intensity I is chosen such that the transition is saturated, establishing a nonlinear dependence on the number of STED photons ($I > 5I_S$ guarantees a depletion probability of > 99%).

In contrast, SMLM does not display nonlinearity in switching as saturating conditions are strictly avoided, but a nonlinear dependence is generated in the emitted fluorescence intensity, as events with too few detected photons are discarded [127]. Thus, the final SMLM image nonlinearly represents the fluorescence emission being rather pointillistic [212, 213] and background free. In contrast, STED imaging always produces a linear representation of the fluorescence emission.

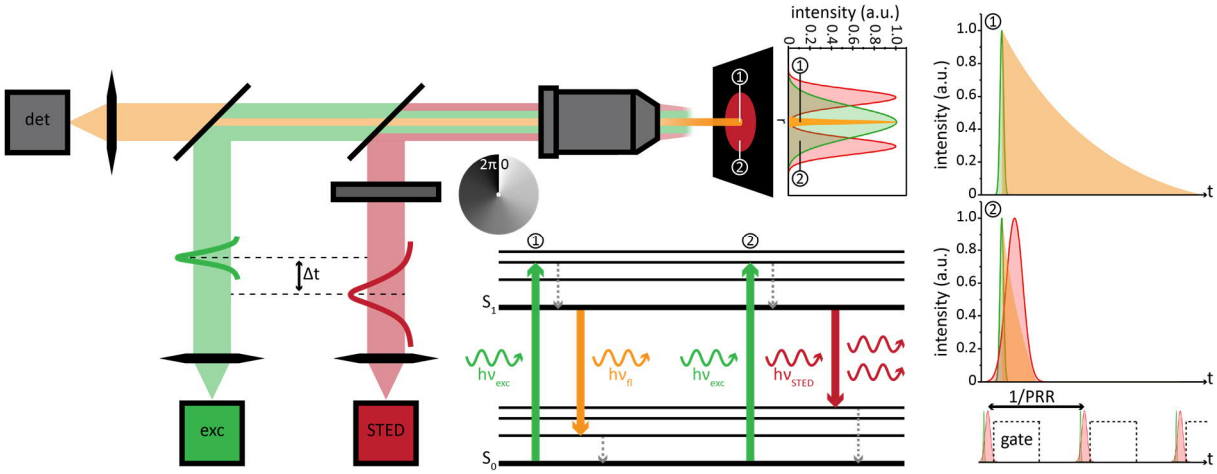

Figure I-6. Schematic illustration of STED nanoscopy and its photophysical foundation.

In the basic 2D implementation of pulsed STED nanoscopy, a regularly focused excitation beam (exc, green) is overlaid with a donut-shaped STED beam (red) featuring a short delay time (Δt). A beam shaping device (e.g. vortex phase plate) in the STED beam path introduces the donut-profile. The STED beam confines the area from which spontaneous emission (orange, ①) is allowed to sub-diffraction dimensions by quenching all excited molecules at the periphery of the excitation spot via stimulated depletion (②). The STED laser delay allows excitation and vibrational relaxation to be completed before STED photons hit the fluorophores while being in the lowest vibrational state of S_1. By opening the detection gate with an additional time delay, early spontaneous emission from the periphery of the excitation spot is discarded. By closing the detection gate after the fluorescence decay, unspecific background signal is reduced. The inverse of the pulse repetition rate (PRR) represents the temporal pulse spacing (bottom right).

As any electronic transition is always a function of its corresponding dipole moment, the emission of every fluorophore depends on its orientation. While freely rotating molecules average out any orientation dependence, both excitation and stimulated emission rates of rotation-hampered fluorophores show a dependence on the direction of the electric field of the lasers. Thus, STED commonly uses circularly polarized light to even out excitation and depletion selection [143]. In any case, potential emission shifts of single fluorophores do not alter the detected position as its coordinates are injected by the STED laser itself. In contrast, SMLM is more prone to potential artefacts originating from the fluorophore's dipole orientation and its localization accuracy is directly affected [214].

In theory, the spatial resolution of STED nanoscopy is unlimited (refer to equation (I-3)). However, with increasing resolution, contrast usually deteriorates. At some point, the signal drowns in noise as the increasingly smaller focal volume contains fewer fluorophores. Sources of noise include autofluorescence of the sample, scattering of laser light, background fluorescence from unspecific labeling and Poisson noise (refer to IV.4) [215]. As an ensemble method, STED does not depend on the

photon flux from single molecules as SMLM methods do [216]. Instead, the emitted photons of all molecules residing within the intensity zero determine the pixel brightness at r_i. However, only a few photons above the noise need to be detected per pixel/voxel.

In SMLM one switching cycle (B→A→B') per molecule is in principle sufficient and theoretically, all emitted photons contribute to image formation. In STED, each fluorophore is switched several times while the intensity zero is scanned over the sample and most of the emitted photons are discarded as they come from stimulated emission. Every emitter cycles only a finite number of times before it irreversibly bleaches, constituting the vulnerable point of STED (refer to I.1.4). However, one of the key strengths of STED nanoscopy is its free choice of depletion intensity, which allows tuning of the spatial resolution to counteract signal loss from photobleaching. By balancing the resolution, STED can be individually adapted to each respective biological question.

STED imaging permits the visualization of cellular structures with an effective image resolution of down to 20 nm [137, 141], opening up avenues for new biological discoveries [152, 202, 217-223]. Even single digit nanometer resolution has been achieved by imaging nitrogen vacancy (NV) centers in diamonds [150, 224, 225]. While these exotic emitters are not only extremely photostable with essentially no photobleaching or dark state transitions, they are also biocompatible [226, 227] and internalized by cells [228-231]. However, the lack of biochemical surface modifications for specific targeting, size and heterogeneity still hamper routine fluorescence imaging application [232]. Yet, STED nanoscopy is also employed outside of biology in nanoscale imaging of inanimate material [233-236] or in solid state physics [237].

I.1.3.2 Technical Implementation

In general, synchronized pulsed excitation and pulsed STED lasers with high repetition rates and narrow STED pulse widths guarantee fast image acquisition and high depletion efficiencies [238]. Yet, the exact timing of the lasers is crucial to optimize the efficiency of stimulated emission and to minimize unwanted influences due to polarization effects, jitters in the timing of the laser pulses, multiphoton processes, nonlinear photobleaching (refer to I.1.4.1 and I.1.4.3) and direct excitation by the STED beam [239]. The bottom line is that the fluorophores' photophysics determine the choice of STED laser and how to operate it.

Depletion is most efficient if the STED pulse hits the fluorophores shortly after excitation and vibrational relaxation within S_1. The delay (approx. a few tens of picoseconds) is necessary due to the width of the excitation pulse and the vibrational lifetime ($k_{IC} \sim 10^{12}$ s^{-1}). STED pulses arriving too early waste STED photons as excitation and/or vibrational relaxation are still ongoing rendering only a fraction of fluorophores susceptible to depletion. STED pulses arriving too late do not entirely suppress spontaneous emission from the periphery, thereby reducing the SNR. Pulse durations must fall in the time frame between vibrational relaxation and spontaneous emission. Pulses shorter than the vibrational lifetime do not deplete efficiently as a fraction of fluorophores has either not vibrationally relaxed yet or already has spontaneously emitted. Moreover, associated high peak intensities increase the chance of immediate re-excitation by the STED laser.

Pulses with durations longer than the fluorescence lifetime of the fluorophore waste STED photons and thus burden the sample with more light than necessary as the later STED photons mainly hit fluorophores that have already spontaneously emitted. Within the reasonable time frame, short pulses deplete efficiently but associated high peak intensities open further pathways for photobleaching. At the same average power, longer pulses lower the probability for nonlinear photobleaching as peak intensities are reduced (refer to I.1.4.1 and I.1.4.3). However, if the STED pulse duration falls in the range of the fluorescence lifetime, time-gated detection becomes necessary to discard early spontaneous emission from the periphery [240]. Concomitantly, early spontaneous emission from the intensity zero is rejected, and thus the SNR is lowered (see below).

The wavelength of the STED laser preferably ensures efficient stimulated emission with no re-excitation. If the wavelength is too short with respect to the fluorophore's spectral properties, depletion intensities are increased as vibrationally excited emitters are also targeted, but pronounced re-excitation promotes nonlinear photobleaching and decreases image contrast [241]. If the STED wavelength is too long, de-excitation becomes inefficient. High pulse repetition rates in the tens of MHz range enable fast imaging but increase linear photobleaching from the triplet state. Lowering the repetition rate decreases linear photobleaching and increases image quality at the expense of a decreased imaging speed.

While implementation of STED nanoscopy is technically and optically more sophisticated than the implementation of SMLM, its usage is straightforward. During imaging, the labeling density does not need to be considered. After imaging, no post-processing is necessary true to the dogma WYSIWYG (`what you see is what you get´). Optionally for STED data, post-processing might be used to increase image quality. Yet, careful application is crucial to avoid the introduction of artefacts. Deconvolution can be used to increase the SNR and the final image resolution; linear unmixing removes crosstalk between different color channels (refer to I.1.3.3).

The first implementation of STED nanoscopy used pulsed excitation and pulsed STED lasers [153]. However, in the early days, continuous wave (CW) lasers simplified the setups and reduced the costs [242]. With CW excitation and CW depletion, a dynamic equilibrium is created that allows for fast imaging and thus potentially less photobleaching. Yet, to attain the same efficiency for stimulated emission as in the pulsed STED case, higher average laser powers have to be applied and thus photobleaching and re-excitation by the STED laser is increased. Moreover, the image contrast is lower than in the pulsed STED case because a non-negligible fraction of the fluorophores spontaneously emits before they can be depleted. The consequence is an unwanted fluorescence in the periphery of the intensity zero and a confocal pedestal in the final image [215].

Combining CW STED with pulsed excitation and time-gating mitigates the drawbacks by discarding the early spontaneous fluorescence. Time-gated detection is a temporal filter that acts like a spatial filter discarding low spatial frequencies. However, as desired photons emitted from the intensity zero region are rejected as well, the SNR is lowered. Furthermore, in CW STED, all fluorophores are constantly exposed to STED photons and thus increase STED-light induced excitation and photobleaching between excitation pulses. Yet, time-gating suppresses the detection of scattered excitation light by opening the gate after the excitation pulse and suppresses the detection of re-excitation by the STED laser by closing it after the fluorescence lifetime.

Improved phase/wave plate designs not only simplified but also rendered STED implementations more compact and robust. Shaping the STED beam without affecting the excitation beam was achieved either by a phase plate consisting of different glass materials with different refractive indices for the excitation and STED wavelengths [243] or by the combination of conventional and segmented wave plates. This birefringent device not only implements the easySTED principle but at the same time infers the fluorophore orientation [244]. Phase/wave plates that modulate only the STED beam co-align the excitation and the STED beam by design. Insensitivity to mechanical drift in the alignment is beneficial, as the SNR and therefore effectively the resolution depends on the nanometer precision overlap of both beams. Other beam-shaping devices enabled the parallelization of STED increasing scanning speed by the number of intensity zeros either modestly [245] or extensively [246, 247].

As switching in STED nanoscopy happens basically instantaneously, the temporal resolution is limited by the scanning speed. With resonant scanners [248] and electro-optical deflectors [249], the pixel dwell time reaches the fluorescence lifetime of the emitter and thus the imaging speed is only dictated by the SNR [211]. As a point scanning method, the acquisition time of STED nanoscopy scales with the FOV. Parallelization of the illumination scheme to accelerate the imaging process is possible since only the intensity zero determines the resolution [245]. With one zero at r_i and the next zero at $r_i \pm \lambda/2NA$, the collective of intensity zeros must only be translated by $\lambda/2NA$ [1]. Yet, in current implementations of parallelization, confocality is lost and thus the image SNR is decreased [246, 247].

As a coordinate-targeted method, STED nanoscopy – except its parallelized version – preserves the aspect of optical sectioning. This quality is highly valuable in biological imaging as most samples are three-dimensional. Yet, in the standard 2D implementation, the axial resolution is still diffraction-limited. To achieve an (quasi-)isotropic resolution, 3D STED imaging can be realized via two approaches. The first one incoherently combines a donut-shaped STED profile confining the effective emission laterally with a bottle-shaped STED profile confining the effective emission axially [233, 250]. The second approach unites 2D STED with 4Pi imaging in isoSTED and is therefore not only technically more demanding but also more sensitive [140, 201-204].

I.1.3.3 Multicolor STED Imaging

Multicolor imaging is essential for biology as it highlights not only a specific structure but visualizes as much cellular context as possible. Various options for color separation exist [251]. In general, different fluorophore types are distinguished based on their spectral properties. Distinct spectral detection windows allow the discrimination based on emission spectra and enable simultaneous recording. Separation solely based on the excitation requires sequential acquisition. However, spectral separation is usually not perfect due to overlapping absorption/emission spectra of the different fluorophore types.

By combining selective excitation with separation of the emission in an appropriate acquisition scheme, only 2nd-order crosstalk remains. Linear unmixing eliminates crosstalk by approximating the signal of each pixel as a linear superposition of signals from the involved fluorophores. This approximation is only valid if the PSFs of the fluorophores are very similar [252]. For STED, the shape of the effective PSF is co-determined by the excitation and STED wavelength and by the light-

fluorophore interaction. The latter varies with the cross sections for absorption and stimulated emission and thus differs between the fluorophore types. Therefore, channel unmixing in STED must take different PSFs into account [251]. Alternative options exploit the differences in the fluorescence lifetimes and include pulse-interleaved excitation (PIE) with time-gated detection or fluorescence lifetime imaging [251, 253].

The possible realizations of dual-color STED imaging comprise the combinations of either two excitation and two STED lines, two excitation and one STED line, or one excitation and one STED line. The first approach requires the most complex setup and proper alignment of four lasers. Yet, it allows for spectrally well-separated fluorophores. Usually, the shorter wavelength STED light strongly excites and drastically bleaches the longer wavelength dye. Hence, sequential imaging is necessary but affords only a single shot [254, 255]. Optimization of the STED wavelengths and reasonable emitter choices reduce photobleaching but forces the handling of more crosstalk [256-258]. The second approach is particularly valuable for colocalization experiments. By using the same STED beam to deplete both excitation channels, their signals are inherently co-aligned. Potential residual chromatic aberrations do not alter the colocalization results as the intensity zero defines the position of effective excitation for both channels [29, 137, 202, 259-262]. Image acquisition is done by (quasi-)simultaneously recording both colors either line-by-line or via a PIE scheme. The third approach separates the channels by spectral detection. Crosstalk is eliminated either by simple channel subtraction [31] or by linear unmixing [263]. A creative alternative employs psFPs with very similar spectral but opposite activation properties to separate the channels by means of photochromism [264].

The more colors are added, the smarter the separation strategies must be. Multicolor STED imaging with three and four colors is made possible by spectrally separating regular fluorophores with long Stokes shift dyes [265, 266], by combining spectral and fluorescence lifetime separation [251], by exploiting photostability differences in excitation-based separation [267] and by applying rigorous mathematical unmixing in emission-based separation [268]. Simplification of multicolor STED imaging can be achieved by the implementation of a supercontinuum laser source for excitation [251, 256]. On the one hand, the respective system becomes very flexible regarding wavelength optimizations; on the other hand, only two lasers must be synchronized in the case of pulsed STED [269, 270].

With every additional color, information content but also complexity increases. Therefore, most multicolor STED experiments with more than two colors have been conducted with fixed samples. Hence, the dimension of cellular context is extended but the temporal dimension is frozen at one specific point in time. To attain actual information on dynamics, live cell imaging must be performed. However, properly imaging living specimens is challenging on many levels and phototoxicity is receiving increasing attention as a major issue relevant to the field of fluorescence nanoscopy.

I.1.4 Phototoxicity in Fluorescence Microscopy

Fluorescence microscopy is generally emphasized in literature to be essentially non-invasive. However, live cell imaging entails two main factors of potential cell damage. While direct chemical toxicity is triggered by the fluorescent label (ligand plus fluorophore) and the imaging buffer, phototoxicity is induced by the light energy deposited in the sample.

The breakthrough from diffraction-limited fluorescence microscopy to diffraction-unlimited fluorescence nanoscopy is directly associated with light doses that are orders of magnitude higher than the light dose biological specimens experience by their very nature (solar flux on earth < 1.4 kW/m^2) [271]. The consequence of the increased photon demand is potential photodamage and phototoxicity meaning impaired sample viability just by looking at it. The biological process, the biological structure or its dynamics of interest might be affected and the imaging results altered, no longer describing biological reality [272]. Amongst all interdependent imaging parameters discussed above (refer to I.1.2 and Figure I-4), cell viability should be of major interest for live cell imaging and parameters like spatiotemporal resolution or contrast optimized for the biological question but not overdone.

I.1.4.1 Photophysical Cause

Upon absorption of a photon, fluorescent markers or endogenous chromophores (e.g. flavins, porphyrins, nicotinamide adenine dinucleotide (phosphate) (NAD(P)H), aromatic amino acids) populate an electronically excited state (usually S_1) with a certain vibrational and rotational configuration ($k_{exc} \sim 10^{15}$ s^{-1}). Most favorable for standard fluorescence microscopy applications is the subsequent relaxation back to the electronic ground state S_0 via emission of a photon ($k_{fl} \sim 10^{9}$ s^{-1}) (Figure I-7). Both, absorption and fluorescence emission obey the Franck-Condon principle (Born-Oppenheimer approximation). The emitted photon is Stokes shifted to longer wavelengths compared to the absorbed photon due to internal conversion and vibrational relaxation ($k_{IC} \sim 10^{12}$ s^{-1}) according to Kasha's rule and due to solvent relaxation following the Franck-Condon principle.

However, as electronically excited fluorophores can also relax via other intermolecular and intramolecular pathways, competing de-excitation processes cause a quantum yield $\phi_F < 1$. Intersystem crossing ($k_{ISC} \sim 10^{8}$ s^{-1}) can disengage the fluorophore from continuous cycling between S_0 and S_1. Entering long-lived dark states like the triplet state T_1 ($k_{ISC} \sim 10^{3}$ s^{-1}) renders the fluorophore more reactive. It becomes prone to react with molecular oxygen generating singlet oxygen via spin flip followed by the build-up of other reactive oxygen species (ROS). Electron transfer reactions produce radical ions of the fluorophore itself and radical ions of surrounding molecules with a lifetime of several seconds to minutes. In the worst case, this photosensitizing process leads to irreversible, photochemical modifications of the fluorophore accompanied by loss of fluorescence (Figure I-7). Photobleaching caps the number of excitation and fluorescence emission cycles. The absolute number of photons emitted and hence signal strength and observation time are limited.

At non-saturating excitation intensities, the photobleaching quantum yield ϕ_B (probability for photobleaching) is small (10^{-7}-10^{-5} for most organic dyes) and can be considered constant under defined conditions. However, saturated excitation, which is commonly reached in confocal microscopy, departs from linear dependencies and promotes photobleaching. Transitions to triplet T_1 or radical ion states $\dot{R}^{+/-}$ increase ϕ_B and photobleaching often starts from these states in reaction with oxygen or ROS. Yet, it is suggested that photobleaching also happens from the excited state via the absorption of a second photon and transition to higher excited states (S_n and T_n) (Figure I-7). The underlying photophysics is complex, nonlinear and strongly dependent on the fluorophore, its concentration and the environment [273-275].

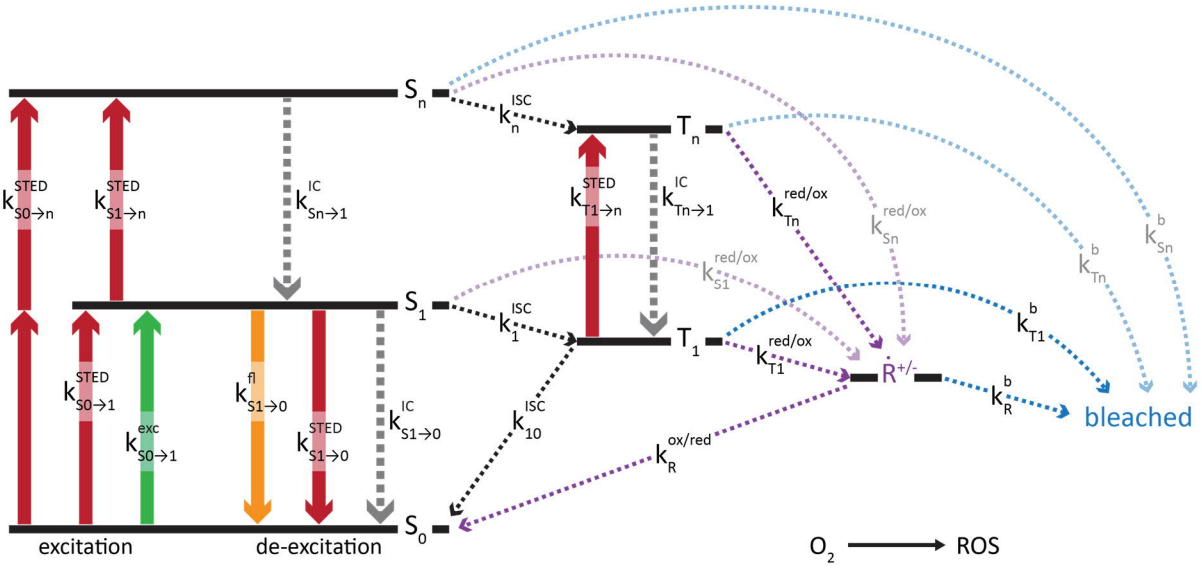

Figure I-7. Major electronic state transitions of common fluorophores.

Radiative transitions are illustrated as solid arrows, non-radiative processes are illustrated as dotted arrows. Excitation from S_0 (singlet ground state) to S_1 (first excited singlet state) is desired upon illumination by the excitation laser ($k_{S0\rightarrow1}^{exc}$~10^{15} s^{-1}). The excited state can relax back to S_0 via the emission of spontaneous fluorescence ($k_{S1\rightarrow0}^{fl}$~10^{9} s^{-1}) or via non-radiative decay processes (e.g. internal conversion, $k_{S1\rightarrow0}^{IC}$). Intersystem crossing (k_1^{ISC}) competes with fluorescence and populates T_1 (lowest triplet state). The excited state can be additionally depleted via stimulated emission ($k_{S1\rightarrow0}^{STED}$) forced by the STED laser. Additionally, the STED laser can induce undesirable excitation from S_0 to S_1 ($k_{S0\rightarrow1}^{STED}$), from S_1 to S_n ($k_{S1\rightarrow n}^{STED}$), from S_0 to S_n (two photon absorption, $k_{S0\rightarrow n}^{STED}$) and from T_1 to T_n ($k_{T1\rightarrow n}^{STED}$). The extended triplet state lifetime promotes the build-up of reactive oxygen species (ROS), and electron transfer reactions ($k_{T1}^{red/ox}$, $k_{Tn}^{red/ox}$, presumably also $k_{S1}^{red/ox}$, $k_{Sn}^{red/ox}$) produce radical ions $\dot{R}^{+/-}$ of the fluorophore. If S_0 is not rescued from T_1 or $\dot{R}^{+/-}$ via triplet quencher (k_{10}^{ISC}) or via redox reaction ($k_{T1}^{red/ox}$, $k_R^{ox/red}$), irreversible photochemical modifications of the fluorophore lead to a loss of fluorescence. Photobleaching presumably also occurs as a consequence of transitions to higher excited states.

I.1.4.2 Physiological Effect

As ROS are a regular metabolic product, cells have a certain buffer capacity which allows their disposal to some extent [276]. A key player on that front is the glutathione disulfide/glutathione (GSSG/GSH) couple. The GSSG/GSH concentration differs between organelles (e.g. 1-10 mM in cytosol) as well as between cell lines [277], but as soon as it is used to capacity, ROS start to accumulate. At low concentrations, ROS interfere with the cell's metabolism and redox state, cell signaling and cell cycle control [278-280]. At higher concentrations, ROS react with surrounding biomolecules (proteins, lipids, DNA) and impair their biological function [281-284]. This oxygen dependent photodamage (type II phototoxicity [285]) is more critical than oxygen independent photodamage (type I phototoxicity [285]), during which the excited state fluorophore directly reacts with neighboring cellular components.

The observation of photobleaching is an unmistakable sign of phototoxicity. However, its absence does not necessarily exclude photodamage [286-288]. Even unlabeled biological samples experience phototoxicity since photosensitizing effects are also mediated by endogenous chromophores [289] (e.g. chemical alterations of DNA upon ultraviolet (UV) illumination like dimerization of thymine base pairs [290]). For the sake of completeness, thermal damage shall be mentioned as an additional

primary consequence of phototoxicity. Yet, it is usually uncritical and only prominent during imaging of strongly absorbing, pigment rich tissue [291].

Taken together, all primary photophysical and photochemical reactions manifest themselves in secondary physiological impacts on cellular homeostasis. Disturbances are expressed in the form of ATP depletion, membrane depolarization [292], cytoplasmatic Ca^{2+} increase [293], morphological changes of mitochondria [294] and eventually cell hydropic swelling and blebbing [289]. If a certain tolerance level is crossed, pathologic changes like DNA mutations accumulate, lead to cell cycle arrest and ultimately to apoptosis or necrosis [295-298].

I.1.4.3 Phototoxicity in STED Nanoscopy

Most fluorescence nanoscopy techniques depend on high irradiation intensities and are therefore susceptible to phototoxicity. Indeed, in biology, they are often applied in short-term experiments and their results are usually considered meaningful as long as the sample is not negatively affected during the experiment. At this point, long-term controls should be handled rather pragmatically than categorically and within the scope of the biological question [289]. Still, long-term validation of cell health will always be supportive of the particular study and is hence desirable [299, 300].

As stimulated emission effectively shortens the excited state lifetime, it theoretically protects the fluorophore from photobleaching compared to the excitation only case. Unfortunately, excited state absorption counteracts this and parasitic transitions to higher electronic states occur even if the cross sections for transitions to S_n and T_n are small. Certainly, not only the combination of excitation and STED lasers photobleaches, but also the STED light alone. Depending on the STED peak intensity, distinct photobleaching mechanisms contribute to different extents. At low STED powers, STED photons mainly de-excite and other interactions of STED photons can be neglected. Photobleaching is intensity-independent, of low-order and associated with dark state population of mainly T_1 [4, 301]. However, STED nanoscopy works under saturating conditions, and excess intensities at the donut crest must be applied to efficiently deplete the fluorophores in the proximity of the intensity zero. Especially this excess exposure promotes the population of T_1, $\dot{R}^{+/-}$, S_n and T_n. via multi-step and/or multi-photon absorption processes of STED light leading to higher-order, intensity-dependent photobleaching [302]. As photobleaching is more pronounced from S_n and T_n reducing the population of any other electronic state than S_1 reduces photobleaching (Figure I-7).

Until now, only one study has extensively dealt with the issue of photodamage in STED nanoscopy [303]. Kilian *et al.* showed that – under the right conditions – STED can be conducted without significant short-term photodamage. Changes in cytoplasmatic Ca^{2+} concentrations were used as a measure for phototoxicity since Ca^{2+} release into the cytosol is one of the earliest stress indications of cells on their way to apoptotic or necrotic cell death [304]. Similar to a previous study examining cell viability under SMLM conditions [305], Kilian *et al.* observed long-term photodamage evident through an increased rate of cell death. However, the study clearly proves that STED imaging does not inevitably cause cell death. However, comprehensive data are missing, and the effects of excitation and STED laser were not assessed separately. Yet, the work by Kilian *et al.* is highly important as it is pointing the way to a systematic characterization of phototoxicity in STED.

I.1.5 Live Cell Imaging

The imaging community is still divided over the question whether true live cell nanoscopy is actually feasible [306] as every increase in resolution comes at the cost of more exposures, longer acquisition times, and higher laser intensities endangering the sample viability [6]. Regardless of the answer, a lot of effort is invested to render existing methods live cell compatible and to come up with new concepts discarding the drawbacks of established techniques and uniting their strengths technically, methodologically [186-188] and computationally [307-309]. Beyond the requirement of a reduced photon burden to achieve diminished phototoxicity (refer to I.1.4 and IV.1), major demands include also an increase in imaging speed to capture the whole temporal range of biological dynamics and an isotropically expanded FOV to capture as much biological context as possible, both without impairing the spatial resolution.

For intermediate resolution gains, SIM is very popular amongst biologists. It is a photon-efficient and thus gentle method using 10^3-10^6 times lower intensities than diffraction-unlimited techniques. SIM provides a high throughput, multicolor, live cell imaging option with acquisition speeds for volumetric imaging of large FOVs, which is compatible with conventional dyes and easily accessible [104, 105, 310-312]. To further speed up acquisition in 3D imaging, multifocus (multiplane) imaging [313] can be combined with SIM [314]. However, SIM is sensitive to out-of-focus light arising from emitting fluorophores above and below the focal plane. This unwanted excitation triggers excess phototoxicity throughout the whole preparation.

In contrast, light sheet fluorescence microscopy (LSFM) [315] and selective plane illumination microscopy (SPIM) [316] illuminate the specimen orthogonally to the detection, thus exciting only the detected fluorophores, which drastically lowers the energy load to the specimen and reduces photobleaching and phototoxicity. LSFM and SPIM are the gentlest fluorescence microscopy techniques available to date [271, 317] and combine unprecedented imaging speed and a high SNR with inherent optical sectioning allowing 3D *in vivo* imaging of small organisms and embryos [318]. Different approaches have been realized to improve the lateral and axial resolution of LSFM/SPIM [194, 319-321]. The combination of LSFM with SIM, lattice light sheet microscopy (LLSM), doubles the lateral resolution in every xy plane [192, 193].

Other options restricting the excitation to the focal plane include TIRF illumination and two-photon excitation (2PE). Imaging in TIRF mode has proven to be less phototoxic than widefield illumination [322, 323], but limits the observation (close) to the basal membrane as the evanescent field penetrates only 100-300 nm into the sample [324]. Imaging with 2PE is advantageous for deep tissue imaging as scattering is reduced at longer wavelengths, but nonlinear photodamage occurs due to the obligatory high peak intensities [325, 326].

I.1.5.1 Live Cell SMLM Imaging

Aiming for high resolution gains requires either live cell SMLM or live cell STED/RESOLFT. In general, the time to acquire a super-resolved image must be faster than the time in which the structure of interest moves one measure of resolution. Otherwise, motion blur compromises image quality and

specifically for SMLM, localization errors and artefacts are the consequence. Typical intensities applied in SMLM range between 1-15 kW/cm^2 at 405-640 nm [18, 41, 42, 327, 328], while the switching/activation rate depends on the laser intensities [329]. TIRF illumination can reduce photodamage but spatially restricts imaging. SMLM collects thousands of camera frames to reconstruct one super-resolved image and potentially long acquisition times constrain its live cell imaging compatibility. Furthermore, adjustment of the switching/activation rates to the labeling density is required to guarantee the desired image and temporal resolutions.

The emitter ON state (OFF state) lifetime in living cells usually ranges between 10-50 ms (0.5-10 s), corresponding to a frame rate of 20-100 Hz [40]. For low fluorophore densities (e.g. labeling of low-copy number proteins) an effective image resolution of 20 nm in combination with a temporal resolution of 0.5-1.0 s can be achieved. However, the fluorophore concentration increases with the abundance of the protein of interest (POI) and thus effective image resolution can only be maintained at the expense of temporal resolution [39].

Clearly, higher laser intensities accelerate switching but technical progress in the means of faster cameras [330] and/or computational development in the sense of new post-processing strategies [331, 332] are necessary to exploit it. Alternatively, super-resolution optical fluctuation imaging (SOFI) [333, 334] and super-resolution radial fluctuation (SRRF) analysis [335] tolerate high labeling densities and still allow a moderate temporal resolution. These approaches analyze fluorescence fluctuations over time to derive additional spatial information. As they do not work strictly at the single molecule level, typical resolution enhancements are limited to 2-3 fold and artefacts can be expected [336].

Specifically for STORM, blinking buffers are not truly live cell compatible as single molecule switching requires an oxygen depleted, redox environment often created by toxic thiols. However, dye selection rules facilitate live cell STORM in different cellular compartments based on the fluorophores' redox potential [337]. Despite the drawbacks hampering routine application of SMLM for living samples, successful live cell SMLM has been performed [37, 38, 41, 42, 337-339].

I.1.5.2 Live Cell STED Imaging

Amongst all nanoscopy techniques, STED is one of the fastest and most suited for live cell imaging and imaging deeper within living tissues or living animals [340]. However, at the beginning of the century, STED was considered not live-cell compatible due to the high STED laser intensities and associated photobleaching [4]. To achieve a resolution in the tens of nanometer range, donut crest intensities up to 1 GW/cm^2 are necessary. Still, 2PE as the method of choice for *in vivo* deep tissue imaging uses even higher doses of light. The live cell compatibility of STED cannot be generally judged as it individually depends on the STED wavelength, the required resolution (i.e. STED laser intensity), the observation time and frequency (i.e. total exposure time), the FOV and the specimen (refer to I.1.4 and IV.1).

After the first proof of live cell STED in 2008 [341], numerous live cell STED experiments have applied FPs [263, 264, 342-349], self-labeling protein tags [29, 30, 32, 33, 259, 260, 350, 351] or small molecule binders [31, 352-354] in both single-color and multicolor approaches [29, 31-33, 260, 263, 264, 342]. The dynamics of different cellular molecules, of molecular assemblies, of structures like the

cytoskeleton, vesicles and the cell membrane, and of organelles such as the endoplasmatic reticulum (ER), mitochondria and peroxisomes have been observed in living cell lines and even in brains of living mice [355, 356]. Deep tissue and *in vivo* STED imaging is mainly challenged by scattering and aberrations degrading the intensity zero, impairing the beam alignment, and thus reducing image contrast and resolution. Adaptive optics using either deformable mirrors or SLMs can correct for sample-induced aberrations from refractive index mismatch [2, 357-362] and 2PE counteracts light scattering [363].

The huge advantage of STED over SMLM is the free choice of the number of simultaneously recorded fluorophores via adaptation of the intensity zero. Individually tuning the spatial resolution allows for matching the respective biological dynamics. (Ultra)fast scanning units enable video-rate STED with a temporal resolution of 80-200 frames per second rendering STED the fastest reported nanoscopy method to date [340, 364, 365]. Alternatively, parallelization of the illumination scheme also speeds up the acquisition [245, 246].

To attain the respective STED intensity for efficient OFF switching around the donut zero, the intensity at the donut crest can be orders of magnitude higher than I_s. Yet, photobleaching, phototoxicity, dark state accumulation and switching fatigue can be lowered by either reducing excess STED photons or protecting the fluorophores (refer to IV.1). For example, in D-Rex (dark state relaxation) [141, 366] and T-Rex (triplet state relaxation) STED [238], low-repetition-pulsed laser light or ultra-fast scanning give the fluorophores time to relax back from dark states and triplet states to S_0. Long pulses in combination with time-gating can reduce STED peak intensities up to one order of magnitude. Other measures to lower the light dose to the sample include sophisticated light exposure schemes applying adaptive illumination (AI), which are conceptually related to controlled light exposure microscopy [286].

Reduction of state transition cycles (RESCue) STED locally adapts the sample exposure by modifying the intensities of the STED and excitation beams. An online decision is taken based on the number of photons detected during a first fraction of the dwell time, which shuts off the STED and excitation beams if the photon flux is lower than a certain threshold. Thus, the fluorophores cycle less often and their exposure to the donut crest is significantly reduced. However, neighboring regions are still negatively affected [367].

By contrast, molecular states for multiple off-state transitions (MOST) nanoscopy exploits the presence of a second (protective) OFF state to prevent designated OFF state fluorophores from populating the ON state. Thereby, neighboring fluorophores are efficiently protected, and resolution and ON-OFF contrast are enhanced. Protected STED combines the MOST concept with STED imaging and introduces the protective OFF state by utilizing the ability of psFPs to reversibly switch between an activated (`fluorescent´) and a deactivated (`dark´) form. In addition to S_0 of the activated form, the deactivated form is implemented as the second OFF state, which efficiently protects the psFPs from photobleaching as the deactivated form either does not absorb the excitation or the STED wavelength or absorption is followed by instantaneous relaxation to S_0. An additional donut-shaped beam restricts the area of psFPs susceptible to the excitation and STED beam to a subdiffraction-sized region by sending all psFPs to their deactivated form except the ones in the center of the donut. The illumination scheme is rather

complex and requires the optimization of numerous parameters, but protected STED enables 2D and 3D live cell imaging of light sensitive samples [368].

STED with minimized FOV and minimized fluorophore exposure to the STED beam (MINFIELD) strongly reduces, as in the case of RESCue STED, the number of excitation and emission suppression cycles. However, MINFIELD records only subdiffraction-sized FOVs determined in advance based on low resolution confocal images. Thereby, the relevant fluorophores are not exposed to the excess intensities of the donut crest and photobleaching is reduced up to 100-fold [369]. STED with dynamic intensity minimum (DyMIN) synergistically combines RESCue and MINFIELD STED without being restricted to subdiffraction-sized FOVs but avoiding excess STED photons. The sample is dynamically probed by confocal scanning with low light intensities and STED power is gradually increased while scanning across a fluorophore. Full STED power is reached only at the moment when the fluorophore is centered in the middle of the donut. Thereby, DyMIN STED reduces the STED laser dose 20-fold in common biological samples. Yet, it works most efficiently in sparsely labeled 2D and 3D samples with STED dose reductions of more than 100-fold [370]. Moreover, refined AI variants of STED nanoscopy exist that are specialized to individual biological problems (e.g. guided STED [371]).

Compared to STED imaging, RESOLFT with psFPs significantly reduces the laser intensities required for efficiently driving the focal switch. It typically exploits the photoinduced *cis-trans* isomerization between a fluorescent and a non-fluorescent psFP chromophore isomer with lifetimes in the ms range. As I_S inversely scales with the lifetime of the involved states, switching intensities are roughly an order of magnitude lower compared to STED imaging assuming that the corresponding cross sections of stimulated depletion and psFP switching are comparable [372]. While every STED switching cycle yields only one photon, psFPs in RESOLFT emit more than one photon per *cis-trans* switching cycle. However, the decreased intensities come at the expense of a reduced imaging speed and near-UV light (for switching). Further limitations potentially appear as crosstalk between ON-OFF switching, photofatigue and FP oligomerization. Any decrease in imaging speed can be compensated by parallelization of the RESOLFT illumination scheme [373, 374].

MINFLUX minimizes the fluorophore input and output by probing single emitters with an excitation light intensity minimum [186, 187]. Therefore, it is at the moment still challenged by samples with background, common for living specimens. Still, the first live cell MINFLUX imaging has recently been published [188].

For successful live cell imaging, the imaging modality must be chosen with respect to the biological question to answer. In any case, minimization of the cells' stress level should be the guiding principle (refer to IV.1) [375]. Besides current technical, methodological and computational innovations, the choices of fluorophore and labeling strategies greatly influence the success of live cell imaging. Further improvements and/or new developments from the (bio)chemical side will strongly advance the progress in the field of live cell imaging.

I.1.6 Specific Targeting in Live Cell Nanoscopy

As a molecular switch is the secret to success for every nanoscopy method, improvements on the fluorophores are one of the major keys to boosting the performance of current methods [376-380]. Spatial resolution is directly linked to the fluorophores' properties regarding state-transfer efficiency, photophysical and photochemical kinetics, photochemical stability, photon yield (i.e. absorption cross section and fluorescence quantum yield) and environmental sensitivity. Thus, there is a strong urge in (bio)chemistry to improve the existing and develop new water-soluble markers that can flexibly be linked to the target of interest.

While every fluorescence nanoscopy method is built on the common principle of the focal switch, the individual demands on the detailed photophysics of the emitters differ between methods. SMLM requires fluorophores with a maximal photon burst in a minimal time and dark times long enough to ensure sufficient spatial separation of single molecule events. MINFLUX depends especially on reliable switching characteristics and strongly benefits from the absence of stochastic blinking behavior.

For all coordinate-targeted methods, a high photostability, a low photobleaching quantum yield ϕ_B and a maximal number of switching cycles is advantageous. The higher the desired effective image resolution is, the higher the STED intensity and the smaller the pixel size must be, thus the more cycles a single fluorophore has to undergo [4, 50]. In particular, STED imaging profits from a high stimulated emission cross section, from low dark state transition possibilities, and from a low cross section for excitation to S_n and T_n [381], characteristics that are mainly found with organic dyes.

As no single fluorophore fulfills all criteria at once, conscious compromises must be taken for each concrete application. Ongoing developments push especially for new organic dyes with beneficial photophysical properties for fluorescence nanoscopy [382-386].

I.1.6.1 Live Dyes

To draw conclusions as close as possible to biological reality, live cell imaging attracts an increasing amount of attention (refer to I.1.5). However, while labeling techniques for living cells were in place, truly biocompatible organic dyes were missing in the early days of fluorescence nanoscopy [387]. Molecular specificity and cell permeability were therefore the two most cited limitations of organic fluorophores for live cell imaging at the end of the last century [388]. The diffusion through cell membranes is either size or charge hampered and, for a long time, only very few cell permeable dyes like TMR-STAR, Oregon Green and ATTO 655 were available. Alternative but invasive strategies deliver the fluorophore inside the cell via cell squeezing [389], biophotonic laser-assisted surgery tool (BLAST) [390], transient membrane pore formation [391], electroporation [392], glass-bead loading [393], membrane transfer [394], micro-/nano-injection [395, 396], cell-penetrating peptides [397], and pinosomelysis [398]. However, these techniques are elaborate, suffer from low efficiency and subject the cells to a high level of stress.

Longer wavelength light unites several characteristics particularly advantageous for live cell, deep tissue and *in vivo* imaging. (Far-)red illumination is less phototoxic and reduces autofluorescence and

scattering [305]. With the beginning of the 2010s, various near-infrared (NIR) synthetic dyes were available, but they were either membrane impermeable or suffered from unspecific binding [260]. Therefore, the development of (far-)red emitting live-cell probes [29-36, 353, 354] and FPs [347-349, 399] for fluorescence nanoscopy has been and still is greatly pushed.

In the field of organic dyes, Lukinavicius *et al.* set the kick-off in 2013 with the synthesis of a far-red silicon-based rhodamine (6-carboxy-tetramethylsiliconrhodamine, SiR-COOH) [30]. The SiR dye is membrane permeable, bright, fluorogenic, photostable, essentially non-toxic, absorbs and emits in the NIR spectral range, and enables no-wash experiments. These characteristics render the SiR dye a potent candidate for NIR live cell STED imaging. It exists in an equilibrium between a non-fluorescent, `cyclized´ spirolactone form and a fluorescent, `open´ zwitterionic form with the dielectric constant of the environment governing the equilibrium's position (Figure I-8a). In the unbound state, which comprises free diffusion in the cytoplasm and binding to off-target proteins or hydrophobic structures, the SiR dye adopts the non-fluorescent form. Upon binding to its target, the fluorescent form is favored. Versatile implementations *in cellulo* and *in vivo* are possible as specific targeting can be achieved with self-labeling protein tags (refer to I.1.6.2) [30], via click chemistry [30] or via small molecule binders [353, 354, 400-403]. Nowadays, the SiR dye is commercially available as a substrate for SNAP-tagged fusion proteins [404].

To expand the color palette of what are colloquially called `live dyes´ and enable multicolor live cell imaging, the development of SiR-related and SiR-inspired fluorophores with different spectral properties has been strongly boosted. On the one hand, red-shifted derivatives of the SiR dye were developed enabling 810 nm STED of cytoskeletal structures [31, 33]. On the other hand, Butkevich *et al.* extended the spectral scope also to shorter wavelengths, synthesized (hydroxylated) rhodamines, carbopyronines, silicorhodamines and germanorhodamines in the same spectral range and introduced the favorable live dye pairs 580CP/SiR and 610CP/640SiRH for live cell dual-color STED with 775 nm de-excitation (Figure I-8b) [29, 32].

To quantify the fluorogenicity of the different derivatives, Butkevich *et al.* defined the measure D0.5. It states the dielectric constant of a dioxane-water mixture with an absorption (or extinction coefficient) of half the maximum absorption (or extinction coefficient) measured for the entire dioxane-water gradient [29]. By investigating the structure-property relationship of the different dye derivatives, Butkevich *et al*. could predict the spectral properties and D0.5 values of new dye derivatives based on a simple additive scheme. The synthesis and characterization of these dyes proved the prediction to be more accurate than current computational methods like density functional theory (DFT) [32].

Additional effort was taken by Grimm *et al.* to improve the brightness and photostability of existing live dyes without changing their spectral properties and cell permeability [34]. The final result was a series of derivatives called Janelia Fluor (JF) dyes [405]. Further development by Grimm *et al.* yielded a photoactivatable SiR dye [36] and photoactivatable variants of the JF dyes [35], enabling fixed cell PALM imaging and live cell single particle tracking (SPT) PALM. Adaptations of the intramolecular nucleophilicity and electrophilicity of the SiR dye tuned the equilibrium constant for the intramolecular spirocyclization and the lifetime of the zwitterionic form, providing the first-in-class spontaneously

blinking HMSiR dye. This rationally designed derivative allows live cell dSTORM without the need for toxic additives or high-intensity laser irradiation to induce blinking [406].

Conjugation of a sulforhodamine fluorophore with the DNA targeting ligand Hoechst yielded the nucleus DNA specific live dye HoeSR. Transient DNA binding results in a fluorescence turn on and allowed for live cell dSTORM imaging of mitosis [37]. The combination of the SiR dye with genetically encoded light-up RNA aptamers provided the remarkably photostable and bright aptamer/ligand pair SiRA, enabling live cell STED imaging of tRNAs and mRNAs [407].

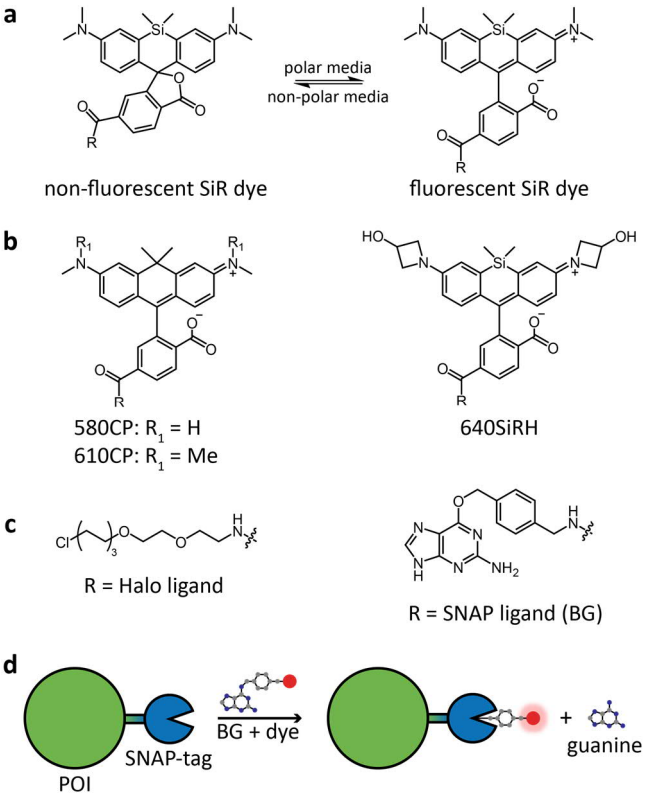

Figure I-8. Structures of selected live dyes and their application via the SNAP-tag technology.

(**a**) The popular silicone rhodamine (SiR) live dye exists in an equilibrium between a `cyclized´ spirolactone form (non-fluorescent) and an `open´ zwitterionic form (fluorescent), which is governed by the polarity of the medium. The excitation and fluorescence emission maxima of the zwitterionic form peak at 645 nm and 661 nm [30]. (**b**) Chemical structures of the three live dyes used in this thesis. The carbopyronines 580CP and 610CP display maximal absorptions at 582 nm and 609 nm and maximal fluorescence emissions at 607 nm and 634 nm [29]. The hydroxylated silicorhodamine 640SiRH shows maximal absorption at 641 nm and maximal fluorescence emission at 662 nm [32]. (**c**) The enzyme specific substrates of HaloTag (chloro-alkanes) and of SNAP-tag (benzylguanine, BG) can be conjugated to the live dyes. (**d**) The protein of interest (POI) is genetically fused to the SNAP-tag (or any other self-labeling protein tag) and the fusion construct is synthesized by the protein expression machinery of the transfected or genetically engineered cell. The BG-dye derivative is supplied with the cell culture medium. The SNAP-tag reacts with its substrate, releases guanine and covalently labels itself with the dye.

I.1.6.2 Targeting Strategies

To visualize a structure or process of interest in cells, tissue or even a whole organism, fluorescent markers must be specifically attached to the respective target. As it is always the emitter that is imaged and not the molecule of interest, the individual targeting strategy greatly influences the results (refer to I.1.2). The `how precisely and accurately´ a biological structure can be visualized with fluorescence nanoscopy, hereinafter referred to as the biological resolution, strongly depends on the label size, the labeling efficiency, the dynamic range, the contrast, the sample's spatial structure and potential biological and/or stage drift. Yet, no consensus has been reached on how exactly to define the biological resolution [408]. It is crucial to emphasize that the resolution of the optical system can strongly differ from the biological resolution (refer to I.1.2).

Intrinsic standards like microtubules are often chosen as a measure for the biological resolution and their FWHM is extracted from line profiles fitted by Gaussian or Lorentzian functions. However, the

results should be handled with caution as firstly, the actual PSF might differ from the Gaussian or Lorentzian description, secondly, the biological resolution may vary within one image and finally, selection of suitable line profiles is biased [99, 132, 409]. More reliable and comparable approaches are based on the Fourier ring correlation, commonly used for assessing the resolution of EM reconstructions [410], which computes the biological resolution directly from the super-resolved image [148, 408, 411, 412].

In all fluorescence nanoscopy methods, selection of suitable labels and thorough sample preparation are significantly more crucial than for diffraction-limited imaging, as the increase in resolution exposes potential, previously unknown labeling artefacts (refer to I.1.2) [413]. To guarantee the best possible biological resolution, an ideal affinity probe is small, live cell compatible, does not induce steric hinderance, targets specifically, binds monovalently, labels quantitatively – and is not known to exist. Therefore, the labeling method must be selected with respect to the biological question, the preparation options for the sample and the required spatial resolution.

FPs revolutionized the field of live cell imaging and since the 1990s have been established as the labeling method of choice for living specimens. Their key strengths are genetic encodability, straightforward expression in fusion constructs with the POI, and autocatalytic chromophore formation rendering additional dye labeling steps redundant. FPs are small compared to antibodies (Table I-1, Figure I-9), but large compared to organic dyes (~1 kDa).

Major efforts in protein engineering have been and still are invested to optimize the photophysical and biochemical properties of FPs, such that today an extensive color palette, various photochromic variants and a large variety of sensor probes are available [21, 22]. Endogenous tagging via genome editing allows for stoichiometric labeling of the POI. Yet, quantitative imaging is only guaranteed if the chromophore maturation efficiency is high. As chromophore maturation depends on the presence of oxygen, its speed sets a temporal limit on the observed processes. Additionally, FP-tagging potentially perturbs folding, stability, interactions and localization of the POI. These problems can be partially to fully circumvented by antibody fragment/FP fusions like fluorobodies or chromobodies [414].

However, the intrinsic tendency of FPs to oligomerize can lead to FP aggregation particularly during overexpression [415]. In general, FPs display more complex photophysics, reduced brightness and lowered photostability compared to organic dyes [416]. Still, rational design and directed evolution with focus on fluorescence nanoscopy applications try to render FPs photophysically compatible with their synthetic counterparts and optimized versions for PALM [417], RESOLFT [138] and STED [347, 348] have been developed. Indeed, STED nanoscopy has been using FPs for a long time as they feature a low excited state absorption for both the excitation and STED wavelengths [341, 345, 418].

Antibodies are the most widely employed affinity probes in fluorescence microscopy as they combine high specificity with enormous flexibility in targeting virtually any cellular compartment. Immunohistochemistry offers the best option for quantitative imaging of endogenous protein levels. While immunostaining is compatible with any organic dye, it is limited to fixed samples as antibodies are not cell membrane permeable. Standard indirect immunofluorescence (IF) with a primary antibody targeting the POI and a fluorescently labeled secondary antibody targeting the primary antibody offers modular staining with strong signal amplification.

However, the primary/secondary complex physically displaces the fluorophore approximately 20-30 nm from the structure of interest. Thus, the imaged coordinates and the structure coordinates are not identical. Furthermore, the primary/secondary complex may sterically hinder labeling of denser regions in the sample where epitopes are not accessible for bulky probes [419, 420]. Incomplete labeling in combination with multiple binding capabilities potentially produce artefacts in nanoscopic imaging [421]. Smaller alternatives recognizing epitopes with monovalent binding can partially to fully circumvent these limitations (Table I-1, Figure I-9) [408].

For certain cellular targets, small molecule binders offer an additional solution to targeting problems. The labels are small as they only consist of a binding motif (often a chemical inhibitor) conjugated to an organic dye. These small molecule binders allow for direct, non-covalent labeling and imaging of living cells, if cell permeable and biocompatible dyes are attached. Yet, compared to the number of targets in a cell, only a very small library is available by now including small molecule binders for organelles (mitochondria, ER, Golgi, endosomes/lysosomes) [31, 38, 422-424], cytoskeleton structures [31, 354], DNA [37, 353] and membranes [422, 425, 426].

More target flexibility is given by click chemistry, which enables fast, irreversible, highly site-specific and direct labeling of proteins and protein subdomains [427-429], of DNA [430], and of lipids [431] in both fixed and living cells with minimal target modification and essentially no label size. Yet, biomolecule labeling via click chemistry is still in its infancy. As soon as it can be routinely applied, click chemistry (or similar approaches) certainly will evolve to the staining method of choice for fluorescence nanoscopy since it alleviates any potential perturbations by bulky tags.

Table I-1. Size comparison of different affinity probes.

label	targeting modality	size [nm]	Mw [kDa]	reference
fluorescent protein	genetic fusion	2-5	27	[432]
SNAP-tag/CLIP-tag	genetic fusion	3-4	20	[23, 24]
HaloTag	genetic fusion	3-5	33	[25]
IgG antibody	epitope recognition	10-15	150	[433]
antibody fragment (Fab)	epitope recognition	9	50	[434]
single-chain variable fragment (scFv)	epitope recognition	6	30	[435]
camelid heavy-chain variable fragments (VHH, nanobody)	epitope recognition	3	13	[436]
designed ankyrin repeat protein (DARPin)	epitope recognition	2-3	10-30	[437]
affibody	epitope recognition	2	6	[438]
fibronectin type III domain (FN3, monobody)	epitope recognition	2	10	[439]
aptamer	epitope recognition	4	15	[421, 440]

Due to the limitations, drawbacks and challenges of the above-mentioned targeting strategies, strong effort has been and still is invested to develop alternative strategies based on genetically encoded protein tags specifically binding their substrates, covalently or non-covalently. Particularly for non-covalently binding tags, fluorogenic ligands are preferred as they keep background minimal even at excess fluorophore concentrations and thus guarantee a high imaging contrast [441].

Reversible binding allows for SMLM at low fluorogen concentrations without the need for special imaging buffers or photoactivation/photoswitching with a second laser [442]. Moreover, reversible binding reduces apparent photobleaching via constant dye renewal, which has been proven to be beneficial for live cell STED imaging [443, 444]. However, as photobleached fluorogens are only replaced and not prevented, ROS are still produced damaging both the sample and the tag itself [445].

Distinction can be made between protein tags that bind endogenous chromophores like flavin-based FPs (FbFPs, iLOV (improved light, oxygen or voltage sensing) domain, miniSOG (mini singlet oxygen generator)) [446-448], bilirubin-binding tags (UnaG (Unagi green FP)) [449] and biliverdin-binding FPs (IFP1.4 (infrared FP 1.4), iRFP (near-infrared FP)) [450-452], and protein tags that bind exogeneous, synthetic fluorophores like the yellow fluorescence-activating and absorption-shifting tag (Y-FAST) [453, 454] and fluorogen activating proteins (FAPs) [455]. Yet, in both cases, substrate and chromophore are identical, imposing no free dye choice, spectral and photophysical constraints and limitations for molecular engineering of the fluorophore. Thus, it is highly beneficial to use tags binding a substrate that can be linked to the desired fluorophore.

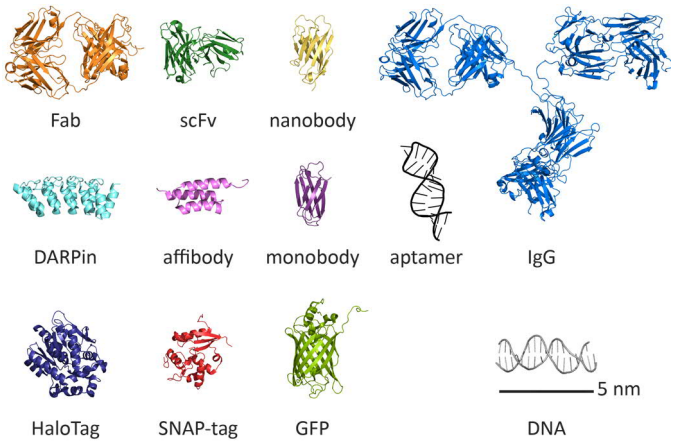

Figure I-9. Label sizes of selected affinity probes.

The different affinity probes commonly used for targeting cellular structures in fluorescence microscopy are shown to scale and in comparison to a short stretch of double-stranded DNA. All crystal structures were obtained from the PDB [Fab 1FDL, scFv 5VF6, nanobody 1MEL, IgG 1IGT, DARPin 5FIN, affibody 2KZJ, monobody 3RZW, aptamer 2JWV, HaloTag 5UY1, SNAP-tag 3KZY, GFP 5DTY, DNA 1W0U].

Self-labeling protein tags like SNAP [23, 24], Halo [25], CLIP [456] and *Escherichia coli* dihydrofolate reductase (eDHFR) [457, 458] covalently bind enzyme specific substrates (benzylguanine (BG), benzylcytosine (BC), chloroalkanes, trimethoprim), which can be conjugated to any freely chosen fluorophore (or any other chemical moiety) (Figure I-8c,d). Certainly, if live cell imaging is the aim, the fluorophore must be cell membrane permeable and biocompatible. All tags originate from enzymes optimized via directed evolution and/or rational protein engineering; SNAP- and CLIP-tags are derivatives of the human DNA repair enzyme O^6-alkylguanine-DNA-alkyltransferase, HaloTag of the bacterial haloalkane dehalogenase from *Rhodococcus rhodochrous*. Hence, the different self-labeling protein tags allow for orthogonal labeling reactions crucial for multicolor imaging. The labeling is typically fast and rather quantitative. Self-labeling protein tags unite the key strengths of FPs and

immunolabeling, namely genetic encoding and bright and photostable organic dyes, while being small, live cell compatible, target specific and modular (Table I-1, Figure I-9).

The category of self-labeling tags further includes tetra-cysteine and tetra-serine tags. These small peptides non-covalently bind the cell-permeable, fluorogenic biarsenical FlAsH (fluorescein arsenical hairpin binder) and ReAsH (resorufin arsenical hairpin binder) dyes [459] and the bis-boronic RhoBo (rhodamine-derived bis-boronic acid) dye [460]. While the tetra-serine/RhoBo system has more background problems through non-specific dye interactions, the tetra-cysteine/FlAsH/ReAsH systems show more cytotoxicity.

All genetically encoded tags must be introduced at the DNA level. Genetic transfection with plasmids encoding for the fusion construct of tag and POI is the faster and easier option but allows only for exogeneous expression of the fusion protein. Thus, labeled and unlabeled proteins expressed from the native locus are simultaneously present in the cell. The native protein level is altered and in extreme cases, overexpression leads to incorrect localization, accumulation and cell stress provoking uncontrolled regulatory effects. Transient transfections are the quick and dirty variant providing for fast and easy, but hard to reproduce and potentially heterogeneous samples; stable transfections are more time consuming but guarantee reproducibility.

In contrast, genome editing enables the site-specific insertion of the tag's sequence in the genome. The most popular molecular scissor is the clustered, regularly interspaced, short palindromic repeats (CRISPR/Cas9) system [461, 462]. Other options make use of meganucleases [463], zinc finger nucleases (ZFNs) [464] or transcription activator-like effector-based nucleases (TALENs) [463, 465]. Genetic engineering allows for stoichiometric labeling in case the specimen has been homozygously tagged. The endogenous protein level remains undisturbed and the fusion protein is expressed at the native transcription level and under the native pattern. Yet, genome editing is often the second choice as it is challenging and time consuming.

I.2 MATERIALS AND METHODS

I.2.1 Materials

I.2.1.1 Machines and Equipment

All standard optics equipment was ordered from Thorlabs (Newton, New Jersey, USA).

Table I-2. Components of the custom-built STED system.

components	company
Onefive Katana 08 HP, 775 nm STED laser	NKT Photonics, Birkerød, Denmark
Solea, supercontinuum laser	PicoQuant, Berlin, Germany
LDH-D-C470, 470 nm diode laser	PicoQuant, Berlin, Germany
ICS-6 Laser Interlock® System	Lasermet, Bournemouth, United Kingdom
525/50 nm BrightLine® single-band bandpass filter	Semrock, Rochester, New York, USA
628/32 nm BrightLine® single-band bandpass filter	Semrock, Rochester, New York, USA
708/75 nm BrightLine® single-band bandpass filter	Semrock, Rochester, New York, USA
775 nm blocking edge BrightLine® shortpass filter	Semrock, Rochester, New York, USA
561 nm laser BrightLine® single-edge super-resolution laser dichroic beamsplitter	Semrock, Rochester, New York, USA
ZT405/473-491/NIRrpc	Chroma Technology, Bellow Falls, Vermont, USA
PCIe-7852, field-programmable gate array (FPGA) based PC board	National Instruments, Austin, Texas, USA
SMARPOD 70.42, hexapod-like positioning system	SmarAct, Oldenburg, Germany
SPCM-AQRH-15/13-FC, avalanche photodiodes (APDs)	Excelitas Technologies, PerkinElmer, Waltham, Massachusetts, USA
MPH16, motorized pinhole	Thorlabs, Newton, New Jersey, USA
HCX PL APO 100×/1.44 Oil CORR CS, objective	Leica, Wetzlar, Germany
Leica DMI6000 CS	Leica, Wetzlar, Germany
EL6000, fluorescence lamp	Leica, Wetzlar, Germany

Table I-3. Further instrumentation and equipment.

equipment	company
Agilent 1100 series, HPLC	Agilent Technologies, Santa Clara, California, USA
LaPrep-System P110, HPLC	VWR International, Radnor, Pennsylvania, USA
NUCLEODUR® Sphinx RP column	VWR International, Radnor, Pennsylvania, USA
Chromolith RP-18e, 100×10 mm	Merck, Darmstadt, Germany
Chromolith RP-18e, 100×4.6 mm	Merck, Darmstadt, Germany
P314, variable UV detector	VWR International, Radnor, Pennsylvania, USA
Sep-Pack C18 cartridge	Waters, Milford, Massachusetts, USA
Avance III, 400 MHz NMR	Bruker Daltonics, Billerica, Massachusetts, USA
APEX-Qe hybrid 9.4 T FT-ICR, mass spectrometer	Bruker Daltonics, Billerica, Massachusetts, USA
Microflex LT, MALDI-MS	Bruker Daltonics, Billerica, Massachusetts, USA
JMS-700 MStation Mass Spectrometer	JEOL, Akishima, Tokyo, Japan
Varian Cary 500 UV-VIS NIR Spectrophotometer	Agilent, Santa Clara, California, USA
Varian Cary Eclipse Fluorescence-Spectrophotometer	Agilent, Santa Clara, California, USA
FluoTime 300 Fluorescence Lifetime Spectrometer	PicoQuant, Berlin, Germany
BD FACS Canto II Flow Cytometer	BD Biosciences, Becton Dickinson, Franklin Lakes, New York, USA
Chef DRII Pulse Field Electrophoresis chamber	BioRad, Hercules, California, USA
Chemi-Doc MP Imaging System	BioRad, Hercules, California, USA
PET-scanner Inveon PET	Siemens, München, Germany
Packard Cobra II, gamma counter	GMI, Ramsey, Minnesota, USA
HoloMonitor® M4 cytometer, holographic microscope	Phase Holographic Imaging, Lund, Sweden
BBD 6220 CO_2 incubator	Thermo Fisher Scientific, Waltham, Massachusetts, USA
Safe 2020 Class II Biological Safety Cabinet	Thermo Fisher Scientific, Waltham, Massachusetts, USA
Countess II FL Automated Cell Counter	Thermo Fisher Scientific, Waltham, Massachusetts, USA
Micro Star 12, microcentrifuge	VWR International, Radnor, Pennsylvania, USA
Megafuge 1.0R, benchtop centrifuge	Heraeus, Hanau, Germany

equipment	company
Sartorius Basic BA 210S FN, analytical balance	Sartorius, Göttingen, Germany
precision balances L4202 and L2001	VWR International, Radnor, Pennsylvania, USA
Vortex-Genie 2	Scientific Industries, Bohemia, New York, USA
PMR-30 platform rocker	Grant Instruments, Shepreth, United Kingdom
INCU-Line® ILS 4, shaking incubator	VWR International, Radnor, Pennsylvania, USA
Slide Moat™, slide hybridizer 240000	Boekel Scientific, Feasterville, Pennsylvania, USA
VWB2 12 water bath, 12 l	VWR International, Radnor, Pennsylvania, USA
PURELAB flex 2 Polisher, ultrapure type I water dispenser	Veolia Water, Paris, France

I.2.1.2 Consumables

Table I-4. Consumables.

consumable	company
4/8-well NUNC™ Lab-Tek™ II Chambered Coverglasses	Thermo Fisher Scientific, Waltham, Massachusetts, USA
4-well NUNC™ Lab-Tek™ II Chamber Slide™ Systems	Thermo Fisher Scientific, Waltham, Massachusetts, USA
96-well filter plate	Millipore, Merck, Darmstadt, Germany
NUNC 24-well cell culture plates	Thermo Fisher Scientific, Waltham, Massachusetts, USA
lumox® 24-well cell culture plates	Sarstedt, Nümbrecht, Germany
PHI HoloLids™	Phase Holographic Imaging, Lund, Sweden
Countess™ Cell Counting Chamber Slides	Thermo Fisher Scientific, Waltham, Massachusetts, USA
CELLSTAR®cell culture flasks with filter cap, T25/T75	Greiner Bio One International, Kremsmünster, Austria
Protein LoBind Tubes	Eppendorf, Hamburg, Germany
SafetySpace™ Low Retention Filter Tips	Sartorius, Göttingen, Germany
Costar® Stripette® serological pipettes	Corning, New York, USA
Menzel #1.5 coverslips, 12 mm diameter	Thermo Fisher Scientific, Waltham, Massachusetts, USA
Menzel microscope slides (76×26 mm)	Thermo Fisher Scientific, Waltham, Massachusetts, USA
ProLong Diamond Antifade Mountant with DAPI	Thermo Fisher Scientific, Waltham, Massachusetts, USA

consumable	company
4/8-well NUNC™ Lab-Tek™ II Chambered Coverglasses	Thermo Fisher Scientific, Waltham, Massachusetts, USA
IMMOIL-F30CC immersion oil	Olympus, Tokyo, Japan
alugram-DC-plates (40×80 mm, RP-18 W/UV_{254}, 0.15 mm)	Machery-Nagel, Düren, Germany
polygram-DC-plates (40×80 mm, SIL G/UV_{254}, 0.2 mm)	Machery-Nagel, Düren, Germany
Matrigel	Becton Dickinson, Franklin Lakes, New York USA
silica gel (0.032 mm–0.062 mm)	Machery-Nagel, Düren, Germany
Biozym Gold Agarose	Biozym Scientific, Hessisch Oldendorf, Germany

I.2.1.3 Buffers, Solutions and Reagents

All commercially available chemicals, reagents and solvents were ordered from Carl Roth (Karlsruhe, Germany), CheMatech (Dijon, France), Iris Biotech (Marktredwitz, Germany), Merck (Darmstadt, Germany), Sigma-Aldrich/Merck (Darmstadt, Germany), VWR International (Radnor, Pennsylvania, USA), AppliChem (Darmstadt, Germany), abcr (Karlsruhe, Germany) and Acros Organics (Geel, Belgium) and were of analytical grade and used as received without further purification. Deuterated solvents were obtained from Deutero (Kastellaun, Germany).

Table I-5. Buffer recipes.

buffer	recipe
phosphate-buffered saline (PBS) pH 7.4	1 tablet (Sigma-Aldrich, Merck, Darmstadt, Germany) per 200 ml ultrapure H_2O yields 0.01 M phosphate buffer, 0.0027 M potassium chloride, 0.137 M sodium chloride
sodium acetate (NaAc) buffer, 0.1 M	13.6 g sodium acetate trihydrate (Sigma-Aldrich, Merck, Darmstadt, Germany) and 5.75 ml glacial acetic acid (Sigma-Aldrich, Merck, Darmstadt, Germany) in ultrapure H_2O, final volume 1 l, pH 4.6
tris-acetate-EDTA (TAE) buffer 1×	50× TAE buffer (BioRad, Hercules, California, USA) diluted 1:50 in ultrapure H_2O
glycine buffer	50 mM glycine (Merck, Darmstadt, Germany) in ultrapure H_2O, pH 2.8
hybridization buffer for PNA FISH	75% formamide in 20 mM NaCl, 20 mM Tris-HCl, 0.1% bovine serum albumin (BSA), pH 7.4
washing buffer for PNA FISH	70% formamide in 10 mM Tris-HCl, pH 7.4
SSC buffer, 2× and 0.1×	premixed powder pack (Santa Cruz Biotechnology, Dallas Texas, USA) dissolved in 1 l ultrapure H_2O yields 20× SSC buffer (3 M NaCl, 300 mM sodium citrate), further diluted 1:10 and 1:100 in ultrapure H_2O

Table I-6. Solutions.

solution	recipe
paraformaldehyde (PFA) solution, 2% and 3.7% (v/v)	diluted in PBS from 37% formaldehyde solution (AppliChem, Darmstadt, Germany)
ethanol (EtOH), 70, 85, 100% (v/v)	EtOH diluted in ultrapure H_2O
goat serum, 10% (v/v)	normal goat serum (Abcam, Cambridge, United Kingdom) diluted 1:10 in PBS
NP-40, 0.002% (v/v)	NP-40 (IGEPAL CA-630, Sigma-Aldrich, Merck, Darmstadt, Germany) diluted 1:50000 in PBS
TritonX-100, 0.1% (v/v)	TritonX-100 (VWR International, Radnor, Pennsylvania, USA) diluted 1:1000 PBS
Tween-20, 0.05% (v/v)	Tween-20 (Sigma-Aldrich, Merck, Darmstadt, Germany) diluted 1:2000 in 2× SSC buffer
propidium iodide (PI) solution	1 mg PI (Thermo Fisher Scientific, Waltham, Massachusetts, USA) in 1 ml ultrapure H_2O
Mowiol	[466]

Table I-7. Specialty chemicals.

chemical	company
STAR 600-NHS-ester	Abberior, Göttingen, Germany
STAR 635P NHS-ester	Abberior, Göttingen, Germany
STAR RED NHS-ester	Abberior, Göttingen, Germany
HBED-CC-tris(*t*Bu)ester[1]	ABX, Radeberg, Germany
PSMA-10 ([Glu-urea-Lys(Ahx)]$_2$-HBED-CC)	ABX, Radeberg, Germany
sevoflurane	Abbott Laboratories, Chicago, Illinois, USA

I.2.1.4 Kits and Dyes

Table I-8. Biochemical kits.

kit	company
Effectene Transfection Reagent Kit	Qiagen, Hilden, Germany
Puregene Core Kit	Qiagen, Hilden, Germany
Telomere Length Assay Kit	Roche, Basel, Switzerland

[1] 3-(3-{[(2-{[5-(2-*tert*-Butoxycarbonyl-ethyl)-2-hydroxy-benzyl]-*tert*-butoxycarbonylmethyl-amino}-ethyl)-*tert*-butoxy-carbonylmethyl-amino]-methyl}-4-hydroxy-phenyl)-propionic acid

Table I-9. Live dyes.

live dye	company/reference
580CP-BG/-Halo	[29]
610CP-BG/-Halo/-BC	[29]
640SiRH-BG/-Halo/-BC	[32]
SNAP-Cell® 647-SiR	New England Biolabs, Ipswich, Massachusetts, USA
LysoTracker™ Green DND-26	Thermo Fisher Scientific, Waltham, Massachusetts, USA
MitoTracker® Green FM	Thermo Fisher Scientific, Waltham, Massachusetts, USA
SiR-Lysosome	Spirochrome, Stein am Rhein, Switzerland

I.2.1.5 Antibodies

Table I-10. Primary antibodies.

antibody	#	company
monoclonal mouse anti-TRF1	GTX10579	GeneTex, Irvine, California, USA
monoclonal mouse anti-TRF1	04-638	Merck, Darmstadt, Germany
monoclonal mouse anti-TRF2	05-521	Merck, Darmstadt, Germany
polyclonal rabbit anti-TRF2	NB110-57130	Novus Biologicals, Centennial, Colorado, USA
polyclonal rabbit anti-PMLIII	sc-5621	Santa Cruz Biotechnology, Dallas Texas, USA
monoclonal mouse anti-PSMA	SAB4200257	Sigma-Aldrich, Merck, Darmstadt, Germany

Table I-11. Secondary antibodies.

antibody	#	company
goat anti-rabbit-IgG coupled to Alexa Fluor 488	A-11034	Thermo Fisher Scientific, Waltham, Massachusetts, USA
goat anti-mouse-IgG coupled to STAR 600	2-0002-010-5	Abberior, Göttingen, Germany
goat anti-rabbit-IgG coupled to STAR 600	2-0012-010-2	Abberior, Göttingen, Germany
goat anti-mouse-IgG coupled to STAR 635P	2-0032-052-6	Abberior, Göttingen, Germany
goat anti-rabbit-IgG coupled to STAR 635P	2-0022-052-9	Abberior, Göttingen, Germany

antibody	#	company
goat anti-mouse-IgG coupled to STAR RED	2-0002-011-2	Abberior, Göttingen, Germany
goat anti-rabbit-IgG coupled to Atto 488	custom labeled	ATTO 488 NHS-ester (ATTO Technology, Amherst, New York, USA) coupled to goat anti-rabbit-IgG (111-005-003, Dianova, Hamburg, Germany)

I.2.1.6 Peptide Nucleic Acid (PNA) Probes

Table I-12. PNA probes.

PNA probe	sequence	company
TelC	$(CCCTAA)_3$-OO	PNA Bio, Thousand Oaks, California, USA
LacO	TTGTTATCCGCTCACAA-OO	PNA Bio, Thousand Oaks, California, USA

I.2.1.7 Plasmids

Table I-13. Plasmids.

plasmid	company/reference
pHTN HaloTag CMV-neo	Promega, Madison, Wisconsin, USA
pSNAPf	New England Biolabs, Ipswich, Massachusetts, USA
SNAP-CLC	[259]

I.2.1.8 Cell Culture

Table I-14. Cell culture reagents.

solution/reagent	company
Dulbecco's modified Eagle medium (DMEM) high glucose/GlutaMAX™/pyruvate	Gibco, Thermo Fisher Scientific, Waltham, Massachusetts, USA
FluoroBrite™ DMEM	Gibco, Thermo Fisher Scientific, Waltham, Massachusetts, USA
Roswell Park Memorial Institute (RPMI) 1640 medium	Gibco, Thermo Fisher Scientific, Waltham, Massachusetts, USA
fetal bovine serum (FBS)	Merck, Darmstadt, Germany
penicillin/streptomycin (100×)	AppliChem, Darmstadt, Germany
sodium pyruvate (100 mM)	Gibco, Thermo Fisher Scientific, Waltham, Massachusetts, USA
GlutaMAX™ Supplement (100×)	Gibco, Thermo Fisher Scientific, Waltham, Massachusetts, USA

solution/reagent	company
trypsin 2.5%, no phenol red (10×)	Gibco, Thermo Fisher Scientific, Waltham, Massachusetts, USA
trypsin 0.05%, ethylenediaminetetraacetic acid (EDTA) 0.02%, with phenol red (1×)	Sigma-Aldrich, Merck, Darmstadt, Germany
poly-L-lysine	Sigma-Aldrich, Merck, Darmstadt, Germany
Trypan Blue stain 0.4%	Invitrogen, Thermo Fisher Scientific, Waltham, Massachusetts, USA
dimethyl sulfoxide (DMSO), sterile	Sigma-Aldrich, Merck, Darmstadt, Germany

Table I-15. Composition of cell culture media.

medium	supplementation
DMEM++	DMEM high glucose/GlutaMAX™/pyruvate + 10% FBS + 1% penicillin/streptomycin
FluoroBrite++	FluoroBrite™ DMEM + 10% FBS + 4 mM GlutaMAX™
RPMI+++	RPMI 1640 medium + 5% FBS + 1% penicillin/streptomycin + 1% sodium pyruvate

Table I-16. Cell lines.

cell line	description	medium	reference
U2OS	human bone osteosarcoma epithelial cells (telomere length ~2-50 kb)	DMEM++	ATCC HTB-96
F6B2	human bone osteosarcoma epithelial cell line with three stably integrated bacterial *lac* operator (*lac*O) repeat arrays at the subtelomeric region (STR) of chromosomes 6q, 11p and 12q	DMEM++	[467]
HeLa	human cervical adenocarcinoma epithelial cells (normal telomere length, ~7 kb)	DMEM++	ATTC CCL-2
HeLa VST	human cervical adenocarcinoma epithelial cells with very short telomeres (~4 kb)	DMEM++	[468]
HeLa LT	human cervical adenocarcinoma epithelial cells with long telomeres (~20 kb)	DMEM++	[468]
LNCaP	PSMA-overexpressing androgen-sensitive human prostate adenocarcinoma cells	RPMI+++	ATCC CRL-1740
PC3	PSMA-negative human prostate adenocarcinoma cells	RPMI+++	ATCC CRL-1435

I.2.1.9 Animals

All animal experiments throughout the thesis complied with the current laws of the Federal Republic of Germany and the German Animal Welfare guidelines were followed.

Table I-17. Animals.

animal	company
BALB/c nu/nu mice, male	Charles River Laboratories, Wilmington, Massachusetts, USA

I.2.1.10 Software

Table I-18. Software.

software	company
Adobe Illustrator CC 22.0.1	Adobe, San José, California, USA
ChemDraw Professional 16.0.1.4	PerkinElmer, Waltham, Massachusetts, USA
Excel 2016	Microsoft, Redmond, Washington, USA
Fiji 1.52n	[469]
GraphPad Prism (version 7)	GraphPad Software, San Diego, California, USA
ImageJ 1.47v	[470]
Imspector 0.11.9825	Abberior Instruments, Göttingen, Germany
LabVIEW™ 2017	National Instruments, Austin, Texas, USA
Octave 5.1.0	[471]
Origin 2017	OriginLab, Northampton, Massachusetts, USA
Python 2.7.15 and 3.6	Python Software Foundation, Wilmington, Delaware, USA
SciPy (scipy.stats)	[472]

I.2.2 Methods

I.2.2.1 STED Microscope System

All confocal and STED data were acquired with a custom-built setup closely related to the one published by Görlitz *et al*. [473] (Figure I-10). It is controlled by a field-programmable gate array (FPGA) based PC board (PCIe-7852R, National Instruments) which guarantees real-time capability down to the nanosecond regime. The FPGA adjusts the pulse timing between excitation (master) and STED (slave) lasers, allows for time-gated detection, and manages beam scanning and focus control. It is operated by a custom application software written in LabVIEW (National Instruments).

The system features a picosecond pulsed supercontinuum laser (Solea, PicoQuant) and a pulsed 470 nm diode laser (LDH-D-C470, PicoQuant) for excitation. The white light laser offers a free choice of excitation wavelengths to individually adapt to the desired fluorophores. For stimulated depletion, a 775 nm pulsed fiber laser (Onefive Katana 08 HP, NKT) guarantees optical stability and reliability. The STED laser provides 700 ps pulses of > 37 nJ pulse energy and can be electronically triggered over a broad frequency range. The pulse repetition rate was set to 40 MHz for all experiments.

An acousto-optical tunable filter (AOTF) selects the desired excitation wavelengths out of the white light spectrum of the supercontinuum laser. The beam passes the AOTF three times in order to suppress efficiently any undesired wavelengths. For excitation of the dye combinations given in Table I-19, the wavelengths 600 nm and 650 nm were chosen. After the AOTF, the beams of the supercontinuum laser and the STED laser are jointly coupled into a polarization maintaining optical fiber while the path of the 470 nm laser runs independently.

Beam shaping is achieved by a segmented (easySTED) waveplate placed between the tube lens and the objective (HCX PL APO 100×/1.44 Oil CORR CS, Leica). While donut-focusing the STED beam, the waveplate leaves the polarization of all excitation wavelengths (mostly) unaffected and thus renders their beams normally focused. The easySTED implementation provides a robust, virtually alignment-free system.

A Quadscanner at the sideport of the microscope body (DMI6000 CS, Leica) beam-scans the sample. Placed in the intermediate image plane, the Quadscanner provides a stationary beam all the way to the side port making scan lenses obsolete and rendering the system compact, robust and effectively alignment-free. By avoiding beam shifting in the pupil, the Quadscanner guarantees a high-quality STED intensity zero over the entire FOV (80×80 µm).

A hexapod-like positioning system (SMARPOD 70.42, SmarAct) translates and rotates the sample in six degrees of freedom while guaranteeing high rigidity, linear repeatability, and absolute accuracy.

A directional beam splitter (DBS) guides the supercontinuum and STED laser light towards the microscope body and the fluorescence emission towards the detection path. The DBS combines a Faraday rotator with two polarizing beam splitters to separate by propagation direction rather than by wavelength. Thereby, it offers flexibility in the choice of excitation wavelengths but avoids degradation of the STED intensity zero. A 561 nm laser BrightLine® single-edge super-resolution laser dichroic beamsplitter (Semrock) separates excitation and fluorescence of the 470 nm beam path.

The detection path contains a motorized pinhole (MPH16, Thorlabs), which allows for flexible adaptation to the brightness of the sample by finding a compromise between signal and contrast. For all experiments, it was set to 125 µm, which corresponds to the size of one Airy. Detection is done via three avalanche photodiodes (APDs) (SPCM-AQRH-15/13-FC, Excelitas Technologies/PerkinElmer). After a 775 nm blocking edge BrightLine® shortpass filter (Semrock) to block the major proportion of the STED laser light, the following double filter combinations are used to guarantee comprehensive extinction of the STED laser light:

- APD1: ZT405/473-491/NIRrpc (Chroma Technology) and 525/50 nm BrightLine® single-band bandpass filter (Semrock)
- APD2: 2× 628/32 nm BrightLine® single-band bandpass filter (Semrock)
- APD3: 2× 708/75 nm BrightLine® single-band bandpass filter (Semrock)

The system is tailored to fluorophores with peak emissions between 600-700 nm. Excitation and depletion in the far-red spectrum are beneficial since scattering, autofluorescence and phototoxicity are reduced as compared to shorter wavelengths. The filter combination enables dual-color recordings of the dye combinations given in Table I-19 with virtually no crosstalk including the delicate combination of 610CP/640SiRH [32]. By using a single STED beam to deplete both excitation channels, their signals are inherently co-aligned and any influence from residual chromatic aberrations is excluded.

For regular diagnostics, the laser power was measured before the beam enters the microscope body using a digital optical power and energy meter (Thorlabs). As the laser beam passes the Quadscanner, further mirrors in the microscope body, the tube lens, and the objective, the laser power decreases due to reflection and transmission losses. An attenuation factor of approximately 0.36 was experimentally determined. The respective power range for excitation and depletion is given in the methods sections of the individual projects (II.4.7, III.4.7, IV.2.3 and IV.4.3).

Table I-19. Organic dye combinations for live cell and fixed cell STED imaging.

The dyes are ordered according to their excitation (exc) wavelength and their detection (det) window (APD2 – 628/32, APD3 – 708/75) of the STED system. The values for absorption (abs) and emission (em) are given for PBS, pH 7.4.

exc 600 nm / det APD2		**exc 650 nm / det APD3**	
dye	**abs/em [nm/nm]**	**dye**	**abs/em [nm/nm]**
580CP [29]	582/607	640SiRH [32]	641/662
610CP [29]	609/634		
Abberior STAR 600	604/623	Abberior STAR RED (KK114) [382]	638/655
		Abberior STAR 635P [382]	638/651

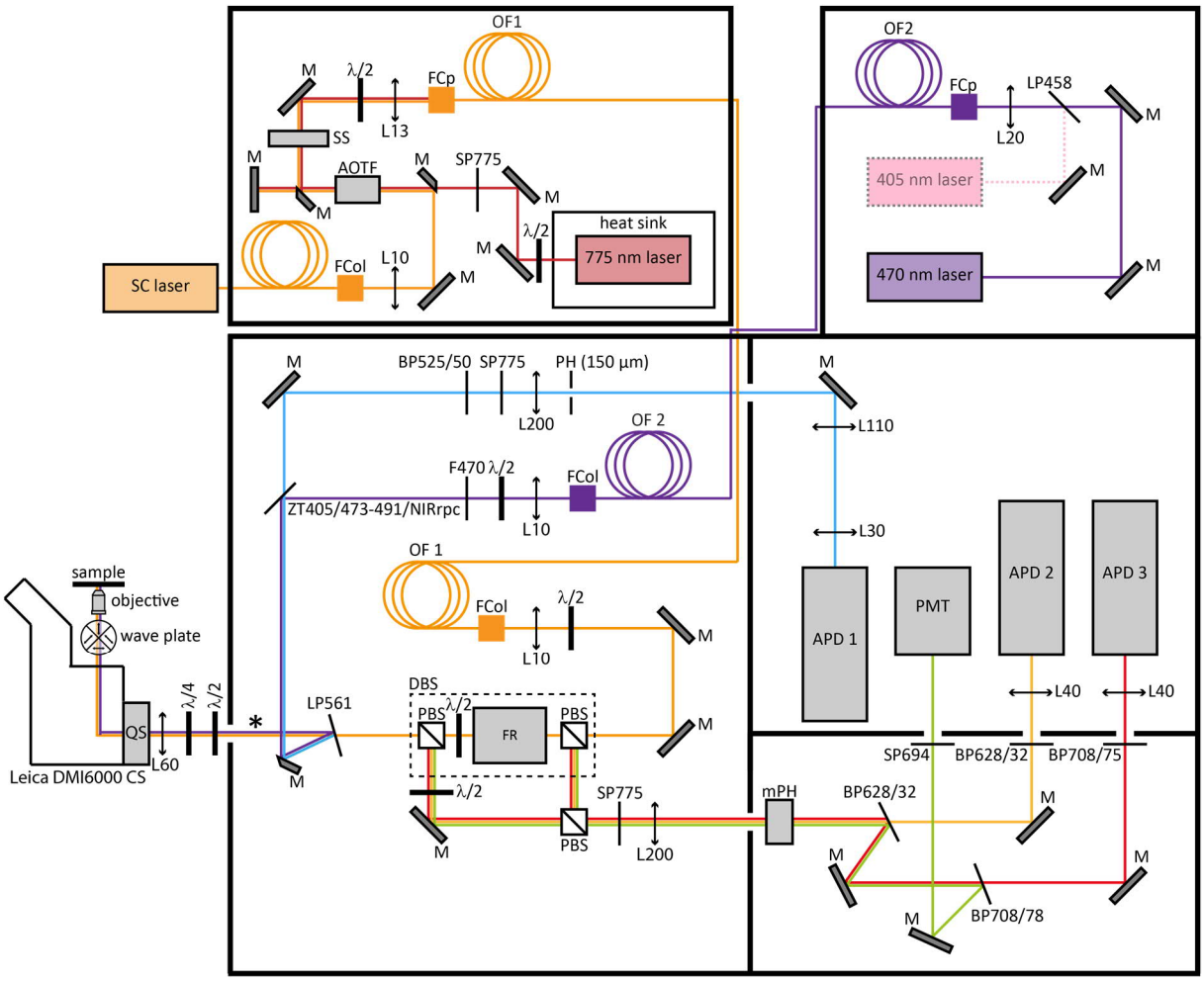

Figure I-10. Schematic description of the custom-built STED system.

The asterisk indicates the position of regular laser power measurements. SC – supercontinuum laser, SS – safety shutter, M – mirror, L – lens with focal length in mm, BP – bandpass filter with bandpass wavelength region given in nm, SP – shortpass filter with cutoff wavelength given in nm, LP – longpass filter with cutoff frequency given in nm, λ/2 – λ/2 plate, λ/4 – λ/4 plate, OF – optical fiber, FCp – fiber coupler, FCol – fiber collimator, DBS – directional beam splitter, PBS – polarizing beam splitter cube, FR – Faraday rotator, AOTF – acousto-optic tunable filter, QS – Quadscanner, (m)PH – (motorized) pinhole, APD – avalanche photodiode, PMT – photomultiplier tube.

I.2.2.2 Data Presentation

All image processing was performed in ImageJ 1.47v [470] and Fiji 1.52n [469] except for linear deconvolution and image smoothing. Unless otherwise stated, all confocal data shown are raw data and all STED data shown are background corrected and linearly deconvolved. Figure I-11 illustrates the post-processing steps on raw STED data for selected examples.

Background correction was performed by subtracting at most 10% of the maximum fluorescence signal. Linear deconvolution (Wiener filter) was performed with the Imspector software (Abberior Instruments) applying a 2D Lorentzian point spread function (PSF)

$$PSF(x,y) = \frac{\left(\frac{FWHM}{2}\right)^2}{(x-X)^2 + (y-Y)^2 + \left(\frac{FWHM}{2}\right)^2} \quad \text{(I-5)}$$

with X and Y determining the peak position and $FWHM$ being the PSF's full width half maximum in lateral dimension. All quantities are specified in compatible units of lengths, e.g. in nanometers. Linear deconvolution was applied only to the extent that data were smoothed, and noise was reduced but image resolution was not increased. Alternatively, smoothing was performed with a Gaussian low pass filter with a width of one pixel in the custom application software of the STED system.

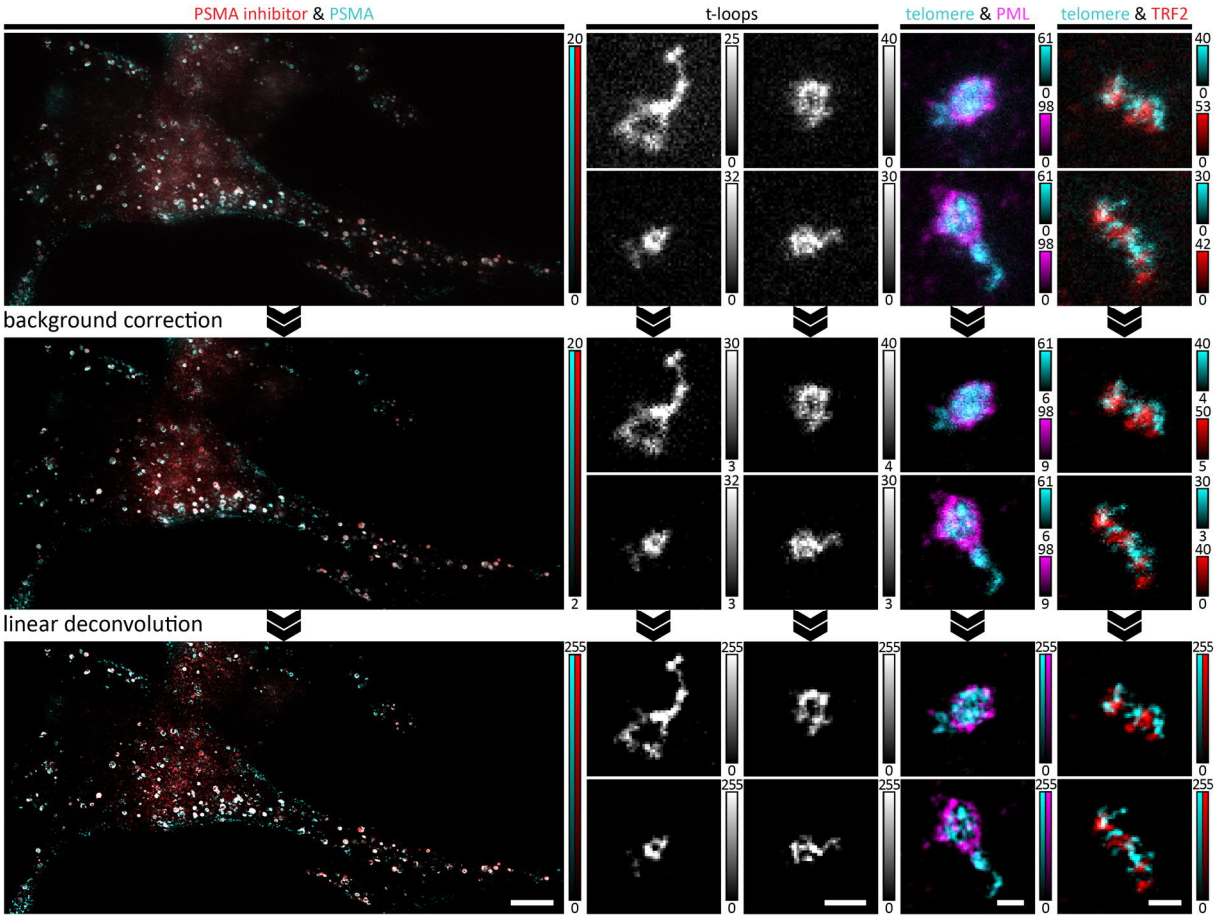

Figure I-11. STED image post-processing steps.

The post-processing steps are exemplified on STED images of PART II and PART III. First, the background is corrected by subtracting at most 10% of the maximum fluorescence signal of each channel. Second, the background corrected images are linearly deconvolved (Wiener filter) by applying a Lorentzian PSF. The respective FWHMs are given in the corresponding methods sections. From left to right: exemplary LNCaP cell STAR 600-immunolabeled for PSMA (cyan) and incubated with PSMA inhibitor (red), scale bar is 5 µm. Next: exemplary t-loops stained via TelC-KK114 PNA FISH, scale bar is 250 nm. Next: exemplary APBs stained for telomere repeats (cyan) via TelC-KK114 PNA FISH and for PML (magenta) via IF with STAR 600, scale bar is 250 nm. Next: exemplary telomeres stained via TelC-KK114 PNA FISH (cyan) decorated with TRF2 stained via IF with STAR 600 (red), scale bar is 250 nm. For abbreviations, see Definition of Abbreviations. For details, refer to respective PART.

Potential color shift between the 470 nm excitation channel and the 600/650 nm excitation channel was corrected for with a custom-written ImageJ routine that correlates the images using the plugin FD Math and shifts them based on the maxima found with the plugin Find Maxima. All line profiles on

STED and confocal data were drawn on raw data and averaged over several pixels (details are given in the individual methods sections II.4, III.4 and IV.2.3).

Data fitting and graphing was performed with Origin 2017 (OriginLab), all chemical structures were drawn with ChemDraw Professional 16.0.1.4 (PerkinElmer) and all figures were composed in Adobe Illustrator CC 22.0.1 (Adobe).

I.2.2.3 Statistical Aspects

All experiments were performed at least in triplicate and quantitative data are expressed as mean ± standard deviation (SD). The respective n-values are given in the corresponding figure or table captions. The Shapiro-Wilk test was used to test the data populations for normality [474]. For normally distributed data, statistical significance was assessed by unpaired, two-tailed Student's *t*-tests [475] or by unpaired, two-tailed Welch's *t*-tests in case of unequal sample sizes [476]. Gaussian error propagation was applied for calculations based on the measurement data. For non-Gaussian data populations, means were compared with the Wilcoxon-Mann-Whitney *U* test [477]. For comparing more than two data populations, the Kruskal-Wallis test was used in a first step to determine whether significant differences exist in general [478]. If so, the Dunn's test was performed as a *post hoc* test to compare all data populations with each other [479]. P-values < 0.05 were marked.

Statistical analysis was performed in GraphPad Prism (Version 7, GraphPad Software), Excel 2016 (Microsoft) and SciPy (scipy.stats) [472].

II – APPLICATION:

THE HUMAN TELOMERE CONFORMATION AT THE NANOSCALE

II.1 INTRODUCTION

As the canonical DNA replication machinery lacks the ability to complete DNA duplication until the very end of linear chromosomes, eukaryotic cells rely on telomeres to shield their genome from replication-associated shortening. Without self-protection, they would be recognized as sites of DNA damage and inappropriately treated by the DNA damage response (DDR) machinery. A comprehensive understanding of nature's solution to the end-protection problem remains elusive and contradicting findings regarding the role of telomere compaction are discussed in the literature [480-482].

Nonetheless, consensus exists that sequestration of the telomeres' 3'-overhang within lariat telomere structures contributes to end protection by masking the chromosome ends. T-loop formation and maintenance has been extensively investigated *in vitro* and mammalian t-loops have been visualized by EM [483, 484] and different fluorescence nanoscopy methods [485, 486], albeit after cross-linking and spreading. However, t-loops have so far not been visualized within intact cells. Moreover, the driving forces for telomere (de)compaction and clustering are not entirely understood and open questions remain concerning the influence of shelterins [480-482] and of the promyelocytic leukemia (PML) protein on the telomeric DNA conformation.

In tumor cells that elongate their telomeres via the telomerase-independent alternative lengthening of telomeres (ALT) mechanism [45], PML associates with telomeres to form ALT-associated PML (APB) complexes [487]. APBs are suggested to play an important role in ALT-related DNA recombination and repair synthesis, but the topology of APBs has not been visualized yet at nanoscale resolution. Investigating telomere conformation and organization in its native environment reduces the chances of investigating preparation artefacts and allows the collection of biological relevant data. Identifying structural differences between healthy and diseased cells may finally lead to a better understanding of structure-function relationships relevant for the deregulation of telomere maintenance in cancer and other telomere dysfunction related diseases and syndromes.

II.2 SURVEY OF THE FIELD

II.2.1 Human Telomere Biology

Human telomeres consist of 2-20 kb double-stranded TTAGGG tandem repeats serving as buffer material at the end of human linear chromosomes. They terminate in a G-rich 3'-overhang due to the unidirectionality of the DNA polymerase. Telomeric repeats are decorated with the six-membered shelterin protein complex. This `telosome' structure ensures genome integrity as it protects the chromosome ends from being processed as double-strand breaks by the DNA repair machinery [488]. At least seven different DDR pathways threaten telomeres but the shelterin complex uses distinct molecular mechanisms to individually block each pathway by targeting the respective initiation step of DNA damage signaling.

The human shelterin complex comprises TRF1 (telomeric repeat binding factor 1), TRF2 (telomeric repeat binding factor 2), RAP1 (repressor/activator protein 1), TIN2 (TRF1-interaction nuclear factor 2), TPP1 (TINT1 (TIN2-interacting protein 1)/PIP1 (POT1-interacting protein 1)/PTOP1 (POT1 and TIN2 organizing protein 1)) and POT1 (protection of telomeres 1) [489]. TRF1 and TRF2 form homodimers and bind with nanomolar affinity to duplex telomeric DNA while POT1 binds single-stranded telomeric DNA (Figure II-1a). TRF1, TRF2, TIN2 and RAP1 are ten times more abundant than TPP1 and POT1 suggesting a core complex of the four proteins [490].

In relation to the overall population of telomeric repeats, shelterin proteins are overabundant and thus, most telomeric DNA is assumed to be decorated [491]. However, the nucleosomal structure of telomeres seems to be unaffected by the presence of shelterin proteins [492]. Human telomeres carry the canonical core histone components, but the nucleosomal repeat length is short and nucleosomes are more mobile [493]. The nucleosomes display heterochromatin-associated histone marks that are similar but not identical to constitutive heterochromatin [494].

The detailed topological organization of the telomere repeats within the telosome is crucial. The 3'-overhang sequesters in an upstream region of the telomere, displacing the G-rich strand in a D-loop to form a lariat telomere structure that masks the chromosome end (Figure II-1b) [489, 495, 496]. As the position of invasion of the 3'-overhang is not strictly defined, the loop's size and tail length varies. The shelterin protein TRF2 is both crucial and sufficient for t-loop formation [485] and necessary for t-loop maintenance as it protects the tail-loop junction from enzymatic cleavage [491].

It is suggested that TRF2 promotes t-loop formation via the low affinity DNA interaction of its TRFH domain, which locally unwinds the double-stranded telomeric DNA by wrapping it around itself, thereby facilitating 3'-overhang invasion (Figure II-1c) [497]. However, the exact structure at the loop-tail junction remains elusive and the minimal telomere length for successful t-loop formation is not known. Indeed, t-loops exist throughout the cell cycle [498] but it is uncertain what fraction of the telomere population adopts this conformation effectively [491].

Telomere replication is performed by the canonical replication machinery and starts from a subtelomeric origin. It is challenged by the G-rich sequence of the telomeric repeats, which is likely to form quadruplex (G4) secondary structures, which potentially stall the replication fork. Yet, TRF1 removes these obstacles by indirectly unwinding G4 structures, promoting telomere replication [491].

However, with each cycle of replication, telomeres progressively shorten due to incomplete lagging strand synthesis, oxidative damage and other factors. Telomere erosion during cell division equips the cell with a `clocking' mechanism, which limits the maximum number of cell divisions. With increased aging, too short telomeres activate DNA damage signals that eventually induce replicative senescence thus setting the initial proliferative barrier to tumor formation [499].

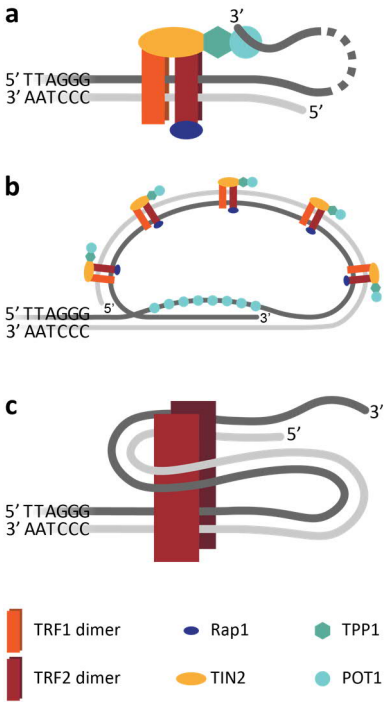

Figure II-1. Schematic illustration of the topology of the human telosome.

(**a**) The six-membered shelterin complex associates with double-stranded telomere repeats via TRF1 and TRF2 and with single-stranded telomere repeats via POT1. (**b**) In the t-loop conformation, the 3'-overhang is sequestered into an upstream region of the duplex-repeat array masking the chromosome end. (**c**) TRF2 presumably promotes t-loop formation by wrapping the telomeric DNA around its TRFH domain. The torsional stress potentially facilitates invasion of the 3'-overhang.

Telomere shortening likewise affects gene regulation. Telomeres exert repressive effects on proximal and distal gene expression, which decline with telomere erosion. The telomere position effect (TPE) is involved in transcriptional repression of genes close to telomeres and is induced by the spreading of heterochromatin to the subtelomeric regions (Figure II-2a) [500, 501]. The concept of telomere position effect over long distances (TPE-OLD) is similar to the long-range interactions within the genome, which modulate gene expression by bringing distal genomic regions into close proximity via 3D chromatin looping involving the CCCTC-binding factor (CTCF) and cohesion [502, 503]. Amongst the different 3D looping interactions of telomeres [504, 505], TPE-OLD mediates telomere interactions with interstitial telomere sequences (ITSs) in distal genomic regions involving the shelterin protein TRF2. Telomeres can only form interstitial telomere loops (ITLs) if they are long enough and ITS interactions are terminated upon telomere erosion [506, 507], thus modulating gene regulation in a telomere length dependent manner (Figure II-2b). Moreover, telomeres are often associated with the nuclear envelope via (in)direct interactions with lamins, the intermediate filaments associated with the inner membrane of the mammalian nucleus, and thereby contribute to higher-order chromatin organization [508].

Cellular growth arrest can be circumvented via the activation of oncogenes and the loss of function of tumor suppressor genes. Further telomere shortening leads to genome instability increasing the risk of cancer. In rare cases, the cells do not die but activate a telomere maintenance mechanism (TMM), which provides unlimited proliferation. A minority of tumors elongate their telomeres via the alternative lengthening of telomeres (ALT) pathway based on telomere recombination (refer to II.2.2) [509]. The vast majority of tumors reactivate and/or upregulate the telomerase reverse transcriptase (TERT) gene encoding for the catalytic component of telomerase [510, 511]. This ribonucleoprotein complex synthesizes telomeric DNA using its integral telomerase RNA component TERC. Telomerase activity in all somatic tissues is restricted to the early stages of human development and silencing occurs during fetal development [512].

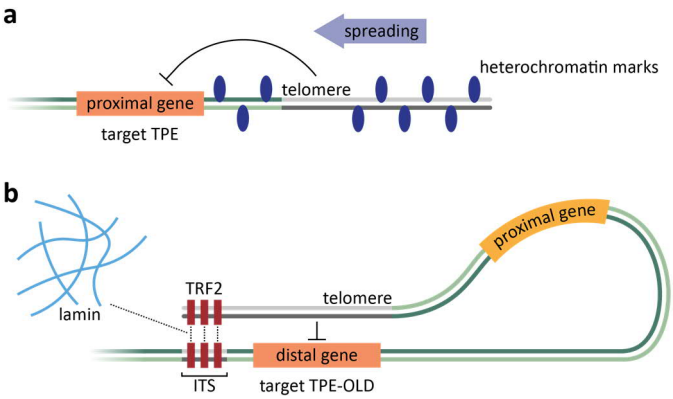

Figure II-2. Telomere position effects.

Telomeres control proximal and distal gene expression as a function of telomere length. With telomere erosion, the repressive influence declines. (**a**) In the classic TPE, telomeric heterochromatin spreads and invades the subtelomeric region, where it silences proximal genes. (**b**) In TPE-OLD, telomeres regulate the expression of distal genes via interactions with interstitial telomere sequences (ITS) mediated by TRF2 and lamins.

Telomere biology evolved to a highly important research field [45] not only due its key role in cancer [513, 514]. A variety of other medical conditions are based on genetic disorders related to mutations in either TMM proteins or telomerase components [515]. These telomere spectrum disorders, also called telomeropathies, display signatures of premature aging. Primary telomeropathies are caused by mutations within the TMM and often combine genetic anticipation and an early stage of onset. Secondary telomeropathies have overlapping syndromes with primary diseases, but are caused by mutations in DNA repair proteins or structural proteins that usually provide telomere preservation [516-518]. A popular example is the telomere-associated premature aging syndrome Hutchinson-Gilford progeria [519]. However, as the network of proteins associated with TMM is so extensive, new telomere disorders are currently and will continue to be identified [520].

A mechanistic understanding of disease pathology requires quantitative methods to measure telomere shortening. The terminal restriction fragment analysis (TRF) is the gold standard for assessing telomere length, although it is impeded by low throughput [521, 522]. In contrast, quantitative polymerase chain reaction (qPCR) allows for greater throughput, but only provides an average telomere length and, thus, it is not sensitive to the shortest telomeres [523, 524]. However, as the shortest telomeres are the ones to trigger senescence, assays sensitive to the shortest telomeres are crucial to understanding the correlation of age-associated pathologies with telomere erosion.

Newer techniques, namely universal single-telomere length analysis (U-STELA) [525] and telomere shortest-length assay (TeSLA) [521], measure the telomere length of every individual chromosome, and hence monitor changes even in the shortest telomeres. However, they again suffer from a lowered throughput. Alternative options include fluorescence *in situ* hybridization (FISH) [526, 527]. It guarantees higher throughput but depends on probe hybridization kinetics and suffers from a detection limit for the shortest telomeres [521, 522]. Yet, FISH is an extremely powerful technique for imaging of telomeres via fluorescence nanoscopy (refer to II.2.3.1).

II.2.2 Alternative Lengthening of Telomeres

The TMM type of a tumor partially correlates with the tumor origin. ALT activity is often found in tumors of mesenchymal and neuroepithelial origin like osteosarcomas, liposarcomas or astrocytomas, but rarely occurs in carcinomas [528, 529]. Only 10-15% of all human cancers employ the ALT pathway to elongate telomeres in the absence of telomerase via DNA recombination and repair processes [509]. ALT-positive tumors feature a set of hallmarks comprising

- a heterogeneous telomere length within one cell [530],
- a globally reduced level of telomere compaction compared to telomerase-positive cells [531],
- extrachromosomal telomeric repeats (ECTRs) [532],
- C-rich 5' overhangs [533],
- mutations of the alpha thalassemia/mental retardation syndrome X-linked (ATRX) chromatin remodeler [534],
- genome instability [535],
- an elevated level of telomere recombination [536],
- increased telomere sister chromatid exchange (T-SCE) [536] and
- the presence of APBs [537, 538].

ECTRs are generated by homologous recombination events and exist in both linear and circular forms [484, 532, 539]. It is suggested that C-rich, (partially) single-stranded telomeric $(CCCTAA)_n$ DNA circles serve as a template for telomere extension in rolling-circle replication [540]. Together with APBs, C-circles are accepted as robust biomarkers for ALT activity [541, 542]. APBs are associations of PML nuclear bodies (PML-NBs) with telomere repeats and, like ECTRs, are solely found in ALT-positive cells.

PML-NBs occur as distinct, spherical subcompartments in the cell nucleus [543]. Imaged with 4Pi microscopy, they display a diameter of approximately 0.2-1.0 µm and a diameter-independent shell thickness of 50-100 nm [544]. Their number varies with cell type, cell cycle phase, differentiation phase and various stimuli, but totals between 5-30 PML-NBs per cell [545]. Excluding disease related exceptions, normal PML-NBs do not contain nucleic acids. The key components of PML-NBs are PML and SP100 (speckled 100 kDa). Both proteins are not tightly bound, but rather exchange steadily [546] and more than 100 other factors have been identified that transiently associate with PML-NBs [547]. These multi-protein complexes are sumoylation hotspots [548]. Post-translational modifications by the small ubiquitin-like modifier (SUMO) equip PML and SP100 with SUMO interacting motifs (SIMs) that allow non-covalent linking with other SIM-containing proteins thereby promoting assembly and stability of PML-NBs. Sumoylation is mediated by the interplay of several enzymes including among others the SUMO E3 ligase MMS21 (methyl methanesulfonate-sensitivity protein 21) [549].

The association of PML-NBs with telomeres in ALT-positive cells occurs presumably also in a SUMO-SIM-interaction-dependent manner, but only for a subset of telomeres and PML-NBs within one cell. Upon APB formation, PML-NB components like PML, SP100 and SUMO as well as telomere-associated proteins such as the shelterin complex are also included into APBs. As imaged with 4Pi microscopy, the entire telomere is enclosed in the PML shell and fully occupies the PML-NB without significantly changing its overall diameter or thickness. APBs are suggested to promote telomere lengthening via repair-associated DNA synthesis [550], as depletion of APBs by long-term PML knockdown promotes telomere erosion in ALT cells [551]. Nevertheless, the molecular and mechanistic details of the ALT pathway are not yet comprehensively understood. However, many key players have been identified including the shelterin complex [552], the SUMO E3 ligase MMS21 [553], several DNA repair proteins [554] and proteins from the heterochromatin protein 1 (HP1) family [555].

It is assumed that partial telomere deprotection is crucial for ALT-related repair processes [556, 557]. While complete TRF2 deletion leads to genome instability, which is apparent in the short term in telomere attrition via T-SCE [558] and in the long term in chromosome fusions via non-homologous

end joining (NHEJ) [532, 559], PML only reduces TRF2 binding thereby creating a favorable intermediate state for ALT. As TRF2 inhibits the ataxia-telangiectasia mutated (ATM) kinase, a central DDR regulator, the reduced TRF2 population in APBs initiates the DDR machinery. Senescence and cell cycle arrest are prevented since ALT activation also coincides with the loss of normal p53 function [560]. PML is further suggested to mediate clustering and compaction of telomeres inside APBs [551]. However, controversial findings exist on the role of (de)compaction and DDR signaling [480-482].

Certainly, APB formation is not sufficient to trigger ALT activity as other deregulation events are likewise involved. APBs rather emerge with ALT initiation, which is presumably connected to several loss of function events affecting the DDR pathway and the telomeric chromatin state [537]. However, exceptions in the form of telomerase-independent telomere maintenance in the absence of APBs and/or other classic ALT hallmarks are known to occur, suggesting the existence of potentially more than one ALT mechanism. While the canonical ALT pathway involves APBs, ECTRs, T-SCEs and a heterogeneous telomere length, non-canonical ALT pathways lack at least one of these classical ALT features [561-563]. For the canonical pathway, T-SCE and homologous recombination dependent DNA synthesis have been proposed as mutually non-exclusive mechanisms for telomere elongation [487]. Different templates for recombination comprise the respective telomere itself via t-loop formation, the telomere of the sister chromatid, the telomere of another chromosome and presumably ECTRs [538, 541, 564, 565]. It is suggested that break-induced telomere synthesis is the underlying mechanism of ALT homologous recombination with a specialized replisome unidirectionally synthesizing long tracts of nascent telomeric DNA [566].

In summary, the following mechanism of APB-mediated telomere lengthening has been proposed (Figure II-3) [551]:

- In a first step, PML encases telomeres and induces compaction and clustering of telomeres and potentially ECTRs [567].
- In a second step, the associated telomeres are partially depleted of TRF2 potentially involving post-translational sumoylation by MMS21 [553].
- In a third step, ATM activation triggers DDR [568, 569].
- In a fourth step, telomeres are elongated via repair-associated DNA synthesis and homologous recombination enabled by telomere clustering.
- Last but not least, APBs disassemble and the extended telomeres regain full TRF2 decoration and thus, protection from DDR.

Indeed, TMMs present an ideal target for clinical purposes and approaches inhibiting telomerase activity have in fact already led to clinical applications [570-574]. However, exploiting ALT key players as targets for diagnostics and therapeutics is challenged by the complexity of the ALT mechanism and by the heterogeneity of ALT tumors [542]. So far, APBs have only been used as a prognostic marker to a very limited extent [575, 576], but they potentially represent a novel target for therapeutics, as disruption of APBs reduces the proliferation potential of tumor cells using the canonical ALT pathway. Moreover, cell populations within initially strictly ALT-negative tumors can transform under treatment with telomerase inhibitors to ALT-positive cells [577]. Thus, comprehensive understanding of the molecular and mechanistic details of the ALT pathway is crucial for the identification of potential diagnostic, prognostic and therapeutic strategies for the respective tumors [542].

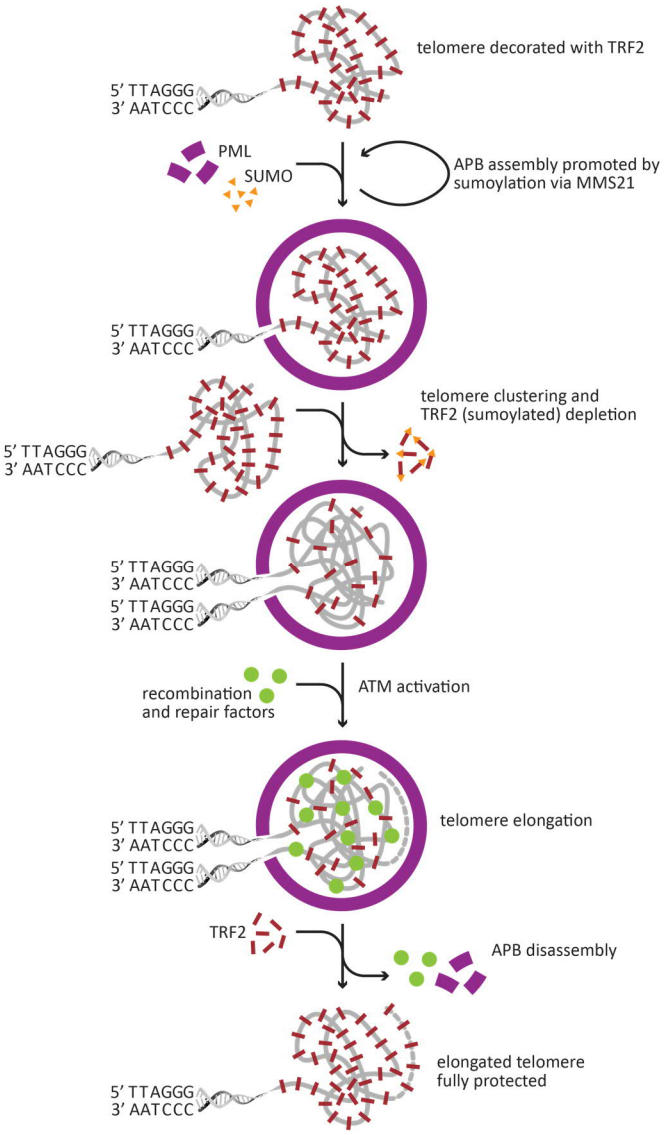

Figure II-3. Proposed mechanism of APB-mediated telomere lengthening in ALT cells.

Before APB formation, telomere protection is ensured by extensive TRF2 (and thus shelterin) decoration. APB assembly is triggered via the sumoylation of telomeric proteins, PML and other APB components by the SUMO E3 ligase MMS21. A sumoylation feedback loop is established through SUMO-SIM interactions. APB formation induces clustering of telomeres (presumably also ECTRs) and promotes partial depletion of TRF2. Telomere deprotection by partial TRF2 depletion is assumed to involve post-translational modifications by the SUMO E3 ligase MMS21. These changes lead to ATM activation, DDR signaling and recruitment of recombination and repair factors to the APB. In the functional APB, telomere elongation occurs via DNA repair processes, non-replicative DNA synthesis and homologous recombination. After telomere extension, the APB disassembles and TRF2 binding is increased thereby reestablishing a fully protected telomere.

II.2.3 Chromatin Imaging

As nuclear structure and nuclear function are two sides of the same coin, any changes in higher-order chromatin organization are either followed or preceded by changes in nuclear function. Therefore, sophisticated imaging strategies for chromatin are highly valuable for the investigation of nuclear structure-function relationships. First insights into nuclear organization were gained with EM [578-580] and current, specialized EM approaches still have and will maintain an essential role in the chromatin imaging field [581-585]. Besides EM, major progress must be attributed to fluorescence nanoscopy techniques currently revolutionizing structure-function studies, as they add specificity combined with the options of multicolor and live imaging [37, 586-589].

By now, most chromatin imaging studies applying advanced fluorescence microscopy or fluorescence nanoscopy techniques have either used SIM [590-592] or SMLM [339, 593-595], as most established DNA labeling strategies require no to only little adaptation to these methods. However, both techniques suffer from background which is drastically elevated by out-of-focus signal when imaging global chromatin with widefield illumination. Yet, this limitation can be overcome by combination with

smart illumination schemes like TIRF or LSFM [192, 596]. In contrast, STED nanoscopy inherently provides optical sectioning, but has been applied only very little in chromatin imaging [353, 597, 598] (for details on the individual imaging modalities, refer to I.1.2, I.1.3 and I.1.5).

II.2.3.1 PNA FISH

FISH has opened the door for cytogenetics to enter the molecular era and multicolor 3D DNA FISH has established itself as the workhorse for sequence specific imaging of chromatin structures and organization [599]. Primarily, FISH is a very general technique based on the hybridization of fluorescently labeled oligonucleotides to their complementary target structures via Watson-Crick base pairing and thus requires denaturation of double-stranded DNA. FISH probes are traditionally generated in a `top down' approach in which genomic DNA fragments of the locus of interest are amplified yielding random short DNA target probes. In the newer `bottom up´ approaches, synthetic oligonucleotides are designed against known sequences, which are often bioinformatically chosen from sequenced genome data [600]. In principle, the probe can be conjugated via a short linker to any desired organic dye, not only rendering DNA FISH highly adaptable to the imaging modality of choice but also placing the fluorophore only a few atoms away from the target structure.

However, as the probe to dye stoichiometry is generally 1:1, basic FISH suffers from an unfavorable SNR for low copy-number targets. Oligopaint amplifies the signal by equipping the probe with non-hybridizing, flanking regions of non-genomic sequences that can be additionally targeted by dye-labeled, complementary, secondary oligonucleotides [601]. With respective probe design, the binding kinetics of the secondary oligonucleotides can be adapted for BALM imaging [602, 603]. Molecular beacon FISH (mbFISH) avoids the background from unbound probes by incorporating a quencher in addition to the fluorophore at the opposite probe end. In the unbound state, the molecular beacon forms a hairpin structure, which brings quencher and fluorophore in close proximity allowing for efficient quenching. Upon binding, the hairpin structure resolves, and fluorescence is resumed [604].

An alternative approach to enhance the performance of DNA FISH is the application of peptide nucleic acid (PNA) probes instead of regular oligonucleotides [605]. This synthetic nucleic acid analogue features a radically altered backbone structure with the sugar-phosphate backbone being replaced by N-(2-aminoethyl)glycine (AEG) units linked by peptide bonds. The natural nucleobases are covalently attached to the backbone via carboxymethyl spacers and thus allow for Watson-Crick base pairing with DNA or RNA. PNA does not occur naturally, but the AEG backbone is found in cyanobacteria and is hypothesized to be the first genetic molecule for life on earth [606]. For FISH, PNA probes are superior to oligonucleotide probes as they provide higher sequence specificity, improved stability, enhanced reproducibility, and lower background. Moreover, PNA probes depend less on the ionic strength of the medium and PNA/DNA duplexes display higher melting temperatures than the corresponding DNA/DNA duplex. The enhanced affinity is at least partially attributed to the neutrally charged AEG backbone, which avoids electrostatic repulsion with its complementary DNA strand [607, 608]. The improved sequence specificity leads to an elevated level of mismatch intolerance and can be translated into shorter probes. Consequently, more dye is recruited to the target structure improving the image SNR [609].

PNA is highly resistant to cleavage by chemicals and in particular by enzymes, as PNA is bio-orthogonal and can withstand both nucleases and proteases. Besides locus-specific chromatin imaging, PNA probes thus provide valuable diagnostic [610-612] and therapeutic [610, 611, 613-616] tools including anticancer, antisense, antigene, antibacterial and antiviral agents with a superior lifetime *in vivo*. The development of modified PNA derivatives has improved the suitability for structure-function studies and medical and biochemical applications [617]. The introduction of chirality into the AEG backbone at the γ carbon atom provides γPNA probes with enhanced affinity and thus increases strand invasion capability. Due to their right-handed helical structure, which already preorganizes the probe for hybridization with its complementary target, γPNA probes can virtually invade any double-stranded DNA sequence [618-621]. Yet, a general problem is the poor membrane permeability and thus limited cellular uptake. To improve delivery into the cell, several measures can be taken including AEG backbone modifications, coupling to cell penetrating peptides or glass bead loading [622].

Using carefully adapted FISH protocols, PNA FISH allows for good preservation of key nuclear characteristics and ultrastructures [590, 623]. However, the overall aim is to either make DNA FISH truly live cell compatible or replace FISH experiments in fixed cells with equally powerful multicolor live cell experiments [624].

II.2.3.2 Alternative Chromatin Targeting Strategies

To visualize definite loci in living cells, the sequence specificity of certain DNA binding proteins must be exploited. Histones restricted to a certain genome region (e.g. centromeres) and other specifically binding proteins characteristic for defined genomic elements can be fused to FPs or self-labeling tags [625-627]. In case the region of interest does not offer an individual protein decoration, artificial target loci (e.g. *lac*O or *tet*O repeats) can be inserted and labeled with the respective transcription factor (e.g. Lac or Tet repressor) fused to FPs or self-labeling tags. Such repressor-operator assays can be either randomly introduced or site-specifically inserted via genome engineering [625-627]. Along the same line, the ParB/INT system is based on the insertion of a 1 kb small INT sequence with ParB not only specifically binding to INT but additionally oligomerizing and thus amplifying the signal [628]. In contrast to targeting strategies relying on the insertion of artificial sites, a series of modular proteins with the ability to specifically recognize DNA sequences permit the targeting of endogenous elements, namely zinc finger proteins (ZFPs) [629, 630], transcription activator-like effectors (TALEs) [631-633], and CRISPR/Cas9 [634-636]. These proteins are established scissors in genome editing, but in the absence of the active form of their nucleases and fused to FPs or self-labeling tags, they offer powerful tools for locus-specific chromatin labeling.

To visualize the global nuclear structure, several sequence unspecific chromatin labeling approaches have been established. Organic dyes either intercalating into DNA or binding the minor or major groove allow for direct chromatin imaging [37, 184, 353, 586, 637-639]. In principle, many sequence independent DNA stains are compatible with SMLM as they are either photoswitchable or transiently binding. Yet, most suffer from low brightness, low photostability and/or low cell membrane permeability. Moreover, intercalating dyes may induce DNA unwinding and elongation [640, 641], potentially interfere with cell cycle progression and initiate DDR in live cell imaging [642]. An

alternative approach for high density, direct labeling of nuclear chromatin, is given by click chemistry with a clickable nucleotide analogue metabolically incorporated into the chromosomal DNA [587, 643]. Furthermore, globally abundant, DNA associated proteins like histones can be targeted via IF [588, 594], with FPs [644] or self-labeling tags [42, 327] in live and fixed cells (for details on targeting strategies in general, refer to I.1.6.2). A pragmatic alternative is label free imaging of chromatin using the intrinsic nucleotide fluorescence [645].

II.2.3.3 Telomere Imaging

As telomeres are unambiguously identified by their repetitive sequence, telomere imaging has been revolutionized by PNA FISH, enabling detailed probing of location, recombination and conformation [522, 622, 646]. The telomere length can be measured via quantitative FISH (Q-FISH), combining the power of PNA probes with software analysis [647, 648]. In general, PNA FISH is limited to fixed samples, but exceptions prove the rule and PNA probes attached to telomeres have been used to observe mitosis in living cells [622]. Telomere PNA FISH is usually performed with organic dyes and in combination with SMLM, reaching an effective image resolution of 20-30 nm [480, 481, 485, 486]. Fewer studies have applied STED, achieving effective image resolutions of only > 50 nm. The fluorophores used, however, were significantly less suitable compared to the current STED dyes of choice [486, 649, 650].

Attaching quantum dots (QDs) to PNA provides photostable telomere probes for SMLM with narrow emission bands ideal for multicolor imaging and without the need for special blinking buffers or a second laser to enable blinking [651]. A more exotic conjugation combines a gold nanoparticle and an organic dye in a dual purpose PNA probe uniting X-ray fluorescence (XRF) for telomere length quantification with SMLM for assessing the biophysical nanometer dimensions of telomeres [652]. Telomere PNA FISH has revealed relevant differences in telomere biology between normal and cancer cells and interesting aspects of DDR at telomeres [567, 653, 654]. It has enabled imaging of human and murine t-loops with STORM, STED, SIM and Airyscan, but only after cell nuclei disruption and telomeric DNA spreading [485, 486, 655]. The first visualization of t-loops was achieved with EM [483] and shortly afterwards with AFM [656], but in both cases also only for isolated human and murine telomeres (Figure II-4).

Imaging of telomeres in living cells is often realized via tagging TRF2 (less often TRF1) with FPs [482, 622, 657, 658]. TALE-based or CRISPR/Cas-based targeting strategies offer a more sophisticated but more complex alternative. While rationally engineered TALEs recognize telomere repeats via a two-amino-acids-one-base-pair code, a single guide RNA (sgRNA) complementary to the telomeric repeats directs the catalytically inert Cas9. Certainly, TALE [631, 632] and Cas9 [659, 660] fusion constructs with FPs or self-labeling tags are frequently applied. Yet, with the CRISPR/Cas-system, the sgRNA can be alternatively labeled with an organic dye and transfected allowing for STED imaging in living cells [661]. A rather exotic option is the tandem hairpin pyrrole-imidazole polyamide probe, a minor groove binder, specifically targeting telomeric DNA. It can be flexibly conjugated to the desired organic dye for labeling telomeres without DNA denaturation and thus is potentially applicable in living cells [662].

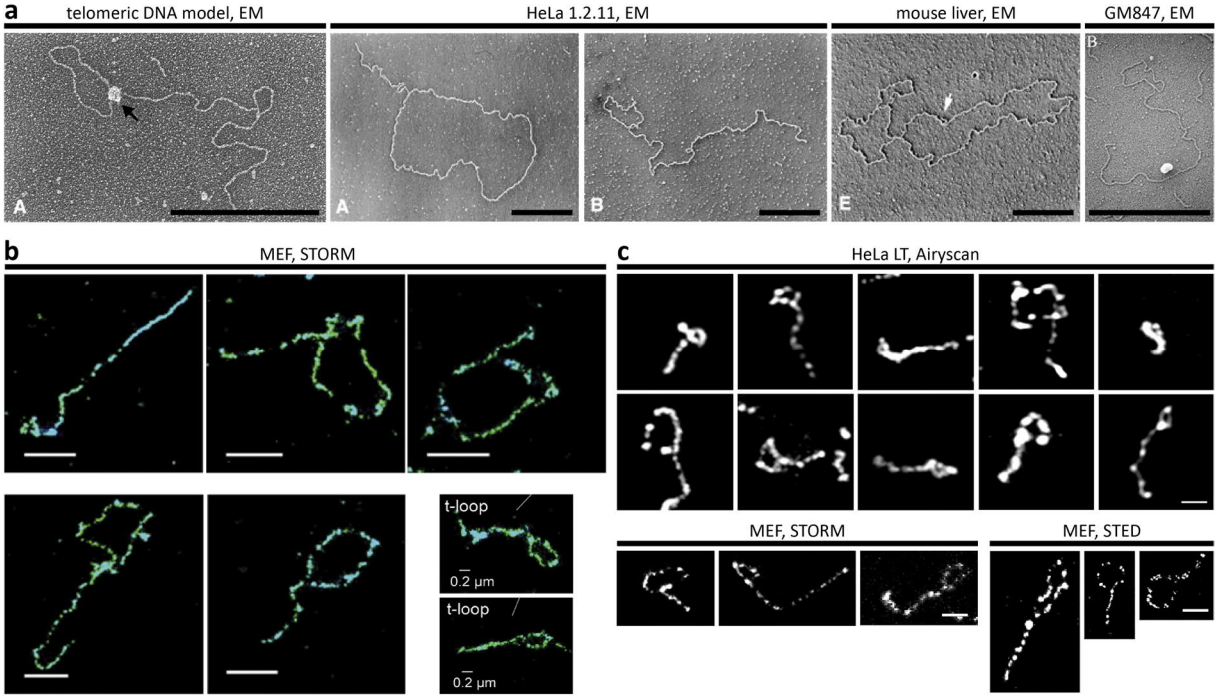

Figure II-4. T-loops as imaged by EM, SMLM, STED and Airyscan microscopy after crosslinking, isolation and spreading.

Until now, t-loops have only been visualized for human and murine telomeres after psoralen crosslinking, disruption of cell nuclei and spreading of telomeric DNA onto a surface. (**a**) EM micrographs of t-loops as imaged by Griffith *et al.* [483] and Cesare *et al*. [484]. From left to right: synthetic telomeric DNA model with TRF2 binding restricted to the loop-tail-junction (black arrow); t-loops from HeLa 1.2.11 cells; t-loop from mouse liver with a short tail (white arrow); t-loop from ALT-positive GM847 cells. All scale bars are 1 kb. (**b**) STORM images of murine t-loops from MEF cells as imaged by Doksani *et al*. [485]. Unless otherwise stated, scale bars are 1 µm. (**c**) Airyscan, STORM and STED images of human and murine t-loops as imaged by Van Ly *et al*. [486]. All scale bars are 1 µm. Figure adapted from [483-486].

II.2.4 Deep Learning in Fluorescence Microscopy

Artificial intelligence (AI) based on deep learning (DL) is slowly invading the field of fluorescence microscopy bringing along the potential to sustainably shape the way data acquisition and image analysis is performed [663]. AI replicates the human ability of recognizing meaning in patterns and adapting prior knowledge to new situations. Machine learning (ML) belongs to AI and extracts relevant information out of large data sets to make predictions or decisions on unseen data [664]. DL based on neural networks (NNs) is in turn a part of ML and is currently becoming increasingly popular as an image classification tool with super-human capabilities [665].

II.2.4.1 Neural Network Basics

While a classic algorithm converts the input data to output data via a known routine with defined rules and parameters, a NN is initially not only confronted with an input data set but additionally with the corresponding desired output (ground truth). After learning from these training data how to map each input into its corresponding output, a NN is subsequently treated with unseen input data and in the process of inference, creates the output of interest (Figure II-5). The generation of the training data

and the training of a NN are the crucial and time-consuming steps. In general, the more comprehensive the training data are, the higher the NN's prediction accuracy is in the end. Still, data augmentation can be used to supplement the training data [663].

NNs consist of complex networks of connected `neurons´ arranged in `layers´. A neuron can be described as a mathematical function featuring adjustable parameters. A layer is the collection of neurons that receive the same input data and operate together passing the output to the subsequent layer. The input layer contains the raw data, the output layer presents the result(s) and the hidden layers do the computation, including nonlinear operations, in between. With each additional layer, the NN depth increases, the representation of the data gains more abstraction, and more complex information can be extracted [664, 665]. Especially for deep NNs, the danger of over-fitting the data, i.e. imprinting the entire training data set instead of learning generalizable features, potentially weakens the predictive power. Thus, the NN architecture must be reasonably adapted to the training data set and during training, the NN performance must be monitored with an unseen validation data set [663].

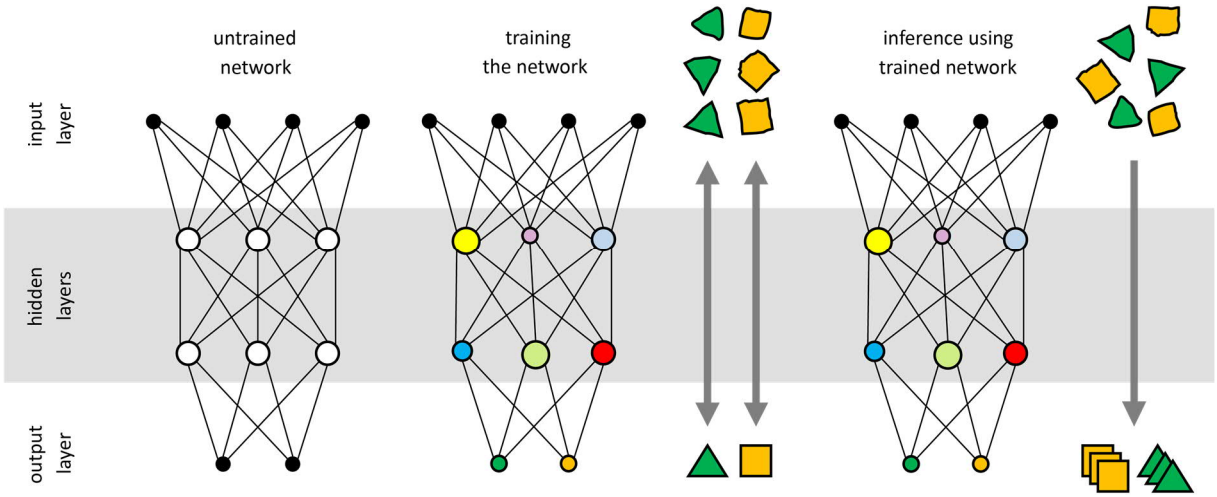

Figure II-5. Schematic of neural network architecture, training and inference.

The neural network design (i.e. number of hidden layers, neuron activation functions) is determined by its future purpose (i.e. data input, desired data output). Network training is performed by providing the desired pairs of input and output data (training data) and determines the neuron input weights and the neuron bias threshold by minimizing the cost function. During inference, the trained network determines from a given input data set the output that is best compatible with the training set.

Certainly, the deeper the NN is, the more parameters it contains and the less trivial its training becomes. For deep NNs, up to millions of parameters must be iteratively adjusted to match the output with the training data to the best possible extent. The source of discrepancies between the output and training data are difficult to localize in the NN structure, but the backpropagation method delivers corrections to the contributions of individual neurons [666]. Subsequent adaptation of the neuron's parameters is achieved via a gradient descent method. Often, the stochastic gradient descent is applied, which iteratively uses a random example from the training data to adjust the neuron's parameters [667].

For image analysis including feature recognition, convolutional NNs (CNNs) are particularly important. Here, successive feature extraction is often combined with data reduction. Convolutional layers extract

image features by performing convolutions on the input image and following pooling layers simplify the feature representation by reducing the number of pixels. The result is a barcode like simplified version of the input image from which the CNN infers the desired output [664, 668].

II.2.4.2 Neural Network Applications in Fluorescence Microscopy

The application of NNs in the field of fluorescence microscopy promises to overcome current limitations in the interdependence of phototoxicity, temporal resolution, spatial resolution, SNR and live cell imaging and to enable unbiased high-throughput analysis, extraction of relevant but complex information, and the handling of big data (for details on current challenges in fluorescence nanoscopy, refer to I.1.2 and I.1.5).

In image segmentation, every pixel of the image is assigned to a structural category, for example signal and background [669, 670]. Thus, NNs are applied to segment cells in co-cultures of multiple cell types [671] or in histopathology with clinical relevance [672-674]. Segmentation is often followed by classification to recognize relevant features in an image and assign an identity. As manual annotation is very time-consuming, biased and limited in throughput, NN classification is highly valuable, e.g. in biomedical imaging for cancer detection [675-677], or for the identification of cellular state or fate from transmitted light data [678, 679].

Furthermore, NNs allow for artificial labeling, i.e. the extraction of cellular structures like plasma membrane, nuclear membrane and mitochondria from label free images. While the task itself is similar to segmentation, the training data strongly differ. For artificial labeling, the respective NN learns with paired images of brightfield and fluorescence data from the same cell. Light sensitive samples in long term live cell imaging strongly benefit from this type of NN-based structure extraction [680, 681] as well as from NN-based image restoration. Here, NNs are applied to increase the SNR and/or the spatial image resolution. The respective NN is often trained with paired images of the same cell acquired at high and low SNR or at high and low spatial resolution [307, 308, 682]. Image restoration can be used to reduce the photon burden in STED imaging [308] or allow for faster data acquisition in densely labeled SMLM samples [683, 684].

The output of any DL application in fluorescence microscopy must be critically considered, especially in terms of resolution enhancing image restoration, as the presence of artefacts in the output images cannot be excluded *per se*. The rigorous identification of potential artefacts is crucial [112, 685]. Yet, only input and output are accessible, but the `in-between´ is not. Due to the abstraction of data representation within deep NNs, the interpretation on how the NN created the output is very difficult. Moreover, the NN performance strongly depends on the quality of the training data, which is usually manually composed by the user. Any bias in the training data will automatically be adopted by the NN.

However, reasonably handled, DL is an extremely versatile and powerful tool to address current challenges of fluorescence microscopy. At the moment, the field of AI is undergoing exponential development and many areas of the latest AI research have not yet been transferred to the imaging community. With the fusion of fluorescence microscopy and AI in its infancy, the application of DL is still bound to experts but the future will lower the accessibility barrier for non-expert users [663].

II.3 AIM

Telomere conformations have direct implications on telomere properties and functions. Thus, dissecting structural features of telomeres and associated proteins in their native cellular environment at the nanoscale opens up new avenues for understanding the role of the respective component in either aging, tumor suppression or telomere maintenance in cancer. Fluorescence nanoscopy has already significantly contributed, but open questions remain: To which extent do t-loops represent the native telomere conformation? Which other telomere conformations exist? How is the telomere conformation triggered? What causes telomere (de)compaction and clustering? Extending the knowledge in these fields will pave the way for the development of alternative diagnostics and treatments for telomere dysfunction related diseases.

The aim of this project was to elucidate the topology of telomere repeats, telomere associated proteins and subtelomeric DNA in fixed and living human cells at the nanoscale. We specifically optimized labeling and imaging conditions for visualizing human t-loops in intact cells with STED nanoscopy and confirmed our results with biological and computational controls. To quantify telomere conformations and highlight structural differences of telomere populations between ALT-positive and ALT-negative cell lines, we performed a neural network classification of the STED data. We further visualized APB topology and quantitatively assessed the perturbing influence of PML on telomere conformation in ALT-positive cells to deduce potential PML participation in telomere maintenance in ALT tumors.

II.4 METHODS

This project was conceived in close collaboration with the DKFZ Division of Chromatin Networks (Heidelberg, Germany) and plasmid cloning as well as TRF analysis were performed in this group. The Monte Carlo simulations were conceptualized in close collaboration with and conducted by Dr. Rifka Vlijm[2]. Data analysis was conducted in close collaboration with Roman Spilger[3]. Detailed information on materials is given in I.2.1.

II.4.1 Plasmids

To create the N-terminal fusion constructs pHTN-HaloTag-TRF2, pHTN-HaloTag-PMLIII, pHTN-HaloTag-LacI, pSNAPf-TRF2, pSNAPf-PMLIII and pSNAPf-LacI, human TRF2, PMLIII and LacI were cloned into pHTN HaloTag CMV-neo (Promega) and pSNAPf (New England Biolabs) vectors from previous plasmid constructs [467]. For confocal imaging of PML-NBs, pEGFP-C1-PMLIII was used [467] (Table II-1).

[2] affiliation: Max Planck Institute for Medical Research, Department of Optical Nanoscopy, Heidelberg, Germany;
current address: University of Groningen, Zernike Institute, Department of Molecular Biophysics, Groningen, Netherlands
[3] University of Heidelberg, BioQuant, IPMB and German Cancer Research Center, Division of Biomedical Computer Vision, Heidelberg, Germany

Table II-1. List of plasmids used for visualizing telomeres, APBs and subtelomeric regions.

plasmid	backbone	insert	fusion	construct
pHTN-HaloTag-TRF2	pHTN HaloTag CMV-neo	TRF2	N-terminal	Halo-TRF2
pHTN-HaloTag-PMLIII	pHTN HaloTag CMV-neo	PMLIII	N-terminal	Halo-PMLIII
pHTN-HaloTag-LacI	pHTN HaloTag CMV-neo	LacI	N-terminal	Halo-LacI
pSNAPf-TRF2	pSNAPf	TRF2	N-terminal	SNAP-TRF2
pSNAPf-PMLIII	pSNAPf	PMLIII	N-terminal	SNAP-PMLIII
pSNAPf-LacI	pSNAPf	LacI	N-terminal	SNAP-LacI

II.4.2 Cell Culture

The cell lines U2OS, F6B2, HeLa (hereinafter referred to as HeLa NT), HeLa VST and HeLa LT (Table I-16) were cultured in Gibco Dulbecco's modified Eagle medium (DMEM) high glucose/GlutaMAX™/ pyruvate (Thermo Fisher Scientific) supplemented with 10% fetal bovine serum (FBS) and 1% penicillin/streptomycin (hereinafter referred to as DMEM++) at 37°C in humidified air with 5% CO_2. All HeLa cells were harvested with trypsin 0.25% (no phenol red, Gibco/Thermo Fisher Scientific); U2OS and F6B2 cells were harvested with trypsin 0.05% ethylenediaminetetraacetic acid (EDTA) 0.02% (with phenol red, Sigma-Aldrich/Merck). A Countess II FL Automated Cell Counter (Thermo Fisher Scientific) was used to count cells and to assess the live-to-dead cell ratio via Trypan Blue stain (0.4%).

For fixed sample preparation, approximately 10^5 cells/well were seeded on #1.5 coverslips in 24-well cell culture plates one day prior to PNA FISH and/or IF staining and kept at 37°C in humidified air with 5% CO_2 until fixation. For live sample preparation, approximately 10^4 cells/well were seeded on 8-well chambered coverglasses one day prior to transfection and kept at 37°C in humidified air with 5% CO_2 until transfection.

II.4.3 Terminal Restriction Fragment (TRF) Analysis

Extraction and purification of genomic DNA was performed after cell lysis with the Puregene Core Kit (Qiagen). Purified DNA (4 µg) was digested with RsaI & HinfII (Telomere Length Assay Kit, Roche) and resolved on a 0.6% agarose gel in 1× tris-acetate-EDTA (TAE) buffer using a Chef DRII Pulse Field Electrophoresis chamber (BioRad) with the following settings: pump 70-80, Volt 4 V/cm, b1 initial switch time 1 s, final switch time 6 s, run time 13 h. The Telomere Length Assay Kit (Roche) was used for Southern blotting and chemiluminescent detection. The blot was visualized via the Chemi-Doc MP System (BioRad).

II.4.4 Immunofluorescence

II.4.4.1 Antibodies

For IF, the following primary antibodies were used: monoclonal mouse anti-TRF2 (05-521, Merck, 1:50, 1 h) in combination with polyclonal rabbit anti-PMLIII (sc-5621, Santa Cruz Biotechnology, 1:50, 30 min), monoclonal mouse anti-TRF1 (GTX10579, GeneTex, 1:50, 1 h) or monoclonal mouse anti-TRF1 (04-638, Merck, 1:50, 1 h) in combination with polyclonal rabbit anti-TRF2 (NB110-57130, Novus Biologicals, 1:50, 1 h).

The following secondary antibodies were used: goat anti-mouse-IgG coupled to STAR 600 (Abberior, 1:50, 1 h), goat anti-rabbit-IgG coupled to STAR 600 (Abberior, 1:50, 1 h), goat anti-mouse-IgG coupled to STAR 635P (Abberior, 1:50, 1 h), goat anti-rabbit-IgG coupled to STAR 635P (Abberior, 1:50, 1 h), goat anti-rabbit-IgG coupled to Alexa Fluor 488 (Thermo Fisher Scientific, 1:50, 1 h) and goat anti-rabbit-IgG coupled to Atto 488 (ATTO 488 NHS-ester (ATTO Technology) custom-coupled to goat anti-rabbit-IgG (111-005-003, Dianova), 1:50, 1 h).

II.4.4.2 Immunofluorescence Staining

After washing three times with phosphate-buffered saline (PBS), the cells were fixed with 3.7% paraformaldehyde (PFA) in PBS for 12 min at room temperature (RT) and subsequently again washed three times with PBS. Permeabilization was performed with 0.1% (v/v) TritonX-100 in PBS for 5 min at RT and unspecific binding was blocked afterwards with 10% goat serum (GS) in PBS for at least 1 h at RT. Subsequently, the primary antibodies were incubated in 10% GS in PBS for 30 min to 1 h in a humid chamber (for individual dilution and incubation time, refer to II.4.4.1). After extensive washing with PBS, additional blocking was performed with 10% GS in PBS for at least 10 min at RT. Subsequently, the secondary antibodies were incubated in 10% GS in PBS for 1 h in a humid chamber (for individual dilution and incubation time, refer to II.4.4.1). Finally, the cells were extensively washed with PBS and the samples were mounted in Mowiol [466].

II.4.5 Fluorescence *in situ* Hybridization (FISH)

The unlabeled TelC PNA probes $(CCCTAA)_3$ (PNA Bio) and the custom-designed and unlabeled LacO PNA probe TTGTTATCCGCTCACAA (PNA Bio) were labeled via O-linker with the fluorescent dyes KK114 [382] and Alexa Fluor 594 at the Facility for Synthetic Chemistry at the Max Planck Institute for Biophysical Chemistry in Göttingen, Germany.

After washing three times with PBS, the cells were fixed with 3.7% PFA in PBS for 12 min at RT, subsequently again washed three times with PBS and permeabilized with ice-cold 0.2% (v/v) TritonX-100 in PBS for 5 min. After washing three times with PBS, dehydration was performed in three steps (70%, 85%, 100% ethanol (EtOH) in H_2O ultrapure) each 2 min long. Air-drying was followed by incubation with 0.1 µM TelC and/or 0.1 µM LacO probe in freshly prepared hybridization buffer (75%

formamide in 20 mM NaCl, 20 mM Tris-HCl, 0.1% bovine serum albumin (BSA), pH 7.4). After 3 min denaturation at 80°C, hybridization was allowed overnight at 30°C.

The next day, the cells were washed twice with freshly prepared 70% formamide in 10 mM Tris-HCl (pH 7.4) for 15 min at RT, once with 2× SSC buffer for 1 min at RT, once with 0.1× SSC buffer for 5 min at 55°C, twice with 0.05% (v/v) Tween-20 in 2× SSC buffer for 5 min at RT and three times with PBS at RT. The samples were either mounted in Mowiol or subjected to subsequent IF staining similar as described in II.4.4.2. Briefly, after blocking and primary antibody incubation, the samples were washed three times with 0.002% (v/v) NP-40 in PBS for 5 min at RT followed by secondary antibody incubation. Finally, the samples were dipped into ultrapure H_2O, dehydrated with 100% EtOH for 1 min, air-dried and mounted in Mowiol [466].

II.4.6 Live Cell Staining

One day prior to live cell imaging, the cells were transiently transfected at 40-60% confluency using the Effectene Transfection Reagent Kit (Qiagen) according to the manufacturer's protocol. At 24 h post transfection, the cells were incubated for 30 min with a 1 µM staining solution of the respective combination of live dyes 580CP-BG [29], 610CP-BG [29] and 640SiRH-Halo [32] (BG = SNAP-tag ligand, Halo = HaloTag ligand) in DMEM++ at 37°C in humidified air with 5% CO_2. The fluorescent live dyes were kindly provided by Dr. Alexey Butkevich[4] and Dr. Vladimir Belov[5]. Following a 10 min washing step with prewarmed Gibco FluoroBrite™ DMEM (Thermo Fisher Scientific) supplemented with 10% FBS and 4 mM Gibco GlutaMAX™ (Thermo Fisher Scientific) (hereinafter referred to as FluoroBrite++) at 37°C in humidified air with 5% CO_2, the cells were either subjected to live cell imaging or were fixed with 3.7% PFA in PBS for 12 min at RT.

II.4.7 STED and Confocal Microscopy

The custom-built STED system is described in detail in I.2.2.1. The power range for all lasers used during live and fixed cell confocal and STED imaging is given in Table II-2. Unless otherwise stated, fixed and live cell confocal and STED imaging was performed with the measurement parameters given in Table II-3. No frame accumulation was used.

[4] Max Planck Institute for Biophysical Chemistry, Department of NanoBiophotonics, Göttingen, Germany;
current address: Max Planck Institute for Medical Research, Department of Optical Nanoscopy, Heidelberg, Germany
[5] Max Planck Institute for Biophysical Chemistry, Department of NanoBiophotonics, Göttingen, Germany;
Facility for Synthetic Chemistry at the Max Planck Institute for Biophysical Chemistry in Göttingen, Germany

Table II-2. Range of laser powers used for fixed and live cell confocal and STED imaging of telomeres and APBs.

The values given describe the estimated laser power in the sample focus based on laser power measurements in front of the microscope body.

	excitation			STED
	470 nm [µW]	**600 nm [µW]**	**650 nm [µW]**	**775 nm [mW]**
confocal, fixed samples	140	0.5-4	0.2-2	---
STED, fixed samples	---	2-12	0.5-12	70-100
confocal, live samples	140	0.5-4	0.2-2	---
STED, live samples	---	2-12	0.5-8	35-70

Table II-3. Standard measurement parameters used for fixed and live cell confocal and STED imaging of telomeres and APBs.

	pixel size [nm]	**dwell time [µs]**	**line accumulation**
confocal, fixed samples	50	50	1
STED, fixed samples	15	10-30	10-20
confocal, live samples	50	30	1
STED, live samples	20	30	1

II.4.8 Monte Carlo Experiments

Monte Carlo simulations of nucleosome chains with subsequent FISH labeling were performed to generate synthetic STED data. On scales ≫ 50nm, the DNA path can be described as a polymer of segments with subsequent segments being uncorrelated in their direction (Figure II-6). Random DNA configurations were simulated for various conditions by building up a chain of segments with the next segment starting where the last segment ended.

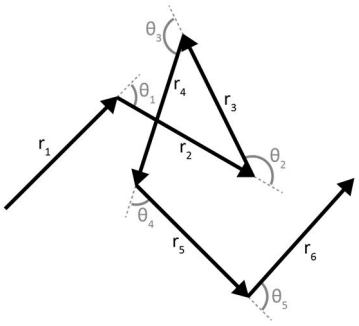

Figure II-6. Polymer chain model of DNA.

Insights into many properties of the genome can be gained by modelling DNA in a coarse-grained procedure. DNA can be described as a polymer with N segments of a certain length called the Kuhn length L_{seg}. Each segment r_i has a direction unrelated to the previous one.

As telomeric DNA is wrapped around nucleosomes, previously estimated values for the polymer-like behavior of DNA with nucleosomes were used (Table II-4) [686]. Any other protein decoration and its effect on the DNA persistence-length were ignored, as these effects are not well understood.

Table II-4. Monte Carlo simulation parameters used to describe nucleosome chains.

simulated DNA lengths (bp)	3864, 9821, 19803, 49749
base pair rise	0.13 nm [686]
persistence length L_p	10.5 nm [686]
Kuhn length ($2 \cdot L_p = L_{seg}$)	21 nm / 162 bp
available bp per Kuhn segment for labeling	$162 \cdot \frac{191-146}{191} = 38$ bp
nucleosome repeat length L_{repeat}	191 bp
length of core DNA L_{core}	146 bp

Randomly picking υ and ν between 0 and 1, the direction of each segment is defined by θ and φ:

$$\theta = 2 \cdot \pi \cdot \upsilon \quad \textbf{(II-1)}$$

$$\varphi = cos^{-1}(2\nu - 1) \quad \textbf{(II-2)}$$

The change in position of each new segment with the length L_{seg} (Kuhn length, refer to Table II-4) is given with respect to the previous position by:

$$dx = L_{seg} \cdot sin(\varphi) \cdot cos(\theta) \quad \textbf{(II-3)}$$

$$dy = L_{seg} \cdot sin(\varphi) \cdot sin(\theta) \quad \textbf{(II-4)}$$

$$dz = L_{seg} \cdot cos(\varphi) \quad \textbf{(II-5)}$$

Based on the different average telomere lengths of the cell lines used (Table I-16), data were generated for roughly N_{bp} = 4, 10, 20 and 50 kb long stretches of DNA.

After simulating the random 3D paths of nucleosome chains, the position of each base pair available for labeling was listed. For nucleosome-DNA, only the linker DNA is available for labeling. The number of base pairs available for labeling is thus defined by the repeat length L_{repeat}, the length of the core DNA L_{core} and the total DNA length N_{bp} (Figure II-7):

$$N_{available\,bp} = \frac{L_{repeat} - L_{core}}{L_{repeat}} N_{bp} \quad \textbf{(II-6)}$$

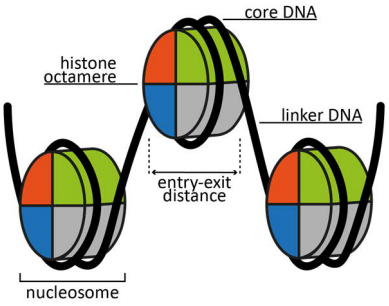

Figure II-7. Schematic illustration of nucleosomal DNA.

The nucleosome constitutes the fundamental packing unit of DNA and consists of the nucleosome core particle and linker DNA. The nucleosome core particle comprises core DNA wrapped around an octamer of core histones.

Next, the number of `dyes´ to be positioned was calculated for different labeling densities n_{label}:

$$N_{dyes} = \frac{N_{available\ bp}}{s_{label}} \cdot n_{label} \qquad \text{(II-7)}$$

The label size s_{label} was chosen to be 18 bp in accordance with the length of the TelC probe used in the actual PNA FISH STED experiments. The labeling density was varied between n_{label} = 10, 20, 30 and 60% of all available base pairs $N_{available\ bp}$.

For each randomly formed nucleosome chain, the decoration with labels was simulated by subsequently choosing random dye locations from the list of base pair positions available for labeling under the following constraint. After a location was chosen, 18 consecutive base pairs were marked as `labeled´ defining these positions are unavailable for any `dye binding´ in all following labeling steps.

After all `dyes´ had been randomly positioned along the simulated nucleosome chain, each dye position was blurred by a Gaussian PSF as it is expected in a STED microscope. Based on the actual STED data, a combined Gaussian PSF of 0.93 times a FWHM of 28 nm and 0.07 times a FWHM of 200 nm was assumed to give the best representation.

After labeling, a 2D projection of the expected photon counts (normalized) was created for each simulated 3D nucleosome chain path. Not all positions of exceptionally large structures can be simultaneously in focus, and thus equally detected. Therefore, `dyes´ within a z-range of 450 nm were fully shown, `dyes´ at positions between 450 and 550 nm were decreasingly represented, and all `dyes´ outside the focal center of 550 nm were excluded in the 2D projection of the 3D nucleosome chain.

In a final step, every resulting 2D representation was binned into 15 nm-squared pixels in accordance to the actual STED data. In total, 20000 synthetic STED images were simulated per condition of DNA length and labeling degree.

II.4.9 Neural Network (NN) Classification

Telomere conformations were analyzed by a deep learning method (Figure II-8). A convolutional NN was used for automatic classification [687] into different telomere classes. The network architecture comprises ten convolutional layers and two fully-connected layers. The convolutional layers are interleaved with three max pooling layers. Between the last convolutional layer and the first fully-connected layer, one global max pooling layer is used. After each convolutional layer, instance normalization is employed [688]. Except for the softmax output layer [689], all nonlinearities are leaky rectified linear units (ReLUs, leakiness 0.3) [690]. The network was trained using a stochastic gradient

descent optimizer and a cosine annealing learning rate scheduler with periodic restarts (learning rates $l_{max} = 10^{-2}$ and $l_{min} = 10^{-6}$) [691]. Overfitting was prevented by employing early stopping and by using a dropout layer ($p_{drop} = 0.25$) [692] after the first fully-connected layer during network training.

Training data for supervised learning were prepared by sorting a fraction of experimentally acquired raw TelC PNA FISH STED data (independent of cell line) into four different classes (namely *loop*, *rod*, *coil*, *globule*) based on the following conformational criteria of the telomere signals (Figure II-8).

- The class ***loop*** comprises lariat telomere signals with similarity to previous super-resolution data confirming the existence of t-loops with isolated telomeric DNA (Figure II-4) [485, 486]. Partially imaged lariat telomere signals were filed as `ambiguous´ and excluded from the training data.
- The class ***rod*** comprises linear telomere signals of fully unfolded telomeres.
- The class ***coil*** comprises heterogeneous telomere signals of decondensed telomeres with an apparent substructure.
- The class ***globule*** comprises compact telomere signals of fully condensed telomeres without any apparent substructure.

After training, the performance of a NN can be described by comparing its prediction with the ground truth. Based on the number of true positives TP, false positives FP and false negatives FN, the measures precision and recall can be calculated by:

$$precision = \frac{TP}{TP + FP} \tag{II-8}$$

$$recall = \frac{TP}{TP + FN} \tag{II-9}$$

To seek a balance between precision and recall, especially for uneven class distributions, the $F1$ score is given by:

$$F1 = 2 \cdot \frac{precision \cdot recall}{precision + recall} \tag{II-10}$$

After training of several NNs that differed in hyperparameters such as number of filters, dropout rate, learning rate scheduling and kernel size, the NN with the highest $F1$ score for *loop* classification was chosen under the premise that precision > recall.

The neural network classification was performed individually for the raw telomere PNA FISH STED data of each cell line and for the raw PNA FISH STED data of the subtelomeric regions (STRs) of the F6B2 cell line. For the U2OS data, no discrimination was initially made between PML-encased and free telomeres. Subsequently, U2OS telomeres were grouped into encased and free telomeres based on dual-color stainings for telomeres (TelC-KK114 PNA FISH) and PML (IF STAR 600). Both groups were individually classified to investigate the influence of PML-encasing on telomere conformation (Figure II-8). To assess the *loop* frequency of the synthetic STED data, sorting was performed identically to the training data of the neural network analysis and the average *loop* frequency was calculated for the different DNA lengths.

II.4.10 Quantitative Image Analysis

II.4.10.1 Determination of Telomere Size

For quantitative analysis, Otsu's thresholding in combination with subsequent morphological operations were used to segment telomere signals. To quantitatively describe the telomere size, different size measures were calculated based on the computed binary images from segmentation:

- The area A of telomere signals was determined by the number of signal-containing pixels of the segmented regions.
- The convex hull area $hullA$ of telomere signals was determined as the area of the minimum circumscribing convex polygon.
- The radius of gyration R_g was determined as the root mean square distance of all signal containing pixels to the center (first moment) of the pixel distribution.
- The convex hull volume $hullV$ was determined by raising the convex hull area to the 3/2 power as previously described [480, 481].

To investigate the influence of PML-encasing on telomere size, the U2OS telomere STED data were grouped into encased and free telomeres based on dual-color stainings for telomeres (TelC-KK114 PNA FISH) and PML (IF STAR 600). For both groups, the four different size measures were calculated (Figure II-8).

II.4.10.2 Estimation of Telomere Volume Density

According to Vancevska *et al.* [481], the ratio of volume densities of telomeric chromatin between two cell lines was estimated by

$$\frac{\rho_1}{\rho_2} = \left(\frac{N_1}{R_{g1}^3}\right)\left(\frac{R_{g2}^3}{N_2}\right) \qquad \textbf{(II-11)}$$

with ρ_1 (ρ_2) being the volume density of cell line 1 (2), N_1 (N_2) being the average telomere length of cell line 1 (2) and R_{g1} (R_{g2}) being the radius of gyration of cell line 1 (2). The average telomere lengths and their errors of HeLa VST, HeLa NT and HeLa LT cells were estimated from the Southern blot of the TRF analysis (refer to II.4.3). For U2OS cells, a rectangular telomere length distribution between 2-50 kb was assumed and the average length and its error accordingly estimated.

II.4.10.3 Determination of T-Loop Diameter

All telomere signals classified as *loop* by NN analysis together with the respective *loop* training data were used to quantify the average size of the loop portion (t-loop without tail) for each cell line. After background subtraction and deconvolution (refer to I.2.2.2), ellipses were fitted to the loops by performing skeletonization [693] and least-squares fitting [694]. The ellipse fitting provided values for the semi-major axis a and the semi-minor axis b of each loop for each cell line (Figure II-8).

Based on these results, the average ellipse circumference C was computed by

$$C = 4aE(\varepsilon) = 4a\int_0^{\pi/2}\sqrt{1-\varepsilon^2\sin^2\theta}\,d\theta \tag{II-12}$$

with E being the complete elliptic integral of the second kind and ε the eccentricity of the ellipse

$$\varepsilon = \sqrt{1-\frac{b^2}{a^2}} \tag{II-13}$$

as implemented in Octave 5.1.0 [471].

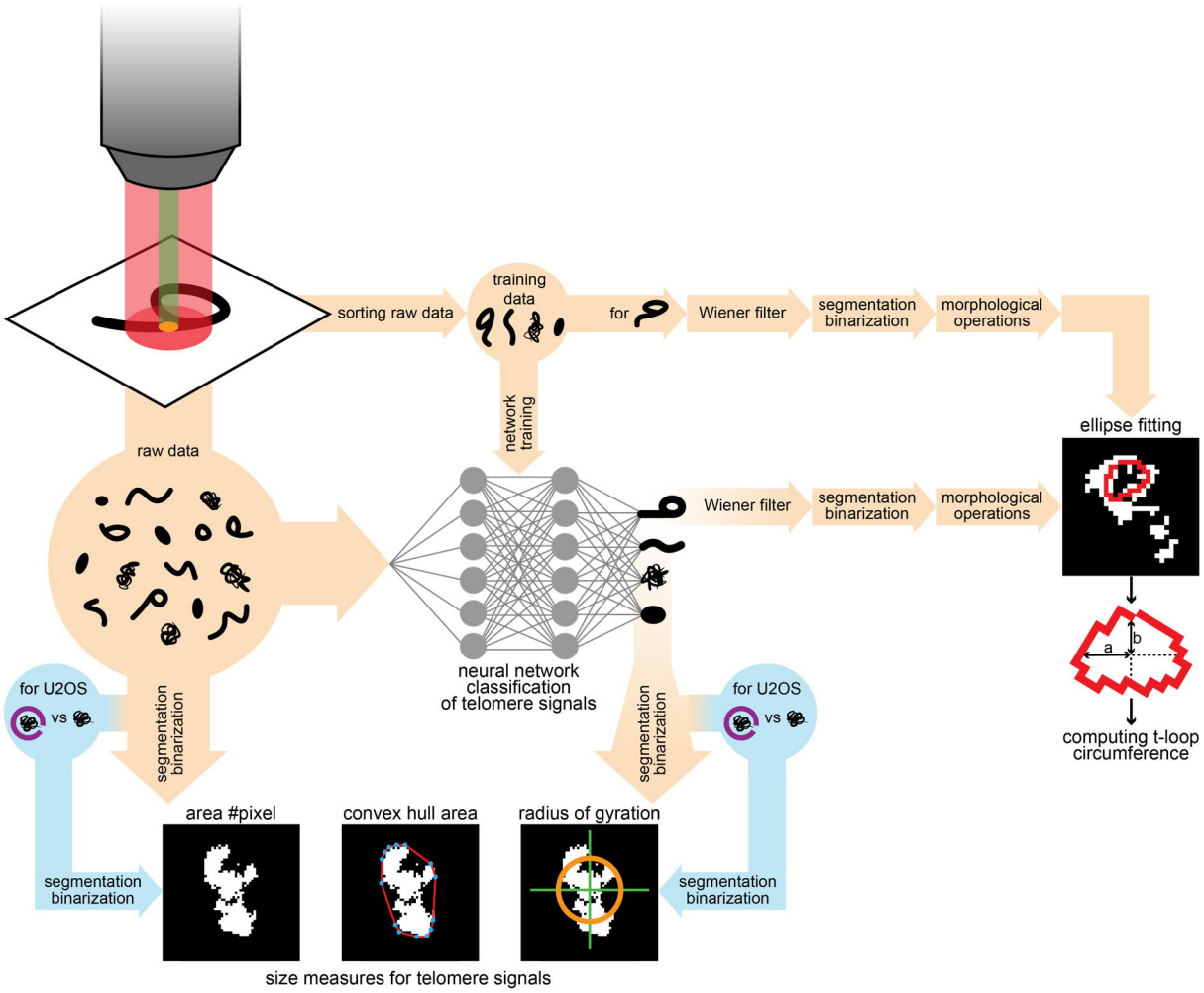

Figure II-8. Schematic illustration of the workflow of data analysis for characterizing human telomere conformations.

After data acquisition, the NN training data were prepared by assigning the raw telomere STED images of a data subset to either the *loop*, *rod*, *coil* or *globule* conformation. After NN training, all raw telomere STED data (light orange), excluding the training data, were classified by NN analysis. The output of the NN as well as the unclassified STED data were subjected to quantitative image analysis after segmentation and binarization to compute the different measures of telomere size. In both cases, the U2OS STED data (light blue) were additionally sorted for PML-encasing. All telomere STED images identified as *loop* by NN analysis as well as the *loop* training data were subjected to ellipse fitting after linear deconvolution (Wiener filter), segmentation and binarization, and morphological operations. Based on the semi-major and semi-minor axes as determined by the ellipse fitting, the average t-loop circumference was calculated.

II.4.11 Colocalization Experiments

For colocalization analysis of immunolabeled TRF1 and TRF2, minor crosstalk of the STAR 635P dye into the shorter wavelength channel (APD2, STAR 600) was corrected for via the linear unmixing algorithm implemented in the custom application software of the STED system (LabVIEW, National Instruments). For colocalization analysis of immunolabeled TRF2 and TelC, potential crosstalk between the STAR 600 dye and the KK114 dye [382] was excluded by single-color stainings and raw data were used for the colocalization analysis. In both cases, the analysis was restricted to regions of interest (ROIs) with relevant signals and the Pearson correlation coefficient (PCC) was calculated with the ImageJ plugin JACoP [470, 695].

II.4.12 Data Presentation

Detailed information on data presentation is given in I.2.2.2. Linear deconvolution of the experimentally acquired STED (confocal) data was performed by applying a Lorentzian PSF (refer to equation (I-5)) with FWHM = 30 nm (FWHM = 250 nm) in lateral dimension. All line profiles were drawn on raw data and averaged over 5 pixels.

II.4.13 Statistical Aspects

Detailed information on general statistical aspects is given in I.2.2.3. NN classification was performed on 699 STED images of HeLa VST telomeres, 427 STED images of HeLa NT telomeres, 697 STED images of HeLa LT telomeres, 1672 STED images of U2OS telomeres (no distinction between encased and free), 780 STED images of free U2OS telomeres, 190 STED images of encased U2OS telomeres and 135 STED images of F6B2 STRs.

The $F1$-score was used as a measure of quality of the classification. The relative frequency of FP and FN determined during neural network training was used to estimate the error in frequency given in the bar plots in the results section (refer to II.5.2 and II.5.5.1) with false positives (negatives) determining the negative (positive) error. The differences between the individual telomere populations as classified by neural network analysis was tested for significance by calculating the log-likelihood ratio (*G*-test) [696]. The difference between two cell lines for a given conformation was tested for significance with a similarity measure (normalized weighted χ^2) based on the histograms of the predicted frequency, the frequency of FP and the frequency of FN for the respective telomere conformation and the respective cell lines (for derivation, refer to VI.1.1).

The *loop* frequency of the synthetic STED data is based on the sorting of 1600 randomly chosen images (100 per condition of DNA length and labeling degree).

II.5 RESULTS

II.5.1 Visualizing Human Telomere Conformations

To study human telomere conformations, five human cancer cell lines were chosen based on their differing average telomere length and TMM. While the three telomerase-positive HeLa cell lines feature either normal telomere length (HeLa NT, literature: ~7 kb), very short telomeres (HeLa VST, literature: ~4 kb) or long telomeres (HeLa LT, literature: ~20 kb) [468], the ALT cell lines U2OS and its derivative F6B2 [467] show a broad telomere length distribution of 2-50 kb for different chromosomes in one cell. While the TRF analysis confirmed the literature values of the average telomere length for HeLa NT and HeLa LT, it revealed a shorter average telomere length for HeLa VST (~2 kb) (Figure II-9). All following calculations are based on the average telomere lengths as estimated from the TRF analysis (for details on average telomere length estimation, refer to II.4.10.2).

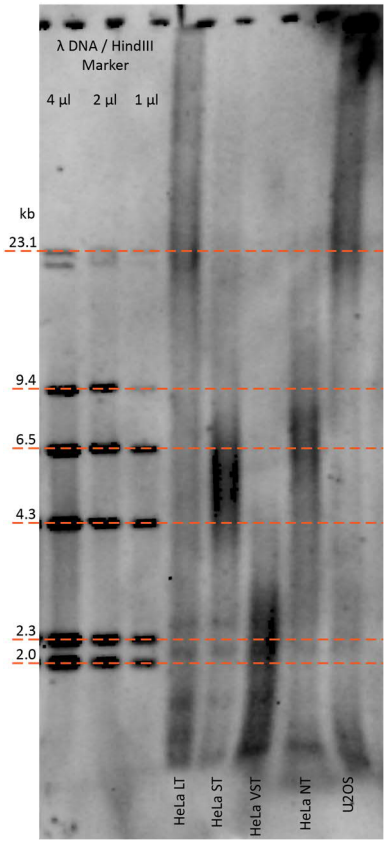

Figure II-9. TRF analysis.

The Southern blot of the terminal restriction fragment analysis compares the different average telomere lengths of the cell lines used in this part of the thesis (HeLa ST cells were not used). HeLa LT and HeLa NT cells display average telomere lengths of approx. 20 kb and 7 kb agreeing well with the literature values. HeLa VST cells show an average telomere length of approx. 2 kb roughly matching the literature value of 4 kb [468]. Typical for ALT cell lines, U2OS cells feature a broader telomere length distribution with most telomeres being > 20 kb.

II.5.1.1 Live Cell STED Imaging of Human Telomeres

Specific targeting of telomeres in living cells was achieved by transiently transfecting and overexpressing a SNAP-tag or HaloTag fusion of the shelterin protein TRF2. Staining with the respective SNAP- or Halo-derivatives of the live dyes 580CP [29], 610CP [29], 640SiRH [32] and SiR [30] allowed for confocal and STED imaging of telomeres in living cells. While single telomeres appeared as blurred diffraction-limited spots without any apparent structure in the confocal images, STED imaging resolved single telomeres with individual structural characteristics (Figure II-10a). To provide complementary fixed cell data, TRF2 was additionally STAR 600- or STAR 635P-immunolabeled and imaged in confocal and STED mode (Figure II-10b).

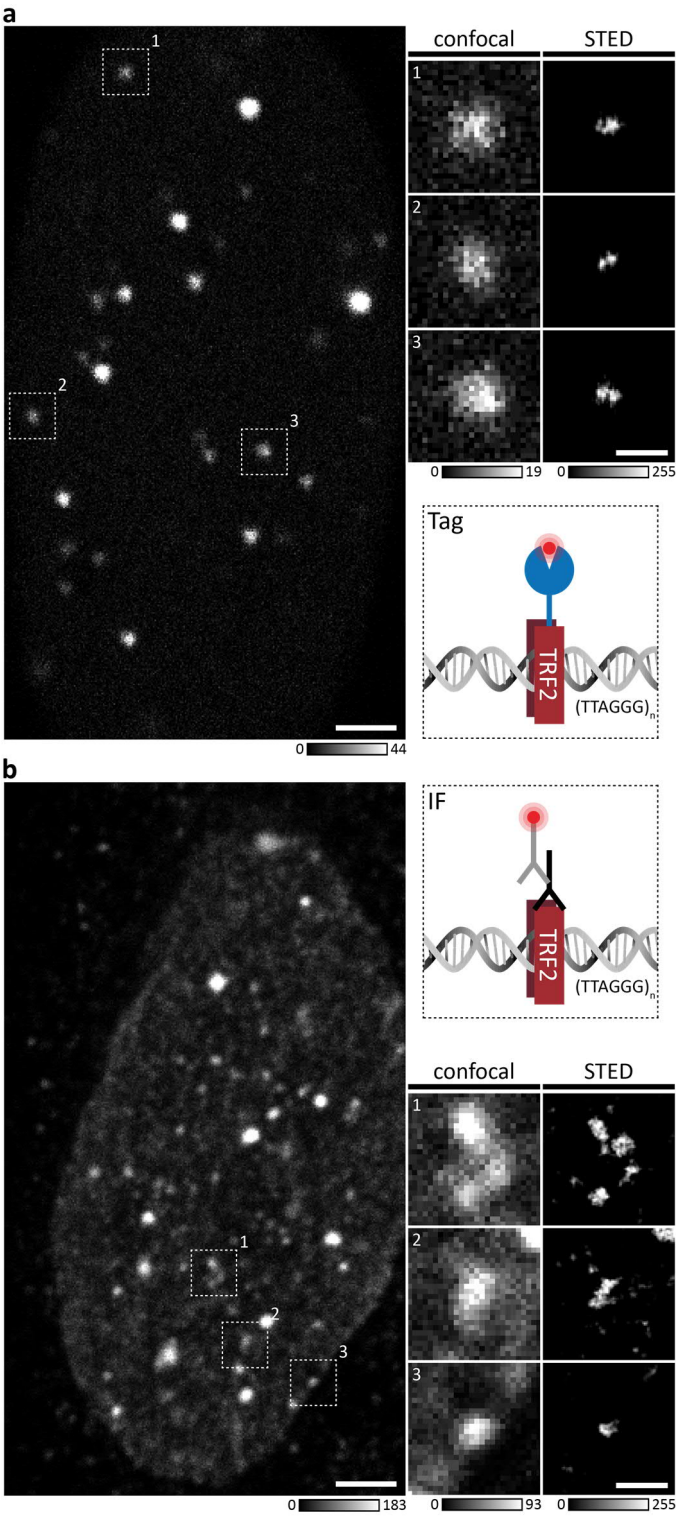

Figure II-10. Live and fixed cell imaging of human telomeres by targeting TRF2.

(**a**) Living U2OS cells were transiently transfected with a SNAP-TRF2 fusion construct, subsequently labeled with the live dye 610CP-BG and subjected to live cell confocal and STED imaging. The three exemplary TRF2 spots marked in the confocal overview (left) are shown as magnified images in confocal and STED mode. (**b**) Fixed U2OS cells were STAR 600-immunolabeled for TRF2. The three exemplary TRF2 spots marked in the confocal overview (left) are shown as magnified images in confocal and STED mode. All confocal data shown are raw data, all STED data shown are background corrected and linearly deconvolved. Scale bars overviews are 2 µm, scale bars close-ups are 500 nm.

To estimate the degree of TRF2 IF labeling, U2OS cells were additionally immunolabeled for TRF1. Both proteins directly bind to double-stranded telomeric DNA and are connected via TIN2 in the shelterin complex. Thus, TRF1 and TRF2 strongly colocalize on the molecular level. Dual-color STED imaging also revealed a prevalent colocalization of the fluorescent signals of the immunolabeled proteins. To quantify colocalization in dual-color fluorescence imaging, the PCC is an established measure with values ranging from -1 (negatively correlated), to 0 (uncorrelated) and 1 (positively correlated) [697]. The average PCC for colocalization of the IF signals of TRF1 and TRF2 of $r = 0.68 \pm 0.07$ ($n = 8$ nuclei) suggests rather quantitative staining of both proteins (Figure II-11).

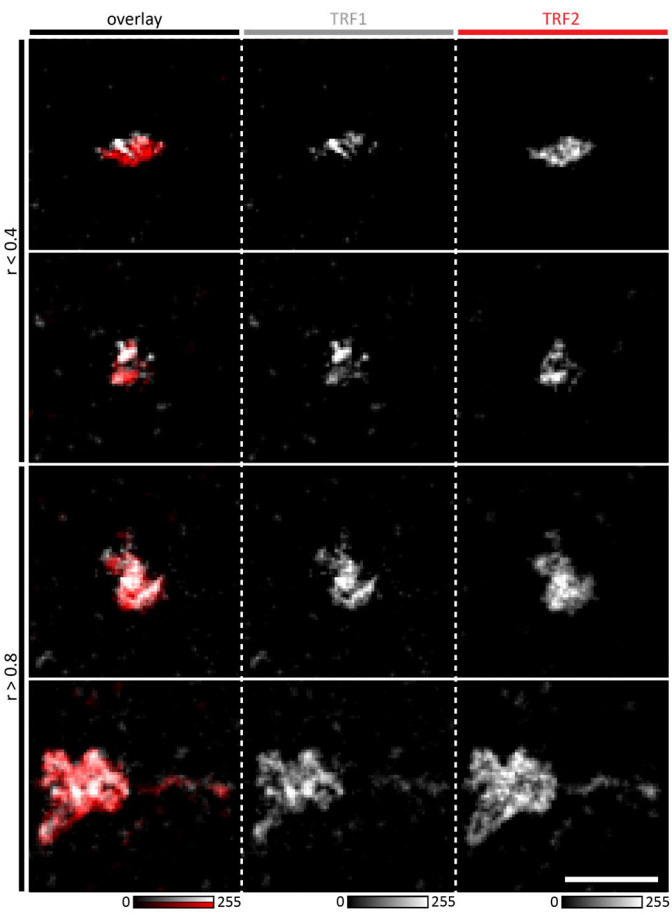

Figure II-11. Colocalization experiments between TRF1 and TRF2.

Fixed U2OS cells were co-stained via IF for TRF1 (STAR 63P, gray) and TRF2 (STAR 600, red). Dual-color STED imaging suggests close to quantitative staining of both shelterin proteins via IF. To quantify the degree of colocalization, the PCC was calculated with an average of r = 0.68 ± 0.07 (n = 8 nuclei). While many TRF1/TRF2 associations show a PCC of r > 0.8 (bottom), only a few show a PCC of r < 0.4 (top). Unless otherwise stated, all STED data shown are background corrected and linearly deconvolved. Scale bar is 500 nm.

Upon comparison of the live cell STED imaging with SNAP- and Halo-tagged TRF2 with the fixed cell STED imaging of immunolabeled TRF2, image quality differences become apparent. The live cell data did not suffer from off-target staining, whereas the IF data showed a background of single, unspecifically bound antibodies. Still, the live data displayed a lower SNR and a decreased spatial resolution. On the one hand, image acquisition must be adapted to living samples implying shorter total dwell times to avoid motion blur due to (sub)cellular dynamics, and lower laser intensities to prevent photobleaching and thus phototoxicity. On the other, the newly developed live cell dyes are less bright and photostable compared to the well-established dyes used for fixed cell STED imaging.

II.5.1.2 PNA FISH STED Imaging of Human Telomeres

As neither SNAP- and Halo-tagging of TRF2 nor IF of TRF1 and TRF2 provided the required biological resolution to analyze conformational details of human telomeres, PNA FISH of telomeres was adapted for STED imaging. In detail, a PNA probe directed against telomere repeats (TelC probe) was conjugated with the STED compatible fluorophores KK114 [382] or Alexa Fluor 594 (Figure II-12a,b).

STED imaging of TelC-KK114 labeled telomeres enabled visualization of conformational details of individual telomeres and differences between cell lines at nanoscale resolution (Figure II-12c-f). In contrast to SNAP- and Halo-tagging or IF staining of TRF2, TelC PNA FISH allowed for the identification of four distinct telomere conformations in all cell lines with STED nanoscopy (Figure II-13a):

- ***loop***: circular and lasso-like telomeres
- ***rod***: linear telomeres
- ***coil***: open and decondensed telomeres
- ***globule***: compact and condensed telomeres

The *loop* conformation is assumed to correspond to t-loop structures and the invasion site of the 3'-overhang determines their circular or lasso-like appearance (Figure II-13b). Partially imaged lariat telomere structures were filed as `ambiguous´ *loop* conformations (Figure II-13c).

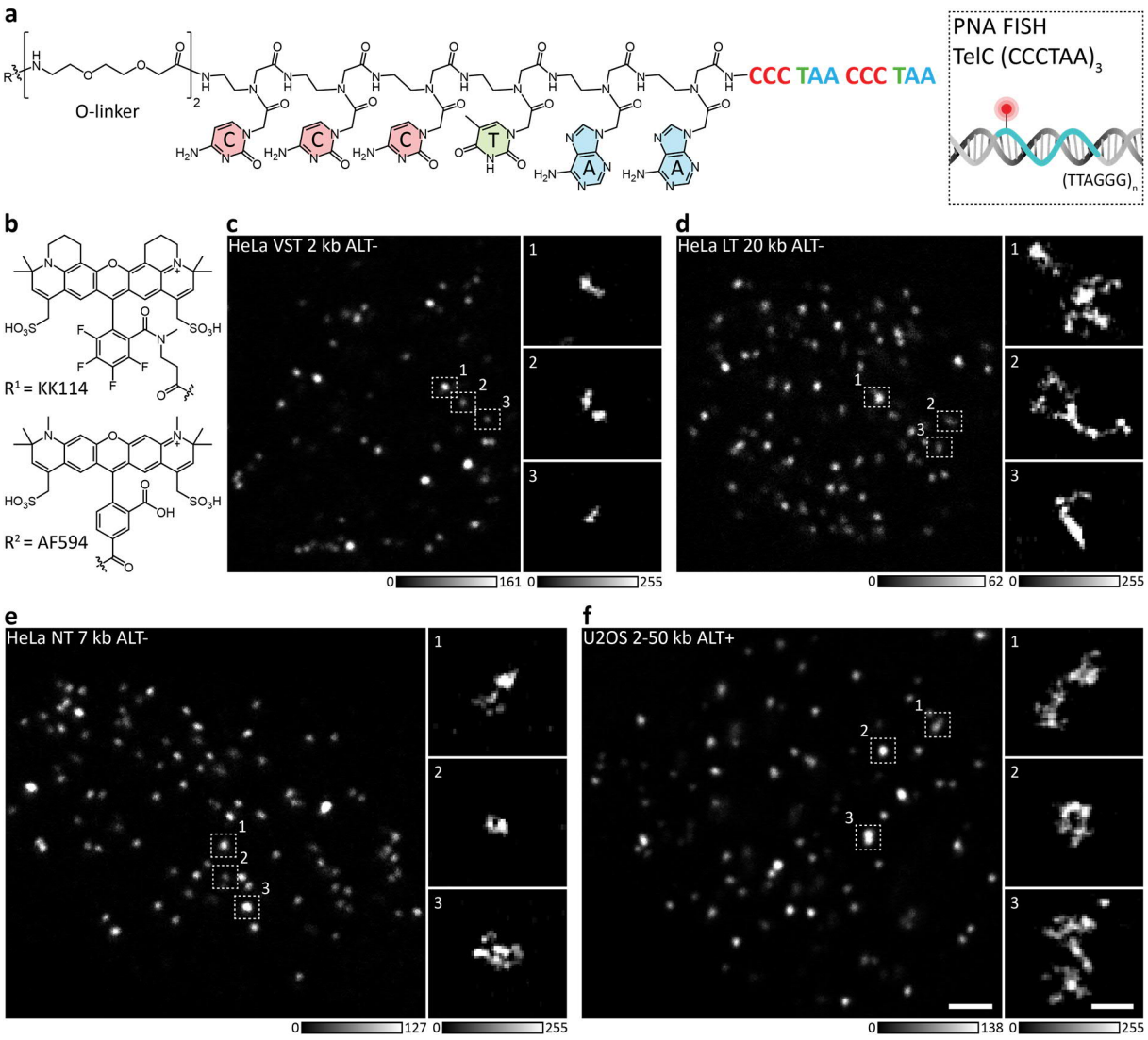

Figure II-12. PNA FISH staining of human telomeres.

(**a**) PNA is a synthetic nucleic acid analogue with the sugar-phosphate backbone being replaced by AEG units linked by peptide bonds. The nucleobases are natural and thus allow for Watson-Crick base pairing with DNA or RNA. The TelC probe (18 bp) specifically binding to telomere repeats places the fluorophores only two O-linker lengths away from the target. (**b**) The fluorescent dyes KK114 [382] and the commercially available Alexa Fluor 594 (AF594) were conjugated to the PNA probe via two O-linkers. (**c**) HeLa VST (**d**) HeLa LT (**e**) HeLa NT and (**f**) U2OS cells were stained for telomeric repeats via TelC-KK114 PNA FISH. Three exemplary telomere spots marked in each confocal overview (left) are shown in magnification (right) as imaged in STED mode. All confocal data shown are raw data, all STED data shown are background corrected and linearly deconvolved. Scale bars overviews are 2 µm, scale bars close-ups are 250 nm.

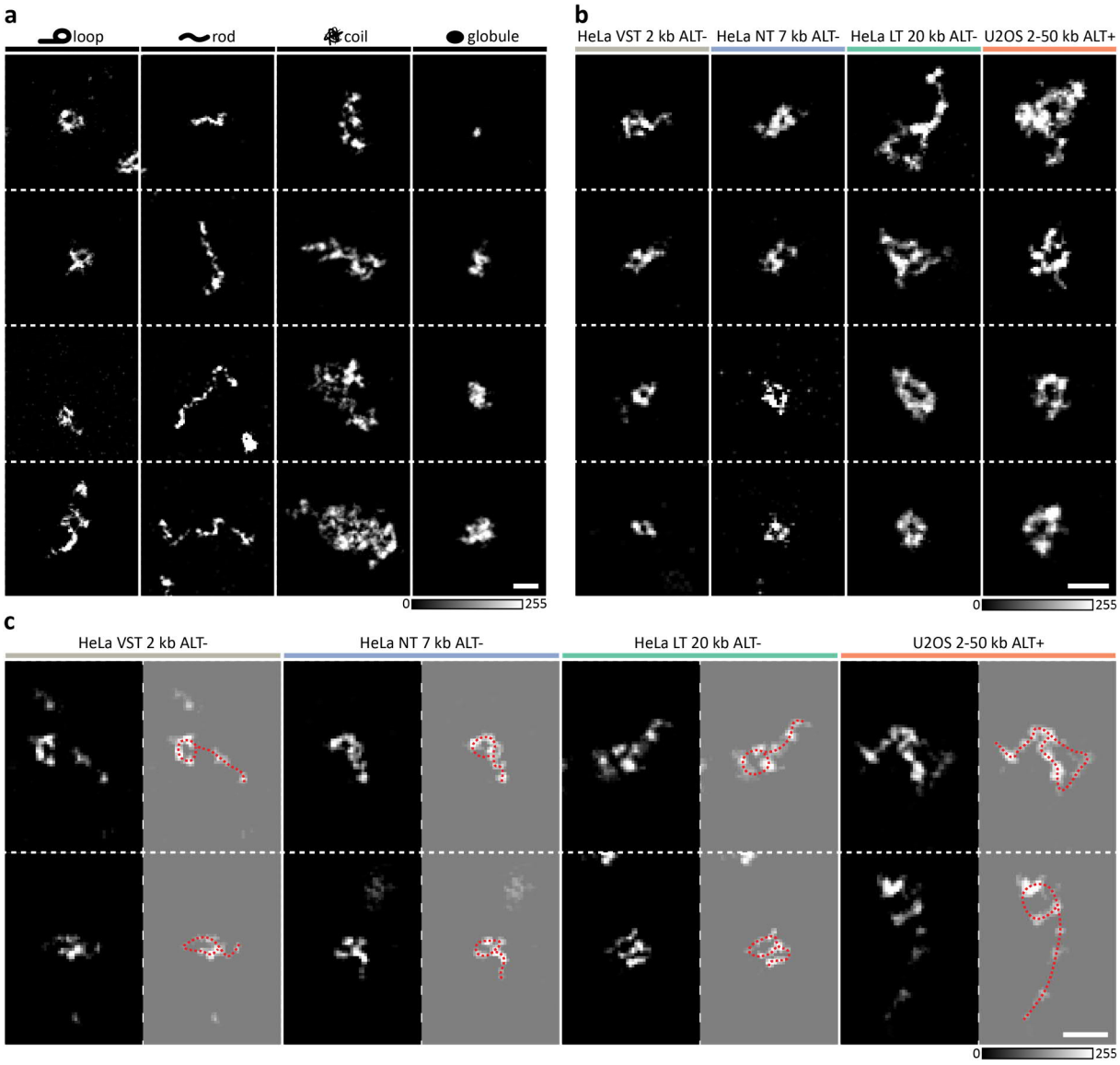

Figure II-13. PNA FISH STED identifies t-loops and other human telomere conformations in intact cells.

(**a**) Exemplary images of the four distinct telomere conformations (from left to right: *loop*, *rod*, *coil*, *globule*) as imaged by STED nanoscopy in TelC-KK114 PNA FISH stained, fixed U2OS cells. (**b**) Exemplary t-loops visualized by STED nanoscopy and TelC-KK114 PNA FISH staining in HeLa VST, HeLa NT, HeLa LT and U2OS cells (left to right). (**c**) Incomplete PNA FISH labeling, occupation of dark states, photobleaching, unfavorable 3D orientation and overlap with other telomere signals complicate the t-loop classification and require exclusion of potential t-loop signals filed as `ambiguous´. The dotted red lines follow their presumed shapes on 50% opaque images. All STED data shown are background corrected and linearly deconvolved. All scale bars are 250 nm.

To investigate the t-loop substructure, U2OS cells were stained for telomeres via PNA FISH and for TRF2 via IF. Overall, STED imaging revealed a surprisingly heterogenous telomere decoration by TRF2 ranging from full TRF2 coverage to almost TRF2-free telomeric DNA (Figure VI-1, Figure VI-2). PCC calculations were performed to quantify the colocalization between the TelC labeled telomere signal and immunolabeled TRF2 signal. The results confirmed the qualitative observation with PCCs from r = 0.16 to r = 0.91 and an average PCC of r = 0.52 ± 0.14 (n = 310 TelC/TRF2 signals) (Figure II-14).

For all t-loop structures identified in the TelC channel of the dual-color STED data, the TRF2 signal displayed two distinct distribution patterns. While TRF2 was diffusely distributed over the t-loop in most cases (Figure II-15a), a small but significant fraction of the data showed a TRF2 signal clearly restricted to the loop-tail junction (Figure II-15b).

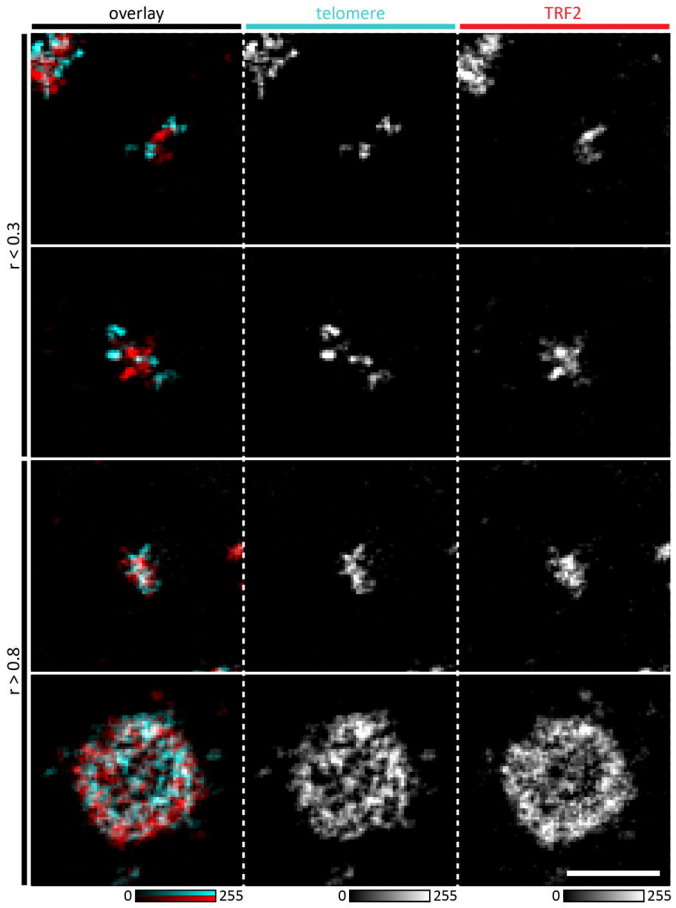

Figure II-14. TRF2 decoration of human telomeres.

Representative dual-color STED images visualizing the heterogeneity of telomere decoration by TRF2 in intact, fixed U2OS cells. Telomeres (cyan) were stained via TelC-KK114 PNA FISH and TRF2 (red) was STAR 600-immunolabeled. To quantify the degree of colocalization, the PCC was calculated ranging from $r < 0.3$ to $r > 0.8$ with an average of $r = 0.52 \pm 0.14$ ($n = 310$ TelC/TRF2 signals). All STED data shown are background corrected and linearly deconvolved. Scale bar is 500 nm.

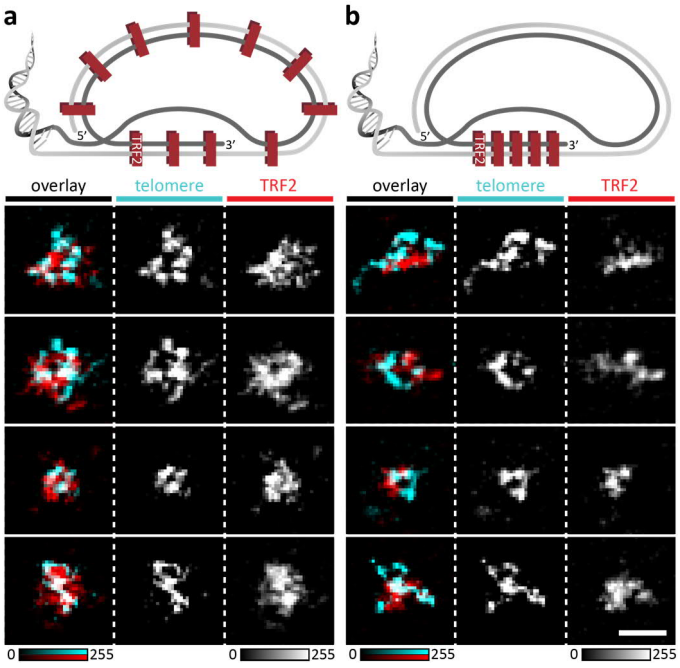

Figure II-15. TRF2 decoration of t-loops in intact human cells.

U2OS telomeres (cyan) were stained via TelC-KK114 PNA FISH and TRF2 (red) was STAR 600-immunolabeled. Dual-color STED imaging distinguishes two different TRF2 binding patterns at t-loops. (**a**) For the majority of t-loops, TRF2 is diffusely distributed over the entire t-loop structure. (**b**) Exclusive TRF2 binding at the loop-tail junction is restricted to a small but significant subset of t-loops. All STED data shown are background corrected and linearly deconvolved. Scale bar is 250 nm.

II.5.2 Classifying Human Telomere Conformations

To quantify the contribution of the different telomere conformations to the entire telomere population of each cell line, a NN-based image analysis was performed. It classified the raw TelC-KK114 STED data into the four predefined conformations (*globule*, *coil*, *rod*, *loop*) with an average scoring parameter $F1 = 0.86 \pm 0.08$. Amongst different NNs with individual sets of hyperparameters, the neural network with the highest $F1$ score for *loop* classification was chosen under the conservative premise that false negatives FN outweigh false positives FP (precision > recall). Table VI-1 summarizes the performance of the NN classification and Figure II-16 shows the corresponding confusion matrix based on the NN training.

Figure II-16. Normalized confusion matrix of NN training for classification of telomere conformations.

The normalized confusion matrix illustrates the performance of the NN training. The diagonal displays the frequency of correct predictions (recall) out of the provided ground truth (true label). The values outside the diagonal represent the frequencies of false positives (column) and false negatives (row) for the respective classes. The results including precision, recall and $F1$ score are further summarized in Table VI-1.

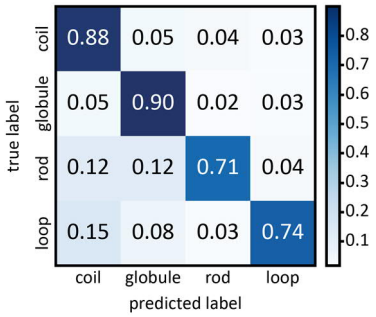

To identify significant differences of the frequency of individual telomere conformations between the cell lines, we introduced a similarity measure based on histograms of the predicted frequency and the frequencies of FP and FN for each telomere conformation of each cell line (refer to VI.1.1).

The results of the NN analysis display a correlation between *loop* frequency and average telomere length. The abundance of the *loop* conformation increased from HeLa VST (5%) and HeLa NT (7%) to HeLa LT (12%) and U2OS (11%) cells. In contrast, the contribution of the *rod* conformation is similar for the four cell lines (5-8%). However, striking differences in the basic composition of the telomere populations between the three HeLa cell lines and the U2OS cell line were observed. U2OS cells featured a more heterogeneous and decondensed telomere population apparent by the approximately ten-fold elevated level of *coil* telomeres (26%) and a corresponding decrease in *globule* conformation (55%). In contrast, all HeLa cell lines displayed only minor frequencies of *coil* telomeres (1-4%) while the *globule* state (80-85%) provided the greatest contribution to the HeLa telomere populations (Figure II-17, Table VI-2, Table VI-3).

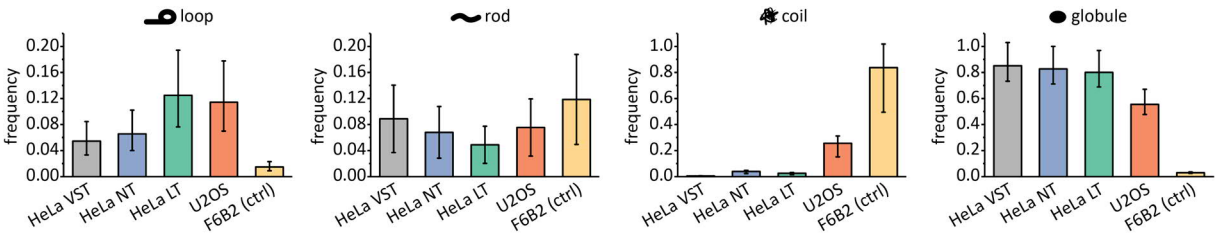

Figure II-17. Classification of human telomere conformations by combining STED imaging and NN analysis.

Neural network analysis classified telomere conformations (*loop*, *rod*, *coil*, *globule*) as visualized by STED imaging of TelC-KK114 PNA FISH stained telomeres in intact HeLa VST (n = 699), HeLa NT (n = 427), HeLa LT (n = 697) and U2OS (n = 1672) cells. The *lac*O repeat arrays at the subtelomeric regions of F6B2 cells were identically labeled and classified serving as biological control (ctrl) (n = 135). Error bars are based on the frequency of false positives (negative error) and false negatives (positive error) identified during NN training. A detailed summary of the results is given in Table VI-2 and Table VI-3.

II.5.3 Validating Human Telomere Conformations

To estimate the level of false positive *loop* contributions due to randomly formed lariat structures and/or imaging artefacts, two fundamentally different controls were conceived. For the biological control, the F6B2 cell line was used which carries three stably integrated bacterial *lac* operator (*lac*O) repeat arrays at the subtelomeric regions (STRs) of chromosomes 6q, 11p and 12q [467]. To label and image the *lac*O arrays analogously to the telomere repeats via PNA FISH STED, a PNA probe against *lac*O repeats (LacO probe) was conjugated with the STED compatible fluorophores KK114 [382] or Alexa Fluor 594. Upon visual inspection of the imaging results, essentially no loop structures were detected and the *lac*O repeats appeared overall less condensed than telomeric DNA (Figure II-18). To quantitatively analyze the conformation of the STRs, the raw LacO PNA FISH STED data were classified with the same NN as the TelC PNA FISH STED data. The results displayed a significantly reduced *loop* frequency of 1% in comparison to the telomere populations of the three HeLa cell lines and the U2OS cell line (Figure II-17, Table VI-2, Table VI-3).

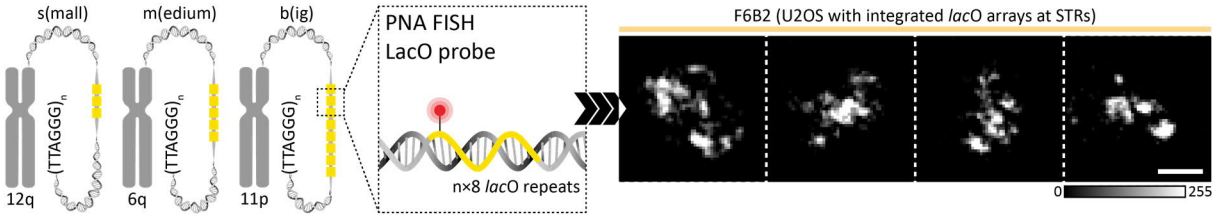

Figure II-18. LacO PNA FISH labeling and STED imaging of STRs.

F6B2 cells carry three stably integrated *lac*O repeat arrays at the STRs of chromosomes 12q, 6q and 11p differing in their number of repeats (s – small, m – medium, b – big) [467]. The *lac*O inserts were labeled via LacO-KK114 PNA FISH and imaged via STED nanoscopy to serve as biological control for assessing the frequency of detecting randomly formed lariat structures and/or false positive *loop* structures. All STED data shown are background corrected and linearly deconvolved. Scale bar is 250 nm.

For the computational control, Monte Carlo simulations of nucleosome chains were conducted generating synthetic telomere PNA FISH STED data for 4, 10, 20 and 50 kb length with labeling degrees of 10, 20, 30 and 60%. The visual appearance of the simulation data corresponded well to the visual appearance of the actual STED data (Figure II-19). Still, classification with the same NN was not possible. The NN sorted the synthetic data into patently incorrect categories. Since the NN was trained with actual data, there was likely a subtle difference between synthetic and actual data, which limits the classification capability of the NN to the actual data alone. Therefore, the synthetic STED data were sorted analogously to the neural network training data revealing a low average frequency of apparent *loop* conformations of 2% (Figure VI-3).

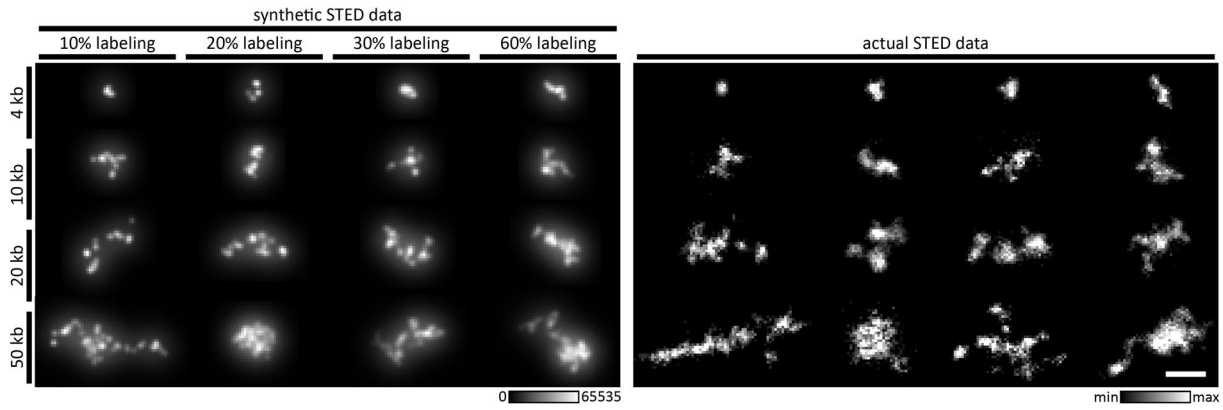

Figure II-19. Comparison of synthetic and actual telomere PNA FISH STED data.

Monte Carlo simulations of nucleosome chains (4, 10, 20, 50 kb) with subsequent PNA FISH labeling (10, 20, 30, 60% labeling degree) generated synthetic telomere STED data that correspond well in visual appearance to the actual telomere PNA FISH STED data. Exemplary images of synthetic (left) and actual (right) data are shown as a composite illustration on black background. Only the actual STED data are background corrected. From left to right and top to bottom, the minimal and maximal (min/max) counts are 13/133, 5/54, 5/59, 5/57, 2/26, 7/71, 3/30, 6/66, 6/67, 17/177, 6/65, 8/85, 4/47, 3/34, 4/45, 8/85. Scale bar is 250 nm.

II.5.4 Quantifying Human Telomere Conformations

To quantitatively characterize the telomere populations and the different conformations of each cell line, several telomere measures were calculated from the TelC PNA FISH STED data. For all conformations, the size of the individual telomere signals was assessed via the area A of the fluorescence signal, the convex hull area $hullA$ and the radius of gyration R_g. The volume density ρ was determined as previously described [481]. Additionally, the t-loop dimensions were determined by ellipse fitting of all STED images of the *loop* conformation.

II.5.4.1 Measures of Telomere Size

All three measures of telomere size (A, $hullA$, R_g) correlated well with an average size increase of the telomere signals with increasing average telomere length from HeLa VST, to HeLa NT, HeLa LT and U2OS. Yet, no direct proportionality between the average telomere length and the average size of the telomere signals was observed. While the average telomere size increased from HeLa VST to HeLa NT and from HeLa NT to HeLa LT by approximately 30%, it increased from HeLa LT to U2OS by more than 80%. To compare the results with previous studies, the convex hull volume $hullV$ was additionally calculated by raising the convex hull area to the power of 3/2 as described in these studies [480, 481] (Figure II-20a, Table VI-4, Table VI-5).

To characterize the size increase in detail, the telomere STED data of each cell line were first classified by NN analysis as described in II.5.2. Subsequently, the size measures were computed individually for the different telomere conformations. As already observed for the entire telomere populations, the average telomere signal size likewise increased for each individual conformation in the order HeLa VST, HeLa NT, HeLa LT and U2OS. Specifically, the *coil* conformation displayed the most prominent increase

with a doubling from HeLa VST and HeLa NT to HeLa LT and an almost doubling from HeLa LT to U2OS. As the *coil* and the *globule* conformations are most closely tied to the level of telomeric DNA (de)compaction, their size measures are displayed in Figure II-20b (Table VI-6, Table VI-7). The average size of *rod* telomere signals increased approximately 20% from cell line to cell line in the order HeLa VST, HeLa NT, HeLa LT and U2OS. For a more tailored size characterization of the *loop* telomere signals, ellipse fitting was performed (refer to II.5.4.3).

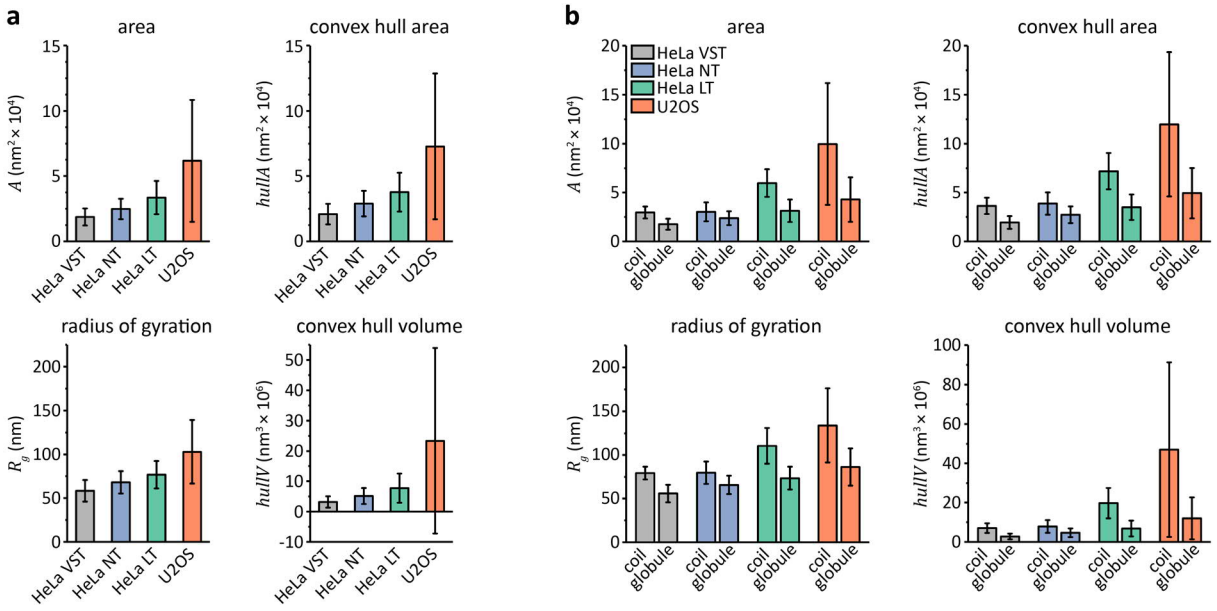

Figure II-20. Measures of telomere size as determined by quantitative STED image analysis.

The area of fluorescent signal A, the convex hull area $hullA$, the radius of gyration R_g and the convex hull volume $hullV$ were calculated based on the TelC-KK114 PNA FISH STED data of (**a**) the entire telomere population for the HeLa VST (n = 699), HeLa NT (n = 427), HeLa LT (n = 697) and U2OS (n = 712) cell line and (**b**) after NN classification for the *coil* conformation (HeLa VST n = 4, HeLa NT n = 17, HeLa LT n = 18, U2OS n = 222) and the *globule* conformation (HeLa VST n = 595, HeLa NT n = 353, HeLa LT n = 558, U2OS n = 366) of each cell line. All results and p-values are summarized in Table VI-4, Table VI-5, Table VI-6 and Table VI-7.

II.5.4.2 Measures of Telomere Density

Based on the average telomere length and the radius of gyration, an estimate of the ratio of volume densities of telomeric chromatin was calculated for all possible cell line combinations (refer to equation (II-11)). Surprisingly, the ratio of HeLa NT and U2OS cells was close to 1:1 implying similar volume densities of telomeric chromatin for both cell lines. Compared to these, the volume density of HeLa VST telomeres was less than half and the volume density of HeLa LT telomeres was approximately double (Figure II-21a, Table VI-8).

To validate the approach of analyzing the (de)compaction level of the telomere populations via NN classification, the ratio of volume densities between *coil* and *globule* telomeres was compared for each cell line. In all cases, the volume density of the *coil* conformation was lower than the volume density of the *globule* conformation. U2OS cells displayed the highest ratio with *coil* telomeres being almost four-fold less dense than *globule* telomeres. The density of the *coil* conformation for HeLa VST and HeLa LT telomeres was approximately three-fold lower compared to the density of the *globule* state.

For HeLa NT cells, the volume density decrease from the *globule* to the *coil* conformation was only two-fold (Figure II-21b, Table VI-9a).

To further analyze the nature of U2OS telomere (de)compaction, the volume density of the U2OS *coil* and *globule* state was compared to the volume densities of the *coil* and *globule* states of the three HeLa cell lines. As expected from the ratio of volume densities between the entire telomere populations, the volume densities of the two telomere conformations were both lower for HeLa VST and higher for HeLa LT. In comparison with HeLa NT, however, U2OS cells displayed a reduced *coil* volume density but an increased *globule* volume density (Figure II-21c, Table VI-9b).

Figure II-21. Ratios of volume densities.

The ratios of volume densities ρ were calculated based on the average telomere length as determined by the TRF analysis (refer to Figure II-9) and the quantitative image analysis results of the radius of gyration R_g (refer to Figure II-20). (**a**) Ratios of ρ (cell line 1 to cell line 2) between the entire telomere populations of the four cell lines studied (HeLa VST n = 699, HeLa NT n = 427, HeLa LT n = 697 and U2OS n = 712). (**b**) Ratios of ρ of the *coil* conformation to *globule* conformation per cell line and (**c**) ratios of ρ of the U2OS *coil* / *globule* conformation to the *coil* / *globule* conformation of the three HeLa cell lines as classified by NN analysis (refer to II.5.2) (*coil* conformation HeLa VST n = 4, HeLa NT n = 17, HeLa LT n = 18, U2OS n = 222; *globule* conformation HeLa VST n = 595, HeLa NT n = 353, HeLa LT n = 558, U2OS n = 366). All results and p-values are summarized in Table VI-8 and Table VI-9.

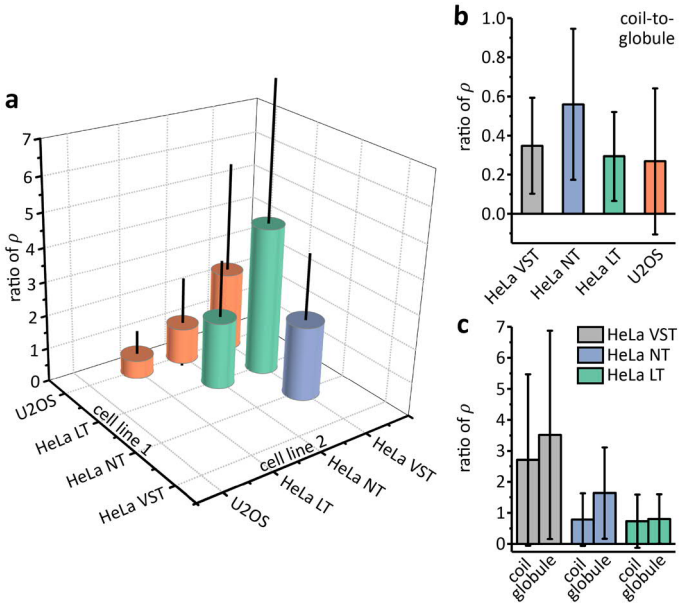

II.5.4.3 T-Loop Dimensions

To determine the average sizes of the loop portion (t-loop without tail) of the four cell lines, ellipse fitting was performed on all t-loop TelC PNA FISH STED images per cell line including both the *loop* output of the NN analysis and the *loop* training data. The fit provided average values and SDs for the semi-major and semi-minor axes, which were used to calculate an average ellipse circumference C for each cell line (Figure II-22). The results increased with increasing telomere length from HeLa VST (C = (267 ± 74) nm) and HeLa NT (C = (241 ± 62) nm) to HeLa LT (C = (312 ± 99) nm) and U2OS cells (C = (342 ± 87) nm) with no significant difference between HeLa VST and HeLa NT (Table VI-10, Table VI-11).

Assuming that telomeric DNA in intact cells is present in the form of unfolded nucleosome chains, the loop size can be expressed in units of base pairs. With a nucleosome repeat length of L_{repeat} = 191 bp, a core DNA length of L_{core} = 146 bp, a linker DNA length of L_{linker} = 45 bp, a base pair rise of $rise_{bare}$ = 0.34 nm for bare DNA, and an entry-exit distance in the nucleosome of approximately d_{nuc} = 9 nm, the base pair rise $rise_{nuc}$ of an unfolded nucleosome chain

$$rise_{nuc} = \frac{(L_{repeat} - L_{core}) \cdot rise_{bare} + d_{nuc}}{L_{repeat}} = 0.13\,nm/bp \quad \text{(II-14)}$$

can be calculated (refer to Figure II-7 and Table II-4) [686]. Table II-5 presents the results of the average t-loop circumference obtained from ellipse fitting divided by $rise_{nuc}$ for each cell line.

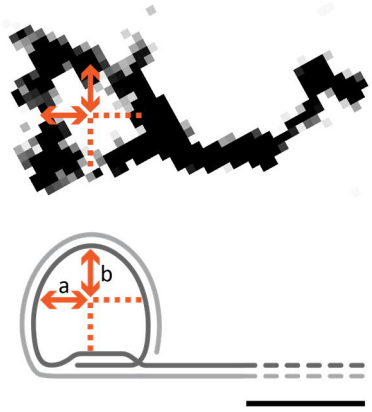

Figure II-22. Quantifying t-loop dimensions by ellipse fitting.

The size of the loop portion of t-loops can be determined by ellipse fitting of the t-loop STED data. The fitting results provide values for the semi-major axis a and the semi-minor axis b, which can be used to calculate the t-loop circumference. Scale bar is 250 nm.

Table II-5. Estimated average t-loop sizes in units of base pairs.

SD – standard deviation.

cell line	mean [kb]	SD [kb]
HeLa VST	2.1	0.6
HeLa NT	1.9	0.5
HeLa LT	2.4	0.8
U2OS	2.6	0.7

II.5.5 Human Telomere Conformations in APBs

To investigate the influence of PML-encasing on the telomere conformation and to resolve the topology of telomere repeats in APBs, ALT-positive U2OS cells were co-stained for telomeres and PML. For live cell confocal and STED imaging, specific targeting of telomeres and PML was achieved by transiently transfecting and overexpressing SNAP-tag or HaloTag fusions of the shelterin protein TRF2 and PML and subsequent staining with the respective SNAP- or Halo-derivatives of the live dyes 580CP [29], 610CP [29], 640SiRH [32] and SiR [30] (Figure II-23a,b, Figure VI-4). For fixed cell STED imaging followed by quantitative image analysis, telomeres were labeled via TelC-KK114 PNA FISH and PML via STAR 600-IF (Figure II-23a,c). Based on the dual-color stainings, telomere signals were sorted into `free´ telomeres not associated with PML and `encased´ telomeres located within APBs.

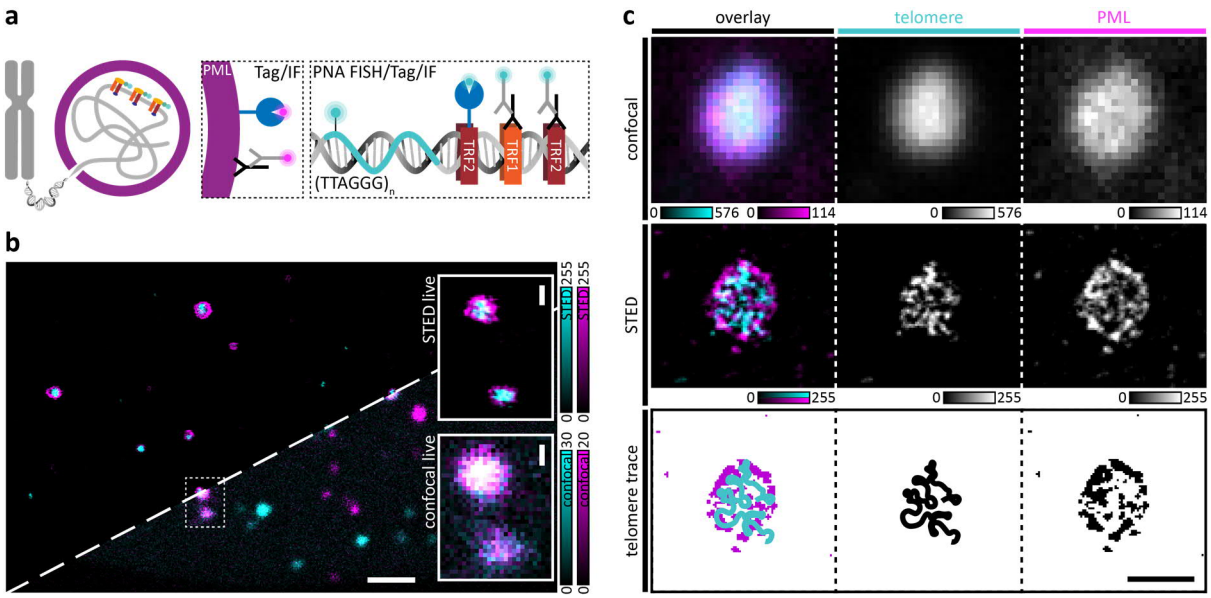

Figure II-23. Live and fixed cell STED imaging of APBs in U2OS cells.

(**a**) To resolve the topology of APBs, PML was targeted via either self-labeling protein tags or antibodies; telomeres were targeted either directly via TelC PNA FISH or indirectly via staining TRF2 through self-labeling protein tags or antibodies. (**b**) Comparison of a representative live cell STED (top) and live cell confocal (bottom) image of telomeres and APBs in a U2OS nucleus expressing a SNAP-tag/TRF2 (cyan) and a HaloTag/PML (magenta) fusion construct labeled with 610CP-BG and 640SiRH-Halo [29, 32]. Magnifications of the marked region in the overview are shown as STED (top) and confocal (bottom) close-ups on the right. Scale bar overview is 2 µm, scale bars close-ups are 250 nm. (**c**) For an exemplary APB stained by PNA FISH (TelC-KK114, cyan) and IF (PML STAR 600, magenta), raw confocal data (top row), and background corrected and linearly deconvolved STED data (middle row) are compared. In the STED image, the telomere trace (drawn by hand) through the PML cavities (segmented and binarized STED image) inside the APB can be followed as illustrated in the bottom row. Scale bar is 500 nm. All confocal data shown are raw data. All STED data shown are background corrected and linearly deconvolved.

II.5.5.1 PML Influence on Telomere Conformation

The groups of free and encased telomeres were separately classified with the same NN as used in II.5.2. In both cases, all four telomere conformations (*loop*, *rod*, *coil*, *globule*) were present (Figure II-24).

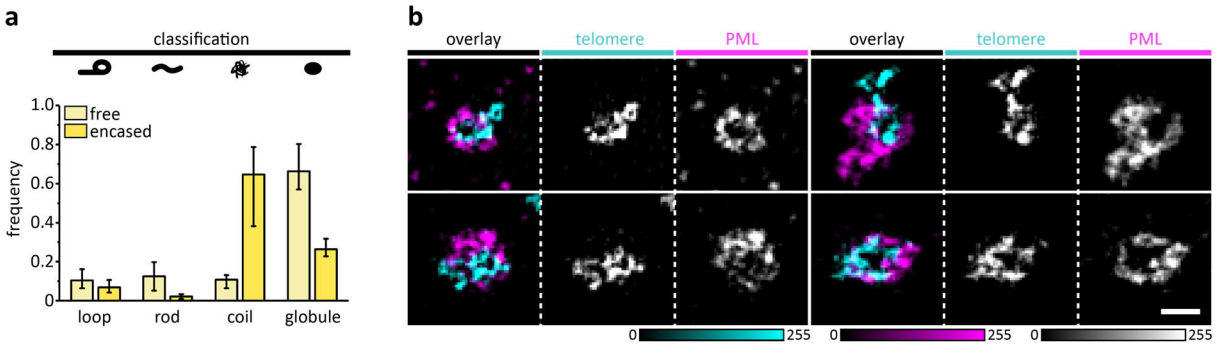

Figure II-24. PML-mediated telomere decompaction.

(**a**) NN analysis classifies telomere conformations (*loop*, *rod*, *coil*, *globule*) as visualized by STED imaging of TelC-KK114 PNA FISH stained free and encased telomeres in intact U2OS cells. PML-encasing drastically increases the frequency of the *coil* conformation at the expense of a declining *rod* and *globule* frequency and thus mediates telomere decompaction. The *loop* frequency is not strongly altered upon APB formation. Error bars are based on the frequency of false positives (negative error) and false negatives (positive error) identified during NN training. The results are summarized in Table VI-12 and Table VI-13. (**b**) Exemplary STED images of undisturbed t-loops within APBs. Telomeres (cyan) were stained via TelC-KK114 PNA FISH and PML (magenta) via STAR 600-IF. All STED data shown are background corrected and linearly deconvolved. Scale bar is 250 nm.

While PML-encasing did not strongly alter the frequency of *loop* telomeres (10% free ↓ 7% encased), essential differences were observed between the abundance of the *rod*, *coil* and *globule* states. In association with APBs, the U2OS telomeres preferred a more decondensed conformation, as was apparent by a six-fold elevation of the *coil* conformation level (11% free ↑ 65% encased) at the expense of the *globule* (67% free ↓ 26% encased) and the *rod* states (12% free ↓ 2% encased, Figure II-24, Table VI-12, Table VI-13).

II.5.5.2 PML Influence on Telomere Size

To study the influence of PML-encasing on the telomere size, the size measures introduced in II.5.4.1 were calculated for free and encased telomeres. The results for the area of the fluorescence signal A, the convex hull area $hullA$ and the radius of gyration R_g consistently displayed almost four times larger telomere signals within APBs (Figure II-25a, Table VI-14).

To investigate the size increase in detail, the three size measures were calculated for the individual conformations of free and encased telomeres as classified by NN analysis (refer to II.5.5.1). Similar to the effect on conformation frequencies, PML-encasing affected the average signal size of *coil* and *globule* telomeres more strongly than the average signal size of *loop* telomeres. For all three size measures, the average size of *coil* telomere signals increased more than three-fold and the average size of *globule* telomere signals more than doubled. The small number (n = 4) of encased telomeres classified as *rod* prevents significant statements on potential differences in the average size of the *rod* conformation between free and encased telomeres (Figure II-25b, Table VI-15).

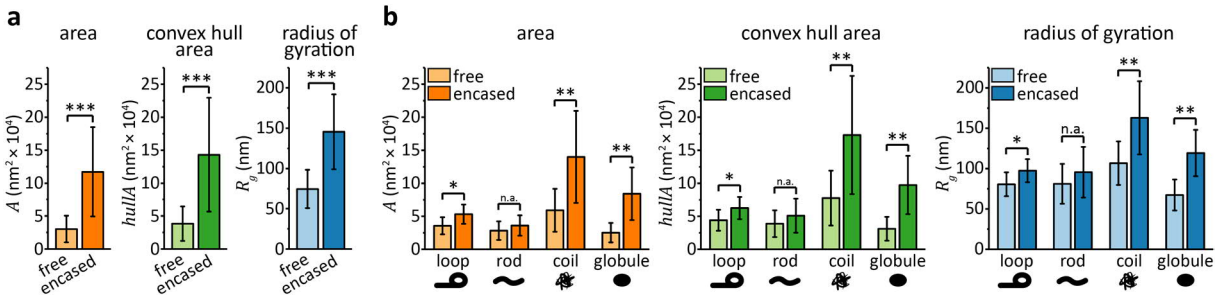

Figure II-25. Size measures of free and encased U2OS telomeres as determined by quantitative STED image analysis.

The area of fluorescent signal A, the convex hull area $hullA$ and the radius of gyration R_g were calculated based on the TelC-KK114 PNA FISH STED data of free and encased U2OS telomeres of (**a**) the entire telomere population (free n = 780, encased n = 190) and (**b**) after NN classification for the *coil* conformation (free n = 83, encased n = 123) and the *globule* conformation (free n = 521, encased n = 50) (* $p < 0.005$, ** $p < 10^{-19}$, *** $p < 10^{-76}$, n.a. p-value not available due to small n). All results and p-values are summarized in Table VI-14 and Table VI-15.

II.5.5.3 APB Topology

Dual-color STED imaging of telomeres and PML revealed a surprisingly high structural heterogeneity of APBs and allowed the identification of four main structural classes for the organization of the telomeric repeats in APBs (Figure II-26):

- ***Globular***. PML forms an intact, spherical shell around the complete telomere, which occupies the entire internal APB space. The *globular* APB appears as a two-component system with clear separation between telomere repeats inside and PML outside.
- ***Partially hollow***. PML forms an intact, spherical shell around the telomere, but for parts of the APB interior, the telomere signal is absent. The `empty space´ strongly varies in size between different *partially hollow* APBs and can take up almost the entire APB interior. The *partially hollow* APB appears as a multicomponent system with clear separation between telomere repeats and `empty space´ inside and PML outside.
- ***Granular***. PML does not form a shell around the telomere. Instead, the telomere displays an `open´ DNA conformation in which the decondensed telomere repeats intermingle with PML. The *granular* APB does not show any distinct separation between telomere and PML.
- ***Clustered***. PML encases repeats from two different telomeres. This structural class is the most diverse and includes APBs with more than one telomeric DNA protrusion, APBs with two discrete telomere spots within one APB, and complexes of two (or more) APBs. The *clustered* APB brings different telomeres together with clear separation between telomere repeats and PML.

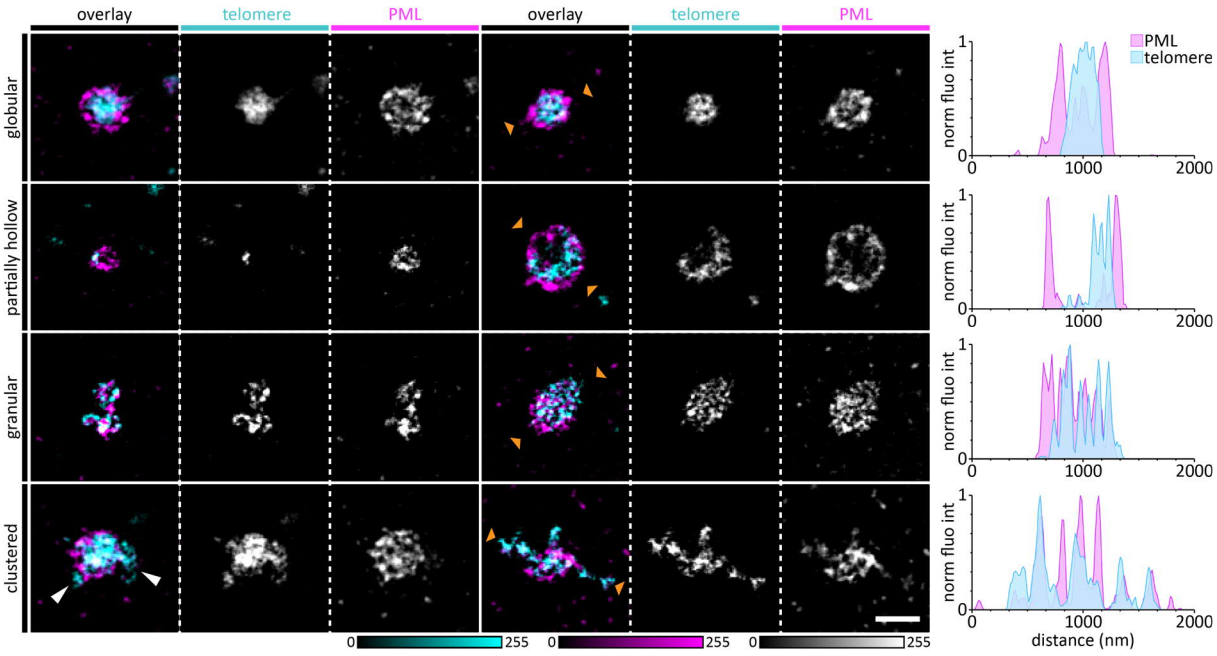

Figure II-26. The four main structural classes for the organization of telomeric repeats within APBs.

STED images of representative examples of the four main structural classes of APBs (*globular*, *partially hollow*, *granular*, *clustered*) in U2OS cells. For *clustered* APBs, two telomere protrusions are marked by white arrows in the first image. Line profiles (right) illustrate the topology of telomere (cyan, TelC-KK114) and PML (magenta, IF STAR600). Line profiles were drawn on raw data (indicated by yellow arrows on overlay) and averaged over 5 pixels. All STED data shown are background corrected and linearly deconvolved. Scale bar is 500 nm.

To confirm the results of the PNA FISH / IF hybrid staining approach, APBs in U2OS cells were additionally visualized by IF only and by live staining of SNAP- and Halo-fusion constructs. In both cases, the telomere had to be indirectly visualized via TRF1/2 targeting. Still, the results of fixed cell STED imaging of immunolabeled APBs and of live cell STED imaging of SNAP- and Halo-tagged APBs qualitatively confirm the presence of the four distinct APB structural classes (Figure II-27).

To investigate potential cell cycle dependence of the presence of the individual APB structural classes, their temporal coincidence in U2OS cell nuclei was investigated. All four APB structural classes were simultaneously observed in individual U2OS nuclei with different staining approaches (Figure VI-5 and Figure VI-6).

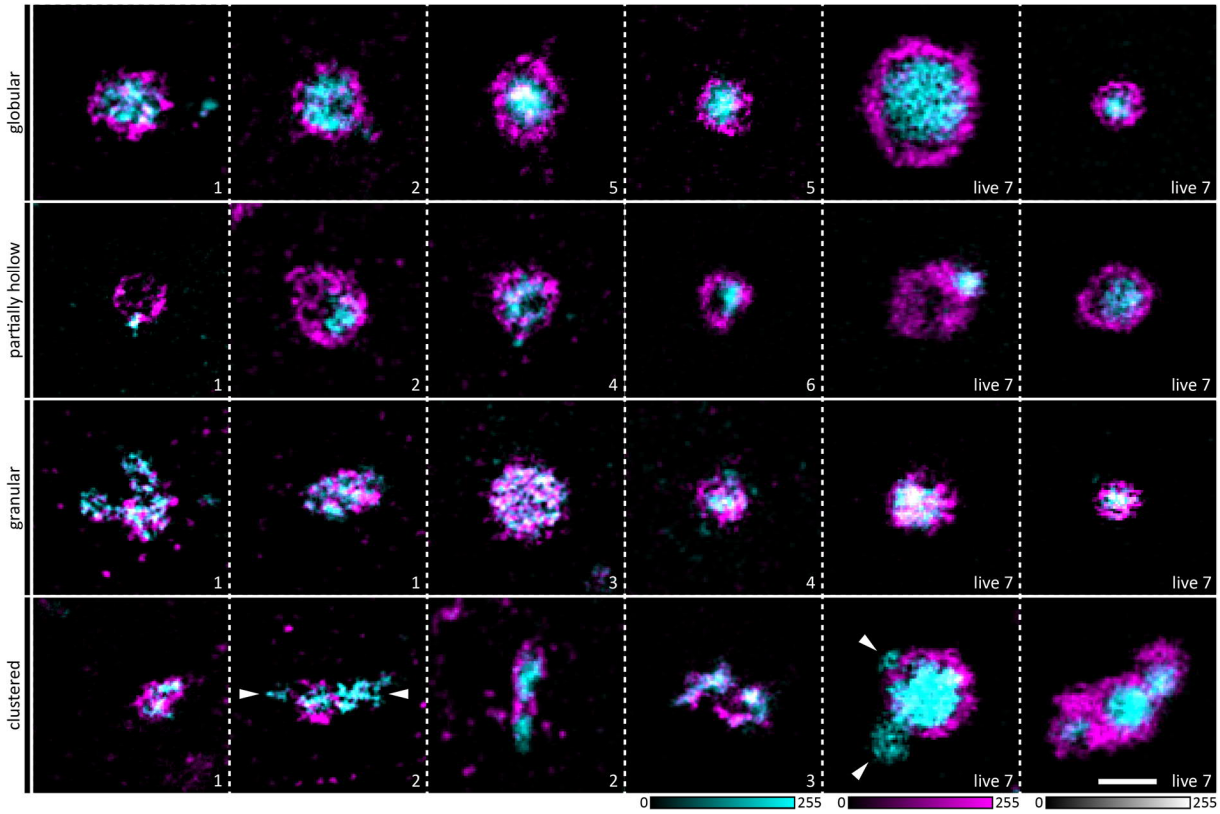

Figure II-27. Further examples for the four main APB structural classes.

Live and fixed cell STED images of representative examples of the four main structural classes of APBs (*globular*, *partially hollow*, *granular*, *clustered*) in U2OS cells. For *clustered* APBs, two telomere protrusions are marked by white arrows in the second and fifth images. The number at the bottom right states the respective labeling approach. 1: TelC-KK114 / PML IF STAR 600, 2: TRF2 IF STAR 600 / PML IF STAR35P, 3: TRF2 IF STAR 635P / PML IF STAR 600, 4: TRF1 IF STAR 600 / PML IF STAR 635P, 5: TRF1 IF STAR 635P / PML IF STAR 600, 6: TRF2-Halo 640SiRH / PML-SNAP 610CP, 7: TRF2-SNAP 610CP / PML-Halo 640SiRH. All STED data shown are background corrected and linearly deconvolved. Scale bar is 500 nm.

Figure II-28. Characterization of the topology of the subtelomeric region of APBs (figure on opposite page).

(**a**) To resolve the topology of APBs and STRs in F6B2 cells, PML was targeted via either fluorescent proteins, self-labeling protein tags or antibodies; telomeres were targeted either directly via TelC PNA FISH or indirectly via staining TRF2 through self-labeling protein tags or antibodies; the *lac*O repeat arrays at the STRs were targeted either directly via LacO PNA FISH or indirectly via LacI fusions with self-labeling protein tags. (**b**) F6B2 cells are *lac*O-tagged directly adjacent to the telomeres of chromosomes 11p (b), 6q (m) and 12q (s) [467]. Triple-color STED/confocal image of a representative F6B2 nucleus of PNA FISH stained telomeres (TelC-Alexa Fluor 594 (AF594), cyan) and STRs (LacO-KK114, yellow), and Alexa Fluor 488-immunolabeled PML (magenta). Bottom left: Telomeres, STRs and PML were imaged in confocal mode. Top right: Telomeres and STRs were imaged in STED mode, PML in confocal mode. The marked telomere/STR in the overview is shown in magnification as imaged in confocal mode (bottom left) and STED mode (top right). (**c**) Representative live and fixed cell close-ups of APBs and STRs. Telomeres and STRs were imaged in STED mode, PML in confocal mode. The number at the bottom right states the respective labeling approach (numbering continued from Figure II-27): 8: TelC Alexa Fluor 594 / LacO KK114 / PML IF Alexa Fluor 488, 9: TRF2-SNAP 610CP / LacI-Halo 640SiRH / PML-eGFP, 10: TRF2-SNAP 580CP / LacI-Halo 640SiRH / PML-eGFP, 11: TRF2-Halo 640SiRH / LacI-SNAP 610CP / PML-eGFP. The STR is either excluded from or (partially) included in the APB. Thus, the content of APBs is not restricted to telomeric repeats. The combined STED and confocal data are background corrected and linearly deconvolved; the confocal only data in (**b**) are raw data. Scale bar nucleus is 2 µm, all scale bars close-ups are 500 nm.

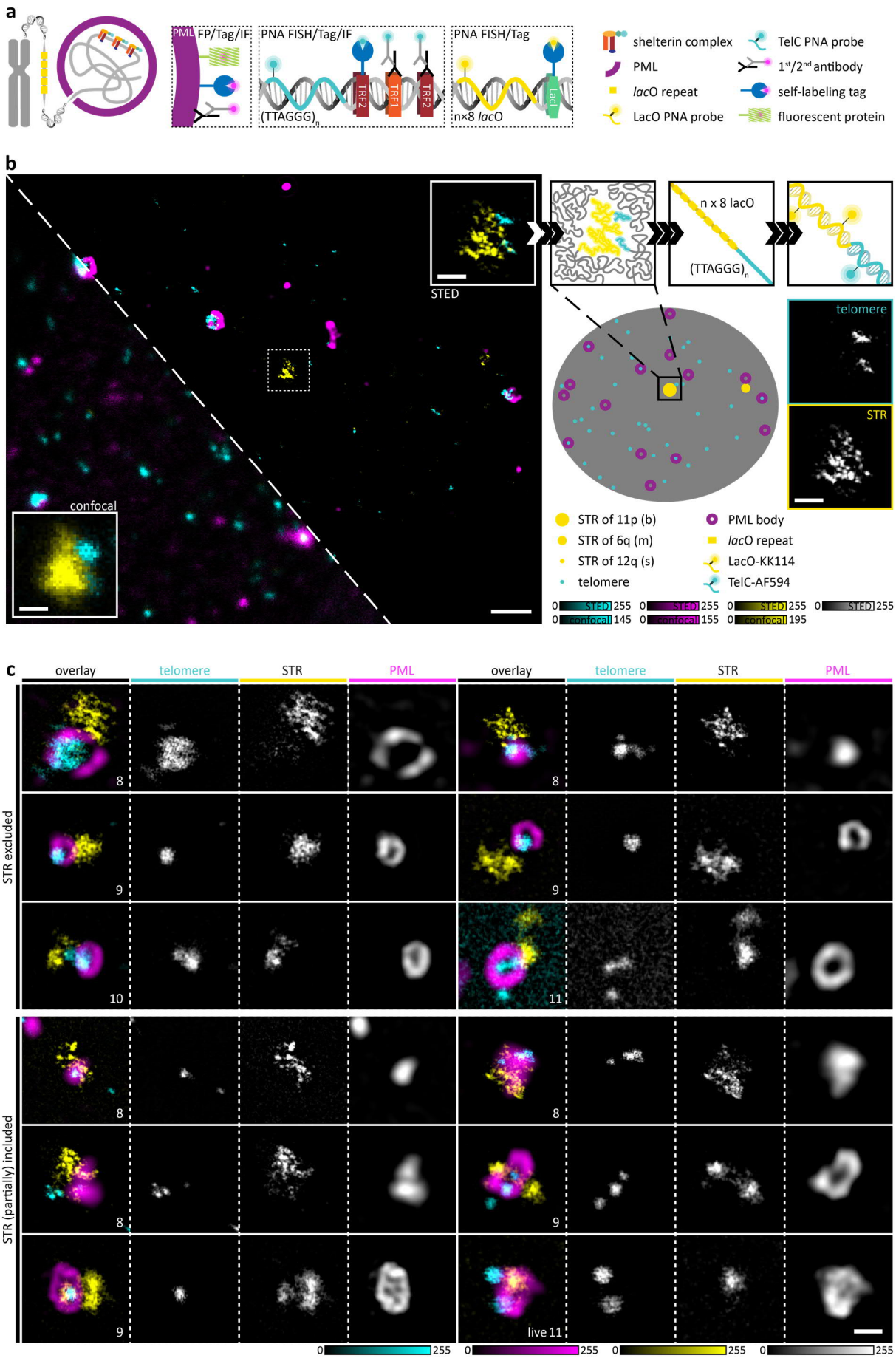
a
PML
FP/Tag/IF
PNA FISH/Tag/IF
TRF2
TRF1
TRF2
(TTAGGG)n
PNA FISH/Tag
LacI
n×8 lacO
shelterin complex
PML
lacO repeat
LacO PNA probe
TelC PNA probe
1st/2nd antibody
self-labeling tag
fluorescent protein
b
STED
confocal
n x 8 lacO
(TTAGGG)n
telomere
STR
STR of 11p (b)
STR of 6q (m)
STR of 12q (s)
telomere
PML body
lacO repeat
LacO-KK114
TelC-AF594
0 STED 255 0 STED 255 0 STED 255 0 STED 255
0 confocal 145 0 confocal 155 0 confocal 195
c
overlay
telomere
STR
PML
STR excluded
STR (partially) included
8
9
10
11
live 11
0 255 0 255 0 255 0 255

To study the spatial organization of the subtelomeric DNA relative to the APB complex, combined STED and confocal imaging of telomeres with three color labels in living and fixed ALT-positive F6B2 cells was performed (Figure II-28). For fixed samples, the telomere repeats and the *lac*O repeats at the STRs were labeled via PNA FISH and imaged in STED mode, whereas PML was immunolabeled and imaged in confocal mode. For live samples, the telomere and *lac*O repeats were indirectly labeled via SNAP-tag or HaloTag fusions of TRF2 and LacI (Lac repressor) and imaged in STED mode, whereas PML was visualized in fusion with eGFP by confocal imaging (Figure II-28a,b).

Both staining approaches provided complementary results showing that APBs do not strictly include or exclude STRs. The F6B2 APB population rather displayed the entire spectrum, comprising fully excluded STRs, partially included STRs and completely included STRs in APBs (Figure II-28c). NN analysis as performed in II.5.2 showed that the repetitive sequences at the STRs were even less compact and more open (*coil* 84%, *globule* 3%) than telomeric DNA within APBs (Figure II-17).

II.6 DISCUSSION

The telomeres at the end of linear human chromosomes assemble with the six-membered shelterin protein complex and buffer the loss of DNA during replication [488, 491]. Yet, comprehensive understanding of nature's solution to the end-protection problem remains elusive and contradicting findings regarding the role of shelterin-mediated telomere compaction have been reported [480-482]. A crucial aspect in this regard is the organization of telomere repeat DNA within the telosome. The sequestration of the 3'-overhang within t-loop structures masks the chromosome ends and thereby protects genome integrity[496].

T-loop structures have been first visualized by EM [483, 484] and more than a decade later by STORM, STED, SIM and Airyscan [485, 486, 655] but solely *in vitro* with purified mammalian telomeric DNA after cross-linking and spreading. These studies have identified TRF2 as the critical factor for t-loop formation and/or maintenance [483, 485, 486]. The majority of these experiments have investigated mouse telomeres. Since the human telomere repeat length (10-15 kb) is significantly shorter than that of mouse cells (40-50 kb), resolving human t-loops is more challenging [486]. So far, t-loop structures have not been imaged within intact cells, neither human nor mouse. Certainly, investigating telomeric structure and organization in the native cellular environment is desirable as it decreases the chances of studying preparation artefacts.

II.6.1 Staining Human Telomeres

Here, we combined STED nanoscopy with NN classification and quantitative image analysis to visualize and characterize telomere conformations in three different telomerase-positive HeLa cell lines and two different ALT-positive U2OS cell lines. Three distinct labeling approaches were tested for their informative value on the topology of telomeres and associated proteins. Certainly, all three labeling approaches guaranteed a significant gain in structural information comparing confocal and STED

imaging. Yet, the level of structural detail in the telomere STED images increased from live cell staining using SNAP-tag and HaloTag fusions of TRF2 over immunolabeled TRF2 to TelC PNA FISH.

In general, telomeres are often indirectly stained for fluorescence imaging by targeting TRF2 with antibodies or FPs [482, 622, 657, 658]. TRF2 specifically binds to double-stranded telomeric DNA, but the finite size of the TRF2/antibody complex or the TRF2/FP fusion protein positions the fluorophore up to tens of nanometers away from the telomere repeats, distances that fall in the range of the STED resolution. Precise determination of the telomere structure is thus impaired in these labeling approaches, as every fluorescence imaging technique never records the structure of interest but always the attached fluorophore itself. In contrast to FP-tagging or IF of TRF2, direct telomeric DNA staining with TelC PNA FISH places the fluorophore only 15 atoms (< 3 nm, two O-linkers) away from the telomere repeats.

Indeed, not only the distance between fluorophore and telomeric DNA matters, but also the labeling density does, i.e. the ratio between the numbers of labels and the number of telomere repeat base pairs. Based on biochemical assays investigating the *in vivo* stoichiometry of telomere repeats and shelterin proteins in human cells, an (over)abundance of the shelterin proteins suggests that most of the telomeric DNA is associated TRF2 [491].

However, we observed a surprisingly high heterogeneity of TRF2 coverage of telomeric DNA represented in a broad distribution of the PCC between TelC-KK114 stained telomeric DNA and STAR 600-immunolabeled TRF2 around $r = 0.52$. Certainly, the results of PCC calculations are additionally affected by the size of TRF2 decorated with primary and secondary antibody displacing STAR 600 away from the telomeric DNA and thus from KK114. Both dyes are comparably bright and photostable, but in STED imaging, the performance of KK114 should be superior to the performance of STAR 600 as the cross section for STED is smaller for STAR 600. Yet, this difference only accounts for a minor change in resolution.

Based on colocalization control experiments with TRF1 and TRF2, we are convinced that the discrepancies between the TelC PNA signal and the TRF2-IF signal are real and not due to incomplete TRF2 staining. As we investigated the TRF2 decoration only for U2OS telomeres, it cannot be excluded that the heterogeneity in TRF2 coverage is a characteristic feature restricted to ALT-positive cells. Indeed, it is suggested that partial telomere deprotection through reduced levels of TRF2 is crucial for initiating ALT-related repair processes [556, 557]. Still, for the purpose of telomere structure determination in U2OS cells, TRF2 represents no valid target and can only be stained to assess telomere positions. Certainly, co-stainings of TRF2 and telomeric DNA provide valuable insights into the telomere decoration by TRF2 allowing to infer structure-function relationships (see below).

With a size of 18 bp, the TelC probe should provide for a high labeling density. In practice, quantitative telomere covering is usually not achieved. Comparing the visual appearance of our actual STED data with the synthetic STED data of the Monte Carlo simulations for different labeling densities, we assume a labeling degree between 30-60%. Moreover, the TelC probes are very likely not homogeneously distributed over the telomere. Human telomeres carry the canonical core histone components and we speculate that the linker DNA is more accessible for PNA FISH than the core DNA wrapped around the histone octamer.

Finally, the level of structural detail in the telomere STED images further depends on the fluorophore's photophysical properties, namely high photostability, low dark state transition probability, and large cross section for stimulated emission. The methods of IF and PNA FISH can freely choose any desired organic dye. In contrast, live cell telomere staining based on SNAP- and Halo-fusions of TRF2 relies on biocompatible and cell membrane permeable fluorophores. Live dyes such as 580CP, 610CP and 640SiRH [29, 32] used in the present study, were just recently developed and hence are not yet as advanced in terms of photostability and brightness as the well-established organic dyes for fixed cell STED imaging. Consequently, the effective image resolution is commonly lower for live cell STED data. However, the amount of information that can be extracted from the live cell imaging data is not only affected by the dyes' photophysical properties. It is further reduced due to the need for faster image acquisition and more conservative imaging parameters to avoid motion blur and phototoxicity.

Summarizing the arguments, PNA FISH in combination with a STED compatible, bright and photostable fluorophore like KK114 [382] is the best choice for STED imaging of telomere repeats. The telomere topology can be resolved with a high level of structural detail as the fluorophore is placed directly at the telomeric DNA. We could thus distinguish separate telomeric DNA strands at distances of 30 nm. The major drawback of PNA FISH of telomeres is its limitation to fixed cells, although exceptions have previously been shown [622].

II.6.2 Visualizing T-Loops in Intact Human Cells

STED imaging of TelC PNA FISH labeled telomeric DNA revealed structural characteristics of individual telomeres and structural variations between the different cell lines at nanoscale resolution. Thus, we could tackle the long-standing question of the existence of t-loops in their native cellular environment. For all cell lines studied, t-loop structures were observed. For each cell line, the loop-to-tail ratio varied, and t-loops appeared either lasso-like or circular, depending on the position of the 3'-overhang sequestration. This observation is in good accordance with results from previous EM and STORM studies on isolated telomeric DNA [483, 485, 496]. Hence, we conclude that during t-loop formation, there is no predefined invasion site for the 3'-overhang along the double-stranded telomeric DNA.

II.6.2.1 T-Loop Frequency

The NN classification allowed us to quantitatively describe the contribution of the t-loop conformation to the telomere population of each cell line. The positive correlation observed between t-loop frequency and average telomere length is consistent with the expectation that for shorter telomere lengths the resolution of smaller loop structures becomes more challenging.

Our experimentally observed t-loop frequencies of 5-12% were lower than the results of previous EM and STORM studies on isolated telomeric DNA stating frequencies of 15-40% for HeLa (S3 and 1.2.11) telomeres and 10-40% for mouse telomeres [483, 485]. Moreover, we did not observe the negative correlation between t-loop presence and telomere decondensation in ALT-positive cells that previous EM and 2D gel electrophoresis studies reported. These experiments observed approximately three-

fold decreased t-loop frequencies in ALT-positive cells as compared to telomerase-positive cells [483, 484, 498].

We can rationalize these discrepancies by noting the following influences and dependences on t-loop detection in intact human cells with 2D STED imaging. It is not only the actual fraction of the telomere population adopting a t-loop conformation that determined our observed t-loop frequency, but additionally, several other aspects affected our results and in summary rather underestimate the actual t-loop frequency of our samples.

First, t-loop imaging in intact cells was significantly hampered by folded up and not `exposed´ t-loops. The chances of detecting t-loops was additionally reduced as we studied human samples with mostly shorter telomeres, thus smaller t-loops, than the previous imaging studies. However, with an elevated level of telomere decompaction in U2OS cells, the probability of t-loop detection was increased as compared to all HeLa cell lines with more compact telomeric DNA. Additionally, ALT cells feature extrachromosomal duplex or single-stranded circular arrays of telomere repeats [487]. These circular ECTRs can be distinguished from t-loop structures by 2D gel electrophoresis but not conclusively by our PNA FISH STED imaging approach. While single-stranded C-circles were not detected by the TelC PNA probe, which only targeted the G-rich strand, the duplex t-circles were detected and thus slightly increased the frequency of imaged loop structures in ALT cells. Theoretically, t-circles can be distinguished from t-loop structures as they are true DNA circles without a tail. However, as the loop-to-tail ratio of t-loops strongly varies and tails can be extremely short [483], we could not decide whether circular fluorescence signals without any apparent tail represented t-circles or t-loops (Figure II-29a). In these aspects, we underestimate the t-loop frequency of the three HeLa cell lines more strongly than the t-loop frequency of the U2OS cells.

Second, comprehensive mapping of each t-loop with TelC PNA FISH was potentially hampered by incomplete telomere labeling, occupation of dark states and/or photobleaching. We decided on stringent sorting criteria that filed partially imaged loop structures as `ambiguous´ and excluded these STED images from the training data. Thereby, we underestimate the t-loop frequency in this aspect.

Third, we recorded samples with unperturbed spatial 3D telomere orientations using a 2D STED imaging approach. For every fluorescence microscopy technique, the detected fluorescence signal is always a 2D projection of the 3D distribution of the fluorophores within the focal volume along z. The number of fluorophores contributing to the detected signal decreases with shrinking focal volume, which is given by the PSF of the respective system. For all 2D fluorescence nanoscopy techniques, the PSF is still diffraction-limited in the axial dimension and measures approximately 550 nm for 2D STED. Thus, within the 3D distribution of loop structures, we detected only the fraction of loops within the focal plane that featured the right orientation towards the focal plane. To be resolved as a lariat structure by our 2D STED system, t-loops had to be roughly aligned with the imaging plane (xy-plane). In perpendicular orientation (i.e. 90° rotated along x or y), t-loops generated rather linear fluorescence signals (Figure II-29b). In this aspect, we underestimate the t-loop frequency.

The fourth point partially relates to the previous one. Not all detected *loop* signals necessarily represented true t-loop structures. It is conceivable that certain non-lariat telomere conformations in 3D (e.g. helical telomere conformation along z) also generated lariat fluorescence signals upon 2D projection. A second source of false positive *loop* signals were random telomeric DNA conformations

incidentally forming lariat structures (Figure II-29c). Consequently, in this aspect we rather overestimate the t-loop frequency.

Fifth, the detected t-loop frequency is further affected by the performance of the NN classification. To be deliberately conservative in our statement concerning the t-loop frequency, we have chosen the NN with the highest $F1$ score but greater precision than recall. As false negatives had outweighed false positives during NN training, the NN also underestimated the t-loop frequency during inference.

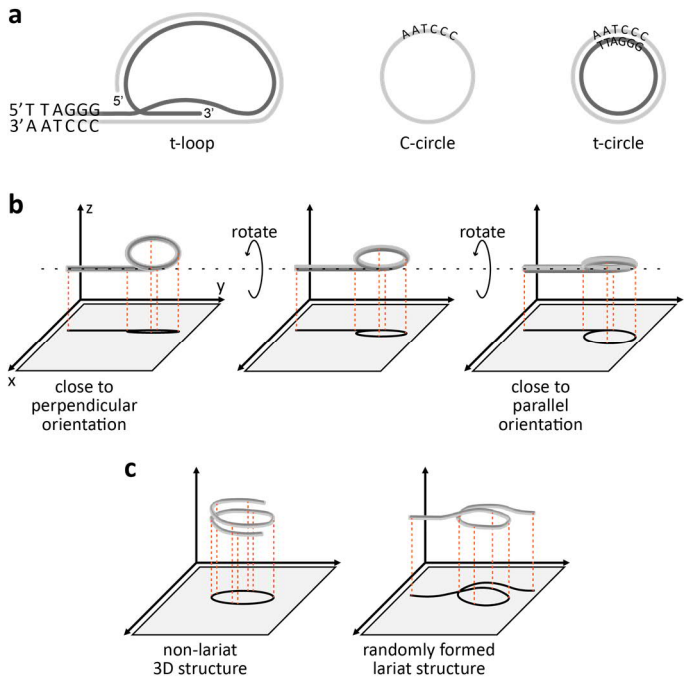

Figure II-29. Different telomere repeat loop structures of ALT cells and the consequences of 2D image acquisition in quantitative t-loop imaging.

(**a**) Besides the universal t-loop structure, ALT cells additionally feature extrachromosomal single-stranded (C-circle) and duplex (t-circle) circular arrays of telomere repeats. (**b**) The 2D detection of t-loops does not resolve lariat structures if the t-loops are perpendicularly oriented with respect to the imaging (xy) plane. The closer the t-loop orientation is towards a parallel orientation (i.e. 90° rotated along x or y), the less perspective distortion the t-loop image displays. (**c**) Certain non-lariat telomere conformations (e.g. helical conformation along z) as well as incidentally formed lariat structures through random telomeric DNA conformations also generate lariat fluorescence signals upon 2D image acquisition. Thus, not all detected *loop* signals necessarily represent true t-loop structures.

With respect to the fourth aspect, the contribution of false positive *loop* structures was estimated in a biological and a computational control. The NN classification of the STED images of LacO PNA FISH labeled STRs in F6B2 cells showed only a minor fraction of the *loop* conformation; the synthetic telomere STED data generated by Monte Carlo simulations revealed a low average frequency of apparent *loop* conformations. We thus conclude that the number of false positive *loop* signals detected in our analysis due to random DNA loop formation and/or due to imaging artefacts is < 2%.

We expect the influence of cell cycle dependent t-loop formation and/or maintenance on our results to be negligible. This assumption is based on biochemical assays in recent literature showing that t-loops are closed throughout the cell cycle and only open in two very short time frames during S phase for replication and during late S/G2 phase for C-strand fill-in DNA synthesis before they immediately refold again [484, 498, 698, 699].

II.6.2.2 T-Loop Size

The increase in t-loop circumference with increasing average telomere length of the four cell lines studied qualitatively confirms previous findings on a correlation between the dimensions of the loop portion of t-loops and the average telomere length [483]. However, our results did not mirror the ratio of the average telomere lengths of HeLa VST, HeLa NT, HeLa LT and U2OS as initially expected. The

differences in the average loop size between the four cell lines were markedly smaller. This can be partially explained by noting that the loop portion of t-loops in ALT-positive cell lines is generally small with respect to the total telomere length [484].

Comparing our results to literature values is not straightforward as previous studies have only characterized t-loops consisting of bare telomeric DNA after isolation and spreading. In contrast, we had to make assumptions on the state of the telomeric DNA in intact cells to derive the number of base pairs contained in the loop portion of t-loops from our results of the ellipse fitting. In accordance to our Monte Carlo simulations, we described the telomeric DNA as nucleosome chains with a defined base pair rise based on established literature values [686].

However, this model deviates from the biological reality as the majority of telomere repeats are organized in an unusual chromatin structure. The nucleosome repeat length is smaller than in bulk DNA and telomeric nucleosomes are more mobile and less stable than regular nucleosomes sliding along the telomeres. Deeper insights into the higher-order organization of telomeric chromatin remain elusive, but the short nucleosomal spacing rather suggests the absence of higher-order chromatin condensation [700, 701].

Therefore, we assume that our results rather underestimate the number of base pairs contained in the loop portion. The comparison with literature values supports this assumption. As we did not use the same cell lines as previous studies did, cell lines with similar average telomere lengths are compared (Table II-6). The most prominent difference is found between the average loop size of HeLa LT cells and the average loop size of HeLa 1.2.11 cells as determined by Griffith *et al.* [483]. Despite a comparable average telomere length, the average loop size of HeLa LT cells is almost six times smaller. In contrast, our results for HeLa NT and U2OS cells are around half of the respective average loop sizes of HeLa S3 cells and normal human peripheral blood leukocytes (PBLs) as determined by Griffith *et al.* [483] and the mean loop size of the ALT-positive cell lines GM847 and GM847-Tert as determined by Cesare *et al.* [484].

Table II-6. Comparison of the average size of the loop portion of t-loops to results from previous studies.

The average telomere length is given as stated in the respective reference. The mean ± SD for the loop size of GM847 and GM847-Tert were estimated from the histogram presented in the respective reference.

this study			literature			
cell line	**average telomere length [kb]**	**loop size [kb]**	**cell line**	**average telomere length [kb]**	**loop size [kb]**	**reference**
HeLa LT	~20	2.4 ± 0.8	HeLa 1.2.11	~23	13.8±6.2	[483]
HeLa NT	~7	1.9 ± 0.5	HeLa S3	~10	5.8±3.5	[483]
			human PBL	~7	2.9±1.9	[483]
U2OS	2-50	2.6 ± 0.7	GM847	10-50	6.4±0.5	[484]
			GM847-Tert	10-50	5.8±0.6	[484]

For HeLa VST, the reviewed literature does not contain any experiments on t-loops from cells that feature a comparable average telomere length. The average circumference of HeLa VST t-loops is similar to the average HeLa VST telomere length as determined by the TRF analysis. However, as we assume systematic underestimation of the number of base pairs contained in the loop portion, we are led to presume a larger number of base pairs in the HeLa VST t-loops than determined by TRF analysis for the average HeLa VST telomere. This observation is certainly explained with the finite resolution of our imaging approach, which sets a lower limit to the detectable t-loop size. Thus, the smallest HeLa VST t-loops are missed. Additionally, we speculate that the shorter the telomere is, the more unlikely t-loop formation gets [702].

Except for the average loop size of HeLa LT, our results are compatible with the results from previous studies for two reasons. On the one hand, the SDs of the literature values reach up to 60% of the calculated means. On the other hand, our approach systematically underestimates the size of the loop portion of t-loops. First, our results for the number of base pairs contained in the loop portion are based on general assumptions on bulk chromatin structure not tailored to the true biological nature of the telomeric chromatin. Second, many of the t-loops imaged in intact cells were likely not fully exposed and still partially folded up thereby hiding their actual size. This aspect is presumably more pronounced with longer telomeres of HeLa LT cells and U2OS cells. Third, all t-loops not perfectly aligned with the imaging plane generated skewed loop images upon 2D projection with circumferences of the *loop* signals smaller than the actual t-loop circumferences (Figure II-29b).

To estimate the maximum error of 2D projection, the idealized assumption of circular t-loops was made. In this approach, the semi-major axis a as determined by fitting to an ellipse represents the radius of the circular t-loop, as we defined the tilting axis to run parallel to a. For the four cell lines studied, the circumference $C_{ideal} = 2\pi a$ of the circular t-loop is ~25% larger than the circumference C calculated from the semi-major and semi-minor axes determined by the ellipse fitting (Table VI-11). However, we assume the error based on compaction and folding of telomeric chromatin to be larger.

II.6.2.3 T-Loop Substructure

Based on several *in vitro* studies, TRF2 is suggested to mediate t-loop formation. In these experiments, TRF2 was shown to remodel artificial telomeric DNA substrates into t-loop like structures [483, 703], to promote supercoiling in telomeric DNA and to induce strand invasion [704-706]. This suggestion was recently supported by two STORM imaging studies with isolated mouse telomeric DNA showing that t-loop formation and/or maintenance critically depend on TRF2 [485, 486]. As Holliday junctions are bound and protected by TRF2 *in vitro* [705, 707], TRF2 presumably functions as `glue´ closing and stabilizing the t-loop structure. However, TRF2 decoration of exclusively the loop-tail junction (the position of 3'-overhang invasion) has yet been visualized only by EM with an artificial telomeric DNA substrate *in vitro* [483].

Thus, we set out to investigate the t-loop substructure with STED nanoscopy and map the localization of TRF2 at t-loops in intact U2OS cells in dual-color STED experiments. The two distinct TRF2 distributions at t-loops suggest cell cycle dependent TRF2 binding patterns. We assume that TRF2 is diffusely distributed over the entire t-loop during most of the cell cycle but accumulates at the loop-

tail junction during specified, short stages. As t-loops are suggested to rapidly unfold and refold twice during the cell cycle (refer to II.6.2.1) [498], we hypothesize that for refolding, TRF2 forms hotspots at the future loop-tail-junction to promote 3'-overhang invasion and thus t-loop formation of the unfolded telomeres. We further speculate the *rod* telomere conformation as classified by NN analysis to represent unfolded t-loops during replication as the *rod* and *loop* frequency are similar for each cell line. Yet, to address this issue in detail, further cell cycle dependent studies will be needed.

To the best of our knowledge, this is the first time that substructural features of t-loops have been visualized in their native cellular environment.

II.6.3 Comparing Human Telomere Populations

All measures of telomere size mirrored the increase in average telomere length ranging from HeLa VST, to HeLa NT, HeLa LT and U2OS cells. Yet, we must note at this point that the area of fluorescent signal, the convex hull area and the radius of gyration each probe slightly different telomere size characteristics. While the convex hull area is sensitive to the compaction state of the telomeres as it only uses the edge points of the telomere signals, i.e. the telomere repeats at the boundary of the telomere spots, the area of fluorescent signal takes into account that telomere outlines have concavities. Similarly, the radius of gyration makes no assumptions on the telomere shape and uses every signal containing pixel to determine the telomere size, but it strongly depends on the level of compaction of the respective telomere. Thus, we only observed a weak proportionality of the three size measures indicating differences in the compaction state of the telomeric chromatin between the four cell lines studied (see below).

To compare our results to previous findings from SMLM studies investigating telomere sizes in intact human cells, we additionally computed the convex hull volume. For HeLa NT and HeLa LT, the convex hull volume and especially the radius of gyration nicely agree with the respective size measures for regular HeLa and HeLa 1.2.11 cells as determined by Bandaria *et al.* [482] and for HeLa S and HeLa L cells as determined by Vancevska *et al.* [481] (Table II-7). For HeLa VST and U2OS, the reviewed literature does not provide any information on measures of telomere size for comparable cell lines.

The absence of direct proportionality between the average telomere length and the measures of telomere size as well as between the size measures themselves indicated changes in the compaction state of telomeric DNA between the four cell lines studied. Based on histone and DNA modifications, it is accepted that telomeres generally exist as heterochromatin [494]. However, biochemical assays have identified telomeric DNA in ALT-positive cells to adopt a less compacted state than in telomerase-positive cells. These results have fueled the speculation that telomeric chromatin decompaction might be one of the driving events of ALT occurrence [531]. Still, contradicting findings exist concerning the correlation between the average telomere lengths and telomere compaction of different HeLa cell lines [481, 482].

While previous telomere SMLM imaging studies have assessed the extent of telomere decompaction by calculating different measures of telomere size from the fluorescence signals [480-482], we investigated an alternative approach based on telomere conformation classification, which has not

been pursued previously. Besides quantifying t-loop frequencies, our NN analysis additionally allowed characterization and comparison of the telomere populations of the individual cell lines studied. The striking difference of the *coil*-to-*globule* ratio between U2OS cells (2:3) and the three HeLa cell lines (> 1:20) strongly points to variations in the level of telomeric chromatin compaction. The ratio of the volume densities of the *coil* and *globule* state unambiguously confirm the *coil* conformation to be less compact and more open than the *globule* conformation. Thus, these results clearly indicate an overall decompaction of U2OS telomeric DNA.

Table II-7. Comparison of the average size of telomere signals to results from previous studies.

The average telomere length is given as stated in the respective reference. The mean ± SD for the convex hull volume of HeLa 1.2.11 was estimated from the bar plot given in the respective reference. The means for the convex hull volume of HeLa S and HeLa L were estimated from the bar plot (no SDs given) in the respective reference. R_g – radius of gyration, $hullV$ – convex hull volume.

this study				literature				
cell line	**average telomere length [kb]**	**R_g [nm]**	**$hullV$ [nm³×10⁶]**	**cell line**	**average telomere length [kb]**	**R_g [nm]**	**$hullV$ [nm³×10⁶]**	**reference**
HeLa NT	~7	68±13	5.1±2.6	HeLa	~6	---	2.3±0.2	[482]
				HeLa S	~11	68±20	4.2	[481]
HeLa LT	~20	77±16	7.7±4.8	HeLa 1.2.11	~20	---	6.1±0.4	[482]
				HeLa L	~33	88±22	10.0	[481]

This conclusion from NN analysis was compared with the measure of volume density of telomeric DNA as defined by Vancevska *et al.* [481]. In contrast to the NN classification results, the ratios of volume densities for the entire telomere populations did not represent the outstanding status of the U2OS cell line regarding the degree of telomere decompaction. On closer examination though, the ratio of *coil*-to-*globule* volume densities confirms that U2OS cells feature an elevated level of decompacted telomeric chromatin. However, bulk telomere population analysis hides this important subpopulation as the U2OS *globule* conformation is strongly decompacted.

This observation demonstrates the importance of studying the characteristics of telomere ensembles based on their individual subpopulations. By analyzing the entire telomere ensemble solely at once, relevant information from subpopulations are averaged out. For HeLa NT and U2OS, the bulk analysis of volume densities did not suggest significant variations in the level of telomere (de)compaction whereas the analysis of the individual telomere conformations revealed important differences in the degree of (de)compaction.

As we compare cell lines with different average telomere lengths, we must consider that the level of telomere (de)compaction presumably correlates to a certain degree with the average telomere length. Vancevska *et al.* have shown that the volume density of telomeric chromatin increases by a factor of 1.4 ± 0.6 from HeLa S (~11 kb) to HeLa L cells (~33 kb) [481]. Our results for the ratios of volume densities between HeLa VST, HeLa NT and HeLa LT qualitatively confirm this finding. However, contradicting conclusions concerning the correlation of telomere compaction and average telomere

length exist. Bandaria *et al.* have not observed an increase in telomere compaction from regular HeLa (~6 kb) to HeLa 1.2.11 cells (~20 kb) [482]. This discrepancy might originate from the fact that Bandaria *et al.* have stained telomeres by fusing TRF2 to the pcFP mEos2 to allow for PALM imaging, while in this work, as in Vancevska *et al.*, telomeres have been stained via PNA FISH.

Strictly speaking, by assuming a correlation between telomere (de)compaction and average telomere length, the volume density of U2OS telomeres should be compared only to the volume density of HeLa LT telomeres. The ratios of volume densities between the U2OS and the HeLa LT cell line for the entire telomere populations as well as for the *coil* and *globule* states strongly support the initial hypothesis that ALT-positive cells feature less compact telomeric DNA than telomerase-positive cells.

Taken together, our NN analysis enabled us to distinguish ALT-positive and telomerase-positive cancer cell lines based on conformational characteristics of their individual telomere populations. To the best of our knowledge, this is the first study to differentiate the two different TMMs using a combination of fluorescence microscopy and deep learning.

II.6.4 Interpreting Human Telomere Conformations

Besides the direct function of t-loops in genome integrity protection, further structure-function relationships are inherently linked to the telomere repeat topology but are only partially understood. The role of telomere decompaction in DDR signaling is still under debate and the driving force for telomere clustering remains elusive [480-482]. The clustering of telomere repeats from different chromosomes is suggested to play a significant role in telomere maintenance via the ALT pathway. The formation of APB complexes is assumed to promote telomere elongation by DNA recombination involving telomere clustering and DNA repair processes [45, 487]. Still, the telomere repeat topology within APBs has not yet been resolved at the nanoscale.

The combination of dual-color STED imaging, neural network classification and quantitative image analysis revealed an additional subpopulation of the U2OS telomere ensemble defined by PML-encasing. The presence of an extra telomere subgroup explains the larger SDs of the measures of U2OS telomere size as observed in the first round of quantitative U2OS telomere image analysis.

PML-encasing correlated with an increased average size of the telomere signal and an elevated average degree of decompaction. While the average size of free U2OS telomeres is in good accordance with our results for HeLa LT telomeres, telomeres within APBs are significantly larger and less compact. Our results do not unambiguously tell if PML preferentially encases longer and more decondensed telomeres or if PML-encasing induces telomere elongation and decompaction. Yet, we speculate that the telomere size difference between free and encased telomeres hints at telomere elongation and/or telomere clustering within APBs. Based on previous suggestions, we further assume that APB formation promotes an open telomeric DNA state, which facilitates ALT-related DNA recombination and/or repair synthesis [531]. As PML-encasing had no significant influence on the classified *loop* frequency but essentially reduced the *rod* and *globule* population, we reason that the t-loop structure is insensitive to PML-induced decompaction.

Although of great interest, we did not calculate the ratio of volume densities between free and encased telomeres as the results of the NN classification and the quantitative image analysis indicate significant differences in both average telomere length and compaction state. By knowing one of the two quantities, the other quantity can be inferred. Certainly, the level of (de)compaction directly influences the convex hull area and the radius of gyration. Therefore, these size measures cannot be used to calculate a ratio of average telomere length between free and encased telomeres. In principle, the area of fluorescent signal is insensitive to the compaction state. However, the nature of 2D image acquisition as discussed above also introduces a dependence of the area of fluorescent signal on the level of (de)compaction. Analyzing fluorescence intensity potentially allows for conclusions on the amount of FISH labeled DNA. Yet, strong differences in the compaction state render the individual telomere populations more or less accessible to the PNA probes making quantitative fluorescence intensity analysis impossible.

The detailed analysis of APBs identified four main structural classes for the PML-DNA topology. *Globular* APBs represent the only structural class that has been characterized previously. Using 4Pi microscopy, Lang *et al.* have pictured APBs as spherical structures of varying size with the PML shell clearly separated from the enclosed telomere, which occupies the entire internal APB space [544]. While our results confirm this topology description for a subgroup of APBs, they further revealed the presence of unknown APB structural classes. These other APB types have previously been missed by Lang *et al.* since the 4Pi imaging approach was limited to a resolution of ~110 nm axially and 150-170 nm laterally [544].

In *partially hollow* APBs, the APB interior displays telomere-free regions. We speculate that this `empty´ space is in fact occupied by other protein complexes presumably involved in ALT telomere maintenance as it is known that APBs colocalize with a long list of factors involved in homologous recombination (e.g. MUS81, replication protein A, RAD51 and RAD52), DNA damage response and DNA damage repair (e.g. 9-1-1 complex, hRAD17, γH2A.X, HP1) [537]. We hypothesize that PML-NBs support efficient telomere recombination by ensuring that the respective repair and recombination factors are at the right location, in the right combination and at the right concentration. This assumption is supported by a recent study showing that repair and recombination factors are client molecules recruited to the APB after APB formation by DDR signaling [708]. As we could show that the APB content occasionally expands to partially include also STRs, we conclude that part of the `empty´ space can be additionally occupied by STRs.

In *granular* APBs, telomere and PML are blended into each other creating a meshwork of both components. We reason that the interaction of PML and telomere (and potentially other ALT specific factors) decondenses the telomeric chromatin. Less compact telomeres are more accessible to proteins involved in ALT-related recombination and repair synthesis as strong condensation efficiently suppresses extensive interactions by simple protein exclusion. Interspersion of the decondensed telomere with PML presumably stabilizes its open DNA conformation and supports the access of ALT-specific factors.

The topology of *clustered* APBs implicates the presence of more than one telomere per APB. This structural class supports previous conclusions about APBs promoting interactions between telomeres. We reason that it displays telomere clustering required for the homologous recombination of

telomeres in the ALT maintenance mechanism by providing repair templates for telomere DNA synthesis. It has been previously shown that APB formation can be triggered by DNA damage at the telomeres induced by either replication stress or double-strand breaks. It entails telomere clustering and telomere elongation within the induced APBs [567]. However, the physical mechanisms underlying telomere clustering remain elusive [468, 567]. We cannot exclude that *clustered* APBs also involve APBs nucleated on ECTRs and telomeres. It can be assumed that ECTRs cluster more efficiently with telomeres, as they are more mobile than telomeres [708].

These APB structural classes commonly underline the fundamental role of PML in the ALT pathway by implicating PML-dependent recruitment of ALT-related factors and promotion of telomere recombination. As the different APB types were simultaneously observed in individual U2OS nuclei, we do not assume any cell cycle dependence. Yet, further cell cycle dependent studies will be needed to address this issue in detail.

Analyzing the nature and spatial localization of the subtelomeric DNA relative to the APB complex provided new insights into the APB topology. Our results suggest that the DNA content of APBs can expand to include subtelomeric DNA sequences beyond the telomere repeats. Fixed and live cell STED data are mutually supportive but certainly display a difference in image quality due to the reasons discussed in II.6.1. However, acquiring large data sets was challenged by the fact that F6B2 cells carry only three stably integrated *lac*O repeat arrays at their STRs and display solely 3-5 APBs per nucleus while featuring chromosome counts in the hypertriploid range.

Based on histone and DNA modifications it is accepted that STRs just like telomeres exist as condensed heterochromatin [494]. However, contradicting findings persist on the methylation pattern at the STRs of ALT-positive cells and its implication for the ALT pathway [531, 709, 710]. As DNA methylation is affiliated with chromatin compaction [711], we speculate that at least for certain ALT cells, hypomethylation causes decompaction of the STRs as revealed by our NN classification analysis for non-lariat telomere and STR structures. The results show an overall elevated level of decompacted DNA conformations of the repetitive sequences at the STRs as compared to the telomere repeats within APBs. The ratio of volume densities was not calculated as the only estimate of the *lac*O insert lengths is based on confocal imaging and the assumption of a bulk chromatin density for the STRs [467], which contradicts our findings.

In summary, by combining PNA FISH, STED imaging, neural network classification and sophisticated image analysis, we quantitatively characterized t-loops and different non-lariat telomere conformations in intact human cells. As our approach did not depend on artificial telomere preparations, we could exclude potential artefacts introduced by psoralen cross-linking, DNA isolation and sample spreading. Characterizing the topology of telomere subpopulations in their native cellular environment is important for the identification of structural differences between different TMMs. As emerging anti-cancer therapies target telomere maintenance, it is crucial to understand the defects that underlie telomeric recombination deregulation in human cells. Disclosing structural differences between healthy and diseased cells may finally lead to a better understanding of telomere dysfunction in aging or cancer and pave the way for new diagnostic and therapeutic developments.

II.7 CONCLUSION

Our telomere STED imaging study afforded the visualization of the structure and organization of telomere repeats in fixed and living cells at the nanoscale. In particular, PNA FISH combined with STED imaging, neural network classification and sophisticated image analysis allowed us to quantitatively distinguish and characterize t-loops and distinct non-lariat telomere structures. To the best of our knowledge, this is the first visualization of t-loops in intact human cells. Dual-color STED experiments further provided the first visual evidence for TRF2-dependent t-loop formation and/or maintenance.

In contrast to artificial *ex cellulo* telomere preparations, our experiments preserved the topology of telomeric DNA throughout the entire telomere population and did not favor one conformation over any other. Our approach excluded artefacts potentially introduced by the established sample preparation method of psoralen cross-linking, DNA isolation and sample spreading onto a surface. Accordingly, we could investigate the structural characteristics of telomere populations in their native environment.

By that very fact, our study further revealed the topology of telomere repeats within APBs of ALT-positive cells. APB complex formation was observed to significantly perturb the organization of telomeric DNA towards an open conformation, which potentially promotes ALT-related DNA repair and recombination. Our NN analysis was able to detect this conformational difference between ALT-positive and telomerase-positive cell lines. For the first time, the two TMMs were distinguished by a combined approach of fluorescence imaging and deep learning. Moreover, our nanoscale STED image analysis obtained additional evidence suggesting telomere elongation within APBs.

In summary, we demonstrated that STED imaging in combination with an adequate labeling approach is a powerful method to investigate the topology of telomeres, associated proteins and subtelomeric DNA. This study provides a combination of tools that will unravel the structural organization of key player proteins at telomeres in their native cellular context. As structure and function are intrinsically connected, any insight into the topology of the telosome will shed light on the role of the respective proteins and telomere conformations in either aging, tumor suppression or telomere maintenance in cancer. Extended knowledge in these fields will pave the way for the development of alternative diagnostics and treatments for telomere dysfunction related diseases.

III – APPLICATION:

THE SUBCELLULAR FATE OF DUAL-LABELED PSMA INHIBITORS AT THE NANOSCALE

III.1 INTRODUCTION

Prostate cancer (PCa) is one of the most prevalent male cancer types and figures among the main causes of cancer-related mortality [712]. In particular, therapeutic options for metastatic, hormone-refractory PCa patients have been limited, but the development of novel prostate-specific membrane antigen (PSMA) inhibitors has revolutionized the diagnostic and treatment regimen of these patients over the last decade [713-717].

Radiolabeling turns these molecules into powerful tools enabling targeted imaging and therapy approaches based on PSMA. The membrane protein represents an attractive target because it is strongly upregulated in poorly differentiated, hormone-refractory and metastasized lesions of almost all PCa types [718-722] and its physiological expression is limited to a few organs, with significantly lower expression levels as compared to cancer tissue [718, 723].

The specificity of PSMA can be further exploited in the surgical removal of PCa lesions, a potential cure for patients with metastatic PCa. However, only precise detection and resection of all malignant tissue guarantee patient survival. These requirements are elegantly met with novel dual-labeled PSMA inhibitors featuring radioactive and/or fluorescent reporter modalities to combine pre-operative imaging with intra-operative guidance (Figure III-1) [48, 724].

However, mechanistic details of PSMA inhibitor internalization and intracellular distribution remain elusive as the subcellular fate of the PSMA/PSMA inhibitor complex has not yet been studied at the nanoscale. Deeper insights are clinically interesting since cell binding and internalization properties as well as the subcellular localization strongly affect the diagnostic and therapeutic efficiency of PSMA inhibitors.

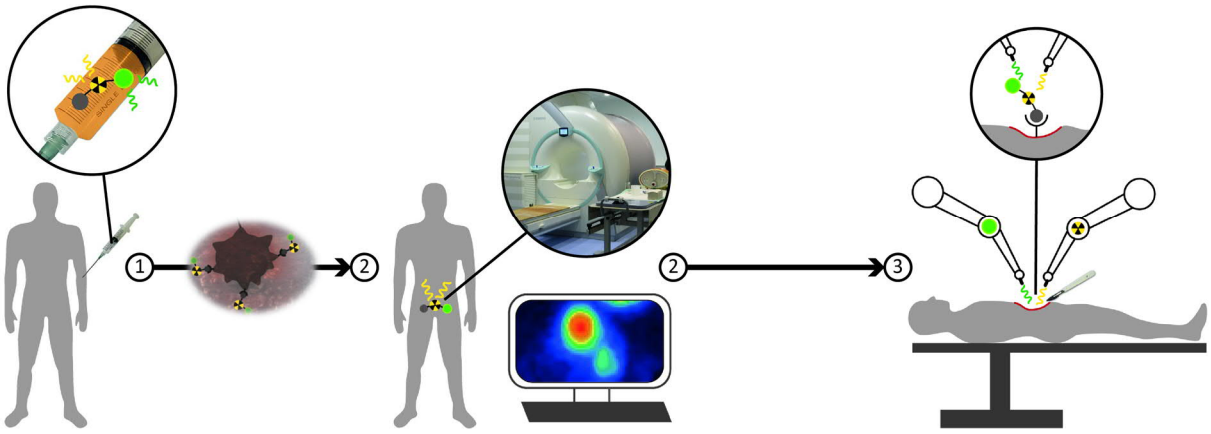

Figure III-1. Concept of clinical application of dual-labeled PSMA inhibitors.

The two modalities of the dual-labeled PSMA inhibitors allow for their detection via both fluorescence and radioactivity. After ① injection of the dual-labeled PSMA inhibitor, ② preoperative imaging such as PET/CT is applied for PCa localization, PCa staging and surgical planning. ③ Intraoperative guidance based on the fluorescence and/or radioactive signal of the PSMA inhibitor allows for the precise localization of the lesions improving surgical accuracy.

III.2 SURVEY OF THE FIELD

III.2.1 Prostate Cancer

Prostate cancer derives from malignant transformation in the epithelium of the prostate, the exocrine gland in the male reproductive system producing the seminal fluid [725]. PCa constitutes one out of five newly diagnosed cancer cases [712] and strongly contributes to the overall cancer-related death rate. Risk factors comprise exogenous influences including dietary habits and socioeconomic factors, as well as endogenous influences including age, chronic inflammation, family history and race [726]. Different molecular pathways for carcinogenesis are discussed [727, 728], with the androgen receptor playing a pivotal role, especially in castration-resistant prostate cancer (CRPCa). PCa feeds on androgens, but mechanistic details in their contribution to carcinogenesis are controversially discussed [729-731].

As PCa is typically a slow-growing cancer with asymptomatic progression at early stages, it is often unnoticed for years. Early detection is crucial, though, since the chances of curative treatment decrease with spreading. The cancer cells can travel through the lymphatic system or the blood stream and the majority of metastases occur in lymph nodes or bones [732]. Yet, early detection is possible by measuring the blood level of prostate-specific antigen (PSA) and by digital rectal exam (DRE). If one of the results is abnormal, further testing is necessary and diagnosis is eventually done by biopsy to determine the stage of the tumor [733, 734].

Clinical staging of PCa is performed according to the Union for International Cancer Control (UICC) via the TNM system, a global classification standard taking into account the size of the primary tumor (T), the number of affected lymph nodes (N), the presence of distal metastases (M), the PSA level and the Gleason score [735]. The Gleason grading system histopathologically compares to which extent the tumor biopsy tissue resembles healthy tissue. The system defines five grades assigned to the morphology of the tumor tissue. With increasing grades, the differentiation of the tumor tissue

decreases, heterogeneity increases, and tissue architecture is lost. The total score is the sum of two grades referring to the dominant cell morphology and to the cell morphology with the highest grade. The higher the Gleason score counts, the more aggressive the tumor is [725, 732]. The clinical staging directly affects the subsequent treatment regimen with options including hormone therapy [736, 737], chemotherapy [738, 739], radiotherapy [740], endoradiotherapy (III.2.5), cryotherapy [741] or resection (III.2.6).

III.2.2 Prostate-Specific Membrane Antigen

PSMA is a type II transmembrane glycoprotein (100–120 kDa) moderately expressed in all types of healthy prostate tissue, but greatly upregulated in PCa, especially in metastatic castration-resistant PCa (mCRPCa) [742]. The level of overexpression correlates with the aggressiveness of the tumor and thus with the Gleason score suggesting PSMA contribution to increasing invasiveness of PCa [718, 743]. Additionally, PSMA displays low expression levels in other organs including kidneys [718], salivary glands [744], spleen [745], small intestine [744], liver [742], testicles [745], ovaries [745] and brain [744]. While the physiological function of PSMA is well understood for the nervous and digestive system, it remains unknown for the other tissues.

PSMA displays two distinct enzymatic functions both resulting in the release of glutamate from the enzyme substrates. As folate hydrolase I (FOLH1), it enables the absorption of dietary folate [743, 746]; as *N*-acetyl-L-aspartyl-L-glutamate peptidase I (NAALADase), it regulates the concentration of the neurotransmitter *N*-acetyl-L-aspartyl-L-glutamate (α-NAAG) in the synaptic cleft [747, 748]. PSMA is further known as glutamate carboxypeptidase II (GCP II) [749]. Its enzymatic activity depends on PSMA dimerization and is additionally affected by the glycosylation pattern [750, 751].

PSMA is an established biomarker for the diagnosis and therapy of PCa [752]. Among other PCa biomarkers, PSMA has proven to be an excellent target structure due to

- its overexpression on PCa,
- absent or low expression rates in healthy tissue [718],
- increasing expression rates with tumor aggressiveness, androgen-independence, metastatic disease as well as disease recurrence [743, 753],
- favorable internalization and binding properties for PSMA-specific ligands [746, 754], and
- significant correlation of PSMA expression and Gleason score [755].

The extensive extracellular domain of PSMA (amino acids 44–750) features several glycosylation sites and consists of an apical, a helical and a protease domain. The active site and substrate-binding cavity is formed with contribution from all three domains (Figure III-2) [756, 757]. Upon ligand binding, PSMA is activated and undergoes clathrin-dependent internalization [723, 754, 758], which is mediated by a novel MXXXL motif of N-terminal amino acids formed by the cytoplasmic tail. The active site is structurally well-characterized allowing for the rational design of PSMA targeting ligands [759-761]. The more interactions a potential ligand offers, the better its affinity to the active site of PSMA [762].

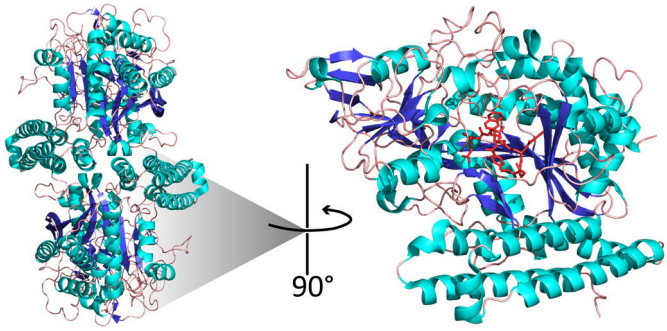

Figure III-2. The PSMA ectodomain.

PSMA is a type II transmembrane protein with a 19-amino-acid internal portion, a 24-amino-acid transmembrane portion and a 706-amino-acid external portion. The ectodomain (shown here) features an active site, which binds substrates such as low molecular weight PSMA inhibitors (shown in red). The crystal structure was obtained from the PDB [PSMA 5O5T].

The first targeted approach exploiting PSMA for diagnosis and therapy of PCa is also the only one that has yet gained approval by the Food and Drug Administration (FDA) [763, 764]. However, the respective antibody targets an intracellular PSMA epitope and thus only binds necrotic cells with disrupted cell membranes strongly limiting its sensitivity [765, 766]. Hence, the subsequent tracer development has especially focused on the extracellular domain and given rise to low molecular weight PSMA inhibitors [767-771], several generations of antibodies [772-775], RNA aptamer conjugates [776, 777], prodrugs [778] and nanoparticles [779-781] with PSMA specificity.

III.2.3 Positron Emission Tomography

Imaging modalities such as ultrasound, computed tomography (CT) and MRI allow the investigation of PCa by visualizing lesion foci, assisting staging, and localizing disease after biochemical recurrence. However, many conventional imaging techniques fail particularly in the detection of metastases. In this regard, positron emission tomography (PET) is a powerful addition to PCa management. It is one of the most common imaging modalities in nuclear medicine for the non-invasive 3D visualization of the spatial distribution of a radiotracer in the patient's body. In combination with suitable targeting strategies, PET imaging allows for quantitative detection of biomarkers and biochemical changes, and for discrimination between physiological and pathological processes with high sensitivity via local radioactivity. The combination with CT or MRI allows for a clear anatomical assignment of the PET data [782]. These hybrid imaging approaches enable individualized treatment regimens with beneficial impact on the therapy outcome.

PET imaging is based on the radioactive β^+ decay, during which a proton p is converted into a neutron n. In this process, a positron e^+ and an electron neutrino v_e are emitted:

$$p \rightarrow n + e^+ + v_e \qquad \textbf{(III-1)}$$

When the positron e^+ collides with an electron e^-, both elementary particles annihilate, emitting two photons γ into opposite directions:

$$e^+ + e^- \rightarrow \gamma + \gamma \qquad \textbf{(III-2)}$$

If the ring-shaped PET scanner, positioned around the patient, detects both photons within a defined time window, they are assigned to the same annihilation event in the patient. This coincidence detection is used to determine the line of response (LOR) along which annihilation occurred (Figure

III-3) [783]. The raw data are a list of LORs, which are organized in a sinogram displaying the superposition of all sinusoids weighted by the amount of activity at each point in the patient. On the level of the sinogram, the data can be corrected for attenuation due to more or denser material. Reconstruction finally yields the radiotracer's *in vivo* distribution [784].

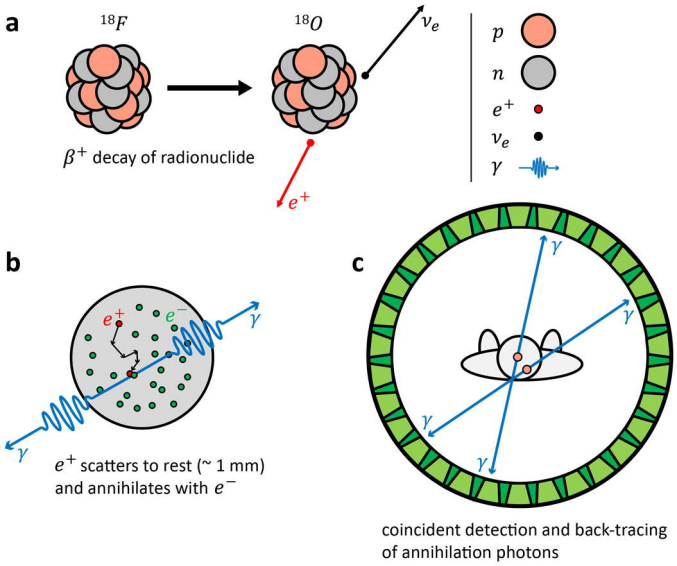

Figure III-3. Function principle of PET imaging.

For positron emission tomography, a radiopharmaceutical is injected intravenously into a patient. (**a**) The isotope (here ^{18}F) distributes in the patient (e.g. according to a carrier molecule) and undergoes β^+ decay. (**b**) The emitted positron scatters through matter, loses energy and annihilates with an electron. Two photons γ (511 keV each) are emitted in almost opposite directions. (**c**) A ring of detectors registers the radiation. The directionality of the annihilation photons allows for localizing their origin as it is assumed that annihilation occurred along the line of response.

Data quality strongly correlates with the choice of tracer, which is usually based on a small molecule that (closely) resembles its biological counterpart. PET tracers either mimic key players of crucial metabolic or signaling pathways, or they specifically bind to target structures including antigens, receptors and other sites of drug action. Labeling of these compounds with a suitable radionuclide creates the radiopharmaceuticals that allow the visualization of metabolic pathways, organ functions, biomarker distributions and other biological processes and structures (tracer principle) [785].

In the design of an efficient radiotracer, good target accessibility, low tracer metabolism, and a suitable radionuclide are desirable. The radionuclide potentially limits measurement time by its half-life and its branching ratio (Table III-1). Despite radiolabeling, the biological activity (e.g. specific target binding or metabolic participation) of the tracer should be maintained. Hence, radioactive isotopes of biologically abundant atoms like ^{11}C, ^{13}N and ^{15}O are potentially favored as they feature little or no sterical hindrance or electronic perturbation of the biological system. However, especially ^{13}N and ^{15}O are very short-lived and hence cannot be included into complex tracer syntheses. The radioisotopes ^{11}C and ^{18}F allow the synthesis of tracers chemically similar and biochemically identical to their biological counterparts, and thus find broad application despite their rather short half-lives [786, 787]. Especially ^{18}F is popular due to its introduction into the glucose analogue [^{18}F]FDG[6]. Tumors are characterized by an elevated glucose metabolism and an upregulated expression of glucose transporters leading to an increased uptake and intracellular accumulation of [^{18}F]FDG in tumor cells [788], which allows distinguishing healthy tissue from tumor tissue.

As an alternative to short-lived radionuclides that usually require a cyclotron on site for generation and application, radionuclide generators like the ^{68}Ge/^{68}Ga generator [789] are an easy to use and cheap option. They are based on a parent-daughter radionuclide pair (^{68}Ge/^{68}Ga) contained in a device

[6] 2-[^{18}F]fluoro-2-deoxy-D-glucose

that permits separation and extraction of the daughter product (^{68}Ga). The daughter activity is replenished continuously by decay of the parent (^{68}Ge) and repeated extraction is possible. However, tracer radiolabeling with radiometals like ^{68}Ga require a chelator, which is large in relation to small molecule tracer structures. To not structurally influence the tracer, chelators are often used together with antibodies and targeting proteins or peptides.

Table III-1. Important PET radionuclides decaying by positron emission (β^+) and electron capture (EC).

radionuclide	half-life	decay	β^+ branching ratio [%]	radionuclide	half-life	decay	β^+ branching ratio [%]
^{11}C	20.3 min	β^+	99	**^{64}Cu**	12.7 h	β^+/EC	19
^{13}N	10.0 min	β^+	100	**^{68}Ga**	68.1 min	β^+	89
^{15}O	2.0 min	β^+	100	**^{89}Zr**	3.3 d	β^+/EC	23
^{18}F	110.0 min	β^+/EC	97	**^{124}I**	4.2 d	β^+/EC	24

III.2.4 Diagnosis of Prostate Cancer

Due to the above-mentioned advantages, PETC/CT and PET/MRI are powerful tools offered by nuclear medicine for the diagnosis of PCa. The applied radiotracers visualize either the increased metabolic activity of PCa tumor cells, PCa specific receptors or antigens such as PSMA, or tissue with angiogenesis or hypoxia [790, 791]. While PCa cells display a low rate of glycolysis making the application of [^{18}F]FDG unsuitable [792, 793], they are characterized by an enhanced uptake of choline, a precursor of the cell membrane lipids phosphatidylcholine and sphingomyelin. The upregulation of choline transporters and the choline kinase allows for the accumulation of choline-based tracers labeled with either ^{11}C or ^{18}F in PCa tumor tissue [791, 794]. General applications of [^{11}C]choline-PET and [^{18}F]choline-PET suffer from limited specificity [795, 796], but both approaches allow for an efficient detection of bone metastases [797].

In contrast, non-metabolic tracers specifically bind to overexpressed target structures preferentially located on the outside of PCa cells. PSMA is the current flagship amongst all PCa biomarkers (refer to III.2.2) with clinical application. Its enzymatic domain can be specifically targeted by diagnostic PET tracers either labeled with ^{68}Ga or ^{18}F [790]. While ^{18}F can be directly integrated into the chemical structure of the tracer, ^{68}Ga depends on complexation. HBED-CC[7] [768] is an efficient radiometal chelator allowing for fast formation of thermodynamically stable complexes with ^{68}Ga at room temperature [798]. The conjugation with a potent urea-based PSMA inhibitor [799] has yielded the novel radiotracer [^{68}Ga]Ga-PSMA-11[8] featuring highly specific tumor internalization and strong tumor signal over background organs (Figure III-4) [800, 801]. It is further characterized by minor accumulation in healthy tissues like small intestine, cervical ganglia, salivary glands and kidneys as well as little internalization in other solid tumors of the salivary gland, colon and kidney, and in

[7] *N,N'*-bis-[2-hydroxy-5-(carboxyethyl)benzyl]ethylenediamine-*N,N'*-diacetic acid
[8] Glu-NH-CO-NH-Lys(Ahx)-[[^{68}Ga]Ga(HBED-CC)]

glioblastomas [715, 802, 803]. [^{68}Ga]Ga-PSMA-11 allows for superior imaging in terms of specificity and sensitivity as compared to established modalities like choline-PET [715, 802, 804-807]. Thus, in diagnostics of all stages of PCa, [^{68}Ga]Ga-PSMA-11 has become the most widely used PET/CT imaging agent [768]. In patients with primary or biochemically recurrent PCa, [^{68}Ga]Ga-PSMA-11 based PET/CT outperforms conventional imaging techniques like CT or MRI in the detection of intraprostatic tumors, malignant lymph nodes and bone metastases [713-716] and is especially powerful in the detection of biochemical recurrence due to its high sensitivity [808]. This new diagnostic approach strongly affects the subsequent treatment regimen and allows for individualized therapy [717].

Figure III-4. Chemical structure of PSMA-11.

The low molecular weight PSMA inhibitor PSMA-11 consists of the binding motif Glu-urea-Lys directly targeting PSMA and the radiometal chelator HBED-CC allowing for complex formation with ^{68}Ga. It is applied as PET/CT imaging agent in non-invasive diagnostics of PCa.

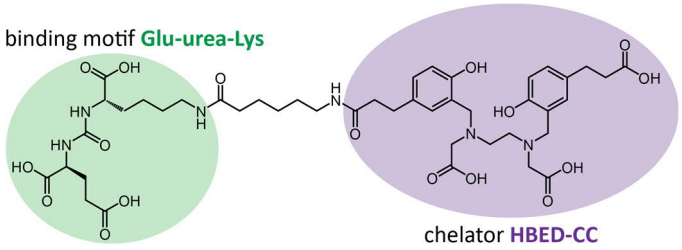

III.2.5 Endoradiotherapy of Prostate Cancer

Exchanging the radionuclides of diagnostic radiotracers with therapeutic radionuclides allows for their application in endoradiotherapy. This systemic approach delivers therapeutically effective radiation doses directly to the target tissue thereby minimizing off-target tissue effects. The concept of theranostics integrates diagnostic imaging and therapy in a single system. Labeled with either γ- or positron-emitters, the tracer is used to identify patients suitable for the respective endoradiotherapy. The selected patients are subsequently treated with the same tracer labeled with either α- or β-emitters.

Radioactive decay occurs in unstable atomic nuclei. In simplified terms, nuclear stability is based on the balance between the electromagnetic and the nuclear force. If the Coulomb repulsion outweighs the attractive nuclear force in elements with high atomic numbers, an α particle is emitted to restore the balance. The α particle is a subatomic fragment consisting of two neutrons and two protons (helium-4-nucleus). It is highly ionizing but relatively heavy and slow, and therefore α radiation shows low tissue penetrating power [809].

In contrast, β particles are less damaging and display greater tissue penetration depths as they carry half the charge of an α particle and typically begin with a lesser initial kinetic energy [810]. The β decay is a consequence of the weak interaction. Unstable atomic nuclei with an excess of neutrons undergo β^- decay, which converts a neutron n into a proton p, emitting an electron e^- and an electron antineutrino $\bar{\nu}_e$ in the process:

$$n \rightarrow p + e^- + \bar{\nu}_e \qquad \textbf{(III-3)}$$

Unstable atomic nuclei with an excess of protons undergo β^+ decay (refer to equation (III-1)). The binding energy per nucleon influences the probability of a nuclide to experience radioactive decay. For any spontaneous particle emission, the final binding energy per nucleon must be larger than in the initial state [811].

The long range of β particles leads to crossfire effects, during which the radiation from one cell also affects the neighboring cells. Crossfire effects are beneficial for heterogeneous tumors in which only a subpopulation of cells can be efficiently targeted by the radiotracer. However, surrounding healthy tissue is likewise subjected to crossfire. Moreover, even non-targeted cells not directly hit by radiation may also exhibit effects of radiation, which is known as the radiation-induced bystander effect (RIBE) [812, 813].

As a second-generation antibody, monoclonal anti-PSMA J591 allows for vascular targeting of PCa by binding to the extracellular domain of PSMA. Labeled with the β^--emitter ^{177}Lu, it has extended patient survival in phase I and II trials. Yet, a broad clinical application of [^{177}Lu]Lu-J591 is limited by adverse events including hematological toxicity and thrombocytopenia. Moreover, the large size of antibodies (150 kDa) generally hampers tumor penetration. Systemic clearance is slow and thus a damaging radiation dose is deposited in the bone marrow [814-816].

In line with the radiotracer development for non-invasive PCa diagnostics, new strategies for endoradiotherapy rely on low molecular weight PSMA inhibitors. Their smaller size provides more rapid pharmacokinetics, an increased tumor penetration and thus high tumor-to-background ratios. For complexation of therapeutic radiometals like the β^--emitters ^{90}Y and ^{177}Lu or the α-emitter ^{225}Ac, HBED-CC is unsuitable and the chelators DOTA[9] or DOTAGA[10] represent the favorable alternatives [762, 769, 770]. The theranostic strategy is realized in the low molecular weight radiotracer PSMA I&T (imaging and therapy) using DOTAGA and the low molecular weight radiotracer PSMA-617 using DOTA. Responses to therapy based on [^{177}Lu]Lu-PSMA I&T include decreasing PSA levels and a reduced tumor burden [817]. Correspondingly, [^{68}Ga]Ga-PSMA I&T can be used for PCa diagnosis but PSMA-11 is more sensitive in the detection of smaller lesions [818].

[^{177}Lu]Lu-PSMA-617 and [^{225}Ac]Ac-PSMA-617 are especially promising for the therapy of late stage mCRPCa patients beyond established treatment options [819-823]. First studies with [^{177}Lu]Lu-PSMA-617 suggest a high efficacy with a favorable safety profile [819, 820] and the radiopharmaceutical has recently entered phase III after successfully passing a phase II multicenter clinical study [819].

III.2.6 Surgical Guidance

For localized PCa, radical prostatectomy is the second treatment option besides radiotherapy [824]. The comprehensive removal of the prostate including all tumor tissue should be favored over `watchful waiting´ [825, 826]. Watchful waiting is a form of active surveillance as PCa often grows very slowly, and especially older men might never need treatment. With parasympathetic nerve-sparing techniques during surgery, adverse side effects like erectile dysfunction and urinary incontinence can be avoided. Laparoscopic surgery allows for a minimally invasive procedure benefiting from smaller incisions, reduced risk for infections, faster recovery times as well as reduced pain and scarring. Challenges like hand-eye coordination, lack of tactile sense, and the projected 2D view of the surgical field [827-829] are addressed with robot-assisted laparoscopic prostatectomy using robotic

[9] 1,4,7,10-tetraazacyclododecane-1,4,7,10-tetraacetic acid
[10] 1,4,7,10-tetraazacyclododececane,1-(glutaric acid)−4,7,10-triacetic acid

telemanipulation systems like the da Vinci robot (Intuitive Surgical, Inc., Sunnyvale, California, USA) [830, 831].

Sentinel lymph nodes are the first lymph node(s) to be infiltrated by cancer cells spreading from a primary tumor. According to the sentinel lymph node concept, tumor-free sentinel lymph nodes imply that downstream lymph nodes are likewise unaffected. Hence, prostatectomy includes a template for sentinel lymph dissection [832]. While the removal of healthy lymph nodes can have adverse effects, remaining malignant lymph nodes are worse as they usually involve follow-up surgery and/or disease reoccurrence [833].

Thus, the precise detection and resection of all malignant tissue directly affect the treatment outcome and patient survival. Both can be strongly improved using surgical guidance by fluorescence or radioactivity (Figure III-5). As the first radiotracer for sentinel lymph node identification labeled also healthy lymph nodes downstream while missing lesions outside the lymph system, the development of PSMA targeting radiotracers for intraoperative guidance was strongly pushed [770, 817, 834, 835].

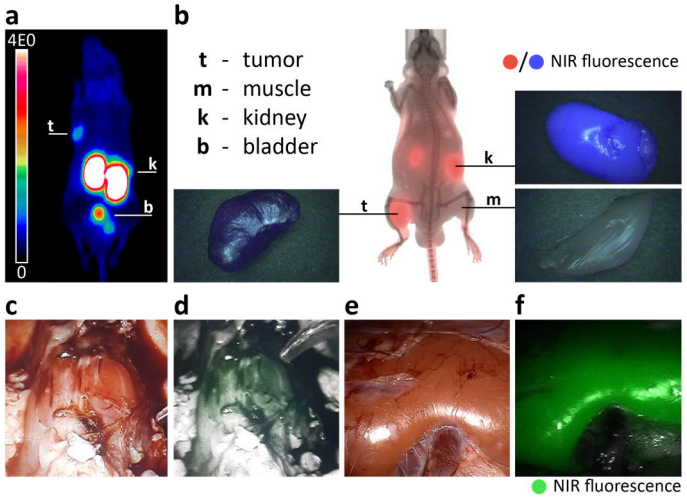

Figure III-5. *In vivo* proof of concept study of dual-labeled PSMA inhibitors.

(**a**) Guidance by radioactivity. Whole-body maximum intensity projection of small-animal PET imaging acquired 120 min p.i. of 0.5 nmol ^{68}Ga-radiolabeled Glu-urea-Lys-HBED-CC-PEG$_2$-IRDye800CW (~50 MBq) in a LNCaP-tumor bearing BALB/c nu/nu mouse model. (**b**) Guidance by fluorescence. NIR-fluorescence detection at 2 h p.i. of 0.5-2 nmol Glu-urea-Lys-HBED-CC-PEG$_2$-IRDye800CW. (**c**-**f**) Proof of concept in a clinical operation theatre at 1 h p.i. of Glu-urea-Lys-HBED-CC-PEG$_2$-IRDye800CW (30 µg/kg) in pigs ((**c**,**d**) prostate, (**e**,**f**) kidney). (**c**,**e**) White light images. (**d**,**f**) Fluorescent tissue could be precisely delineated from surrounding tissue using the da Vinci FireFly system.

Low molecular weight compounds like [^{111}In]In-PSMA I&T and its refined variant [^{99m}Tc]Tc-PSMA I&S (imaging and surgery) enable the intraoperative detection of small lesions that were initially identified using PET/CT [834-837]. However, gamma probes (hand-held detection device) suffer from a high sensitivity towards background, which is especially increased in the area of injection or the renal pathway. Thus, the detection of lesions in these regions is particularly impaired. The exact localization and precise distinction from healthy tissue is further hampered as gamma probes produce only acoustic and no visual signals. Moreover, the patient and the medical staff is exposed to radioactivity [838, 839].

In contrast, fluorescence-guided surgery allows for the visualization of the tracer's signal and thus facilitates the precise detection of malignant tissue. Furthermore, fluorescent dyes are not subjected to short half-lives as radionuclides are. They offer easy handling, repetitive excitation and detection as well as high sensitivity. NIR dyes are favored as scattering, absorption by endogenous chromophores and autofluorescence decrease with increasing wavelength, allowing for comparatively deep tissue penetration with a good SNR (refer to I.1.6.1). A large Stokes shift is desired to guarantee a good separation of excitation and emission [840-844]. Currently, the only clinically approved NIR dye is

indocyanine green (ICG) [845]. Similar to radionuclides in diagnosis or therapy, ICG can be specifically targeted to PCa tissue via conjugation to the J591 antibody [846] or to low molecular weight PSMA inhibitors [847-853].

Disadvantages of fluorescence-only surgical guidance include photobleaching, residual absorption and scattering, background due to stray light, and a limited tissue penetration depth as compared to γ-rays [828, 841, 854, 855]. Moreover, conjugation with the fluorescent dye can affect the pharmacokinetic and binding properties. Thus, hybrid approaches were developed combining γ-emitter and fluorescent dye in one compound to unite the strengths of both guiding modalities and bypass the individual weaknesses. These dual-modality tracers allow for pre-operative imaging and intraoperative (radio- or fluorescence-) guidance, and guarantee precise detection and resection to the best possible extent [832, 854, 856].

The first approaches suffered from unspecific distribution in sentinel lymph nodes and from the photophysical and chemical drawbacks of ICG such as low photostability, small Stokes shift, and aggregation in aqueous solutions [839, 857]. The subsequently developed dual-modality antibodies and nanoparticles specifically targeting PSMA used IRDye800CW as fluorescent reporter. Both strategies have enabled the visualization of tumor tissue, but only with time delay, as antibodies and nanoparticles feature extended systemic circulation times (refer to III.2.5) [858, 859].

In contrast, low molecular weight tracers offer more rapid pharmacokinetics and fast systemic clearance, allowing for a high contrast at early time points. Thus, dual-modality PSMA inhibitors featuring radioactive and fluorescent reporter entities, namely [^{68}Ga]Ga-Glu-urea-Lys-HBED-CC-PEG$_2$-IRDye800CW and [^{68}Ga]Ga-PSMA I&F (imaging and fluorescence), have recently been developed and are currently in preparation for clinical translation [48, 724]. The new class of dual-labeled low molecular weight PSMA inhibitors promises huge advances in the diagnosis and therapy of PCa. However, the conjugation with chelator and fluorescent moiety can easily affect the biological and pharmacological properties of the low molecular weight compounds. Thus, in the design of low weight hybrid approaches, special care must be taken to preserve the pharmacokinetics and tumor-specific accumulation of the original tracer.

III.3 Aim

Targeted imaging and therapy based on novel PSMA inhibitors have been a game changer in diagnostics and treatment of PCa, but the subcellular fate of PSMA/PSMA inhibitor complexes remains an open question. Yet, the exact mechanism of internalization and intracellular distribution is of great clinical interest to provide deeper insight into the mode of action during endoradiotherapy. Dual-modality PSMA inhibitors in particular promise huge advances in the diagnostic and treatment regimen of PCa as they combine pre-operative imaging with intra-operative guidance.

Thus, this project sought to follow the trafficking of PSMA and of dual-modality PSMA inhibitors at the molecular level. Therefore, we designed, synthesized and comprehensively characterized STED compatible dual-modality PSMA inhibitors mimicking clinically applied PSMA inhibitors. Binding,

internalization and retention properties were assessed in fixed and live cell confocal and STED experiments, radioactive biodistribution studies, small PET-imaging experiments and flow cytometry studies. The PSMA inhibitors' subcellular fate was analyzed via long-term internalization experiments and colocalization studies with PSMA and other relevant components of the endocytic pathway by developing a novel non-standard live cell staining protocol and applying fixed and live cell STED nanoscopy.

As of September 2019, the work presented in the following sections has been submitted for publication as Matthias, J., Engelhardt, J., Schäfer, M., Bauder-Wüst, U., Meyer, P.T., Haberkorn, U., Eder, M., Kopka, K., Hell, S.W., Eder, A.C., *The intracellular fate of PSMA inhibitors as revealed by STED nanoscopy*.

III.4 METHODS

This project was conceived and conducted in close collaboration with Dr. Ann-Christin Eder, previously Baranski[11]. The synthesis, the compound characterization based on radioactive properties and the flow cytometry studies were performed by Dr. Ann-Christin Eder. The fluorescence microscopy samples were prepared together with Dr. Ann-Christin Eder. Detailed information on materials is given in I.2.1.

III.4.1 Synthesis

Preparative HPLC (high performance liquid chromatography) was carried out with a LaPrep-System P110 (VWR International) equipped with a NUCLEODUR® Sphinx RP column and a variable UV detector (P314, VWR International) with a flow rate of 20 ml/min. For semipreparative HPLC, the system Agilent 1100 series (Agilent Technologies) was equipped with a Chromolith RP-18e (100×10 mm, Merck), for analytical HPLC with a Chromolith RP-18e (100×4.6 mm, Merck). UV absorbance was measured at wavelengths of 214 nm and 254 nm. The dual-labeled dye conjugates were derived from PSMA-11 and synthesized as described by Baranski *et al.* [48]:

Briefly, starting with bis-tetrafluorophenyl (TFP)-functionalized HBED-CC, the synthesis of the precursor Glu-urea-Lys[Fe(HBED-CC)]-PEG_2 was performed by reaction of the TFP activated sites with tri-*tert*-butyl protected Glu-urea-Lys (0.9 eq., ABX) and subsequently with an excess of 2,2'-(ethylenedioxy)bis(ethylamine) in *N,N*-dimethylformamide (DMF). Incubation with trifluoroacetic acid (TFA) for 3 h at RT removed the tri-*tert*-butyl protecting groups. STAR RED-NHS-ester (1 eq., 1 mg, Abberior) was conjugated to Glu-urea-Lys[Fe(HBED-CC)]-PEG_2 (3 eq.) in DMF (300 µl) and *N,N*-diisopropylethylamine (DIPEA) (15 µl) for 24 h at RT. STAR 635P-NHS-ester (1 eq., 1 mg, Abberior) was

[11] German Cancer Research Center, Division of Radiopharmaceutical Chemistry, Heidelberg, Germany;
current address: University Medical Center Freiburg, Department of Nuclear Medicine, University of Freiburg, Faculty of Medicine, Freiburg, Germany;
German Cancer Consortium, partner site Freiburg, and German Cancer Research Center, Division of Radiopharmaceutical Development, Heidelberg, Germany

dissolved in 50 µl dimethyl sulfoxide (DMSO) and conjugated to Glu-urea-Lys[Fe(HBED-CC)]-PEG_2 (3 eq.) in PBS (pH 8.5) for 24 h at RT. Complexed Fe^{3+} was removed on a Sep-Pack C18 cartridge (Waters) with 1 M HCl as previously described [860]. Reversed-phase HPLC (RP-HPLC) and matrix-assisted laser desorption/ionization mass spectrometry (MALDI-MS, Bruker) were used for purification and analytics of the final compounds.

III.4.2 Radiolabeling

^{68}Ga (half-life 68 min, β^+ 89%, $E_{\beta+}$ max. 1.9 MeV) was obtained from a $^{68}Ge/^{68}Ga$ generator based on a pyrogallol resin support [789]. For radiolabeling with ^{68}Ga, Glu-urea-Lys-HBED-CC-PEG_2-STAR RED or -STAR 635P (1 nmol in 4-(2-hydroxyethyl)piperazine-1-ethanesulfonic acid (HEPES buffer) (580 mg/ml) with 5 mg ascorbic acid, 90 µl) was added to 40 µl $[^{68}Ga]Ga^{3+}$ eluate (~40 MBq). The pH of the labeling solution was adjusted with NaOH to pH 3.8 and incubated at 98°C for 10 min. Analytical RP-HPLC was used to determine the radiochemical yield (RCY). The lipophilicity of the ^{68}Ga-radiolabeled PSMA inhibitors was determined via the 2-phase system n-octanol and PBS.

III.4.3 Fluorescence Properties

Glu-urea-Lys-HBED-CC-PEG_2-STAR RED and -STAR 635P were diluted to 10 µM in PBS (pH 7.4) or sodium acetate (NaAc) buffer (0.1 M, pH 4.6) and measured in standard 1 cm quartz cuvettes. The absorbance of the compounds was recorded with a Varian Cary 500 UV-VIS NIR Spectrophotometer (Agilent) equipped with the software Cary 500 (EPROM Version 8.01) in the 200-1000 nm interval. The fluorescence emission of the compounds was measured with a Varian Cary Eclipse Fluorescence-Spectrophotometer (Agilent) equipped with the software Cary Eclipse (Version 1.1) with excitation at 590 nm in the 600-1000 nm interval. To additionally determine potential temperature and pH dependence of the fluorescence properties, the compounds were incubated for 6 h at RT or 37°C in PBS or NaAc prior to absorbance and fluorescence emission recordings.

III.4.4 Cell Culture

PSMA-overexpressing androgen-sensitive human prostate adenocarcinoma cells (LNCaP cells, ATCC CRL-1740) and PSMA-negative human prostate adenocarcinoma cells (PC3 cells, ATCC CRL-1435) were grown in Roswell Park Memorial Institute (RPMI) 1640 medium (Thermo Fisher Scientific) enriched with 5% FBS, 1% penicillin/streptomycin and 1% sodium pyruvate (hereinafter referred to as RPMI+++) at 37°C in humidified air with 5% CO_2. The cells were harvested using trypsin (0.25%, no phenol red). A Countess II FL Automated Cell Counter (Thermo Fisher Scientific) was used to count cells and to determine the live-to-dead cell ratio via Trypan Blue stain (0.4%).

For fixed sample preparation, 10^5 cells/well were seeded two days prior to imaging on poly-L-Lysine (Sigma-Aldrich/Merck) coated 4-well removable chamber slides (Nunc Lab-Tek II Chamber Slides, Thermo Fisher Scientific) and kept at 37°C in humidified air with 5% CO_2 until fixation. For live cell

sample preparation, 10^5 cells/well were seeded two days prior to imaging on poly-L-lysine (Sigma-Aldrich/Merck) coated 4-well chambered coverslips (Nunc Lab-Tek II chambered coverglasses, Thermo Fisher Scientific) and kept at 37°C and 5% CO_2 until live cell staining.

III.4.5 Cell Binding and Internalization

The competitive cell binding assay and internalization experiments were performed according to Eder *et al*. [768].

III.4.5.1 Cell Binding Assay

For competitive binding, 10^5 LNCaP cells/well were incubated with various concentrations (0, 0.5, 1, 2.5, 5, 10, 25, 50, 100, 500, 1000, 5000 nM) of Glu-urea-Lys-HBED-CC-PEG_2-STAR RED or -STAR 635P in the presence of 0.75 nM ^{68}Ga-labeled radioligand [Glu-urea-Lys(Ahx)]$_2$-HBED-CC (PSMA-10, ABX) [860] on 96-well filter plates for 45 min at RT. After washing twice with ice-cold PBS, the radioactivity of the punched filters was assessed via gamma counter (Packard Cobra II, GMI). The half maximal inhibitory concentration (IC_{50}) was determined via nonlinear regression. The IC_{50} values were converted to the binding affinities K_i of the PSMA inhibitors by

$$K_i = \frac{IC_{50}}{1 + \frac{c_{PSMA-10}}{K_d}} \quad \textbf{(III-4)}$$

with $c_{PSMA-10}$ = 0.75 nM being the concentration of the ^{68}Ga-labeled radioligand PSMA-10 and K_d = 3.8 ±1 .8 nM being the dissociation constant of the ^{68}Ga-labeled radioligand PSMA-10 [860].

III.4.5.2 Internalization Assay

To determine the internalization properties, LNCaP cells were incubated with 30 nM ^{68}Ga-radiolabeled Glu-urea-Lys-HBED-CC-PEG_2-STAR RED or -STAR 635P for 45 min at 37°C. For blocking studies, 500 µM of the highly efficient PSMA inhibitor 2-(phosphonomethyl)-pentanedioic acid (2-PMPA) were co-incubated. Subsequently, cells were washed with ice-cold PBS and the membrane bound fraction was collected via glycine (pH 2.8) washes. The internalized fraction was collected via cell lysis with 0.3 M NaOH. The radioactivity of the collected fractions was measured using a gamma counter (Packard Cobra II, GMI) and expressed as percent of applied radioactivity (%IA) bound to 10^5 cells.

III.4.6 Biodistribution and PET Imaging Studies

For the *in vivo* mouse tumor model, 5×10^6 LNCaP or PC3 cells (in 50% Matrigel) were subcutaneously inoculated into the right trunk of 7- to 8-week-old male BALB/c nu/nu mice (Charles River Laboratories). The tumors were allowed to grow until reaching a size of approximately 1 cm^3.

III.4.6.1 Biodistribution

To analyze the biodistribution of ^{68}Ga-labeled Glu-urea-Lys-HBED-CC-PEG$_2$-STAR RED or -STAR 635P, the radiolabeled compounds (in 0.9% NaCl, pH 7) were injected into the tail vein of LNCaP or PC3 tumor-bearing mice (per mouse 1-2 MBq, 60 pmol). The animals were sacrificed 1 h post injection (p.i.) and blood was collected. The organs/tissues of interest (heart, lung, spleen, liver, kidney, muscle, small intestine, brain, tumor) were dissected, blotted dry, and weighed. A gamma counter (Packard Cobra II, GMI) was used to measure the radioactivity. The data were corrected for the half-life of ^{68}Ga and the results were expressed as the mean percent injected dose per gram of tissue (%ID/g).

III.4.6.2 PET Imaging

For small-animal PET studies, LNCaP or PC3 tumor-bearing mice were anaesthetized with 2% sevoflurane (Abbott) and placed into a PET scanner (Inveon PET, Siemens). After a 10 min transmission scan, 0.5 nmol of ^{68}Ga-labeled Glu-urea-Lys-HBED-CC-PEG$_2$-STAR RED or -STAR 635P (0.9% NaCl, pH 7) were injected into the tail vein. A 60 min dynamic scan as well as a static scan between 120 to 140 min p.i. were recorded. Image reconstruction was done iteratively (16 subsets, 4 iterations) by applying median root prior correction. The results were converted to standardized uptake value (SUV) images.

III.4.7 STED and Confocal Microscopy

The custom-built STED system is described in detail in I.2.2.1. The power range for all lasers used during live and fixed cell confocal and STED imaging is given in Table III-2. Unless otherwise stated, fixed and live cell confocal and STED imaging was performed with the measurement parameters given in Table III-3. No frame accumulation was used.

Table III-2. Range of laser powers used for fixed and live cell confocal and STED imaging of PSMA, PSMA inhibitors and components of the endosomal pathway.

The values given describe the estimated laser power in the sample focus based on laser power measurements in front of the microscope body.

	excitation			STED
	470 nm [µW]	**600 nm [µW]**	**650 nm [µW]**	**775 nm [mW]**
confocal, fixed samples	140	8-10	15-20	---
STED, fixed samples	---	8-10	15-20	70-100
confocal, live samples	140	2-10	0.5 (SiR-Lysosome) 15-20 (conjugate **RED**/**635P**)	---
STED, live samples	---	2-10	1.5 (SiR-Lysosome) 15-20 (conjugate **RED**/**635P**)	35-70

Table III-3. Standard measurement parameters used for fixed and live cell confocal and STED imaging of PSMA, PSMA inhibitors and components of the endosomal pathway.

	pixel size [nm]	dwell time [µs]	line accumulation
confocal, fixed samples	50	30-50	1
STED, fixed samples	20	30	1
confocal, live samples	50	20	1
STED, live samples	20	20	1

III.4.8 Determination of Vesicle Diameter

The vesicle diameter was measured for different internalization times (30, 45, 60 min) by fitting a two-dimensional ring function to the raw fluorescence signal of individual vesicles

$$R(x,y) = a_1 + a_2\left(a_3 + \frac{(x-a_4)^2 + (y-a_5)^2}{2a_6^2}\right)e^{-\frac{(x-a_4)^2+(y-a_5)^2}{2a_6^2}} \qquad \textbf{(III-5)}$$

with fit parameters a_1 to a_6. The fit algorithm is implemented in the custom application software (LabVIEW, National Instruments) of the STED system.

III.4.9 Time and Concentration Dependence

To study the time dependence of the internalization process via fluorescence imaging, LNCaP cells were incubated with 50 nM Glu-urea-Lys-HBED-CC-PEG_2-STAR RED in RPMI+++ for 5, 15, 30 and 45 min at RT. To analyze the concentration dependence of internalization, the PSMA inhibitor was incubated for 45 min at the concentrations 50, 100, 250 and 500 nM in RPMI+++. After incubation, cells were washed with PBS and fixed for 10 min with 2% PFA in PBS at RT. Following three PBS washing steps, the samples were mounted in ProLong Diamond Antifade Mountant containing DAPI (Thermo Fisher Scientific).

III.4.10 Live Cell Imaging

For live cell imaging, LNCaP and PC3 cells were washed once with PBS and were incubated with 50 nM or 100 nM Glu-urea-Lys-HBED-CC-PEG_2-STAR RED in RPMI+++ for 20 min on ice to prevent premature internalization. After washing three times with PBS on ice, the cells were immediately imaged in FluoroBrite++. To verify specific uptake of Glu-urea-Lys-HBED-CC-PEG_2-STAR RED, the cells were additionally co-incubated with 500 µM 2-PMPA in block experiments. Confocal time series were recorded with 0.5 fpm or 1 fpm for a total time of 2 h.

III.4.11 Live Cell Immunofluorescence

III.4.11.1 Antibodies

For live cell IF staining of PSMA, the primary monoclonal mouse antibody anti-PSMA (clone 107-1A4, SAB4200257, Sigma-Aldrich/Merck, 1:50, 1 h) was used in combination with the secondary antibodies goat anti-mouse-IgG coupled to STAR 600 (Abberior, 1:50, 1 h) and goat anti-mouse-IgG coupled to STAR RED (Abberior, 1:50, 1 h).

III.4.11.2 Immunofluorescence Staining

The following live cell IF protocol selectively stains the membrane bound PSMA fraction. The entire protocol was performed on ice to prevent premature internalization of PSMA. After washing once with ice-cold 10% goat serum in PBS, LNCaP and PC3 cells were incubated for 1 h with the primary antibody in 10% GS in PBS. After washing three times with ice-cold 10% GS in PBS, the secondary antibody was incubated for 1 h in 10% GS. After washing three times with ice-cold 10% GS in PBS, PSMA internalization was triggered by incubation at 37°C in humidified air with 5% CO_2 for various times.

III.4.12 Colocalization Experiments

III.4.12.1 Clathrin/PSMA Inhibitor Colocalization

To stain clathrin in living LNCaP cells, the cells were transiently transfected with the N-terminal fusion construct SNAP-tag/clathrin light chain (SNAP-CLC). The plasmid was kindly provided by Francesca Bottanelli[12] [259].

Transient transfection was performed 24 h prior to imaging with 300 ng of the SNAP-CLC plasmid using the Effectene Transfection Reagent Kit (Qiagen) according to the manufacturer's protocol. On the day of the experiment, the cells were stained with a 1 µM staining solution of the live dye 610CP-BG (BG = SNAP-tag ligand) [29] in RPMI+++ for 45 min at 37°C in humidified air with 5% CO_2. The live dye was kindly provided by Dr. Alexey Butkevich[13] and Dr. Vladimir Belov[14]. After washing three times with preheated RPMI+++, the cells were incubated with 50 nM Glu-urea-Lys-HBED-CC-PEG_2-STAR RED for different durations (10, 15, 20 min) at 37°C in humidified air with 5% CO_2.

To visualize the colocalization between Glu-urea-Lys-HBED-CC-PEG_2-STAR RED and clathrin, live dual-color confocal images were recorded. Single-color stainings were used to quantify minor crosstalk between the two color channels. Color correction was performed with the linear unmixing algorithm

[12] Yale University School of Medicine, Rothman Laboratory, New Haven, USA;
current address: Freie Universität Berlin, Department of Biology, Chemistry, Pharmacy, Bottanelli Group – Membrane trafficking, Berlin, Germany
[13] Max Planck Institute for Biophysical Chemistry, Department of NanoBiophotonics, Göttingen, Germany;
current address: Max Planck Institute for Medical Research, Department of Optical Nanoscopy, Heidelberg, Germany
[14] Max Planck Institute for Biophysical Chemistry, Department of NanoBiophotonics, Göttingen, Germany;
Facility for Synthetic Chemistry at the Max Planck Institute for Biophysical Chemistry in Göttingen, Germany

implemented in the data analysis section of the custom application software (LabVIEW, National Instruments) of the STED system. To quantify the colocalization, the PCC was calculated for the corrected images using the ImageJ plugin JACoP [470, 695].

III.4.12.2 LysoTracker/PSMA Colocalization

To visualize endosomal PSMA recycling, the protein was first immunolabeled according to III.4.11.2. After secondary antibody (STAR 600-labeled) incubation, LNCaP cells were washed three times with 10% GS in PBS and incubated with 500 nM LysoTracker™ Green DND-26 (Thermo Fisher Scientific) or 1 µM SiR-Lysosome (Spirochrome) in FluoroBrite++ at 37°C in humidified air with 5% CO_2 to allow for endosomal/lysosomal staining and trigger internalization simultaneously. For selected experiments, the LysoTracker was co-incubated with 500 µM 2-PMPA, 50 nM Glu-urea-Lys-HBED-CC-PEG_2-STAR RED or 50 nM Glu-urea-Lys-HBED-CC-PEG_2-STAR 635P.

After 1 h and after > 20 h of internalization time, colocalization was visualized in live cell dual-color confocal and STED experiments. STED (confocal) time series were recorded for a total time of up to 15 min (up to 30 min) with 1.1 and 1.2 fpm (2.1 and 2.6 fpm).

Single-color stainings confirmed the absence of crosstalk between the two color channels. Color shift correction between the 470 nm excitation channel (LysoTracker™ Green DND-26) and the 600 nm excitation channel (immunolabeled PSMA) was performed as described in I.2.2.2. The PCC of the corrected images was calculated with the ImageJ plugin JACoP [470, 695].

III.4.12.3 PSMA/PSMA Inhibitor Colocalization

To analyze colocalization between Glu-urea-Lys-HBED-CC-PEG_2-STAR RED/-STAR 635P and PSMA, LNCaP cells were first immunolabeled for PSMA according to III.4.11.2. The primary antibody was co-incubated with 100 nM Glu-urea-Lys-HBED-CC-PEG_2-STAR RED/-STAR 635P. After secondary antibody (STAR 600-labeled) incubation, the samples were washed three times with 10% GS in PBS and the cells were either directly fixed for 10 min with 3.7% PFA in PBS at RT or subjected to internalization. For internalization, the cells were incubated for 30 min, 45 min, 1 h, 3 h, 6 h or 24 h in RPMI+++ at 37°C in humidified air with 5% CO_2. After fixation with 3.7% PFA in PBS for 10 min at RT and three subsequent PBS washing steps, the samples were mounted in ProLong Diamond Antifade Mountant containing DAPI (Thermo Fisher Scientific). The absence of crosstalk between the two color channels was confirmed by single-color stainings of Glu-urea-Lys-HBED-CC-PEG_2-STAR RED, Glu-urea-Lys-HBED-CC-PEG_2-STAR 635P, STAR 600-immunolabeled PSMA and STAR RED-immunolabeled PSMA prepared under the same conditions as the dual-color stainings.

Images with a maximum fluorescence intensity < 20 counts were excluded from colocalization analysis. Background subtraction of two counts was performed prior to PCC calculation to correct for homogeneous background. The ImageJ plugin JACoP [470, 695] was used to calculate the PCC of the corrected images. For calculation of the average PCC for each time point, all results scattering by more than double the SD were excluded.

Pixel fluorograms (hereinafter referred to as fluorograms) can be generated to illustrate colocalization trends in dual-color fluorescence images [861]. Each pixel in a fluorogram represents the number of pixels in the corresponding dual-color fluorescence image that shows an intensity of dye 1 (dye 2) according to the x-axis (y-axis) of the fluorogram. Pixels with similar intensities in both channels of the fluorescence image (colocalization) appear in the diagonal area of the fluorogram. In contrast, pixels close the x-axis (y-axis) of the fluorogram represent pixels with single-color staining of dye 1 (dye 2).

Time-dependent changes in colocalization were visualized in dual-color image fluorograms calculated with the custom application software (LabVIEW, National Instruments) of the STED system. Below a phasor line of 20° slope, all pixels in the fluorogram are considered single staining of the PSMA inhibitor. Above a phasor line of 70° slope, all pixels in the fluorogram are considered single staining of PSMA. All pixels falling between these lines are considered colocalized. The area below the quarter circle in the fluorogram indicates the fluorescence image background defined as the average intensity of Glu-urea-Lys-HBED-CC-PEG_2-STAR RED in the cytoplasm after 24 h of internalization. Colocalization can be quantified by calculating the integral of the fluorescence intensities in the area between the phasor lines divided by the total fluorescence intensity [861].

The time-dependent changes of the relative integrated fluorescence intensity for each channel were calculated on smoothed images for each of the resulting six sections

- PSMA signal only foreground
- PSMA signal only background
- colocalizing signal foreground
- colocalizing signal background
- PSMA inhibitor signal only foreground
- PSMA inhibitor signal only background

as well as in the entire foreground and in the entire background. For calculating the average integrated relative fluorescence intensity for each time point, channel and section, all results differing by more than double the SD were excluded. The ratio between the integrated fluorescence intensities of both channels in the entire image was calculated and compared for each time point to assess potential photobleaching and externalization.

III.4.13 Cytotoxicity Studies

The duration and frequency of LNCaP cell division was analyzed via holographic time-lapse imaging using a HoloMonitor® M4 cytometer (Phase Holographic Imaging) to assess potential cytotoxicity of Glu-urea-Lys-HBED-CC-PEG_2-STAR RED and –STAR 635P. Two days prior to the experiment, LNCaP cells were seeded in RPMI+++ in poly-L-Lysine (Sigma-Aldrich/Merck) coated lumox® 24-well plates (Sarstedt) and kept at 37°C in humidified air with 5% CO_2 until the experiment. Holographic imaging was conducted at 37°C in humidified air with 5% CO_2 in the absence or presence of either 100 nM Glu-urea-Lys-HBED-CC-PEG_2-STAR RED or 100 nM Glu-urea-Lys-HBED-CC-PEG_2-STAR 635P in RPMI+++ for a total of 48 h with 15 min between image captures. During the experiment, PHI HoloLids™ (Phase Holographic Imaging) were used to close the well plate to ensure optimal image quality. Data analysis

was performed with the HstudioM4 software (Phase Holographic Imaging) including cell segmentation, tracking of dividing cells, confluency measurement, and cell counting.

III.4.14 Flow Cytometry Studies

III.4.14.1 PSMA Binding Affinity

Using flow cytometry, the binding affinity was determined as the half maximal effective concentration (EC_{50}). An ascending series of concentrations (0, 0.5, 1, 2.5, 5, 10, 25, 50, 100, 500 nM) of Glu-urea-Lys-HBED-CC-PEG_2-STAR RED and -STAR 635P was diluted in RPMI+++ and LNCaP cells were incubated with the respective concentrations for 45 min. After centrifugation (800 rpm, 2 min), the supernatant was decanted, and the cells were resuspended in RPMI+++. This procedure was repeated twice but the cells were resuspended in PBS in each case. Finally, propidium iodide solution (PI, 1 mg/ml) was added as a nucleic acid intercalator marking dead cells. For PSMA inhibitor concentrations of 0.5, 5 and 50 nM, 500 µM 2-PMPA was additionally co-incubated to demonstrate the specificity of the binding.

The samples were measured using a BD FACS Canto II Flow Cytometer (BD Biosciences) and 2×10^3 living cells were selected for analysis in the forward scatter (FSC) *vs.* side scatter (SSC) plot. The mean fluorescence intensities (as median fluorescence intensities) of the PSMA inhibitors were measured and the binding affinity was determined at least three times. The data are presented as EC_{50} ± SD.

III.4.14.2 PSMA Binding pH Dependence

The pH dependence of the binding to PSMA on LNCaP cells was analyzed for Glu-urea-Lys-HBED-CC-PEG_2-STAR RED and -STAR 635P and the antibody complex consisting of primary antibody decorated either with STAR 600- or STAR RED-labeled secondary antibody (refer to III.4.11.1). The incubation scheme is summarized in Table III-4. Both incubation steps (incubation 1 and 2) were conducted in a volume of 50 µl on ice for 1 h; the cells were washed by centrifugation (800 rpm, 2 min) with 10% GS in PBS between steps. After washing once with 10% GS in PBS and twice with PBS by centrifugation (800 rpm, 2 min), the cells were resuspended with PBS and PI (1 mg/ml) was added.

The samples were measured using a BD FACS Canto II Flow Cytometer (BD Biosciences) and 2×10^3 living cells were selected for analysis in the FSC-SSC plot. The mean fluorescence intensities (as median fluorescence intensities) of the PSMA inhibitors and the secondary antibodies were assessed, and the measurements were repeated at least three times. The data are presented as the percentage binding at pH 4.6 normalized to binding at pH 7.4.

Table III-4. Incubation scheme for the analysis of the pH dependence of PSMA binding for PSMA inhibitors and antibody complex.

1stAB – primary antibody, 2ndAB – secondary antibody

sample	incubation 1	incubation 2
control 1	10% GS in PBS pH 7.4	10% GS in PBS pH 7.4
control 2	10% GS in PBS pH 4.6	10% GS in PBS pH 4.6
control 3	10% GS in PBS pH 7.4	2ndAB-STAR RED (1:50) in 10% GS in PBS pH 7.4
control 4	10% GS in PBS pH 4.6	2ndAB-STAR RED (1:50) in 10% GS in PBS pH 4.6
control 5	10% GS in PBS pH 7.4	2ndAB-STAR 600 (1:50) in 10% GS in PBS pH 7.4
control 6	10% GS in PBS pH 4.6	2ndAB-STAR 600 (1:50) in 10% GS in PBS pH 4.6
Glu-urea-Lys-HBED-CC-PEG_2-STAR RED pH 7.4	50 nM in 10% GS in PBS pH 7.4	10% GS in PBS pH 7.4
Glu-urea-Lys-HBED-CC-PEG_2-STAR RED pH 4.6	50 nM in 10% GS in PBS pH 4.6	10% GS in PBS pH 4.6
Glu-urea-Lys-HBED-CC-PEG_2-STAR 635P pH 7.4	50 nM in 10% GS in PBS pH 7.4	10% GS in PBS pH 7.4
Glu-urea-Lys-HBED-CC-PEG_2-STAR 635P pH 4.6	50 nM in 10% GS in PBS pH 4.6	10% GS in PBS pH 4.6
1stAB + 2ndAB-STAR RED pH 7.4	1stAB (1:50) in 10% GS in PBS pH 7.4	2ndAB-STAR RED (1:50) in 10% GS in PBS pH 7.4
1stAB + 2ndAB-STAR RED pH 4.6	1stAB (1:50) in 10% GS in PBS pH 4.6	2ndAB-STAR RED (1:50) in 10% GS in PBS pH 4.6
1stAB + 2ndAB-STAR 600 pH 7.4	1stAB (1:50) in 10% GS in PBS pH 7.4	2ndAB-STAR 600 (1:50) in 10% GS in PBS pH 7.4
1stAB + 2ndAB-STAR 600 pH 4.6	1stAB (1:50) in 10% GS in PBS pH 4.6	2ndAB-STAR 600 (1:50) in 10% GS in PBS pH 4.6

III.4.15 Data Presentation

Detailed information on data presentation is given in I.2.2.2. Linear deconvolution of the STED (confocal) data was performed by applying a Lorentzian PSF (refer to equation (I-5)) with FWHM = 60 nm (FWHM = 200 nm) in lateral dimension. All line profiles were drawn on raw data and averaged over 3 pixels.

If necessary, the single images of the live confocal and STED time series were corrected for photobleaching using the ImageJ Plugin CorrectBleach V2.0.2 applying histogram matching as correction mode [470, 862]. The images of all time series were corrected for background and the STED data were additionally linearly deconvolved.

III.4.16 Statistical Aspects

Detailed information on general statistical aspects is given in I.2.2.3.

III.5 RESULTS

III.5.1 Synthesis and Radiolabeling

For the design of dual-modality PSMA inhibitors suitable for 775 nm STED, derivatives based on Glu-urea-Lys-HBED-CC-PEG_2-IRDye800CW were chosen as an exemplary model. Compared to clinically established molecules such as PSMA-11 or PSMA-617, Glu-urea-Lys-HBED-CC-PEG_2-IRDye800CW shows similar cell binding, internalization, and pharmacokinetic properties as well as comparable specific tumor enrichment [48, 768, 769].

High-quality STED imaging depends, among other things, on photostable dyes with a low dark state transition probability and a large cross section for stimulated emission. Due to their superior performance in 775 nm STED, the commercially available Abberior dyes STAR RED and STAR 635P were conjugated to the precursor Glu-urea-Lys[Fe(HBED-CC)]-PEG_2-NH_2. The chemical purity of the final products

- Glu-urea-Lys-HBED-CC-PEG_2-STAR RED (hereinafter referred to as `conjugate **RED**´) and
- Glu-urea-Lys-HBED-CC-PEG_2-STAR 635P (hereinafter referred to as `conjugate **635P**´)

was determined to be > 95%. Table VI-16 summarizes the analytical data of the final products and Figure III-6a shows their chemical structure. The radiochemical yields of ^{68}Ga-labeling exceeded 99% and the molar activities of the radiolabeled conjugates measured 50 GBq/µmol. The lipophilicity was determined as log*D* in octanol/PBS at pH 7.4 and ranged from -1.93 ± 0.44 for [^{68}Ga]Ga-conjugate **RED** to -2.88 ± 0.09 for [^{68}Ga]Ga-conjugate **635P**.

III.5.2 Fluorescence Properties

The absorbance and fluorescence emission of the STAR RED dye and STAR 635P dye underwent a slight red-shift upon conjugation to Glu-urea-Lys[Fe(HBED-CC)]-PEG_2-NH_2. The absorbance of conjugate **RED** peaked at 641 nm and the fluorescence emission at 660 nm in PBS at pH 7.4 (uncoupled dye 638 nm/655 nm in PBS pH 7.4); the absorbance of conjugate **635P** peaked at 639 nm and the fluorescence emission at 660 nm in PBS at pH 7.4 (uncoupled dye 638 nm/651 nm in PBS pH 7.4) (Figure III-6b,c). The UV-active HBED-CC chelator moiety caused an additional absorbance peak around 280 nm, which was used to normalize the spectra and correct for slight variations in concentration (Figure VI-7).

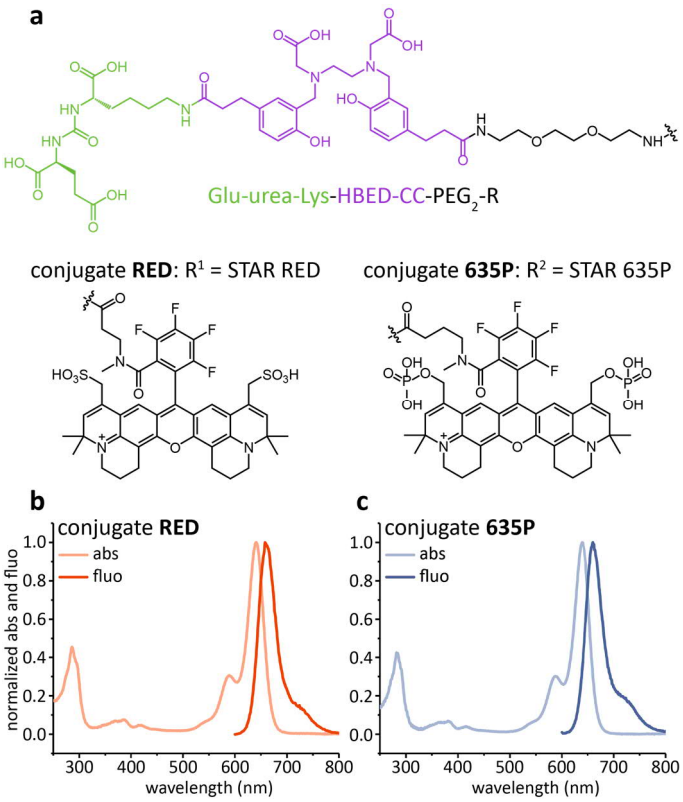

Figure III-6. Chemical structures and spectral properties of conjugate RED and conjugate 635P.

(**a**) The conjugates consist of the PSMA binding motif Glu-urea-Lys (green), the radiometal chelator HBED-CC (purple) and the fluorescence moiety conjugated via a PEG_2 linker. (**b**) Conjugate **RED** displays absorbance and fluorescence emission maxima at 641 nm and 660 nm. (**c**) Conjugate **635P** displays absorbance and fluorescence emission maxima at 639 nm and 660 nm. The conjugates were measured in PBS at pH 7.4. The absorbance spectra are baseline corrected. All spectra are normalized to their maximum.

III.5.3 Specific Cell Binding and Internalization *in vitro*

Incubation of LNCaP cells with either ^{68}Ga[Ga]-conjugate **RED** or ^{68}Ga[Ga]-conjugate **635P** (30 nM, 45 min, 37°C) resulted for both conjugates in significant and specific cell surface binding. Competitive cell binding studies revealed high affinities to PSMA in the low nanomolar range (expressed as K_i values calculated from cellular IC_{50} values). For both conjugates, a large fraction specifically internalized in addition. Table III-5 summarizes the fractions of specifically bound and specifically internalized ^{68}Ga-radiolabeled conjugate **RED** and ^{68}Ga-radiolabeled conjugate **635P**.

Table III-5. Cell binding and internalization properties of ^{68}Ga-radiolabeled conjugate RED and conjugate 635P.

Data are expressed as mean ± SD (n = 3), * ^{68}Ga-radiolabeled conjugates. Specific cell uptake was determined by blockage using 500 µM 2-PMPA. Values are expressed as % of applied radioactivity (IA) bound to 10^5 cells, † free inhibitors, competitive cell binding against [^{68}Ga]Ga-PSMA-10, ‡ free inhibitors, PSMA binding FACS study.

	specifically cell surface bound [%IA/10^5 cells]*	specifically internalized [%IA/10^5 cells]*	K_i [nM]†	EC_{50} [nM]‡
conjugate **RED**	2.98 ± 0.66	8.94 ± 3.33	36.77 ± 2.28	30.36 ± 7.48
conjugate **635P**	6.94 ± 1.51	17.15 ± 1.45	45.73 ± 3.15	63.19 ± 4.02

III.5.4 Localization to LNCaP Xenograft Tumors *in vivo*

Biodistribution studies were performed to analyze the specific targeting ability of conjugate **RED** and conjugate **635P** to PSMA *in vivo* at 1 h p.i.. The performance of both conjugates was comparable. The tumor uptake in PSMA-positive LNCaP xenograft tumors was high with a mean percent injected dose per gram of tissue of around 5%ID/g. The liver uptake was negligible, whereas the kidney uptake was high, suggesting elimination via the renal pathway (Figure III-7). The results of the biodistribution studies are summarized Table VI-17.

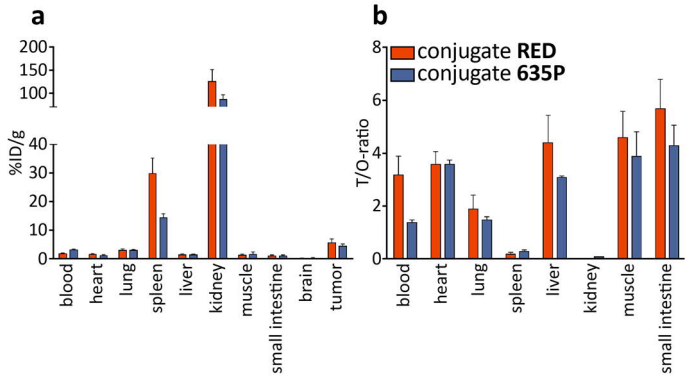

Figure III-7. Organ distribution at 1 h p.i. of ^{68}Ga-radiolabeled conjugate RED and conjugate 635P.

(**a**) Organ distribution of 60 pmol ^{68}Ga[Ga]-conjugate **RED** (red) and 60 pmol ^{68}Ga[Ga]-conjugate **635P** (blue) (data are expressed as mean %ID/g tissue ± SD (n=3)) and (**b**) corresponding tumor-to-organ ratios (T/O-ratios). All plotted values including SDs and p-values are summarized in Table VI-17.

As conjugate **RED** displayed higher photostability and better contrast in the fluorescence imaging experiments (refer to III.5.6, III.5.7 and III.5.8), its specificity of *in vivo* tumor uptake was additionally proven with PSMA-negative PC3 tumor xenografts. The uptake of conjugate **RED** was comparable for PSMA-negative tumor tissue and muscle tissue (Table VI-18).

III.5.5 Small-Animal PET Imaging

In the next step of *in vivo* characterization, the performance of ^{68}Ga-radiolabeled conjugate **RED** was evaluated in small-animal PET imaging studies. High imaging contrast was observed at early time points as [^{68}Ga]Ga-conjugate **RED** combines selective tumor uptake in the LNCaP xenograft model with rapid clearance from off-target tissue (Figure III-8a). High PSMA specificity was confirmed, as no measurable [^{68}Ga]Ga-conjugate **RED** uptake was detected in PSMA-negative PC3 xenografts during the experiments (Figure III-8b). While the corresponding time activity curves illustrate rapid clearance from tissues of liver, heart and muscle, they display continuous accumulation of [^{68}Ga]Ga-conjugate **RED** in the tissues of kidney and bladder. This observation agrees well with the biodistribution studies indicating the renal pathway to be the most likely elimination mechanism (Figure III-8c,d).

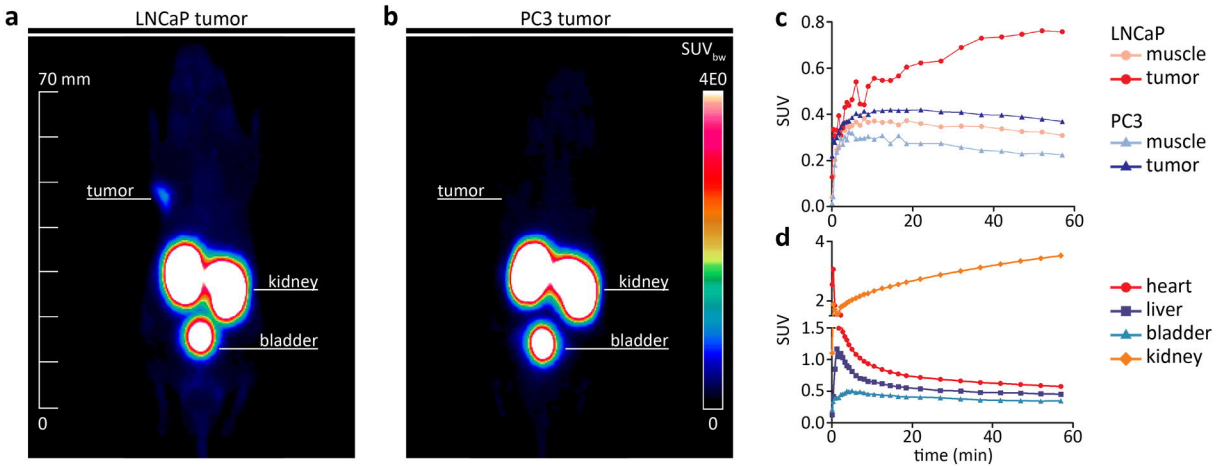

Figure III-8. Small-animal PET imaging study of [^{68}Ga]Ga-conjugate RED.

Whole-body maximum intensity projections of small-animal PET imaging acquired 120 min p.i. of 0.5 nmol ^{68}Ga-radiolabeled conjugate **RED** (~50 MBq) in (**a**) LNCaP- and (**b**) PC3-tumor-bearing (right trunk) athymic nude mice (SUV – standardized uptake value). Corresponding time activity curves are shown in (**c**) for tumor and muscle (LNCaP and PC3) and in (**d**) for heart, liver, kidney and bladder (LNCaP).

III.5.6 From Antigen Binding to Internalization and Cellular Accumulation

In fluorescence imaging experiments, conjugate **RED** displayed superior contrast and photostability as compared to conjugate **635P**. Thus, all following confocal and STED data were acquired with this conjugate. Confocal fluorescence imaging confirmed the time activity curves shown in Figure III-8c,d by detecting an increasing accumulation of conjugate **RED** in LNCaP cells over time. Saturation of the biological system was reached after 15 min of incubation. At later time points, neither further signal increase of the membrane bound nor of the internalized fraction was detected (Figure III-9a).

The concentration of conjugate **RED** did not affect its cellular accumulation and for the tested concentration range (50-250 nM), a blocking effect was not observed (Figure III-9b). The specificity of PSMA binding and internalization was proven in confocal microscopy blocking studies in the presence of 500 µM 2-PMPA and in confocal microscopy internalization experiments with PSMA-negative PC3 cells (Figure VI-8).

While in confocal imaging, the PSMA distribution in the cell membrane as visualized by conjugate **RED** bound antigen appeared homogeneous, STED imaging resolved details of the antigen distribution. Areas of higher and lower PSMA density were indicated by the heterogeneous distribution of the fluorescence signal along the cell membrane. Round to oval-shaped antigen clusters of varying sizes were detected located within the patches of high PSMA density (Figure III-10).

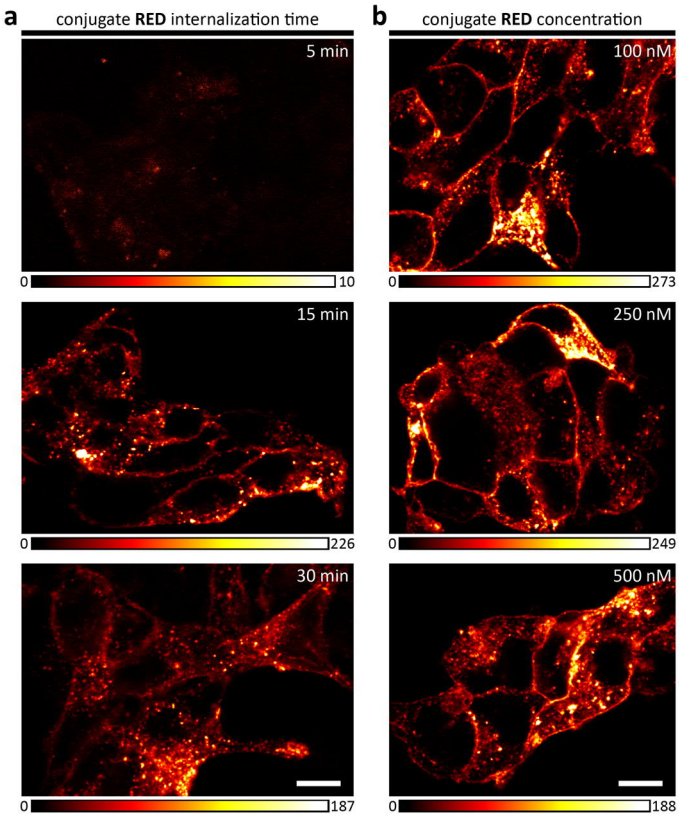

Figure III-9. Time and concentration dependence of conjugate RED internalization.

(**a**) Confocal imaging after 5/15/30 min of conjugate **RED** incubation (50 nM) determined cell saturation at 15 min of internalization time. (**b**) Confocal imaging after incubation with 100/250/500 nM conjugate **RED** (45 min) did not detect any apparent differences in membrane binding and internalization in the concentration range tested. All data shown are raw data and were acquired using the same imaging parameters. All scale bars are 10 µm.

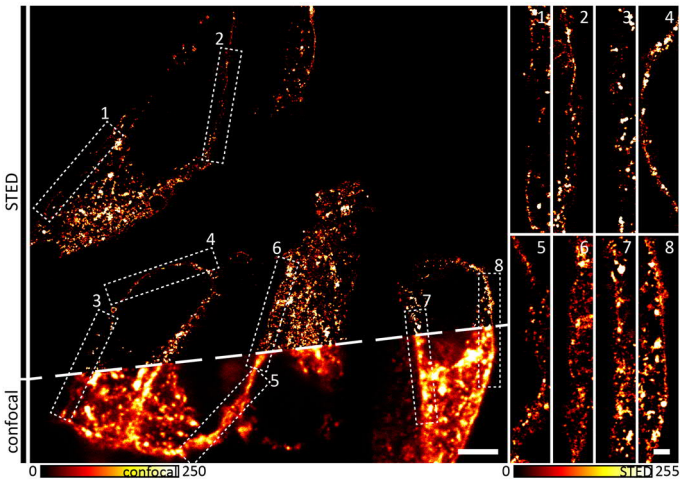

Figure III-10. PSMA distribution in the cell membrane.

Overview image of LNCaP cells after incubation with conjugate **RED** (100 nM) for 45 min. Comparing STED (top left) with confocal (bottom left) demonstrates the gain in resolution. A heterogeneous distribution of conjugate **RED** bound PSMA with areas of higher and lower antigen density is resolved by STED imaging. The patches of high PSMA density consisted of round to oval-shaped PSMA clusters of varying sizes. Magnifications of the marked regions in the overview are shown as STED close-ups on the right. All STED data shown are background corrected and linearly deconvolved. All confocal data shown are raw data Scale bar overview is 5 µm, scale bar close-ups is 1 µm.

The relationship of internalized conjugate **RED** and PSMA was assessed by additional STAR 600-immunolabeling of the antigen. We developed a novel antibody staining protocol that enabled us to simultaneously target PSMA in living LNCaP cells with antibodies and dual-labeled PSMA inhibitors (refer to III.4.11). The fluorescent signals of the putative PSMA/PSMA inhibitor complex were initially localized to cytosolic vesicles visualized as blurred diffraction-limited spots by confocal imaging. In contrast, STED imaging allowed for the nanometer resolution of defined, hollow, spherical structures and revealed that the antigen-inhibitor complex was initially vesicle membrane bound. The vesicle distribution in the cytosol was heterogeneous and regions of higher and lower vesicle density were observed. In particular cellular filopodia accumulated increased concentrations of vesicles as opposed to the nucleus, which always remained free of any conjugate **RED** signal (Figure III-11).

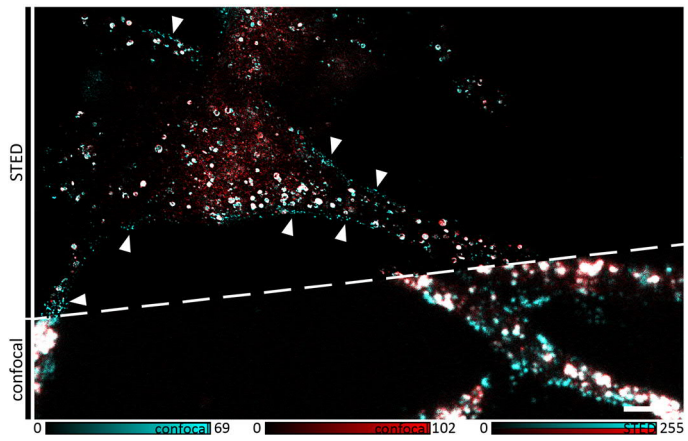

Figure III-11. Distribution of PSMA/PSMA inhibitor carrying vesicles in the cytosol.

After IF staining for PSMA (STAR 600, cyan) and conjugate **RED** (red) incubation (100 nM) for 1 h of internalization, STED (top) and confocal (bottom) imaging visualize different vesicle densities in the cytosol of LNCaP cells. Accumulation was pronounced in filopodia. The vesicles were resolved as defined, hollow, spherical structures by STED imaging. While conjugate **RED** has already started to disperse homogeneously in the cytosol, a fraction of internalized PSMA inhibitor was still PSMA bound after 1 h of incubation. Distinct patches of round to oval-shaped (non-colocalizing) PSMA signal clusters of varying size on the cell membrane indicated recycled protein (white arrows). All STED data shown are background corrected and linearly deconvolved. All confocal data shown are raw data. Scale bar is 5 µm.

The improvement in resolution gained by STED is illustrated by line profiles of vesicles derived from raw confocal and STED data (Figure III-12). Describing the line profiles by Lorentzian fitting confirmed a spatial resolution far below the diffraction limit allowing for determination of the average vesicle diameter. As PSMA internalization is mediated by clathrin-dependent endocytosis [723, 758] and clathrin-coated vesicles (CCVs) are characterized by a well-defined diameter, the degree of progress along the endocytic pathway can be judged by the diameter of PSMA inhibitor carrying endocytic vesicles. Thus, the vesicle diameter was computed by fitting a two-dimensional ring function (refer to equation (III-5)) to the fluorescence signal of conjugate **RED** incubated for different internalization times and imaged by STED nanoscopy. Within the first hour of internalization, the average diameter d did not differ significantly (Table III-6, Table VI-19). For later time points especially, the large SDs represent a broad diameter distribution in the overall vesicle population ranging from d < 150 nm to d > 500 nm (Figure VI-9). These results are in the range of but always lager than the CCV diameter of ~100 nm as previously determined by EM [863, 864].

To complement the fixed cell imaging data, the internalization and cellular accumulation of conjugate **RED** were additionally studied in live cell imaging experiments. LNCaP cells were incubated with conjugate **RED** for 20 min on ice. The low temperature prevented premature antigen internalization during staining of the membrane bound PSMA fraction. Confocal imaging of the washed samples detected steady internalization confirming the fixed cell data (Figure III-13). Neither significant externalization of conjugate **RED** nor signs of impaired cell viability (e.g. morphological changes) were observed during the experiment.

Table III-6. Diameter of endocytic vesicles carrying conjugate RED bound PSMA.

Data are expressed as mean ± SD (n = 50).

internalization time [min]	d [nm]
30	274 ± 71
45	262 ± 82
60	298 ± 97

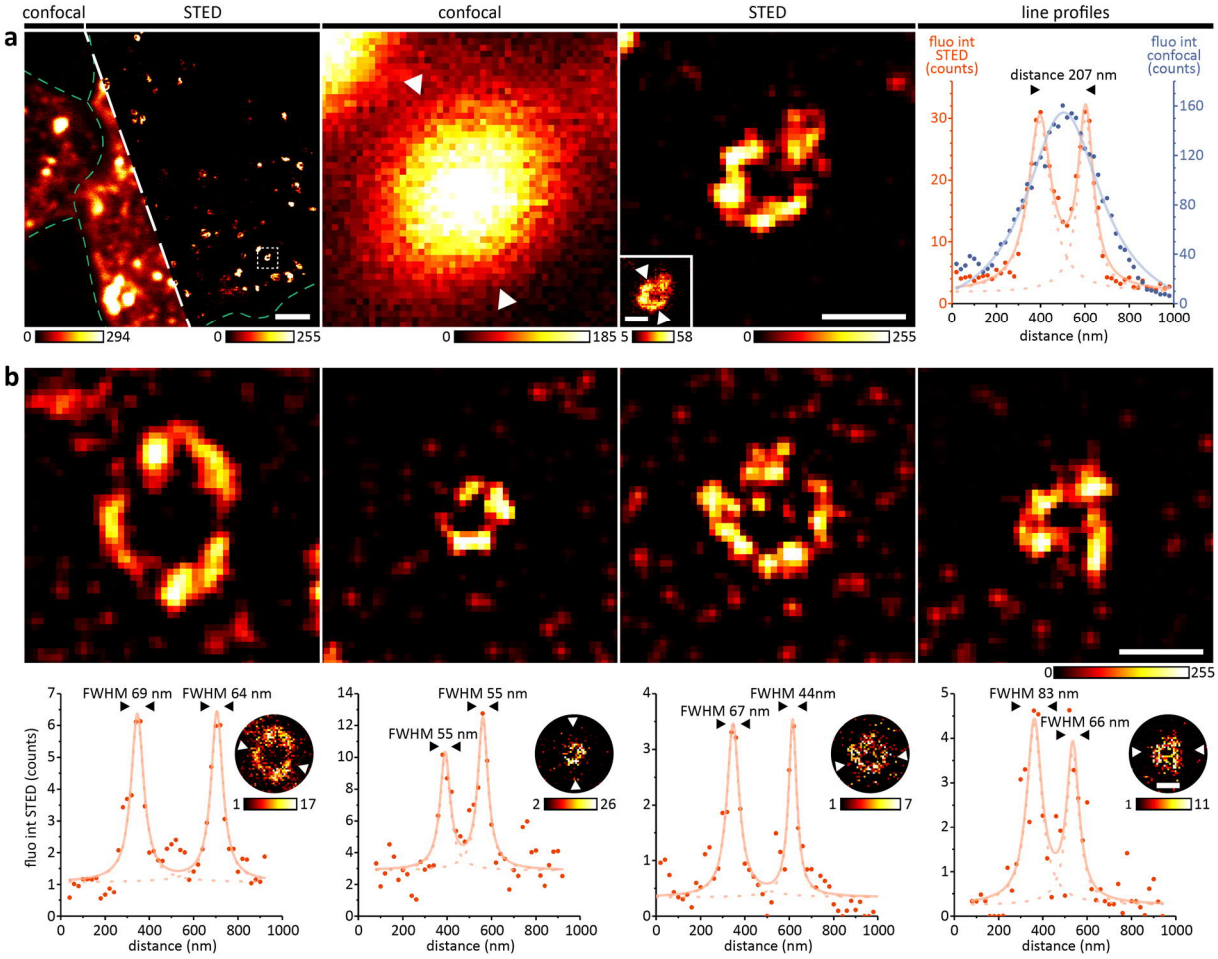

Figure III-12. STED imaging resolves endocytic vesicles after internalization of conjugate RED bound PSMA.

(**a**) Comparison of STED and confocal imaging of LNCaP cells stained with conjugate **RED** (100 nM) for 45 min of internalization time. From left to right: overview image showing internalized vesicles in a lamellipodium (cell outline sketched with dashed green line) imaged in confocal and STED mode; next: magnification of the vesicle marked in the overview as recorded in confocal imaging; next: same vesicle as recorded in STED imaging; next: line profiles of the STED (red) and confocal (blue) data as marked in the magnified vesicle images by white arrows. While confocal imaging did not resolve the vesicle, STED imaging revealed a diameter of approx. 207 nm. Pixel size was identical for confocal and STED image (20 nm). Scale bar overview is 2 µm, scale bars close-ups are 250 nm. (**b**) Additional examples of endocytic vesicles as resolved by STED imaging with the corresponding line profiles depicted below the respective STED image, scale bars are 250 nm. The line profiles of (**a**) and (**b**) were drawn on raw data (marked by white arrows), averaged over three pixels and fitted with a single (for confocal data) or a double (for STED data) Lorentzian function. For the STED data, the FWHMs illustrate a resolution significantly below the diffraction limit. Except for the insets displaying the direction of line profiles, which are background corrected only, all STED data shown in (**a**) and (**b**) are background corrected and linearly deconvolved. All confocal data are raw data.

For rigorous exclusion of potential conjugate **RED** cytotoxicity, LNCaP proliferation was followed using holographic time-lapse imaging. To determine the duration and frequency of cell division, cells were imaged for 48 h in the presence of either conjugate **RED** or conjugate **635P**. The results were compared to the proliferation behavior of untreated cells. The data suggest absence of cytotoxicity for both conjugates. Surprisingly, the presence of particularly conjugate **RED** even accelerated LNCaP proliferation (Figure III-14, Figure III-15) (for details on cytotoxicity testing of live dyes in general, refer to IV.3).

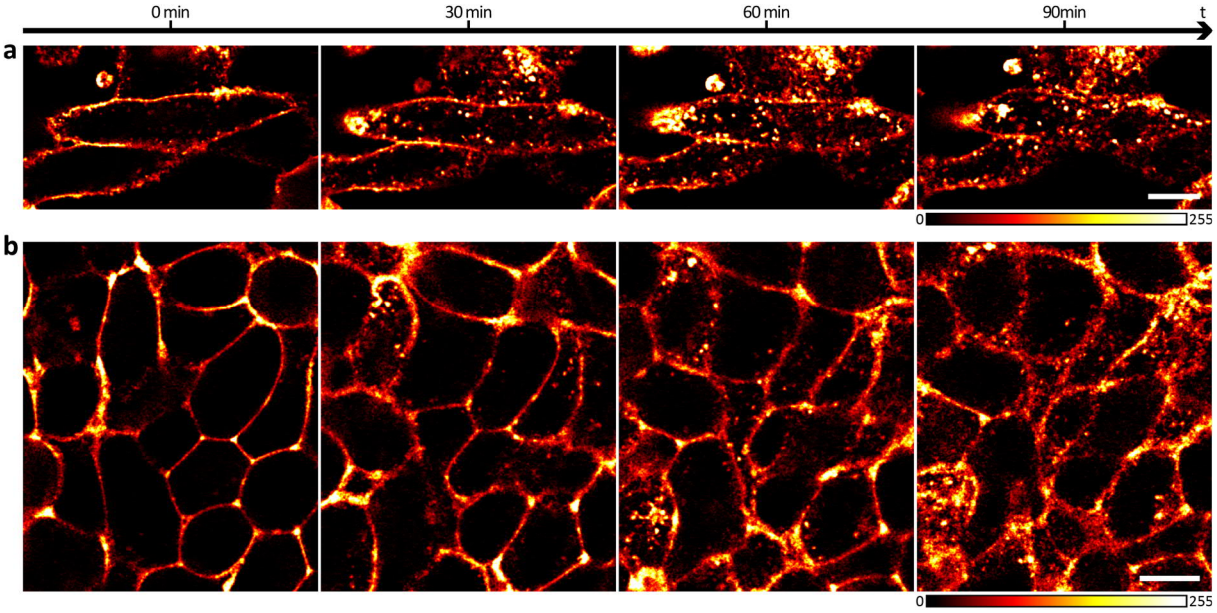

Figure III-13. Live cell confocal imaging of conjugate RED internalization.

LNCaP cells were incubated on ice for 20 min with (**a**) 100 nM or (**b**) 50 nM conjugate **RED**. The focal plane was set into the cell volume and confocal time series were recorded with a frequency of (**a**) 1 fpm or (**b**) 0.5 fpm for a duration of (**a**) 120 min or (**b**) 90 min. Steady internalization was observed. To smooth the data and reduce the noise, all confocal images shown are linearly deconvolved. Scale bars are 10 µm.

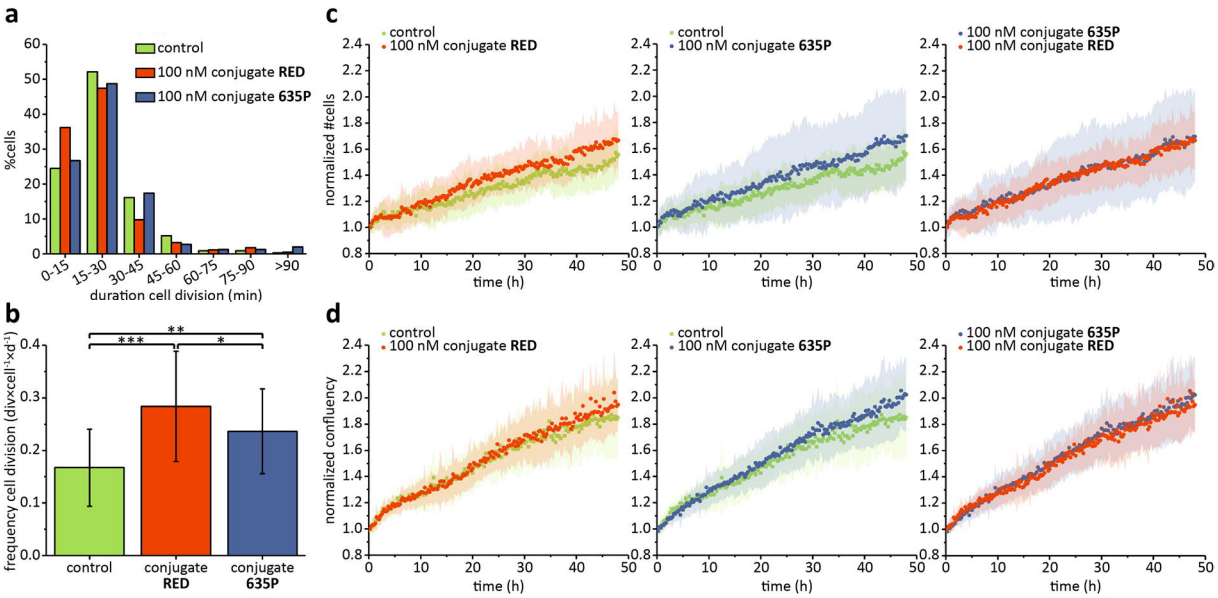

Figure III-14. Assessment of the cytotoxicity of conjugate RED and conjugate 635P.

Cytotoxicity data are based on holographic time-lapse series (duration 48 h, frequency 15 min) of LNCaP proliferation in the absence (green) or presence of 100 nM conjugate **RED** (red) or 100 nM conjugate **635P** (blue) (e.g. Figure III-15). (**a**) Duration of cell division of untreated (n = 347), conjugate **RED** treated (n = 624) and conjugate **635P** treated (n = 408) LNCaP cells. P-values indicate no significant difference between the untreated and the conjugate **635P** treated condition, but a significant shortening in cell division duration by conjugate **RED**. (**b**) Frequency of cell division of untreated (n = 347), conjugate **RED** treated (n = 624) and conjugate **635P** treated (n = 408) LNCaP cells. The results display an increase in cell division frequency for both conjugates (* p <0 .5, ** p <0 .05, ***p <0 .005). (**c**) Cell count and (**d**) confluency of untreated (n = 13), conjugate **RED** treated (n = 16) and conjugate **635P** treated (n = 14) LNCaP cells. Both measures were normalized to the first frame (t = 0). The results were averaged and SDs are displayed as shadows in the graphs. P-values indicate no significant difference between untreated and treated LNCaP cells. All data strongly support the absence of cytotoxicity. All results and p-values are summarized in Table VI-20, Table VI-21 and Table VI-22.

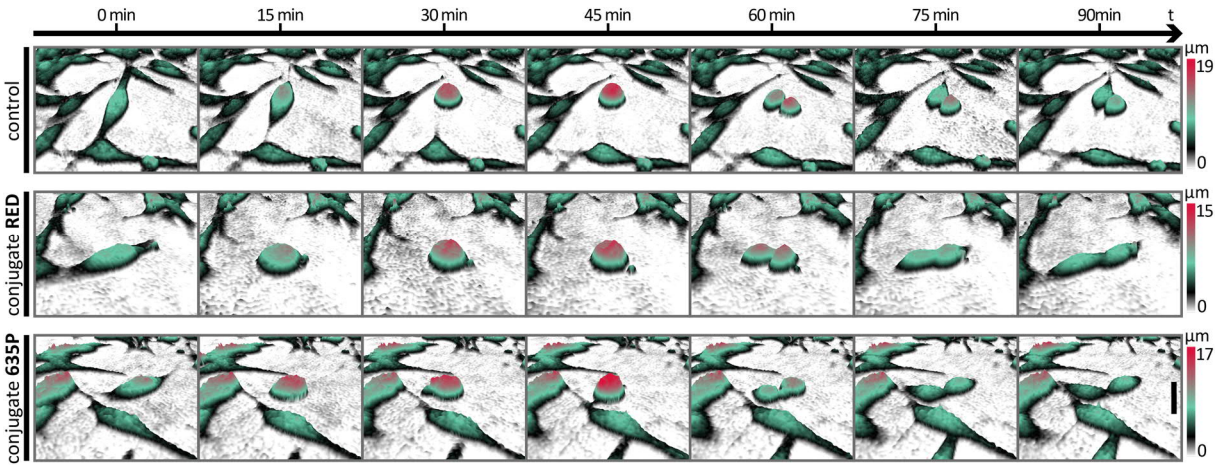

Figure III-15. LNCaP cell division in the absence and presence of PSMA inhibitors.

Using holographic time-lapse cytometry with a HoloMonitor® M4 microscope, LNCaP cell proliferation was followed for a total of 48 h in the absence (control) and in the presence of either 100 nM conjugate **RED** or conjugate **635P**. In the exemplary sequences (duration 1.5 h, frequency 15 min), dividing cells round up and thus can be distinguished from non-dividing cells by height (color coded). Scale bar is 50 µm.

III.5.7 Along the Endocytic Pathway

To study the PSMA inhibitor internalization pathway, colocalization of conjugate **RED** with clathrin was assessed in live cell confocal experiments with LNCaP cells transiently transfected with a SNAP-tag fusion of clathrin labeled with the live dye 610CP-BG [29]. For early time points of internalization, a significant signal overlap between conjugate **RED** and clathrin was observed (Figure III-16). With progressing internalization time, the degree of colocalization decreased. For quantitative analysis of the colocalization, the PCC was calculated. From 10 min to 15 min of internalization, the PCC significantly ($p = 10^{-8}$) dropped from $r = 0.70 \pm 0.08$ ($n = 7$) to $r = 0.23 \pm 0.11$ ($n = 14$). This result indicates clathrin-dependent endocytosis with rapid clathrin uncoating after internalization. Uncoated endocytic vesicles can fuse with early endosomes (Figure III-17) [865, 866].

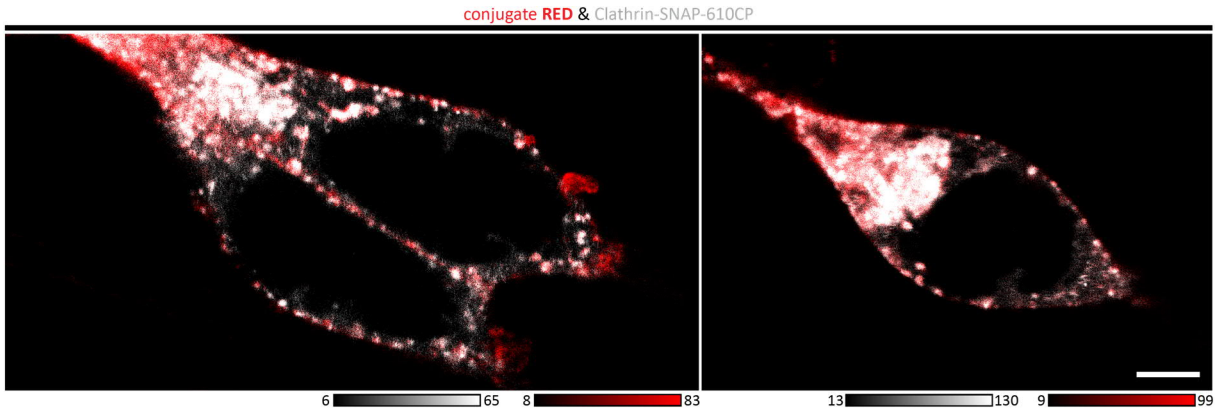

Figure III-16. Colocalization experiments confirming clathrin-mediated uptake of conjugate RED bound PSMA.

To prove clathrin-mediated uptake of PSMA inhibitors, colocalization between conjugate **RED** (red) and clathrin (gray) was investigated. SNAP-CLC transiently transfected LNCaP cells were labeled with 610CP-BG and incubated with conjugate **RED** (50 nM). Live cell confocal imaging showed strong colocalization after 10 min of internalization time. All confocal data shown are background corrected. Scale bar is 5 µm.

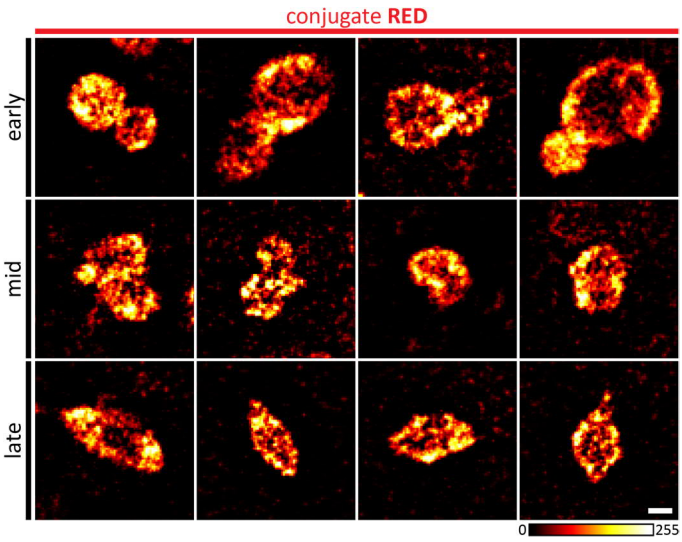

Figure III-17. Fusion of endocytic vesicles carrying conjugate RED bound PSMA.

After cellular uptake and clathrin uncoating, vesicles fuse along the endosomal pathway. STED imaging resolved early stages (upper row), intermediate stages (middle row) and late stages (bottom row) of vesicle fusion in LNCaP cells incubated with conjugate **RED** (100 nM) for 1 h of internalization time. All data are background corrected and linearly deconvolved. Scale bar is 250 nm.

In live cell confocal experiments, endosomal colocalization of PSMA was investigated for different internalization times by co-staining with LysoTracker™ Green DND-26, which is selective for both endosomes and lysosomes. With progressing internalization time, the degree of colocalization between the PSMA signal and the endosomal signal increased. Additionally, non-colocalizing LysoTracker™ Green DND-26 signal was detected. On the one hand, the PSMA population of the samples was not comprehensively labeled due to the nature of the IF staining approach. On the other hand, the samples also contained non-PSMA-carrying lysosomes (Figure III-18a, Figure VI-10).

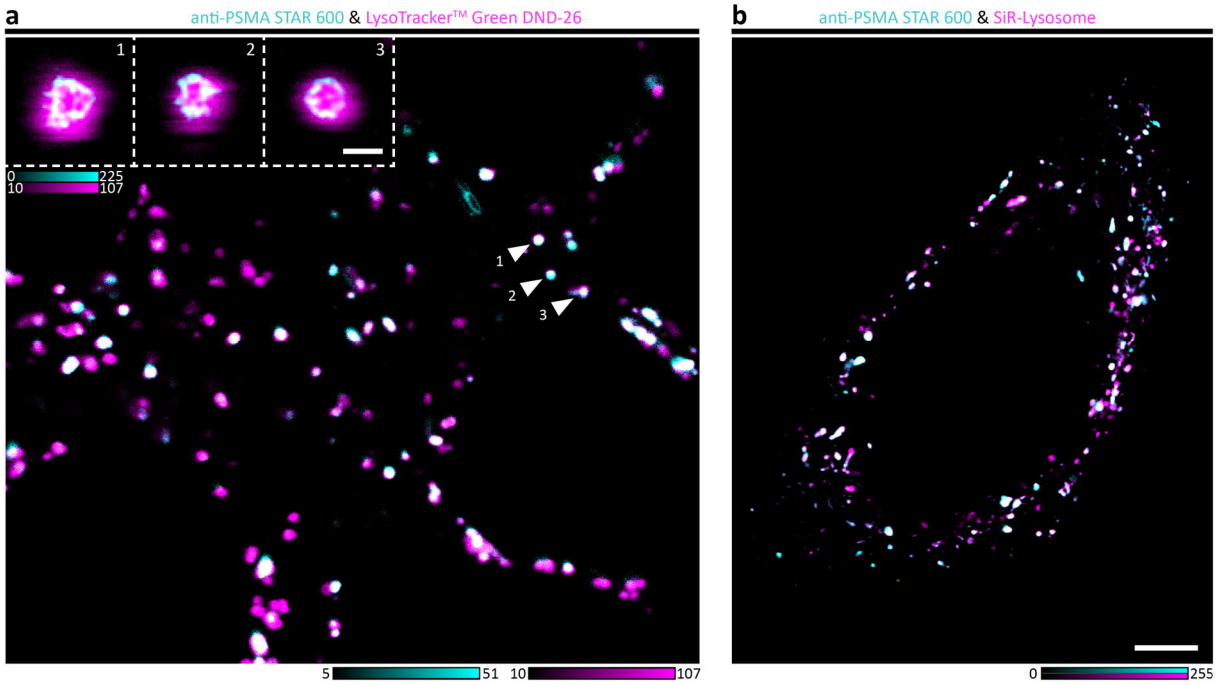

Figure III-18. Colocalization experiments confirming endosomal recycling of PSMA.

Colocalization between PSMA (cyan) and two commercially available endosomal/lysosomal probes (magenta) was analyzed to confirm endosomal PSMA recycling. LNCaP cells were STAR 600-immunolabled for PSMA on ice and subsequently incubated with (**a**) LysoTracker™ Green DND-26 (500 nM) or (**b**) SiR-Lysosome (1 µM) at 37°C to trigger internalization and allow for endosomal/lysosomal staining. After > 20 h of internalization time, strong colocalization was recorded between PSMA and (**a**) LysoTracker™ Green DND-26 in confocal mode and between PSMA and (**b**) SiR-Lysosome in STED mode. The insets in (**a**) represent magnifications of the endosomes marked by white arrows in the confocal overview image. While the PSMA signal is shown in STED mode, the endosome signal is diffraction-limited as LysoTracker™ Green DND-26 is not STED compatible. Scale bar overviews is 5 µm, scale bar close-ups is 500 nm. All confocal data shown are background corrected; all STED data shown are additionally linearly deconvolved.

Co-incubation with 2-PMPA, conjugate **RED** or conjugate **635P** did not significantly affect the PCC for endosomal colocalization of PSMA (Table VI-23). Average PCCs were thus taken over these four different experimental conditions (+ nothing, + 2-PMPA, + conjugate **RED**, + conjugate **635P**). From 1 h to > 20 h of internalization, the PCC for endosomal colocalization of PSMA significantly ($p = 10^{-15}$) climbed from r = 0.39 ± 0.05 (n = 21) to r = 0.71 ± 0.11 (n=26) indicating endosomal PSMA recycling.

Live cell dual-color confocal and STED colocalization experiments with STAR 600-immunolabeled PSMA and the SiR-Lysosome probe, which also targets both endosomes and lysosomes, confirmed the results obtained with LysoTracker™ Green DND-26 (Figure III-18b, Figure VI-11). Moreover, PSMA recycling was additionally supported by the appearance of clustered, non-colocalizing antigen signal at the cell membrane in STED imaging experiments after 45 min of internalization time (Figure III-11).

After live cell STED imaging, low light intensity confocal times-series of lysosomal dynamics were recorded to exclude potential phototoxic influence during the STED imaging process. Compared to control samples not exposed to high STED laser intensities, qualitative differences in lysosomal dynamics were not detected (Figure VI-12, Figure VI-13 and Figure VI-14).

III.5.8 Intracellular Fate of PSMA Inhibitors

To investigate the intracellular continuance of the PSMA/PSMA inhibitor complex, the extent and duration of colocalization of conjugate **RED** with PSMA was studied in dual-color STED experiments during and after the internalization process. LNCaP cells were simultaneously incubated with conjugate **RED** and STAR 600-immunolabeled for PSMA. After different internalization times, STED imaging visualized the intracellular distribution of the PSMA inhibitor and PSMA. The internalization times were well-defined by accurate temperature control of the endocytic process. No evidence of mutual blocking effects was observed upon internalization of both conjugate **RED** and the primary/secondary antibody complex.

In the following, qualitative trends are described rather than quantitative numbers stated due to biological heterogeneity. At early times of internalization, the strongest colocalization was observed with an average PCC peaking at 30 min with r = 0.65 ± 0.08 (n = 9).The signals continued to colocalize at the vesicle membrane during the first 60 min of internalization with an average PCC of r = 0.54 ± 0.09 (n = 43). After 60 min of internalization, colocalization progressively decreased as the conjugate **RED** signal started to gradually disperse homogeneously inside the endocytic vesicles, whereas the PSMA antibody signal remained at the vesicle membrane (Figure III-19). At later times of internalization (6 h, 24 h), the degree of colocalization between conjugate **RED** and PSMA was significantly reduced with an average PCC of r = 0.25 ± 0.12 (n = 18). The conjugate **RED** signal displayed a homogenous cytosolic distribution. In contrast, the PSMA antibody signal was still localized to the vesicle membrane. Additionally, new patches of dotted PSMA antibody signal appeared at the cell membrane indicating recycled antigen (Figure III-11).

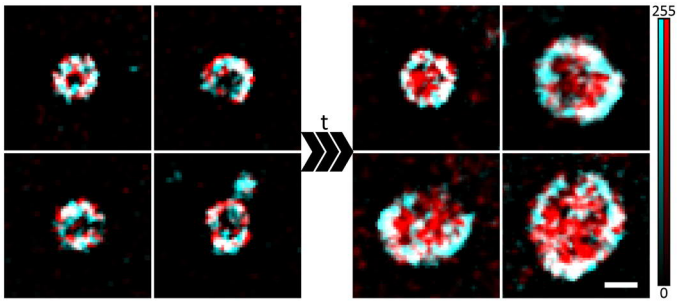

Figure III-19. Vesicular fate of the conjugate RED/PSMA complex.

LNCaP cells were STAR 600-immunolabeled for PSMA (cyan) and incubated with conjugate **RED** (100 nM, red). At early times of internalization, PSMA and conjugate **RED** colocalized at the vesicle membrane. Within the first hour of internalization, conjugate **RED** detached from PSMA and distributed homogeneously in the vesicles before it diffused into the cytosol. All STED data shown are background corrected and linearly deconvolved. Scale bar is 250 nm.

As fluorograms nicely illustrate colocalization trends (refer to III.4.12.3), the dual-color STED data of conjugate **RED** and STAR 600-immunolabeled PSMA were used to generate the corresponding fluorograms to the fluorescence images of all internalization times. For describing the internalization-time-dependent changes in the colocalization of conjugate **RED** and PSMA, all fluorograms were segmented in three defined sections separating:

- The top section represents the PSMA signal only.
- The middle section represents the colocalizing signal.
- The bottom section represents the conjugate **RED** signal only.

The background (quarter circle in left corner) was defined as the value of the average conjugate **RED** intensity after 24 h of internalization time (Figure III-20).

For short internalization times, the fluorograms displayed one colocalized fraction (white) falling into the middle section of the fluorogram. This corresponds to strong colocalization between the conjugate **RED** signal (red) and the PSMA signal (cyan) and represents specific binding of conjugate **RED** to PSMA in the cell and vesicle membrane. At 45 min of internalization time, the relative integrated intensity of the colocalizing fraction started to decline significantly in favor of an increasing cyan fraction (PSMA) in the top section of the fluorograms. This represents PSMA gradually releasing conjugate **RED** to recycle back to the cell membrane. In contrast, the red fraction (PSMA inhibitor) slowly vanished into the background as conjugate **RED** initially distributed homogeneously in the vesicles after detaching from PSMA to subsequently disperse in the cytosol of the cells (Figure III-21).

Taken together, the relative integrated intensities of conjugate **RED** and PSMA signal in the foreground of the middle section of the fluorogram significantly receded with progressing internalization time. While the relative integrated intensity of the conjugate **RED** signal in the entire background of the fluorogram (all three background sections taken together) significantly increased, it declined in the entire foreground (all three foreground sections taken together). On the contrary, the relative integrated intensity of the PSMA signal was steady in both the entire foreground and the entire background. No significant further changes of the signal distribution were detected after 6 h of internalization time (Figure VI-15).

As the ratio of the integrated fluorescence intensities did not drastically change with progressing internalization time (average of 1.17 ± 0.35 for PSMA to conjugate **RED**, n = 57), photobleaching and externalization were negligible. Still, rigorous quantification is challenging as the third dimension was ignored by the 2D imaging approach.

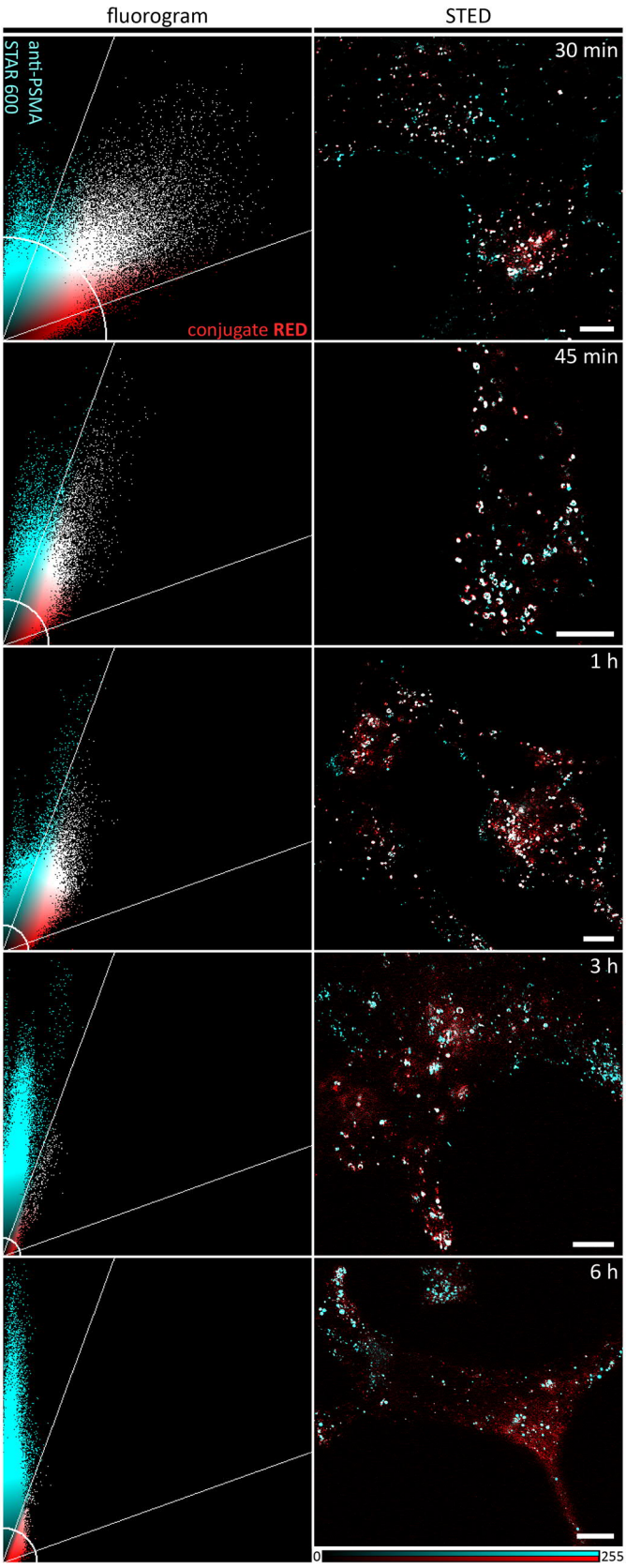

Figure III-20. Intracellular fate of the conjugate RED/PSMA complex.

LNCaP cells were STAR 600-immunolabeled for PSMA (cyan) and incubated with conjugate **RED** (100 nM, red). Exemplary dual-color STED images (left) with their corresponding fluorograms (right) are shown for 30 min, 45 min, 1 h, 3 h and 6 h of internalization time. Each fluorogram is subdivided into three defined sections representing PSMA signal only (top, cyan), colocalizing signal (middle, white) and conjugate **RED** signal only (bottom, red). Background (quarter circle bottom left) was set to the average conjugate **RED** fluorescence intensity in the cytosol after 24 h of internalization time. With progressing internalization time, the colocalizing fraction declined and the PSMA fraction increased as PSMA gradually released conjugate **RED** and recycled back to the cell membrane. The conjugate **RED** signal vanished into the background due to homogeneous cytosolic dispersion. All STED data shown are background corrected and linearly deconvolved. Scale bars are 5 µm.

Exchanging the fluorescent labels between the PSMA inhibitor and immunolabeled PSMA (i.e. Glu-urea-Lys-HBED-CC-PEG_2-STAR 600 and STAR RED-immunolabeled PSMA) would have been of great interest to further exclude dye-dependent effects. However, conjugation of the Abberior dye STAR 600 to the precursor Glu-urea-Lys[Fe(HBED-CC)]-PEG_2-NH_2 killed the fluorescence properties of STAR 600. Hence, conjugate **635P** was used to substantiate the results of conjugate **RED**. As the spectral properties of the STAR RED dye and the STAR 635P dye are very similar though (refer to III.5.2), PSMA had to be immunolabeled with STAR 600. The colocalization data for conjugate **635P** and STAR 600-immunolabeled PSMA after 30 min of internalization support the results for conjugate **RED** by displaying an average PCC of r = 53 ± 0.09 (n = 10) (Figure VI-16). For STAR RED-immunolabeled PSMA, the intracellular localization had to be assessed individually in single-color experiments due to non-fluorescent Glu-urea-Lys-HBED-CC-PEG_2-STAR 600. The data confirm the results for STAR 600-immunolabeled PSMA (Figure VI-16).

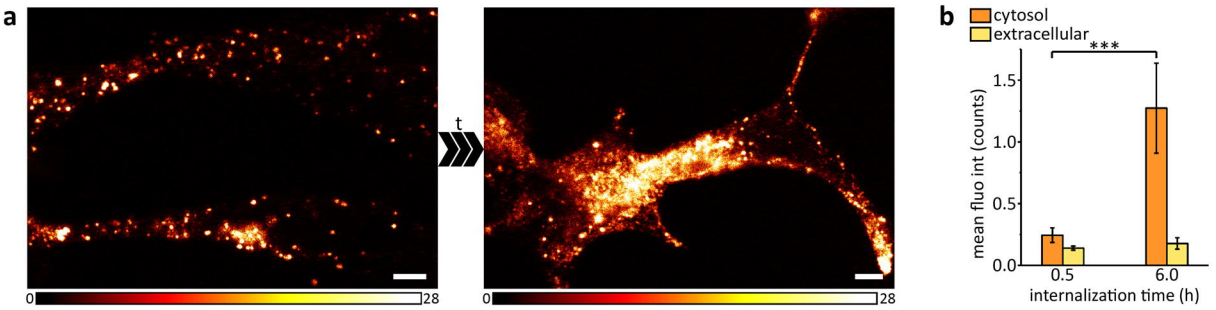

Figure III-21. Cytosolic fate of conjugate RED.

(**a**) Exemplary confocal images of a LNCaP cells incubated with conjugate **RED** (100 nM) for either 30 min of internalization time (right) or for 6 h of internalization time (left). The results illustrate the homogeneous cytosolic distribution of conjugate **RED** at later internalization times. All confocal data shown are raw data. Scale bars are 5 µm. (**b**) Comparison of the cytosolic and extracellular backgrounds of LNCaP cells for STED images after 30 min and 6 h of conjugate **RED** internalization time (cytosol, 30 min n = 32; extracellular, 30 min n = 32; cytosol, 6 h n = 48; extracellular, 6 h n = 48). The cytosolic fraction significantly (*** $p < 10^{-25}$) increased over time. All results and p-values are summarized in Table VI-24.

III.5.9 pH Dependence of PSMA Binding

The decreasing pH in endosomes potentially promoted the separation of the PSMA/PSMA inhibitor complex as suggested by the homogeneous cytosolic conjugate **RED** distribution for internalization times < 3 h. To prove this hypothesis, the binding properties of conjugate **RED**, conjugate **635P** and the primary/secondary antibody complexes to PSMA on LNCaP cells were tested for the putative pH dependence. The fluorescence signals of the PSMA inhibitors and secondary antibodies were exploited in flow cytometry studies to determine the fraction bound at pH 4.6 in percent of the fraction bound at pH 7.0. An acidic pH of 4.6 did not significantly affect the binding of the primary/secondary antibody complexes to PSMA. However, for conjugate **RED** and conjugate **635P**, the binding to PSMA was reduced by up to a factor of five at pH 4.6 (Table III-7, Figure VI-17).

Additionally, potential changes in the spectral properties of conjugate **RED** and conjugate **635P** were analyzed after incubation at different pH and temperature combinations to exclude pH and/or temperature dependent fluorophore degradation of the PSMA inhibitors. Neither the absorbance nor the fluorescence emission of conjugate **RED** and conjugate **635P** significantly changed at acidic pH and elevated temperature (Figure VI-18).

Table III-7. Influence of pH on the PSMA binding affinity of conjugate RED, conjugate 635P and the antibody complex.

Fraction of PSMA inhibitor or antibody complex bound at pH 4.6 given in percent of fraction bound at pH 7.0, data are expressed as mean ± SD (n = 3), p-values are given in Table VI-25.

	% binding at pH 4.6
anti-PSMA-STAR 600	83.29 ± 12.58
anti-PSMA-STAR RED	102.08 ± 16.58
conjugate **RED**	20.14 ± 2.24
conjugate **635P**	24.05 ± 1.36

III.6 DISCUSSION

The clinical limitations of non-targeted molecular imaging agents for PCa underscore the urgent need for reliable targeted probes for both PET and MRI of PCa [867]. Over the past decade, this awareness has stimulated the development of a plethora of investigational targeted imaging agents in both preclinical and clinical research [868]. Due to its remarkable efficacy in the detection, staging, and active surveillance of PCa, especially targeted PET imaging outperforms conventional imaging modalities strongly influencing further patient management and treatment regimen [713-717].

In particular, the discovery of strong PSMA upregulation on PCa cells has boosted seminal progress of targeted molecular imaging strategies [869]. PSMA has emerged as one of the most promising key players in targeted nuclear medicine. Its upregulation on PCa cells correlates with the stage and grade of tumor progression, especially in androgen-independent, advanced and metastatic disease [718-722]. Only a few organs physiologically express PSMA, but solely at significantly lower levels as compared to cancer tissue [718, 723].

During the last years, research focus has shifted from monoclonal anti-PSMA antibodies to low molecular weight PSMA-targeting probes, fueling the development and clinical translation of various tracers for the detection and treatment of PCa by means of radioligand imaging, radioligand therapy or radioguided surgery [870]. Low molecular weight inhibitors with high PSMA affinity inherently combine fast tumor uptake and rapid excretion. The exponential increase of imaging and therapy approaches based on these molecules has revolutionized the diagnosis and the treatment of metastatic, hormone-refractory PCa patients. Especially for late stage mCRPCa patients beyond established treatment options, endoradiotherapy based on α- or β-emitter radiolabeled PSMA inhibitors offers a promising treatment approach [819, 820].

The diagnostic and therapeutic strength of PCa targeting probes is strongly affected by both their cell binding and internalization properties as well as their subcellular localization. Certainly, strong and specific probe internalization is desired as it guarantees not only enrichment in the target cells over time but also protection of healthy tissue. Applied in endoradiotherapy, the probes' intracellular distributions co-determine the efficiency of the treatment. Potent DNA damage and subsequent apoptosis is ensured by a more target-oriented application of effectively higher local radiation doses. The relevant molecular framework is provided by cytosolic probe accumulation and localization in nuclear proximity. For the application of sufficient radiation, for example with high linear energy transfer α-particles, the enrichment adjacent to the nucleus is considered as particularly crucial.

III.6.1 Preclinical Characterization of STED Compatible Dual-Labeled PSMA Inhibitors

Equipping PSMA inhibitors with an additional fluorescent moiety has successfully introduced a second imaging modality to the established class of low molecular weight PSMA inhibitors in the clinical routine [48, 724, 871]. These dual-labeled PSMA inhibitors preserve specific PSMA binding and

internalization, high tumor uptake and favorable pharmacokinetic properties comparable to the clinically applied agents PSMA-11 and PSMA-617 [48, 768, 769].

From the clinical perspective, the additional fluorescence property allows for intraoperative fluorescence guidance during surgical resection of primary PCa and regional lymph node metastases. From the preclinical research perspective, the additional fluorescence property allows for intracellular tracking of these molecules. Combined with sophisticated fluorescence imaging approaches and complemented with elaborate PSMA staining strategies, these dual-labeled PSMA inhibitors represent attractive model compounds for studying the subcellular fate of low molecular weight PSMA inhibitors at the nanoscale. To the best of our knowledge, the detailed subcellular fate of PSMA/PSMA inhibitor complexes for low molecular weight PSMA inhibitors has so far not been investigated with fluorescence nanoscopy. The only basic knowledge of PSMA internalization and its intracellular distribution is based on diffraction-limited confocal microscopy studies [772, 872].

Certainly, the resolution of conventional diffraction-limited fluorescence microscopy is good enough to visualize the coarse localization of PSMA and its inhibitors inside cells over time. However, it is not sufficient for precisely investigating localization details such as cluster substructures and the molecular colocalization of PSMA and its inhibitors. Here, STED nanoscopy is the method of choice. Indeed, it provides the required spatial resolution; but moreover, STED nanoscopy is particularly valuable for colocalization experiments as compared to other fluorescence nanoscopy and related resolution-enhancing techniques. By using one STED donut to deplete both excitation channels, their signals are inherently co-aligned. Since the STED zero defines the position of the fluorescently active molecules and thus the position of effective excitation for all channels, the colocalization results are not altered by residual chromatic aberrations [137].

To meet the special demands of STED imaging on the applied fluorophores such as high photostability, large cross section for stimulated emission and low dark state transition probabilities [381], we synthesized PSMA-11 based dual-labeled PSMA inhibitors conjugated with the STED compatible Abberior dyes STAR RED and STAR 635P. For a start, we preclinically characterized our conjugates by exploiting their radioactive properties. Conjugate **RED** as well as conjugate **635P** displayed high binding affinities specific to PSMA and large internalized fractions in PSMA-positive cells. In addition to these promising targeting characteristics, the tumor uptake in PSMA-positive lesions was specific. The high tumor-to-background ratios at early time points are comparable to those of the reference compounds [48, 768, 769]. We thus conclude that the additional fluorescence moiety did not significantly alter the important characteristics of our conjugates. As pharmacokinetic properties and tumor accumulation remained unaffected, conjugate **RED** and conjugate **635P** are suitable to mimic clinically applied PSMA inhibitors for studying their intracellular fate using STED nanoscopy.

As a function of time, confocal and STED microscopy afforded the investigation of the intracellular distribution of PSMA and of our PSMA inhibitors in PSMA-overexpressing cells. Independently of the concentrations tested, the internalized PSMA inhibitor fraction increased with progressing incubation time. The data obtained in the *in vitro* radioassays, namely cell binding and internalization studies with our ^{68}Ga-radiolabeled PSMA inhibitors, support the fluorescence imaging results. As we did not observe any blocking effects between our PSMA inhibitors and the anti-PSMA antibody, we conclude that the antibody binding site essentially differs from the substrate cavity binding the PSMA inhibitors.

III.6.2 Visualizing PSMA Clustering

STED nanoscopy of our conjugates and/or of immunolabeled PSMA further revealed structural subtleties of the membrane bound antigen fraction. Instead of being homogeneously distributed along the cell membrane, the PSMA signal was rather spread into patches. These patches consisted of oval- to round-shaped signals of different sizes and were observed both before internalization and after PSMA recycling. We assume these single signals to comprise a varying number of PSMA molecules grouped in antigen clusters at the cell surface.

Previous findings obtained in biochemical assays have suggested PSMA clustering at the cell membrane. In these experiments, PSMA clustering was artificially induced with antibodies to study its consequences. It has been concluded that PSMA clustering is crucial not only for PSMA activation and subsequent antigen internalization. Additionally, it is involved in many downstream signaling pathways that directly or indirectly affect cell proliferation [873-875].

Here, we visualized PSMA clustering at the cell membrane for the first time. It was either induced by our PSMA inhibitors or by antibodies as consequence of PSMA IF. During our colocalization experiments between immunolabeled PSMA and endosomal/lysosomal probes, endosomal PSMA colocalization did not significantly differ, independently of the presence or absence of PSMA inhibitors and 2-PMPA. This observation is indeed not surprising as IF of PSMA already induces antigen clustering and thus PSMA activation and internalization. Moreover, antibody binding is not affected by 2-PMPA as this compound specifically blocks the binding cavity of PSMA inhibitors, which differs from the antibody binding site.

However, we speculate that the holographic cytometry studies indirectly revealed effects of PSMA clustering. The proliferation of PSMA-positive cells was slightly but significantly accelerated in the presence of our PSMA inhibitors as compared to the proliferation of untreated PSMA-positive cells. While PSMA clustering and thus activation (together with its impact on cell proliferation) was induced in the presence of our conjugates, it was not in the case of untreated cells.

III.6.3 Following the Endosomal Pathway

During the early phase of PSMA/PSMA inhibitor complex internalization, endocytic vesicle formation was observed. Based on our colocalization studies, we assume that the PSMA-specific uptake of low molecular weight PSMA inhibitors depends on clathrin-mediated endocytosis. Moreover, we confirmed previous suggestions that PSMA itself travels the endosomal pathway to be either finally degraded in lysosomes or recycled back to the cell surface [758, 872].

The endocytic vesicles were readily resolved by STED imaging allowing for their size quantification. The average vesicle diameter of our samples is more than twice the value for the diameter of CCVs as described in literature [863, 864]. However, the large SD indicates a very heterogeneous population of endocytic vesicles in our samples. By targeting the extracellular domain of PSMA with both PSMA inhibitor and antibodies, our labeling strategy rather underestimates the vesicle diameter (refer to III.6.4, Figure III-22). Upon endocytosis of PSMA, invagination of the cell membrane locates the PSMA

ectodomain and thus the fluorophores in the vesicle interior. Still, the FWHMs of selected vesicle line profiles indicate an effective image resolution high enough to resolve vesicles with approximately 100 nm in diameter. Since CCVs rapidly uncoat, subsequently fuse and become early endosomes featuring diameters larger than CCVs, we conclude that the recorded vesicle population mainly consisted of early endosomes.

After PSMA inhibitor internalization, cellular retention without significant externalization is suggested by both long-term internalization confocal and STED experiments as well as by biodistribution and small-animal PET imaging studies. The *in vivo* time course of tumor accumulation not only confirms a long-term accumulation of the PSMA inhibitors in PCa tumor cells, but additionally revealed a high tumor-to-background ratio. The signal of the specifically internalized fraction remained, whereas the non-specific signal of unbound PSMA inhibitors declined with progressing time. Off-target internalization occured only for a very limited set of tissues, but for these cases, our holographic cytometry data indicate absence of cytotoxicity.

III.6.4 The Subcellular Fate of PSMA Inhibitors

To visualize the subcellular distribution of our PSMA inhibitors in relation to PSMA at the molecular level, we developed a novel non-standard live cell IF staining protocol (Figure III-22). We note that in general, IF staining is restricted to fixed cells as it depends on cell membrane permeabilization. The intact cell membrane of living cells is a permissive barrier for macromolecules such as antibodies and can only be passed via active uptake by the cell.

Here, we exploited the metabolic peculiarity of LNCaP cells to withstand low temperatures while pausing PSMA internalization. Hence, the membrane bound PSMA fraction could be comprehensively labeled by incubating LNCaP cells on ice without impairing cell health. The internalization of the complex consisting of PSMA, primary antibody, secondary antibodies and PSMA inhibitor was triggered by a subsequent temperature increase.

Generally, IF provides a strong fluorescent signal amplification as the primary antibody recruits more than one secondary antibody, which each in turn is decorated with more than one fluorophore. In contrast, our PSMA inhibitors contribute only one fluorophore per PSMA molecule. Surprisingly, the brightness and SNR of the PSMA inhibitor signal was only slightly reduced in comparison to the immunolabeled PSMA signal despite the essential difference in fluorophore stoichiometry. We conclude that in particular for conjugate **RED**, dye coupling to the PSMA inhibitor scaffold did not significantly alter the photophysical properties of the bright and photostable STED dye STAR RED.

A rough sketch of PSMA and PSMA inhibitor trafficking could be drawn by diffraction-limited confocal microscopy. However, to elucidate in detail the subcellular fate of PSMA and PSMA inhibitor after their binding at the cell surface, STED nanoscopy was necessary.

At early time points of internalization, PSMA and the PSMA inhibitors strongly colocalized. With progressing time, the degree of colocalization declined. At later time points of internalization, colocalization eventually vanished. The PSMA inhibitors displayed a gradual cytosolic distribution over time, whereas immunolabeled PSMA remained localized to the endocytic vesicle membrane to be

either recycled back to the cell surface or to be degraded in lysosomes. Internalization and vesicle formation of antibody-targeted PSMA has previously been reported on by Rajasekaran *et al.* after 2 h of incubation [872]. Our results confirm these findings but additionally visualize PSMA localization at later time points up to 24 h including antigen recycling.

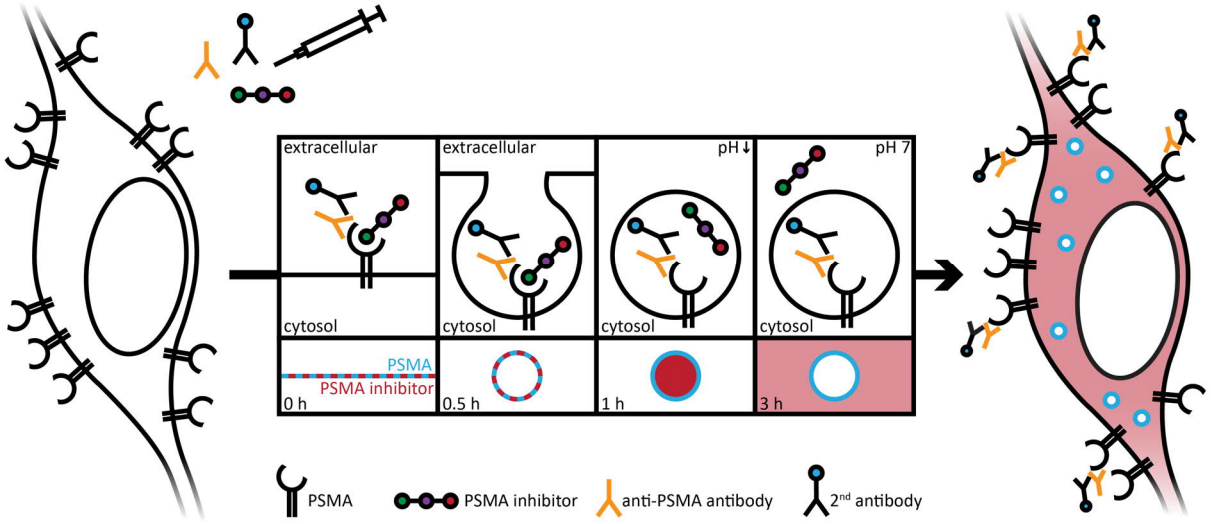

Figure III-22. Sketch illustrating the labeling strategy for PSMA/PSMA inhibitor colocalization studies.

To assess the colocalization between our PSMA inhibitors and PSMA, live LNCaP cells were immunolabeled for PSMA and co-incubated with either conjugate **RED** or conjugate **635P**. As both affinity labels are not cell membrane permeable, only the membrane fraction of PSMA was targeted. Passive passage through the cell membrane was impaired as antibodies are too large and as PSMA inhibitors are too charged at neutral pH. Premature internalization of PSMA was prevented by labeling on ice. Internalization of the antibody/PSMA/PSMA inhibitor complex was triggered by incubation at 37°C. Initially, PSMA inhibitor and primary (1^{st}, anti-PSMA) / secondary (2^{nd}) antibody were PSMA bound. Upon endocytosis, invagination of the cell membrane placed the extracellular domain of PSMA inside the endocytic vesicles. Thus, the PSMA inhibitor and the $1^{st}/2^{nd}$ antibody complex pointed inwards. The size of the low molecular weight PSMA inhibitor can be neglected (approx. 2 nm), but due to the non-negligible size of antibodies ($1^{st}/2^{nd}$ antibody complex approx. 30 nm) and the PSMA ectodomain (amino acids 44-750), the actual positions of the fluorophores and the vesicle membrane did not coincide. Thus, our labeling approach rather underestimated the vesicle diameter. The pH decline along the endosomal pathway stimulated segregation of the PSMA/PSMA inhibitor complex while the $1^{st}/2^{nd}$ antibodies remained attached to PSMA. After detaching, the PSMA inhibitor homogeneously distributed inside the vesicle in a first step. The acidic pH in endosomes protonated the acidic moieties of the PSMA inhibitor rendering it neutral and thus cell membrane permeable. In a second step, the PSMA inhibitor diffused through the vesicle membrane and dispersed homogeneously in the cytosol. Due to a neutral cytosolic pH, the acidic moieties of the PSMA inhibitor deprotonated again trapping the tracer inside the cytosol. In contrast, PSMA was either recycled back to the cell surface or degraded in lysosomes.

III.6.5 Mechanistic Model for the Cytosolic Distribution of PSMA Inhibitors

Strikingly, low molecular weight PSMA inhibitors apparently display an essentially different distribution pattern on the subcellular level as compared to PSMA antibodies used in immunotherapy of PCa. During the antigen recycling process, the PSMA/PSMA inhibitor complex dissociates in the endosomal compartment.

Remarkably, antibody complex and low molecular weight inhibitors display significant differences in the pH dependence of their PSMA binding affinity. While PSMA binding of the anti-PSMA antibody/secondary antibody complex remained unaffected at acidic pH, the interaction between PSMA inhibitor and PSMA drastically suffered. We conclude that our low molecular weight PSMA inhibitors detach from PSMA upon pH decrease in the endosomes after clathrin-based endocytosis to initially distribute in endosomes but gradually disperse homogeneously in the cytosol without binding to other structures. We further speculate our conjugates to be intrinsically inert to lysosomal digestion as they are unnatural inhibitors of PSMA.

Reduction of the PSMA binding affinity of the PSMA inhibitors at acidic pH certainly shifts the equilibrium between bound and unbound PSMA inhibitor towards the unbound state. For a closed system and thus within an established steady-state equilibrium, the dynamic fraction of PSMA bound PSMA inhibitor would simply shrink but in its diminished size continuing to exist. However, the endosome appears to be a closed system only at first glance.

Due to their acidic moieties (Figure III-6a), our PSMA inhibitors are charged at neutral pH, rendering the molecules membrane impermeable. Initially, the PSMA inhibitors thus cannot cross the cell membrane from the cell medium into the cytosol specifically limiting their uptake to internalization via PSMA. However, the acidic moieties of the PSMA inhibitors are mostly protonated at endosomal acidic pH, rendering the molecules membrane permeable. Hence, the PSMA inhibitors can passively diffuse through the endosome membrane and cytosolically disperse, a process simply driven by entropy. By this, unbound PSMA inhibitors are continuously withdrawn from the PSMA bound/unbound equilibrium inside the endosomes. Thereby, the position of the equilibrium is pushed further and further towards the unbound state until finally the entire PSMA inhibitor population is located inside the cytosol. The neutral pH inside the cytosol deprotonates the acidic moieties of the PSMA inhibitors again rendering the molecules once more membrane impermeable and finally trapping the PSMA inhibitors in the cytosol of the cell.

We exclude any dye-dependent effects as interchanging the fluorescent labels for immunolabeled PSMA and PSMA inhibitor did not alter our results. Moreover, neither absorption nor fluorescence emission properties of the PSMA inhibitors displayed sensitivity to acidic pH and/or elevated temperatures.

The striking difference between the subcellular fate of PSMA antibodies and PSMA inhibitors will presumably translate into an enhanced therapeutic efficiency of low molecular weight PSMA inhibitors. For preventing off-target tissue effects and achieving high imaging contrasts, a long retention in PCa cells is crucial in imaging and therapy approaches based on PSMA inhibitors. Of particular interest for endoradiotherapy is the homogenous dispersion of low molecular weight PSMA inhibitors in PCa cells after internalization, which we have demonstrated here for the first time. Especially with α-particles, effectively high local radiation doses throughout the targeted cell are afforded. By providing valuable insights for the design of improved PCa targeting strategies, we expect our findings to stimulate further ligand development, not only in the field of PCa.

III.7 CONCLUSION

PSMA-based diagnosis and treatment of PCa is the textbook example for the potential of targeted imaging and therapy approaches to bridge the shortcomings of established cancer treatment. The development of pharmaceuticals specifically targeting PSMA has evolved as one of the most vigorous and vibrant radiopharmaceutical research fields during the last decade. Numerous applications have already successfully demonstrated the efficient targetability of PSMA. Not only focused clinical development programs but also industrial companies foster and encourage the academic research.

To date, the urea-based binding motif and the phosphonate-based binding motif characterize the two main classes of PSMA inhibitors that offer the most promising properties. For PSMA-targeted imaging, several different tracers are currently available. With respect to imaging characteristics, availability, access and cost, the most suitable tracer must be still identified. However, a prosaic clinical and chemical view might even conclude that the tracer improvement for PSMA-targeted imaging is almost exhausted balancing the limits of chemical feasibility and the clinical necessity [870].

On the contrary, the efficiency of endoradiotherapy strategies will greatly benefit from further tracer optimization. The major restriction among all PSMA inhibitors for their application in endoradiotherapy are high binding affinities to kidneys and to salivary glands. These challenges are currently addressed by different approaches stimulating the development of a `second generation´ of PSMA inhibitors with optimized pharmacokinetic profiles and lower off-target uptake [876].

Optimized endoradiotherapy strategies most likely pave the way for α-particle therapy. Future research must evaluate the potential of this treatment approach, develop selective and efficient therapy strategies for improved patient care and explore the value of combination therapies with antiandrogenic drugs. Additionally, longer follow-up periods are crucial to analyze the long-term results and toxicities. To facilitate therapy response assessment, expanded insights into the effects of various treatments on PSMA expression are needed. By that, current imaging and therapy protocols will evolve and improve.

Inspired by the gap between the current state and the target state of radiopharmaceutical PCa research, we designed a study to track and clarify the intracellular fate of PSMA/PSMA inhibitor complexes. In particular, elucidating the subcellular PSMA inhibitor distribution is crucial for obtaining a detailed understanding of the mechanism of action during endoradiotherapy.

Our study is the first to give insight into intracellular distribution patterns of PSMA and of low molecular weight PSMA inhibitors at clinically relevant time points resolved up to the molecular level by STED nanoscopy. The principles uncovered and the novel imaging method described in this work offer extensive utility and contribute valuable knowledge to the field of PCa research. Our findings hopefully boost the future design and development of novel radiopharmaceutical agents for refined and/or new diagnostic and therapeutic approaches, acting as theranostics for molecular targeted PCa therapy and aiming at selective and efficient therapy strategies for improved patient care.

IV – METHODOLOGY:

ASPECTS OF LIVE CELL STED NANOSCOPY

IV.1 INTRODUCTION

The potential of STED nanoscopy in live cell imaging is far from being fully exploited. While satisfying demands regarding temporal resolution and optical sectioning, live cell STED imaging like any other live cell fluorescence nanoscopy technique is challenged by phototoxicity mainly mediated through photobleaching (refer to I.1.4). Thus, suitable fluorophores reliably withstanding high light intensities/light doses are desperately required and it is the (bio)chemistry that must catch up with the current state in optics.

Certain measures can be taken to reduce the risk of photodamage. Upfront, any stress prior to imaging should be kept as low as possible. Experimental settings and conditions not only affect phototoxicity but already by themselves potentially cause stress (e.g. overexpression) [272]. Therefore, cell health of `dark´ controls should be additionally assessed and maximized. As light sensitivity is strongly sample dependent and varies with the organism, developmental stage [877, 878], cell type [305], cell age and cell cycle phase [289], the sample choice should be reasonably considered.

During imaging, experimental conditions (e.g. exposure to drugs) might increase the specimen's sensitivity to light. Therefore, optimal cell culture conditions should be provided to keep additional stress at a minimum. Further biochemical measures include both scavenging and prevention of ROS and $\dot{R}^{+/-}$ in the sample by removal of photosensitizing compounds (e.g. riboflavin, pyridoxal) from the imaging medium [879] and addition of empirically determined antifading agents [880], antioxidants (e.g. ascorbic acid [881], n-propyl-gallate [879, 882]), radical state quenchers, and reducing and oxidizing systems (ROXS). ROXS buffers efficiently depopulate the reactive intermediate state (often T_1) and restore S_0 via complementary electron transfer reactions [419, 880, 881, 883]. T_1 quenching is additionally favorable for the SNR since the population of any dark state disengages fluorophores from the image formation process. Ironically, oxygen is the main triplet quencher in biological samples [884, 885] but at the same a key player in phototoxicity.

The build-up of ROS can potentially be prevented by either enzymatic [886, 887] or technical [888] oxygen removal. Yet, oxygen must be replaced by an efficient triplet quencher (e.g. Trolox [889-891] or cyclooctatetraene [882]) to prevent T_1 accumulation and photon yield impairment. However, most living specimens require oxygen for respiration and thus complete removal is usually not an option. Furthermore, cytotoxicity sets limits on the additives' concentrations. Indeed, to ensure efficient scavenging, depletion and protection, any additive must be supplied in high concentration guaranteeing frequent collisions with its target. This conflict can be avoided by strongly decreasing the concentration via direct coupling of the additive to the fluorophore, as successfully demonstrated in the concept of self-healing dyes [892].

The induced phototoxicity and the counteracting effects of additives heavily depend on the fluorophore type, its cellular localization, local concentration, and on its biomolecular target. Fluorophores with low photobleaching probabilities, low STED absorption cross sections of S_0, S_1 and T_1, and low dark state population probabilities are desirable [893-895]. Certainly, illumination conditions are decisive and exposure concepts that mitigate photobleaching in conventional diffraction-limited microscopy are not necessarily ideal for STED nanoscopy. The following optical measures go hand in hand with the biochemical approach and must be tailored to the particular dye and its environment.

Photodamage is wavelength-dependent and more pronounced at shorter wavelengths due to higher photon energy and increased absorbance by endogenous chromophores [298, 305, 896]. Thus, excitation and depletion in the far-red spectral range are less harmful. Specifically adapting the STED wavelength outside of the $S_1 \rightarrow S_n$ and $T_1 \rightarrow T_n$ bands is additionally favorable but quickly renders multicolor STED imaging highly complex. Clearly, less light exposure is always advantageous and conservative laser intensities should be used for tuning the spatial resolution only to the level necessary to answer the biological question of interest. If applicable, limiting the light exposure only to the focal plane of interest further reduces phototoxicity (refer to I.1.4). To better compare phototoxicity between different experimental implementations, it is advisable to measure the irradiance at the sample level.

As the cellular ROS buffering system can cope better with the same amount of ROS spread over a longer period, exposure times should be extended at the expense of peak intensities. Indeed, this measure reduces the temporal resolution and renders motion blur more likely. In summary, the total light dose is not as important as the duration for which the total light dose is applied [292, 298, 877]. Here, pulsed or intermittent instead of continuous illumination is beneficial [301, 366, 897, 898]. Especially low-repetition-rate pulses allow the fluorophores in metastable dark states to relax back to the ground state between pulses. Thus, dark state build-up and the rate of photobleaching via this route are reduced [141, 238, 366, 898]. Yet, more time-efficient triplet state relaxation is possible via ultrafast scanning as one fluorophore's relaxation time is the other fluorophore's excitation time. The irradiation is distributed more evenly and the total exposure time is controlled by line or frame accumulation [141, 249, 301].

Longer pulse durations lower the peak intensity and hence the probability of transitions to S_n and T_n without drastically decreasing the depletion efficiency [239]. In combination with time-gating, a similar resolution as with shorter pulses can be maintained, yet at the expense of a lowered SNR [899]. Making

compromises is necessary and different measures must be taken to counteract lower-order and higher-order photobleaching. For low average powers (i.e. lower-order photobleaching) shorter pulses guarantee the best temporal and spatial resolution. Dark state population is the main source of photobleaching and best hindered via low-repetition-rate pulses or ultrafast scanning and additives. For high average powers (i.e. higher-order photobleaching) longer pulses reduce multi-step and/or multiphoton processes to S_n and T_n [302].

Besides rationally following these guidelines, the challenge of photobleaching and associated phototoxicity must additionally be met with the design of refined and/or novel bright and photostable live cell imaging probes (refer to IV.2). The sample health should receive the highest priority during both sample preparation and image acquisition. Thus, to guarantee the recording of an unaltered biological reality, first, potential cytotoxicity of these live dyes must be excluded (refer to IV.3) and second, conservative live cell imaging parameters must be chosen. Due to the latter, live cell imaging data often suffer a reduced SNR in comparison to fixed cell imaging data. To maximize the extraction of biological information, the quality of such `degraded´ live cell images can be improved by image restoration (refer to IV.4).

IV.2 Novel Probes for Live Cell STED Imaging

IV.2.1 Motivation

For all fluorescence nanoscopy methods, the focal switch represents the key that unlocks the diffraction limit and renders the nanometer resolution regime accessible. Thus, further improvement of the performance of current nanoscopy methods strongly depends on the development of new and/or refined fluorophores with optimized (bio)chemical and photophysical properties [376-380]. In particular, live cell STED nanoscopy can only exploit its full potential with fluorophores that combine biocompatibility and membrane permeability with high photostability, low photobleaching probabilities, a maximal number of switching cycles, low dark state transition possibilities, a high cross section for stimulated emission, and a low cross section for excitation to S_n and T_n [381].

To date, no single fluorophore fulfills all requirements at once, and thus reasonable choices must be made for each concrete application. Current research pushes especially for new organic dyes with the optimal combination of (bio)chemical and photophysical properties to guarantee selective, sensitive, and stable live cell STED imaging [29-34, 353, 354, 405].

In particular, the criterion of cell permeability limits the variety of organic dyes applicable for intracellular labeling of living cells. Since their first synthesis by Fu *et al*. [900], silicon xanthenes and the subsequently developed silicon rhodamines (SiR) [30] have drawn a lot of attention as promising fluorescence labels penetrating the outer plasma membranes of intact cells and thus offering a broad field of application. SiR dyes come close to the optimal live cell STED probe as they are bright, photostable, fluorogenic, membrane permeable, essentially non-toxic, biocompatible, biologically stable, and absorb and emit in the far-red spectral range. These properties render SiR dyes not only attractive for live cell fluorescence nanoscopy [29-33, 36, 38, 901, 902], but likewise allow their

application as direct probes for various biomolecules [403, 903-905], or as sensors for metal ions [906-910], pH [908], voltage [911] or metabolites [912-915].

With the aim to control the dyes' photophysical properties by rational design, correlations between structural features and photophysical properties were investigated in several attempts partially supported by DFT calculations [34, 914, 916, 917]. These studies resulted in new SiR derivatives with optimized and fine-tuned photophysical properties. The introduction of methyl, methoxy or dimethylamine groups into the benzene moiety of SiR dyes tunes the highest occupied molecular orbital (HOMO) energy level and thereby affects the quantum yield while leaving absorption and emission bands unchanged. The extent of the effect depends on the oxidation potential and the HOMO energy level of the benzene moiety. Hence, the negative value of the HOMO energy level and/or the oxidation potential are directly connected to the quantum yield [907]. Certainly, the quantum yield is also influenced by other factors. Non-radiative quenching (e.g. via bond rotation) competes with fluorescence emission and lowers the quantum yield by effectively contributing to the depopulation of S_1 [918]. Despite the theoretical and experimental efforts of the past years, the rational trends for radiative and non-radiative decays remain difficult to predict [919].

In analogy to BODIPY fluorophores [920], we initially hypothesized that a constrained rotation around the xanthene-aryl bond should lead to an improved quantum yield of SiR dyes. Table IV-1 together with Figure IV-1 compile SiR dyes with high quantum yields and their structural analogues with lower quantum yields.

Azetidine substituents at the xanthene moiety of dyes **5**, **7** and **9** not only improve the quantum yield of these dyes but also red-shift the spectral properties as compared to the *N,N*-dimethylaniline analogue dyes **1**, **3** and **4** (Table IV-1, entry 1 *vs.* 5, 3 *vs.* 7, and 4 *vs.* 9). On the contrary, the fluoroazetidine moiety in dye **10** (JF635) does not affect the high quantum yield but induces a hypsochromic shift as compared to the azetidine analogue dye **9** (JF646) (Table IV-1, entry 9 *vs.* 10). However, restricted rotation around the xanthene–benzene bond leads to a drastic improvement of the quantum yield from 0.10 to 0.31 when comparing the phenyl substituted rhodamine dye **2** with its 2'-methyl substituted analogue dye **3** (Table 1, entry 2 *vs.* 3). Accordingly, 2'-substituents with A-values between a proton and a methyl group (such as F and Cl) result in quantum yields from 0.19 (for F) [915] to 0.30 (for Cl) [915] for rhodamines like dyes **3**, **4**, **11** or **12** (Table IV-1, entries 3, 4, 11 and 12). Remarkably, dye **1**, dye **5** and dye **6** do not possess any benzene moiety but display moderate to high quantum yields (Table IV-1, entries 1, 5 and 6).

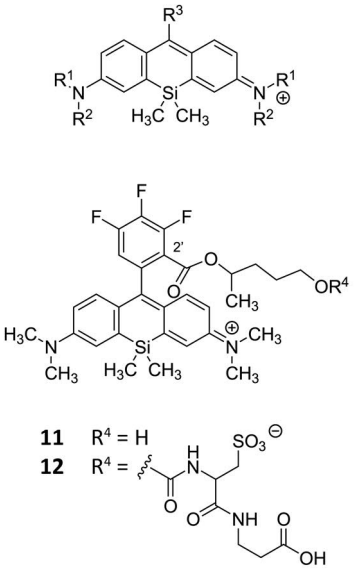

Figure IV-1. Chemical structures of SiR derivatives belonging to Table IV-1.

Table IV-1 specifies the individual groups R^1, R^2 and R^3 and gives the respective photophysical properties of the corresponding SiR derivative.

To the best of our knowledge, dyes **11** and **12** feature the highest quantum yields known amongst SiR dyes with values of 0.66 and 0.70 (Table IV-1, entries 11 and 12). This might be explained by the

bulkiness of the ester group in the 2'-position (isopropyl ester derivative), and/or by the effects of the fluorine atoms and the ester group on the HOMO energy level of the benzene moiety.

Table IV-1. Comparison of the photophysical properties of different SiR derivatives.

Figure IV-1 provides the corresponding chemical structures for this table. λ_{abs} – absorption wavelength, λ_{em} – fluorescence emission wavelength, ϕ – quantum yield. * In PBS at pH 7.4; † cresyl violet in methanol used as reference dye; ‡ in PBS; ¥ in HEPES at pH 7.3; ¤ in water; § quantum yield determined by absolute measurement; £ corresponding isopropyl ester showed a quantum yield of 0.60; ‖ quantum yield determined in water with reference dye Atto AZ 237.

entry	NR^1R^2	R^3	dye	λ_{abs} [nm]	λ_{em} [nm]	ϕ	reference
1	$N(CH_3)_2$	H	**1** (SiP)	634	648	0.42*,†	[907]
2	$N(CH_3)_2$	Ph	**2**	646	667	0.10‡,†	[921]
3	$N(CH_3)_2$	2-CH_3-Ph	**3**	646	660	0.31*,†	[907]
4	$N(CH_3)_2$	2-COOH-Ph	**4**	643	662	0.41¥,§	[34]
5	azetidine	H	**5**	636	649	0.62¥,§	[922]
6	azetidine	COOH	**6**	641	657	0.26¥,§	[922]
7	azetidine	2-CH_3-Ph	**7**	649	663	0.47¥,§	[922]
8	azetidine	2-CH_3-6-CH_3-Ph	**8**	651	664	0.51¥,§	[922]
9	azetidine	2-COOH-Ph	**9** (JF646)	646	664	0.54¥,§	[34]
10	3-F-azetidine	2-COOH-Ph	**10** (JF635)	635	652	0.56¥,§	[916]
11			**11**	662	680	0.66¤,£,‖	[923]
12			**12**	663	680	0.70¤,‖	[923]
13	$N(CH_3)_2$	pyridin-4-yl	**13**	655	680	0.12‡,§	[924]
14	azetidine	3-CH_3-pyridin-4-yl	**14**	656	670	0.48¥,§	[922]

Consequently, this work was based on a presumed positive correlation between quantum yield and bulkiness of the phenylic 2'-substituent of SiR dyes and speculated that the 2'-substituent constrains the rotation around the xanthene–benzene bond more strongly the larger it is. In detail, we strived for the development of the pyridinyl-substituted SiR dye **15**, which allows for the easy radiofluorination of the 2-halopyridine moiety and thus the generation of the PET-active dye **16** (Figure IV-2).

Such PET-active NIR dyes allow for bimodal medical imaging (PET/optical imaging (OI)) and promise huge advances in diagnostic and treatment regimens in the field of cancer as they combine precise pre-operative imaging of lesions with medical interventions such as intra-operative guidance or sentinel lymph node detection. The precise detection and resection of all malignant tissue directly affect the treatment outcome and patient survival, and both can be strongly improved by using surgical

guiding by dual-modality probes (refer to III.2.6). Moreover, the fluorescence modality can be additionally exploited for histopathological analyses of biopsy material.

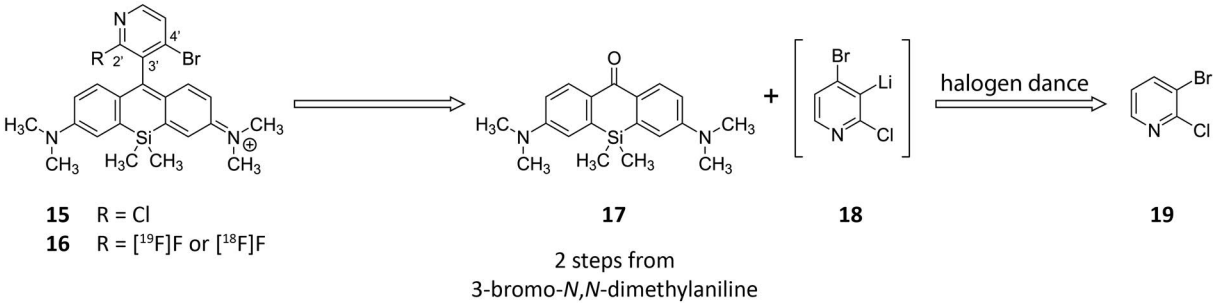

Figure IV-2. Retrosynthetic analysis of the dual-modality SiR dye 16.

This scheme depicts the retrosynthesis of the proposed small molecule dual-modality probe [^{18}F]SiR dye **16** for hybrid medical imaging (PET/OI) of cancer cells with up-regulated mitochondrial activity. For examples on radiolabeling of 2-halopyridines (here **15** to **16**) refer to [925-927].

Only two pyridinyl-substituted SiR dyes have been published to date. Dye **13** (Table IV-1, entry 13) combines good water solubility with an intrinsic targeting ability to lysosomes, but only features a quantum yield of 0.12 [924]. In contrast, dye **14** (Table IV-1, entry 14) displays an enhanced quantum yield of 0.48 [922], presumably due to both the azetidine substituents at the xanthene moiety and the restricted bond rotation owing to the 3'-methyl group (pyridine numbering).

The 2-chloropyridinyl moiety of dye **15** not only introduces a convenient fluorination option, but presumably the additional intrinsic targeting ability to acidic cellular compartments analogously to the lysosomal-selective dye **13**. Due to its increased lipophilic nature as compared to dye **13** (Table IV-2), we assumed that our proposed dual-modality fluorophore possesses better selectivity for mitochondria. Driven by the mitochondrial plasma membrane potential, lipophilic cations such as the phosphonium cation or rhodamines selectively accumulate within mitochondria [928, 929]. Diffusion through the cell and mitochondrial membranes is facilitated by the lipophilicity of these cations. By conjugating ten different amines with varying lipophilicity to the SiR core, Sung *et al.* recently determined clog*P* values between 5.50 and 6.33 to be optimal for mitochondrial targeting and developed a SiR dye (SiR-Mito 8) selectively staining mitochondria [930].

Mitochondria are bounded by an outer and an inner membrane separated by the intermembrane space. The inner membrane is highly convoluted and forms invaginations (cristae) that extend into the mitochondrial matrix (Figure IV-3). Mitochondria are dynamic organelles that continuously undergo fission and fusion events [931, 932]. Their morphology depends on cell function and disease states and thus can be exploited as a biological marker.

Table IV-2. Comparison of the lipophilicity of dye 13, SiR dye 15 and SiR dye 16.

* calculated log*P* values.

	dye 13	SiR dye 15	SiR dye 16
clog*P**	2.136	3.712	3.142

Medical imaging of mitochondrial activity is highly informative for various indications, including neurodegenerative and metabolic diseases, ischemic injuries, necrosis, therapy response and cancer [928, 929, 933-935]. With regard to bimodal medical imaging in the field of cancer, our proposed dual-

modality probe will potentially achieve a reasonable tumor-to-background ratio, as many cancer cells have a higher mitochondrial membrane potential than non-transformed cells [933, 936, 937].

Figure IV-3. Schematic illustration of a mitochondrion.

Mitochondria are enclosed by an outer and an inner membrane dividing these organelles into a narrow intermembrane space and a larger internal matrix. The inner membrane is highly convoluted forming numerous infoldings called cristae. Mitochondria are responsible for the ATP synthesis of a cell and organize into an extensive intertwined network in the cytoplasm.

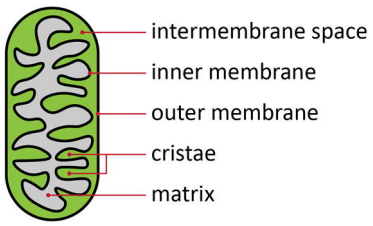

Designing SiR dye **15** and its radiofluorinated analogue SiR dye **16**, we chose a molecule with an additional bulky 4'-substituent such as bromine, since the smaller 2'-fluorine substituent in SiR dye **16** should lead to a decrease in quantum yield as compared to SiR dye **15** featuring the larger 2'-chlorine. The HOMO energy level of SiR dye **15** and SiR dye **16** should not be negatively altered by the presence of a 4'-bromine atom. Moreover, the additional substituent can be further used for functionalization.

To date, no SiR dyes have been reported that feature two phenylic halogen substituents (any combination of F, Cl, Br) at the positions adjacent to the xanthene-benzene bond. The same holds for rhodamines bearing a dihalogenated pyridinyl motif, although halogenated pyridines are highly interesting for further functionalization or vector conjugation by nucleophilic aromatic substitution.

For the introduction of the dihalogenated pyridine motif into the SiR scaffold, we decided on a halogen dance (HD) reaction of 3-bromo-2-chloropyridine (compound **19**) to compound **18** followed by a condensation with silicon xanthone **17**, which is accessible in a two-step reaction from 3-bromo-*N,N*-dimethylaniline. Initially published and investigated by Mallet *et al.*, the rearrangement of halo pyridine **19**, initiated by a halogen-metal exchange with *n*-BuLi, is also termed `homotransmetallation´ [938]. For the synthesis of highly substituted carbo- and heterocyclic systems (e.g. tetrasubstituted pyridines [939]) with substitution patterns difficult to obtain otherwise [940-942], the HD rearrangement reaction commonly offers an excellent approach.

IV.2.2 Aim

The performance of live cell STED nanoscopy strongly depends on the biochemical and photophysical properties of the applied fluorophores. Those that provide many photons while reliably sustaining high light intensities/light doses are most promising for further progress in the field of live cell STED imaging. In this regard, silicon xanthenes and in particular the subsequently developed silicon rhodamines are highly attractive starting points for further dye development. In recent years, several live cell STED compatible SiR derivatives specifically labeling different cellular structures and organelles have been reported [31, 353, 354, 423]. However, to the best of our knowledge, none of these new STED compatible SiR probes target mitochondria.

Thus, the aim of this project was the design of a live cell STED compatible SiR derivative specifically staining mitochondria. As medical imaging of these organelles is highly informative for various indications, we further strived for additional applicability in multimodal (PET/OI) medical imaging.

Therefore, a dihalogenated fluorinatable pyridinyl SiR dye was synthesized by the application of a halogen dance rearrangement. The product was analytically and photophysically characterized. To confirm its specific mitochondrial targeting ability, colocalization experiments with MitoTracker® Green FM and LysoTrackerTM Green DND-26 were performed in two human cell lines. STED compatibility was assessed in live cell imaging experiments. To exclude cytotoxicity, the potential influence on the proliferation behavior of human cell lines was evaluated in long-term holographic cytometry experiments.

The work presented in the following sections has recently been published as Matthias, J., Kanagasundaram, T., Kopka, K., Kramer, C. S., *Synthesis of a di-halogenated pyridinyl silicon rhodamine for mitochondrial imaging by a halogen dance rearrangement*. Beilstein Journal of Organic Chemistry, 2019. **15**: p. 2333-2343. [943].

IV.2.3 Methods

This project was conceived and conducted in close collaboration with Dr. Carsten S. Kramer[15]. The synthesis and the analytical characterization were performed by Dr. Carsten S. Kramer. Detailed information on materials is given in I.2.1.

IV.2.3.1 Synthesis

Unless otherwise stated, reactions requiring exclusion of oxygen and moisture were conducted in heat-gun flasks dried under argon gas atmosphere using the Schlenk technique.

In a flame-dried flask and under argon, 3-bromo-2-chloropyridine (**19** in Figure IV-2) (249 mg, 1.29 mmol, 20 eq.) was dissolved in 3.0 ml anhydrous tetrahydrofuran (THF). After cooling the solution to -78°C, *tert*-butyllithium (*t*-BuLi) (1.7 M in pentane, 2.59 mmol, 1.52 ml, 40 eq.) was added dropwise.

CAUTION: solutions of *t*-BuLi react explosively with water and may ignite in moist air.

The mixture (brown-red) was stirred at -78°C and after 30 min, silicon xanthone (**17** in Figure IV-2) [30] dissolved in anhydrous THF (2.0 ml) was added drop-wise at the same temperature (mixture turned deep red). After 2 min, the mixture was brought to RT (mixture turned dark) and the reaction was stirred for 4 h. Subsequently, water and dichloromethane (DCM) were added. After adding some drops of 1 N HCl (organic phase turned deep blue), the organic phase was separated, and the water phase was extracted with DCM several times. Brine and sodium sulfate were used for drying of the organic phase. Following filtration, the solvents were evaporated *in vacuo*. Flash column chromatography (silica gel, 0.032 mm–0.062 mm, 1% to 10% methanol in DCM) was used for purification of the product (**15** in Figure IV-2) (deep blue solid) using manual techniques.

[15] German Cancer Research Center, Division of Radiopharmaceutical Chemistry, Heidelberg, Germany

IV.2.3.2 Analytics

Nuclear magnetic resonance (NMR) spectra were acquired on an Avance III 400 MHz NMR spectrometer (Bruker Daltonics) at RT. The chemical shifts are given relative to methanol-d_4 in units of δ (δ_H = 3.31; δ_C = 49.0) [944]. For the first-order analysis, the following abbreviations were used: s – singlet, d – doublet, t – triplet, dd – doublet of doublet, etc., m – multiplet. The coupling constants *J* refer to H,H-couplings and are reported in Hz. Distortionless enhancement by polarization transfer (DEPT) and heteronuclear single quantum correlation (HSQC) experiments were used for assignment (CH, CH_2, CH_3, C_{quart}).

Mass spectra were acquired in the Department of Organic Chemistry, University of Heidelberg, (Heidelberg, Germany) using the electrospray ionization (ESI) method with an Apex-Qe hybrid 9.4 T FT-ICR mass spectrometer (Bruker Daltonics). High-resolution mass spectrometry (HRMS) was performed with a JMS-700 MStation mass spectrometer (JEOL). The molecule fragments are given in mass-to-charge (m/z) ratio.

Analytical thin-layer chromatography (TLC) was conducted on polygram-DC-plates (40 × 80 mm, SIL G/UV254, 0.2 mm layer thickness, Machery-Nagel). UV light (254 nm or 366 nm) was used for detection. Reversed-phase TLC was performed on alugram-DC-plates (40 × 80 mm, RP-18 W/UV254, 0.15 mm layer thickness, Machery-Nagel).

For computing clog*P*, ChemDraw Professional 16.0.1.4 (PerkinElmer) was used.

IV.2.3.3 Spectral Properties

The SiR dye **15** stock solution (4.67 mM in acetonitrile (MeCN)) was diluted in either PBS pH 7.4 or MeCN to 15.5 µM for UV–vis/NIR absorbance recording or to 4.7 µM for fluorescence emission recording. Dilutions were measured in standard 1 cm quartz cuvettes. The absorbance of SiR dye **15** was recorded in the 200-800 nm interval with a Varian Cary 500 UV-VIS NIR Spectrophotometer (Agilent) equipped with the software Cary 500 (EPROM Version 8.01). With excitation at 600 nm, the fluorescence emission of SiR dye **15** was measured in the 610-800 nm interval with a Varian Cary Eclipse Fluorescence-Spectrophotometer (Agilent) equipped with the software Cary Eclipse (Version 1.1). The extinction coefficient ε_{max} was calculated for the absorbance maximum according to Lambert–Beer.

IV.2.3.4 Fluorescence Quantum Yield

Determination of the fluorescence quantum yield was performed via relative measurements following the literature procedure [945, 946]. Nile blue (ϕ_{ref} = 0.27) was used as reference standard dye [947]. Considering an absorbance between 0.01 and 0.1 at the excitation wavelength of 600 nm, the stock solutions of SiR dye **15** (4.67 mM in MeCN) and Nile Blue (1 mM in DMSO) were diluted as follows:

- SiR dye **15**: 4-5 dilutions, 0.8 µM – 4.7 µM in PBS pH 7.4 or MeCN

- Nile blue: 4-5 dilutions, 0.2 µM – 1.0 µM in 5% (v/v) 0.1 M HCl in EtOH

The absorbance of each dilution was measured in the 200-800 nm interval with a Varian Cary 500 UV-VIS NIR Spectrophotometer (Agilent) equipped with the software Cary 500 (EPROM Version 8.01). Subsequently, with excitation at 600 nm, the emission of the respective dilution was measured in the 610-800 nm interval with a Varian Cary Eclipse Fluorescence-Spectrophotometer (Agilent) equipped with the software Cary Eclipse (Version 1.1). The measurement parameters were kept constant throughout all measurements.

To determine the fluorescence quantum yield, the wavelength-integrated fluorescence intensity ($\int F$) was plotted versus the absorbance at 600 nm (A_{600}). The data were fitted by linear regression. The slopes as determined by the linear fit were used to calculate the fluorescence quantum yield of SiR dye **15** according to

$$\phi = \phi_{ref}\left(\frac{m}{m_{ref}}\right)\left(\frac{n}{n_{ref}}\right)^2 \qquad \textbf{(IV-1)}$$

with ϕ (ϕ_{ref}) being the fluorescence quantum yield, m (m_{ref}) the slope of the linear regression and n (n_{ref}) the refractive index of the solvent of SiR dye **15** (Nile Blue).

IV.2.3.5 Fluorescence Lifetime

Fluorescence lifetime was determined by time-correlated single photon counting (TCSPC) using a FluoTime 300 Fluorescence Lifetime Spectrometer (PicoQuant). The stock solution of SiR dye **15** (4.67 mM in MeCN) was diluted to 4.7 µM in either PBS pH 7.4 or MeCN. The fluorescence intensity decay $F(t)$ was recorded with excitation at 640 nm and subsequently fitted using an additive superposition of exponential functions

$$F(t) = \int_{-\infty}^{t} IRF(t') \sum_{i=1}^{n} A_i e^{-\frac{t-t'}{\tau_i}} dt' \qquad \textbf{(IV-2)}$$

with τ_i being the (possibly) n different fluorescence lifetimes of SiR dye **15**, A_i the corresponding amplitudes of the individual exponential decays and IRF the instrument response function.

IV.2.3.6 Cell Culture

The cell lines HeLa and U2OS (Table I-16) were cultured in DMEM++ at 37°C in humidified air with 5% CO_2. HeLa cells were harvested with trypsin 0.25% (no phenol red, Gibco/Thermo Fisher Scientific); U2OS cells were harvested with trypsin 0.05% EDTA 0.02% (with phenol red, Sigma-Aldrich/Merck). A Countess II FL Automated Cell Counter (Thermo Fisher Scientific) was used to count cells and to assess the live-to-dead cell ratio via Trypan Blue stain (0.4%). For live sample preparation, approximately 10^4 cells/well were seeded on 8-well chambered coverglasses one day prior to the experiment and kept at 37°C in humidified air with 5% CO_2 until live cell staining.

IV.2.3.7 Confocal and STED Microscopy

The custom-built STED system is described in detail in I.2.2.1. The power range for all lasers used during live cell confocal and STED imaging is given in Table IV-3. Unless otherwise stated, live cell confocal and STED imaging was performed with the measurement parameters given in Table IV-4. No frame accumulation was used.

Table IV-3. Range of laser powers used for live cell confocal and STED imaging of SiR dye 15, MitoTracker® Green FM and LysoTracker™ Green DND-26.

The values given describe the estimated laser power in the sample focus based on laser power measurements in front of the microscope body.

	excitation		STED
	470 nm [µW]	**650 nm [µW]**	**775 nm [mW]**
confocal, live samples	140 (MitoTracker) 20 (LysoTracker)	2.7	---
STED, live samples	---	5.4	15

Table IV-4. Standard measurement parameters used for live cell confocal and STED imaging of SiR dye 15, MitoTracker® Green FM and LysoTracker™ Green DND-26.

	pixel size [nm]	**dwell time [µs]**	**line accumulation**
confocal, live samples	50	10 (MitoTracker) 20 (LysoTracker)	1
STED, live samples	20	10	1

IV.2.3.8 Colocalization Experiments

For assessing mitochondrial colocalization, HeLa and U2Os cells were stained for 30 min with 1 µM SiR dye **15** and 100 nM MitoTracker® Green FM (Thermo Fisher Scientific) in FluoroBrite++ at 37°C in humidified air with 5% CO_2. After washing three times with prewarmed FluoroBrite++, the samples were subjected to live cell dual-color confocal imaging.

For assessing endosomal/lysosomal colocalization, HeLa and U2OS cells were stained for 30 min with 1 µM SiR dye **15** in FluoroBrite++ at 37°C in humidified air with 5% CO_2. After washing three times with prewarmed FluoroBrite++, the samples were imaged live by confocal microscopy in FluoroBrite++ supplemented with 500 nM LysoTracker™ Green DND-26 (Thermo Fisher Scientific).

For quantifying mitochondrial and endosomal/lysosomal colocalization, the color shift between the 470 nm excitation channel (MitoTracker® Green FM and LysoTracker™ Green DND-26) and the 650 nm excitation channel (SiR dye **15**) was performed as described in I.2.2.2. The PCC of the corrected images was calculated with the ImageJ plugin JACoP [470, 695].

IV.2.3.9 Live Cell STED Imaging

HeLa cells were stained for 1 h with 1 µM SiR dye **15** in FluoroBrite++ at 37°C in humidified air with 5% CO_2. After washing three times with prewarmed FluoroBrite++, the cells were subjected to live cell STED imaging.

IV.2.3.10 Cytotoxicity Studies

To assess potential cytotoxicity of SiR dye **15**, the duration and frequency of cell division was followed by holographic time-lapse imaging using a HoloMonitor® M4 cytometer (Phase Holographic Imaging). One day prior to the experiment, U2OS cells were seeded in DMEM++ in lumox® 24-well plates (Sarstedt) and kept at 37°C in humidified air with 5% CO_2. On the day of the experiment, the old medium of one half of the wells was replaced with fresh DMEM++ containing 1 µM SiR dye **15** and the old medium of the other half of the wells was replaced with fresh DMEM++ without dye. After 1 h of incubation at 37°C in humidified air with 5% CO_2, all wells were washed three times with DMEM++ before holographic time-lapse imaging was started for a total of 14.5 h with 30 min between image captures at 37°C in humidified air with 5% CO_2. During the experiment, PHI HoloLids™ (Phase Holographic Imaging) were used to close the well plate to ensure optimal image quality. Data analysis was performed with the HstudioM4 software (Phase Holographic Imaging) including cell segmentation, tracking of dividing cells, confluency measurement, and cell counting.

IV.2.3.11 Data Presentation

Detailed information on data presentation is given in I.2.2.2. Linear deconvolution of the STED data was performed by applying a Lorentzian PSF (refer to equation (I-5)) with FWHM = 40 nm in lateral dimension. All line profiles were drawn on raw data and averaged over 5 pixels.

IV.2.3.12 Statistical Aspects

Detailed information on general statistical aspects is given in I.2.2.3.

IV.2.4 Results and Discussion

IV.2.4.1 Approaches to Synthesize SiR Dye 15

The experimental procedure towards an optimized synthesis of the radiofluorinatable NIR SiR dye **15** is summarized in Table IV-5 and Figure IV-4. In the first step, 3-bromo-2-chloropyridine (compound **19**) was lithiated at -78°C to initiate the HD reaction. In the second step, the silicon xanthone **17** was added after 30 min. Subsequently, the reaction mixture was brought to room temperature and stirred for different durations t_r. Using *t*-BuLi as a lithiation reagent provided the desired product SiR dye **15** as a deep blue solid but only at 14% yield (Table IV-5, entry 1).

The HD rearrangement of compound **19** is usually performed with substoichiometric amounts of the lithiating agent (0.5 eq. *n*-BuLi for 1 eq. compound **19**) due to the homotransmetallation mechanism [938, 940]. Therefore, in the second approach, we used 0.9 eq. of *t*-BuLi (Table IV-5, entry 2) and 0.5 eq. of *n*-BuLi (Table IV-5, entry 3). However, SiR dye **15** was again obtained at poor yield together with unreacted xanthone **17**. The mechanism of the halogen–metal exchange with *t*-BuLi states that one equivalent of the base is used for the lithiation, while a second equivalent of base eliminates hydrogen bromide from the resulting *t*-BuBr. According to this, our second approach represents the use of approximately 0.5 eq. of base for 1 eq. of compound **19** (Table IV-5, entry 2 and 3).

Optimization of the reaction was finally achieved by applying more equivalents of the base. After lithiation of compound **19**, the metallated intermediate (2-chloropyridin-3-yl)lithium reacts again with unreacted compound **19**. After several steps of the halogen dance, the lithiated pyridine intermediate **18** results, which can add to the silicon xanthone **17**. If more equivalents of the base are used, low temperatures are crucial for the HD reaction to maintain a coexistence of compound **19** and its lithiated analogue. By using a large excess of compound **19**, the reaction was forced to completeness. The dihalogenated pyridinyl SiR dye **15** was obtained at 85% yield without monohalogenated byproduct and without the need for purification (Table IV-5, entry 4). The analytical data of SiR dye **15** are summarized in Table VI-26, Table VI-27, Figure VI-19 and Figure VI-20.

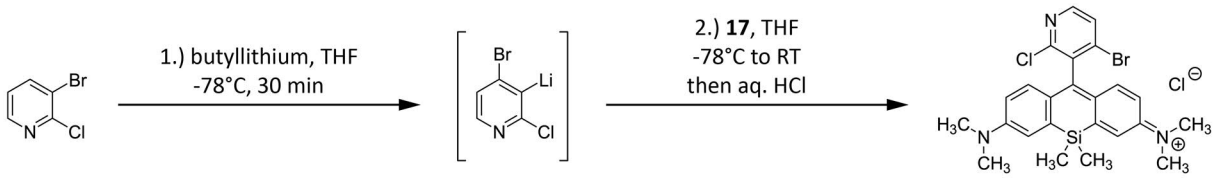

Figure IV-4. Synthesis of SiR dye 15 via HD rearrangement of compound 19.

Optimization of the synthesis of SiR dye **15** is outlined in Table IV-5.

Although the bromine offers the option of further coupling or functionalization of SiR dye **15** via a nucleophilic substitution, we additionally investigated if the ester analogue *tert*-butyl 5-bromo-6-chloronicotinate undergoes a HD reaction and subsequent xanthone addition. The reaction did not yield any product, neither with *n*-BuLi nor with *t*-BuLi. Also, HD reactions of nicotinic acids have not been reported in the literature. In fact, only methyl groups are tolerated as carbon substituents when using 2,3-dihalogenated pyridines as the starting material for the HD rearrangement.

Table IV-5. Optimization of the synthesis of SiR dye 15 via HD rearrangement of compound 19.

Figure IV-4 provides the corresponding scheme of the chemical reaction for this table. * Reaction time after addition of 1 eq. xanthone **17**, † yield based on recovered starting material of xanthone **17**.

entry	eq. of lithiation reagent	eq. of compound 19	t_r [h]*	yield of SiR dye 15 [%]
1	20 *t*-BuLi	10	1.5	14
2	9 *t*-BuLi	10	24	14 28†
3	5 *n*-BuLi	10	5	11
4	40 *t*-BuLi	20	4	85

IV.2.4.2 Fluorescence Properties of SiR Dye 15

The dihalogenated pyridinyl SiR dye **15** displays an absorbance maximum at 665 nm with a corresponding extinction coefficient of ε_{max} = 34000 $M^{-1}cm^{-1}$ and a fluorescence emission maximum at 681 nm with a corresponding fluorescence lifetime of τ = 1.9 ns measured in PBS at pH 7.4 (Figure IV-5,Figure VI-21, Table VI-28). Compared to the azetidine-substituted pyridinyl dye **14**, SiR dye **15** shows a red-shift of approximately 10 nm in both absorption and fluorescence emission; compared to the pyridinyl dye **13**, SiR dye **15** shows a 10 nm red-shifted absorption with unchanged fluorescence emission.

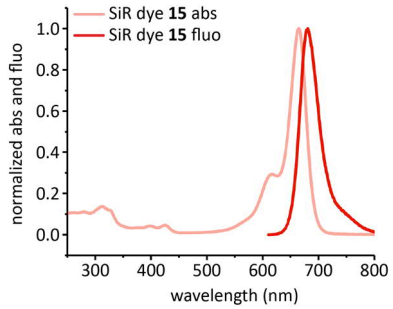

Figure IV-5. Absorbance and fluorescence emission of SiR dye 15.

The absorbance and fluorescence emission of SiR dye **15** in PBS at pH 7.4 peak at 665 nm and 681 nm. The absorbance spectrum is baseline corrected. Both spectra are normalized to their maximum.

With ϕ = 0.34, the quantum yield of SiR dye **15** measured in PBS at pH 7.4 is remarkably higher than that of pyridinyl dye **13** (Figure VI-22, Table VI-29). We assume that the increased quantum yield is based on a rotation restriction around the pyridinyl–xanthene bond and/or on beneficial effects of the halogens on the HOMO energy level. Due to the additional contributions of the azetidine rings, the pyridinyl SiR dye **14** still displays an enhanced quantum yield as compared to SiR dye **15**.

Figure VI-21, Figure VI-22, Figure VI-23, Table VI-28 and Table VI-29 comprise the photophysical properties of SiR dye **15** measured in MeCN.

IV.2.4.3 Mitochondrial Targeting Ability of SiR Dye 15

To study the predicted targeting ability of SiR dye **15** to mitochondria, HeLa and U2OS cells were co-stained with SiR dye **15** and the mitochondria staining reagent MitoTracker® Green FM. In live cell confocal experiments, the colocalization between these two probes was assessed (Figure IV-6). The average PCC of each cell line was calculated based on the confocal data. With r = 0.85 ± 0.05 (n = 22) for HeLa cells and r = 0.81 ± 0.05 (n = 27) for U2OS cells, the PCC results are reasonably high, which confirms the predicted targeting ability of SiR dye **15** to mitochondria.

For selective mitochondria staining, PCCs of r > 0.8 have been correlated with an increased lipophilicity of clog*P* > 5 of the respective mitochondrial probe. In this regard, the recently published SiR-Mito 8 especially stands out featuring a PCC of r ≥ 0.9 for mitochondrial colocalization [930]. SiR-Mito 8 offers a comparable quantum yield to SiR dye **15** (ε not available) but is not proven to be STED compatible. In contrast, SiR dye **15** combines the advantages of further red-shifted absorption and emission properties with an increased photostability thus making it suitable for application in live cell STED nanoscopy of the mitochondrial network (refer to IV.2.4.4).

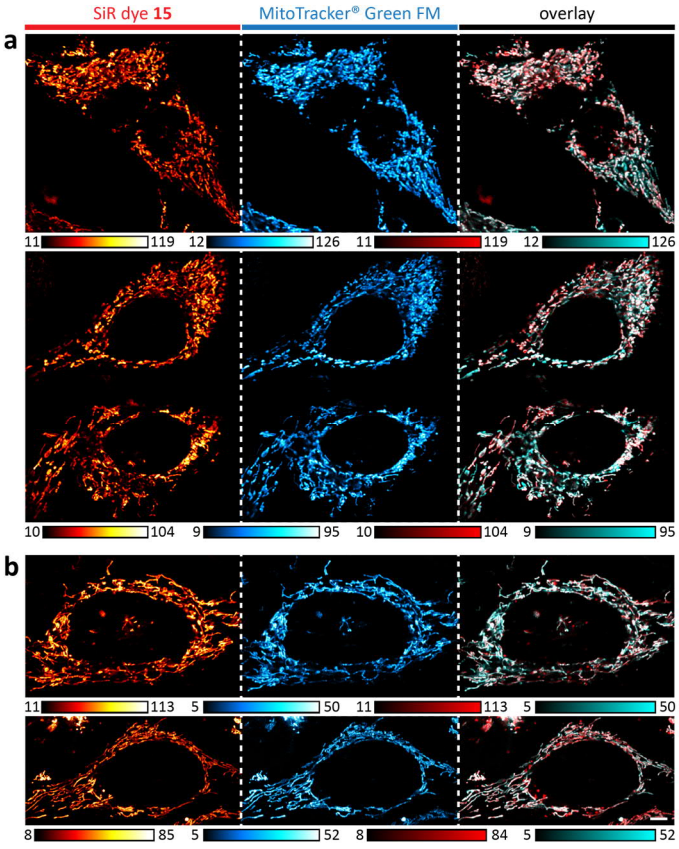

Figure IV-6. SiR dye 15 specifically targets mitochondria in living human cell lines.

Confocal colocalization experiments of SiR dye **15** (red) and MitoTracker® Green FM (cyan) in (**a**) living HeLa and (**b**) U2OS cells. The results support the application of SiR dye **15** as a specific NIR mitochondrial probe. Confocal data are corrected for color shift and background, scale bar is 5 µm.

In general, the 2-chloropyridinyl moiety in SiR dye **15** targets acidic cellular compartments. To exclude a potential affinity of SiR dye 15 to endosomes or lysosomes, HeLa and U2OS cells were co-stained with SiR dye **15** and the endosomal/lysosomal staining reagent LysoTracker™ Green DND-26. The colocalization of the two probes was visualized in live cell confocal experiments and the average PCC of each cell line was calculated based on the confocal data (Figure IV-7).

With r = 0.35 ± 0.06 (n = 13) for HeLa cells and r = 0.38 ± 0.04 (n = 13) for U2OS cells, the PCC results prove the absence of lysosomal targeting ability, confirming specific mitochondrial staining and supporting the application of SiR dye **15** as a specific NIR mitochondrial probe (Figure IV-8). We additionally note that the PCC for endosomal/lysosomal colocalization overestimates the lysosomal targeting ability of SiR dye **15** as LysoTracker™ Green DND-26 shows mild but additional mitochondrial staining.

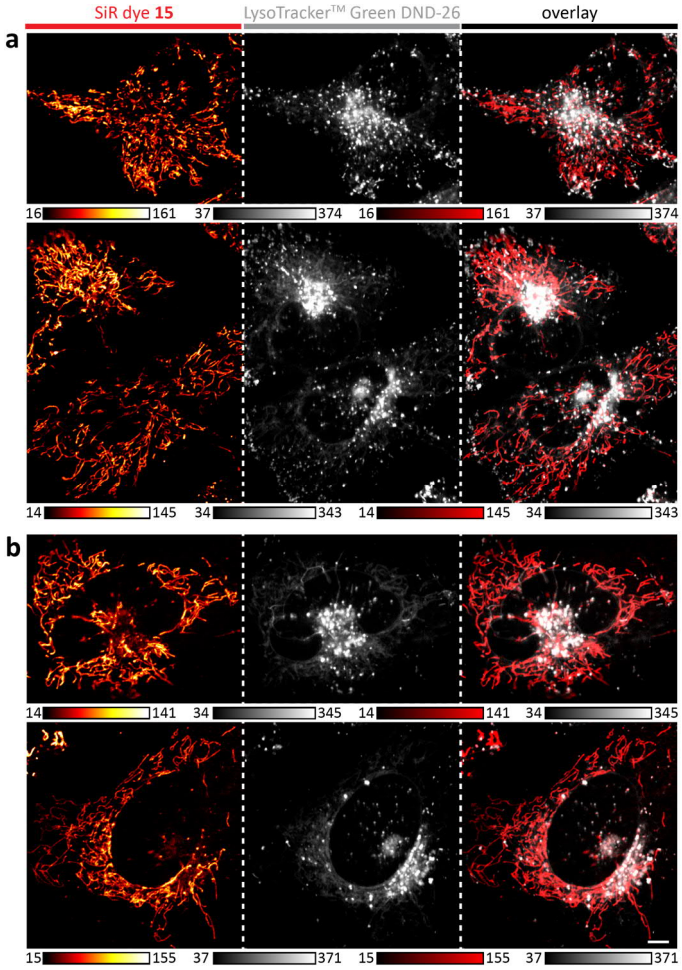

Figure IV-7. SiR dye 15 displays no targeting ability for endosomes or lysosomes in living human cell lines.

Confocal colocalization experiments of SiR dye **15** (red) and LysoTracker™ Green DND-26 (gray) in (**a**) living HeLa and (**b**) U2OS cells. The results strongly suggest the absence of an endosomal/lysosomal targeting ability of SiR dye **15** and confirm its specificity for mitochondria. Confocal data are corrected for color shift and background, scale bar is 5 µm.

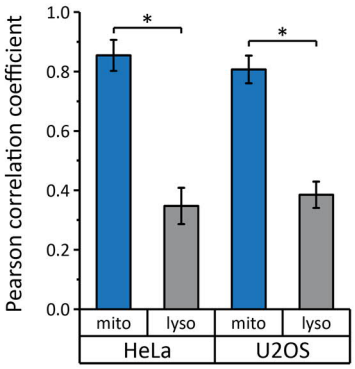

Figure IV-8. Pearson correlation coefficients of mitochondrial and endosomal/lysosomal colocalization of SiR dye 15.

Average PCCs for SiR dye **15**/MitoTracker® Green FM (blue, mito) and SiR dye **15**/LysoTracker™ Green DND-26 (gray, lyso) colocalization in HeLa and U2OS cells. The PCC of each color shift corrected confocal image was calculated with the ImageJ plugin JACoP [470, 695]. Data are expressed as mean ± SD. Mitochondrial colocalization HeLa n = 22, U2OS n = 27; lysosomal colocalization HeLa n = 13, U2OS n = 13; * $p < 10^{-22}$. All results and p-values are summarized in Table VI-30.

IV.2.4.4 STED Compatibility of SiR Dye 15

Medical agents must undergo an expensive regulatory process before they attain approval for the market. Thus, medical imaging probes that can address multiple questions or be applied for different purposes are highly interesting. In this regard, our probe design aimed not only for the combination of PET imaging and macroscopic fluorescence imaging. Instead, we strived for a dual-modality PET tracer that additionally offers the option for application in STED nanoscopy. Histopathological examinations of biopsy material with subcellular detail require a sufficiently high image resolution and it has been

shown that mitochondrial morphology constitutes a valid biomarker for cancer phenotype classification and for drug response analysis [948].

To prove STED compatibility of SiR dye **15**, HeLa cells were stained with SiR dye **15** and subjected to live cell STED imaging. The tubular structure of mitochondria in living HeLa cells was successfully resolved. We note that the STED power was set as low as possible to avoid photobleaching but as high as necessary to resolve these structures. Figure IV-9 compares STED images of the mitochondrial network with their corresponding confocal images. The STED data suggest that SiR dye **15** presumably targets the outer membrane as it does not visualize cristae. We conclude that SiR dye **15** is a potent probe for live cell STED imaging of mitochondria.

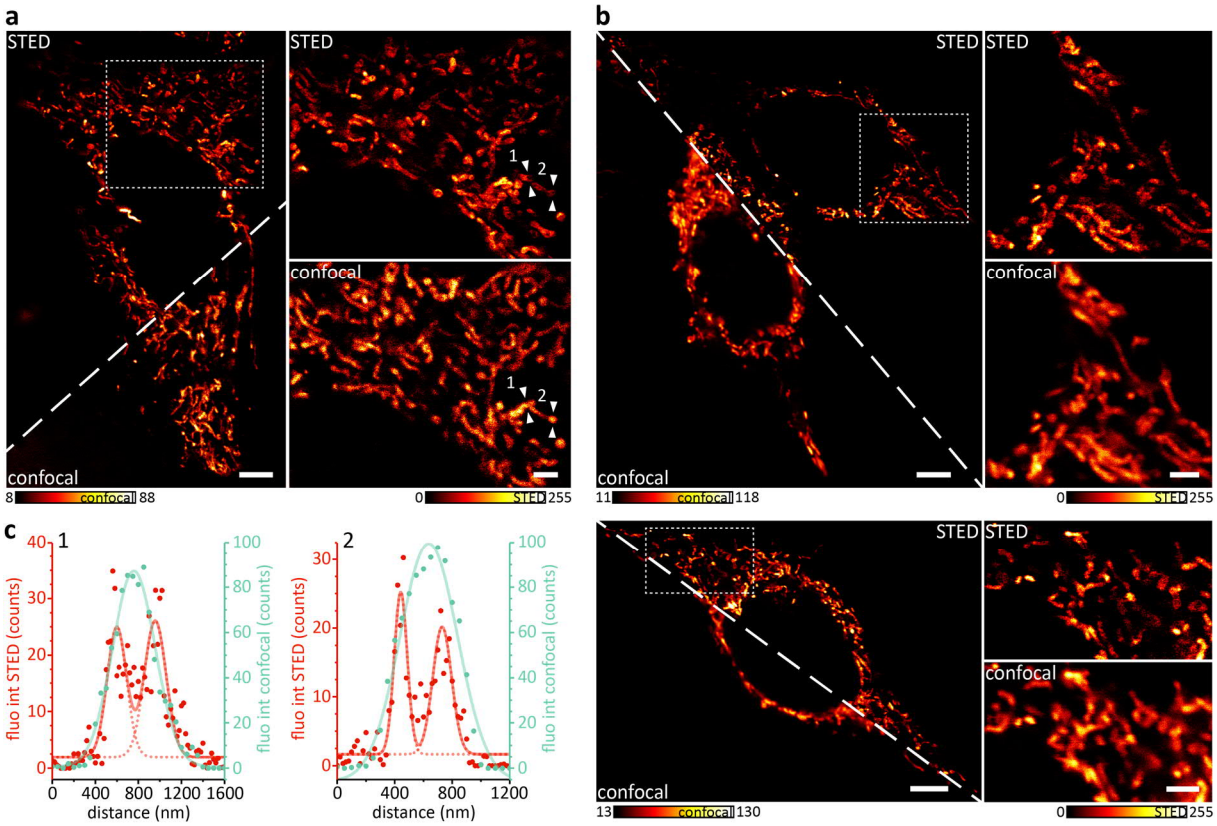

Figure IV-9. STED imaging of the mitochondrial network in living HeLa cells stained with SiR dye 15.

(**a**,**b**) Exemplary STED images (top) of the mitochondrial network in living HeLa cells stained with SiR dye **15** and their corresponding confocal data (bottom). To the right of each overview image, a magnification of the marked region is shown in STED (top) and confocal (bottom) mode. Pixel size (**a**) STED 20 nm, confocal 50 nm, (**b**) STED and confocal 20 nm. Scale bar overviews are 5 µm, scale bar close-ups are 2 µm. Note that the overall structure of the mitochondrial network in the corresponding STED and confocal images in (**a**) slightly differs due to mitochondrial dynamics and time-sequential recording (confocal after STED). All STED data are background corrected and linearly deconvolved, all confocal data are background corrected only. (**c**) Line profiles (as marked in the close-ups in (**a**) by white arrows) prove the gain in spatial resolution by STED (red) compared to confocal (cyan). Line profiles were drawn on background corrected (not deconvolved) data and counts were averaged over five pixels. The data were fitted with a single (confocal) or double (STED) Gaussian function. The STED power was set as low as possible to avoid photobleaching but as high as necessary to resolve the tubular structure of mitochondria.

IV.2.4.5 Cytotoxicity of SiR Dye 15

In contrast to PET imaging, which only requires pico- to nanomolar amounts of the radiopharmaceutical compound, medical applications of fluorescence imaging (e.g. fluorescence-guided interventions) depend on larger amounts of the fluorescent probe. Thus, the absence of cytotoxicity is a crucial requirement for our proposed dual-modality probe SiR dye **16**. Therefore, we evaluated the degree of cytotoxicity of its precursor, SiR dye **15**, based on the frequency and duration of cell division. U2OS cell proliferation was followed by holographic time-lapse imaging and quantitatively compared for treated and untreated cells (Figure IV-10) (for details on cytotoxicity testing of live dyes in general, refer to IV.3).

Neither the duration nor the frequency of U2OS cell division were significantly affected by the treatment with SiR dye **15**. This observation is additionally supported by cell count and confluency analysis (Figure IV-11). As SiR dye **15** does not affect U2OS cell proliferation, we assume that SiR dye **15** does not induce significant cytotoxic effects in human cells and speculate the same for its fluorinated derivative.

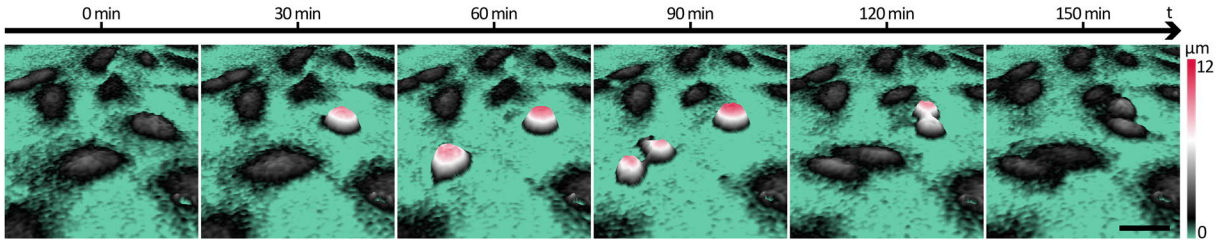

Figure IV-10. U2OS cell division after treatment with SiR dye 15.

Using holographic time-lapse cytometry with a HoloMonitor® M4 microscope, U2OS cell proliferation was followed for a total of 14.5 h after 1 h treatment with 1 µM SiR dye **15**. The exemplary image sequence (duration 2.5 h, frequency 30 min) displays two subsequent cell divisions; dividing cells round up and thus can be distinguished from non-dividing cells by height (color coded). Scale bar is 50 µm.

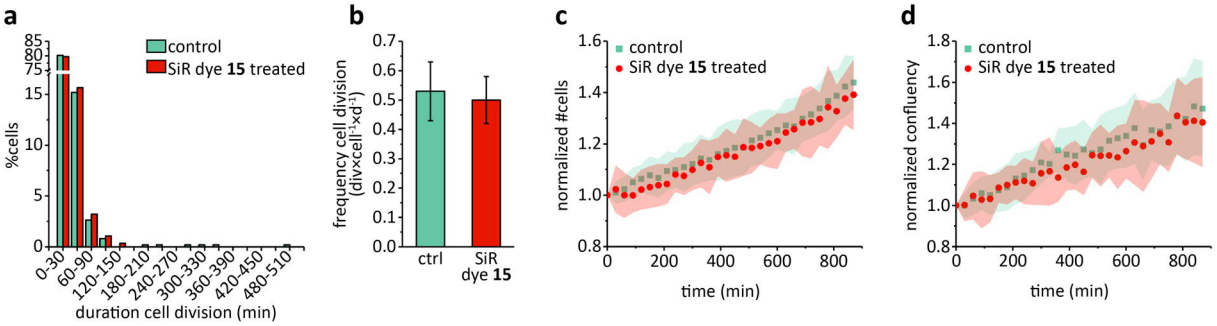

Figure IV-11. Assessment of the cytotoxicity of SiR dye 15.

Cytotoxicity data are based on holographic time-lapse series (duration 14.5 h, frequency 30 min) of the proliferation of U2OS cells untreated (cyan) or SiR dye **15** treated (red). (**a**) Duration of cell division (untreated n = 494, SiR dye **15** treated n = 281). P-values indicate no significant difference between the untreated and the SiR dye **15** treated conditions. (**b**) Frequency of cell division (untreated n = 494, SiR dye **15** treated n = 281). P-values indicate no significant difference between the untreated and the SiR dye **15** treated condition. (**c**) Cell count and (**d**) confluency of untreated (n = 11) and SiR dye **15** treated (n = 8) U2OS cells. Both measures were normalized to the first frame (t = 0). The results were averaged and SDs are displayed as shadows in the graphs. P-values indicate no significant difference between untreated and treated U2OS cells. All data strongly support the absence of cytotoxicity. All results and p-values are summarized in Table VI-31.

IV.2.5 Conclusion

To exploit the full potential of live cell STED imaging, (bio)chemical progress optimizing both targeting strategies and fluorophore performance is indispensable. Extending the palette of bright, photostable, cell permeable, and biocompatible far-red STED fluorophores with derivatives featuring novel targeting abilities and exceptional characteristics such as dual-modalities, will not only broaden the application of live cell STED nanoscopy in common life sciences research but also introduce STED imaging to applications such as clinical diagnostics so far unexplored by STED nanoscopy.

Here, we synthesized and extensively characterized SiR dye **15**, a pyridinyl silicon rhodamine dye featuring the option of implementing a second modality. The application of a halogen dance rearrangement allowed for the introduction of two halogen atoms adjacent to the xanthene–pyridine bond of SiR dye **15**. The chlorine atom in 2'-position allows for the introduction of the PET radionuclide ^{18}F, potentially yielding a dual-modality PET tracer for hybrid medical imaging approaches (PET/OI). The bromine atom in 4'-position not only constrains the rotation around the xanthene–pyridine bond but also serves as a leverage point for further linkage. Our optimized synthesis procedure provided SiR dye **15** at high yield and without the necessity of further purification.

The improved molecule rigidity introduced by the bulky bromine should reduce non-radiative decay processes and thus raise the quantum yield of SiR dye **15**. Surprisingly, despite being reasonably high, the quantum yield of SiR dye **15** does not outperform the quantum yield of the monosubstituted pyridine SiR **14**. Additional experiments combined with DFT calculations must address the orbital effects of both halogens and the nitrogen position in the pyridine ring to explain these findings with confidence.

Just like the recently published squaraine dye variant MitoESq-635 [949], our SiR dye **15** provides the option for live cell STED imaging of mitochondria without the necessity of an additional tagging step. In contrast to MitoESq-635, SiR dye **15** presumably targets the outer membrane and does not visualize cristae. Still, SiR dye **15** selectively stains mitochondria without background from unspecific membrane staining as is the case for MitoESq-635. However, due to a higher photostability and a lower saturation intensity I_S for STED, MitoESq-635 shows better performance in time-lapse live cell STED imaging of mitochondria. Different from MitoESq-635, the recently published SiR-Mito 8 offers highly specific mitochondrial targeting without background from unspecific membrane staining, but SiR-Mito 8 is not proven to be STED compatible. Thus, our SiR dye **15** represents a valid compromise between MitoESq-635 and SiR-Mito 8 by offering biocompatible, specific mitochondrial staining in live cell STED imaging.

Compared to other NIR SiR dyes with similar spectral properties [29, 31, 33], our SiR dye **15** displays photophysical properties (ε, ϕ, τ) in the same range, but rather at the lower end. However, its photophysical performance is in line with the group of SiR probes directly targeting certain cellular structures or organelles [31, 353, 354, 423]. Amongst these STED compatible SiR probes, to the best of our knowledge, none target mitochondria and thus SiR dye **15** is the first to extend the list of STED compatible SiR probes for direct labeling with a NIR mitochondrial SiR probe.

Taken together, we synthesized and characterized a biocompatible, non-toxic, STED compatible NIR SiR dye specifically targeting mitochondria in living cells. SiR dye **15** not only features excellent optical properties for biomedical imaging but additionally provides the option of subsequent radiolabeling.

Due to the intrinsic mitochondrial targeting ability of SiR dye **15**, its radiolabeled analogue could be applied for diagnostic and therapeutic purposes in medical multimodal (PET/OI) imaging of mitochondria in, e.g., cancer patients. In this scenario, the STED compatibility would allow for the histopathological examination of biopsy material with highest detail after the localization of lesions via PET imaging. The (radio)fluorination of SiR dye **15** is the subject of current research.

IV.3 Cytotoxicity in Live Cell STED Imaging

IV.3.1 Motivation

Like any other live cell fluorescence nanoscopy technique, live cell STED imaging is confronted with two main factors of potential cell damage. While phototoxicity accounts for any damage induced by the light energy deposited in the sample (refer to I.1.4), cytotoxicity refers to the direct chemical toxicity induced by the fluorescent label (ligand plus fluorophore) and the imaging buffer.

In both cases, the biological subject of interest is potentially affected and the imaging results are altered, no longer describing the biological reality of a viable cell [272]. In general, the sample health should be of major interest for any live cell imaging application and other imaging parameters must certainly be optimized for the biological question but not overdone (refer to I.1.5). Both phototoxicity and cytotoxicity are well-known aspects of fluorescence microscopy. However, phototoxicity has just recently started to gain increasing attention in the live cell imaging community with particular focus on fluorescence nanoscopy [289, 303, 305, 879, 891, 950, 951]. In comparison, cytotoxicity in live cell fluorescence nanoscopy is still addressed insufficiently.

Comprehensive studies that systematically quantify the cytotoxicity of live dyes applicable in fluorescence nanoscopy and further correlate the results to their structural features remain to be reported. It is suggested that neutral, hydrophobic fluorophores and anionic fluorophores induce less cytotoxicity than cationic fluorophores [952]. However, many positively charged lipophilic dyes display membrane association and bind non-specifically [953]. Anionic fluorophores (usually sulfonates or phosphates) are essentially restricted to fixed cell staining as these probes are not cell membrane permeable. Hence, choosing the appropriate dye is crucial to prevent biasing effects of the dyes on cellular interactions and processes eventually leading to misinterpretations when comparing data obtained with different probes.

Most of the live dyes published during the last few years are electronically neutral, hydrophilic and designed with particular attention to compatibility with living cells [29-36, 353, 354, 405, 916, 922] (refer to I.1.6.1). Still, amongst this valuable flood of reports on novel probes for live cell fluorescence nanoscopy, only a few studies have rigorously investigated the cytotoxicity of their newly proposed live dyes [32, 353, 354, 954]. As the field is still in its infancy though, follow-up studies on the cytotoxicity of already published live dyes can be expected.

The selected studies that include cytotoxicity assessment have evaluated the sample health consequences of targeted labeling with their novel live dyes. Thus, the results always represent the

combined cytotoxic effect of the dye itself and the affinity probe (e.g. docetaxel as a small molecule binder for tubulin) [32, 353, 354, 954]. These insights are exceptionally valuable as it is eventually the combination of dye and targeting strategy that must be non-toxic to the cell. However, for further dye optimization and novel dye design, it is crucial to understand the dyes' individual contribution to cytotoxicity and relate it to specific features of the dyes' chemical structure.

Cell viability refers to the fraction of healthy cells in a sample and numerous cytotoxicity assays have been established to monitor this parameter. Many of these assays exploit general cell functions such as enzyme activity, cell membrane integrity, NADH concentration and ATP production. The common drawback of all metabolic assays is their inability to differentiate between actively dividing and quiescent cells. Some of these methods even constitute terminal assays as they interfere with or destroy the cell's functioning [955].

In contrast, the non-invasive observation and the quantitative analysis of cell proliferation avoids these downsides. Cell proliferation offers not only a universal but also a sensitive measure for cell viability. The finely tuned coordination of different cell cycle checkpoints and in particular the transitions from the growth phase 1 (G1) to the DNA synthesis phase (S) and from the growth phase 2 (G2) to mitosis (M) are essential for maintaining genome integrity and thus represent crucial prerequisites for a successful cell division. DNA replication itself is a delicate process requiring the highest fidelity as it is orchestrated by a complex replisome that must ensure not only complete duplication of the genetic material but also the maintenance and propagation of chromatin states [956].

Digital holographic microscopy provides the technique to observe cell proliferation over extended time periods. Its technology is based on quantitative phase imaging and offers label-free, non-invasive visualization and quantification of living cells without compromising cell integrity. Digital holographic microscopy is an interferometric imaging technique that records amplitude and phase information of an object wave in form of holograms. As living, unstained cells are rather translucent and do not absorb, emit or scatter light to any significant extent, the amplitude change of a sample beam passing through these cells can be neglected. However, as the refractive index of cells (especially of the nucleus) differs from the surrounding medium, the cells imprint a phase-shift onto the sample beam. From the hologram, this phase delay can be numerically reconstructed into a phase image displaying the morphology and 3D optical properties of the cells (Figure IV-12) [957].

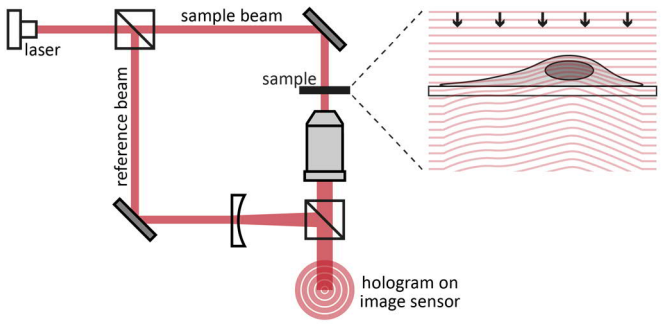

Figure IV-12. Schematic illustration of digital holographic microscopy.

A low-intensity laser beam is split into a reference beam and a sample beam. The phase of the sample beam is delayed upon passing through the sample as the cells' interiors feature a different optical density as compared to the surrounding medium. Once combined, the reference beam and the phase-shifted sample beam interfere and create a hologram on the image sensor, which is used to compute the 3D phase image.

IV.3.2 Aim

To not alter the imaging results by affecting the biological process, the biological structure or its dynamics of interest, sample health should be treated as the essential parameter during live cell experiments. Any impairment of cell viability might eventually lead to the acquisition of biological artefacts. Besides phototoxicity, potential cytotoxicity of the applied fluorophores must be also excluded to achieve thoroughly biocompatible imaging conditions. As DNA replication is a sensitive process depending on a properly functioning cell proliferation machinery, the cell division frequency and duration provide meaningful measures to assess cytotoxic effects.

The aim of this project was to evaluate potential cytotoxicity of several recently developed live cell STED compatible dyes. Therefore, the influence of different concentrations of these probes on the proliferation behavior of U2OS cells was investigated. To non-invasively assess the effect on the frequency and duration of U2OS cell division, holographic cytometry studies were conducted, different proliferation parameters quantified, and the results compared to those of proliferation measurements of untreated U2OS cells.

The work presented in the following section has not been published yet but extends the already published work of Butkevich, A.N., Belov, V. N., Kolmakov, K., Sokolov, V. V., Shojaei, H., Sidenstein, S. C., Kamin, D., Matthias, J., Vlijm, R., Engelhardt, J., Hell, S. W., *Hydroxylated Fluorescent Dyes for Live-Cell Labeling: Synthesis, Spectra and Super-Resolution STED*. Chemistry, 2017. 23(50): p. 12114-12119. [32].

IV.3.3 Methods

Detailed information on materials is given in I.2.1.

IV.3.3.1 Cell Culture

The cell line U2OS (Table I-16) was cultured in DMEM++ at 37°C in humidified air with 5% CO_2. The cells were harvested with trypsin 0.05% EDTA 0.02% (with phenol red, Sigma-Aldrich/Merck). A Countess II FL Automated Cell Counter (Thermo Fisher Scientific) was used to count cells and to assess the live-to-dead cell ratio via Trypan Blue stain (0.4%). For sample preparation, approximately 10^5 cells/well were seeded one day prior to the experiment in DMEM++ in lumox® 24-well plates (Sarstedt) and kept at 37°C in humidified air with 5% CO_2 until holographic time-lapse imaging.

IV.3.3.2 Cytotoxicity Studies

To assess potential cytotoxicity of the new live dyes 580CP-BG/-Halo, 610CP-BG/-BC/-Halo, 640SiRH-BG/-BC/-Halo [29, 32] (BG = SNAP-tag ligand, BC = CLIP-tag ligand, Halo = HaloTag ligand) and SNAP-

Cell® 647-SiR (New England Biolabs) [404], the duration and frequency of U2OS cell division was followed by holographic time-lapse imaging using a HoloMonitor® M4 cytometer (Phase Holographic Imaging). The old medium was replaced with fresh DMEM++ containing either 1 µM or 5 µM of the respective live dye and holographic time-lapse imaging was started for a total of 48 h with 15 min between image captures at 37°C in humidified air with 5% CO_2. During the experiment, PHI HoloLids™ (Phase Holographic Imaging) were used to close the well plate to ensure optimal image quality. Data analysis was performed with the HstudioM4 software (Phase Holographic Imaging) including cell segmentation, tracking of dividing cells, confluency measurement, and cell counting.

IV.3.3.3 Data Presentation

Detailed information on data presentation is given in I.2.2.2.

IV.3.3.4 Statistical Aspects

Detailed information on general statistical aspects is given in I.2.2.3.

IV.3.4 Results and Discussion

To evaluate potential cytotoxic effects of the popular SiR dye [30, 404] and of the recently published live cell STED compatible dyes 580CP, 610CP [29] and 640SiRH [32], U2OS cells were incubated for 48 h with 1 µM and 5 µM of the respective SNAP, CLIP and Halo derivatives. Holographic time-lapse cytometry enabled concurrent observation of the cell proliferation. The system used (HoloMonitor® M4) illuminates the sample with a 635 nm laser. At this wavelength, the absorption of 580CP is negligible. However, 610CP absorbs mildly and 640SiRH and SiR absorb strongly at 635 nm. A significant impact of phototoxicity on the measurement results can be excluded though as the laser excites under non-saturating conditions (0.2 mW/cm^2) (refer to I.1.4).

U2OS cell proliferation was observed for all tested conditions. Figure IV-13 shows exemplary holographic image sequences of U2OS cell divisions in the presence of either 1 µM 610CP-BG or 1 µM 640SiRH-Halo. As dividing cells contract upon mitotic chromatin condensation, they can be distinguished by shape and height from non-dividing cells. Cell segmentation of the corresponding 2D data allowed for cell counting and cell tracking and thus the quantitative analysis of cell proliferation.

Based on the initial number of cells at the beginning of the experiment (t = 0) and the total number of observed cell divisions during the experiment, the average frequency of cell division per cell and day was computed for each condition. The results were compared to those of control measurements of the proliferation of untreated U2OS cells (Figure IV-14a). At the tested concentrations of 1 µM and 5 µM, none of the investigated dye derivatives significantly reduced the U2OS cell division frequency. Surprisingly, 1 µM 580CP-BG and 1 µM 640SiRH-BC even slightly increased the division rate. As these

two derivatives share neither obvious commonalities in the dye moiety (carbopyronine *vs.* silicon rhodamine) nor in the enzyme specific substrate moiety (benzylguanine *vs.* benzylcytosine), a direct correlation between influence on division frequency and structural features could not be identified.

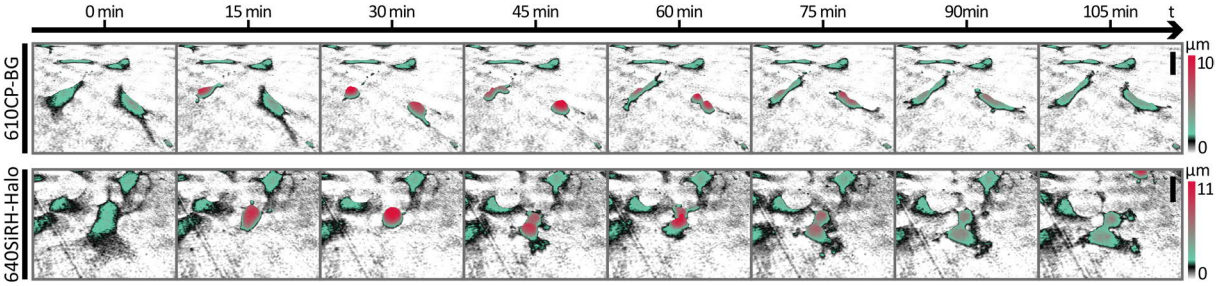

Figure IV-13. U2OS cell divisions in the presence of the live dyes 610CP-BG and 640SiRH-Halo.

Using holographic time-lapse cytometry with a HoloMonitor® M4 microscope, U2OS cell proliferation was followed for a total of 48 h in the presence of the recently published [29, 32] live cell STED compatible dyes 610CP-BG (1 µM, top) and 640SiRH-Halo (1 µM, bottom) (BG = SNAP-tag ligand, Halo = HaloTag ligand). In the exemplary image sequences (duration 1.75 h, frequency 15 min), dividing cells round up and thus can be distinguished from non-dividing cells by height (color coded). Scale bars are 50 µm.

Individual tracking of dividing cells enabled the quantitative analysis of the duration of U2OS cell division. Figure IV-14b illustrates the results as histograms for each derivative binning the relative number of divided cells into time windows of the length of the inverse image acquisition frequency (15 min). Except for 5 µM 610CP-Halo, none of the tested derivatives significantly slowed down U2OS cell division. In contrast, 1 µM 580CP-BG, 1 µM and 5 µM 610CP-BG, 1 µM 610CP-Halo and 1 µM 640SiRH-BG even decreased the division duration. Interestingly, most of these division accelerating derivatives are carbopyronines coupled to benzylguanine. However, to correlate these characteristics with certainty, further studies are pending.

As the results of the division duration do not entirely mirror the results of the division frequency, it is evident that the rate and the duration of cell division are not necessarily dependent and can be individually affected. Thus, these parameters are not redundant, and it is worthwhile analyzing both to assess cytotoxic effects.

Based on the segmented phase images, the time series of the cell count (Figure IV-15) and of the confluency (Figure VI-24) were computed for each condition. It should be noted that the time series of the cell count is directly linked to the cell division frequency. Still, the analyses towards these parameters differ and thus the time series of the cell count was used to confirm the results of the division rate. The cell count itself further correlates with the confluency of the sample. However, the cell area additionally affects the confluency and thus the time series of the cell count and of the confluency are only redundant under the assumption of an unchanged cell area, which is not necessarily given.

As expected from the results of the U2OS division rate analysis, the cell count time series of all tested derivative conditions do not strongly deviate from the result of the control measurements. Due to the increased frequency of U2OS cell division in the presence of 1 µM 580CP-BG and 1 µM 640SiRH-BC, the data points of the cell count time series of these two conditions lie above the data points of the control time series. The results of the U2OS cell division duration are not mirrored in the time series of the cell count.

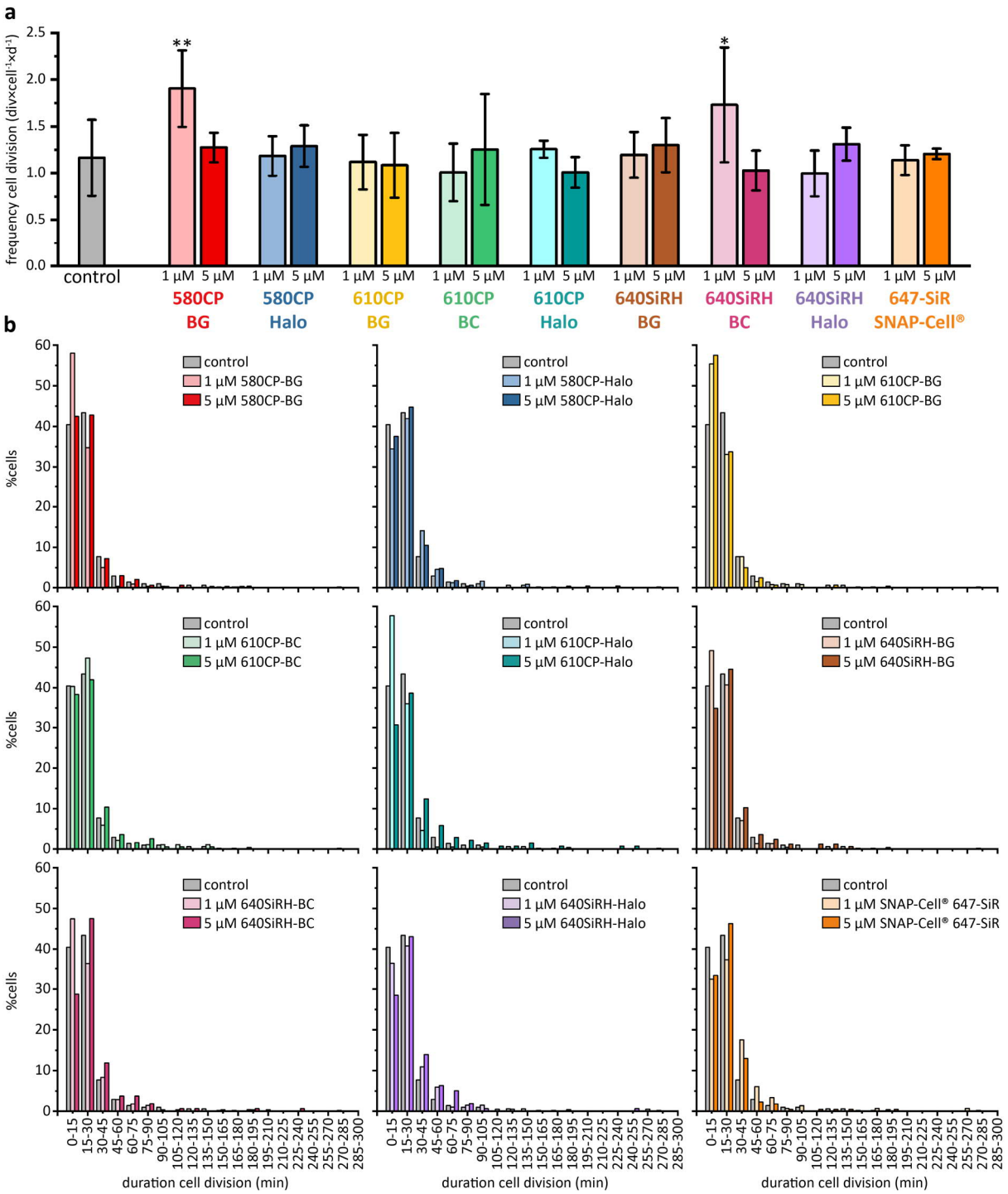

Figure IV-14. Duration and frequency of U2OS cell division in the presence of various live cell STED compatible dyes.

Cytotoxicity data are based on holographic time-lapse series (duration 48 h, frequency 15 min) of U2OS cell proliferation in the presence of 1 µM and 5 µM of SNAP (BG), CLIP (BC) and Halo derivatives of the popular SiR dye [30, 404] and the recently published [29, 32] live cell STED compatible organic dyes 580CP, 610CP and 640SiRH. The data are compared to the control measurements of the proliferation of untreated U2OS cells (gray). (**a**) Frequency of cell division. P-values indicate no significant difference between the control and the dye treated conditions, except for the 1 µM 580CP-BG and 1 µM 640SiRH-BC conditions (* $p < 0.05$, ** $p < 0.005$). (**b**) Duration of cell division. P-values comparing the average duration of the control and the dye treated conditions indicate a retardation of U2OS cell divisions for the condition 5 µM 610CP-Halo and an acceleration of U2OS cell divisions for the conditions 1 µM 580CP-BG, 1 µM and 5 µM 610CP-BG, 1 µM 610CP-Halo and 1 µM 640SiRH-BG. All results, n-values and p-values are summarized in Table VI-32.

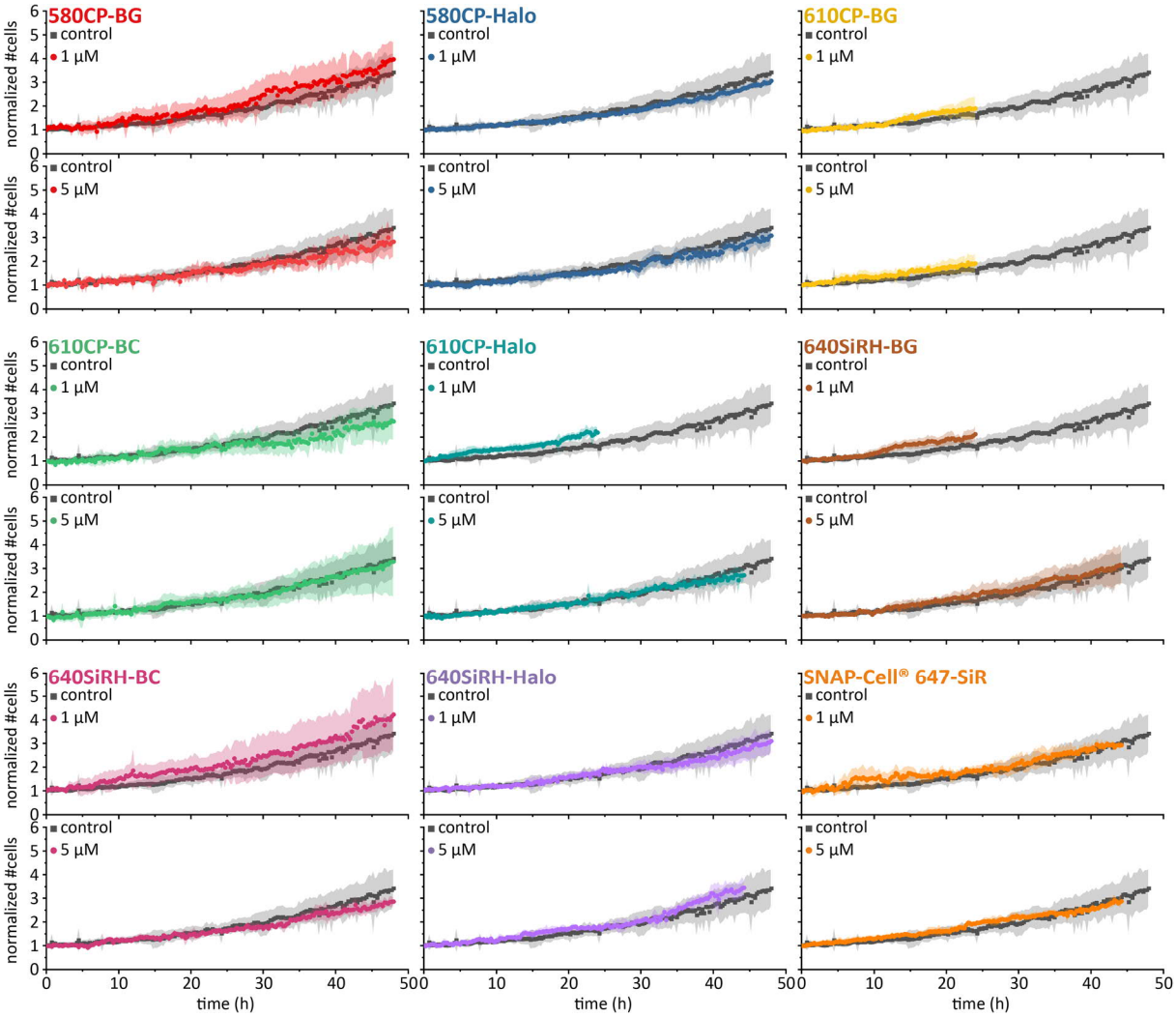

Figure IV-15. Time series of the U2OS cell count in the presence of various live cell STED compatible dyes.

Cytotoxicity data are based on holographic time-lapse series (duration 24/44.25/48 h, frequency 15 min) of U2OS cell proliferation in the presence of 1 µM and 5 µM of SNAP (BG), CLIP (BC) and Halo derivatives of the popular SiR dye [30, 404] and the recently published [29, 32] live cell STED compatible organic dyes 580CP, 610CP and 640SiRH. The data are compared to the control measurements of the proliferation of untreated U2OS cells (dark gray data points). The cell count (#cells) was normalized to the first frame (t = 0). The results were averaged and SDs are displayed as shadows in the graphs. Average p-values indicate no significant difference between untreated and treated U2OS cells. All results, n-values and p-values are summarized in Table VI-32.

To analyze significant differences between the cell count time series of the control measurements and the cell count time series of the tested dye derivatives, the p-values were computed for each time point and averaged over the experiment duration (Table VI-32). The average p-values suggest no significant differences between the tested conditions and the control in the time series of the cell count. However, in this approach, the correlation of the cell count over time is lost. As soon as the curve of a time series of a certain condition constantly lies below or above the curve of the control time series, it can be assumed that a significant difference exists. Consequently, the data displayed in Figure IV-15 suggest that especially 5 µM 580CP-BG and 1 µM 610CP-BC slightly compromise U2OS cell proliferation whereas especially 1 µM 580CP-BG, 1 µM 610CP-Halo and 640SiRH-BC slightly stimulate U2OS cell proliferation.

Overall, the confluency time series confirm the results of the cell count analysis (Figure VI-24). Minor differences (e.g. 1 µM 580CP-BG) as well as the larger SDs are assigned to imprecise cell segmentation. The confluency measure more strongly relies on precise cell segmentation than the cell count does. The cell count solely requires the correct identification of individual cells whereas the confluency additionally depends on a proper sketch of the cell outline. Changing image quality during a measurement series can significantly hamper a consistently precise segmentation of the cell area, which directly affects the confluency but not the cell count.

Taken together, the results of the holographic cytometry studies strongly suggest the absence of pronounced cytotoxicity of SNAP, CLIP and Halo derivatives of the live cell STED compatible dyes 580CP, 610CP, 640SiRH and SiR at concentrations up to 5 µM. Literature only provides comparable cytotoxicity data acquired with 5 µM of the free carboxylic acid dyes 580CP-COOH and SiR-COOH. In the respective study, both dyes were also proven to be non-toxic in experiments analyzing the population distribution over the cell cycle [954].

Although none of the tested dye derivatives unambiguously induced cytotoxic effects, namely severe retardation of cell proliferation, inhibition of cell proliferation, apoptosis or necrosis, certain derivatives influenced U2OS cell proliferation more than others. Table IV-6 provides an overview of the results. In particular, 580CP-BG and 610CP-Halo affected the cell proliferation behavior the most, whereas 580CP-Halo, 640SiRH-Halo and SNAP-Cell® 647-SiR did not significantly alter it. From these results, the proliferation influence cannot be conclusively linked to a certain dye, dye type or enzyme specific substrate. However, it must be emphasized that regardless of the direction of deviation from the control (retardation or acceleration), changed cell proliferation behaviors are first signals of cell stress. The cellular stress response includes an increased production of ROS. At low levels, ROS even stimulate proliferation, while at higher levels they cause senescence or even cell death [958, 959].

Table IV-6. Summary of the results of the cytotoxicity study of SNAP, CLIP and Halo derivatives of selected live cell STED compatible organic dyes.

Green – no apparent effect on U2OS cell proliferation, red – U2OS cell proliferation is slightly impaired, yellow – U2OS cell proliferation is slightly stimulated; * SNAP-Cell® 647-SiR [404].

	580CP				610CP						640SiRH						SiR*	
	BG		Halo		BG		BC		Halo		BG		BC		Halo		BG	
c [µM]	1	5	1	5	1	5	1	5	1	5	1	5	1	5	1	5	1	5
frequency																		
duration																		
#cells																		

IV.3.5 Conclusion

Live cell STED nanoscopy is attracting an increasing amount of attention as it enables the extraction of information at unprecedented detail as close as possible to biological reality given the absence of phototoxicity and cytotoxicity (refer to I.1.5). In the early days of STED nanoscopy, live cell labeling techniques were already available, but truly biocompatible organic dyes were missing [387]. In recent years though, rapid progress in the field of live cell STED compatible organic dye development has provided a color palette of photostable, bright and cell membrane permeable dyes [29-34, 353, 354, 916, 954]. If not conjugated to small molecule binders, these dyes are commonly applied as SNAP, CLIP or Halo derivatives to specifically stain fusion constructs of the respective self-labeling protein tags.

So far, no study has systematically investigated potential cytotoxic effects of these live dye derivatives. However, the absence of cytotoxicity is a prerequisite for drawing biologically meaningful conclusions from live cell imaging data. Therefore, this project studied the influence of SNAP, CLIP and Halo derivatives of the live cell STED compatible NIR dyes 580CP [29] 610CP [29], 640SiRH [32] and SiR [30] on the proliferation behavior of U2OS cells. All tested dye derivatives did not induce pronounced cytotoxic effects at concentrations up to 5 µM. However, certain derivatives, namely 580CP-BG and 610CP-Halo, slightly affected the proliferation behavior of U2OS cells. For sensitive specimens and delicate biological questions, these dye derivatives should rather be avoided, favoring instead derivatives such as 580CP-Halo, 640SiRH-Halo and SNAP-Cell® 647-SiR, which did not alter the proliferation behavior in the present study.

The results only provide hints towards a general accelerating effect on the cell division duration by carbopyronines conjugated to benzylguanine. To confirm this speculation and to potentially identify other correlations between structural features and altered proliferation behaviors, further dedicated studies are required. Moreover, repeating the experiments with other cell lines is necessary to confirm the current results. Complementary cytotoxicity studies using the tested derivatives in the labeling of well-selected cellular targets are crucial to understanding the individual contributions of the single components of live cell sample preparations. Certainly, this also involves testing of the potential cytotoxicity of sample preparation agents that are added to protect the fluorophores from photobleaching (e.g. ROXS) or to prevent the cells from actively clearing their cytosol of dye (e.g. verapamil).

As the field of live cell STED compatible organic dyes is still young and the awareness for the importance of cell viability is continuously growing in the live cell imaging community, comprehensive cytotoxicity studies of live dyes can be expected in the near future. The results of this current project together with the results of these pending studies will facilitate the choice of the right dye for the individual biological application. The more comprehensively the available live dyes are characterized, the easier the choice, as it is not only the photostability, the brightness, the spectral properties, and the cell permeability that matters in live cell STED nanoscopy.

IV.4 IMAGE RESTORATION IN LIVE CELL STED IMAGING

IV.4.1 Motivation

The information content of fluorescence images is not only determined by the resolving power of the optical system used. Indeed, the final image quality and the effective image resolution in live cell fluorescence microscopy is strongly affected by several partially interdependent imaging parameters comprising the temporal resolution, observation time, SNR, FOV, imaging depth, fluorophore performance, fluorophore density and sample health [289, 951].

Simultaneous optimization of all imaging parameters is impossible, and trade-offs are thus inevitable. To a certain extent, these compromises can be alleviated by optimizing hardware and data acquisition strategies. However, physics sets limits that cannot easily be overcome with living and moving samples. Rationally applied, computational approaches enhancing the final image quality can be used to restore biological information. Sophisticated strategies comprise resolution-enhancing post-processing algorithms as applied in the diverse variants of SIM [98], SOFI [333] and SRRF [335], deconvolution [960-962], surface projection algorithms [963, 964], denoising methods [965-967] and image restoration based on deep learning [308, 682-684]. It must be noted that in image processing terms `super-resolution´ refers to algorithms performing resolution enhancing post-processing operations (e.g. SIM, SOFI, SRRF) and should not be confused with the optical methods of nanoscopy. In the remaining part of this section, `super-resolution´ is used in the sense of image processing.

The term `image restoration´ generally describes the recovery of the original signal from a degraded observation. Image restoration differs essentially from image enhancement with the latter being simply concerned with making the image look more pleasing to the observer without the scientific intent to produce realistic data. In order to enhance the information content of an image, as is the objective in image restoration, obviously this information must be provided from a source other than the actual image of degraded quality. Thus, the typical image restoration problem is decomposed into the question of accurately matching the structures in the image and into the question of reintroducing as far as possible the information that was lost during the process of data acquisition (degradation). In image processing terms, the former is referred to as achieving `data fidelity´ and the latter is referred to as achieving `regularization´.

For the design of a restoration algorithm,

- a mathematical model for the degradation process must be formulated,
- a quality metric that sets the goal of the restoration process must be defined,
- a regularization procedure that accounts for typical detail structures of the images under consideration must be developed, and
- a mathematical algorithm that achieves this goal must be implemented [968].

As a lens-based method, fluorescence microscopy is confronted with the phenomenon of diffraction and thus with image degradation caused by optical blurring, which is characterized by the individual PSF of the respective optical system (refer to I.1.1). Further sources of blur comprise sample motion and out-of-focus signal. Acquired by photon-counting detectors such as APDs, fluorescence images are usually degraded by noise with mixed Poisson-Gaussian statistics. Compared to photography (~10^5

photons per pixel), the signal in fluorescence microscopy (~10^2 photons per pixel) is generally weak and the fluorescence signal is quantized due to the discrete nature of photons. While Gaussian noise dominates in photography, it is Poisson noise, also referred to as shot noise, that prevails in fluorescence microscopy.

Poisson-Gaussian noise has been extensively addressed by numerous denoising methods [969-971], and joint approaches additionally adding deconvolution [972-975] or super-resolution [976] have been proposed. Most of these methods are designed within a maximum *a posteriori* (MAP) framework [971, 973-976]. MAP approaches require the manual adaptation of a regularization parameter defining the trade-off between the data fidelity term and the regularization term to guarantee best performance. This problem can be bypassed by approximating the minimum mean square error (MMSE) estimate [969, 972] and Marnissi *et al.* have used variational Bayesian approximation to compute the MMSE estimate and the regularization parameter [977].

Often, image restoration problems are treated through an application of Bayes' theorem [978] relating the conditional probabilities p between two separate events or logical conditions A and B

$$p(A|B) = \frac{p(B|A) \cdot p(A)}{p(B)} \tag{IV-3}$$

where $p(A|B)$ is the conditional probability that A occurs (is fulfilled) given that B has occurred (is fulfilled) and vice versa for $p(B|A)$. Further, $p(A)$ and $p(B)$ are the probabilities of observing A and B independently without knowledge of prior events or conditions.

In the application of image restoration, A represents the true image to be approximated by the restored image and B represents the acquired, degraded image. Note that $p(B)$ can be ignored since the availability of a degraded image can be assumed:

$$p(A|B) \propto p(B|A) \cdot p(A) \tag{IV-4}$$

Importantly, $p(A|B)$ is interpreted as the quantity to be maximized such that A becomes the most probable estimate of the true image, i.e. the restored image, and is often referred to as the posterior distribution. On the other hand, $p(B|A)$ represents the probability that the ideal image A leads to the observed image B, including degrading effects of noise, motion blur and PSF. The factor $p(A)$, referred to as the prior distribution, encodes correlations typical for true images in the relevant domain. This includes the expected behavior of contrast, textures and colors.

A Bayesian MMSE estimate is statistically more sound than a MAP estimate as it is based on the whole model distribution and thus exploits more information. For non-convex problems though, MMSE estimate computing is difficult. A trained non-convex probabilistic generative image prior has been applied in methods for denoising and deblurring of additive Gaussian noise [979, 980]. In these approaches, an efficient block Gibbs sampler has been used to average model samples for approximating the MMSE estimate. A regularization parameter has not been needed as the MMSE estimation operates in a purely generative setting. Due to its more complex statistics, Poisson-Gaussian noise cannot be addressed by the Gibbs sampler though.

IV.4.2 Aim

Fluorescence microscopy is confronted with Poisson-Gaussian noise with a dominating Poisson contribution due to its inherently weak signal. Particularly live cell data are affected by a degraded SNR as sample health demands conservative imaging parameters. The performance of deconvolution or denoising approaches that consider only one type of noise is usually insufficient for images suffering from noise of mixed Poisson-Gaussian statistics.

Thus, the aim of this project was the validation of a novel Bayesian method that restores images with mixed Poisson-Gaussian noise by simultaneously applying deconvolution, denoising as well as super-resolution. The restoration model was conceived based on a likelihood approximated by a superposition of Gaussians to model the statistics of Poisson-Gaussian noise and a generative Markov random field image prior. For efficient inference, a block Gibbs sampler was defined, and image restoration was performed by approximating the Bayesian minimum mean squared error estimate in a sampling-based scheme. To characterize the performance of the newly developed method, it was applied to live cell STED data of U2OS telomeres indirectly stained via a SNAP-tag/TRF2 fusion construct.

The work presented in the following sections has been published as Gao, Q., Eck, S., Matthias, J., Chung, I., Engelhardt, J., Rippe, K., Rohr, K. , *Bayesian Joint Super-Resolution, Deconvolution, and Denoising of Images with Poisson-Gaussian Noise.* 2018 IEEE 15th International Symposium on Biomedical Imaging (ISBI 2018), 2018: p. 938-942. [981].

IV.4.3 Methods

This project was conducted in close collaboration with the DKFZ Division of Biomedical Computer Vision (Heidelberg, Germany), who initiated and directed the effort. Detailed information on materials is given in I.2.1.

IV.4.3.1 Model Formulation and Sampling-Based Inference

For a detailed formulation of the model and an in-depth description of the sampling-based inference, refer to the methods section in Gao *et al.* [981]. Briefly, the image restoration is based on the posterior distribution in a Bayesian framework:

$$p(\mathbf{x}|\mathbf{y}) \propto p_L(\mathbf{y}|\mathbf{x};\boldsymbol{\Theta}) \cdot p_P(\mathbf{x};\boldsymbol{\Omega}) \qquad \textbf{(IV-5)}$$

with $\mathbf{y} \in \mathbb{R}^N$ being the degraded (noisy, blurry, low-resolution) image, $\mathbf{x} \in \mathbb{R}^{r^2N}$ being the true image to be restored, $\boldsymbol{\Theta}$ being the likelihood distribution parameters and $\boldsymbol{\Omega}$ being the prior distribution parameters. Above, N represents the number of pixels in the degraded image and $r > 1$ represents the linear super-resolution scaling factor. For super-resolution, every pixel in the degraded image is mapped onto $r \times r$ pixels in the higher resolution image. Clearly, a meaningful increase in image

resolution must draw on additional information not present in the degraded image. This role is taken by the prior distribution p_P.

The likelihood model is inferred by assuming Poisson-Gaussian noise. Thus, the intensity of each pixel y_i in the observed image $\mathbf{y}$ can be described by:

$$y_i = \alpha t_i + n_i \tag{IV-6}$$

with t_i following a Poisson distribution, α being a gain factor that controls the Poisson noise strength and $n_i \sim \mathcal{N}(\mu_n, \sigma_n^2)$ being additive Gaussian noise. The convolution of $\mathbf{x}$ with the PSF $\mathbf{k}$ and the discretization $\mathbf{S}$ into image pixels is represented by:

$$\tilde{\mathbf{x}} = \frac{1}{\alpha}\mathbf{S}(\mathbf{k} \otimes \mathbf{x}) = \frac{1}{\alpha}\mathbf{H}\mathbf{x} \tag{IV-7}$$

where $\mathbf{H}$ represents a linear operator combining the effects of the PSF $\mathbf{k}$ and the downsampling $\mathbf{S} \in \mathbb{R}^{N \times r^2 N}$. With pixels in $\mathbf{y}$ assumed to being mutually independent, the likelihood model is defined by:

$$p_L(\mathbf{y}|\mathbf{x}; \boldsymbol{\Theta}) = \prod_i p(y_i|\tilde{x}_i) \tag{IV-8}$$

For the prior model, a filter-based, high-order Markov random field (MRF) image prior is used as described previously [982]. The model parameters $\boldsymbol{\Omega}$ of the prior distribution are obtained from unsupervised learning from training images.

The image $\mathbf{x}$ is restored to the best estimate $\hat{\mathbf{x}}$ from the degraded image $\mathbf{y}$ by using the Bayesian MMSE estimate

$$\mathrm{E}(\mathbf{x}|\mathbf{y}) = \arg\min_{\hat{\mathbf{x}}} \int |\hat{\mathbf{x}} - \mathbf{x}|^2 \, p(\mathbf{x}|\mathbf{y}; \boldsymbol{\Theta}, \boldsymbol{\Omega}) \, d\mathbf{x} \tag{IV-9}$$

Sampling-based approximation of the MMSE is necessary as it cannot be expressed in a closed form. The likelihood is approximated by a superposition of Gaussians. Together with the MRF image prior, it allows to define a block Gibbs sampler for efficient inference.

IV.4.3.2 Cell Culture

U2OS cells (Table I-16) were cultured in DMEM++ at 37°C in humidified air with 5% CO_2. The cells were harvested with trypsin 0.05% EDTA 0.02% (with phenol red, Sigma-Aldrich/Merck). A Countess II FL Automated Cell Counter (Thermo Fisher Scientific) was used to count cells and to assess the live-to-dead cell ratio via Trypan Blue stain (0.4%). For live sample preparation, approximately 10^4 cells/well were seeded on 8-well chambered coverglasses one day prior to transfection and kept at 37°C in humidified air with 5% CO_2 until transfection.

IV.4.3.3 Live Cell Staining

One day prior to live cell imaging, the cells were transiently transfected at 40-60% confluency with the N-terminal fusion constructs pSNAPf-TRF2 (refer to II.4.1) using the Effectene Transfection Reagent Kit (Qiagen) according to the manufacturer's protocol. At 24 h post transfection, the cells were incubated for 30 min with a 1 µM staining solution of SNAP-Cell® 647-SiR (New England Biolabs) in DMEM++ at 37°C in humidified air with 5% CO_2. Following a 10 min washing step with prewarmed FluoroBrite++ at 37°C in humidified air with 5% CO_2, the cells were subjected to live cell STED imaging.

IV.4.3.4 Live Cell STED Microscopy

The custom-built STED system is described in detail in I.2.2.1. The samples were excited at 650 nm with 10 µW and depleted at 775 nm with 54 mW. The values given describe the estimated laser power in the sample focus based on laser power measurements in front of the microscope body (refer to I.2.2.1). The pixel size was set to 15 nm and the dwell time to 100 µs. No frame or line accumulation was used.

IV.4.4 Results and Discussion

Image restoration with the novel method was applied to both synthetic images and actual STED images. A 3×3 MRF was used as prior and eight filters were learned from natural images as described previously [982]. Retraining of the prior parameters on the STED data did not improve the results suggesting that the local image structures of natural and fluorescence microscopy images are similar.

The likelihood was approximated by a superposition of three Gaussians. For the synthetic data, the image noise parameters α, μ_n, σ_n and $\mathbf{H}$ were assumed to be given. For the actual STED data, the parameters were estimated. No additional parameter adaptation was required. To evaluate the novel image restoration method, its performance was compared to that of popular denoising and deconvolution methods using synthetic images. The essence of the comparison is presented here; for further details on the results of the validation, refer to the experimental section of Gao *et al.* [981].

For denoising, $\mathbf{H}$ represents an identity matrix. The superposition of three Gaussians for likelihood approximation offered a peak SNR gain of up to 0.45 dB as compared to the application of a single Gaussian likelihood. Thus, the restoration performance crucially depends on the accuracy of likelihood modelling. In comparison to the popular Poisson-Gaussian denoising method PURE-LET [972] and especially for strong noise, the present approach generated fewer artefacts in the restored images.

For deconvolution, $\mathbf{H}$ represents a convolution matrix generated from a blur kernel. In comparison to GLIAM [983], a deconvolution method for Poissonian images, the novel method was robust with respect to increased Gaussian noise contribution.

For super-resolution, $\mathbf{H}$ represents a Gaussian blurring and downsampling matrix allowing for additional denoising. In comparison to a sequential scheme of denoising with the present approach ($\mathbf{H}$ as identity matrix) and subsequent bicubic interpolation, the joint scheme of super-resolution and denoising yielded sharper edges in the restored images.

To validate the performance of the newly developed method with actual fluorescence microscopy data, image restoration of live cell STED telomere data was conducted. In such practical applications, the noise parameters α, μ_n and σ_n are not accessible. Thus, they must be estimated from the original images and different methods are available that offer the direct estimation [984, 985]. For joint super-resolution (scaling factor r = 2), deconvolution and denoising of the live cell STED telomere images, the noise parameters were estimated to be $\alpha \approx 3.2$ and $\sigma_n \approx 4.9$. Both noise and blur were significantly reduced by the joint image restoration process. In comparison to the raw data, the image resolution of the restored images increased by a factor of two (Figure IV-16).

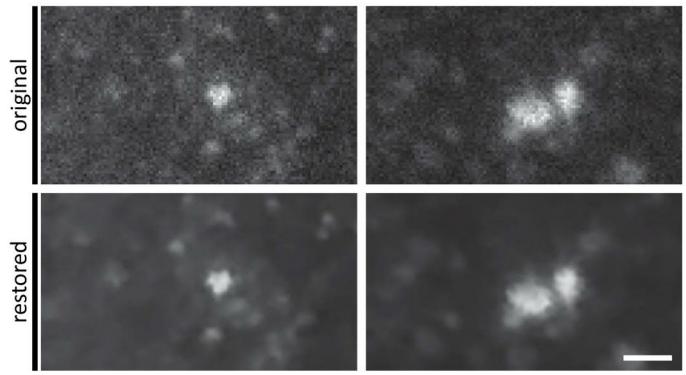

Figure IV-16. Super-resolution, deconvolution and denoising of live cell telomere STED data.

Application of the joint scheme for the restoration of live cell STED images of U2OS telomeres indirectly stained via a SNAP-tag/TRF2 fusion construct labeled with SNAP-Cell® 647-SiR. The top row shows the original images, the bottom row shows the corresponding restored images. The noise parameters were estimated as previously suggested [985]: $\alpha \approx 3.2$, $\sigma_n \approx 4.9$. Scale bar is 250 nm. Adapted from [981].

To test if the biological information content became more accessible for subsequent image analysis, the restored images as well as the raw images were subjected to segmentation and shape analysis of telomeres using a previously proposed model fitting approach [986]. This approach analytically describes the shape and intensity of heterochromatin foci and its model is based on a Fourier representation. The Fourier coefficients reflecting the foci shape are determined by fitting the model to the image intensities. Application of the model fitting approach to restored and raw data revealed that the determination of the Fourier coefficients was more accurate and robust for the restored images as compared to the raw images. Thus it was concluded that the novel Bayesian method for joint deconvolution, denoising and super-resolution is able to efficiently recover information from noise and blur degraded live cell STED images.

IV.4.5 Conclusion

The newly developed Bayesian method introduces a joint restoration model for super-resolution, deconvolution, and denoising of images with mixed Poisson-Gaussian noise.

The statistics of Poisson-Gaussian noise are well described by a superposition of Gaussians, which thus can be used to approximate the likelihood. The use of a generative probabilistic image prior renders an additional regularization parameter unnecessary. The likelihood and the prior allow for the design

of an efficient Gibbs sampler for inference. Degraded images are restored by computing the MMSE solution. The method can be directly adjusted to image restoration problems with other types of noise by the usage of an application-neutral generative image prior. Additionally, super-resolution is integrated into the model framework to simultaneously afford super-resolution, deconvolution and denoising.

The strength of this novel image restoration method was successfully demonstrated on different types of synthetic data in direct comparison to established methods. The joint scheme is superior to a sequential application of denoising and super-resolution. Especially the deconvolution performance can compete with state-of-the-art methods. The application of the joint scheme to actual STED data underlined its ability to restore biological information in degraded live cell fluorescence microscopy images and to make this information available to further sophisticated image analysis methods.

V – PERSPECTIVE

This thesis exemplifies the power of an integrated design approach for fluorescence nanoscopy imaging studies. Pooling the expertise of (bio)chemistry, biology, (photo)physics and (bio)informatics and uniting this knowledge into a coordinated workflow from sample preparation to image acquisition and finally data analysis creates a reliable platform for deriving meaningful conclusions in complex biological questions. This work demonstrates the value of iterative adaptation of individual components in the operational chain to optimize the significance of the output in the respective biological field. Creatively combining the strengths of existing methods and approaching biological questions with wide-ranging perspectives and techniques strongly boosts the quality of the results.

This thesis addresses hot topics in biomedical research in the spirit described. The individual projects in this work treat different aspects of cancer research of both direct and indirect clinical interest, while sharing methodological commonalities. Live cell STED imaging was achieved in different fashions confirming the results of sophisticated fixed staining methods. However, potential phototoxicity was not rigorously assessed as the structures of interest were not obviously affected during imaging. While this relaxed attitude might be partially justifiable, it cannot be ignored that photodamage begins prior to any visual indication.

To ultimately judge the relevance and extent of phototoxicity measures, the photophysical background must be understood to the best possible extent. Yet, comprehensive information on the relationship of photobleaching and phototoxicity in STED is difficult to assess as numerous parameters heavily influence the results while being only partially controllable. In particular, biological, biochemical, photophysical and photochemical heterogeneity demand the acquisition of enormous amounts of data for a tightly restricted set of variables under extremely well-defined conditions to generate meaningful statistics. Moreover, technical heterogeneity renders the deduction of the absolute importance of different imaging parameters and conditions from disparate STED experiments and STED implementations highly intricate.

Although phototoxicity is a known aspect of fluorescence microscopy, widely witnessed and substantially understood, it is generally covered insufficiently [950]. A more comprehensive and quantitative approach is required but difficult to draft as phototoxicity is the result of complex, nonlinear photophysical and biochemical processes. Qualitative knowledge has been collected abundantly but no common agreement on a universal measure of cell health and phototoxicity has been established to date. Two different conceptions regarding the assessment of phototoxicity presently challenge one another. The less rigorous notion considers imaging non-damaging if the structure or process of interest remains undisturbed during and directly after imaging. Yet, photodamage does not necessarily become evident during the experiment itself and short-term monitoring neglects long-term effects on cell viability [300, 305, 878, 987]. The more rigorous notion takes these long-term effects into account even though they do not affect the actual imaging results.

In the future, phototoxicity assessments will be increasingly in demand as mandatory additions to live cell imaging. This raises the requirement for some sort of measurement standard. To evaluate and compare established and newly introduced imaging techniques, specification of dose and illumination intensity at standardized samples is desirable. However, to assess potential phototoxicity in biological studies, establishing a universal assay is impossible as phototoxicity strongly varies with the sample, the setup and the biological question.

Still, common principles and guidelines should be shared in the live cell imaging community and first attempts have already been taken [877, 988]. Global changes like cell blebbing, nuclear fragmentation and cell death are often chosen to assess photodamage, but these only offer soft criteria as the sample physiology is long affected before any morphological changes or obvious photobleaching become visible [272, 298, 300, 951]. In contrast, species and stage specific dose-response curves of the structure or process of interest provide a phototoxicity threshold that reflects the point where the sample's ROS scavenging capacity is exceeded [299, 877, 987]. As this approach is complex and highly individual, a more general approach could consider the timing of the cell cycle, or in case of whole organisms, the timing of developmental stages. Since DNA replication is a delicate process relying on a properly functioning cell proliferation machinery, observing the division frequency and mitosis length should be a sensitive figure of merit and thus a harsher criterion [951, 989-995]. However, these parameters are not immediately observable and more direct disclosure is given by changed cytoskeletal dynamics, a slowed metabolism, an increased intracellular calcium level or the activation of stress-sensitive transcription factors [288, 305, 992, 996-998].

In the long run, the live cell imaging community benefits from a common perception and evaluation of phototoxicity. Different imaging approaches will be more comparable, the choice of the right approach will be easier, the risk of producing artefacts will be reduced, reliable and reproducible data will be generated, and the quality of biologically meaningful discovery will be improved.

VI – APPENDICES

VI.1 SUPPLEMENTARY MATERIAL FOR PART II

VI.1.1 Histogram Similarity Measure

To compare the results of the NN classification for individual telomere conformations between the different cell lines, it is crucial to have a measure of significance. While the inference provides a predicted frequency for each conformation and each cell line, the NN training provides the frequency of false positives and false negatives for each conformation. These three values are histogrammed as a footprint of the NN performance for each conformation of each cell line. To establish a measure of similarity between the footprints of a given conformation between the different cell lines, we chose a normalized weighted least squares sum (normalized weighted χ^2). Weighting in the terms of the sum comes from the statistical uncertainty associated with the finite training set of the NN [999].

Our training data set t consists of $N^{(t)}$ = 286 telomere STED images manually sorted into the four predefined conformations (Table VI-1):

$$N^{(t)} = \sum_{k=1}^{4} N_k^{(t)} \qquad \textbf{(VI-1)}$$

where $N_k^{(t)}$ is the number of manually sorted images (ground truth) for class (= conformation) k. Table VI-1 provides $N_k^{(t)}$ under `support´. During training, the NN classified each of these images into exactly one class. For a given class k, the ground truth images $N_k^{(t)}$ are thus given by the number of true positives $TP_k^{(t)}$ and false negatives $FN_k^{(t)}$:

$$N_k^{(t)} = TP_k^{(t)} + FN_k^{(t)} \qquad \textbf{(VI-2)}$$

Consequently, false positives $FP_k^{(t)}$ from class k must be `missing´ from other classes k' as false negatives $FN_{k'}^{(t)}$:

$$\sum_k FN_k^{(t)} = \sum_{k'} FP_{k'}^{(t)} \tag{VI-3}$$

Assuming that repetitions of generating additional ground truth data of the same nature and training the network on it would lead to a distribution of results of $TP_k^{(t)}$, $FN_k^{(t)}$ and $FP_k^{(t)}$ that follows counting statistics (Poisson statistics), the absolute errors on the quantities would be given by:

$$\Delta TP_k^{(t)} = \sqrt{TP_k^{(t)}} \tag{VI-4}$$

$$\Delta FN_k^{(t)} = \sqrt{FN_k^{(t)}} \tag{VI-5}$$

$$\Delta FP_k^{(t)} = \sqrt{FP_k^{(t)}} \tag{VI-6}$$

and the relative errors by:

$$\delta TP_k^{(t)} = \frac{\Delta TP_k^{(t)}}{TP_k^{(t)}} = \frac{1}{\sqrt{TP_k^{(t)}}} \tag{VI-7}$$

$$\delta FN_k^{(t)} = \frac{\Delta FN_k^{(t)}}{FN_k^{(t)}} = \frac{1}{\sqrt{FN_k^{(t)}}} \tag{VI-8}$$

$$\delta FP_k^{(t)} = \frac{\Delta FP_k^{(t)}}{FP_k^{(t)}} = \frac{1}{\sqrt{FP_k^{(t)}}} \tag{VI-9}$$

Next, we consider the quantities of true positives, false negatives and false positives in the application of the NN to the data to be classified. As noted above, the performance of the NN on a given image in our data set is characterized by $TP_k^{(j)}$, $FN_k^{(j)}$ and $FP_k^{(j)}$ for the conformation k and the cell line j. While $TP_k^{(j)}$ is a direct result of the inference, the estimated values of $FN_k^{(j)}$ and $FP_k^{(j)}$ must be scaled from the results of the NN training:

$$FN_k^{(j)} = FN_k^{(t)} \frac{TP_k^{(j)}}{TP_k^{(t)}} \tag{VI-10}$$

$$FP_k^{(j)} = FP_k^{(t)} \frac{TP_k^{(j)}}{TP_k^{(t)}} \tag{VI-11}$$

The relative uncertainties in $TP_k^{(j)}$, $FN_k^{(j)}$ and $FP_k^{(j)}$ are given by (Gaussian error propagation):

$$\delta TP_k^{(j)} = \frac{\Delta TP_k^{(j)}}{TP_k^{(j)}} = \frac{1}{\sqrt{TP_k^{(j)}}} \quad \textbf{(VI-12)}$$

$$\delta FN_k^{(j)} = \sqrt{\left(\delta FN_k^{(t)}\right)^2 + \left(\delta TP_k^{(j)}\right)^2 + \left(\delta TP_k^{(t)}\right)^2} \quad \textbf{(VI-13)}$$

$$\delta FP_k^{(j)} = \sqrt{\left(\delta FP_k^{(t)}\right)^2 + \left(\delta TP_k^{(j)}\right)^2 + \left(\delta TP_k^{(t)}\right)^2} \quad \textbf{(VI-14)}$$

In the following, we define the three histogram channels and their uncertainties to which we will apply our similarity analysis:

$$h_k^{(j)}(1) = \frac{TP_k^{(j)}}{N^{(j)}} \quad \textbf{(VI-15)}$$

$$h_k^{(j)}(2) = \frac{FN_k^{(j)}}{N^{(j)}} \quad \textbf{(VI-16)}$$

$$h_k^{(j)}(3) = \frac{FP_k^{(j)}}{N^{(j)}} \quad \textbf{(VI-17)}$$

where the histogram channels $i \in \{1, 2, 3\}$ are normalized by $N^{(j)}$, the total number of images per cell line j. Due to the statistical uncertainties in the finite training set and also in the classified data set, the absolute uncertainties in the histogram channels are given by:

$$\Delta h_k^{(j)}(1) = h_k^{(j)}(1)\sqrt{\left(\delta TP_k^{(j)}\right)^2 + \left(\delta N^{(j)}\right)^2} \quad \textbf{(VI-18)}$$

$$\Delta h_k^{(j)}(2) = h_k^{(j)}(2)\sqrt{\left(\delta FN_k^{(j)}\right)^2 + \left(\delta N^{(j)}\right)^2} \quad \textbf{(VI-19)}$$

$$\Delta h_k^{(j)}(3) = h_k^{(j)}(3)\sqrt{\left(\delta FP_k^{(j)}\right)^2 + \left(\delta N^{(j)}\right)^2} \quad \textbf{(VI-20)}$$

where $\delta N^{(j)} = \Delta N^{(j)}/N^{(j)}$ and $\Delta N^{(j)} = \sqrt{N^{(j)}}$ (Poisson statistics of data sample).

The simple difference between two corresponding histogram channels i of two different cell lines j and j' for the conformation k is:

$$d_k^{(j,j')}(i) = \left(h_k^{(j)}(i) - h_k^{(j')}(i)\right) \quad \textbf{(VI-21)}$$

with its corresponding uncertainty:

$$\Delta d_k^{(j,j')}(i) = \sqrt{\left(\Delta h_k^{(j)}(i)\right)^2 + \left(\Delta h_k^{(j')}(i)\right)^2} \quad \textbf{(VI-22)}$$

This distance measure is finally used to construct the weighted similarity measure χ^2:

$$(\chi^2)_k^{(j,j')} = \sum_{i=1}^{3} \frac{\left(d_k^{(j,j')}(i)\right)^2}{\left(\Delta d_k^{(j,j')}(i)\right)^2} = \sum_{i=1}^{3} \frac{\left(h_k^{(j)}(i) - h_k^{(j')}(i)\right)^2}{\left[\left(\Delta h_k^{(j)}(i)\right)^2 + \left(\Delta h_k^{(j')}(i)\right)^2\right]} \quad \textbf{(VI-23)}$$

When normalizing χ^2 by the number of data points, we obtain the measure

$$(\hat{\chi}^2)_k^{(j,j')} = \frac{(\chi^2)_k^{(j,j')}}{3} \quad \textbf{(VI-24)}$$

for which values on the order of unity indicate significant similarity and values $\gg 1$ indicate significant differences between the cell lines j and j' for the conformation k. The results are given in Table VI-3.

When the different telomere conformations are compared between free and encased U2OS telomeres, the above formalism can be used to assess significant differences between free and encased telomeres for a given conformation k. Here, j and j' represent free and encased telomeres. The results are given in Table VI-13.

VI.1.2 Supplementary Figures

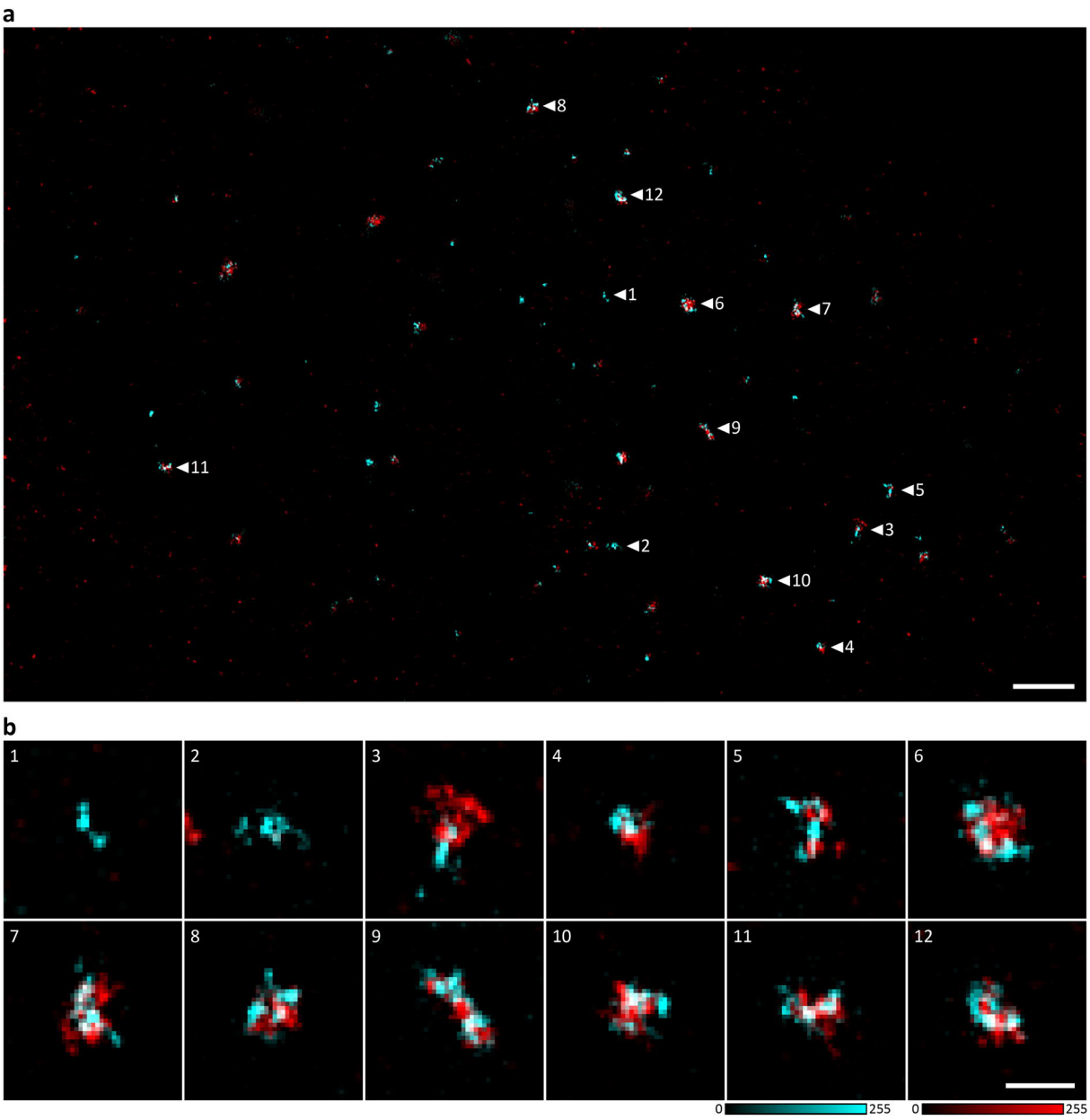

Figure VI-1. Heterogeneous TRF2 coverage of telomeres in a U2OS nucleus.

(**a**) Exemplary U2OS nucleus with telomeres stained via TelC-KK114 PNA FISH (cyan) and TRF2 stained via STAR 600-IF (red). Dual-color STED imaging revealed a heterogeneous decoration of telomeres by TRF2. (**b**) Magnifications of the telomeres marked in (**a**) by white arrows. The close-ups are arranged by increasing PCC from r(1) = -0.02 to r(12) = 0,721. All STED data shown are background corrected and linearly deconvolved. Scale bar overview is 1 µm, scale bar close-ups is 250 nm.

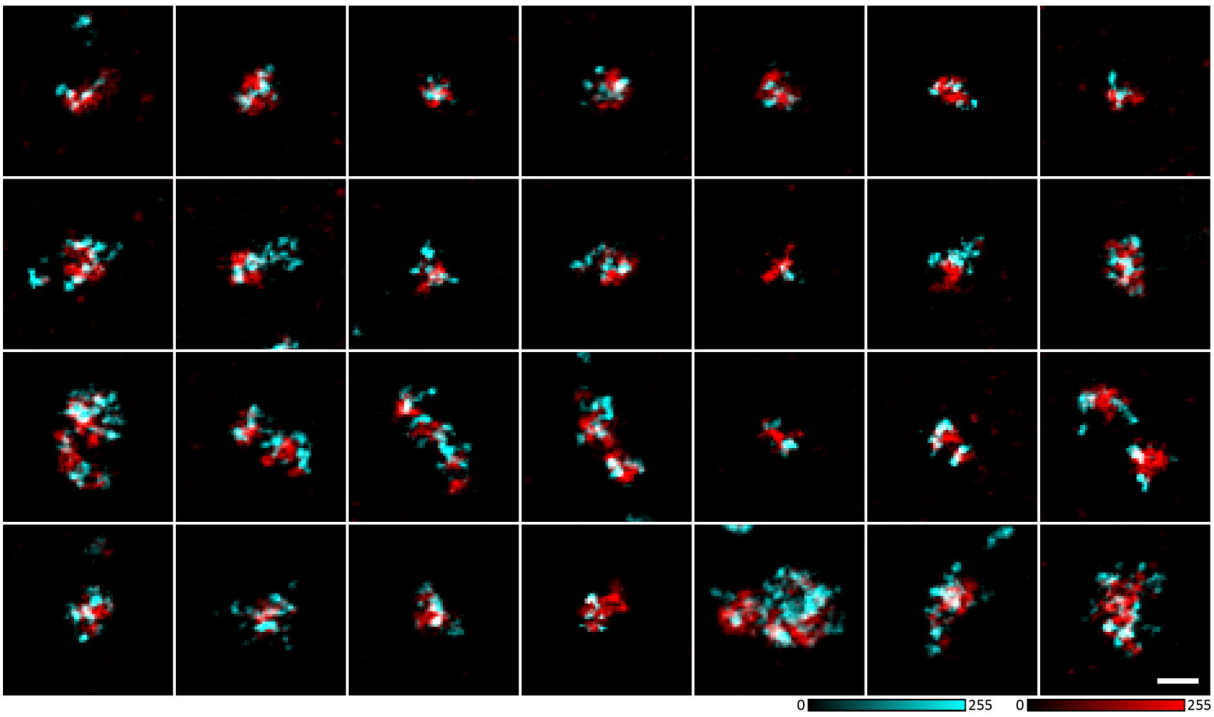

Figure VI-2. Heterogeneous TRF2 coverage of individual U2OS telomeres.

Dual-color STED close-ups of exemplary U2OS telomeres stained via TelC-KK114 PNA FISH (cyan) and bound by STAR 600-immunolabeled TRF2 (red) illustrate a heterogeneous decoration of telomeres by TRF2. All STED data shown are background corrected and linearly deconvolved. Scale bar is 250 nm.

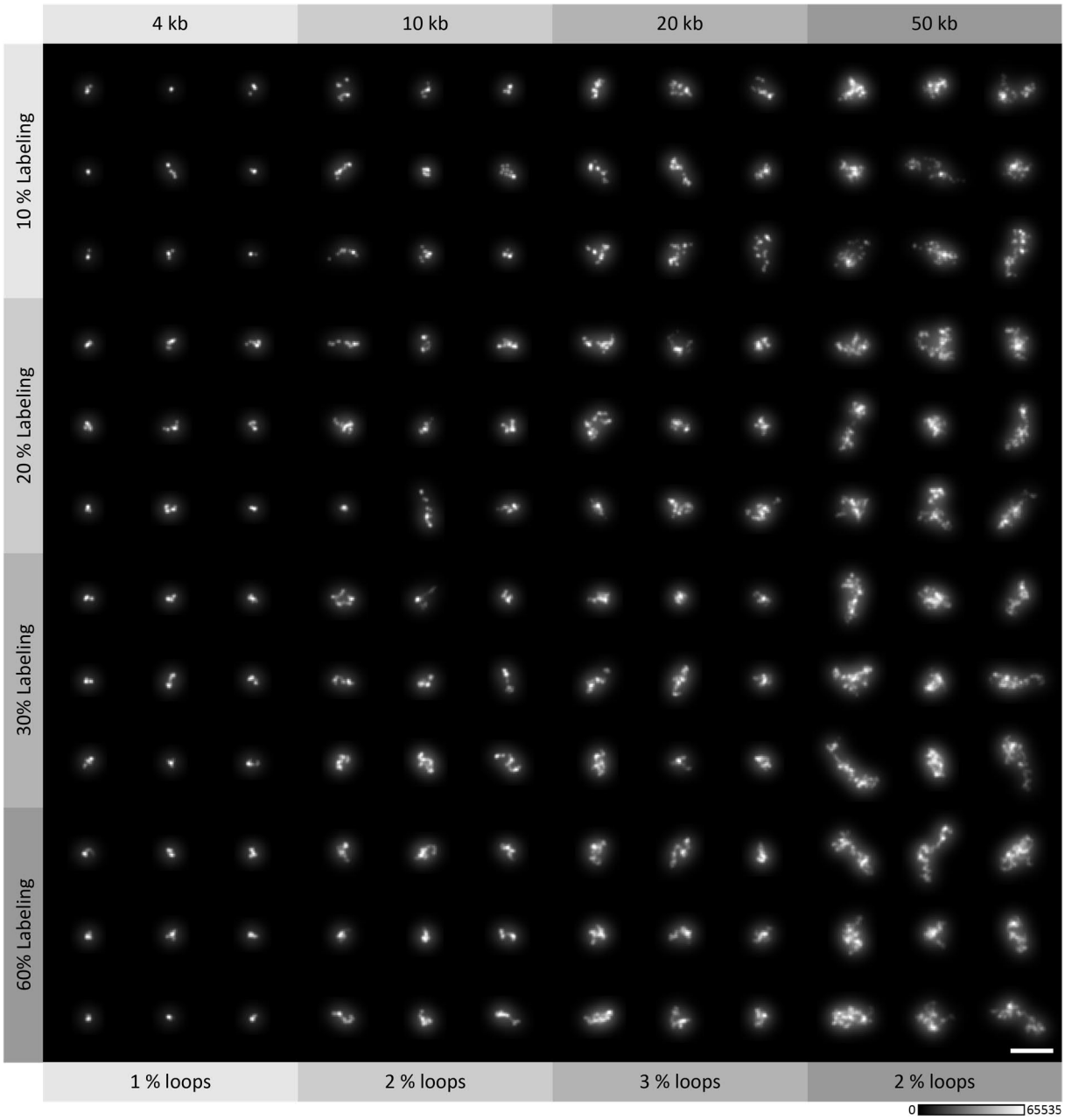

Figure VI-3. Exemplary results of the synthetic STED data generated by Monte Carlo simulations.

Representative images of the synthetic STED data generated by Monte Carlo simulations of nucleosome chains (4, 10, 20, 50 kb) and subsequent PNA FISH labeling (10, 20, 30, 60% labeling degree). The synthetic STED data were sorted identically to the NN training data and display significantly reduced *loop* frequencies of around 2% as compared to the actual STED data. This result confirms the biological control experiment. Together, these controls render the contribution of randomly formed DNA loops and/or false positives to the observed t-loop frequencies of our actual STED data assessable. Scale bar is 500 nm.

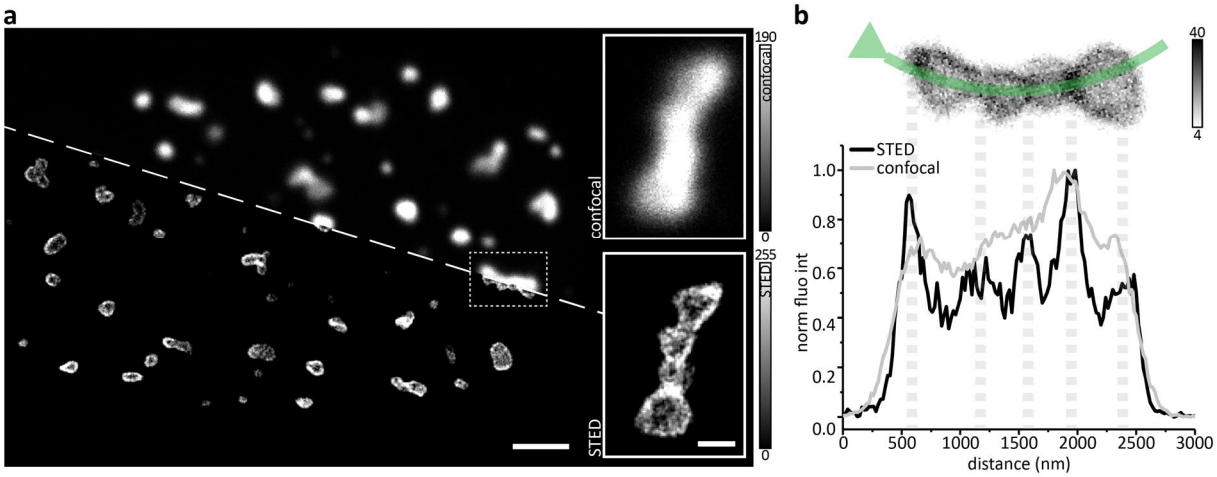

Figure VI-4. PML nuclear bodies in a living U2OS cell.

(**a**) Representative nucleus of a live U2OS cell expressing a SNAP-tag fusion construct of PML labeled with the STED compatible live dye 610CP [29]. PML-NBs appear as diffraction-limited spots in confocal (top). STED imaging reveals their hollow nature. Aggregation of several PML-NBs might promote telomere clustering as exemplified by the close-up of the PML-NB marked in the overview. (**b**) Line profiles of the confocal and STED data of the close-up shown in (**a**) illustrating the gain in structural information by STED. The line profiles were drawn on raw data and averaged over 5 pixels. All confocal data shown are raw data. All STED data shown are background corrected and linearly deconvolved, except for (**b**) showing only background corrected STED data. Scale bar nucleus is 2 µm, scale bar close-ups is 500 nm.

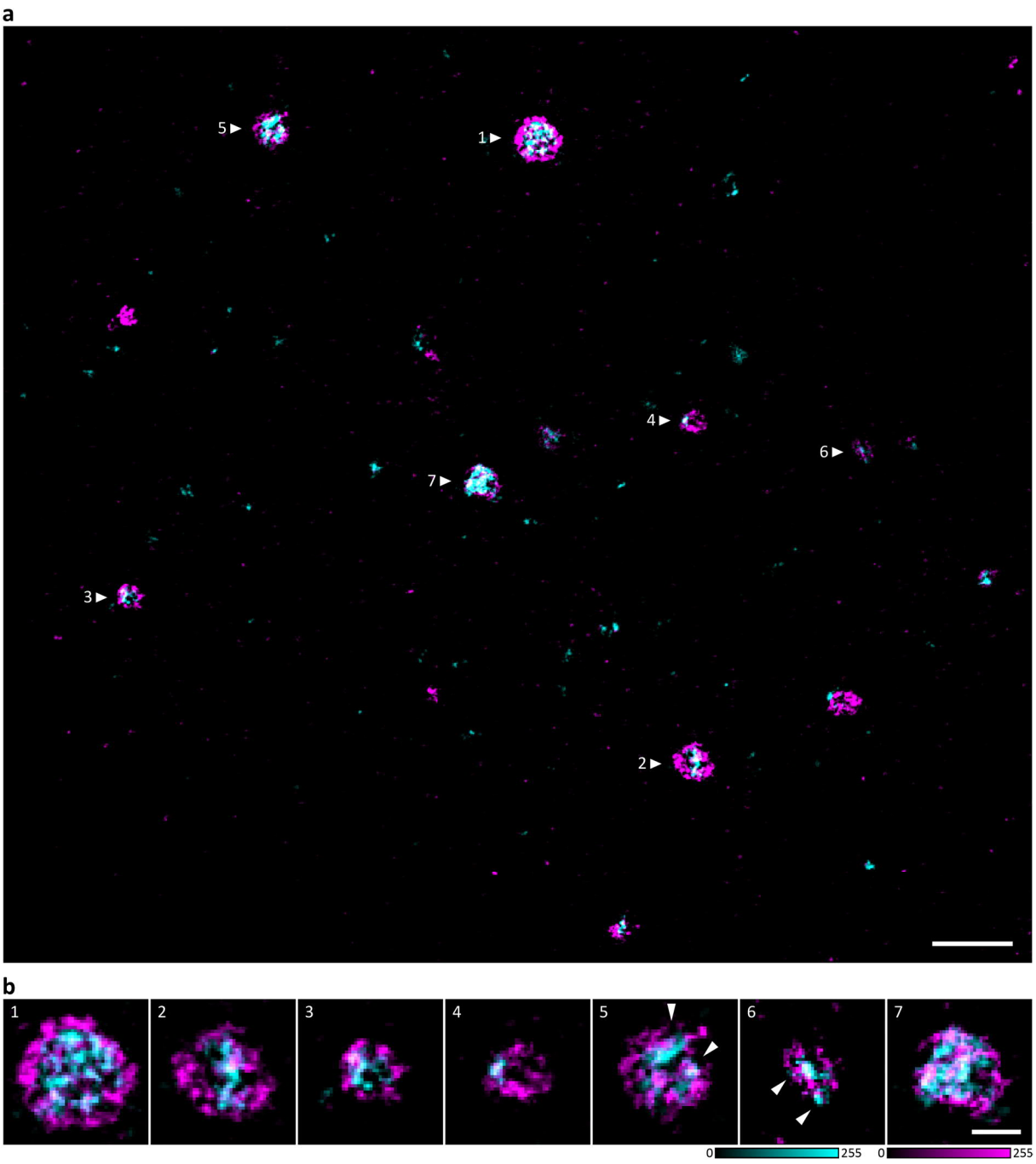

Figure VI-5. U2OS nucleus containing the four main structural classes of APBs stained by PNA FISH and IF.

(**a**) Exemplary U2OS nucleus displaying the four main structural classes of APBs as well as non-associated telomeres (TelC-KK114, cyan) and PML-NBs (IF STAR 600, magenta). (**b**) Magnifications of the APBs marked by white arrows in (**a**). Cell cycle dependent appearance of APB types can be excluded since *globular* (1), *partially hollow* (2-4), *clustered* (5, 6) and *granular* APBs (7) are simultaneously present in the same U2OS nucleus. For *clustered* APBs, the two telomeres are marked by white arrows. All STED data shown are background corrected and linearly deconvolved. Scale bar overview is 1 µm, scale bar close-ups is 250 nm.

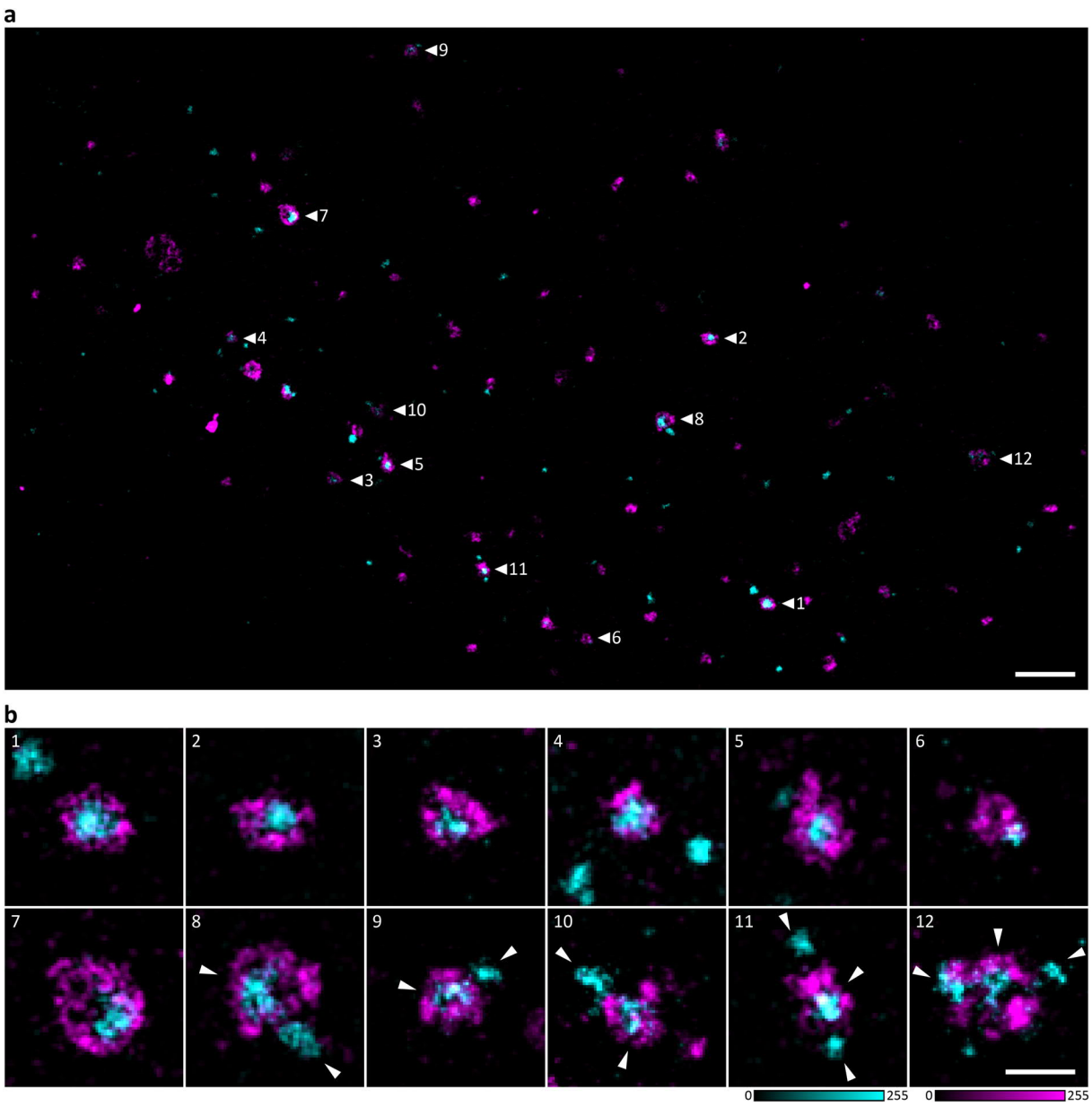

Figure VI-6. U2OS nucleus containing three of the four main structural classes of APBs stained by IF.

(**a**) Exemplary U2OS nucleus displaying three of the four main structural classes of APBs as well as non-associated telomeres (STAR 600-immunolabeled TRF2, cyan) and PML-NBs (IF STAR 635P, magenta). (**b**) Magnifications of the APBs marked by white arrows in (**a**). Cell cycle dependent appearance of APB types can be excluded since *globular* (1-5), *partially hollow* (6-8) and *clustered* (8-12) are simultaneously present in the same U2OS nucleus. For *clustered* APBs, the two (three) telomeres are marked by white arrows. Note that a single APB can comprise characteristics of two structural classes (8). All STED data shown are background corrected and linearly deconvolved. Scale bar overview is 2 µm, scale bar close-ups is 500 nm.

VI.1.3 Supplementary Tables

Table VI-1. Report of the NN training for telomere classification.

TP – true positives, FP – false positives, FN – false negatives, SD – standard deviation.

				#images			
	precision	**recall**	***F*1**	**TP**	**FP**	**FN**	**support**
loop	0.81	0.74	0.77	29	7	10	39
rod	0.71	0.71	0.71	17	7	7	24
coil	0.80	0.88	0.84	66	17	9	75
globule	0.93	0.90	0.91	133	10	15	148
average	0.81	0.81	0.81				
SD	0.08	0.08	0.08				

Table VI-2. Results of the NN classification of telomere/STR conformations for HeLa VST/NT/LT, U2OS and F6B2 cells.

FP (false positives) and FN (false negatives) are calculated according to equations (VI-10) and (VI-11) and rounded to the nearest integer.

		#images				frequency			
		loop	***rod***	***coil***	***globule***	***loop***	***rod***	***coil***	***globule***
HeLa VST	**predicted**	38	62	4	595	0.054	0.089	0.006	0.851
	FP	7	18	1	42	0.011	0.026	0.001	0.060
	FN	11	18	0	62	0.015	0.026	0.001	0.089
HeLa NT	**predicted**	28	29	17	353	0.066	0.068	0.040	0.827
	FP	5	8	3	25	0.013	0.020	0.008	0.058
	FN	8	8	2	37	0.018	0.020	0.004	0.087
HeLa LT	**predicted**	87	34	18	558	0.125	0.049	0.026	0.801
	FP	17	10	4	39	0.024	0.014	0.005	0.056
	FN	24	10	2	59	0.035	0.014	0.003	0.084
U2OS	**predicted**	191	126	428	927	0.114	0.075	0.256	0.554
	FP	37	37	88	65	0.022	0.022	0.052	0.039
	FN	53	37	46	97	0.032	0.022	0.028	0.058
F6B2	**predicted**	2	16	113	4	0.015	0.119	0.837	0.030
	FP	0	5	23	0	0.003	0.035	0.171	0.002
	FN	1	5	12	0	0.004	0.035	0.091	0.003

Table VI-3. $\hat{\chi}^2$ similarity measure for the NN classification results.

All values on the order of unity and below indicate significant similarity (shaded red) and values $\gg 1$ indicate significant differences (shaded progressively green) between the cell lines for the given conformation.

loop	HeLa VST	HeLa NT	HeLa LT	U2OS	F6B2
HeLa VST	---	---	---	---	---
HeLa NT	0.23	---	---	---	---
HeLa LT	6.90	3.89	---	---	---
U2OS	8.47	3.84	0.15	---	---
F6B2	4.23	4.89	15.85	20.54	---

rod	HeLa VST	HeLa NT	HeLa LT	U2OS	F6B2
HeLa VST	---	---	---	---	---
HeLa NT	0.57	---	---	---	---
HeLa LT	2.98	0.65	---	---	---
U2OS	0.36	0.10	2.20	---	---
F6B2	0.37	1.09	2.28	0.85	---

coil	HeLa VST	HeLa NT	HeLa LT	U2OS	F6B2
HeLa VST	---	---	---	---	---
HeLa NT	6.66	---	---	---	---
HeLa LT	5.29	0.86	---	---	---
U2OS	110.71	58.59	82.17	---	---
F6B2	26.16	23.90	24.85	12.40	---

globule	HeLa VST	HeLa NT	HeLa LT	U2OS	F6B2
HeLa VST	---	---	---	---	---
HeLa NT	0.04	---	---	---	---
HeLa LT	0.21	0.04	---	---	---
U2OS	11.23	6.64	8.29	---	---
F6B2	97.51	62.91	93.11	130.42	---

Table VI-4. Measures of telomere size for the entire telomere populations.

A – area of fluorescent signal, $hullA$ – convex hull area, R_g – radius of gyration, $hullV$ – convex hull volume, SD – standard deviation.

		HeLa VST	HeLa NT	HeLa LT	U2OS
	n	699	427	697	712
$\boldsymbol{A}$ **[10^4 × nm^2]**	**mean**	1.9	2.5	3.4	6.2
	SD	0.7	0.8	1.3	4.7
$\boldsymbol{hullA}$ **[10^4 × nm^2]**	**mean**	2.1	2.9	3.8	7.3
	SD	0.8	1.0	1.5	5.6
$\boldsymbol{R_g}$ **[nm]**	**mean**	58	68	77	103
	SD	12	13	16	36
$\boldsymbol{hullV}$ **[10^6 × nm^3]**	**mean**	3.2	5.1	7.7	23.3
	SD	1.9	2.6	4.8	30.6

Table VI-5. P-values for the measures of telomere size of the entire telomere populations.

A – area of fluorescent signal, $hullA$ – convex hull area, R_g – radius of gyration, $hullV$ – convex hull volume.

		HeLa VST	HeLa NT	HeLa LT	U2OS
$\boldsymbol{A}$	**HeLa VST**	---	---	---	---
	HeLa NT	5×10^{-41}	---	---	---
	HeLa LT	8×10^{-132}	2×10^{-34}	---	---
	U2OS	2×10^{-181}	8×10^{-99}	2×10^{-57}	---
$\boldsymbol{hullA}$	**HeLa VST**	---	---	---	---
	HeLa NT	4×10^{-46}	---	---	---
	HeLa LT	7×10^{-128}	1×10^{-25}	---	---
	U2OS	2×10^{-183}	2×10^{-96}	4×10^{-65}	---
$\boldsymbol{R_g}$	**HeLa VST**	---	---	---	---
	HeLa NT	1×10^{-37}	---	---	---
	HeLa LT	3×10^{-108}	2×10^{-21}	---	---
	U2OS	8×10^{-171}	3×10^{-90}	4×10^{-63}	---
$\boldsymbol{hullV}$	**HeLa VST**	---	---	---	---
	HeLa NT	4×10^{-46}	---	---	---
	HeLa LT	7×10^{-128}	1×10^{-25}	---	---
	U2OS	2×10^{-183}	2×10^{-96}	4×10^{-65}	---

Table VI-6. Measures of telomere size for the individual telomere conformations.

(**a**) HeLa VST, (**b**) HeLa NT, (**c**) HeLa LT, (**d**) U2OS. A – area of fluorescent signal, $hullA$ – convex hull area, R_g – radius of gyration, $hullV$ – convex hull volume, SD – standard deviation.

(a)		***loop***	***rod***	***coil***	***globule***
HeLa VST	**n**	38	62	4	595
$\boldsymbol{A}$ **[10^4 × nm^2]**	**mean**	2.6	2.4	3.0	1.8
	SD	0.8	0.7	0.6	0.6
$\boldsymbol{hullA}$ **[10^4 × nm^2]**	**mean**	3.0	2.8	3.6	1.9
	SD	0.9	0.9	0.8	0.7
$\boldsymbol{R_g}$ **[nm]**	**mean**	70	74	79	56
	SD	11	15	7	10
$\boldsymbol{hullV}$ **[10^6 × nm^3]**	**mean**	5.4	5.0	7.0	2.8
	SD	2.6	2.4	2.4	1.5

(b)		***loop***	***rod***	***coil***	***globule***
HeLa NT	**n**	28	29	17	353
$\boldsymbol{A}$ **[10^4 × nm^2]**	**mean**	3.0	2.9	3.0	2.4
	SD	0.9	1.0	1.0	0.7
$\boldsymbol{hullA}$ **[10^4 × nm^2]**	**mean**	3.6	3.7	3.9	2.7
	SD	1.0	1.3	1.1	0.9
$\boldsymbol{R_g}$ **[nm]**	**mean**	75	82	80	66
	SD	10	21	13	11
$\boldsymbol{hullV}$ **[10^6 × nm^3]**	**mean**	7.0	7.3	7.9	4.7
	SD	3.0	3.9	3.2	2.2

continued on next page

(c)		*loop*	*rod*	*coil*	*globule*
HeLa LT	**n**	87	34	18	558
A **[10^4 × nm²]**	**mean**	4.2	3.5	6.0	3.1
	SD	1.1	1.0	1.4	1.1
$hullA$ **[10^4 × nm²]**	**mean**	4.6	4.3	7.2	3.5
	SD	1.3	1.5	1.9	1.3
R_g **[nm]**	**mean**	85	91	111	73
	SD	12	21	21	13
$hullV$ **[10^6 × nm³]**	**mean**	10.2	9.3	19.7	6.8
	SD	4.3	5.2	7.7	4.0

(d)		*loop*	*rod*	*coil*	*globule*
U2OS	**n**	98	26	222	366
A **[10^4 × nm²]**	**mean**	5.1	4.3	10.0	4.3
	SD	1.6	2.0	6.2	2.3
$hullA$ **[10^4 × nm²]**	**mean**	5.9	5.5	12.0	4.9
	SD	1.9	3.0	7.4	2.6
R_g **[nm]**	**mean**	95	102	134	86
	SD	16	36	42	21
$hullV$ **[10^6 × nm³]**	**mean**	1.5	1.4	4.7	1.2
	SD	0.7	1.1	4.4	1.1

Table VI-7. P-values for the measures of telomere size of the *coil* and *globule* telomere conformations.

Comparison of the measures of telomere size of the (**a**) *coil* conformation and (**b**) *globule* conformation between the four cell lines studied. (**c**) Comparison between the measures of the *coil* and *globule* telomere size within each cell line. A – area of fluorescent signal, $hullA$ – convex hull area, R_g – radius of gyration, $hullV$ – convex hull volume.

(a) *coil vs. coil*		**HeLa VST**	**HeLa NT**	**HeLa LT**	**U2OS**
$\boldsymbol{A}$	**HeLa VST**	---	---	---	---
	HeLa NT	0.823	---	---	---
	HeLa LT	0.003	3×10^{-6}	---	---
	U2OS	0.002	3×10^{-9}	0.009	---
$\boldsymbol{hullA}$	**HeLa VST**	---	---	---	---
	HeLa NT	0.622	---	---	---
	HeLa LT	0.003	3×10^{-6}	---	---
	U2OS	0.002	6×10^{-9}	0.006	---
$\boldsymbol{R_g}$	**HeLa VST**	---	---	---	---
	HeLa NT	0.823	---	---	---
	HeLa LT	0.003	6×10^{-6}	---	---
	U2OS	0.003	1×10^{-8}	0.016	---
$\boldsymbol{hullV}$	**HeLa VST**	---	---	---	---
	HeLa NT	0.622	---	---	---
	HeLa LT	0.003	3×10^{-6}	---	---
	U2OS	0.002	6×10^{-9}	0.006	---

continued on next page

(b) *globule vs. globule*		HeLa VST	HeLa NT	HeLa LT	U2OS
A	HeLa VST	---	---	---	---
	HeLa NT	1×10^{-40}	---	---	---
	HeLa LT	9×10^{-116}	2×10^{-26}	---	---
	U2OS	1×10^{-109}	4×10^{-52}	3×10^{-20}	---
$hullA$	HeLa VST	---	---	---	---
	HeLa NT	6×10^{-46}	---	---	---
	HeLa LT	3×10^{-115}	1×10^{-20}	---	---
	U2OS	4×10^{-112}	3×10^{-51}	2×10^{-24}	---
R_g	HeLa VST	---	---	---	---
	HeLa NT	3×10^{-41}	---	---	---
	HeLa LT	7×10^{-104}	7×10^{-18}	---	---
	U2OS	2×10^{-106}	2×10^{-48}	3×10^{-24}	---
$hullV$	HeLa VST	---	---	---	---
	HeLa NT	6×10^{-46}	---	---	---
	HeLa LT	3×10^{-115}	1×10^{-20}	---	---
	U2OS	4×10^{-112}	3×10^{-51}	2×10^{-24}	---

(c) *coil vs. globule*	HeLa VST	HeLa NT	HeLa LT	U2OS
A	0.001	0.001	7×10^{-11}	1×10^{-42}
$hullA$	7×10^{-4}	1×10^{-5}	2×10^{-11}	2×10^{-46}
R_g	7×10^{-4}	2×10^{-6}	1×10^{-11}	2×10^{-47}
$hullV$	7×10^{-4}	1×10^{-5}	2×10^{-11}	2×10^{-46}

Table VI-8. Ratio of volume densities of the entire telomere populations.

The SDs (standard deviations) were calculated by Gaussian error propagation using the computed SDs of the radii of gyration and the following SD estimates for the average telomere lengths: HeLa VST 2.0 ± 0.5 kb (TRF analysis), HeLa NT 7.0 ± 0.5 kb (TRF analysis), HeLa LT 20 ± 1 kb (TRF analysis), U2OS 26 ± 13 kb (rectangular telomere length distribution between 2-50 kb); HeLa VST n = 699, HeLa NT n = 427, HeLa LT n = 697 and U2OS n = 712.

		HeLa VST	HeLa NT	HeLa LT	U2OS
HeLa VST	**mean**	---	---	---	---
	SD	---	---	---	---
HeLa NT	**mean**	2.2	---	---	---
	SD	2.0	---	---	---
HeLa LT	**mean**	4.4	2.0	---	---
	SD	4.0	1.7	---	---
U2OS	**mean**	2.4	1.1	0.5	---
	SD	3.2	1.4	0.7	---

Table VI-9. Ratio of volume densities of the *coil* and *globule* telomere conformations.

(**a**) *Coil*-to-*globule* ratio of volume densities for each cell line. (**b**) Ratio of volume densities between the *coil* (*globule*) conformation of each cell line and the U2OS *coil* (*globule*) conformation. The SDs (standard deviations) were calculated by Gaussian error propagation using the computed SDs of the radii of gyration and the following SD estimates for the average telomere lengths: HeLa VST 2.0 ± 0.5 kb (TRF analysis), HeLa NT 7.0 ± 0.5 kb (TRF analysis), HeLa LT 20 ± 1 kb (TRF analysis), U2OS 26 ± 13 kb (rectangular telomere length distribution between 2-50 kb); *coil* conformation HeLa VST n = 4, HeLa NT n = 17, HeLa LT n = 18, U2OS n = 222; *globule* conformation HeLa VST n = 595, HeLa NT n = 353, HeLa LT n = 558, U2OS n = 366.

(a)		HeLa VST	HeLa NT	HeLa LT	U2OS
coil*-to-*globule	**mean**	0.3	0.6	0.3	0.3
	SD	0.2	0.4	0.2	0.4

(b)			HeLa VST	HeLa NT	HeLa LT	U2OS
U2OS	***coil*-to-*coil***	**mean**	2.7	0.8	0.7	---
	globule*-to-*globule	**SD**	2.8	0.8	0.9	---

Table VI-10. Results and p-values of ellipse fitting and t-loop circumference C calculation.

a – semi-major axis, b – semi-minor axis, C – circumference, data are expressed as mean ± SD.

				p-values			
	a [nm]	b [nm]	C [nm]	HeLa VST	HeLa NT	HeLa LT	U2OS
HeLa VST	55 ± 17	36 ± 9	267 ± 74	---	---	---	---
HeLa NT	48 ± 13	34 ± 10	241 ± 62	0.092	---	---	---
HeLa LT	63 ± 22	44 ± 14	312 ± 99	0.017	4×10^{-4}	---	---
U2OS	68 ± 19	49 ± 13	342 ± 87	4×10^{-7}	3×10^{-9}	0.010	---

Table VI-11. Estimation of the maximum error of t-loop circumference introduced by 2D projection.

C – circumference calculated from results of ellipse fitting, C_{ideal} – circumference of circular t-loop with radius a (semi-major axis of ellipse fitting), data are expressed as mean ± SD.

	a [nm]	C [nm]	$C_{ideal} = 2\pi a$ [nm]	C/C_{ideal}
HeLa VST	55 ± 17	267 ± 74	343 ± 109	0.78
HeLa NT	48 ± 13	241 ± 62	302 ± 82	0.80
HeLa LT	63 ± 22	312 ± 99	395 ± 135	0.79
U2OS	68 ± 19	342 ± 87	429 ± 119	0.80

Table VI-12. Results of the NN classification of telomere conformations for free and encased U2OS telomeres.

FP – false positives, FN – false negatives.

		#images				frequency			
		loop	*rod*	*coil*	*globule*	*loop*	*rod*	*coil*	*globule*
free	**predicted**	80	96	83	521	0.103	0.123	0.106	0.668
	FP	16	28	17	36	0.020	0.036	0.022	0.047
	FN	22	28	9	55	0.028	0.036	0.012	0.070
encased	**predicted**	13	4	123	50	0.068	0.021	0.647	0.263
	FP	3	1	25	3	0.013	0.006	0.133	0.018
	FN	4	1	13	5	0.019	0.006	0.070	0.028

Table VI-13. $\hat{\chi}^2$ similarity measure for the NN classification results for free and encased U2OS telomeres.

All values on the order of unity and below indicate significant similarity (shaded red) and values $\gg 1$ indicate significant differences (shaded progressively green) between free and encased telomere for the given conformation.

	loop	*rod*	*coil*	*globule*
free *vs.* encased	1.00	13.97	21.14	19.44

Table VI-14. Measures of telomere size for free and encased U2OS telomeres without discrimination of conformations.

A – area of fluorescent signal, $hullA$ – convex hull area, R_g – radius of gyration, $hullV$ – convex hull volume, SD – standard deviation, free n = 780, encased n = 190.

		free	encased	p-values
$\boldsymbol{A}$**[10⁴ × nm²]**	**mean**	3.0	11.7	6×10^{-81}
	SD	2.0	6.8	
$\boldsymbol{hullA}$ **[10⁴ × nm²]**	**mean**	3.8	14.3	6×10^{-79}
	SD	2.6	8.6	
$\boldsymbol{R_g}$ **[nm]**	**mean**	75	146	6×10^{-77}
	SD	24	46	
$\boldsymbol{hullV}$ **[10⁶ × nm³]**	**mean**	8.6	60.9	6×10^{-79}
	SD	10.2	59.3	

Table VI-15. Measures of telomere size for the individual conformations of free and encased U2OS telomeres.

A – area of fluorescent signal, $hullA$ – convex hull area, R_g – radius of gyration, $hullV$ – convex hull volume, SD – standard deviation.

		loop		*rod*		*coil*		*globule*	
		free	**encased**	**free**	**encased**	**free**	**encased**	**free**	**encased**
	n	80	13	96	4	83	123	521	50
$\boldsymbol{A}$ **[10^4 × nm^2]**	**mean**	3.6	5.3	2.8	3.6	5.9	14.0	2.5	8.4
	SD	1.3	1.5	1.4	1.5	3.3	7.0	1.5	4.0
$\boldsymbol{hullA}$ **[10^4 × nm^2]**	**mean**	4.4	6.2	3.9	5.1	7.8	17.3	3.1	9.7
	SD	1.6	1.7	2.0	2.6	4.2	9.0	1.8	4.4
$\boldsymbol{R_g}$ **[nm]**	**mean**	81	97	81	96	107	163	67	119
	SD	15	14	25	31	27	45	19	29
$\boldsymbol{hullV}$ **[10^6 × nm^3]**	**mean**	9.7	16.0	8.4	12.3	23.7	78.7	6.1	32.6
	SD	5.3	6.4	6.5	8.8	21.1	65.5	5.6	22.6

p-values				
$\boldsymbol{A}$	8×10^{-5}	---	6×10^{-22}	9×10^{-26}
$\boldsymbol{hullA}$	3×10^{-4}	---	1×10^{-20}	4×10^{-25}
$\boldsymbol{R_g}$	0.001	---	1×10^{-20}	2×10^{-24}
$\boldsymbol{hullV}$	3×10^{-4}	---	1×10^{-20}	4×10^{-25}

VI.2 Supplementary Material for Part III

VI.2.1 Supplementary Figures

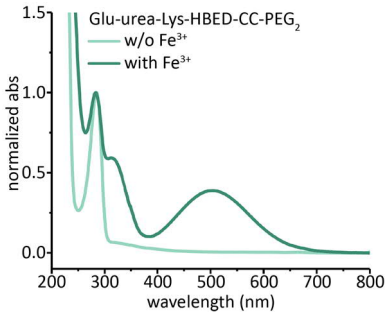

Figure VI-7. Absorbance of Glu-urea-Lys-HBED-CC-PEG$_2$ with Fe $^{3+}$ and without Fe^{3+}.

UV/vis absorbance was recorded in PBS at pH 7.4. Raw data were baseline corrected and normalized to the peak around 280 nm, which is attributed to the UV-active HBED-CC chelator moiety.

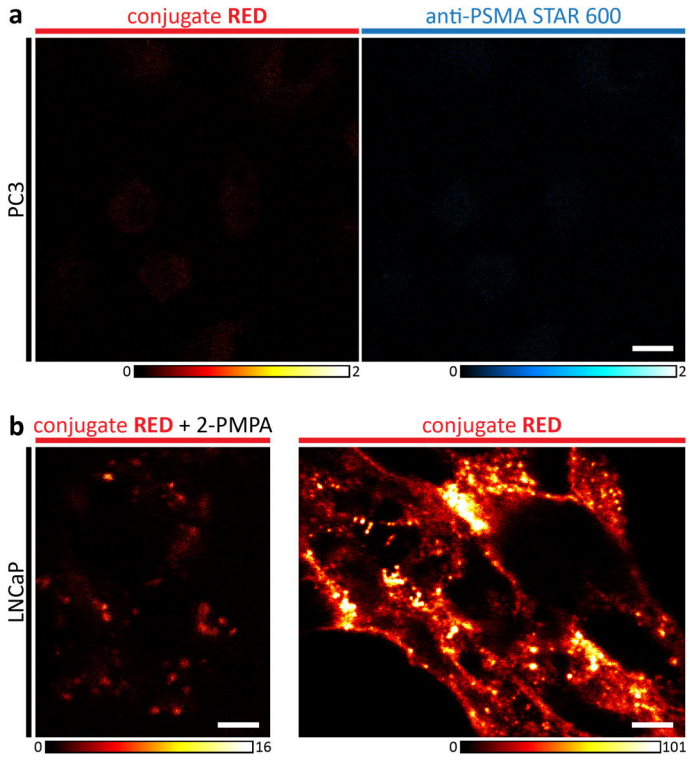

Figure VI-8. PC3 cell incubation and PMPA blocking confirm conjugate RED specificity.

The negative controls confirm specific PSMA binding and internalization of conjugate **RED**. (**a**) PSMA binding and internalization specificity of conjugate **RED** was confirmed by staining PSMA-negative PC3 cells via IF for PSMA (STAR 600, cyan, right) and incubation with conjugate **RED** (100 nM, red, left) for 1 h of internalization time with subsequent PFA fixation. Confocal imaging did not detect significant binding or internalization of conjugate **RED** with PC3 cells. Scale bar is 10 µm. (**b**) Left: LNCaP cells were co-incubated with conjugate **RED** (50 nM) and 2-PMPA (500 µM) on ice. Internalization of the PSMA/PSMA inhibitor complex should be triggered by subsequent temperature increase, but live confocal imaging did not detect significant binding or internalization of conjugate **RED** after 20 min. Right: Positive control showing live LNCaP cells incubated with conjugate **RED** (50 nM) for 15 min of internalization time. Scale bars are 5 µm. All confocal data shown are raw data.

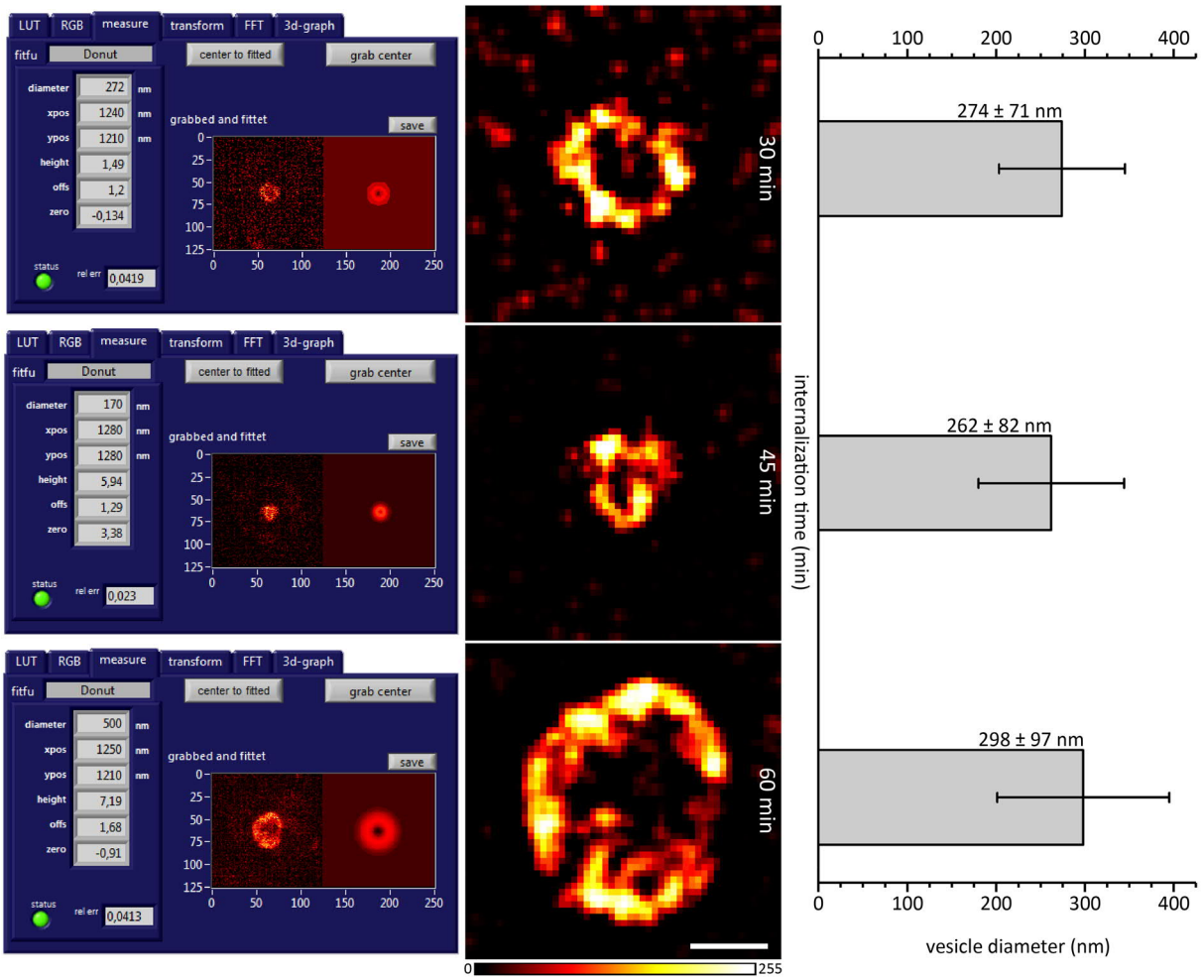

Figure VI-9. Average diameter d of endocytic vesicles carrying conjugate RED bound PSMA.

LNCaP cells were incubated with conjugate **RED** (100 nM) for 30 min (top), 45 min (middle) or 60 min (bottom). The vesicle diameter was assessed by fitting a two-dimensional ring function (refer to equation (III-5)) to the raw fluorescence signal of individual vesicles. The results were averaged for every internalization time (n = 50). The average diameter d of the different internalization times did not differ significantly ($p > 0.05$). The large SDs of the results suggest a broad diameter distribution in the samples. The STED data shown in the user interface of the fit program are smoothed with a Gaussian low pass filter (width of one pixel), the remaining STED data are background corrected and linearly deconvolved. Scale bar is 250 nm.

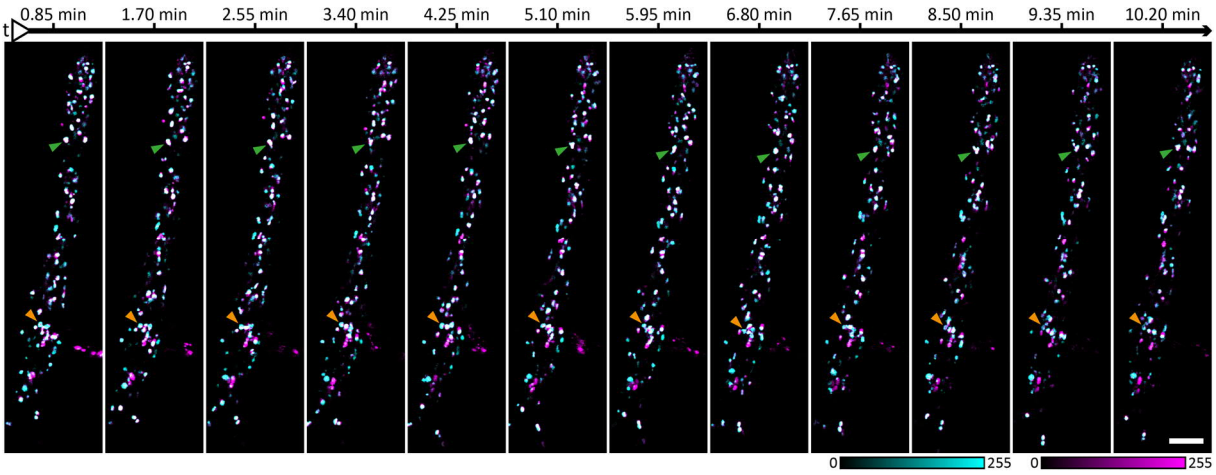

Figure VI-10. STED/confocal time-lapse sequence of PSMA/LysoTracker™ Green DND-26 colocalization experiment.

To assess endosomal/lysosomal colocalization of PSMA, LNCaP cells were STAR 600-immunolabeled for PSMA (cyan) and imaged in the presence of LysoTracker™ Green DND-26 (500 nM, magenta) after > 20 h of internalization. Live STED (anti-PSMA STAR 600) and confocal (LysoTracker™ Green DND-26) time-lapse sequences were recorded for 10 min with 1.2 fpm. The green and yellow arrows follow two dual-labeled endosomes/lysosomes. STED and confocal data are background corrected and linearly deconvolved. Scale bar is 5 µm.

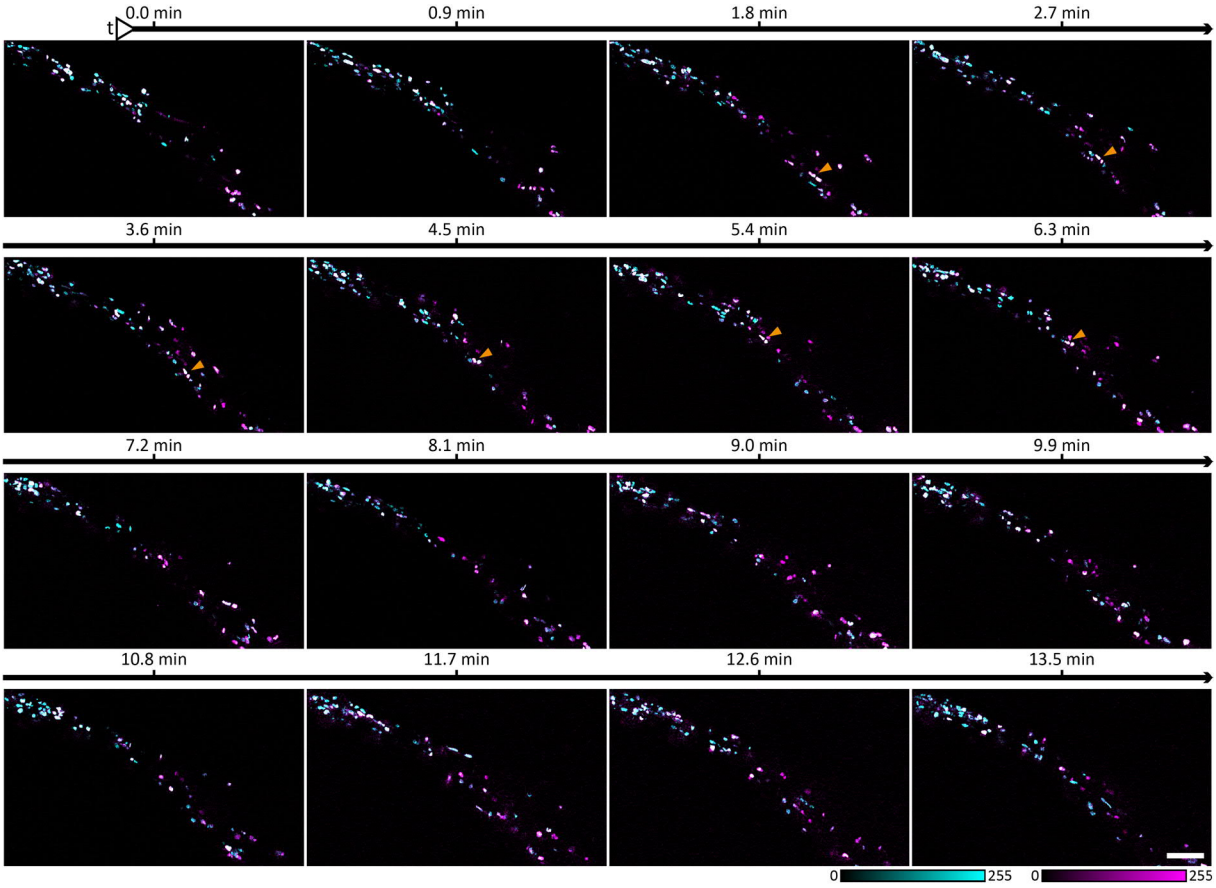

Figure VI-11. STED time-lapse sequence of PSMA/SiR-Lysosome colocalization experiment.

To assess endosomal/lysosomal colocalization of PSMA, LNCaP cells were STAR 600-immunolabeled for PSMA (cyan) and stained with SiR-Lysosome (1 µM, magenta) after > 20 h of internalization. Live STED time-lapse sequences were recorded for 13.5 min with 1.1 fpm. The yellow arrow follows a dual-labeled endosome/lysosome. STED data are photobleaching and background corrected and linearly deconvolved. Scale bar is 5 µm.

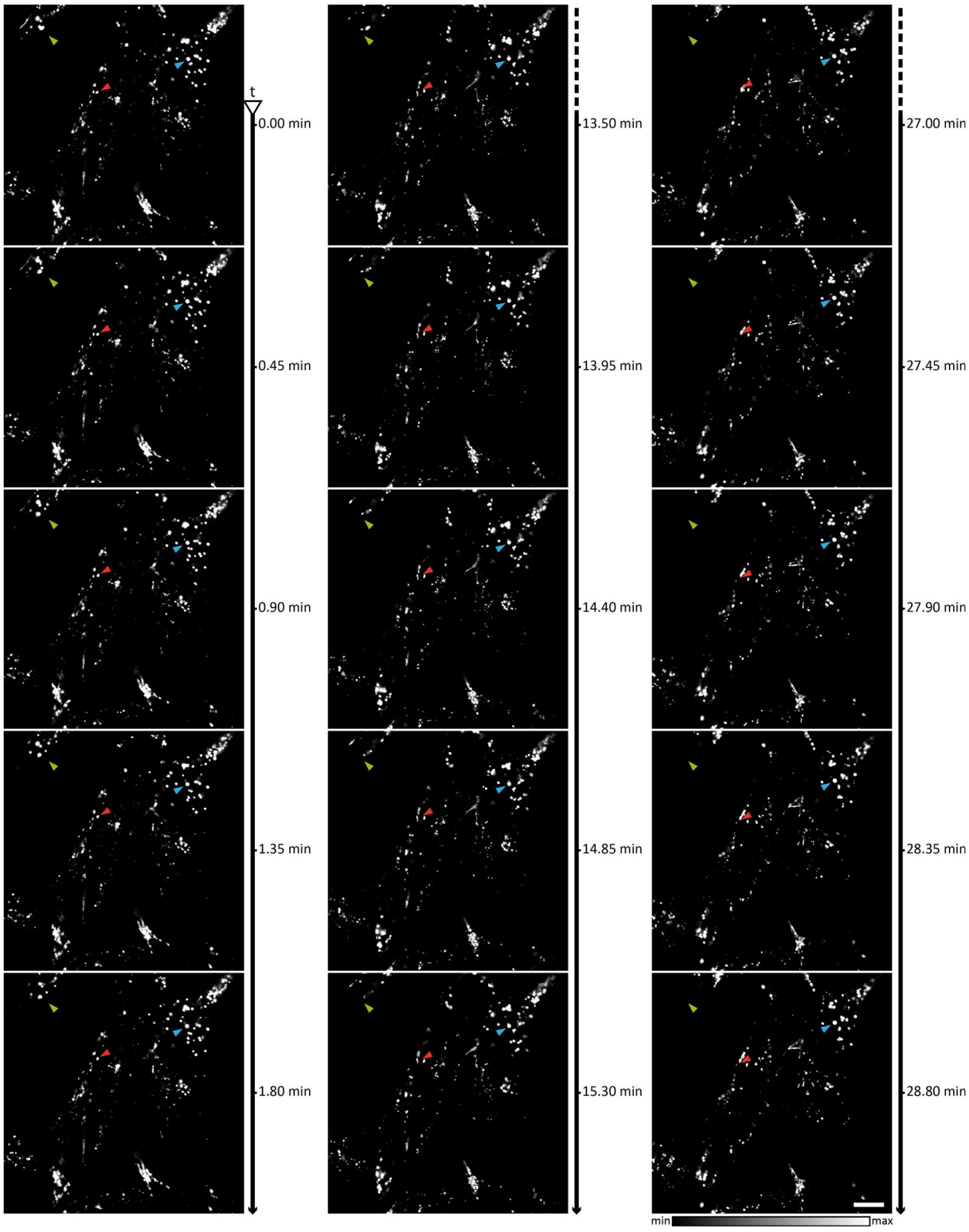

Figure VI-12. Confocal time-lapse sequence of SiR-Lysosome stained endosomes and lysosomes.

Low light confocal control time-lapse series (28.8 min, 2.1 fpm) of LNCaP cells stained with SiR-Lysosome (1 µM). Sequences of five consecutive images are displayed for the beginning (1st column), the middle (2nd column) and the end (3rd column) of the time-lapse data. Red and blue arrows follow two rather stationary endosomes/lysosomes with only local dynamics; green arrows mark a region of increased dynamics with more mobile endosomes/lysosomes. The dynamics were qualitatively compared to those of low light confocal time-lapse series after STED imaging (Figure VI-13). Confocal data are background corrected. From left to right/top to bottom, the minimal and maximal (min/max) counts are 19/196, 19/192, 19/192, 19/198, 18/189, 18/180, 19/190, 18/180, 18/181, 182/180, 16/168, 16/169, 16/166, 16/168, 16/166. Scale bar is 10 µm.

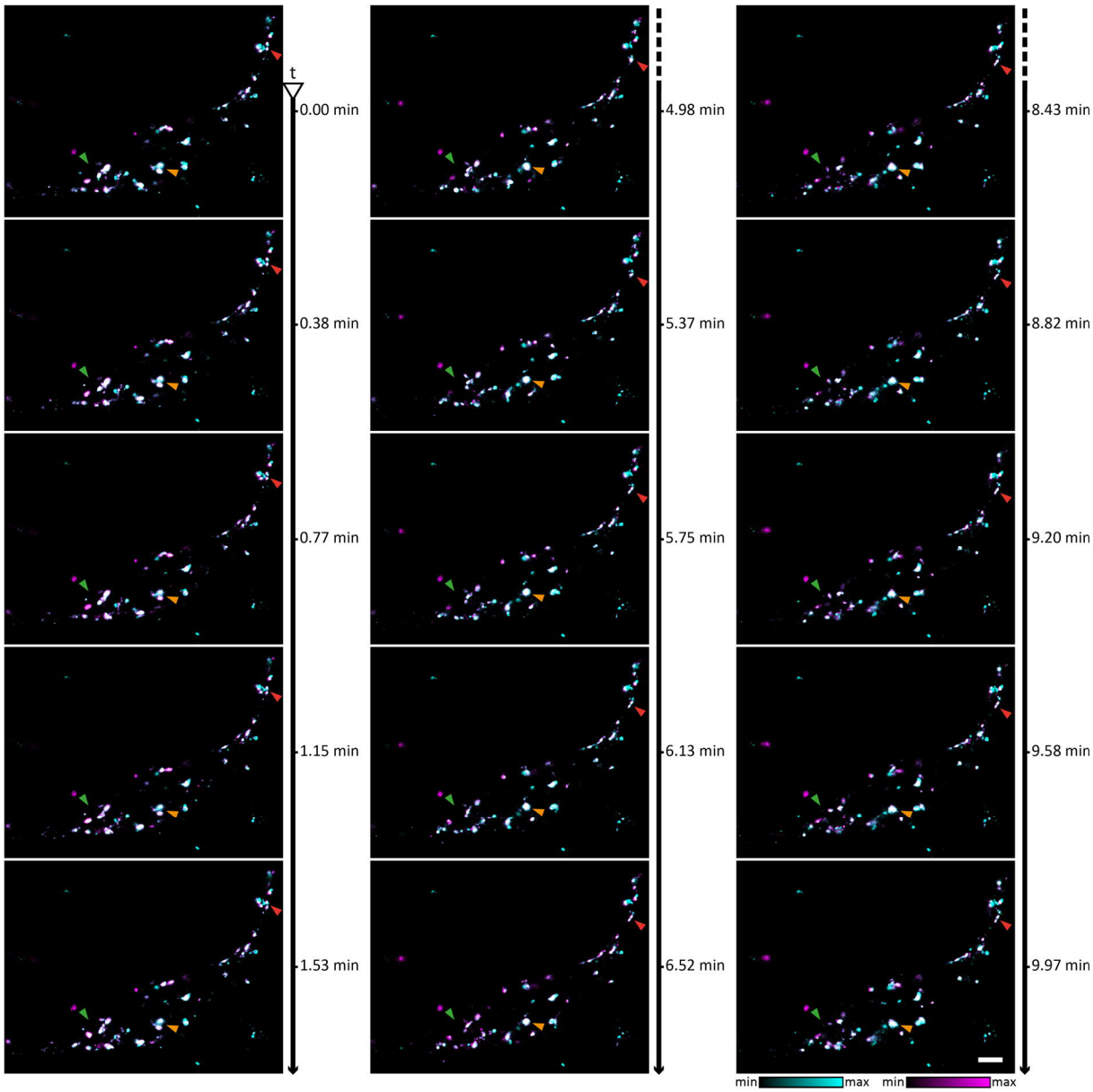

Figure VI-13. Confocal time-lapse sequence of PSMA/SiR-Lysosome colocalization after STED imaging.

To evaluate cell viability after PSMA/SiR-Lysosome STED colocalization experiments, low intensity confocal time-lapse series were recorded for 10 min with 2.6 fpm after STED imaging. Anti-PSMA STAR 600 is shown in cyan, SiR-Lysosome is shown in magenta. Sequences of five consecutive images are displayed for the beginning (first column), the middle (second column) and the end (third column) of the time-lapse data. Red and yellow arrows follow two rather stationary dual-labeled endosomes/lysosomes with only local dynamics; green arrows mark a region of increased dynamics with more mobile endosomes/lysosomes. The dynamics were qualitatively compared to confocal control time-lapse series (Figure VI-12). No significant differences were observed. Figure VI-14 shows the corresponding live cell dual-color STED image. Confocal data are background corrected. From left to right/top to bottom, the minimal and maximal (min/max) counts for the STAR 600 and SiR channel (STAR 600//SiR) are 5/54//5/54, 5/58//4/49, 6/68//5/51, 6/66//5/55, 6/61//4/49, 5/52//5/52, 5/52//5/56, 5/55//5/57, 5/54//5/56, 6/67//4/44, 6/64//4/47, 5/50//5/53, 5/56//4/44, 5/54//4/49, 5/50//5/50. Scale bar is 5 µm.

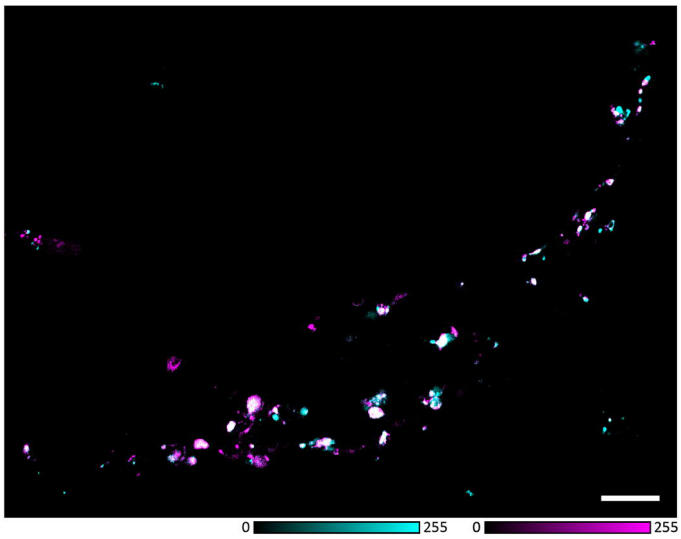

Figure VI-14. Corresponding live cell dual-color STED image to the confocal time-lapse sequence shown in Figure VI-13.

Dual-color STED image of a live LNCaP cell STAR 600-immunolabeled for PSMA and stained with SiR-Lysosome (1 µM) after > 20 h of internalization time. After STED acquisition, the lysosomal/endosomal dynamics were followed via low light intensity confocal time-lapse imaging to evaluate potential phototoxicity. The corresponding image sequence is shown in Figure VI-13. The STED data shown are background corrected and linearly deconvolved. Scale bar is 5 µm.

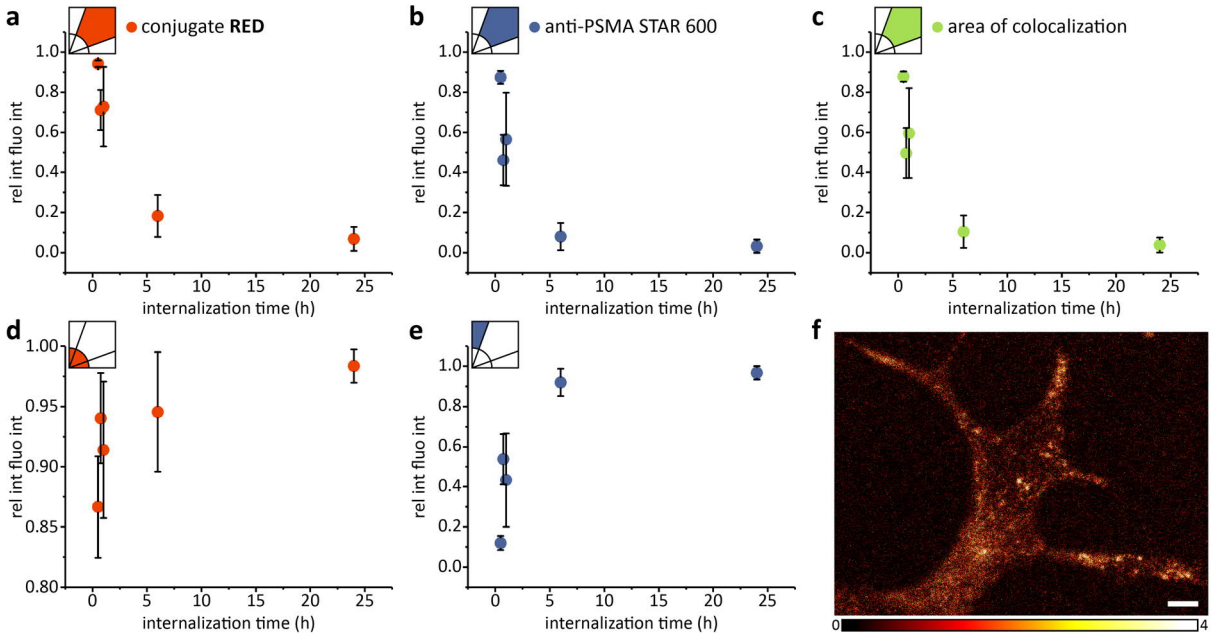

Figure VI-15. Corresponding time curves to the fluorogram analysis of conjugate RED/PSMA colocalization.

The time curves represent the internalization time-dependent changes of the relative integrated fluorescence intensity of STAR 600-immunolabeled PSMA and conjugate **RED** in the different sections of the fluorograms shown in (Figure III-20). Upon progressive segregation of the PSMA/PSMA inhibitor complex, the relative integrated fluorescence intensity of (**a**) conjugate **RED** (red) and of (**b**) PSMA (blue) declines in the colocalizing section of the fluorogram. (**c**) Consequently, the area of colocalizing signal decreases. (**d**) Simultaneously, the relative integrated fluorescence intensity of conjugate **RED** in the background increases upon cytosolic conjugate **RED** distribution. (**e**) In contrast, the relative integrated fluorescence intensity of PSMA increases in the `PSMA signal only´ section of the fluorogram since the primary/secondary antibody/PSMA complex remains intact. All changes in the relative integrated fluorescence intensity from 30 min to 45 min and from 1 h to 6 h (except for (d)), are significant ($p < 0.005$). No significant changes occur from 45 min to 1 h (30 min n = 8, 45 min n = 11, 1 h n = 24, 6 h n = 10, 24 h n = 4). (**f**) Exemplary confocal image of conjugate **RED** after 24 h of internalization time confirming cytosolic distribution and long-time retention of conjugate **RED**. Raw data are shown. Scale bar is 5 µm.

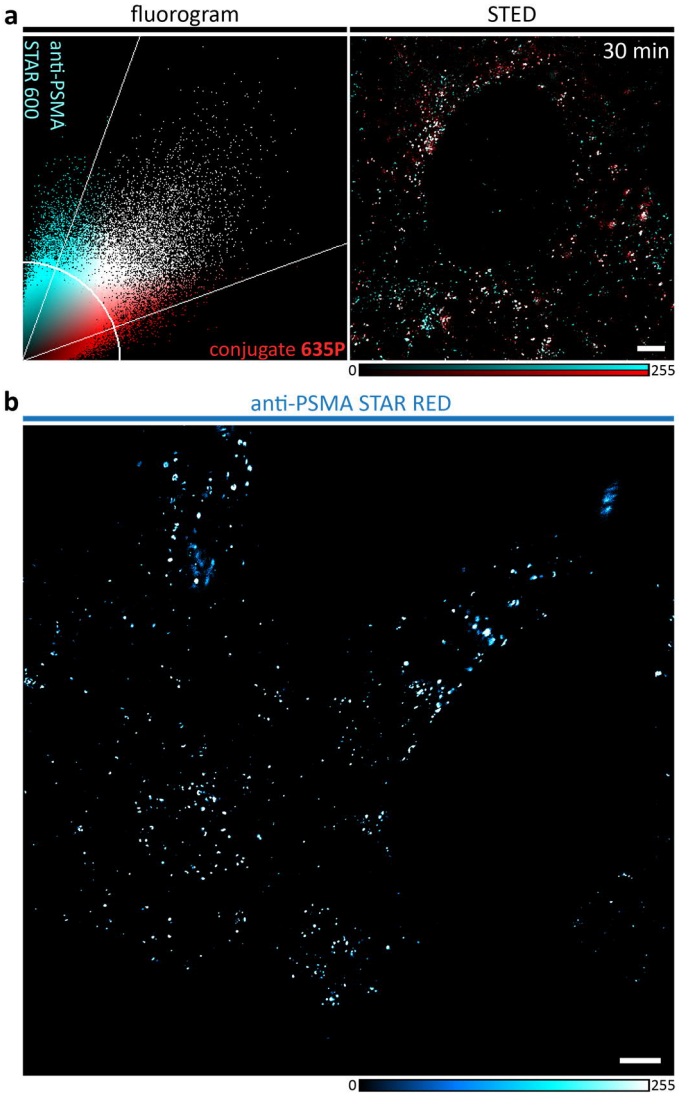

Figure VI-16. Excluding dye dependence of PSMA/PSMA inhibitor colocalization.

(**a**) Exemplary dual-color STED image with its corresponding fluorogram is shown for LNCaP cells STAR 600-immunolabeled for PSMA (cyan) and incubated with conjugate **635P** (100 nM, red) for 30 min of internalization time. The fluorogram is subdivided into three defined sections representing PSMA signal only (top, cyan), colocalizing signal (middle, white) and conjugate **635P** signal only (bottom, red). Background (quarter circle bottom left) was set to the average conjugate **RED** fluorescence intensity in the cytosol after 24 h of internalization time. The quantification of conjugate **635P**/PSMA colocalization via fluorogram analysis supports the results obtained for conjugate **RED**. (**b**) Exemplary STED image of LNCaP cells after 1 h of internalization STAR RED-immunolabeled for PSMA. Between STAR-600- and STAR RED-immunolabeled PSMA, qualitative differences could not be observed. Taken together, these results indicate the absence of dye dependent effects on the PSMA/PSMA inhibitor colocalization results. All STED data shown are background corrected and linearly deconvolved. Scale bars are 5 µm.

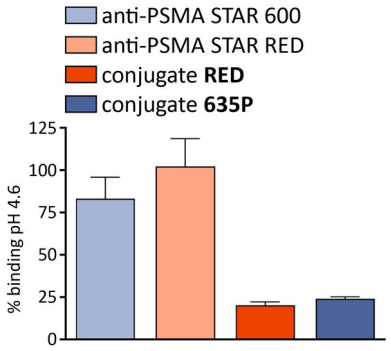

Figure VI-17. Influence of pH on the PSMA binding affinity of conjugate RED, conjugate 635P and the antibody complex.

Characterization of pH dependent binding of the primary/secondary antibody complexes (primary anti-PSMA antibody + secondary IgG-STAR 600, primary anti-PSMA antibody + secondary IgG-STAR RED antibody, all antibodies 1:50), of conjugate **RED** (50 nM) and of conjugate **635P** (50 nM) to PSMA on LNCaP cells. Flow cytometry determined the binding percentage at pH 4.6 normalized to the binding percentage at pH 7.0. Data are expressed as mean ± SD (n = 3). The antibody complexes did not show a strong pH dependence of PSMA binding, whereas both PSMA inhibitors displayed significantly weaker PSMA binding at acidic pH.

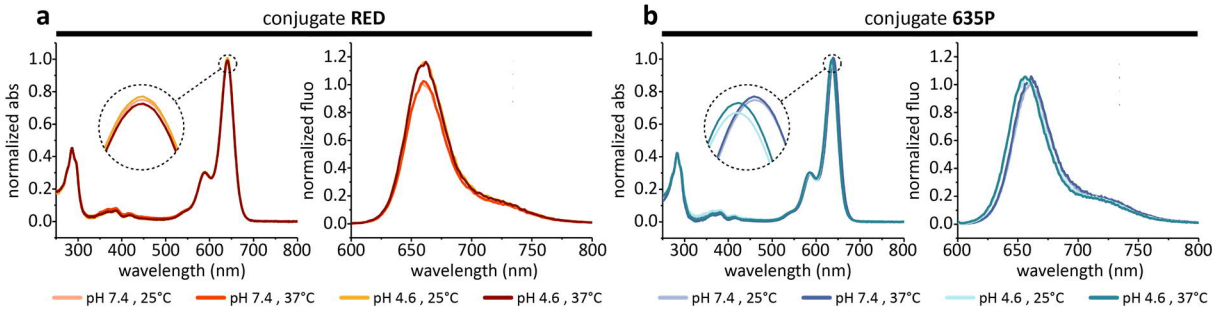

Figure VI-18. Influence of pH and temperature on the spectral properties of conjugate RED and conjugate 635P.

Conjugate **RED** and conjugate **635P** (both 10 µM) were incubated for 6 h in the dark at different pH and temperature combinations (PBS pH 7.4 at 25°C, PBS pH 7.4 at 37°C, NaAc buffer pH 4.6 at 25°C, NaAc buffer pH 4.6 at 37°C). During the experiment, (**a**) the conjugate **RED** absorbance did not display strong pH and/or temperature dependence and the conjugate **RED** fluorescence emission was not affected by temperature but slightly increased upon acidification. (**b**) The conjugate **635P** absorbance did not show strong temperature dependence but a small hypsochromic shift of 3 nm upon acidification, and the conjugate **635P** fluorescence emission did not display a strong temperature dependence but a small hypsochromic shift of 4 nm upon acidification. All absorbance spectra are baseline corrected, individually normalized on the HBED-CC concentration and collectively normalized on the absorbance maximum at pH 7.4, 25°C. All fluorescence emission spectra are individually normalized on the HBED-CC concentration and collectively normalized on the fluorescence emission maximum at pH 7.4, 25°C.

VI.2.2 Supplementary Tables

Table VI-16. Analytical data of conjugate RED and conjugate 635P.

Conjugate **RED** – Glu-urea-Lys-HBED-CC-PEG_2-STAR RED, conjugate **635P** – Glu-urea-Lys-HBED-CC-PEG_2-STAR 635P, * mass spectrometry of non-labeled ligand, † chemical yields refer to the dye conjugation to Glu-urea-Lys[Fe(HBED-CC)]-PEG_2, ‡ lipophilicity at pH 7.4 of ^{68}Ga-radiolabeled ligand.

	m/z (g/mol, M_{calc})	m/z* (M_{found})	chemical yield [%]†	lipophilicity log*D* n-octanol/PBS‡
conjugate RED	1850.9	1851.1	9	-1.93 ± 0.44
conjugate 635P	1882.8	1882.7	29	-2.88 ± 0.09

Table VI-17. Organ distribution of [^{68}Ga]Ga-conjugate RED and [^{68}Ga]Ga-conjugate 635P in LNCaP-tumor bearing BALB/c nu/nu mice 1 h p.i..

Conjugate **RED** – Glu-urea-Lys-HBED-CC-PEG$_2$-STAR RED, conjugate **635P** – Glu-urea-Lys-HBED-CC-PEG$_2$-STAR 635P, data are expressed as mean %ID/g tissue ± SD (n=3) and tumor-to-organ ratios.

	[^{68}Ga]Ga-conjugate RED [%ID/g]	[^{68}Ga]Ga-conjugate 635P [%ID/g]	p-values	[^{68}Ga]Ga-conjugate RED tumor-to-organ ratio	[^{68}Ga]Ga-conjugate 635P tumor-to-organ ratio	p-values
blood	1.81 ± 0.35	3.13 ± 0.43	0.797	3.19 ± 1.19	1.43 ± 0.14	0.027
heart	1.55 ± 0.31	1.25 ± 0.25	0.820	3.57 ± 0.78	3.61 ± 0.25	0.178
lung	3.14 ± 0.62	3.02 ± 0.44	0.699	1.91 ± 0.89	1.49 ± 0.17	0.069
spleen	29.83 ± 9.34	14.50 ± 2.06	0.094	0.21 ± 0.10	0.32 ± 0.08	0.781
liver	1.37 ± 0.46	1.45 ± 0.32	0.581	4.41 ± 1.82	3.10 ± 0.07	0.003
kidney	126.09 ± 43.10	86.96 ± 16.05	0.244	0.05 ± 0.01	0.05 ± 0.00	---
muscle	1.32 ± 0.50	1.58 ± 1.32	0.251	4.57 ± 1.75	3.92 ± 1.58	0.927
intestine	1.06 ± 0.40	1.11 ± 0.36	0.895	5.66 ± 1.95	4.30 ± 1.32	0.651
brain	0.24 ± 0.05	0.33 ± 0.08	0.781	24.54 ± 10.11	13.61 ± 1.32	0.034
tumor	5.65 ± 2.33	4.53 ± 1.07	0.356	---	---	---

Table VI-18. Organ distribution of [^{68}Ga]Ga-conjugate RED in PC3-tumor bearing BALB/c nu/nu mice 1 h p.i..

Conjugate **RED** – Glu-urea-Lys-HBED-CC-PEG$_2$-STAR RED, data are expressed as mean %ID/g tissue ± SD (n=3).

	blood	heart	lung	spleen	liver	kidney	muscle	intestine	brain	tumor
[^{68}Ga]Ga-conjugate RED [%ID/g]	0.63 ± 0.35	0.52 ± 0.16	1.54 ± 0.59	6.69 ± 2.38	0.51 ± 0.15	84.94 ± 30.91	0.82 ± 0.37	0.67 ± 0.16	0.12 ± 0.05	0.89 ± 0.17

Table VI-19. P-values of average diameters of endocytic vesicles carrying conjugate RED bound PSMA.

internalization time	30 min	45 min	60 min
30 min	---	---	---
45 min	0.448	---	---
60 min	0.169	0.054	---

Table VI-20. Results and p-values of the duration of LNCaP cell division.

Conjugate **RED** – Glu-urea-Lys-HBED-CC-PEG_2-STAR RED, conjugate **635P** – Glu-urea-Lys-HBED-CC-PEG_2-STAR 635P, data are expressed as mean ± SD.

		untreated	+ 100 nM conjugate RED	+ 100 nM conjugate 635P
n		347	624	408
cell division duration [min]		33 ± 34	29 ± 18	40 ± 107
p-values	**untreated**	---	---	---
	+ 100 nM conjugate RED	0.040	---	---
	+ 100 nM conjugate 635P	0.228	0.015	---

Table VI-21. Results and p-values of the frequency of LNCaP cell division.

Conjugate **RED** – Glu-urea-Lys-HBED-CC-PEG_2-STAR RED, conjugate **635P** – Glu-urea-Lys-HBED-CC-PEG_2-STAR 635P, data are expressed as mean ± SD.

		untreated	+ 100 nM conjugate RED	+ 100 nM conjugate 635P
n		347	624	408
cell division frequency [divisions per cell per day]		0.17 ± 0.07	0.28 ± 0.10	0.24 ± 0.08
p-values	**untreated**	---	---	---
	+ 100 nM conjugate RED	0.003	---	---
	+ 100 nM conjugate 635P	0.035	0.195	---

Table VI-22. Results and p-values of the cell count and confluency of LNCaP cell proliferation.

(**a**) Results and average p-values of the cell count given as mean ± SD, (**b**) results and average p-values of the confluency given as mean ± SD. * Given as fold change comparing the value at t = 48 h to the value at t = 0 h. Conjugate **RED** – Glu-urea-Lys-HBED-CC-PEG_2-STAR RED, conjugate **635P** – Glu-urea-Lys-HBED-CC-PEG_2-STAR 635P.

(a)		**untreated**	**+ 100 nM conjugate RED**	**+ 100 nM conjugate 635P**
cell count [fold change]*		1.56 ± 0.19	1.67 ± 0.22	1.70 ± 0.35
p-values	**untreated**	---	---	---
	+ 100 nM conjugate RED	0.698 ± 0.207	---	---
	+ 100 nM conjugate 635P	0.644 ± 0.240	0.629 ± 0.216	---

(b)		**untreated**	**+ 100 nM conjugate RED**	**+ 100 nM conjugate 635P**
confluency [fold change]*		1.85 ± 0.31	1.95 ± 0.21	2.02 ± 0.28
p-values	**untreated**	---	---	---
	+ 100 nM conjugate RED	0.580 ± 0.178	---	---
	+ 100 nM conjugate 635P	0.446 ± 0.303	0.436 ± 0.290	---

Table VI-23. PCCs and p-values of endosomal colocalization between PSMA and LysoTracker™ Green DND-26.

Conjugate **RED** – Glu-urea-Lys-HBED-CC-PEG_2-STAR RED, conjugate **635P** – Glu-urea-Lys-HBED-CC-PEG_2-STAR 635P, PCC – Pearson correlation coefficient, * data are expressed as mean PCC r ± SD, † without any additive (1 h n = 4, +20 h n = 8), ‡ with 500 µM 2-PMPA (1 h n = 3, +20 h n = 8), ¤ with 50 nM conjugate **RED** (1 h n = 7, +20 h n = 4) or conjugate **635P** (1 h n = 7, +20 h n = 6).

Pearson r	r(1h)*	r(+20h)*	p-values
w/o†	0.38 ± 0.02	0.64 ± 0.11	2×10^{-3}
+ 2-PMPA‡	0.42 ± 0.02	0.76 ± 0.09	3×10^{-4}
+ conjugate RED¤	0.39 ± 0.04	0.77 ± 0.04	4×10^{-7}
+ conjugate 635P¤	0.39 ± 0.07	0.71 ± 0.10	7×10^{-5}

p-values 1 h	w/o†	+ 2-PMPA‡	+ conjugate RED¤	+ conjugate 635P¤
w/o†	---	0.145	0.815	0.883
+ 2-PMPA‡	---	---	0.413	0.571
+ conjugate RED¤	---	---	---	0.990
+ conjugate 635P¤	---	---	---	---

p-values +20 h	w/o†	+ 2-PMPA‡	+ conjugate RED¤	+ conjugate 635P¤
w/o†	---	0.051	0.080	0.308
+ 2-PMPA‡	---	---	0.922	0.389
+ conjugate RED¤	---	---	---	0.375
+ conjugate 635P¤	---	---	---	---

Table VI-24. Results and p-values of the cytosolic and extracellular background determination.

Conjugate **RED** – Glu-urea-Lys-HBED-CC-PEG_2-STAR RED, conjugate **635P** – Glu-urea-Lys-HBED-CC-PEG_2-STAR 635P, data are given as mean ± SD (0.5 h n = 32, 6 h n = 48).

			0.5 h internalization time		6 h internalization time	
			cytosol	extracellular	cytosol	extracellular
		background [counts]	0.24± 0.06	0.14± 0.18	1.27 ± 0.36	0.18± 0.05
p-values	0.5 h internalization time	cytosol	---	---	---	---
		extracellular	1×10^{-13}	---	---	---
	6 h internalization time	cytosol	7×10^{-26}	1×10^{-28}	---	---
		extracellular	3×10^{-7}	5×10^{-5}	2×10^{-36}	---

Table VI-25. P-values of the influence of pH on the PSMA binding affinity of conjugate RED, conjugate 635P and the antibody complex.

The fractions of PSMA inhibitor or antibody complex bound at pH 4.6 are compared. Conjugate **RED** – Glu-urea-Lys-HBED-CC-PEG_2-STAR RED, conjugate **635P** – Glu-urea-Lys-HBED-CC-PEG_2-STAR 635P.

	anti-PSMA-STAR 600	anti-PSMA-STAR RED	conjugate RED	conjugate 635P
anti-PSMA-STAR 600	---	---	---	---
anti-PSMA-STAR RED	0.731	---	---	---
conjugate RED	0.062	0.036	---	---
conjugate 635P	0.023	0.013	0.539	---

VI.3 SUPPLEMENTARY MATERIAL FOR PART IV

VI.3.1 Supplementary Figures to IV.2

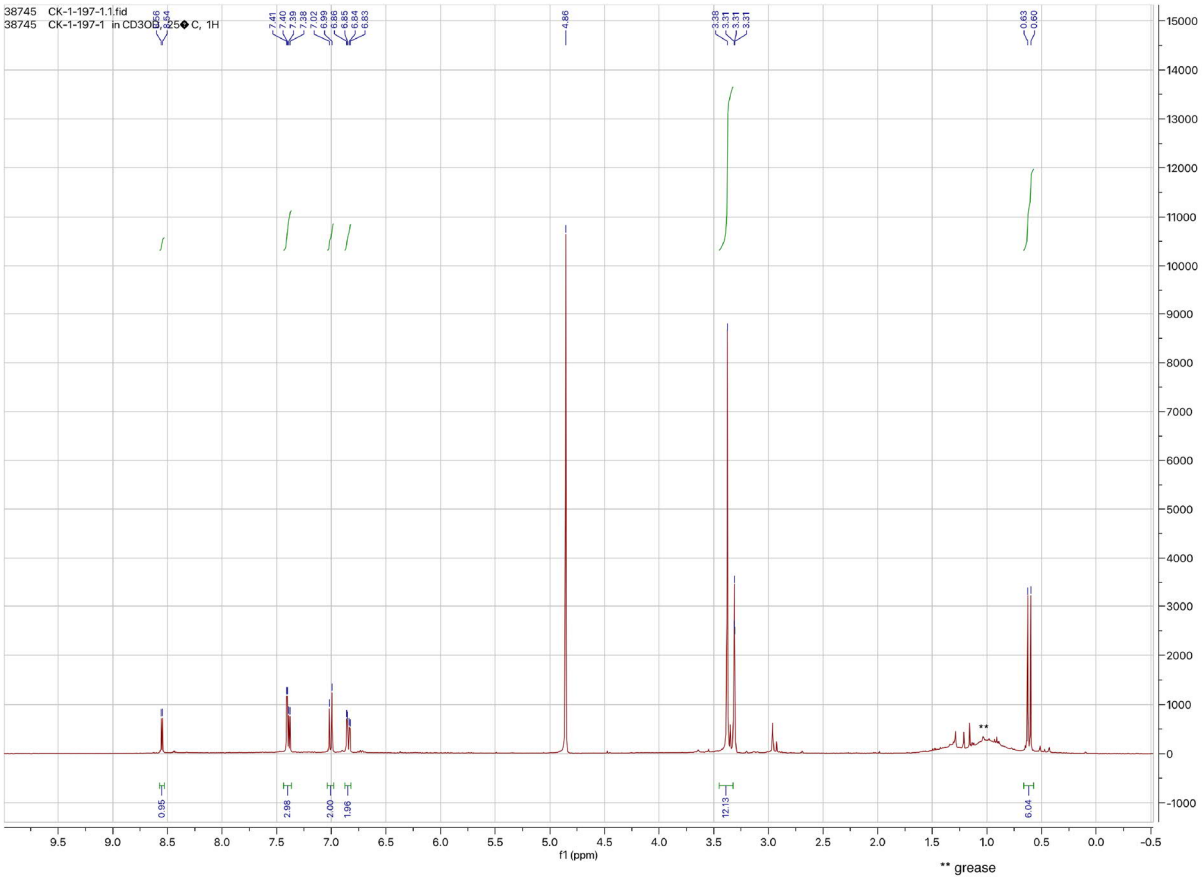

Figure VI-19. ^{1}H NMR spectrum of SiR dye 15.

The ^{1}H NMR (400 MHz, methanol-d_4) spectrum of SiR dye **15** is shown. The data are summarized in Table VI-27.

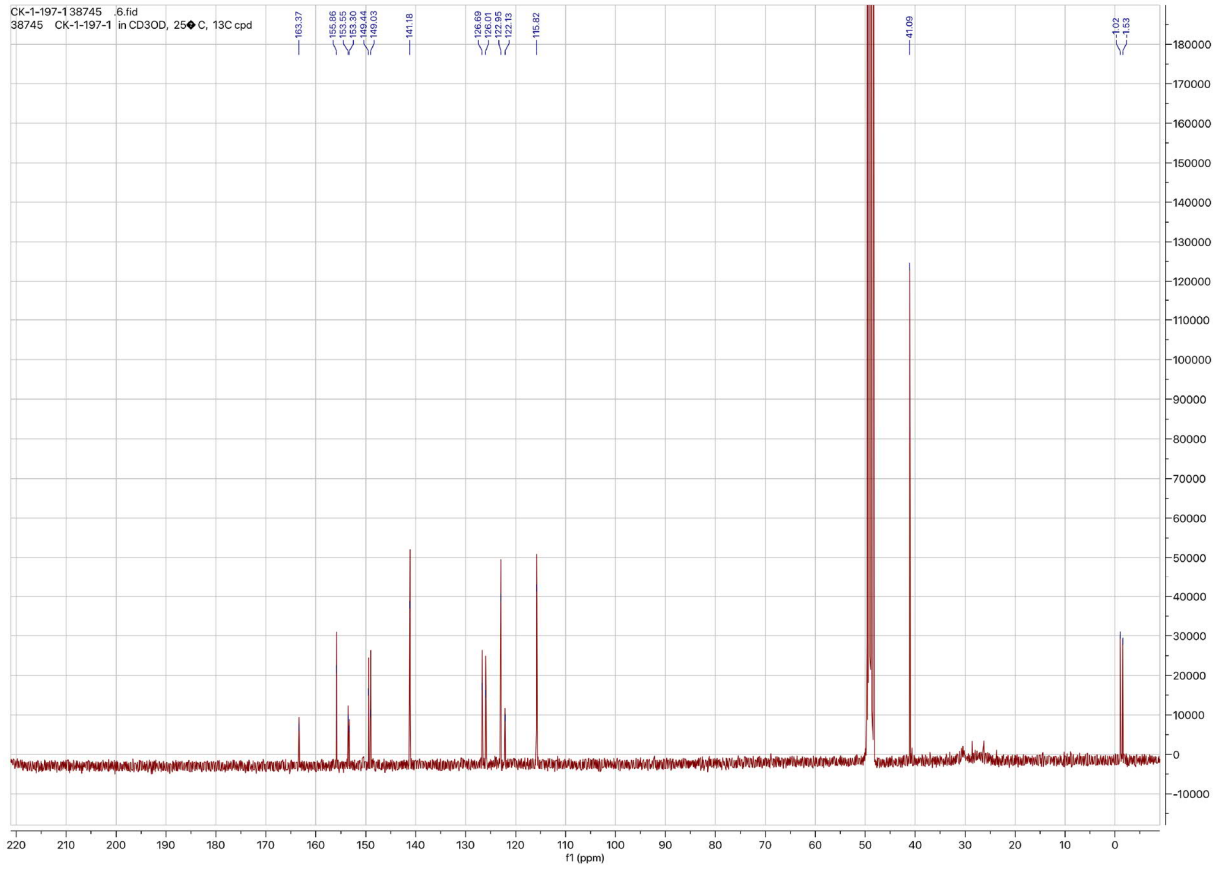

Figure VI-20. ^{13}C NMR spectrum of SiR dye 15.

The ^{13}C NMR (101 MHz, methanol-d_4) spectrum of SiR dye **15** is shown. The data are summarized in Table VI-27.

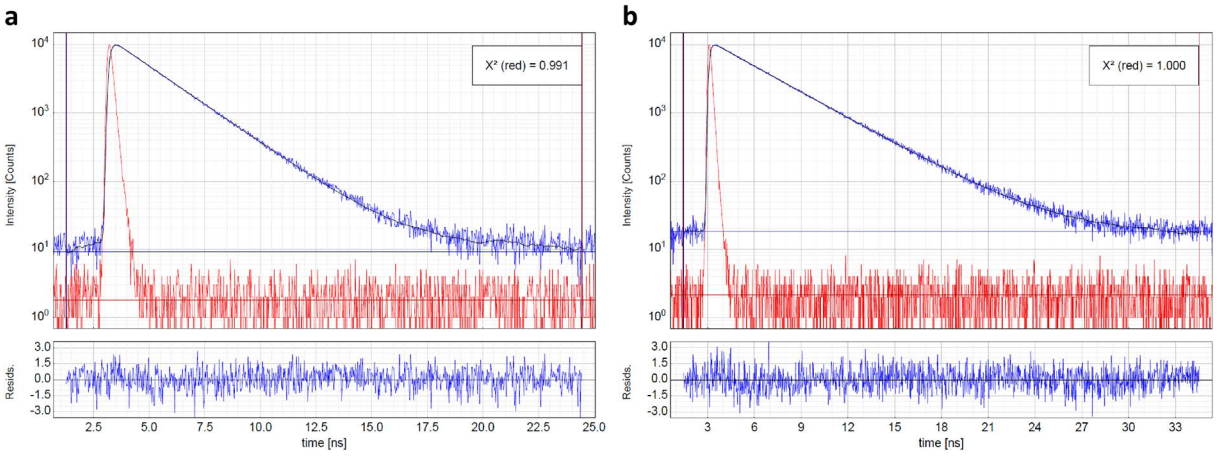

Figure VI-21. Fluorescence intensity decay of SiR dye 15.

The fluorescence intensity $F(t)$ decay of SiR dye **15** is shown in blue as measured in (**a**) PBS at pH 7.4 and in (**b**) MeCN. The fluorescence lifetime is determined by fitting the data with an additive superposition of exponential functions revealing a mono-exponential decay in both solvents. The fit results are summarized in Table VI-28. The instrument response function is shown in red.

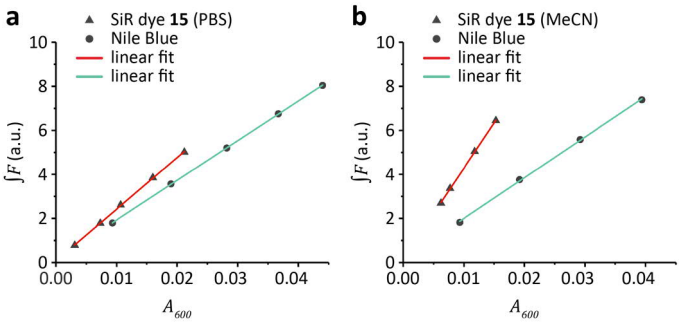

Figure VI-22. Relative measurement of the quantum yield of SiR dye 15.

The quantum yield ϕ of SiR dye **15** in (**a**) PBS at pH 7.4 and in (**b**) MeCN was determined in relative measurements using Nile Blue as reference standard. The wavelength-integrated fluorescence intensity $\int F$ is plotted versus the absorbance at 600 nm A_{600} and fitted by linear regression. The linear fit results are summarized in Table VI-29.

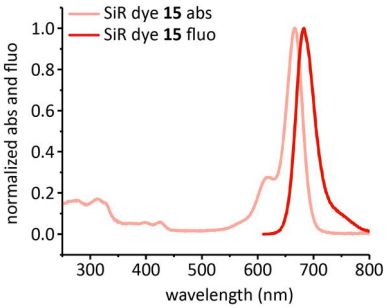

Figure VI-23. Spectral properties of SiR dye 15 in MeCN.

The absorbance and fluorescence emission of SiR dye **15** in MeCN peak at 667 nm and 683 nm. The absorbance spectrum is baseline corrected. Both spectra are normalized to their maximum.

VI.3.2 Supplementary Tables to IV.2

Table VI-26. Analytical data of SiR dye 15.

* Calculated for $C_{24}H_{26}BrClN_3Si$ [M^+], † ESI-HRMS, ‡ retardation factor (methanol : DCM = 1 : 9), ¥ calculated log*P*.

	m/z* (g/mol, M_{calc})	m/z† (M_{found})	chemical yield [%]	R_f‡	lipophilicity clog*P*¥
SiR dye 15	498.0768	498.0722	85	0.44	3.712

Table VI-27. NMR data of SiR dye 15.

Chemical shifts δ are given relative to methanol-d_4 (δ_H = 3.31, δ_C = 49.0). Analysis followed first (s – singlet, d – doublet, dd – doublet of doublet). Coupling constants *J* refer to H,H-couplings. Assignment was done via DEPT and HSQC experiments.

^{1}H NMR (400 MHz)				^{13}C NMR (101 MHz)	
δ	multiplets	*J* [Hz]	assignment	δ	assignment
8.55	d	4.8	1H	163.4	C_{quart}
7.41	d	2.8	2H	155.9	C_{quart}
7.38	d	4.8	1H	153.55	C_{quart}
7.01	d	9.7	2H	153.3	C_{quart}
6.84	dd	9.6, 2.9	2H	149.4	C_{quart}
3.38	s	---	12H	149.0	CH
0.63	s	---	3H	141.2	CH
0.60	s	---	3H	126.69	C_{quart}
				126.0	CH
				123.0	CH
				122.1	C_{quart}
				115.8	CH
				41.1	CH_3
				-1.0	CH_3
				-1.5	CH_3

Table VI-28. Fit parameter of the exponential fit of the fluorescence decay of SiR dye 15.

The fluorescence lifetime τ of SiR dye **15** was determined by TCSPC in PBS pH 7.4 and in MeCN. Fitting of the fluorescence intensity $F(t)$ decay with an additive superposition of exponential functions revealed a mono-exponential decay (n = 1) for both solvents. IRF – instrument response function.

solvent	PBS pH 7.4	MeCN
equation	$F(t) = \int_{-\infty}^{t} IRF(t') \sum_{i=1}^{n} A_i e^{-\frac{t-t'}{\tau_i}} dt'$	
A [counts]	12251 ± 61	11556 ± 54
τ [ns]	1.933 ± 0.007	3.425 ± 0.012
background decay [counts]	9.14 ± 0.86	18.04 ± 1.19
background IRF [counts]	1.79 ± 0.11	2.15 ± 0.09
shift IRF [ns]	0.021 ± 0.002	-0.013 ± 0.003
A scat [counts]	3390 ± 1260	6040 ± 1550
χ^2	0.991	1.000

Table VI-29. Fit parameter of the relative measurement of the quantum yield of SiR dye 15.

The quantum yield ϕ of SiR dye **15** was determined relative to the reference standard Nile Blue in PBS pH 7.4 and in MeCN. COD – coefficient of determination, $\int F$ – wavelength-integrated fluorescence intensity, A_{600} – absorbance at 600 nm.

	PBS pH 7.4		MeCN	
	SiR dye 15	Nile Blue	SiR dye 15	Nile Blue
equation	$\int F = a + m\, A_{600}$			
weight	no weighting			
intercept a	743 ± 273	1249 ± 179	1700 ± 470	1517 ± 818
slope m	(2.34 ± 0.02)×10^6	(1.80 ± 0.01)×10^6	(4.11 ± 0.04)×10^6	(1.85 ± 0.03)×10^6
residual sum of squares	257461	80813	190738	941642
Pearson's r	0.99988	0.99998	0.99989	0.99973
R^2 (COD)	0.99977	0.99997	0.99978	0.99945
adjusted R^2	0.99969	0.99996	0.99967	0.99918

Table VI-30. Results and p-values of the PCC calculation for mitochondrial and endosomal/lysosomal colocalization of SiR dye 15.

Data are expressed as mean ± SD. Note that the PCC for endosomal/lysosomal colocalization overestimates the lysosomal targeting ability of SiR dye **15** as LysoTracker™ Green DND-26 mildly stains mitochondria additionally.

	mitochondrial colocalization		endosomal/lysosomal colocalization		
cell lines	**n**	**PCC**	**n**	**PCC**	**p-value**
HeLa	22	0.85 ± 0.05	13	0.35 ± 0.06	3×10^{-23}
U2OS	27	0.81 ± 0.05	13	0.38 ± 0.04	3×10^{-26}

Table VI-31. Results and p-values of the duration and frequency of U2OS cell division and of the cell count and confluency of U2OS cell proliferation after treatment with SiR dye 15.

Data are expressed as mean ± SD. * Given as fold change comparing the value at t = 14.5 h to the value at t = 0 h, † Average p-value expressed as mean ± SD.

	untreated	**+ 1 µM SiR dye 15**	**p-value**
n(divisions)	494	281	---
n(experiments)	11	8	---
cell division duration [min]	40 ± 37	38 ± 18	0.300
cell division frequency [divisions per cell per day]	0.53 ± 0.10	0.50 ± 0.08	0.555
cell count [fold change]*	1.44 ± 0.10	1.39 ± 0.14	$0.521 \pm 0.204^{\dagger}$
confluency [fold change]*	1.47 ± 0.23	1.41 ± 0.22	$0.574 \pm 0.262^{\dagger}$

VI.3.3 Supplementary Figures to IV.3

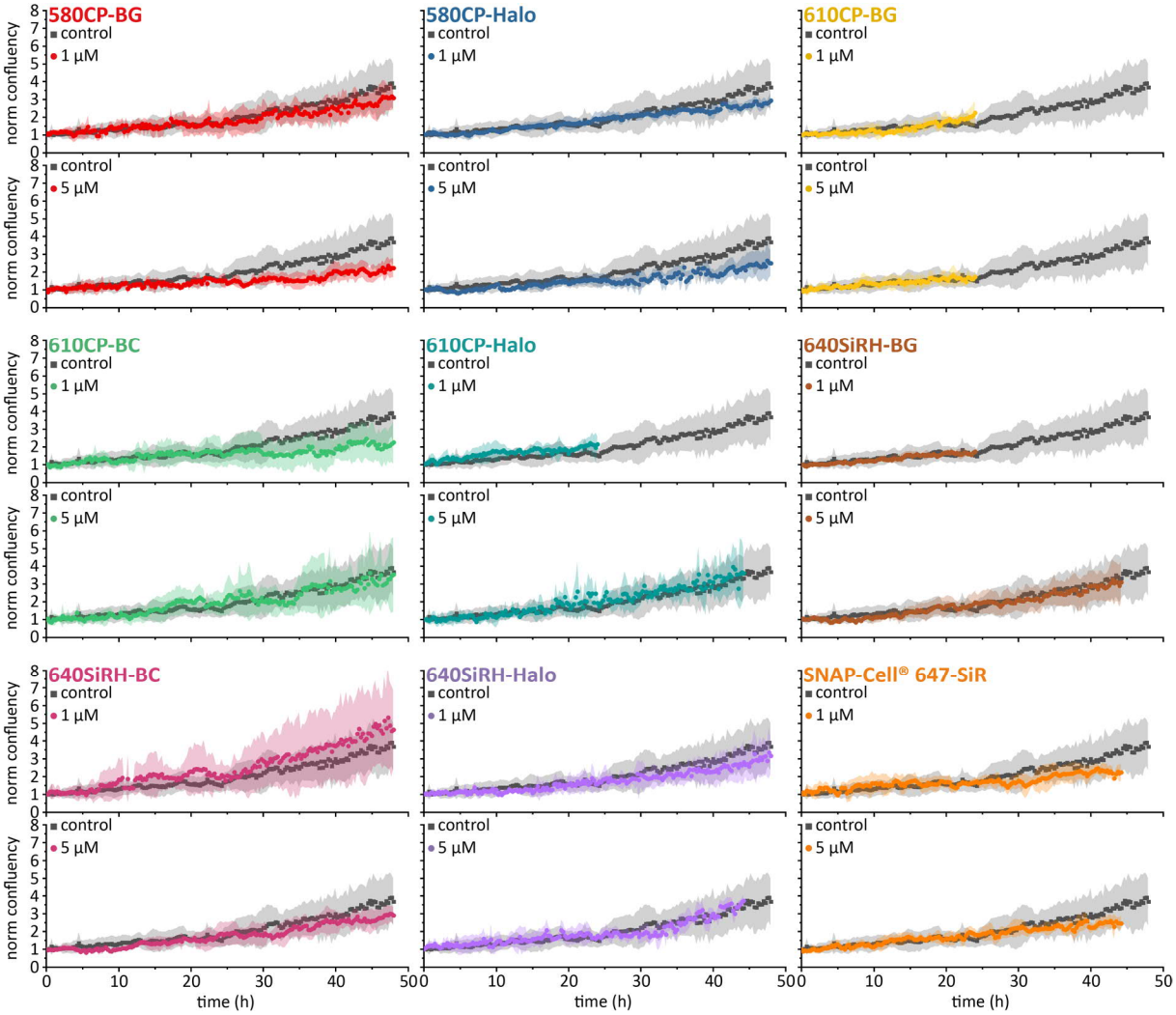

Figure VI-24. Time series of U2OS confluency in the presence of various live cell STED compatible dyes.

Cytotoxicity data are based on holographic time-lapse series (duration 24/44.25/48 h, frequency 15 min) of U2OS cell proliferation in the presence of 1 µM and 5 µM of SNAP (BG), Halo and CLIP (BC) derivatives of the popular SiR dye [30, 404] and recently published [29, 32] live cell STED compatible organic dyes. The data are compared to the control measurements of the proliferation of untreated U2OS cells. The confluency was normalized to the first frame (t = 0). The results were averaged and SDs are displayed as shadows in the graphs. Average p-values indicate no significant difference between untreated and treated U2OS cells. All results, n-values and p-values are summarized in Table VI-32.

VI.3.4 Supplementary Tables to IV.3

Table VI-32. Results and p-values of the duration and frequency of U2OS cell division and of the cell count and confluency of U2OS cell proliferation in the presence of selected SNAP, CLIP and Halo live dye derivatives.

Data are expressed as mean ± SD and p-values compare the dye treated condition with the untreated control; div – division, exp – experiment. * Fold change comparing the value at t = 24 h to the value at t = 0 h, ** Fold change comparing the value at t = 44.25 h to the value at t = 0 h, *** Fold change comparing the value at t = 48 h to the value at t = 0 h,† Average p-value expressed as mean ± SD.

		n		cell division			
		div.	exp.	duration [min]	frequency [divisions per cell per day]	cell count [fold change]	confluency [fold change]
untreated (control)	**results**	507	12	31 ± 27	1.16 ± 0.41	1.6 ± 0.2* 3.0 ± 0.7** 3.4 ± 0.8***	1.5 ± 0.4* 3.3 ± 1.2** 3.7 ± 1.3***
+ 1 µM 580CP-BG	**results**	555	6	23 ± 14	1.90 ± 0.41	1.8 ± 0.5* 4.0 ± 0.7***	1.5 ± 0.7* 3.1 ± 0.6***
	p-values	---	---	5×10^{-9}	0.004	0.338 ± 0.246†	0.594 ± 0.237†
+ 5 µM 580CP-BG	**results**	332	4	29 ± 21	1.27 ± 0.16	1.6 ± 0.2* 2.8 ± 0.6***	1.5 ± 0.3* 2.2 ± 0.5***
	p-values	---	---	0.237	0.631	0.537 ± 0.238†	0.397 ± 0.308†
+ 1 µM 580CP-Halo	**results**	241	4	33 ± 27	1.18 ± 0.21	1.6 ± 0.1* 3.1 ± 0.2***	1.9 ± 0.4* 2.9 ± 0.4***
	p-values	---	---	0.338	0.936	0.633 ± 0.211†	0.638 ± 0.227†
+ 5 µM 580CP-Halo	**results**	333	4	29 ± 14	1.29 ± 0.22	1.5 ± 0.2* 3.1 ± 0.3***	1.5 ± 0.4* 2.5 ± 0.7***
	p-values	---	---	0.132	0.594	0.560 ± 0.242†	0.365 ± 0.239†
+ 1 µM 610CP-BG	**results**	130	4	25 ± 15	1.12 ± 0.29	1.9 ± 0.5*	2.2 ± 0.7*
	p-values	---	---	0.010	0.848	0.442 ± 0.306†	0.635 ± 0.231†
+ 5 µM 610CP-BG	**results**	160	4	24 ± 14	1.08 ± 0.35	1.9 ± 0.4*	1.7 ± 0.4*
	p-values	---	---	0.001	0.744	0.251 ± 0.176†	0.764 ± 0.161†
+ 1 µM 610CP-BC	**results**	186	6	29 ± 22	1.01 ± 0.31	1.6 ± 0.3* 2.7 ± 0.8***	1.7 ± 0.9* 2.2 ± 1.2***
	p-values	---	---	0.416	0.448	0.424 ± 0.273†	0.459 ± 0.311†
+ 5 µM 610CP-BC	**results**	193	6	31 ± 20	1.25 ± 0.59	1.6 ± 0.3* 3.3 ± 1.5***	1.8 ± 0.7* 3.5 ± 2.1***
	p-values	---	---	0.868	0.732	0.693 ± 0.236†	0.567 ± 0.263†
+ 1 µM 610CP-Halo	**results**	194	4	23 ± 12	1.26 ± 0.09	2.2 ± 0.2*	2.1 ± 0.4*
	p-values	---	---	5×10^{-5}	0.684	0.085 ± 0.177†	0.348 ± 0.227 †

		n		cell division			
		div.	**exp.**	**duration [min]**	**frequency [divisions per cell per day]**	**cell count [fold change]**	**confluency [fold change]**
+ 5 µM 610CP-Halo	**results**	137	5	44 ± 55	1.01 ± 0.16	1.7 ± 0.3* 2.7 ± 0.3**	1.9 ± 0.4* 3.6 ± 1.5**
	p-values	---	---	2×10^{-4}	0.446	0.656 ± 0.210†	0.593 ± 0.251†
+ 1 µM 640SiRH-BG	**results**	226	4	25 ± 12	1.20 ± 0.24	2.1 ± 0.3*	1.7 ± 0.1*
	p-values	---	---	0.001	0.896	0.260 ± 0.291†	0.727 ± 0.184†
+ 5 µM 640SiRH-BG	**results**	166	4	32 ± 23	1.30 ± 0.29	1.9 ± 0.4* 3.1 ± 0.8**	2.0 ± 0.6* 3.1 ± 1.2**
	p-values	---	---	0.582	0.573	0.536 ± 0.247†	0.656 ± 0.250†
+ 1 µM 640SiRH-BC	**results**	276	6	29 ± 24	1.73 ± 0.61	2.1 ± 0.6* 4.2 ± 1.6***	1.9 ± 0.7* 4.6 ± 2.2***
	p-values	---	---	0.313	0.044	0.225 ± 0.176†	0.436 ± 0.238†
+ 5 µM 640SiRH-BC	**results**	160	4	35 ± 28	1.03 ± 0.21	1.7 ± 0.1* 2.9 ± 0.1***	1.9 ± 0.7* 2.9 ± 0.5***
	p-values	---	---	0.107	0.555	0.540 ± 0.232†	0.534 ± 0.238†
+ 1 µM 640SiRH-Halo	**results**	201	5	35 ± 44	1.00 ± 0.24	1.8 ± 0.2* 3.1 ± 0.5***	1.6 ± 0.4* 3.2 ± 1.1***
	p-values	---	---	0.128	0.433	0.598 ± 0.222†	0.532 ± 0.235†
+ 5 µM 640SiRH-Halo	**results**	158	4	35 ± 26	1.31 ± 0.18	1.7 ± 0.1* 3.4 ± 0.4**	1.7 ± 0.1* 3.7 ± 0.4**
	p-values	---	---	0.094	0.525	0.455 ± 0.255†	0.644 ± 0.233†
+ 1 µM SNAP-Cell® 647-SiR	**results**	148	4	35 ± 29	1.14 ± 0.16	1.8 ± 0.2* 2.9 ± 0.1**	1.7 ± 0.2* 2.2 ± 0.5**
	p-values	---	---	0.102	0.911	0.435 ± 0.304†	0.503 ± 0.247†
+ 5 µM SNAP-Cell® 647-SiR	**results**	216	4	34 ± 36	1.21 ± 0.06	1.9 ± 0.1* 2.9 ± 0.2**	1.8 ± 0.3* 2.4 ± 0.4**
	p-values	---	---	0.253	0.852	0.447 ± 0.257†	0.633 ± 0.228†

REFERENCES

1. Hell, S.W., *Far-field optical nanoscopy.* Science, 2007. **316**(5828): p. 1153-8.
2. Hell, S.W., et al., *The 2015 super-resolution microscopy roadmap.* Journal of Physics D-Applied Physics, 2015. **48**(44).
3. Nienhaus, K. and G.U. Nienhaus, *Where Do We Stand with Super-Resolution Optical Microscopy?* Journal of Molecular Biology, 2016. **428**(2): p. 308-322.
4. Eggeling, C., et al., *Lens-based fluorescence nanoscopy.* Quarterly Reviews of Biophysics, 2015. **48**(2): p. 178-243.
5. Sahl, S.J., S.W. Hell, and S. Jakobs, *Fluorescence nanoscopy in cell biology.* Nature Reviews Molecular Cell Biology, 2017. **18**(11): p. 685-701.
6. Schermelleh, L., et al., *Super-resolution microscopy demystified.* Nature Cell Biology, 2019. **21**(1): p. 72-84.
7. Heinisch, J.J., et al., *Atomic force microscopy - looking at mechanosensors on the cell surface.* Journal of Cell Science, 2012. **125**(18): p. 4189-4195.
8. Shibata, M., et al., *Long-tip high-speed atomic force microscopy for nanometer-scale imaging in live cells.* Scientific Reports, 2015. **5**.
9. Dufrene, Y.F., et al., *Five challenges to bringing single-molecule force spectroscopy into living cells.* Nature Methods, 2011. **8**(2): p. 123-127.
10. de Jonge, N. and D.B. Peckys, *Live Cell Electron Microscopy Is Probably Impossible.* Acs Nano, 2016. **10**(10): p. 9061-9063.
11. Kourkoutis, L.F., J.M. Plitzko, and W. Baumeister, *Electron Microscopy of Biological Materials at the Nanometer Scale.* Annual Review of Materials Research, Vol 42, 2012. **42**: p. 33-58.
12. Hell, S.W. and J. Wichmann, *Breaking the Diffraction Resolution Limit by Stimulated-Emission - Stimulated-Emission-Depletion Fluorescence Microscopy.* Optics Letters, 1994. **19**(11): p. 780-782.
13. Rust, M.J., M. Bates, and X.W. Zhuang, *Sub-diffraction-limit imaging by stochastic optical reconstruction microscopy (STORM).* Nature Methods, 2006. **3**(10): p. 793-795.
14. Shimomura, O., F.H. Johnson, and Y. Saiga, *Extraction, Purification and Properties of Aequorin, a Bioluminescent Protein from Luminous Hydromedusan, Aequorea.* Journal of Cellular and Comparative Physiology, 1962. **59**(3): p. 223-&.
15. Chalfie, M., et al., *Green Fluorescent Protein as a Marker for Gene-Expression.* Science, 1994. **263**(5148): p. 802-805.
16. Heim, R., D.C. Prasher, and R.Y. Tsien, *Wavelength Mutations and Posttranslational Autoxidation of Green Fluorescent Protein.* Proceedings of the National Academy of Sciences of the United States of America, 1994. **91**(26): p. 12501-12504.
17. Tsien, R.Y., *The green fluorescent protein.* Annual Review of Biochemistry, 1998. **67**: p. 509-544.
18. Betzig, E., et al., *Imaging intracellular fluorescent proteins at nanometer resolution.* Science, 2006. **313**(5793): p. 1642-1645.
19. Deschout, H., et al., *Complementarity of PALM and SOFI for super-resolution live-cell imaging of focal adhesions.* Nat Commun, 2016. **7**: p. 13693.
20. Hofmann, M., et al., *Breaking the diffraction barrier in fluorescence microscopy at low light intensities by using reversibly photoswitchable proteins.* Proceedings of the National Academy of Sciences of the United States of America, 2005. **102**(49): p. 17565-17569.
21. Chudakov, D.M., et al., *Fluorescent proteins and their applications in imaging living cells and tissues.* Physiol Rev, 2010. **90**(3): p. 1103-63.
22. Rodriguez, E.A., et al., *The Growing and Glowing Toolbox of Fluorescent and Photoactive Proteins.* Trends Biochem Sci, 2017. **42**(2): p. 111-129.
23. Keppler, A., et al., *A general method for the covalent labeling of fusion proteins with small molecules in vivo.* Nat Biotechnol, 2003. **21**(1): p. 86-9.

24. Juillerat, A., et al., *Directed evolution of O6-alkylguanine-DNA alkyltransferase for efficient labeling of fusion proteins with small molecules in vivo.* Chem Biol, 2003. **10**(4): p. 313-7.
25. Los, G.V., et al., *HaloTag: a novel protein labeling technology for cell imaging and protein analysis.* ACS Chem Biol, 2008. **3**(6): p. 373-82.
26. Cramer, L.P., *Role of actin-filament disassembly in lamellipodium protrusion in motile cells revealed using the drug jasplakinolide.* Current Biology, 1999. **9**(19): p. 1095-1105.
27. Barasoain, I., J.F. Diaz, and J.M. Andreu, *Fluorescent taxoid probes for microtubule research.* Methods Cell Biol, 2010. **95**: p. 353-72.
28. Liberman, E.A., et al., *Mechanism of coupling of oxidative phosphorylation and the membrane potential of mitochondria.* Nature, 1969. **222**(5198): p. 1076-8.
29. Butkevich, A.N., et al., *Fluorescent Rhodamines and Fluorogenic Carbopyronines for Super-Resolution STED Microscopy in Living Cells.* Angew Chem Int Ed Engl, 2016. **55**(10): p. 3290-4.
30. Lukinavicius, G., et al., *A near-infrared fluorophore for live-cell super-resolution microscopy of cellular proteins.* Nat Chem, 2013. **5**(2): p. 132-9.
31. Lukinavicius, G., et al., *Fluorogenic Probes for Multicolor Imaging in Living Cells.* J Am Chem Soc, 2016. **138**(30): p. 9365-8.
32. Butkevich, A.N., et al., *Hydroxylated Fluorescent Dyes for Live-Cell Labeling: Synthesis, Spectra and Super-Resolution STED.* Chemistry, 2017. **23**(50): p. 12114-12119.
33. Butkevich, A.N., et al., *Two-Color 810 nm STED Nanoscopy of Living Cells with Endogenous SNAP-Tagged Fusion Proteins.* ACS Chem Biol, 2018. **13**(2): p. 475-480.
34. Grimm, J.B., et al., *A general method to improve fluorophores for live-cell and single-molecule microscopy.* Nat Methods, 2015. **12**(3): p. 244-50, 3 p following 250.
35. Grimm, J.B., et al., *Bright photoactivatable fluorophores for single-molecule imaging.* Nat Methods, 2016. **13**(12): p. 985-988.
36. Grimm, J.B., et al., *Synthesis of a Far-Red Photoactivatable Silicon-Containing Rhodamine for Super-Resolution Microscopy.* Angew Chem Int Ed Engl, 2016. **55**(5): p. 1723-7.
37. Zhang, X., et al., *A targetable fluorescent probe for dSTORM super-resolution imaging of live cell nucleus DNA.* Chem Commun (Camb), 2019. **55**(13): p. 1951-1954.
38. Takakura, H., et al., *Long time-lapse nanoscopy with spontaneously blinking membrane probes.* Nature Biotechnology, 2017. **35**(8): p. 773-780.
39. Sauer, M. and M. Heilemann, *Single-Molecule Localization Microscopy in Eukaryotes.* Chem Rev, 2017. **117**(11): p. 7478-7509.
40. van de Linde, S., M. Heilemann, and M. Sauer, *Live-Cell Super-Resolution Imaging with Synthetic Fluorophores.* Annual Review of Physical Chemistry, Vol 63, 2012. **63**: p. 519-540.
41. Jones, S.A., et al., *Fast, three-dimensional super-resolution imaging of live cells.* Nature Methods, 2011. **8**(6): p. 499-U96.
42. Wombacher, R., et al., *Live-cell super-resolution imaging with trimethoprim conjugates.* Nature Methods, 2010. **7**(9): p. 717-719.
43. Halabi, E.A., D. Pinotsi, and P. Rivera-Fuentes, *Photoregulated fluxional fluorophores for live-cell super-resolution microscopy with no apparent photobleaching.* Nat Commun, 2019. **10**(1): p. 1232.
44. Shay, J.W., *Role of Telomeres and Telomerase in Aging and Cancer.* Cancer Discovery, 2016. **6**(6): p. 584-593.
45. Shay, J.W. and W.E. Wright, *Telomeres and telomerase: three decades of progress.* Nat Rev Genet, 2019. **20**(5): p. 299-309.
46. Gaspar, T.B., et al., *Telomere Maintenance Mechanisms in Cancer.* Genes, 2018. **9**(5).
47. Roake, C.M. and S.E. Artandi, *DNA repair: Telomere-lengthening mechanism revealed.* Nature, 2016. **539**(7627): p. 35-36.
48. Baranski, A.C., et al., *PSMA-11-Derived Dual-Labeled PSMA Inhibitors for Preoperative PET Imaging and Precise Fluorescence-Guided Surgery of Prostate Cancer.* J Nucl Med, 2018. **59**(4): p. 639-645.

49. Baranski, A.C., et al., *Improving the Imaging Contrast of (68)Ga-PSMA-11 by Targeted Linker Design: Charged Spacer Moieties Enhance the Pharmacokinetic Properties.* Bioconjug Chem, 2017. **28**(9): p. 2485-2492.
50. Turkowyd, B., D. Virant, and U. Endesfelder, *From single molecules to life: microscopy at the nanoscale.* Analytical and Bioanalytical Chemistry, 2016. **408**(25): p. 6885-6911.
51. Milo, R., et al., *BioNumbers--the database of key numbers in molecular and cell biology.* Nucleic Acids Res, 2010. **38**(Database issue): p. D750-3.
52. McRobbie, D., et al., *MRI from Picture to Proton*. 2017, Cambridge: Cambridge University Press.
53. Bailey, D.L., et al., *Positron Emission Tomography: Basic Sciences*. 2005: Springer London.
54. Drexler, W., *Optical Coherence Tomography*. Technology and Applications. 2015: Springer International Publishing.
55. Knoll, M. and E. Ruska, *The Electron Microscope.* Zeitschrift Fur Physik, 1932. **78**(5-6): p. 318-339.
56. Binnig, G., C.F. Quate, and C. Gerber, *Atomic force microscope.* Phys Rev Lett, 1986. **56**(9): p. 930-933.
57. Meyer, G. and N.M. Amer, *Novel Optical Approach to Atomic Force Microscopy.* Applied Physics Letters, 1988. **53**(12): p. 1045-1047.
58. Binnig, G. and H. Rohrer, *Scanning Tunneling Microscopy.* Surface Science, 1983. **126**(1-3): p. 236-244.
59. Ash, E.A. and G. Nicholls, *Super-Resolution Aperture Scanning Microscope.* Nature, 1972. **237**(5357): p. 510-&.
60. Synge, E.H., *A suggested method for extending microscopic resolution into the ultra-microscopic region.* Philosophical Magazine, 1928. **6**(35): p. 356-362.
61. Voigtländer, B., *Scanning Probe Microscopy: Atomic Force Microscopy and Scanning Tunneling Microscopy*. 2015: Springer Berlin Heidelberg.
62. Muller, D.J. and Y.F. Dufrene, *Atomic force microscopy: a nanoscopic window on the cell surface.* Trends in Cell Biology, 2011. **21**(8): p. 461-469.
63. Dykstra, M. and L. Reuss, *Biological Electron Microscopy*. Theory, Techniques, and Troubleshooting. 2003: Springer US.
64. Specht, E.A., E. Braselmann, and A.E. Palmer, *A Critical and Comparative Review of Fluorescent Tools for Live-Cell Imaging.* Annual Review of Physiology, Vol 79, 2017. **79**: p. 93-117.
65. Liu, Z., L.D. Lavis, and E. Betzig, *Imaging live-cell dynamics and structure at the single-molecule level.* Mol Cell, 2015. **58**(4): p. 644-59.
66. Medintz, I.L. and N. Hildebrandt, *FRET - Förster Resonance Energy Transfer: From Theory to Applications*. 2013: Wiley.
67. Lippincott-Schwartz, J., E. Snapp, and A. Kenworthy, *Studying protein dynamics in living cells.* Nat Rev Mol Cell Biol, 2001. **2**(6): p. 444-56.
68. Sprague, B.L. and J.G. McNally, *FRAP analysis of binding: proper and fitting.* Trends Cell Biol, 2005. **15**(2): p. 84-91.
69. Shen, H., et al., *Single Particle Tracking: From Theory to Biophysical Applications.* Chem Rev, 2017. **117**(11): p. 7331-7376.
70. Becker, W., *Fluorescence lifetime imaging--techniques and applications.* J Microsc, 2012. **247**(2): p. 119-36.
71. Elson, E.L., *Fluorescence correlation spectroscopy: past, present, future.* Biophys J, 2011. **101**(12): p. 2855-70.
72. Ishikawa-Ankerhold, H.C., R. Ankerhold, and G.P. Drummen, *Advanced fluorescence microscopy techniques--FRAP, FLIP, FLAP, FRET and FLIM.* Molecules, 2012. **17**(4): p. 4047-132.
73. Dean, K.M. and A.E. Palmer, *Advances in fluorescence labeling strategies for dynamic cellular imaging.* Nature Chemical Biology, 2014. **10**(7): p. 512-523.
74. Chen, X. and Y.W. Wu, *Selective chemical labeling of proteins.* Organic & Biomolecular Chemistry, 2016. **14**(24): p. 5417-5439.

75. Nienhaus, G.U. and K. Nienhaus, *Fluorescence Labeling*, in *Fluorescence Microscopy: From Principles to Biological Applications*, U. Kubitscheck, Editor. 2017, Wiley. p. 133-164.
76. Airy, G.B., *On the Diffraction of an Object-glass with Circular Aperture.* Transactions of the Cambridge Philosophical Society, 1835. **5**: p. 283.
77. Rayleigh, L., *On the theory of optical images, with special reference to the microscope.* Philosophical Magazine, 1896. **42**(255): p. 167-195.
78. Abbe, E., *Beiträge zur Theorie des Mikroskops und der mikroskopischen Wahrnehmung.* Archiv für mikroskopische Anatomie, 1873. **9**(1): p. 413-418.
79. von Helmholtz, H., *Die theoretische Grenze für die Leistungsfähigkeit der Mikroskope.* Annalen Der Physik, 1874(Jubelband J.C. Poggendorf gewidmet).
80. Alberts, B., et al., *Visualizing Cells, Chapter 9*, in *Molecular Biology of the Cell*. 2002, Garland Science: New York.
81. Hermann, R.J. and M.J. Gordon, *Nanoscale Optical Microscopy and Spectroscopy Using Near-Field Probes.* Annual Review of Chemical and Biomolecular Engineering, Vol 9, 2018. **9**: p. 365-387.
82. Betzig, E., et al., *Near-field fluorescence imaging of cytoskeletal actin.* Bioimaging, 1993. **1**(3): p. 129-135.
83. Betzig, E., et al., *Near Field Scanning Optical Microscopy (NSOM): Development and Biophysical Applications.* Biophys J, 1986. **49**(1): p. 269-79.
84. Lewis, A., et al., *Development of a 500-a Spatial-Resolution Light-Microscope .1. Light Is Efficiently Transmitted through Gamma-16 Diameter Apertures.* Ultramicroscopy, 1984. **13**(3): p. 227-231.
85. Pohl, D.W., W. Denk, and M. Lanz, *Optical Stethoscopy - Image Recording with Resolution Lambda/20.* Applied Physics Letters, 1984. **44**(7): p. 651-653.
86. Minsky, M., *Memoir on Inventing the Confocal Scanning Microscope.* Scanning, 1988. **10**(4): p. 128-138.
87. Marvin, M., *Microscopy apparatus*. 1961, Marvin, Minsky: United States.
88. Pawley, J., *Handbook of Biological Confocal Microscopy*. 2013: Springer US.
89. Denk, W., J.H. Strickler, and W.W. Webb, *Two-photon laser scanning fluorescence microscopy.* Science, 1990. **248**(4951): p. 73-6.
90. Hoover, E.E. and J.A. Squier, *Advances in multiphoton microscopy technology.* Nat Photonics, 2013. **7**(2): p. 93-101.
91. Hell, S. and E.H.K. Stelzer, *Properties of a 4pi Confocal Fluorescence Microscope.* Journal of the Optical Society of America a-Optics Image Science and Vision, 1992. **9**(12): p. 2159-2166.
92. Hell, S.W., *Double-confocal scanning microscope.* 1992, Euorpean Patent 0491289.
93. Gustafsson, M.G.L., D.A. Agard, and J.W. Sedat, *Sevenfold Improvement of Axial Resolution in 3d Widefield Microscopy Using 2 Objective Lenses.* Three-Dimensional Microscopy: Image Acquisition and Processing Ii, 1995. **2412**: p. 147-156.
94. Gustafsson, M.G.L., D.A. Agard, and J.W. Sedat, *3D widefield microscopy with two objective lenses: Experimental verification of improved axial resolution.* Three-Dimensional Microscopy: Image Acquisition and Processing Iii, 1996. **2655**: p. 62-66.
95. Gustafsson, M.G.L., D.A. Agard, and J.W. Sedat, *(IM)-M-5: 3D widefield light microscopy with better than 100 nm axial resolution.* Journal of Microscopy, 1999. **195**: p. 10-16.
96. Bailey, B., et al., *Enhancement of Axial Resolution in Fluorescence Microscopy by Standing-Wave Excitation.* Nature, 1993. **366**(6450): p. 44-48.
97. Frohn, J.T., H.F. Knapp, and A. Stemmer, *True optical resolution beyond the Rayleigh limit achieved by standing wave illumination.* Proceedings of the National Academy of Sciences of the United States of America, 2000. **97**(13): p. 7232-7236.
98. Gustafsson, M.G.L., *Surpassing the lateral resolution limit by a factor of two using structured illumination microscopy.* Journal of Microscopy, 2000. **198**: p. 82-87.
99. Gustafsson, M.G.L., et al., *Three-dimensional resolution doubling in wide-field fluorescence microscopy by structured illumination.* Biophysical Journal, 2008. **94**(12): p. 4957-4970.

100. Lukosz, W., *Optical Systems with Resolving Powers Exceeding Classical Limit.* Journal of the Optical Society of America, 1966. **56**(11): p. 1463-&.
101. Schermelleh, L., et al., *Subdiffraction multicolor imaging of the nuclear periphery with 3D structured illumination microscopy.* Science, 2008. **320**(5881): p. 1332-1336.
102. Muller, C.B. and J. Enderlein, *Image scanning microscopy.* Phys Rev Lett, 2010. **104**(19): p. 198101.
103. York, A.G., et al., *Resolution doubling in live, multicellular organisms via multifocal structured illumination microscopy.* Nat Methods, 2012. **9**(7): p. 749-54.
104. Schulz, O., et al., *Resolution doubling in fluorescence microscopy with confocal spinning-disk image scanning microscopy.* Proc Natl Acad Sci U S A, 2013. **110**(52): p. 21000-5.
105. York, A.G., et al., *Instant super-resolution imaging in live cells and embryos via analog image processing.* Nat Methods, 2013. **10**(11): p. 1122-6.
106. De Luca, G.M., et al., *Re-scan confocal microscopy: scanning twice for better resolution.* Biomed Opt Express, 2013. **4**(11): p. 2644-56.
107. Sahl, S.J., et al., *Comment on "Extended-resolution structured illumination imaging of endocytic and cytoskeletal dynamics".* Science, 2016. **352**(6285).
108. Pospisil, J., K. Fliegel, and M. Klima, *Analysis of image reconstruction artifacts in structured illumination microscopy.* Applications of Digital Image Processing Xl, 2017. **10396**.
109. Heintzmann, R. and T. Huser, *Super-Resolution Structured Illumination Microscopy.* Chemical Reviews, 2017. **117**(23): p. 13890-13908.
110. Schaefer, L.H., D. Schuster, and J. Schaffer, *Structured illumination microscopy: artefact analysis and reduction utilizing a parameter optimization approach.* Journal of Microscopy, 2004. **216**: p. 165-174.
111. Karras, C., et al., *Successful optimization of reconstruction parameters in structured illumination microscopy - A practical guide.* Optics Communications, 2019. **436**: p. 69-75.
112. Culley, S., et al., *Quantitative mapping and minimization of super-resolution optical imaging artifacts.* Nature Methods, 2018. **15**(4): p. 263-+.
113. Lang, M.C., et al., *4Pi microscopy with negligible sidelobes.* New Journal of Physics, 2008. **10**.
114. Bewersdorf, J., R. Schmidt, and S.W. Hell, *Comparison of I5M and 4Pi-microscopy.* J Microsc, 2006. **222**(Pt 2): p. 105-17.
115. Yi, X. and S. Weiss, *Cusp-artifacts in high order Superresolution Optical Fluctuation Imaging.* bioRxiv, 2019: p. 545574.
116. Yi, X., et al., *Moments reconstruction and local dynamic range compression of high order Superresolution Optical Fluctuation Imaging.* bioRxiv, 2018: p. 500819.
117. Burns, D.H., et al., *Strategies for Attaining Superresolution Using Spectroscopic Data as Constraints.* Applied Optics, 1985. **24**(2): p. 154-161.
118. Betzig, E., *Proposed Method for Molecular Optical Imaging.* Optics Letters, 1995. **20**(3): p. 237-239.
119. van Oijen, A.M., et al., *Far-field fluorescence microscopy beyond the diffraction limit.* Journal of the Optical Society of America a-Optics Image Science and Vision, 1999. **16**(4): p. 909-915.
120. Hell, S.W., *Strategy for far-field optical imaging and writing without diffraction limit.* Physics Letters A, 2004. **326**(1-2): p. 140-145.
121. Hell, S.W., S. Jakobs, and L. Kastrup, *Imaging and writing at the nanoscale with focused visible light through saturable optical transitions.* Applied Physics a-Materials Science & Processing, 2003. **77**(7): p. 859-860.
122. Boyer, D., et al., *Photothermal imaging of nanometer-sized metal particles among scatterers.* Science, 2002. **297**(5584): p. 1160-3.
123. Hell, S.W., *Toward fluorescence nanoscopy.* Nature Biotechnology, 2003. **21**(11): p. 1347-1355.
124. Hell, S.W., M. Dyba, and S. Jakobs, *Concepts for nanoscale resolution in fluorescence microscopy.* Curr Opin Neurobiol, 2004. **14**(5): p. 599-609.
125. Heisenberg, W., *The Physical Principles of the Quantum Theory*. 1930: Ill., The University of Chicago Press.

126. Bobroff, N., *Position Measurement with a Resolution and Noise-Limited Instrument.* Review of Scientific Instruments, 1986. **57**(6): p. 1152-1157.
127. Hell, S.W., *Microscopy and its focal switch.* Nature Methods, 2009. **6**(1): p. 24-32.
128. Schnell, U., et al., *Immunolabeling artifacts and the need for live-cell imaging.* Nature Methods, 2012. **9**(2): p. 152-158.
129. Winter, P.W. and H. Shroff, *Faster fluorescence microscopy: advances in high speed biological imaging.* Current Opinion in Chemical Biology, 2014. **20**: p. 46-53.
130. Nyquist, H., *Certain Topics in Telegraph Transmission Theory* Transactions of the American Institute of Electrical Engineers, 1928. **47**(2): p. 617 - 644
131. Shannon, C.E., *Communication in the Presence of Noise.* Proceedings of the Institute of Radio Engineers, 1949. **37**(1): p. 10-21.
132. Demmerle, J., et al., *Assessing resolution in super-resolution imaging.* Methods, 2015. **88**: p. 3-10.
133. Deschout, H., et al., *Precisely and accurately localizing single emitters in fluorescence microscopy.* Nat Methods, 2014. **11**(3): p. 253-66.
134. Baddeley, D. and J. Bewersdorf, *Biological Insight from Super-Resolution Microscopy: What We Can Learn from Localization-Based Images.* Annu Rev Biochem, 2018. **87**: p. 965-989.
135. Vreja, I.C., et al., *Super-resolution Microscopy of Clickable Amino Acids Reveals the Effects of Fluorescent Protein Tagging on Protein Assemblies.* Acs Nano, 2015. **9**(11): p. 11034-11041.
136. Harke, B., et al., *Resolution scaling in STED microscopy.* Optics Express, 2008. **16**(6): p. 4154-4162.
137. Gottfert, F., et al., *Coaligned Dual-Channel STED Nanoscopy and Molecular Diffusion Analysis at 20 nm Resolution.* Biophysical Journal, 2013. **105**(1): p. L1-L3.
138. Grotjohann, T., et al., *rsEGFP2 enables fast RESOLFT nanoscopy of living cells.* Elife, 2012. **1**: p. e00248.
139. Testa, I., et al., *Dual Channel RESOLFT Nanoscopy by Using Fluorescent State Kinetics.* Nano Letters, 2015. **15**(1): p. 103-106.
140. Dyba, M. and S.W. Hell, *Focal spots of size lambda/23 open up far-field florescence microscopy at 33 nm axial resolution.* Physical Review Letters, 2002. **88**(16).
141. Donnert, G., et al., *Macromolecular-scale resolution in biological fluorescence microscopy.* Proceedings of the National Academy of Sciences of the United States of America, 2006. **103**(31): p. 11440-11445.
142. Bretschneider, S., C. Eggeling, and S.W. Hell, *Breaking the diffraction barrier in fluorescence microscopy by optical shelving.* Phys Rev Lett, 2007. **98**(21): p. 218103.
143. Westphal, V. and S.W. Hell, *Nanoscale resolution in the focal plane of an optical microscope.* Phys Rev Lett, 2005. **94**(14): p. 143903.
144. Gustafsson, M.G.L., *Nonlinear structured-illumination microscopy: Wide-field fluorescence imaging with theoretically unlimited resolution.* Proceedings of the National Academy of Sciences of the United States of America, 2005. **102**(37): p. 13081-13086.
145. Brakemann, T., et al., *A reversibly photoswitchable GFP-like protein with fluorescence excitation decoupled from switching.* Nature Biotechnology, 2011. **29**(10): p. 942-U132.
146. Bossi, M., et al., *Breaking the diffraction resolution barrier in far-field microscopy by molecular optical bistability.* New Journal of Physics, 2006. **8**.
147. Grotjohann, T., et al., *Diffraction-unlimited all-optical imaging and writing with a photochromic GFP.* Nature, 2011. **478**(7368): p. 204-208.
148. Tortarolo, G., et al., *Evaluating image resolution in stimulated emission depletion microscopy.* Optica, 2018. **5**(1): p. 32-35.
149. Wildanger, D., et al., *Solid immersion facilitates fluorescence microscopy with nanometer resolution and sub-angstrom emitter localization.* Adv Mater, 2012. **24**(44): p. OP309-13.
150. Rittweger, E., et al., *STED microscopy reveals crystal colour centres with nanometric resolution.* Nature Photonics, 2009. **3**(3): p. 144-147.

151. Klar, T.A., et al., *Fluorescence microscopy with diffraction resolution barrier broken by stimulated emission.* Proceedings of the National Academy of Sciences of the United States of America, 2000. **97**(15): p. 8206-8210.
152. Willig, K.I., et al., *STED microscopy reveals that synaptotagmin remains clustered after synaptic vesicle exocytosis.* Nature, 2006. **440**(7086): p. 935-939.
153. Klar, T.A. and S.W. Hell, *Subdiffraction resolution in far-field fluorescence microscopy.* Opt Lett, 1999. **24**(14): p. 954-6.
154. Ioannides, A.A., et al., *Magnetic field tomography of cortical and deep processes: examples of "real-time mapping" of averaged and single trial MEG signals.* Int J Psychophysiol, 1995. **20**(3): p. 161-75.
155. Heintzmann, R., T.M. Jovin, and C. Cremer, *Saturated patterned excitation microscopy - a concept for optical resolution improvement.* Journal of the Optical Society of America a-Optics Image Science and Vision, 2002. **19**(8): p. 1599-1609.
156. Kwon, J.W., et al., *RESOLFT nanoscopy with photoswitchable organic fluorophores.* Scientific Reports, 2015. **5**.
157. van de Linde, S., et al., *Direct stochastic optical reconstruction microscopy with standard fluorescent probes.* Nat Protoc, 2011. **6**(7): p. 991-1009.
158. Bates, M., et al., *Multicolor super-resolution imaging with photo-switchable fluorescent probes.* Science, 2007. **317**(5845): p. 1749-1753.
159. Folling, J., et al., *Photochromic rhodamines provide nanoscopy with optical sectioning.* Angewandte Chemie-International Edition, 2007. **46**(33): p. 6266-6270.
160. Vaughan, J.C., S. Jia, and X. Zhuang, *Ultrabright photoactivatable fluorophores created by reductive caging.* Nat Methods, 2012. **9**(12): p. 1181-4.
161. Axelrod, D., *Cell-Substrate Contacts Illuminated by Total Internal-Reflection Fluorescence.* Journal of Cell Biology, 1981. **89**(1): p. 141-145.
162. Tokunaga, M., N. Imamoto, and K. Sakata-Sogawa, *Highly inclined thin illumination enables clear single-molecule imaging in cells.* Nat Methods, 2008. **5**(2): p. 159-61.
163. Huang, B., et al., *Three-dimensional super-resolution imaging by stochastic optical reconstruction microscopy.* Science, 2008. **319**(5864): p. 810-813.
164. Pavani, S.R.P., et al., *Three-dimensional, single-molecule fluorescence imaging beyond the diffraction limit by using a double-helix point spread function.* Proceedings of the National Academy of Sciences of the United States of America, 2009. **106**(9): p. 2995-2999.
165. Juette, M.F., et al., *Three-dimensional sub-100 nm resolution fluorescence microscopy of thick samples.* Nature Methods, 2008. **5**(6): p. 527-529.
166. Shroff, H., et al., *Dual-color superresolution imaging of genetically expressed probes within individual adhesion complexes.* Proceedings of the National Academy of Sciences of the United States of America, 2007. **104**(51): p. 20308-20313.
167. Burgert, A., et al., *Artifacts in single-molecule localization microscopy.* Histochem Cell Biol, 2015. **144**(2): p. 123-31.
168. Hell, S.W., J. Soukka, and P.E. Haenninen, *Two- and multiphoton detection as an imaging mode and means of increasing the resolution in far-field light microscopy: A study based on photon-optics.* Bioimaging, 1995. **3**(2): p. 64-69.
169. Hess, S.T., T.P.K. Girirajan, and M.D. Mason, *Ultra-high resolution imaging by fluorescence photoactivation localization microscopy.* Biophysical Journal, 2006. **91**(11): p. 4258-4272.
170. Folling, J., et al., *Fluorescence nanoscopy with optical sectioning by two-photon induced molecular switching using continuous-wave lasers.* Chemphyschem, 2008. **9**(2): p. 321-326.
171. Bates, M., T.R. Blosser, and X.W. Zhuang, *Short-range spectroscopic ruler based on a single-molecule optical switch.* Physical Review Letters, 2005. **94**(10).
172. Dempsey, G.T., et al., *Evaluation of fluorophores for optimal performance in localization-based super-resolution imaging.* Nature Methods, 2011. **8**(12): p. 1027-+.
173. Bock, H., et al., *Two-color far-field fluorescence nanoscopy based on photoswitchable emitters.* Applied Physics B-Lasers and Optics, 2007. **88**(2): p. 161-165.

174. Egner, A., et al., *Fluorescence nanoscopy in whole cells by asynchronous localization of photoswitching emitters.* Biophysical Journal, 2007. **93**(9): p. 3285-3290.
175. Folling, J., et al., *Fluorescence nanoscopy by ground-state depletion and single-molecule return.* Nature Methods, 2008. **5**(11): p. 943-945.
176. Heilemann, M., et al., *Subdiffraction-resolution fluorescence imaging with conventional fluorescent probes.* Angewandte Chemie-International Edition, 2008. **47**(33): p. 6172-6176.
177. Sharonov, A. and R.M. Hochstrasser, *Wide-field subdiffraction imaging by accumulated binding of diffusing probes.* Proceedings of the National Academy of Sciences of the United States of America, 2006. **103**(50): p. 18911-18916.
178. Giannone, G., et al., *Dynamic Superresolution Imaging of Endogenous Proteins on Living Cells at Ultra-High Density.* Biophysical Journal, 2010. **99**(4): p. 1303-1310.
179. Jungmann, R., et al., *Single-Molecule Kinetics and Super-Resolution Microscopy by Fluorescence Imaging of Transient Binding on DNA Origami.* Nano Letters, 2010. **10**(11): p. 4756-4761.
180. Jungmann, R., et al., *Quantitative super-resolution imaging with qPAINT.* Nature Methods, 2016. **13**(5): p. 439-+.
181. Jungmann, R., et al., *Multiplexed 3D cellular super-resolution imaging with DNA-PAINT and Exchange-PAINT.* Nature Methods, 2014. **11**(3): p. 313-U292.
182. Schueder, F., et al., *Universal Super-Resolution Multiplexing by DNA Exchange.* Angewandte Chemie-International Edition, 2017. **56**(14): p. 4052-4055.
183. Schoen, I., et al., *Binding-activated localization microscopy of DNA structures.* Nano Lett, 2011. **11**(9): p. 4008-11.
184. Szczurek, A., et al., *Imaging chromatin nanostructure with binding-activated localization microscopy based on DNA structure fluctuations.* Nucleic Acids Res, 2017. **45**(8): p. e56.
185. Feynman, R.P., *There's plenty of room at the bottom.* Engineering and Science, 1960. **23**: p. 22-26.
186. Balzarotti, F., et al., *Nanometer resolution imaging and tracking of fluorescent molecules with minimal photon fluxes.* Science, 2017. **355**(6325): p. 606-612.
187. Eilers, Y., et al., *MINFLUX monitors rapid molecular jumps with superior spatiotemporal resolution.* Proc Natl Acad Sci U S A, 2018. **115**(24): p. 6117-6122.
188. Gwosch, K.C., et al., *MINFLUX nanoscopy delivers multicolor nanometer 3D-resolution in (living) cells.* bioRxiv, 2019: p. 734251.
189. Friedrich, M., et al., *STED-SPIM: Stimulated Emission Depletion Improves Sheet Illumination Microscopy Resolution.* Biophysical Journal, 2011. **100**(8): p. L43-L45.
190. Hoyer, P., et al., *Breaking the diffraction limit of light-sheet fluorescence microscopy by RESOLFT.* Proceedings of the National Academy of Sciences of the United States of America, 2016. **113**(13): p. 3442-3446.
191. Legant, W.R., et al., *High-density three-dimensional localization microscopy across large volumes.* Nature Methods, 2016. **13**(4): p. 359-365.
192. Chen, B.C., et al., *Lattice light-sheet microscopy: Imaging molecules to embryos at high spatiotemporal resolution.* Science, 2014. **346**(6208): p. 439-+.
193. Chang, B.J., V.D. Perez Meza, and E.H.K. Stelzer, *csiLSFM combines light-sheet fluorescence microscopy and coherent structured illumination for a lateral resolution below 100 nm.* Proc Natl Acad Sci U S A, 2017. **114**(19): p. 4869-4874.
194. Li, D., et al., *ADVANCED IMAGING. Extended-resolution structured illumination imaging of endocytic and cytoskeletal dynamics.* Science, 2015. **349**(6251): p. aab3500.
195. Cnossen, J., et al., *Localization microscopy at doubled precision with patterned illumination.* bioRxiv, 2019: p. 554337.
196. Halpern, A.R., et al., *Hybrid Structured Illumination Expansion Microscopy Reveals Microbial Cytoskeleton Organization.* Acs Nano, 2017. **11**(12): p. 12677-12686.

197. Cahoon, C.K., et al., *Superresolution expansion microscopy reveals the three-dimensional organization of the Drosophila synaptonemal complex.* Proceedings of the National Academy of Sciences of the United States of America, 2017. **114**(33): p. E6857-E6866.
198. Unnersjo-Jess, D., et al., *Confocal super-resolution imaging of the glomerular filtration barrier enabled by tissue expansion.* Kidney International, 2018. **93**(4): p. 1008-1013.
199. Gao, M.F., et al., *Expansion Stimulated Emission Depletion Microscopy (ExSTED).* Acs Nano, 2018. **12**(5): p. 4178-4185.
200. Gambarotto, D., et al., *Imaging cellular ultrastructures using expansion microscopy (U-ExM).* Nature Methods, 2019. **16**(1): p. 71-+.
201. Dyba, M., J. Keller, and S.W. Hell, *Phase filter enhanced STED-4Pi fluorescence microscopy: theory and experiment.* New Journal of Physics, 2005. **7**.
202. Schmidt, R., et al., *Spherical nanosized focal spot unravels the interior of cells.* Nat Methods, 2008. **5**(6): p. 539-44.
203. Curdt, F., et al., *isoSTED nanoscopy with intrinsic beam alignment.* Opt Express, 2015. **23**(24): p. 30891-903.
204. Dyba, M., S. Jakobs, and S.W. Hell, *Immunofluorescence stimulated emission depletion microscopy.* Nature Biotechnology, 2003. **21**(11): p. 1303-1304.
205. Bohm, U., S.W. Hell, and R. Schmidt, *4Pi-RESOLFT nanoscopy.* Nature Communications, 2016. **7**.
206. Aquino, D., et al., *Two-color nanoscopy of three-dimensional volumes by 4Pi detection of stochastically switched fluorophores.* Nature Methods, 2011. **8**(4): p. 353-+.
207. Shtengel, G., et al., *Interferometric fluorescent super-resolution microscopy resolves 3D cellular ultrastructure.* Proc Natl Acad Sci U S A, 2009. **106**(9): p. 3125-30.
208. Huang, F., et al., *Ultra-High Resolution 3D Imaging of Whole Cells.* Cell, 2016. **166**(4): p. 1028-1040.
209. Gu, L., et al., *Molecular resolution imaging by repetitive optical selective exposure.* Nature Methods, 2019.
210. Bianchini, P., et al., *STED nanoscopy: a glimpse into the future.* Cell Tissue Res, 2015. **360**(1): p. 143-50.
211. Vicidomini, G., P. Bianchini, and A. Diaspro, *STED super-resolved microscopy.* Nat Methods, 2018. **15**(3): p. 173-182.
212. Lidke, K.A., et al., *Superresolution by localization of quantum dots using blinking statistics.* Optics Express, 2005. **13**(18): p. 7052-7062.
213. Heintzmann, R. and G. Ficz, *Breaking the resolution limit in light microscopy.* Brief Funct Genomic Proteomic, 2006. **5**(4): p. 289-301.
214. Engelhardt, J., et al., *Molecular orientation affects localization accuracy in superresolution far-field fluorescence microscopy.* Nano Lett, 2011. **11**(1): p. 209-13.
215. Leutenegger, M., C. Eggeling, and S.W. Hell, *Analytical description of STED microscopy performance.* Opt Express, 2010. **18**(25): p. 26417-29.
216. Moerner, W.E., *Single-molecule mountains yield nanoscale cell images.* Nat Methods, 2006. **3**(10): p. 781-2.
217. Blom, H., et al., *Spatial distribution of Na+-K+-ATPase in dendritic spines dissected by nanoscale superresolution STED microscopy.* Bmc Neuroscience, 2011. **12**.
218. Kellner, R.R., et al., *Nanoscale organization of nicotinic acetylcholine receptors revealed by stimulated emission depletion microscopy.* Neuroscience, 2007. **144**(1): p. 135-143.
219. Kittel, R.J., et al., *Bruchpilot promotes active zone assembly, Ca2+ channel clustering, and vesicle release.* Science, 2006. **312**(5776): p. 1051-1054.
220. Lau, L., et al., *STED Microscopy with Optimized Labeling Density Reveals 9-Fold Arrangement of a Centriole Protein.* Biophysical Journal, 2012. **102**(12): p. 2926-2935.
221. Schmidt, R., et al., *Mitochondrial cristae revealed with focused light.* Nano Lett, 2009. **9**(6): p. 2508-10.

222. Sieber, J.J., et al., *The SNARE motif is essential for the formation of syntaxin clusters in the plasma membrane.* Biophys J, 2006. **90**(8): p. 2843-51.
223. Wagner, E., et al., *Stimulated emission depletion live-cell super-resolution imaging shows proliferative remodeling of T-tubule membrane structures after myocardial infarction.* Circ Res, 2012. **111**(4): p. 402-14.
224. Han, K.Y., et al., *Dark state photophysics of nitrogen-vacancy centres in diamond.* New Journal of Physics, 2012. **14**.
225. Arroyo-Camejo, S., et al., *Stimulated Emission Depletion Microscopy Resolves Individual Nitrogen Vacancy Centers in Diamond Nanocrystals.* Acs Nano, 2013. **7**(12): p. 10912-10919.
226. Zhu, Y., et al., *The Biocompatibility of Nanodiamonds and Their Application in Drug Delivery Systems.* Theranostics, 2012. **2**(3): p. 302-312.
227. Mohan, N., et al., *In Vivo Imaging and Toxicity Assessments of Fluorescent Nanodiamonds in Caenorhabditis elegans.* Nano Letters, 2010. **10**(9): p. 3692-3699.
228. McGuinness, L.P., et al., *Quantum measurement and orientation tracking of fluorescent nanodiamonds inside living cells.* Nature Nanotechnology, 2011. **6**(6): p. 358-363.
229. Pope, I., et al., *Coherent anti-Stokes Raman scattering microscopy of single nanodiamonds.* Nature Nanotechnology, 2014. **9**(11): p. 940-946.
230. Hemelaar, S.R., et al., *The interaction of fluorescent nanodiamond probes with cellular media.* Microchimica Acta, 2017. **184**(4): p. 1001-1009.
231. Faklaris, O., et al., *Detection of Single Photoluminescent Diamond Nanoparticles in Cells and Study of the Internalization Pathway.* Small, 2008. **4**(12): p. 2236-2239.
232. Hemelaar, S.R., et al., *Nanodiamonds as multi-purpose labels for microscopy.* Scientific Reports, 2017. **7**.
233. Harke, B., et al., *Three-dimensional nanoscopy of colloidal crystals.* Nano Lett, 2008. **8**(5): p. 1309-13.
234. Ullal, C.K., et al., *Block copolymer nanostructures mapped by far-field optics.* Nano Lett, 2009. **9**(6): p. 2497-500.
235. Ullal, C.K., et al., *Flexible Microdomain Specific Staining of Block Copolymers for 3D Optical Nanoscopy.* Macromolecules, 2011. **44**(19): p. 7508-7510.
236. Friedemann, K., et al., *Characterization via Two-Color STED Microscopy of Nanostructured Materials Synthesized by Colloid Electrospinning.* Langmuir, 2011. **27**(11): p. 7132-7139.
237. Wildanger, D., J.R. Maze, and S.W. Hell, *Diffraction Unlimited All-Optical Recording of Electron Spin Resonances.* Physical Review Letters, 2011. **107**(1).
238. Donnert, G., C. Eggeling, and S.W. Hell, *Triplet-relaxation microscopy with bunched pulsed excitation.* Photochem Photobiol Sci, 2009. **8**(4): p. 481-5.
239. Dyba, M. and S.W. Hell, *Photostability of a fluorescent marker under pulsed excited-state depletion through stimulated emission.* Applied Optics, 2003. **42**(25): p. 5123-5129.
240. Vicidomini, G., et al., *STED nanoscopy with time-gated detection: theoretical and experimental aspects.* PLoS One, 2013. **8**(1): p. e54421.
241. Vicidomini, G., et al., *STED with wavelengths closer to the emission maximum.* Opt Express, 2012. **20**(5): p. 5225-36.
242. Willig, K.I., et al., *STED microscopy with continuous wave beams.* Nat Methods, 2007. **4**(11): p. 915-8.
243. Wildanger, D., et al., *A STED microscope aligned by design.* Opt Express, 2009. **17**(18): p. 16100-10.
244. Reuss, M., J. Engelhardt, and S.W. Hell, *Birefringent device converts a standard scanning microscope into a STED microscope that also maps molecular orientation.* Opt Express, 2010. **18**(2): p. 1049-58.
245. Bingen, P., et al., *Parallelized STED fluorescence nanoscopy.* Opt Express, 2011. **19**(24): p. 23716-26.
246. Bergermann, F., et al., *2000-fold parallelized dual-color STED fluorescence nanoscopy.* Opt Express, 2015. **23**(1): p. 211-23.

247. Yang, B., et al., *Large parallelization of STED nanoscopy using optical lattices.* Opt Express, 2014. **22**(5): p. 5581-9.
248. Moneron, G., et al., *Fast STED microscopy with continuous wave fiber lasers.* Opt Express, 2010. **18**(2): p. 1302-9.
249. Schneider, J., et al., *Ultrafast, temporally stochastic STED nanoscopy of millisecond dynamics.* Nat Methods, 2015. **12**(9): p. 827-30.
250. Wildanger, D., et al., *A compact STED microscope providing 3D nanoscale resolution.* J Microsc, 2009. **236**(1): p. 35-43.
251. Buckers, J., et al., *Simultaneous multi-lifetime multi-color STED imaging for colocalization analyses.* Opt Express, 2011. **19**(4): p. 3130-43.
252. Neher, R. and E. Neher, *Optimizing imaging parameters for the separation of multiple labels in a fluorescence image.* J Microsc, 2004. **213**(1): p. 46-62.
253. Niehorster, T., et al., *Multi-target spectrally resolved fluorescence lifetime imaging microscopy.* Nat Methods, 2016. **13**(3): p. 257-62.
254. Donnert, G., et al., *Two-color far-field fluorescence nanoscopy.* Biophysical Journal, 2007. **92**(8): p. L67-L69.
255. Meyer, L., et al., *Dual-color STED microscopy at 30-nm focal-plane resolution.* Small, 2008. **4**(8): p. 1095-100.
256. Neumann, D., et al., *Two-color STED microscopy reveals different degrees of colocalization between hexokinase-I and the three human VDAC isoforms.* PMC Biophys, 2010. **3**(1): p. 4.
257. Osseforth, C., et al., *Simultaneous dual-color 3D STED microscopy.* Opt Express, 2014. **22**(6): p. 7028-39.
258. Blom, H., et al., *Spatial distribution of DARPP-32 in dendritic spines.* PLoS One, 2013. **8**(9): p. e75155.
259. Bottanelli, F., et al., *Two-colour live-cell nanoscale imaging of intracellular targets.* Nat Commun, 2016. **7**: p. 10778.
260. Pellett, P.A., et al., *Two-color STED microscopy in living cells.* Biomed Opt Express, 2011. **2**(8): p. 2364-71.
261. D'Este, E., et al., *Subcortical cytoskeleton periodicity throughout the nervous system.* Sci Rep, 2016. **6**: p. 22741.
262. D'Este, E., et al., *STED nanoscopy reveals the ubiquity of subcortical cytoskeleton periodicity in living neurons.* Cell Rep, 2015. **10**(8): p. 1246-51.
263. Tonnesen, J., et al., *Two-Color STED Microscopy of Living Synapses Using A Single Laser-Beam Pair.* Biophysical Journal, 2011. **101**(10): p. 2545-2552.
264. Willig, K.I., et al., *Dual-Label STED Nanoscopy of Living Cells Using Photochromism.* Nano Letters, 2011. **11**(9): p. 3970-3973.
265. Galiani, S., et al., *Super-resolution Microscopy Reveals Compartmentalization of Peroxisomal Membrane Proteins.* J Biol Chem, 2016. **291**(33): p. 16948-62.
266. Sidenstein, S.C., et al., *Multicolour Multilevel STED nanoscopy of Actin/Spectrin Organization at Synapses.* Sci Rep, 2016. **6**: p. 26725.
267. Ronnlund, D., et al., *Multicolor fluorescence nanoscopy by photobleaching: concept, verification, and its application to resolve selective storage of proteins in platelets.* ACS Nano, 2014. **8**(5): p. 4358-65.
268. Winter, F.R., et al., *Multicolour nanoscopy of fixed and living cells with a single STED beam and hyperspectral detection.* Sci Rep, 2017. **7**: p. 46492.
269. Wildanger, D., et al., *STED microscopy with a supercontinuum laser source.* Opt Express, 2008. **16**(13): p. 9614-21.
270. Auksorius, E., et al., *Stimulated emission depletion microscopy with a supercontinuum source and fluorescence lifetime imaging.* Opt Lett, 2008. **33**(2): p. 113-5.
271. Stelzer, E.H., *Light-sheet fluorescence microscopy for quantitative biology.* Nat Methods, 2015. **12**(1): p. 23-6.

272. Magidson, V. and A. Khodjakov, *Circumventing photodamage in live-cell microscopy.* Methods Cell Biol, 2013. **114**: p. 545-60.
273. Eggeling, C., et al., *Photobleaching of Fluorescent Dyes under Conditions Used for Single-Molecule Detection: Evidence of Two-Step Photolysis.* Anal Chem, 1998. **70**(13): p. 2651-9.
274. Eggeling, C., A. Volkmer, and C.A. Seidel, *Molecular photobleaching kinetics of Rhodamine 6G by one- and two-photon induced confocal fluorescence microscopy.* Chemphyschem, 2005. **6**(5): p. 791-804.
275. Widengren, J. and R. Rigler, *Photobleaching investigations of dyes using fluorescence correlation spectroscopy (FCS).* Progress in Biophysics & Molecular Biology, 1996. **65**: p. Ph109-Ph109.
276. Turrens, J.F., *Mitochondrial formation of reactive oxygen species.* J Physiol, 2003. **552**(Pt 2): p. 335-44.
277. Schafer, F.Q. and G.R. Buettner, *Redox environment of the cell as viewed through the redox state of the glutathione disulfide/glutathione couple.* Free Radic Biol Med, 2001. **30**(11): p. 1191-212.
278. Riley, P.A., *Free radicals in biology: oxidative stress and the effects of ionizing radiation.* Int J Radiat Biol, 1994. **65**(1): p. 27-33.
279. Poli, G., et al., *Oxidative stress and cell signalling.* Curr Med Chem, 2004. **11**(9): p. 1163-82.
280. Burhans, W.C. and N.H. Heintz, *The cell cycle is a redox cycle: linking phase-specific targets to cell fate.* Free Radic Biol Med, 2009. **47**(9): p. 1282-93.
281. Davies, M.J., *Reactive species formed on proteins exposed to singlet oxygen.* Photochem Photobiol Sci, 2004. **3**(1): p. 17-25.
282. Pattison, D.I., A.S. Rahmanto, and M.J. Davies, *Photo-oxidation of proteins.* Photochem Photobiol Sci, 2012. **11**(1): p. 38-53.
283. Smith, W.L. and R.C. Murphy, *Oxidized lipids formed non-enzymatically by reactive oxygen species.* J Biol Chem, 2008. **283**(23): p. 15513-4.
284. Cadet, J. and J.R. Wagner, *DNA base damage by reactive oxygen species, oxidizing agents, and UV radiation.* Cold Spring Harb Perspect Biol, 2013. **5**(2).
285. Björn, L.O., *Photobiology: The Science of Light and Life*. 2012: Springer Netherlands.
286. Hoebe, R.A., et al., *Controlled light-exposure microscopy reduces photobleaching and phototoxicity in fluorescence live-cell imaging.* Nat Biotechnol, 2007. **25**(2): p. 249-53.
287. Kuznetsova, D.S., et al., *Photobleaching and phototoxicity of KillerRed in tumor spheroids induced by continuous wave and pulsed laser illumination.* J Biophotonics, 2015. **8**(11-12): p. 952-60.
288. Logg, K., et al., *Investigations on light-induced stress in fluorescence microscopy using nuclear localization of the transcription factor Msn2p as a reporter.* FEMS Yeast Res, 2009. **9**(6): p. 875-84.
289. Laissue, P.P., et al., *Assessing phototoxicity in live fluorescence imaging.* Nat Methods, 2017. **14**(7): p. 657-661.
290. Pattison, D.I. and M.J. Davies, *Actions of ultraviolet light on cellular structures.* EXS, 2006(96): p. 131-57.
291. Bixler, J.N., et al., *Assessment of tissue heating under tunable near-infrared radiation.* J Biomed Opt, 2014. **19**(7): p. 070501.
292. Koester, H.J., et al., *Ca2+ fluorescence imaging with pico- and femtosecond two-photon excitation: signal and photodamage.* Biophys J, 1999. **77**(4): p. 2226-36.
293. Knight, M.M., et al., *Live cell imaging using confocal microscopy induces intracellular calcium transients and cell death.* Am J Physiol Cell Physiol, 2003. **284**(4): p. C1083-9.
294. Wakabayashi, T., *Structural changes of mitochondria related to apoptosis: swelling and megamitochondria formation.* Acta Biochim Pol, 1999. **46**(2): p. 223-37.
295. Nichols, M.G., E.E. Barth, and J.A. Nichols, *Reduction in DNA synthesis during two-photon microscopy of intrinsic reduced nicotinamide adenine dinucleotide fluorescence.* Photochem Photobiol, 2005. **81**(2): p. 259-69.

296. Tirlapur, U.K., et al., *Femtosecond near-infrared laser pulses elicit generation of reactive oxygen species in mammalian cells leading to apoptosis-like death.* Exp Cell Res, 2001. **263**(1): p. 88-97.
297. Batista, L.F., et al., *How DNA lesions are turned into powerful killing structures: insights from UV-induced apoptosis.* Mutat Res, 2009. **681**(2-3): p. 197-208.
298. Dixit, R. and R. Cyr, *Cell damage and reactive oxygen species production induced by fluorescence microscopy: effect on mitosis and guidelines for non-invasive fluorescence microscopy.* Plant J, 2003. **36**(2): p. 280-90.
299. Goldman, R.D., J. Swedlow, and D.L. Spector, *Live Cell Imaging: A Laboratory Manual*. 2010: Cold Spring Harbor Laboratory Press.
300. Carlton, P.M., et al., *Fast live simultaneous multiwavelength four-dimensional optical microscopy.* Proc Natl Acad Sci U S A, 2010. **107**(37): p. 16016-22.
301. Wu, Y., et al., *Resonant Scanning with Large Field of View Reduces Photobleaching and Enhances Fluorescence Yield in STED Microscopy.* Sci Rep, 2015. **5**: p. 14766.
302. Oracz, J., et al., *Photobleaching in STED nanoscopy and its dependence on the photon flux applied for reversible silencing of the fluorophore.* Sci Rep, 2017. **7**(1): p. 11354.
303. Kilian, N., et al., *Assessing photodamage in live-cell STED microscopy.* Nature Methods, 2018. **15**(10): p. 755-756.
304. Orrenius, S., B. Zhivotovsky, and P. Nicotera, *Regulation of cell death: The calcium-apoptosis link.* Nature Reviews Molecular Cell Biology, 2003. **4**(7): p. 552-565.
305. Waldchen, S., et al., *Light-induced cell damage in live-cell super-resolution microscopy.* Sci Rep, 2015. **5**: p. 15348.
306. Strack, R., *Death by super-resolution imaging.* Nature Methods, 2015. **12**(12): p. 1111-1111.
307. Ouyang, W., et al., *Deep learning massively accelerates super-resolution localization microscopy.* Nat Biotechnol, 2018. **36**(5): p. 460-468.
308. Wang, H., et al., *Deep learning enables cross-modality super-resolution in fluorescence microscopy.* Nat Methods, 2019. **16**(1): p. 103-110.
309. Jia, S., B. Han, and J.N. Kutz, *Example-Based Super-Resolution Fluorescence Microscopy.* Sci Rep, 2018. **8**(1): p. 5700.
310. Shao, L., et al., *Super-resolution 3D microscopy of live whole cells using structured illumination.* Nat Methods, 2011. **8**(12): p. 1044-6.
311. Fiolka, R., et al., *Time-lapse two-color 3D imaging of live cells with doubled resolution using structured illumination.* Proc Natl Acad Sci U S A, 2012. **109**(14): p. 5311-5.
312. Huang, X., et al., *Fast, long-term, super-resolution imaging with Hessian structured illumination microscopy.* Nat Biotechnol, 2018. **36**(5): p. 451-459.
313. Abrahamsson, S., et al., *Fast multicolor 3D imaging using aberration-corrected multifocus microscopy.* Nat Methods, 2013. **10**(1): p. 60-3.
314. Abrahamsson, S., et al., *Multifocus structured illumination microscopy for fast volumetric super-resolution imaging.* Biomedical Optics Express, 2017. **8**(9): p. 4135-4140.
315. Voie, A.H., D.H. Burns, and F.A. Spelman, *Orthogonal-plane fluorescence optical sectioning: three-dimensional imaging of macroscopic biological specimens.* J Microsc, 1993. **170**(Pt 3): p. 229-36.
316. Huisken, J., et al., *Optical sectioning deep inside live embryos by selective plane illumination microscopy.* Science, 2004. **305**(5686): p. 1007-9.
317. Power, R.M. and J. Huisken, *A guide to light-sheet fluorescence microscopy for multiscale imaging.* Nat Methods, 2017. **14**(4): p. 360-373.
318. Keller, P.J., et al., *Reconstruction of zebrafish early embryonic development by scanned light sheet microscopy.* Science, 2008. **322**(5904): p. 1065-9.
319. Planchon, T.A., et al., *Rapid three-dimensional isotropic imaging of living cells using Bessel beam plane illumination.* Nat Methods, 2011. **8**(5): p. 417-23.
320. Gao, L., et al., *Noninvasive imaging beyond the diffraction limit of 3D dynamics in thickly fluorescent specimens.* Cell, 2012. **151**(6): p. 1370-85.

321. Gustavsson, A.K., et al., *3D single-molecule super-resolution microscopy with a tilted light sheet.* Nat Commun, 2018. **9**(1): p. 123.
322. Schneckenburger, H., et al., *Light exposure and cell viability in fluorescence microscopy.* J Microsc, 2012. **245**(3): p. 311-8.
323. Wagner, M., et al., *Light dose is a limiting factor to maintain cell viability in fluorescence microscopy and single molecule detection.* Int J Mol Sci, 2010. **11**(3): p. 956-66.
324. Ambrose, E.J., *A surface contact microscope for the study of cell movements.* Nature, 1956. **178**(4543): p. 1194.
325. Hopt, A. and E. Neher, *Highly nonlinear photodamage in two-photon fluorescence microscopy.* Biophys J, 2001. **80**(4): p. 2029-36.
326. Debarre, D., et al., *Mitigating phototoxicity during multiphoton microscopy of live Drosophila embryos in the 1.0-1.2 microm wavelength range.* PLoS One, 2014. **9**(8): p. e104250.
327. Klein, T., et al., *Live-cell dSTORM with SNAP-tag fusion proteins.* Nat Methods, 2011. **8**(1): p. 7-9.
328. Shroff, H., et al., *Live-cell photoactivated localization microscopy of nanoscale adhesion dynamics.* Nat Methods, 2008. **5**(5): p. 417-23.
329. van de Linde, S. and M. Sauer, *How to switch a fluorophore: from undesired blinking to controlled photoswitching.* Chem Soc Rev, 2014. **43**(4): p. 1076-87.
330. Huang, F., et al., *Video-rate nanoscopy using sCMOS camera-specific single-molecule localization algorithms.* Nat Methods, 2013. **10**(7): p. 653-8.
331. Holden, S.J., S. Uphoff, and A.N. Kapanidis, *DAOSTORM: an algorithm for high- density super-resolution microscopy.* Nat Methods, 2011. **8**(4): p. 279-80.
332. Zhu, L., et al., *Faster STORM using compressed sensing.* Nat Methods, 2012. **9**(7): p. 721-3.
333. Dertinger, T., et al., *Fast, background-free, 3D super-resolution optical fluctuation imaging (SOFI).* Proceedings of the National Academy of Sciences of the United States of America, 2009. **106**(52): p. 22287-22292.
334. Geissbuehler, S., et al., *Live-cell multiplane three-dimensional super-resolution optical fluctuation imaging.* Nature Communications, 2014. **5**.
335. Gustafsson, N., et al., *Fast live-cell conventional fluorophore nanoscopy with ImageJ through super-resolution radial fluctuations.* Nature Communications, 2016. **7**.
336. Geissbuehler, S., C. Dellagiacoma, and T. Lasser, *Comparison between SOFI and STORM.* Biomedical Optics Express, 2011. **2**(3): p. 408-420.
337. van de Linde, S., et al., *The effect of photoswitching kinetics and labeling densities on super-resolution fluorescence imaging.* J Biotechnol, 2010. **149**(4): p. 260-6.
338. Wilmes, S., et al., *Triple-color super-resolution imaging of live cells: resolving submicroscopic receptor organization in the plasma membrane.* Angew Chem Int Ed Engl, 2012. **51**(20): p. 4868-71.
339. Nozaki, T., et al., *Dynamic Organization of Chromatin Domains Revealed by Super-Resolution Live-Cell Imaging.* Mol Cell, 2017. **67**(2): p. 282-+.
340. Westphal, V., et al., *Video-rate far-field optical nanoscopy dissects synaptic vesicle movement.* Science, 2008. **320**(5873): p. 246-9.
341. Hein, B., K.I. Willig, and S.W. Hell, *Stimulated emission depletion (STED) nanoscopy of a fluorescent protein-labeled organelle inside a living cell.* Proc Natl Acad Sci U S A, 2008. **105**(38): p. 14271-6.
342. Bethge, P., et al., *Two-photon excitation STED microscopy in two colors in acute brain slices.* Biophys J, 2013. **104**(4): p. 778-85.
343. Morozova, K.S., et al., *Far-red fluorescent protein excitable with red lasers for flow cytometry and superresolution STED nanoscopy.* Biophys J, 2010. **99**(2): p. L13-5.
344. Nagerl, U.V., et al., *Live-cell imaging of dendritic spines by STED microscopy.* Proc Natl Acad Sci U S A, 2008. **105**(48): p. 18982-7.
345. Rankin, B.R., et al., *Nanoscopy in a living multicellular organism expressing GFP.* Biophys J, 2011. **100**(12): p. L63-5.

346. Urban, N.T., et al., *STED nanoscopy of actin dynamics in synapses deep inside living brain slices.* Biophys J, 2011. **101**(5): p. 1277-84.
347. Hense, A., et al., *mGarnet, A Far-Red Fluorescent Protein for Live-Cell Sted Imaging.* Biophysical Journal, 2016. **110**(3): p. 488a-488a.
348. Matela, G., et al., *A far-red emitting fluorescent marker protein, mGarnet2, for microscopy and STED nanoscopy.* Chemical Communications, 2017. **53**(5): p. 979-982.
349. Kamper, M., et al., *Near-infrared STED nanoscopy with an engineered bacterial phytochrome.* Nature Communications, 2018. **9**.
350. Hein, B., et al., *Stimulated Emission Depletion Nanoscopy of Living Cells Using SNAP-Tag Fusion Proteins.* Biophysical Journal, 2010. **98**(1): p. 158-163.
351. Schroder, J., et al., *In Vivo Labeling Method Using a Genetic Construct for Nanoscale Resolution Microscopy.* Biophysical Journal, 2009. **96**(1): p. L1-L3.
352. Heine, J., et al., *Three dimensional live-cell STED microscopy at increased depth using a water immersion objective.* Review of Scientific Instruments, 2018. **89**(5).
353. Lukinavicius, G., et al., *SiR-Hoechst is a far-red DNA stain for live-cell nanoscopy.* Nature Communications, 2015. **6**.
354. Lukinavicius, G., et al., *Fluorogenic probes for live-cell imaging of the cytoskeleton.* Nature Methods, 2014. **11**(7): p. 731-U168.
355. Berning, S., et al., *Nanoscopy in a living mouse brain.* Science, 2012. **335**(6068): p. 551.
356. Wegner, W., et al., *In vivo mouse and live cell STED microscopy of neuronal actin plasticity using far-red emitting fluorescent proteins.* Sci Rep, 2017. **7**(1): p. 11781.
357. Ji, N., D.E. Milkie, and E. Betzig, *Adaptive optics via pupil segmentation for high-resolution imaging in biological tissues.* Nature Methods, 2010. **7**(2): p. 141-U84.
358. Booth, M.J., *Adaptive optical microscopy: the ongoing quest for a perfect image.* Light-Science & Applications, 2014. **3**.
359. Gould, T.J., et al., *Adaptive optics enables 3D STED microscopy in aberrating specimens.* Optics Express, 2012. **20**(19): p. 20998-21009.
360. Antonello, J., et al., *Coma aberrations in combined two- and three-dimensional STED nanoscopy.* Opt Lett, 2016. **41**(15): p. 3631-4.
361. Patton, B.R., et al., *Is phase-mask alignment aberrating your STED microscope?* Methods and Applications in Fluorescence, 2015. **3**(2).
362. Lenz, M.O., et al., *3-D stimulated emission depletion microscopy with programmable aberration correction.* Journal of Biophotonics, 2014. **7**(1-2): p. 29-36.
363. Loew, L.M. and S.W. Hell, *Superresolving Dendritic Spines.* Biophysical Journal, 2013. **104**(4): p. 741-743.
364. Lauterbach, M.A., et al., *Comparing video-rate STED nanoscopy and confocal microscopy of living neurons.* J Biophotonics, 2010. **3**(7): p. 417-24.
365. Westphal, V., et al., *Dynamic far-field fluorescence nanoscopy.* New Journal of Physics, 2007. **9**.
366. Donnert, G., C. Eggeling, and S.W. Hell, *Major signal increase in fluorescence microscopy through dark-state relaxation.* Nat Methods, 2007. **4**(1): p. 81-6.
367. Staudt, T., et al., *Far-field optical nanoscopy with reduced number of state transition cycles.* Opt Express, 2011. **19**(6): p. 5644-57.
368. Danzl, J.G., et al., *Coordinate-targeted fluorescence nanoscopy with multiple off states.* Nature Photonics, 2016. **10**(2): p. 122-+.
369. Gottfert, F., et al., *Strong signal increase in STED fluorescence microscopy by imaging regions of subdiffraction extent.* Proceedings of the National Academy of Sciences of the United States of America, 2017. **114**(9): p. 2125-2130.
370. Heine, J., et al., *Adaptive-illumination STED nanoscopy.* Proceedings of the National Academy of Sciences of the United States of America, 2017. **114**(37): p. 9797-9802.
371. Schloetel, J.G., et al., *Guided STED nanoscopy enables super-resolution imaging of blood stage malaria parasites.* Sci Rep, 2019. **9**(1): p. 4674.

372. Schwentker, M.A., et al., *Wide-field subdiffraction RESOLFT microscopy using fluorescent protein photoswitching.* Microscopy Research and Technique, 2007. **70**(3): p. 269-280.
373. Chmyrov, A., et al., *Nanoscopy with more than 100,000 'doughnuts'.* Nat Methods, 2013. **10**(8): p. 737-40.
374. Chmyrov, A., et al., *Achromatic light patterning and improved image reconstruction for parallelized RESOLFT nanoscopy.* Sci Rep, 2017. **7**: p. 44619.
375. Rieder, C.L. and R.W. Cole, *Cold-shock and the Mammalian cell cycle.* Cell Cycle, 2002. **1**(3): p. 169-75.
376. Endesfelder, U., et al., *Chemically Induced Photoswitching of Fluorescent Probes-A General Concept for Super-Resolution Microscopy.* Molecules, 2011. **16**(4): p. 3106-3118.
377. Fernandez-Suarez, M. and A.Y. Ting, *Fluorescent probes for super-resolution imaging in living cells.* Nature Reviews Molecular Cell Biology, 2008. **9**(12): p. 929-943.
378. Yang, Z.G., et al., *Super-resolution fluorescent materials: an insight into design and bioimaging applications.* Chemical Society Reviews, 2016. **45**(17): p. 4651-4667.
379. Uno, S.N., et al., *A guide to use photocontrollable fluorescent proteins and synthetic smart fluorophores for nanoscopy.* Microscopy, 2015. **64**(4): p. 263-277.
380. Nienhaus, K. and G.U. Nienhaus, *Fluorescent proteins for live-cell imaging with super-resolution.* Chemical Society Reviews, 2014. **43**(4): p. 1088-1106.
381. Hotta, J., et al., *Spectroscopic rationale for efficient stimulated-emission depletion microscopy fluorophores.* J Am Chem Soc, 2010. **132**(14): p. 5021-3.
382. Wurm, C.A., et al., *Novel red fluorophores with superior performance in STED microscopy.* Optical Nanoscopy, 2012. **1**(1): p. 7.
383. Kolmakov, K., et al., *Red-emitting rhodamines with hydroxylated, sulfonated, and phosphorylated dye residues and their use in fluorescence nanoscopy.* Chemistry, 2012. **18**(41): p. 12986-98.
384. Kolmakov, K., et al., *Red-emitting rhodamine dyes for fluorescence microscopy and nanoscopy.* Chemistry, 2010. **16**(1): p. 158-66.
385. Kolmakov, K., et al., *A Versatile Route to Red-Emitting Carbopyronine Dyes for Optical Microscopy and Nanoscopy.* European Journal of Organic Chemistry, 2010(19): p. 3593-3610.
386. Mitronova, G.Y., et al., *New Fluorinated Rhodamines for Optical Microscopy and Nanoscopy.* Chemistry-a European Journal, 2010. **16**(15): p. 4477-4488.
387. Hinner, M.J. and K. Johnsson, *How to obtain labeled proteins and what to do with them.* Current Opinion in Biotechnology, 2010. **21**(6): p. 766-776.
388. Giepmans, B.N., et al., *The fluorescent toolbox for assessing protein location and function.* Science, 2006. **312**(5771): p. 217-24.
389. Kollmannsperger, A., et al., *Live-cell protein labelling with nanometre precision by cell squeezing.* Nature Communications, 2016. **7**.
390. Wu, Y.C., et al., *Massively parallel delivery of large cargo into mammalian cells with light pulses.* Nature Methods, 2015. **12**(5): p. 439-+.
391. Teng, K.W., et al., *Labeling proteins inside living cells using external fluorophores for microscopy.* Elife, 2016. **5**.
392. Crawford, R., et al., *Long-Lived Intracellular Single-Molecule Fluorescence Using Electroporated Molecules.* Biophysical Journal, 2013. **105**(11): p. 2439-2450.
393. Mcneil, P.L. and E. Warder, *Glass-Beads Load Macromolecules into Living Cells.* Journal of Cell Science, 1987. **88**: p. 669-678.
394. Barber, K., et al., *Delivery of membrane-impermeant fluorescent probes into living neural cell populations by lipotransfer.* Neuroscience Letters, 1996. **207**(1): p. 17-20.
395. Zhang, D.H., P. Wadsworth, and P.K. Hepler, *Microtubule Dynamics in Living Dividing Plant-Cells - Confocal Imaging of Microinjected Fluorescent Brain Tubulin.* Proceedings of the National Academy of Sciences of the United States of America, 1990. **87**(22): p. 8820-8824.
396. Bruckbauer, A., et al., *Nanopipette delivery of individual molecules to cellular compartments for single-molecule fluorescence tracking.* Biophysical Journal, 2007. **93**(9): p. 3120-3131.

397. Richard, J.P., et al., *Cell-penetrating peptides. A reevaluation of the mechanism of cellular uptake.* J Biol Chem, 2003. **278**(1): p. 585-90.
398. Okada, C.Y. and M. Rechsteiner, *Introduction of Macromolecules into Cultured Mammalian-Cells by Osmotic Lysis of Pinocytic Vesicles.* Cell, 1982. **29**(1): p. 33-41.
399. Wannier, T.M., et al., *Monomerization of far-red fluorescent proteins.* Proceedings of the National Academy of Sciences of the United States of America, 2018. **115**(48): p. E11294-E11301.
400. Erdmann, R.S., et al., *Super-resolution imaging of the Golgi in live cells with a bioorthogonal ceramide probe.* Angew Chem Int Ed Engl, 2014. **53**(38): p. 10242-6.
401. Wang, B., et al., *A general approach to spirolactonized Si-rhodamines.* Chem Commun (Camb), 2014. **50**(92): p. 14374-7.
402. Kim, E., et al., *Red Si-rhodamine drug conjugates enable imaging in GFP cells.* Chem Commun (Camb), 2014. **50**(34): p. 4504-7.
403. Kim, E., et al., *Optimized Near-IR Fluorescent Agents for in Vivo Imaging of Btk Expression.* Bioconjug Chem, 2015. **26**(8): p. 1513-8.
404. *SNAP-Cell® 647-SiR, New England Biolabs*. 2019; Available from: www.international.neb.com.
405. Grimm, J.B., et al., *Synthesis of Janelia Fluor HaloTag and SNAP-Tag Ligands and Their Use in Cellular Imaging Experiments.* Super-Resolution Microscopy: Methods and Protocols, 2017. **1663**: p. 179-188.
406. Uno, S.N., et al., *A spontaneously blinking fluorophore based on intramolecular spirocyclization for live-cell super-resolution imaging.* Nat Chem, 2014. **6**(8): p. 681-9.
407. Wirth, R., et al., *SiRA - A Silicon Rhodamine-Binding Aptamer for Live-Cell Super-Resolution RNA Imaging.* J Am Chem Soc, 2019.
408. Fornasiero, E.F. and F. Opazo, *Super-resolution imaging for cell biologists: concepts, applications, current challenges and developments.* Bioessays, 2015. **37**(4): p. 436-51.
409. Barentine, A.E.S., et al., *Simultaneously Measuring Image Features and Resolution in Live-Cell STED Images.* Biophys J, 2018. **115**(6): p. 951-956.
410. Saxton, W.O. and W. Baumeister, *The correlation averaging of a regularly arranged bacterial cell envelope protein.* J Microsc, 1982. **127**(Pt 2): p. 127-38.
411. Banterle, N., et al., *Fourier ring correlation as a resolution criterion for super-resolution microscopy.* J Struct Biol, 2013. **183**(3): p. 363-367.
412. Nieuwenhuizen, R.P.J., et al., *Measuring image resolution in optical nanoscopy.* Nature Methods, 2013. **10**(6): p. 557-+.
413. Stadler, C., et al., *Immunofluorescence and fluorescent-protein tagging show high correlation for protein localization in mammalian cells.* Nature Methods, 2013. **10**(4): p. 315-+.
414. Kaiser, P.D., et al., *Recent progress in generating intracellular functional antibody fragments to target and trace cellular components in living cells.* Biochim Biophys Acta, 2014. **1844**(11): p. 1933-1942.
415. Wiedenmann, J., F. Oswald, and G.U. Nienhaus, *Fluorescent proteins for live cell imaging: opportunities, limitations, and challenges.* IUBMB Life, 2009. **61**(11): p. 1029-42.
416. Remington, S.J., *Fluorescent proteins: maturation, photochemistry and photophysics.* Curr Opin Struct Biol, 2006. **16**(6): p. 714-21.
417. Zhang, X., et al., *Highly photostable, reversibly photoswitchable fluorescent protein with high contrast ratio for live-cell superresolution microscopy.* Proc Natl Acad Sci U S A, 2016. **113**(37): p. 10364-9.
418. Willig, K.I., et al., *Nanoscale resolution in GFP-based microscopy.* Nat Methods, 2006. **3**(9): p. 721-3.
419. Kasper, R., et al., *Single-molecule STED microscopy with photostable organic fluorophores.* Small, 2010. **6**(13): p. 1379-84.
420. Xu, L., et al., *Resolution, target density and labeling effects in colocalization studies - suppression of false positives by nanoscopy and modified algorithms.* FEBS J, 2016. **283**(5): p. 882-98.

421. Opazo, F., et al., *Aptamers as potential tools for super-resolution microscopy.* Nat Methods, 2012. **9**(10): p. 938-9.
422. Shim, S.H., et al., *Super-resolution fluorescence imaging of organelles in live cells with photoswitchable membrane probes.* Proceedings of the National Academy of Sciences of the United States of America, 2012. **109**(35): p. 13978-13983.
423. Erdmann, R.S., D. Toomre, and A. Schepartz, *STED Imaging of Golgi Dynamics with Cer-SiR: A Two-Component, Photostable, High-Density Lipid Probe for Live Cells.* Methods Mol Biol, 2017. **1663**: p. 65-78.
424. Wang, C., et al., *A photostable fluorescent marker for the superresolution live imaging of the dynamic structure of the mitochondrial cristae.* Proc Natl Acad Sci U S A, 2019. **116**(32): p. 15817-15822.
425. Revelo, N.H., et al., *A new probe for super-resolution imaging of membranes elucidates trafficking pathways.* J Cell Biol, 2014. **205**(4): p. 591-606.
426. Vicidomini, G., et al., *STED-FLCS: An Advanced Tool to Reveal Spatiotemporal Heterogeneity of Molecular Membrane Dynamics.* Nano Lett, 2015. **15**(9): p. 5912-8.
427. Nikic, I. and E.A. Lemke, *Genetic code expansion enabled site-specific dual-color protein labeling: superresolution microscopy and beyond.* Current Opinion in Chemical Biology, 2015. **28**: p. 164-173.
428. Uttamapinant, C., et al., *Genetic code expansion enables live-cell and super-resolution imaging of site-specifically labeled cellular proteins.* J Am Chem Soc, 2015. **137**(14): p. 4602-5.
429. Beatty, K.E., et al., *Fluorescence visualization of newly synthesized proteins in mammalian cells.* Angew Chem Int Ed Engl, 2006. **45**(44): p. 7364-7.
430. Salic, A. and T.J. Mitchison, *A chemical method for fast and sensitive detection of DNA synthesis in vivo.* Proc Natl Acad Sci U S A, 2008. **105**(7): p. 2415-20.
431. Neef, A.B. and C. Schultz, *Selective fluorescence labeling of lipids in living cells.* Angew Chem Int Ed Engl, 2009. **48**(8): p. 1498-500.
432. Hink, M.A., et al., *Structural dynamics of green fluorescent protein alone and fused with a single chain Fv protein.* J Biol Chem, 2000. **275**(23): p. 17556-60.
433. Milstein, C., *The hybridoma revolution: an offshoot of basic research.* Bioessays, 1999. **21**(11): p. 966-73.
434. Porter, R.R., *The hydrolysis of rabbit y-globulin and antibodies with crystalline papain.* Biochem J, 1959. **73**: p. 119-26.
435. Clackson, T., et al., *Making Antibody Fragments Using Phage Display Libraries.* Nature, 1991. **352**(6336): p. 624-628.
436. Ries, J., et al., *A simple, versatile method for GFP-based super-resolution microscopy via nanobodies.* Nature Methods, 2012. **9**(6): p. 582-+.
437. Jost, C. and A. Pluckthun, *Engineered proteins with desired specificity: DARPins, other alternative scaffolds and bispecific IgGs.* Curr Opin Struct Biol, 2014. **27**: p. 102-12.
438. Nord, K., et al., *A combinatorial library of an alpha-helical bacterial receptor domain.* Protein Eng, 1995. **8**(6): p. 601-8.
439. Koide, A., et al., *The fibronectin type III domain as a scaffold for novel binding proteins.* Journal of Molecular Biology, 1998. **284**(4): p. 1141-1151.
440. Ellington, A.D. and J.W. Szostak, *In vitro selection of RNA molecules that bind specific ligands.* Nature, 1990. **346**(6287): p. 818-22.
441. Jullien, L. and A. Gautier, *Fluorogen-based reporters for fluorescence imaging: a review.* Methods Appl Fluoresc, 2015. **3**(4): p. 042007.
442. Yan, Q., et al., *Localization microscopy using noncovalent fluorogen activation by genetically encoded fluorogen-activating proteins.* Chemphyschem, 2014. **15**(4): p. 687-695.
443. Saurabh, S., et al., *Super-resolution Imaging of Live Bacteria Cells Using a Genetically Directed, Highly Photostable Fluoromodule.* J Am Chem Soc, 2016. **138**(33): p. 10398-401.
444. Fitzpatrick, J.A., et al., *STED nanoscopy in living cells using Fluorogen Activating Proteins.* Bioconjug Chem, 2009. **20**(10): p. 1843-1847.

445. Pimenta, F.M., et al., *Chromophore Renewal and Fluorogen-Binding Tags: A Match Made to Last.* Sci Rep, 2017. **7**(1): p. 12316.
446. Chapman, S., et al., *The photoreversible fluorescent protein iLOV outperforms GFP as a reporter of plant virus infection.* Proc Natl Acad Sci U S A, 2008. **105**(50): p. 20038-43.
447. Shu, X., et al., *A genetically encoded tag for correlated light and electron microscopy of intact cells, tissues, and organisms.* PLoS Biol, 2011. **9**(4): p. e1001041.
448. Buckley, A.M., et al., *LOV-based reporters for fluorescence imaging.* Curr Opin Chem Biol, 2015. **27**: p. 39-45.
449. Kumagai, A., et al., *A bilirubin-inducible fluorescent protein from eel muscle.* Cell, 2013. **153**(7): p. 1602-11.
450. Filonov, G.S., et al., *Bright and stable near-infrared fluorescent protein for in vivo imaging.* Nat Biotechnol, 2011. **29**(8): p. 757-61.
451. Shcherbakova, D.M. and V.V. Verkhusha, *Near-infrared fluorescent proteins for multicolor in vivo imaging.* Nat Methods, 2013. **10**(8): p. 751-4.
452. Shu, X., et al., *Mammalian expression of infrared fluorescent proteins engineered from a bacterial phytochrome.* Science, 2009. **324**(5928): p. 804-7.
453. Li, C., et al., *Dynamic multicolor protein labeling in living cells.* Chem Sci, 2017. **8**(8): p. 5598-5605.
454. Plamont, M.A., et al., *Small fluorescence-activating and absorption-shifting tag for tunable protein imaging in vivo.* Proc Natl Acad Sci U S A, 2016. **113**(3): p. 497-502.
455. Xu, S. and H.Y. Hu, *Fluorogen-activating proteins: beyond classical fluorescent proteins.* Acta Pharm Sin B, 2018. **8**(3): p. 339-348.
456. Gautier, A., et al., *An engineered protein tag for multiprotein labeling in living cells.* Chem Biol, 2008. **15**(2): p. 128-36.
457. Miller, L.W., et al., *In vivo protein labeling with trimethoprim conjugates: a flexible chemical tag.* Nat Methods, 2005. **2**(4): p. 255-7.
458. Chen, Z., et al., *Second-generation covalent TMP-tag for live cell imaging.* J Am Chem Soc, 2012. **134**(33): p. 13692-9.
459. Adams, S.R. and R.Y. Tsien, *Preparation of the membrane-permeant biarsenicals FlAsH-EDT2 and ReAsH-EDT2 for fluorescent labeling of tetracysteine-tagged proteins.* Nat Protoc, 2008. **3**(9): p. 1527-34.
460. Halo, T.L., et al., *Selective recognition of protein tetraserine motifs with a cell-permeable, pro-fluorescent bis-boronic acid.* J Am Chem Soc, 2009. **131**(2): p. 438-9.
461. Cong, L., et al., *Multiplex Genome Engineering Using CRISPR/Cas Systems.* Science, 2013. **339**(6121): p. 819-823.
462. Mali, P., et al., *RNA-Guided Human Genome Engineering via Cas9.* Science, 2013. **339**(6121): p. 823-826.
463. Stoddard, B.L., *Homing Endonucleases: From Microbial Genetic Invaders to Reagents for Targeted DNA Modification.* Structure, 2011. **19**(1): p. 7-15.
464. Urnov, F.D., et al., *Genome editing with engineered zinc finger nucleases.* Nature Reviews Genetics, 2010. **11**(9): p. 636-646.
465. Joung, J.K. and J.D. Sander, *INNOVATION TALENs: a widely applicable technology for targeted genome editing.* Nature Reviews Molecular Cell Biology, 2013. **14**(1): p. 49-55.
466. *Mowiol embedding medium.* Cold Spring Harbor Protocols, 2010. **2010**(1): p. pdb.rec12110.
467. Jegou, T., et al., *Dynamics of telomeres and promyelocytic leukemia nuclear bodies in a telomerase-negative human cell line.* Mol Biol Cell, 2009. **20**(7): p. 2070-82.
468. O'Sullivan, R.J., et al., *Rapid induction of alternative lengthening of telomeres by depletion of the histone chaperone ASF1.* Nat Struct Mol Biol, 2014. **21**(2): p. 167-74.
469. Schindelin, J., et al., *Fiji: an open-source platform for biological-image analysis.* Nat Methods, 2012. **9**(7): p. 676-82.
470. Schneider, C.A., W.S. Rasband, and K.W. Eliceiri, *NIH Image to ImageJ: 25 years of image analysis.* Nat Methods, 2012. **9**(7): p. 671-5.

471. Eaton, J.W., et al., *GNU Octave version 5.1.0 manual: a high-level interactive language for numerical computations*. 2019.
472. Jones, E., et al., *SciPy: Open source scientific tools for Python*. 2001.
473. Gorlitz, F., et al., *A STED microscope designed for routine biomedical applications.* . Prog Electromagn Res, 2014. **147**: p. 57-68.
474. Shapiro, S.S. and M.B. Wilk, *An analysis of variance test for normality (complete samples).* Biometrika, 1965. **52**(3-4): p. 591-611.
475. Student, *The Probable Error of a Mean.* Biometrika, 1908. **6**(1): p. 1-25.
476. Welch, B.L., *The Generalization of `Student's' Problem when Several Different Population Variances are Involved.* Biometrika, 1947. **34**(1/2): p. 28-35.
477. Mann, H.B. and D.R. Whitney, *On a test of whether one of two random variables is stochastically larger than the other.* Annals of Mathematical Statistics, 1947. **18**: p. 50-60.
478. Kruskal, W.H. and W.A. Wallis, *Use of Ranks in One-Criterion Variance Analysis.* Journal of the American Statistical Association, 1952. **47**(260): p. 583-621.
479. Dunn, O.J., *Multiple Comparisons among Means.* Journal of the American Statistical Association, 1961. **56**(293): p. 52-64.
480. Timashev, L.A., et al., *The DDR at telomeres lacking intact shelterin does not require substantial chromatin decompaction.* Genes Dev, 2017. **31**(6): p. 578-589.
481. Vancevska, A., et al., *The telomeric DNA damage response occurs in the absence of chromatin decompaction.* Genes Dev, 2017. **31**(6): p. 567-577.
482. Bandaria, J.N., et al., *Shelterin Protects Chromosome Ends by Compacting Telomeric Chromatin.* Cell, 2016. **164**(4): p. 735-46.
483. Griffith, J.D., et al., *Mammalian telomeres end in a large duplex loop.* Cell, 1999. **97**(4): p. 503-514.
484. Cesare, A.J. and J.D. Griffith, *Telomeric DNA in ALT cells is characterized by free telomeric circles and heterogeneous t-loops.* Mol Cell Biol, 2004. **24**(22): p. 9948-57.
485. Doksani, Y., et al., *Super-Resolution Fluorescence Imaging of Telomeres Reveals TRF2-Dependent T-loop Formation.* Cell, 2013. **155**(2): p. 345-356.
486. Van Ly, D., et al., *Telomere Loop Dynamics in Chromosome End Protection.* Mol Cell, 2018. **71**(4): p. 510-525 e6.
487. Cesare, A.J. and R.R. Reddel, *Alternative lengthening of telomeres: models, mechanisms and implications.* Nat Rev Genet, 2010. **11**(5): p. 319-30.
488. Palm, W. and T. de Lange, *How shelterin protects mammalian telomeres.* Annu Rev Genet, 2008. **42**: p. 301-34.
489. de Lange, T., *Shelterin: the protein complex that shapes and safeguards human telomeres.* Genes Dev, 2005. **19**(18): p. 2100-10.
490. Takai, K.K., et al., *In vivo stoichiometry of shelterin components.* J Biol Chem, 2010. **285**(2): p. 1457-67.
491. de Lange, T., *Shelterin-Mediated Telomere Protection.* Annu Rev Genet, 2018. **52**: p. 223-247.
492. Wu, P. and T. De Lange, *No overt nucleosome eviction at deprotected telomeres.* Mol Cell Biol, 2008. **18**: p. 5724-35.
493. Pisano, S., et al., *Telomeric nucleosomes are intrinsically mobile.* J Mol Biol, 2007. **369**(5): p. 1153-62.
494. Blasco, M.A., *The epigenetic regulation of mammalian telomeres.* Nat Rev Genet, 2007. **8**(4): p. 299-309.
495. Greider, C.W., *Telomeres.* Curr Opin Cell Biol, 1991. **3**(3): p. 444-51.
496. de Lange, T., *T-loops and the origin of telomeres.* Nat Rev Mol Cell Biol, 2004. **5**(4): p. 323-9.
497. Benarroch-Popivker, D., et al., *TRF2-Mediated Control of Telomere DNA Topology as a Mechanism for Chromosome-End Protection.* Mol Cell, 2016. **61**(2): p. 274-86.
498. Zhang, Z., et al., *2D gel electrophoresis reveals dynamics of t-loop formation during the cell cycle and t-loop in maintenance regulated by heterochromatin state.* J Biol Chem, 2019. **294**(16): p. 6645-6656.

499. Maciejowski, J. and T. de Lange, *Telomeres in cancer: tumour suppression and genome instability.* Nat Rev Mol Cell Biol, 2017. **18**(3): p. 175-186.
500. Kulkarni, A., et al., *Effect of telomere proximity on telomere position effect, chromosome healing, and sensitivity to DNA double-strand breaks in a human tumor cell line.* Mol Cell Biol, 2010. **30**(3): p. 578-89.
501. Baur, J.A., et al., *Telomere position effect in human cells.* Science, 2001. **292**(5524): p. 2075-7.
502. Dekker, J. and L. Mirny, *The 3D Genome as Moderator of Chromosomal Communication.* Cell, 2016. **164**(6): p. 1110-1121.
503. Rowley, M.J. and V.G. Corces, *The three-dimensional genome: principles and roles of long-distance interactions.* Curr Opin Cell Biol, 2016. **40**: p. 8-14.
504. Robin, J.D., et al., *Telomere position effect: regulation of gene expression with progressive telomere shortening over long distances.* Genes Dev, 2014. **28**(22): p. 2464-76.
505. Kim, W. and J.W. Shay, *Long-range telomere regulation of gene expression: Telomere looping and telomere position effect over long distances (TPE-OLD).* Differentiation, 2018. **99**: p. 1-9.
506. Bolzan, A.D., *Interstitial telomeric sequences in vertebrate chromosomes: Origin, function, instability and evolution.* Mutat Res, 2017. **773**: p. 51-65.
507. Burla, R., M. La Torre, and I. Saggio, *Mammalian telomeres and their partnership with lamins.* Nucleus, 2016. **7**(2): p. 187-202.
508. van Steensel, B. and A.S. Belmont, *Lamina-Associated Domains: Links with Chromosome Architecture, Heterochromatin, and Gene Repression.* Cell, 2017. **169**(5): p. 780-791.
509. Bryan, T.M., et al., *Evidence for an alternative mechanism for maintaining telomere length in human tumors and tumor-derived cell lines.* Nat Med, 1997. **3**(11): p. 1271-4.
510. Shay, J.W. and S. Bacchetti, *A survey of telomerase activity in human cancer.* Eur J Cancer, 1997. **33**(5): p. 787-91.
511. Kim, N.W., et al., *Specific association of human telomerase activity with immortal cells and cancer.* Science, 1994. **266**(5193): p. 2011-5.
512. Wright, W.E., et al., *Telomerase activity in human germline and embryonic tissues and cells.* Dev Genet, 1996. **18**(2): p. 173-9.
513. Shay, J.W. and W.E. Wright, *Telomerase therapeutics for cancer: challenges and new directions.* Nat Rev Drug Discov, 2006. **5**(7): p. 577-84.
514. Shay, J.W. and W.E. Wright, *Mechanism-based combination telomerase inhibition therapy.* Cancer Cell, 2005. **7**(1): p. 1-2.
515. Calado, R.T. and N.S. Young, *Telomere diseases.* N Engl J Med, 2009. **361**(24): p. 2353-65.
516. Opresko, P.L. and J.W. Shay, *Telomere-associated aging disorders.* Ageing Res Rev, 2017. **33**: p. 52-66.
517. Garcia, C.K., W.E. Wright, and J.W. Shay, *Human diseases of telomerase dysfunction: insights into tissue aging.* Nucleic Acids Res, 2007. **35**(22): p. 7406-16.
518. Armanios, M. and E.H. Blackburn, *The telomere syndromes.* Nat Rev Genet, 2012. **13**(10): p. 693-704.
519. Chojnowski, A., et al., *Progerin reduces LAP2alpha-telomere association in Hutchinson-Gilford progeria.* Elife, 2015. **4**.
520. Holohan, B., W.E. Wright, and J.W. Shay, *Cell biology of disease: Telomeropathies: an emerging spectrum disorder.* J Cell Biol, 2014. **205**(3): p. 289-99.
521. Lai, T.P., et al., *A method for measuring the distribution of the shortest telomeres in cells and tissues.* Nat Commun, 2017. **8**(1): p. 1356.
522. Aubert, G., M. Hills, and P.M. Lansdorp, *Telomere length measurement-caveats and a critical assessment of the available technologies and tools.* Mutat Res, 2012. **730**(1-2): p. 59-67.
523. Cawthon, R.M., *Telomere measurement by quantitative PCR.* Nucleic Acids Res, 2002. **30**(10): p. e47.
524. Verhulst, S., et al., *Commentary: The reliability of telomere length measurements.* Int J Epidemiol, 2015. **44**(5): p. 1683-6.

525. Bendix, L., et al., *The load of short telomeres, estimated by a new method, Universal STELA, correlates with number of senescent cells.* Aging Cell, 2010. **9**(3): p. 383-97.
526. Baird, D.M., *New developments in telomere length analysis.* Exp Gerontol, 2005. **40**(5): p. 363-8.
527. Baerlocher, G.M., et al., *Flow cytometry and FISH to measure the average length of telomeres (flow FISH).* Nat Protoc, 2006. **1**(5): p. 2365-76.
528. Johnson, J.E. and D. Broccoli, *Telomere maintenance in sarcomas.* Curr Opin Oncol, 2007. **19**(4): p. 377-82.
529. Heaphy, C.M., et al., *Prevalence of the alternative lengthening of telomeres telomere maintenance mechanism in human cancer subtypes.* Am J Pathol, 2011. **179**(4): p. 1608-15.
530. Bryan, T.M., et al., *Telomere elongation in immortal human cells without detectable telomerase activity.* EMBO J, 1995. **14**(17): p. 4240-8.
531. Episkopou, H., et al., *Alternative Lengthening of Telomeres is characterized by reduced compaction of telomeric chromatin.* Nucleic Acids Res, 2014. **42**(7): p. 4391-405.
532. Wang, R.C., A. Smogorzewska, and T. de Lange, *Homologous recombination generates T-loop-sized deletions at human telomeres.* Cell, 2004. **119**(3): p. 355-68.
533. Oganesian, L. and J. Karlseder, *Mammalian 5' C-rich telomeric overhangs are a mark of recombination-dependent telomere maintenance.* Mol Cell, 2011. **42**(2): p. 224-36.
534. Heaphy, C.M., et al., *Altered telomeres in tumors with ATRX and DAXX mutations.* Science, 2011. **333**(6041): p. 425.
535. Lovejoy, C.A., et al., *Loss of ATRX, genome instability, and an altered DNA damage response are hallmarks of the alternative lengthening of telomeres pathway.* PLoS Genet, 2012. **8**(7): p. e1002772.
536. Londono-Vallejo, J.A., et al., *Alternative lengthening of telomeres is characterized by high rates of telomeric exchange.* Cancer Res, 2004. **64**(7): p. 2324-7.
537. Chung, I., et al., *PML body meets telomere: the beginning of an ALTernate ending?* Nucleus, 2012. **3**(3): p. 263-75.
538. Yeager, T.R., et al., *Telomerase-negative immortalized human cells contain a novel type of promyelocytic leukemia (PML) body.* Cancer Res, 1999. **59**(17): p. 4175-9.
539. Groff-Vindman, C., et al., *Recombination at long mutant telomeres produces tiny single- and double-stranded telomeric circles.* Mol Cell Biol, 2005. **25**(11): p. 4406-12.
540. Natarajan, S. and M.J. McEachern, *Recombinational telomere elongation promoted by DNA circles.* Mol Cell Biol, 2002. **22**(13): p. 4512-21.
541. Henson, J.D., et al., *DNA C-circles are specific and quantifiable markers of alternative-lengthening-of-telomeres activity.* Nat Biotechnol, 2009. **27**(12): p. 1181-5.
542. Pompili, L., et al., *Diagnosis and treatment of ALT tumors: is Trabectedin a new therapeutic option?* J Exp Clin Cancer Res, 2017. **36**(1): p. 189.
543. Koken, M.H., et al., *The t(15;17) translocation alters a nuclear body in a retinoic acid-reversible fashion.* EMBO J, 1994. **13**(5): p. 1073-83.
544. Lang, M., et al., *Three-dimensional organization of promyelocytic leukemia nuclear bodies.* J Cell Sci, 2010. **123**(Pt 3): p. 392-400.
545. Kim, J., et al., *Tudor, MBT and chromo domains gauge the degree of lysine methylation.* EMBO Rep, 2006. **7**(4): p. 397-403.
546. Weidtkamp-Peters, S., et al., *Dynamics of component exchange at PML nuclear bodies.* J Cell Sci, 2008. **121**(Pt 16): p. 2731-43.
547. Lallemand-Breitenbach, V. and H. de The, *PML nuclear bodies.* Cold Spring Harb Perspect Biol, 2010. **2**(5): p. a000661.
548. Van Damme, E., et al., *A manually curated network of the PML nuclear body interactome reveals an important role for PML-NBs in SUMOylation dynamics.* Int J Biol Sci, 2010. **6**(1): p. 51-67.
549. Shen, T.H., et al., *The mechanisms of PML-nuclear body formation.* Mol Cell, 2006. **24**(3): p. 331-9.

550. Chung, I., H. Leonhardt, and K. Rippe, *De novo assembly of a PML nuclear subcompartment occurs through multiple pathways and induces telomere elongation.* J Cell Sci, 2011. **124**(Pt 21): p. 3603-18.
551. Osterwald, S., et al., *PML induces compaction, TRF2 depletion and DNA damage signaling at telomeres and promotes their alternative lengthening.* J Cell Sci, 2015. **128**(10): p. 1887-900.
552. Jiang, W.Q., et al., *Identification of candidate alternative lengthening of telomeres genes by methionine restriction and RNA interference.* Oncogene, 2007. **26**(32): p. 4635-47.
553. Potts, P.R. and H. Yu, *The SMC5/6 complex maintains telomere length in ALT cancer cells through SUMOylation of telomere-binding proteins.* Nat Struct Mol Biol, 2007. **14**(7): p. 581-90.
554. Nabetani, A. and F. Ishikawa, *Alternative lengthening of telomeres pathway: recombination-mediated telomere maintenance mechanism in human cells.* J Biochem, 2011. **149**(1): p. 5-14.
555. Jiang, W.Q., et al., *Induction of alternative lengthening of telomeres-associated PML bodies by p53/p21 requires HP1 proteins.* J Cell Biol, 2009. **185**(5): p. 797-810.
556. Cesare, A.J. and R.R. Reddel, *Telomere uncapping and alternative lengthening of telomeres.* Mech Ageing Dev, 2008. **129**(1-2): p. 99-108.
557. Cesare, A.J., et al., *Spontaneous occurrence of telomeric DNA damage response in the absence of chromosome fusions.* Nat Struct Mol Biol, 2009. **16**(12): p. 1244-51.
558. Zeng, S., et al., *Telomere recombination requires the MUS81 endonuclease.* Nat Cell Biol, 2009. **11**(5): p. 616-23.
559. Stagno D'Alcontres, M., et al., *Lack of TRF2 in ALT cells causes PML-dependent p53 activation and loss of telomeric DNA.* J Cell Biol, 2007. **179**(5): p. 855-67.
560. Mekeel, K.L., et al., *Inactivation of p53 results in high rates of homologous recombination.* Oncogene, 1997. **14**(15): p. 1847-57.
561. Cerone, M.A., et al., *A human cell line that maintains telomeres in the absence of telomerase and of key markers of ALT.* Oncogene, 2005. **24**(53): p. 7893-901.
562. Fasching, C.L., K. Bower, and R.R. Reddel, *Telomerase-independent telomere length maintenance in the absence of alternative lengthening of telomeres-associated promyelocytic leukemia bodies.* Cancer Res, 2005. **65**(7): p. 2722-9.
563. Marciniak, R.A., et al., *A novel telomere structure in a human alternative lengthening of telomeres cell line.* Cancer Res, 2005. **65**(7): p. 2730-7.
564. Dunham, M.A., et al., *Telomere maintenance by recombination in human cells.* Nat Genet, 2000. **26**(4): p. 447-50.
565. Muntoni, A., et al., *Telomere elongation involves intra-molecular DNA replication in cells utilizing alternative lengthening of telomeres.* Hum Mol Genet, 2009. **18**(6): p. 1017-27.
566. Dilley, R.L., et al., *Break-induced telomere synthesis underlies alternative telomere maintenance.* Nature, 2016. **539**(7627): p. 54-58.
567. Cho, N.W., et al., *Interchromosomal homology searches drive directional ALT telomere movement and synapsis.* Cell, 2014. **159**(1): p. 108-121.
568. Karlseder, J., et al., *The telomeric protein TRF2 binds the ATM kinase and can inhibit the ATM-dependent DNA damage response.* PLoS Biol, 2004. **2**(8): p. E240.
569. Denchi, E.L. and T. de Lange, *Protection of telomeres through independent control of ATM and ATR by TRF2 and POT1.* Nature, 2007. **448**(7157): p. 1068-71.
570. Ruden, M. and N. Puri, *Novel anticancer therapeutics targeting telomerase.* Cancer Treat Rev, 2013. **39**(5): p. 444-56.
571. Ward, R.J. and C. Autexier, *Pharmacological telomerase inhibition can sensitize drug-resistant and drug-sensitive cells to chemotherapeutic treatment.* Mol Pharmacol, 2005. **68**(3): p. 779-86.
572. Joseph, I., et al., *The telomerase inhibitor imetelstat depletes cancer stem cells in breast and pancreatic cancer cell lines.* Cancer Res, 2010. **70**(22): p. 9494-504.
573. Dikmen, Z.G., et al., *In vivo inhibition of lung cancer by GRN163L: a novel human telomerase inhibitor.* Cancer Res, 2005. **65**(17): p. 7866-73.

574. Pascolo, E., et al., *Mechanism of human telomerase inhibition by BIBR1532, a synthetic, non-nucleosidic drug candidate.* J Biol Chem, 2002. **277**(18): p. 15566-72.
575. Cairney, C.J., et al., *High level of telomerase RNA gene expression is associated with chromatin modification, the ALT phenotype and poor prognosis in liposarcoma.* Br J Cancer, 2008. **98**(8): p. 1467-74.
576. Venturini, L., et al., *Prognostic relevance of ALT-associated markers in liposarcoma: a comparative analysis.* BMC Cancer, 2010. **10**: p. 254.
577. Hu, J., et al., *Antitelomerase therapy provokes ALT and mitochondrial adaptive mechanisms in cancer.* Cell, 2012. **148**(4): p. 651-63.
578. Monneron, A. and W. Bernhard, *Fine structural organization of the interphase nucleus in some mammalian cells.* J Ultrastruct Res, 1969. **27**(3): p. 266-88.
579. Olins, D.E., et al., *Electron microscope tomography: transcription in three dimensions.* Science, 1983. **220**(4596): p. 498-500.
580. Smetana, K. and F. Hermansky, *A Contribution to the Knowledge of the Ultrastructure of Leukaemic Lymphocytes.* Neoplasma, 1963. **10**: p. 405-11.
581. Rouquette, J., et al., *Revealing the high-resolution three-dimensional network of chromatin and interchromatin space: a novel electron-microscopic approach to reconstructing nuclear architecture.* Chromosome Res, 2009. **17**(6): p. 801-10.
582. Bazett-Jones, D.P., et al., *Elucidating chromatin and nuclear domain architecture with electron spectroscopic imaging.* Chromosome Res, 2008. **16**(3): p. 397-412.
583. Schroeder-Reiter, E., et al., *Focused ion beam (FIB) combined with high resolution scanning electron microscopy: a promising tool for 3D analysis of chromosome architecture.* J Struct Biol, 2009. **165**(2): p. 97-106.
584. Joti, Y., et al., *Chromosomes without a 30-nm chromatin fiber.* Nucleus, 2012. **3**(5): p. 404-10.
585. Maeshima, K., S. Hihara, and M. Eltsov, *Chromatin structure: does the 30-nm fibre exist in vivo?* Curr Opin Cell Biol, 2010. **22**(3): p. 291-7.
586. Szczurek, A.T., et al., *Single molecule localization microscopy of the distribution of chromatin using Hoechst and DAPI fluorescent probes.* Nucleus, 2014. **5**(4): p. 331-40.
587. Zessin, P.J., K. Finan, and M. Heilemann, *Super-resolution fluorescence imaging of chromosomal DNA.* J Struct Biol, 2012. **177**(2): p. 344-8.
588. Xu, J., et al., *Super-Resolution Imaging of Higher-Order Chromatin Structures at Different Epigenomic States in Single Mammalian Cells.* Cell Rep, 2018. **24**(4): p. 873-882.
589. Boettiger, A.N., et al., *Super-resolution imaging reveals distinct chromatin folding for different epigenetic states.* Nature, 2016. **529**(7586): p. 418-22.
590. Markaki, Y., et al., *The potential of 3D-FISH and super-resolution structured illumination microscopy for studies of 3D nuclear architecture: 3D structured illumination microscopy of defined chromosomal structures visualized by 3D (immuno)-FISH opens new perspectives for studies of nuclear architecture.* Bioessays, 2012. **34**(5): p. 412-26.
591. Hansen, A.S., et al., *CTCF and cohesin regulate chromatin loop stability with distinct dynamics.* Elife, 2017. **6**.
592. Chapman, J.R., et al., *BRCA1-associated exclusion of 53BP1 from DNA damage sites underlies temporal control of DNA repair.* J Cell Sci, 2012. **125**(Pt 15): p. 3529-34.
593. Nagashima, R., et al., *Single nucleosome imaging reveals loose genome chromatin networks via active RNA polymerase II.* J Cell Biol, 2019. **218**(5): p. 1511-1530.
594. Ricci, M.A., et al., *Chromatin fibers are formed by heterogeneous groups of nucleosomes in vivo.* Cell, 2015. **160**(6): p. 1145-58.
595. Prakash, K., et al., *Superresolution imaging reveals structurally distinct periodic patterns of chromatin along pachytene chromosomes.* Proc Natl Acad Sci U S A, 2015. **112**(47): p. 14635-40.
596. Cella Zanacchi, F., et al., *Live-cell 3D super-resolution imaging in thick biological samples.* Nat Methods, 2011. **8**(12): p. 1047-9.

597. Mitchell-Jordan, S., et al., *Features of endogenous cardiomyocyte chromatin revealed by super-resolution STED microscopy.* J Mol Cell Cardiol, 2012. **53**(4): p. 552-8.
598. Persson, F., et al., *Fluorescence nanoscopy of single DNA molecules by using stimulated emission depletion (STED).* Angew Chem Int Ed Engl, 2011. **50**(24): p. 5581-3.
599. Gall, J.G. and M.L. Pardue, *Formation and detection of RNA-DNA hybrid molecules in cytological preparations.* Proc Natl Acad Sci U S A, 1969. **63**(2): p. 378-83.
600. Beliveau, B.J., et al., *OligoMiner provides a rapid, flexible environment for the design of genome-scale oligonucleotide in situ hybridization probes.* Proc Natl Acad Sci U S A, 2018. **115**(10): p. E2183-E2192.
601. Beliveau, B.J., et al., *Versatile design and synthesis platform for visualizing genomes with Oligopaint FISH probes.* Proc Natl Acad Sci U S A, 2012. **109**(52): p. 21301-6.
602. Beliveau, B.J., et al., *Single-molecule super-resolution imaging of chromosomes and in situ haplotype visualization using Oligopaint FISH probes.* Nat Commun, 2015. **6**: p. 7147.
603. Beliveau, B.J., et al., *In Situ Super-Resolution Imaging of Genomic DNA with OligoSTORM and OligoDNA-PAINT.* Methods Mol Biol, 2017. **1663**: p. 231-252.
604. Ni, Y., et al., *Super-resolution imaging of a 2.5 kb non-repetitive DNA in situ in the nuclear genome using molecular beacon probes.* Elife, 2017. **6**.
605. Nielsen, P.E., et al., *Sequence-selective recognition of DNA by strand displacement with a thymine-substituted polyamide.* Science, 1991. **254**(5037): p. 1497-500.
606. Banack, S.A., et al., *Cyanobacteria produce N-(2-aminoethyl)glycine, a backbone for peptide nucleic acids which may have been the first genetic molecules for life on Earth.* PLoS One, 2012. **7**(11): p. e49043.
607. Egholm, M., et al., *PNA hybridizes to complementary oligonucleotides obeying the Watson-Crick hydrogen-bonding rules.* Nature, 1993. **365**(6446): p. 566-8.
608. Tomac, S., et al., *Ionic Effects on the Stability and Conformation of Peptide Nucleic Acid Complexes.* J Am Chem Soc, 1996. **118**(24): p. 5544-5552.
609. Annoni, C., et al., *Triplex-forming peptide nucleic acid modified with 2-aminopyridine as a new tool for detection of A-to-I editing.* Chem Commun (Camb), 2016. **52**(51): p. 7935-8.
610. Marchelli, R., et al., *Gene Modulation by Peptide Nucleic Acids (PNAs) Targeting microRNAs (miRs)*, in *Targets in Gene Therapy*, Y. You, Editor. 2011, IntechOpen. p. 26-46.
611. Janson, C. and M. During, *Peptide Nucleic Acids, Morpholinos and Related Antisense Biomolecules*. 2006: Springer US.
612. Shi, H., et al., *A review: fabrications, detections and applications of peptide nucleic acids (PNAs) microarray.* Biosens Bioelectron, 2015. **66**: p. 481-9.
613. Maekawa, K., et al., *Antisense peptide nucleic acid-peptide conjugates for functional analyses of genes in Pseudomonas aeruginosa.* Bioorg Med Chem, 2015. **23**(22): p. 7234-9.
614. Wang, H., et al., *Inhibition of gene expression and growth of multidrug-resistant Acinetobacter baumannii by antisense peptide nucleic acids.* Mol Biol Rep, 2014. **41**(11): p. 7535-41.
615. Ahn, D.G., et al., *Interference of ribosomal frameshifting by antisense peptide nucleic acids suppresses SARS coronavirus replication.* Antiviral Res, 2011. **91**(1): p. 1-10.
616. Zeng, Z., et al., *A Tat-conjugated Peptide Nucleic Acid Tat-PNA-DR Inhibits Hepatitis B Virus Replication In Vitro and In Vivo by Targeting LTR Direct Repeats of HBV RNA.* Mol Ther Nucleic Acids, 2016. **5**: p. e295.
617. Gupta, A., A. Mishra, and N. Puri, *Peptide nucleic acids: Advanced tools for biomedical applications.* J Biotechnol, 2017. **259**: p. 148-159.
618. Dragulescu-Andrasi, A., et al., *A simple gamma-backbone modification preorganizes peptide nucleic acid into a helical structure.* J Am Chem Soc, 2006. **128**(31): p. 10258-67.
619. Yeh, J.I., et al., *Crystal structure of chiral gammaPNA with complementary DNA strand: insights into the stability and specificity of recognition and conformational preorganization.* J Am Chem Soc, 2010. **132**(31): p. 10717-27.
620. He, G., et al., *Strand invasion of extended, mixed-sequence B-DNA by gammaPNAs.* J Am Chem Soc, 2009. **131**(34): p. 12088-90.

621. Bahal, R., et al., *Sequence-unrestricted, Watson-Crick recognition of double helical B-DNA by (R)-miniPEG-gammaPNAs.* Chembiochem, 2012. **13**(1): p. 56-60.
622. Molenaar, C., et al., *Visualizing telomere dynamics in living mammalian cells using PNA probes.* EMBO J, 2003. **22**(24): p. 6631-41.
623. Markaki, Y., et al., *Fluorescence in situ hybridization applications for super-resolution 3D structured illumination microscopy.* Methods Mol Biol, 2013. **950**: p. 43-64.
624. Cremer, T., et al., *The 4D nucleome: Evidence for a dynamic nuclear landscape based on co-aligned active and inactive nuclear compartments.* FEBS Lett, 2015. **589**(20 Pt A): p. 2931-43.
625. Robinett, C.C., et al., *In vivo localization of DNA sequences and visualization of large-scale chromatin organization using lac operator/repressor recognition.* J Cell Biol, 1996. **135**(6 Pt 2): p. 1685-700.
626. Gasser, S.M., *Visualizing chromatin dynamics in interphase nuclei.* Science, 2002. **296**(5572): p. 1412-6.
627. Roukos, V., et al., *Spatial dynamics of chromosome translocations in living cells.* Science, 2013. **341**(6146): p. 660-4.
628. Saad, H., et al., *DNA dynamics during early double-strand break processing revealed by non-intrusive imaging of living cells.* PLoS Genet, 2014. **10**(3): p. e1004187.
629. Lindhout, B.I., et al., *Live cell imaging of repetitive DNA sequences via GFP-tagged polydactyl zinc finger proteins.* Nucleic Acids Res, 2007. **35**(16): p. e107.
630. Casas-Delucchi, C.S., et al., *Targeted manipulation of heterochromatin rescues MeCP2 Rett mutants and re-establishes higher order chromatin organization.* Nucleic Acids Res, 2012. **40**(22): p. e176.
631. Ma, H., P. Reyes-Gutierrez, and T. Pederson, *Visualization of repetitive DNA sequences in human chromosomes with transcription activator-like effectors.* Proc Natl Acad Sci U S A, 2013. **110**(52): p. 21048-53.
632. Miyanari, Y., C. Ziegler-Birling, and M.E. Torres-Padilla, *Live visualization of chromatin dynamics with fluorescent TALEs.* Nat Struct Mol Biol, 2013. **20**(11): p. 1321-4.
633. Thanisch, K., et al., *Targeting and tracing of specific DNA sequences with dTALEs in living cells.* Nucleic Acids Res, 2014. **42**(6): p. e38.
634. Anton, T., et al., *Visualization of specific DNA sequences in living mouse embryonic stem cells with a programmable fluorescent CRISPR/Cas system.* Nucleus, 2014. **5**(2): p. 163-72.
635. Ma, H., et al., *Multicolor CRISPR labeling of chromosomal loci in human cells.* Proc Natl Acad Sci U S A, 2015. **112**(10): p. 3002-7.
636. Knight, S.C., et al., *Dynamics of CRISPR-Cas9 genome interrogation in living cells.* Science, 2015. **350**(6262): p. 823-6.
637. Flors, C., *DNA and chromatin imaging with super-resolution fluorescence microscopy based on single-molecule localization.* Biopolymers, 2011. **95**(5): p. 290-7.
638. Flors, C., *Super-resolution fluorescence imaging of directly labelled DNA: from microscopy standards to living cells.* J Microsc, 2013. **251**(1): p. 1-4.
639. Berdnikova, D.V., et al., *Governing the DNA-binding mode of styryl dyes by the length of their alkyl substituents - from intercalation to major groove binding.* Org Biomol Chem, 2018. **16**(4): p. 545-554.
640. Gunther, K., M. Mertig, and R. Seidel, *Mechanical and structural properties of YOYO-1 complexed DNA.* Nucleic Acids Res, 2010. **38**(19): p. 6526-32.
641. Reuter, M. and D.T. Dryden, *The kinetics of YOYO-1 intercalation into single molecules of double-stranded DNA.* Biochem Biophys Res Commun, 2010. **403**(2): p. 225-9.
642. Sen, O., A.T. Saurin, and J.M.G. Higgins, *The live cell DNA stain SiR-Hoechst induces DNA damage responses and impairs cell cycle progression.* Sci Rep, 2018. **8**(1): p. 7898.
643. Vranken, C., et al., *Super-resolution optical DNA Mapping via DNA methyltransferase-directed click chemistry.* Nucleic Acids Res, 2014. **42**(7): p. e50.
644. Watanabe, S., et al., *Protein localization in electron micrographs using fluorescence nanoscopy.* Nat Methods, 2011. **8**(1): p. 80-4.

645. Dong, B., et al., *Superresolution intrinsic fluorescence imaging of chromatin utilizing native, unmodified nucleic acids for contrast.* Proc Natl Acad Sci U S A, 2016. **113**(35): p. 9716-21.
646. Williams, E.S., et al., *CO-FISH, COD-FISH, ReD-FISH, SKY-FISH.* Methods Mol Biol, 2011. **735**: p. 113-24.
647. Poon, S.S. and P.M. Lansdorp, *Quantitative fluorescence in situ hybridization (Q-FISH).* Curr Protoc Cell Biol, 2001. **Chapter 18**: p. Unit 18 4.
648. Slijepcevic, P., *Telomere length measurement by Q-FISH.* Methods Cell Sci, 2001. **23**(1-3): p. 17-22.
649. Wang, S., et al., *Superresolution imaging of telomeres with continuous wave stimulated emission depletion (STED) microscope.* Science China Chemistry, 2016. **59**(11): p. 1519-1524.
650. Anderson, R., et al., *Length-independent telomere damage drives cardiomyocyte senescence.* bioRxiv, 2018: p. 394809.
651. Wang, L., et al., *Single molecule localization imaging of telomeres and centromeres using fluorescence in situ hybridization and semiconductor quantum dots.* Nanotechnology, 2018. **29**(28): p. 285602.
652. Jeynes, J.C.G., et al., *Nanoscale Properties of Human Telomeres Measured with a Dual Purpose X-ray Fluorescence and Super Resolution Microscopy Gold Nanoparticle Probe.* ACS Nano, 2017. **11**(12): p. 12632-12640.
653. Lajoie, V., et al., *LMP1 mediates multinuclearity through downregulation of shelterin proteins and formation of telomeric aggregates.* Blood, 2015. **125**(13): p. 2101-10.
654. Dimitrova, N., et al., *53BP1 promotes non-homologous end joining of telomeres by increasing chromatin mobility.* Nature, 2008. **456**(7221): p. 524-8.
655. Phipps, M.L., et al., *Super-resolution optical microscopy study of telomere structure.* J Biomed Opt, 2016. **21**(9): p. 94003.
656. Chen, A., et al., *Direct visualization of telomeric DNA loops in cells by AFM*, in *APSIAC 2000: Asia–Pacific Surface and Interface Analysis Conference*. 2001: Beijing, China. p. 32-37.
657. Avogaro, L., et al., *Live-cell imaging reveals the dynamics and function of single-telomere TERRA molecules in cancer cells.* RNA Biol, 2018. **15**(6): p. 787-796.
658. Schmidt, J.C., A.J. Zaug, and T.R. Cech, *Live Cell Imaging Reveals the Dynamics of Telomerase Recruitment to Telomeres.* Cell, 2016. **166**(5): p. 1188-1197 e9.
659. Chen, B., et al., *Dynamic imaging of genomic loci in living human cells by an optimized CRISPR/Cas system.* Cell, 2013. **155**(7): p. 1479-91.
660. Deng, W., et al., *CASFISH: CRISPR/Cas9-mediated in situ labeling of genomic loci in fixed cells.* Proc Natl Acad Sci U S A, 2015. **112**(38): p. 11870-5.
661. Wang, S., et al., *Multiplexed Superresolution CRISPR Imaging of Chromatin in Living Cells.* CCS Chem, 2019. **1**(3): p. 278-285.
662. Maeshima, K., S. Janssen, and U.K. Laemmli, *Specific targeting of insect and vertebrate telomeres with pyrrole and imidazole polyamides.* EMBO J, 2001. **20**(12): p. 3218-28.
663. von Chamier, L., R.F. Laine, and R. Henriques, *Artificial intelligence for microscopy: what you should know.* Biochemical Society Transactions, 2019: p. BST20180391.
664. LeCun, Y., Y. Bengio, and G. Hinton, *Deep learning.* Nature, 2015. **521**(7553): p. 436-44.
665. Krizhevsky, A., I. Sutskever, and G.E. Hinton, *ImageNet classification with deep convolutional neural networks*, in *Proceedings of the 25th International Conference on Neural Information Processing Systems - Volume 1*. 2012, Curran Associates Inc.: Lake Tahoe, Nevada. p. 1097-1105.
666. Rumelhart, D.E., G.E. Hinton, and R.J. Williams, *Learning representations by back-propagating errors.* Nature, 1986. **323**(6088): p. 533-536.
667. Bottou, L. *Large-Scale Machine Learning with Stochastic Gradient Descent*. 2010. Heidelberg: Physica-Verlag HD.
668. Nichols, J.A., H.W. Herbert Chan, and M.A.B. Baker, *Machine learning: applications of artificial intelligence to imaging and diagnosis.* Biophys Rev, 2019. **11**(1): p. 111-118.

669. Falk, T., et al., *Author Correction: U-Net: deep learning for cell counting, detection, and morphometry.* Nat Methods, 2019. **16**(4): p. 351.
670. Falk, T., et al., *U-Net: deep learning for cell counting, detection, and morphometry.* Nat Methods, 2019. **16**(1): p. 67-70.
671. Van Valen, D.A., et al., *Deep Learning Automates the Quantitative Analysis of Individual Cells in Live-Cell Imaging Experiments.* PLoS Comput Biol, 2016. **12**(11): p. e1005177.
672. Xu, J., et al., *A Deep Convolutional Neural Network for segmenting and classifying epithelial and stromal regions in histopathological images.* Neurocomputing, 2016. **191**: p. 214-223.
673. Naylor, P., et al., *Segmentation of Nuclei in Histopathology Images by Deep Regression of the Distance Map.* IEEE Trans Med Imaging, 2019. **38**(2): p. 448-459.
674. Chen, H., et al. *DCAN: Deep Contour-Aware Networks for Accurate Gland Segmentation*. arXiv e-prints, 2016.
675. Wang, D., et al. *Deep Learning for Identifying Metastatic Breast Cancer*. arXiv e-prints, 2016.
676. Esteva, A., et al., *Corrigendum: Dermatologist-level classification of skin cancer with deep neural networks.* Nature, 2017. **546**(7660): p. 686.
677. Esteva, A., et al., *Dermatologist-level classification of skin cancer with deep neural networks.* Nature, 2017. **542**(7639): p. 115-118.
678. Eulenberg, P., et al., *Reconstructing cell cycle and disease progression using deep learning.* Nat Commun, 2017. **8**(1): p. 463.
679. Richmond, D., et al. *DeadNet: Identifying Phototoxicity from Label-free Microscopy Images of Cells using Deep ConvNets*. arXiv e-prints, 2017.
680. Christiansen, E.M., et al., *In Silico Labeling: Predicting Fluorescent Labels in Unlabeled Images.* Cell, 2018. **173**(3): p. 792-803 e19.
681. Ounkomol, C., et al., *Label-free prediction of three-dimensional fluorescence images from transmitted-light microscopy.* Nat Methods, 2018. **15**(11): p. 917-920.
682. Weigert, M., et al., *Content-aware image restoration: pushing the limits of fluorescence microscopy.* Nat Methods, 2018. **15**(12): p. 1090-1097.
683. Nehme, E., et al., *Deep-STORM: super-resolution single-molecule microscopy by deep learning.* Optica, 2018. **5**(4): p. 458-464.
684. Boyd, N., et al., *DeepLoco: Fast 3D Localization Microscopy Using Neural Networks.* bioRxiv, 2018: p. 267096.
685. Azulay, A. and Y. Weiss *Why do deep convolutional networks generalize so poorly to small image transformations?* arXiv e-prints, 2018.
686. Erdel, F., K. Muller-Ott, and K. Rippe, *Establishing epigenetic domains via chromatin-bound histone modifiers.* Ann N Y Acad Sci, 2013. **1305**: p. 29-43.
687. Simonyan, K. and A. Zisserman *Very Deep Convolutional Networks for Large-Scale Image Recognition*. arXiv e-prints, 2014.
688. Ulyanov, D., A. Vedaldi, and V. Lempitsky *Instance Normalization: The Missing Ingredient for Fast Stylization*. arXiv e-prints, 2016.
689. Bishop, C.M., *Pattern Recognition and Machine Learning*. 2006: Springer.
690. Maas, A.L., A.Y. Hannun, and A.Y. Ng, *Rectifier nonlinearities improve neural network acoustic models*, in *ICML Workshop on Deep Learning for Audio, Speech and Language Processing*. 2013.
691. Loshchilov, I. and F. Hutter *SGDR: Stochastic Gradient Descent with Warm Restarts*. arXiv e-prints, 2016.
692. Srivastava, N., et al., *Dropout: A Simple Way to Prevent Neural Networks from Overfitting.* Journal of Machine Learning Research, 2014. **15**: p. 1929-1958.
693. Lee, T.C., R.L. Kashyap, and C.N. Chu, *Building Skeleton Models via 3-D Medial Surface Axis Thinning Algorithms.* CVGIP: Graphical Models and Image Processing, 1994. **56**(6): p. 462-478.
694. Fitzgibbon, A.W. and R.B. Fisher, *A buyer's guide to conic fitting*, in *Proc. 5th British Machine Vision Conference, Birmingham*. 1995: University of Edinburgh, Department of Artificial Intelligence. p. 513-522.

695. Bolte, S. and F.P. Cordelieres, *A guided tour into subcellular colocalization analysis in light microscopy.* J Microsc, 2006. **224**(Pt 3): p. 213-32.
696. Woolf, B., *The Log Likelihood Ratio Test (The G-Test).* Annals of Human Genetics, 1957. **21**(4): p. 397-409.
697. Dunn, K.W., M.M. Kamocka, and J.H. McDonald, *A practical guide to evaluating colocalization in biological microscopy.* Am J Physiol Cell Physiol, 2011. **300**(4): p. C723-42.
698. Vannier, J.B., et al., *RTEL1 dismantles T loops and counteracts telomeric G4-DNA to maintain telomere integrity.* Cell, 2012. **149**(4): p. 795-806.
699. Dai, X., et al., *Molecular steps of G-overhang generation at human telomeres and its function in chromosome end protection.* EMBO J, 2010. **29**(16): p. 2788-801.
700. Cacchione, S., A. Biroccio, and A. Rizzo, *Emerging roles of telomeric chromatin alterations in cancer.* J Exp Clin Cancer Res, 2019. **38**(1): p. 21.
701. Galati, A., E. Micheli, and S. Cacchione, *Chromatin structure in telomere dynamics.* Front Oncol, 2013. **3**: p. 46.
702. Greider, C.W., *Telomeres do D-loop-T-loop.* Cell, 1999. **97**(4): p. 419-22.
703. Stansel, R.M., T. de Lange, and J.D. Griffith, *T-loop assembly in vitro involves binding of TRF2 near the 3' telomeric overhang.* EMBO J, 2001. **20**(19): p. 5532-40.
704. Amiard, S., et al., *A topological mechanism for TRF2-enhanced strand invasion.* Nat Struct Mol Biol, 2007. **14**(2): p. 147-54.
705. Poulet, A., et al., *TRF2 promotes, remodels and protects telomeric Holliday junctions.* EMBO J, 2009. **28**(6): p. 641-51.
706. Verdun, R.E. and J. Karlseder, *The DNA damage machinery and homologous recombination pathway act consecutively to protect human telomeres.* Cell, 2006. **127**(4): p. 709-20.
707. Fouche, N., et al., *The basic domain of TRF2 directs binding to DNA junctions irrespective of the presence of TTAGGG repeats.* J Biol Chem, 2006. **281**(49): p. 37486-95.
708. Zhang, H., et al., *Liquid condensation drives telomere clustering during ALT.* bioRxiv, 2019: p. 633040.
709. Tilman, G., et al., *Subtelomeric DNA hypomethylation is not required for telomeric sister chromatid exchanges in ALT cells.* Oncogene, 2009. **28**(14): p. 1682-93.
710. Gonzalo, S., et al., *DNA methyltransferases control telomere length and telomere recombination in mammalian cells.* Nat Cell Biol, 2006. **8**(4): p. 416-24.
711. Jimenez Useche, I., et al., *Effects of DNA Methylation Patterns on Chromatin Compaction.* Biophysical Journal, 2013. **104**(2): p. 39a.
712. Siegel, R.L., K.D. Miller, and A. Jemal, *Cancer statistics, 2019.* CA Cancer J Clin, 2019. **69**(1): p. 7-34.
713. Zamboglou, C., et al., *Comparison of (68)Ga-HBED-CC PSMA-PET/CT and multiparametric MRI for gross tumour volume detection in patients with primary prostate cancer based on slice by slice comparison with histopathology.* Theranostics, 2017. **7**(1): p. 228-237.
714. Zamboglou, C., et al., *(68)Ga-HBED-CC-PSMA PET/CT Versus Histopathology in Primary Localized Prostate Cancer: A Voxel-Wise Comparison.* Theranostics, 2016. **6**(10): p. 1619-28.
715. Maurer, T., et al., *Diagnostic Efficacy of (68)Gallium-PSMA Positron Emission Tomography Compared to Conventional Imaging for Lymph Node Staging of 130 Consecutive Patients with Intermediate to High Risk Prostate Cancer.* J Urol, 2016. **195**(5): p. 1436-1443.
716. Pyka, T., et al., *Comparison of bone scintigraphy and (68)Ga-PSMA PET for skeletal staging in prostate cancer.* Eur J Nucl Med Mol Imaging, 2016. **43**(12): p. 2114-2121.
717. Hope, T.A., et al., *Impact of (68)Ga-PSMA-11 PET on Management in Patients with Biochemically Recurrent Prostate Cancer.* J Nucl Med, 2017. **58**(12): p. 1956-1961.
718. Silver, D.A., et al., *Prostate-specific membrane antigen expression in normal and malignant human tissues.* Clin Cancer Res, 1997. **3**(1): p. 81-5.
719. Wright, G.L., Jr., et al., *Expression of prostate-specific membrane antigen in normal, benign, and malignant prostate tissues.* Urol Oncol, 1995. **1**(1): p. 18-28.

720. Sweat, S.D., et al., *Prostate-specific membrane antigen expression is greatest in prostate adenocarcinoma and lymph node metastases.* Urology, 1998. **52**(4): p. 637-40.
721. Mhawech-Fauceglia, P., et al., *Prostate-specific membrane antigen (PSMA) protein expression in normal and neoplastic tissues and its sensitivity and specificity in prostate adenocarcinoma: an immunohistochemical study using mutiple tumour tissue microarray technique.* Histopathology, 2007. **50**(4): p. 472-83.
722. Minner, S., et al., *High level PSMA expression is associated with early psa recurrence in surgically treated prostate cancer.* Prostate, 2011. **71**(3): p. 281-8.
723. Ghosh, A. and W.D. Heston, *Tumor target prostate specific membrane antigen (PSMA) and its regulation in prostate cancer.* J Cell Biochem, 2004. **91**(3): p. 528-39.
724. Schottelius, M., et al., *Synthesis and Preclinical Characterization of the PSMA-Targeted Hybrid Tracer PSMA-I&F for Nuclear and Fluorescence Imaging of Prostate Cancer.* J Nucl Med, 2019. **60**(1): p. 71-78.
725. Litwin, M.S. and H.J. Tan, *The Diagnosis and Treatment of Prostate Cancer: A Review.* JAMA, 2017. **317**(24): p. 2532-2542.
726. Bostwick, D.G., et al., *Human prostate cancer risk factors.* Cancer, 2004. **101**(10 Suppl): p. 2371-490.
727. Ramsay, A.K. and H.Y. Leung, *Signalling pathways in prostate carcinogenesis: potentials for molecular-targeted therapy.* Clinical Science, 2009. **117**(5-6): p. 209-228.
728. Packer, J.R. and N.J. Maitland, *The molecular and cellular origin of human prostate cancer.* Biochimica Et Biophysica Acta-Molecular Cell Research, 2016. **1863**(6): p. 1238-1260.
729. Isbarn, H., et al., *Testosterone and Prostate Cancer: Revisiting Old Paradigms.* European Urology, 2009. **56**(1): p. 48-56.
730. Wang, D.P. and D.J. Tindall, *Androgen Action During Prostate Carcinogenesis.* Androgen Action: Methods and Protocols, 2011. **776**: p. 25-44.
731. Huggins, C. and C.V. Hodges, *Studies on prostatic cancer. I. The effect of castration, of estrogen and androgen injection on serum phosphatases in metastatic carcinoma of the prostate.* CA Cancer J Clin, 1972. **22**(4): p. 232-40.
732. Heidenreich, A., et al., *EAU guidelines on prostate cancer. Part 1: screening, diagnosis, and treatment of clinically localised disease.* Eur Urol, 2011. **59**(1): p. 61-71.
733. Stewart, R.W., et al., *Screening for prostate cancer.* Semin Oncol, 2017. **44**(1): p. 47-56.
734. Carroll, P.R., et al., *NCCN Guidelines Insights: Prostate Cancer Early Detection, Version 2.2016.* J Natl Compr Canc Netw, 2016. **14**(5): p. 509-19.
735. Edge, S.B. and C.C. Compton, *The American Joint Committee on Cancer: the 7th edition of the AJCC cancer staging manual and the future of TNM.* Ann Surg Oncol, 2010. **17**(6): p. 1471-4.
736. Brawer, M.K., *Hormonal therapy for prostate cancer.* Rev Urol, 2006. **8 Suppl 2**: p. S35-47.
737. Wirth, M.P., O.W. Hakenberg, and M. Froehner, *Antiandrogens in the treatment of prostate cancer.* Eur Urol, 2007. **51**(2): p. 306-13; discussion 314.
738. Shelley, M., et al., *Chemotherapy for hormone-refractory prostate cancer.* Cochrane Database Syst Rev, 2006(4): p. CD005247.
739. Tannock, I.F., et al., *Chemotherapy with mitoxantrone plus prednisone or prednisone alone for symptomatic hormone-resistant prostate cancer: a Canadian randomized trial with palliative end points.* J Clin Oncol, 1996. **14**(6): p. 1756-64.
740. Wolff, R.F., et al., *A systematic review of randomised controlled trials of radiotherapy for localised prostate cancer.* Eur J Cancer, 2015. **51**(16): p. 2345-67.
741. Cho, S. and S.H. Kang, *Current status of cryotherapy for prostate and kidney cancer.* Korean J Urol, 2014. **55**(12): p. 780-8.
742. Sokoloff, R.L., et al., *A dual-monoclonal sandwich assay for prostate-specific membrane antigen: levels in tissues, seminal fluid and urine.* Prostate, 2000. **43**(2): p. 150-7.
743. Pinto, J.T., et al., *Prostate-specific membrane antigen: a novel folate hydrolase in human prostatic carcinoma cells.* Clin Cancer Res, 1996. **2**(9): p. 1445-51.

744. Troyer, J.K., M.L. Beckett, and G.L. Wright, Jr., *Detection and characterization of the prostate-specific membrane antigen (PSMA) in tissue extracts and body fluids.* Int J Cancer, 1995. **62**(5): p. 552-8.
745. Pangalos, M.N., et al., *Isolation and expression of novel human glutamate carboxypeptidases with N-acetylated alpha-linked acidic dipeptidase and dipeptidyl peptidase IV activity.* J Biol Chem, 1999. **274**(13): p. 8470-83.
746. Yao, V., et al., *Expression of prostate-specific membrane antigen (PSMA), increases cell folate uptake and proliferation and suggests a novel role for PSMA in the uptake of the non-polyglutamated folate, folic acid.* Prostate, 2010. **70**(3): p. 305-16.
747. Luthi-Carter, R., et al., *Molecular characterization of human brain N-acetylated alpha-linked acidic dipeptidase (NAALADase).* J Pharmacol Exp Ther, 1998. **286**(2): p. 1020-5.
748. Slusher, B.S., et al., *Rat brain N-acetylated alpha-linked acidic dipeptidase activity. Purification and immunologic characterization.* J Biol Chem, 1990. **265**(34): p. 21297-301.
749. Rawlings, N.D. and A.J. Barrett, *Structure of membrane glutamate carboxypeptidase.* Biochim Biophys Acta, 1997. **1339**(2): p. 247-52.
750. Schulke, N., et al., *The homodimer of prostate-specific membrane antigen is a functional target for cancer therapy.* Proc Natl Acad Sci U S A, 2003. **100**(22): p. 12590-5.
751. Ghosh, A. and W.D. Heston, *Effect of carbohydrate moieties on the folate hydrolysis activity of the prostate specific membrane antigen.* Prostate, 2003. **57**(2): p. 140-51.
752. Kularatne, S.A., et al., *Prostate-specific membrane antigen targeted imaging and therapy of prostate cancer using a PSMA inhibitor as a homing ligand.* Mol Pharm, 2009. **6**(3): p. 780-9.
753. Ross, J.S., et al., *Correlation of primary tumor prostate-specific membrane antigen expression with disease recurrence in prostate cancer.* Clin Cancer Res, 2003. **9**(17): p. 6357-62.
754. Goodman, O.B., Jr., et al., *Interaction of prostate specific membrane antigen with clathrin and the adaptor protein complex-2.* Int J Oncol, 2007. **31**(5): p. 1199-203.
755. Bravaccini, S., et al., *PSMA expression: a potential ally for the pathologist in prostate cancer diagnosis.* Sci Rep, 2018. **8**(1): p. 4254.
756. Barinka, C., et al., *Identification of the N-glycosylation sites on glutamate carboxypeptidase II necessary for proteolytic activity.* Protein Sci, 2004. **13**(6): p. 1627-35.
757. Kinoshita, Y., et al., *Targeting epitopes in prostate-specific membrane antigen for antibody therapy of prostate cancer.* Prostate Cancer Prostatic Dis, 2005. **8**(4): p. 359-63.
758. Liu, H., et al., *Constitutive and antibody-induced internalization of prostate-specific membrane antigen.* Cancer Res, 1998. **58**(18): p. 4055-60.
759. Davis, M.I., et al., *Crystal structure of prostate-specific membrane antigen, a tumor marker and peptidase.* Proc Natl Acad Sci U S A, 2005. **102**(17): p. 5981-6.
760. Barinka, C., et al., *Interactions between human glutamate carboxypeptidase II and urea-based inhibitors: structural characterization.* J Med Chem, 2008. **51**(24): p. 7737-43.
761. Mesters, J.R., et al., *Structure of glutamate carboxypeptidase II, a drug target in neuronal damage and prostate cancer.* EMBO J, 2006. **25**(6): p. 1375-84.
762. Benesova, M., et al., *Linker Modification Strategies To Control the Prostate-Specific Membrane Antigen (PSMA)-Targeting and Pharmacokinetic Properties of DOTA-Conjugated PSMA Inhibitors.* J Med Chem, 2016. **59**(5): p. 1761-75.
763. Ellis, R.J., et al., *Ten-year outcomes: the clinical utility of single photon emission computed tomography/computed tomography capromab pendetide (Prostascint) in a cohort diagnosed with localized prostate cancer.* Int J Radiat Oncol Biol Phys, 2011. **81**(1): p. 29-34.
764. Sodee, D.B., et al., *Multicenter ProstaScint imaging findings in 2154 patients with prostate cancer. The ProstaScint Imaging Centers.* Urology, 2000. **56**(6): p. 988-93.
765. Troyer, J.K., M.L. Beckett, and G.L. Wright, Jr., *Location of prostate-specific membrane antigen in the LNCaP prostate carcinoma cell line.* Prostate, 1997. **30**(4): p. 232-42.
766. Bouchelouche, K., P.L. Choyke, and J. Capala, *Prostate specific membrane antigen- a target for imaging and therapy with radionuclides.* Discov Med, 2010. **9**(44): p. 55-61.

767. Hillier, S.M., et al., *123I-MIP-1072, a small-molecule inhibitor of prostate-specific membrane antigen, is effective at monitoring tumor response to taxane therapy.* J Nucl Med, 2011. **52**(7): p. 1087-93.
768. Eder, M., et al., *68Ga-complex lipophilicity and the targeting property of a urea-based PSMA inhibitor for PET imaging.* Bioconjug Chem, 2012. **23**(4): p. 688-97.
769. Benesova, M., et al., *Preclinical Evaluation of a Tailor-Made DOTA-Conjugated PSMA Inhibitor with Optimized Linker Moiety for Imaging and Endoradiotherapy of Prostate Cancer.* J Nucl Med, 2015. **56**(6): p. 914-20.
770. Weineisen, M., et al., *Synthesis and preclinical evaluation of DOTAGA-conjugated PSMA ligands for functional imaging and endoradiotherapy of prostate cancer.* EJNMMI Res, 2014. **4**(1): p. 63.
771. Foss, C.A., et al., *Radiolabeled small-molecule ligands for prostate-specific membrane antigen: in vivo imaging in experimental models of prostate cancer.* Clin Cancer Res, 2005. **11**(11): p. 4022-8.
772. Smith-Jones, P.M., et al., *In vitro characterization of radiolabeled monoclonal antibodies specific for the extracellular domain of prostate-specific membrane antigen.* Cancer Res, 2000. **60**(18): p. 5237-43.
773. Tykvart, J., et al., *Comparative analysis of monoclonal antibodies against prostate-specific membrane antigen (PSMA).* Prostate, 2014. **74**(16): p. 1674-90.
774. Pandit-Taskar, N., et al., *(8)(9)Zr-huJ591 immuno-PET imaging in patients with advanced metastatic prostate cancer.* Eur J Nucl Med Mol Imaging, 2014. **41**(11): p. 2093-105.
775. Behe, M., et al., *In vivo testing of 177Lu-labelled anti-PSMA antibody as a new radioimmunotherapeutic agent against prostate cancer.* In Vivo, 2011. **25**(1): p. 55-9.
776. Wu, X., et al., *Second-generation aptamer-conjugated PSMA-targeted delivery system for prostate cancer therapy.* Int J Nanomedicine, 2011. **6**: p. 1747-56.
777. Baek, S.E., et al., *RNA aptamer-conjugated liposome as an efficient anticancer drug delivery vehicle targeting cancer cells in vivo.* J Control Release, 2014. **196**: p. 234-42.
778. Kularatne, S.A., et al., *Synthesis and biological analysis of prostate-specific membrane antigen-targeted anticancer prodrugs.* J Med Chem, 2010. **53**(21): p. 7767-77.
779. Kasten, B.B., et al., *Targeting prostate cancer cells with PSMA inhibitor-guided gold nanoparticles.* Bioorg Med Chem Lett, 2013. **23**(2): p. 565-8.
780. Mukherjee, A., et al., *Development and screening of a series of antibody-conjugated and silica-coated iron oxide nanoparticles for targeting the prostate-specific membrane antigen.* ChemMedChem, 2014. **9**(7): p. 1356-60.
781. Hrkach, J., et al., *Preclinical development and clinical translation of a PSMA-targeted docetaxel nanoparticle with a differentiated pharmacological profile.* Sci Transl Med, 2012. **4**(128): p. 128ra39.
782. Townsend, D.W., et al., *PET/CT today and tomorrow.* J Nucl Med, 2004. **45 Suppl 1**: p. 4S-14S.
783. Rich, D.A., *A brief history of positron emission tomography.* J Nucl Med Technol, 1997. **25**(1): p. 4-11.
784. Tong, S., A.M. Alessio, and P.E. Kinahan, *Image reconstruction for PET/CT scanners: past achievements and future challenges.* Imaging Med, 2010. **2**(5): p. 529-545.
785. Leitha, T., *Nuclear medicine: proof of principle for targeted drugs in diagnosis and therapy.* Curr Pharm Des, 2009. **15**(2): p. 173-87.
786. Ametamey, S.M., M. Honer, and P.A. Schubiger, *Molecular imaging with PET.* Chem Rev, 2008. **108**(5): p. 1501-16.
787. Nayak, T.K. and M.W. Brechbiel, *Radioimmunoimaging with longer-lived positron-emitting radionuclides: potentials and challenges.* Bioconjug Chem, 2009. **20**(5): p. 825-41.
788. Groves, A.M., et al., *Non-[18F]FDG PET in clinical oncology.* Lancet Oncol, 2007. **8**(9): p. 822-30.
789. Schuhmacher, J. and W. Maier-Borst, *A new Ge-68/Ga-68 radioisotope generator system for production of Ga-68 in dilute HCl.* Int J Appl Radiat Isot, 1981. **32**: p. 31–36.

790. Bednarova, S., et al., *Positron emission tomography (PET) in primary prostate cancer staging and risk assessment.* Transl Androl Urol, 2017. **6**(3): p. 413-423.
791. Jadvar, H., *Molecular imaging of prostate cancer: PET radiotracers.* AJR Am J Roentgenol, 2012. **199**(2): p. 278-91.
792. von Mallek, D., et al., *[Technical limits of PET/CT with 18FDG in prostate cancer].* Aktuelle Urol, 2006. **37**(3): p. 218-21.
793. Jadvar, H., *Molecular imaging of prostate cancer with 18F-fluorodeoxyglucose PET.* Nat Rev Urol, 2009. **6**(6): p. 317-23.
794. Ackerstaff, E., et al., *Detection of increased choline compounds with proton nuclear magnetic resonance spectroscopy subsequent to malignant transformation of human prostatic epithelial cells.* Cancer Res, 2001. **61**(9): p. 3599-603.
795. Castellucci, P., et al., *Early biochemical relapse after radical prostatectomy: which prostate cancer patients may benefit from a restaging 11C-Choline PET/CT scan before salvage radiation therapy?* J Nucl Med, 2014. **55**(9): p. 1424-9.
796. Suardi, N., et al., *Long-term outcomes of salvage lymph node dissection for clinically recurrent prostate cancer: results of a single-institution series with a minimum follow-up of 5 years.* Eur Urol, 2015. **67**(2): p. 299-309.
797. Wondergem, M., et al., *A literature review of 18F-fluoride PET/CT and 18F-choline or 11C-choline PET/CT for detection of bone metastases in patients with prostate cancer.* Nucl Med Commun, 2013. **34**(10): p. 935-45.
798. Eder, M., et al., *Novel Preclinical and Radiopharmaceutical Aspects of [68Ga]Ga-PSMA-HBED-CC: A New PET Tracer for Imaging of Prostate Cancer.* Pharmaceuticals (Basel), 2014. **7**(7): p. 779-96.
799. Kozikowski, A.P., et al., *Design of remarkably simple, yet potent urea-based inhibitors of glutamate carboxypeptidase II (NAALADase).* J Med Chem, 2001. **44**(3): p. 298-301.
800. Afshar-Oromieh, A., et al., *PET imaging with a [68Ga]gallium-labelled PSMA ligand for the diagnosis of prostate cancer: biodistribution in humans and first evaluation of tumour lesions.* Eur J Nucl Med Mol Imaging, 2013. **40**(4): p. 486-95.
801. Afshar-Oromieh, A., et al., *[68Ga]Gallium-labelled PSMA ligand as superior PET tracer for the diagnosis of prostate cancer: comparison with 18F-FECH.* Eur J Nucl Med Mol Imaging, 2012. **39**(6): p. 1085-6.
802. Afshar-Oromieh, A., et al., *The diagnostic value of PET/CT imaging with the (68)Ga-labelled PSMA ligand HBED-CC in the diagnosis of recurrent prostate cancer.* Eur J Nucl Med Mol Imaging, 2015. **42**(2): p. 197-209.
803. Demirci, E., et al., *(68)Ga-PSMA PET/CT imaging of metastatic clear cell renal cell carcinoma.* Eur J Nucl Med Mol Imaging, 2014. **41**(7): p. 1461-2.
804. Afshar-Oromieh, A., et al., *Comparison of PET imaging with a (68)Ga-labelled PSMA ligand and (18)F-choline-based PET/CT for the diagnosis of recurrent prostate cancer.* Eur J Nucl Med Mol Imaging, 2014. **41**(1): p. 11-20.
805. Bluemel, C., et al., *68Ga-PSMA-PET/CT in Patients With Biochemical Prostate Cancer Recurrence and Negative 18F-Choline-PET/CT.* Clin Nucl Med, 2016. **41**(7): p. 515-21.
806. Eiber, M., et al., *Simultaneous (68)Ga-PSMA HBED-CC PET/MRI Improves the Localization of Primary Prostate Cancer.* Eur Urol, 2016. **70**(5): p. 829-836.
807. Eiber, M., et al., *Evaluation of Hybrid (6)(8)Ga-PSMA Ligand PET/CT in 248 Patients with Biochemical Recurrence After Radical Prostatectomy.* J Nucl Med, 2015. **56**(5): p. 668-74.
808. Perera, M., et al., *Sensitivity, Specificity, and Predictors of Positive (68)Ga-Prostate-specific Membrane Antigen Positron Emission Tomography in Advanced Prostate Cancer: A Systematic Review and Meta-analysis.* Eur Urol, 2016. **70**(6): p. 926-937.
809. L'Annunziata, M.F., *Chapter 4 - Alpha Radiation*, in *Radioactivity (Second Edition)*, M.F. L'Annunziata, Editor. 2016, Elsevier: Boston. p. 123-134.
810. Particle Data, G., et al., *Review of Particle Physics.* Physical Review D, 2018. **98**(3): p. 030001.

811. L'Annunziata, M.F., *Chapter 6 - Beta Radiation and Beta Decay*, in *Radioactivity (Second Edition)*, M.F. L'Annunziata, Editor. 2016, Elsevier: Boston. p. 167-201.
812. Haberkorn, U., et al., *Endoradiotherapy with peptides - status and future development.* Curr Med Chem, 2008. **15**(3): p. 219-34.
813. Haberkorn, U., et al., *New Strategies in Prostate Cancer: Prostate-Specific Membrane Antigen (PSMA) Ligands for Diagnosis and Therapy.* Clin Cancer Res, 2016. **22**(1): p. 9-15.
814. Vallabhajosula, S., et al., *Radioimmunotherapy of prostate cancer using 90Y- and 177Lu-labeled J591 monoclonal antibodies: effect of multiple treatments on myelotoxicity.* Clin Cancer Res, 2005. **11**(19 Pt 2): p. 7195s-7200s.
815. Bander, N.H., et al., *Phase I trial of 177lutetium-labeled J591, a monoclonal antibody to prostate-specific membrane antigen, in patients with androgen-independent prostate cancer.* J Clin Oncol, 2005. **23**(21): p. 4591-601.
816. Tagawa, S.T., et al., *Phase II study of Lutetium-177-labeled anti-prostate-specific membrane antigen monoclonal antibody J591 for metastatic castration-resistant prostate cancer.* Clin Cancer Res, 2013. **19**(18): p. 5182-91.
817. Weineisen, M., et al., *68Ga- and 177Lu-Labeled PSMA I&T: Optimization of a PSMA-Targeted Theranostic Concept and First Proof-of-Concept Human Studies.* J Nucl Med, 2015. **56**(8): p. 1169-76.
818. McCarthy, M., et al., *Comparison of PSMA-HBED and PSMA-I&T as diagnostic agents in prostate carcinoma.* Eur J Nucl Med Mol Imaging, 2017. **44**(9): p. 1455-1462.
819. Rahbar, K., et al., *German Multicenter Study Investigating 177Lu-PSMA-617 Radioligand Therapy in Advanced Prostate Cancer Patients.* J Nucl Med, 2017. **58**(1): p. 85-90.
820. Baum, R.P., et al., *177Lu-Labeled Prostate-Specific Membrane Antigen Radioligand Therapy of Metastatic Castration-Resistant Prostate Cancer: Safety and Efficacy.* J Nucl Med, 2016. **57**(7): p. 1006-13.
821. Kratochwil, C., et al., *Targeted alpha-Therapy of Metastatic Castration-Resistant Prostate Cancer with (225)Ac-PSMA-617: Swimmer-Plot Analysis Suggests Efficacy Regarding Duration of Tumor Control.* J Nucl Med, 2018. **59**(5): p. 795-802.
822. Kratochwil, C., et al., *Targeted alpha-Therapy of Metastatic Castration-Resistant Prostate Cancer with (225)Ac-PSMA-617: Dosimetry Estimate and Empiric Dose Finding.* J Nucl Med, 2017. **58**(10): p. 1624-1631.
823. Kratochwil, C., et al., *225Ac-PSMA-617 for PSMA-Targeted alpha-Radiation Therapy of Metastatic Castration-Resistant Prostate Cancer.* J Nucl Med, 2016. **57**(12): p. 1941-1944.
824. Heidenreich, A., et al., *EAU guidelines on prostate cancer. part 1: screening, diagnosis, and local treatment with curative intent-update 2013.* Eur Urol, 2014. **65**(1): p. 124-37.
825. Wilt, T.J., et al., *Radical prostatectomy versus observation for localized prostate cancer.* N Engl J Med, 2012. **367**(3): p. 203-13.
826. Holmberg, L., et al., *Results from the Scandinavian Prostate Cancer Group Trial Number 4: a randomized controlled trial of radical prostatectomy versus watchful waiting.* J Natl Cancer Inst Monogr, 2012. **2012**(45): p. 230-3.
827. Abdul-Muhsin, H.M. and M.R. Humphreys, *Advances in laparoscopic urologic surgery techniques.* F1000Res, 2016. **5**.
828. Schols, R.M., et al., *Advanced intraoperative imaging methods for laparoscopic anatomy navigation: an overview.* Surg Endosc, 2013. **27**(6): p. 1851-9.
829. Sodergren, M., G.Z. Yang, and A. Darzi, *Perception and orientation in minimally invasive surgery.* Arch Surg, 2012. **147**(3): p. 210-1.
830. Freschi, C., et al., *Technical review of the da Vinci surgical telemanipulator.* Int J Med Robot, 2013. **9**(4): p. 396-406.
831. Gandaglia, G., et al., *Novel Technologies in Urologic Surgery: a Rapidly Changing Scenario.* Curr Urol Rep, 2016. **17**(3): p. 19.
832. Munbauhal, G., et al., *Current perspectives of sentinel lymph node dissection at the time of radical surgery for prostate cancer.* Cancer Treat Rev, 2016. **50**: p. 228-239.

833. Yossepowitch, O., et al., *Positive surgical margins in radical prostatectomy: outlining the problem and its long-term consequences.* Eur Urol, 2009. **55**(1): p. 87-99.
834. Schottelius, M., et al., *[(111)In]PSMA-I&T: expanding the spectrum of PSMA-I&T applications towards SPECT and radioguided surgery.* EJNMMI Res, 2015. **5**(1): p. 68.
835. Robu, S., et al., *Preclinical Evaluation and First Patient Application of 99mTc-PSMA-I&S for SPECT Imaging and Radioguided Surgery in Prostate Cancer.* J Nucl Med, 2017. **58**(2): p. 235-242.
836. Maurer, T., et al., *Prostate-specific membrane antigen-radioguided surgery for metastatic lymph nodes in prostate cancer.* Eur Urol, 2015. **68**(3): p. 530-4.
837. Rauscher, I., et al., *Value of (111) In-prostate-specific membrane antigen (PSMA)-radioguided surgery for salvage lymphadenectomy in recurrent prostate cancer: correlation with histopathology and clinical follow-up.* BJU Int, 2017. **120**(1): p. 40-47.
838. Brouwer, O.R., et al., *Feasibility of intraoperative navigation to the sentinel node in the groin using preoperatively acquired single photon emission computerized tomography data: transferring functional imaging to the operating room.* J Urol, 2014. **192**(6): p. 1810-6.
839. Lutje, S., et al., *Targeted radionuclide and fluorescence dual-modality imaging of cancer: preclinical advances and clinical translation.* Mol Imaging Biol, 2014. **16**(6): p. 747-55.
840. Bai, M. and D.J. Bornhop, *Recent advances in receptor-targeted fluorescent probes for in vivo cancer imaging.* Curr Med Chem, 2012. **19**(28): p. 4742-58.
841. Keereweer, S., et al., *Optical image-guided surgery--where do we stand?* Mol Imaging Biol, 2011. **13**(2): p. 199-207.
842. Fomina, N., et al., *Low power, biologically benign NIR light triggers polymer disassembly.* Macromolecules, 2011. **44**(21): p. 8590-8597.
843. Jo, D. and H. Hyun, *Structure-Inherent Targeting of Near-Infrared Fluorophores for Image-Guided Surgery.* Chonnam Med J, 2017. **53**(2): p. 95-102.
844. Luo, S., et al., *A review of NIR dyes in cancer targeting and imaging.* Biomaterials, 2011. **32**(29): p. 7127-38.
845. Polom, K., et al., *Current trends and emerging future of indocyanine green usage in surgery and oncology: a literature review.* Cancer, 2011. **117**(21): p. 4812-22.
846. Nakajima, T., et al., *Targeted, activatable, in vivo fluorescence imaging of prostate-specific membrane antigen (PSMA) positive tumors using the quenched humanized J591 antibody-indocyanine green (ICG) conjugate.* Bioconjug Chem, 2011. **22**(8): p. 1700-5.
847. Chen, Y., et al., *Synthesis and biological evaluation of low molecular weight fluorescent imaging agents for the prostate-specific membrane antigen.* Bioconjug Chem, 2012. **23**(12): p. 2377-85.
848. Chen, Y., et al., *A low molecular weight PSMA-based fluorescent imaging agent for cancer.* Biochem Biophys Res Commun, 2009. **390**(3): p. 624-9.
849. Neuman, B.P., et al., *Real-time, near-infrared fluorescence imaging with an optimized dye/light source/camera combination for surgical guidance of prostate cancer.* Clin Cancer Res, 2015. **21**(4): p. 771-80.
850. Kelderhouse, L.E., et al., *Development of tumor-targeted near infrared probes for fluorescence guided surgery.* Bioconjug Chem, 2013. **24**(6): p. 1075-80.
851. Liu, T., et al., *A targeted low molecular weight near-infrared fluorescent probe for prostate cancer.* Bioorg Med Chem Lett, 2010. **20**(23): p. 7124-6.
852. Humblet, V., et al., *High-affinity near-infrared fluorescent small-molecule contrast agents for in vivo imaging of prostate-specific membrane antigen.* Mol Imaging, 2005. **4**(4): p. 448-62.
853. Wang, X., et al., *Development of targeted near-infrared imaging agents for prostate cancer.* Mol Cancer Ther, 2014. **13**(11): p. 2595-606.
854. Lutje, S., et al., *PSMA Ligands for Radionuclide Imaging and Therapy of Prostate Cancer: Clinical Status.* Theranostics, 2015. **5**(12): p. 1388-401.
855. Schaafsma, B.E., et al., *The clinical use of indocyanine green as a near-infrared fluorescent contrast agent for image-guided oncologic surgery.* J Surg Oncol, 2011. **104**(3): p. 323-32.

856. Vidal-Sicart, S. and R.A. Valdes Olmos, *Sentinel node approach in prostate cancer.* Rev Esp Med Nucl Imagen Mol, 2015. **34**(6): p. 358-71.
857. Kelloff, G.J., et al., *The progress and promise of molecular imaging probes in oncologic drug development.* Clin Cancer Res, 2005. **11**(22): p. 7967-85.
858. Lutje, S., et al., *Dual-Modality Image-Guided Surgery of Prostate Cancer with a Radiolabeled Fluorescent Anti-PSMA Monoclonal Antibody.* J Nucl Med, 2014. **55**(6): p. 995-1001.
859. Banerjee, S.R., et al., *(111)In- and IRDye800CW-Labeled PLA-PEG Nanoparticle for Imaging Prostate-Specific Membrane Antigen-Expressing Tissues.* Biomacromolecules, 2017. **18**(1): p. 201-209.
860. Schafer, M., et al., *A dimerized urea-based inhibitor of the prostate-specific membrane antigen for 68Ga-PET imaging of prostate cancer.* EJNMMI Res, 2012. **2**(1): p. 23.
861. Demandolx, D. and J. Davoust, *Multicolour analysis and local image correlation in confocal microscopy.* Journal of Microscopy, 1997. **185**: p. 21-36.
862. Miura K; Rueden C; Hiner M, S.J., Rietdorf J *ImageJ Plugin CorrectBleach V2.0.2 (Version v2.0.2).* Zenodo, 2014.
863. Bertelsen, V., et al., *A chimeric pre-ubiquitinated EGF receptor is constitutively endocytosed in a clathrin-dependent, but kinase-independent manner.* Traffic, 2011. **12**(4): p. 507-20.
864. Miller, S.E., et al., *CALM regulates clathrin-coated vesicle size and maturation by directly sensing and driving membrane curvature.* Dev Cell, 2015. **33**(2): p. 163-75.
865. Pastan, I.H. and M.C. Willingham, *Receptor-mediated endocytosis of hormones in cultured cells.* Annu Rev Physiol, 1981. **43**: p. 239-50.
866. Mellman, I., *Endocytosis and molecular sorting.* Annu Rev Cell Dev Biol, 1996. **12**: p. 575-625.
867. Grubmuller, B., et al., *PSMA Ligand PET/MRI for Primary Prostate Cancer: Staging Performance and Clinical Impact.* Clin Cancer Res, 2018. **24**(24): p. 6300-6307.
868. Dulaney, C.R., et al., *Prostate Radiotherapy in the Era of Advanced Imaging and Precision Medicine.* Prostate Cancer, 2016. **2016**: p. 4897515.
869. Eder, M., et al., *PSMA as a target for radiolabelled small molecules.* Eur J Nucl Med Mol Imaging, 2013. **40**(6): p. 819-23.
870. Wester, H.J. and M. Schottelius, *PSMA-Targeted Radiopharmaceuticals for Imaging and Therapy.* Semin Nucl Med, 2019. **49**(4): p. 302-312.
871. Banerjee, S.R., et al., *Sequential SPECT and optical imaging of experimental models of prostate cancer with a dual modality inhibitor of the prostate-specific membrane antigen.* Angew Chem Int Ed Engl, 2011. **50**(39): p. 9167-70.
872. Rajasekaran, S.A., et al., *A novel cytoplasmic tail MXXXL motif mediates the internalization of prostate-specific membrane antigen.* Mol Biol Cell, 2003. **14**(12): p. 4835-45.
873. Perico, M.E., et al., *Prostate-specific membrane antigen (PSMA) assembles a macromolecular complex regulating growth and survival of prostate cancer cells "in vitro" and correlating with progression "in vivo".* Oncotarget, 2016. **7**(45): p. 74189-74202.
874. Schmidt, S., et al., *Discriminatory Role of Detergent-Resistant Membranes in the Dimerization and Endocytosis of Prostate-Specific Membrane Antigen.* PLoS One, 2013. **8**(6): p. e66193.
875. Colombatti, M., et al., *The prostate specific membrane antigen regulates the expression of IL-6 and CCL5 in prostate tumour cells by activating the MAPK pathways.* PLoS One, 2009. **4**(2): p. e4608.
876. Wustemann, T., et al., *Targeting prostate cancer: Prostate-specific membrane antigen based diagnosis and therapy.* Med Res Rev, 2019. **39**(1): p. 40-69.
877. Tinevez, J.Y., et al., *A quantitative method for measuring phototoxicity of a live cell imaging microscope.* Methods Enzymol, 2012. **506**: p. 291-309.
878. Bianchi, J.I., et al., *Reliable Screening of Dye Phototoxicity by Using a Caenorhabditis elegans Fast Bioassay.* PLoS One, 2015. **10**(6): p. e0128898.
879. Stockley, J.H., et al., *Surpassing light-induced cell damage in vitro with novel cell culture media.* Sci Rep, 2017. **7**(1): p. 849.

880. Cordes, T., et al., *Mechanisms and advancement of antifading agents for fluorescence microscopy and single-molecule spectroscopy.* Phys Chem Chem Phys, 2011. **13**(14): p. 6699-709.
881. Vogelsang, J., et al., *A reducing and oxidizing system minimizes photobleaching and blinking of fluorescent dyes.* Angew Chem Int Ed Engl, 2008. **47**(29): p. 5465-9.
882. Widengren, J., et al., *Strategies to improve photostabilities in ultrasensitive fluorescence spectroscopy.* J Phys Chem A, 2007. **111**(3): p. 429-40.
883. Cordes, T., J. Vogelsang, and P. Tinnefeld, *On the mechanism of Trolox as antiblinking and antibleaching reagent.* J Am Chem Soc, 2009. **131**(14): p. 5018-9.
884. Zheng, Q., et al., *The contribution of reactive oxygen species to the photobleaching of organic fluorophores.* Photochem Photobiol, 2014. **90**(2): p. 448-454.
885. Wilkinson, F., D.J. Mcgarvey, and A.F. Olea, *Excited Triplet-State Interactions with Molecular-Oxygen - Influence of Charge-Transfer on the Bimolecular Quenching Rate Constants and the Yields of Singlet Oxygen (O-2(Asterisk),(1)Delta(G)) for Substituted Naphthalenes in Various Solvents.* Journal of Physical Chemistry, 1994. **98**(14): p. 3762-3769.
886. Harada, Y., et al., *Mechanochemical coupling in actomyosin energy transduction studied by in vitro movement assay.* J Mol Biol, 1990. **216**(1): p. 49-68.
887. Aitken, C.E., R.A. Marshall, and J.D. Puglisi, *An oxygen scavenging system for improvement of dye stability in single-molecule fluorescence experiments.* Biophys J, 2008. **94**(5): p. 1826-35.
888. Lemke, E.A., et al., *Microfluidic device for single-molecule experiments with enhanced photostability.* J Am Chem Soc, 2009. **131**(38): p. 13610-2.
889. Rasnik, I., S.A. McKinney, and T. Ha, *Nonblinking and long-lasting single-molecule fluorescence imaging.* Nat Methods, 2006. **3**(11): p. 891-3.
890. Vandelinder, V. and G.D. Bachand, *Photodamage and the importance of photoprotection in biomolecular-powered device applications.* Anal Chem, 2014. **86**(1): p. 721-8.
891. Douthwright, S. and G. Sluder, *Live Cell Imaging: Assessing the Phototoxicity of 488 and 546 nm Light and Methods to Alleviate it.* J Cell Physiol, 2017. **232**(9): p. 2461-2468.
892. Tinnefeld, P. and T. Cordes, *'Self-healing' dyes: intramolecular stabilization of organic fluorophores.* Nat Methods, 2012. **9**(5): p. 426-7; author reply 427-8.
893. Dittrich, P.S. and P. Schwille, *Photobleaching and stabilization of fluorophores used for single-molecule analysis with one- and two-photon excitation.* Applied Physics B-Lasers and Optics, 2001. **73**(8): p. 829-837.
894. Eggeling, C., et al., *Photostability of Fluorescent Dyes for Single-Molecule Spectroscopy: Mechanisms and Experimental Methods for Estimating Photobleaching in Aqueous Solution*, in *Applied Fluorescence in Chemistry, Biology and Medicine*. 1999, Springer Berlin Heidelberg: Berlin, Heidelberg. p. 193-240.
895. Eggeling, C., et al., *Analysis of photobleaching in single-molecule multicolor excitation and Forster resonance energy transfer measurements.* J Phys Chem A, 2006. **110**(9): p. 2979-95.
896. Khodjakov, A. and C.L. Rieder, *Imaging the division process in living tissue culture cells.* Methods, 2006. **38**(1): p. 2-16.
897. Waters, J. and T. Wittmann, *Quantitative Imaging in Cell Biology*. 2014: Elsevier Science.
898. Boudreau, C., et al., *Excitation Light Dose Engineering to Reduce Photo-bleaching and Photo-toxicity.* Sci Rep, 2016. **6**: p. 30892.
899. Castello, M., et al., *Gated-sted microscopy with subnanosecond pulsed fiber laser for reducing photobleaching.* Microsc Res Tech, 2016. **79**(9): p. 785-91.
900. Fu, M., et al., *A design concept of long-wavelength fluorescent analogs of rhodamine dyes: replacement of oxygen with silicon atom.* Chem Commun (Camb), 2008(15): p. 1780-2.
901. Thompson, A.D., et al., *Long-Term Live-Cell STED Nanoscopy of Primary and Cultured Cells with the Plasma Membrane HIDE Probe DiI-SiR.* Angew Chem Int Ed Engl, 2017. **56**(35): p. 10408-10412.
902. Kozma, E., et al., *Bioorthogonal double-fluorogenic siliconrhodamine probes for intracellular super-resolution microscopy.* Chem Commun (Camb), 2017. **53**(50): p. 6696-6699.

903. Shieh, P., et al., *Imaging bacterial peptidoglycan with near-infrared fluorogenic azide probes.* Proc Natl Acad Sci U S A, 2014. **111**(15): p. 5456-61.
904. Iwatate, R.J., et al., *Silicon Rhodamine-Based Near-Infrared Fluorescent Probe for gamma-Glutamyltransferase.* Bioconjug Chem, 2018. **29**(2): p. 241-244.
905. Hanaoka, K., et al., *Synthesis of unsymmetrical Si-rhodamine fluorophores and application to a far-red to near-infrared fluorescence probe for hypoxia.* Chem Commun (Camb), 2018. **54**(50): p. 6939-6942.
906. Du, M., et al., *A near-infrared fluorescent probe for selective and quantitative detection of fluoride ions based on Si-Rhodamine.* Anal Chim Acta, 2018. **1030**: p. 172-182.
907. Koide, Y., et al., *Evolution of Group 14 Rhodamines as Platforms for Near-Infrared Fluorescence Probes Utilizing Photoinduced Electron Transfer.* ACS Chemical Biology, 2011. **6**(6): p. 600-608.
908. Wang, T., et al., *Spirolactonized Si-rhodamine: a novel NIR fluorophore utilized as a platform to construct Si-rhodamine-based probes.* Chemical Communications, 2012. **48**(70): p. 8781-8783.
909. Wang, B., et al., *A six-membered-ring incorporated Si-rhodamine for imaging of copper(ii) in lysosomes.* Org Biomol Chem, 2016. **14**(28): p. 6720-8.
910. Egawa, T., et al., *Development of a far-red to near-infrared fluorescence probe for calcium ion and its application to multicolor neuronal imaging.* J Am Chem Soc, 2011. **133**(36): p. 14157-9.
911. Huang, Y.L., A.S. Walker, and E.W. Miller, *A Photostable Silicon Rhodamine Platform for Optical Voltage Sensing.* J Am Chem Soc, 2015. **137**(33): p. 10767-76.
912. Zhang, H., et al., *Imaging lysosomal highly reactive oxygen species and lighting up cancer cells and tumors enabled by a Si-rhodamine-based near-infrared fluorescent probe.* Biomaterials, 2017. **133**: p. 60-69.
913. Huo, Y., et al., *Selective and sensitive visualization of endogenous nitric oxide in living cells and animals by a Si-rhodamine deoxylactam-based near-infrared fluorescent probe.* Chem Sci, 2017. **8**(10): p. 6857-6864.
914. Koide, Y., et al., *Development of an Si-rhodamine-based far-red to near-infrared fluorescence probe selective for hypochlorous acid and its applications for biological imaging.* J Am Chem Soc, 2011. **133**(15): p. 5680-2.
915. Umezawa, K., et al., *Rational design of reversible fluorescent probes for live-cell imaging and quantification of fast glutathione dynamics.* Nat Chem, 2017. **9**(3): p. 279-286.
916. Grimm, J.B., et al., *A general method to fine-tune fluorophores for live-cell and in vivo imaging.* Nat Methods, 2017. **14**(10): p. 987-994.
917. Chi, W., et al., *A Photoexcitation-Induced Twisted Intramolecular Charge Shuttle.* Angew Chem Int Ed Engl, 2019. **58**(21): p. 7073-7077.
918. Lavis, L.D. and R.T. Raines, *Bright ideas for chemical biology.* ACS Chem Biol, 2008. **3**(3): p. 142-55.
919. Savarese, M., et al., *Fluorescence lifetimes and quantum yields of rhodamine derivatives: new insights from theory and experiment.* J Phys Chem A, 2012. **116**(28): p. 7491-7.
920. Zhao, N., et al., *Enhanced Hypsochromic Shifts, Quantum Yield, and π–π Interactions in a meso,β-Heteroaryl-Fused BODIPY.* The Journal of Organic Chemistry, 2017. **82**(7): p. 3880-3885.
921. Fischer, C. and C. Sparr, *Direct Transformation of Esters into Heterocyclic Fluorophores.* Angewandte Chemie International Edition, 2018. **57**(9): p. 2436-2440.
922. Grimm, J.B., et al., *General Synthetic Method for Si-Fluoresceins and Si-Rhodamines.* ACS Cent Sci, 2017. **3**(9): p. 975-985.
923. Kolmakov, K., et al., *Far-Red Emitting Fluorescent Dyes for Optical Nanoscopy: Fluorinated Silicon-Rhodamines (SiRF Dyes) and Phosphorylated Oxazines.* Chemistry, 2015. **21**(38): p. 13344-56.
924. Zhang, H., et al., *Pyridine-Si-xanthene: A novel near-infrared fluorescent platform for biological imaging.* Chinese Chemical Letters, 2019. **30**(5): p. 1063-1066.

925. Dolci, L., et al., *2-[18F]fluoropyridines by no-carrier-added nucleophilic aromatic substitution with [18F]FK-K222—a comparative study.* Journal of Labelled Compounds and Radiopharmaceuticals, 1999. **42**(10): p. 975-985.
926. Olberg, D.E., et al., *One Step Radiosynthesis of 6-[18F]Fluoronicotinic Acid 2,3,5,6-Tetrafluorophenyl Ester ([18F]F-Py-TFP): A New Prosthetic Group for Efficient Labeling of Biomolecules with Fluorine-18.* Journal of Medicinal Chemistry, 2010. **53**(4): p. 1732-1740.
927. Naumiec, G.R., et al., *Quinuclidine and DABCO Enhance the Radiofluorination of 5-Substituted 2-Halopyridines.* European Journal of Organic Chemistry, 2017. **2017**(45): p. 6593-6603.
928. Zielonka, J., et al., *Mitochondria-Targeted Triphenylphosphonium-Based Compounds: Syntheses, Mechanisms of Action, and Therapeutic and Diagnostic Applications.* Chemical Reviews, 2017. **117**(15): p. 10043-10120.
929. Murphy, M.P., *Targeting lipophilic cations to mitochondria.* Biochimica et Biophysica Acta (BBA) - Bioenergetics, 2008. **1777**(7): p. 1028-1031.
930. Sung, J., et al., *A New Infrared Probe Targeting Mitochondria via Regulation of Molecular Hydrophobicity.* Bioconjugate Chemistry, 2019. **30**(1): p. 210-217.
931. Youle, R.J. and A.M. van der Bliek, *Mitochondrial fission, fusion, and stress.* Science, 2012. **337**(6098): p. 1062-5.
932. Westermann, B., *Mitochondrial fusion and fission in cell life and death.* Nat Rev Mol Cell Biol, 2010. **11**(12): p. 872-84.
933. Murphy, M.P. and R.A.J. Smith, *Drug delivery to mitochondria: the key to mitochondrial medicine.* Advanced Drug Delivery Reviews, 2000. **41**(2): p. 235-250.
934. Murayama, C., et al., *Monitoring Mitochondrial Complex-I Activity Using Novel PET Probe 18F-BCPP-EF Allows Early Detection of Radiotherapy Effect in Murine Squamous Cell Carcinoma.* PLoS One, 2017. **12**(1): p. e0170911.
935. Li, J., J. Lu, and Y. Zhou, *Mitochondrial-Targeted Molecular Imaging in Cardiac Disease.* Biomed Res Int, 2017. **2017**: p. 5246853.
936. Murphy, M.P., *Selective targeting of bioactive compounds to mitochondria.* Trends Biotechnol, 1997. **15**(8): p. 326-30.
937. Rideout, D.C., et al., *Phosphonium salts exhibiting selective anti-carcinoma activity in vitro.* Anticancer Drug Des, 1989. **4**(4): p. 265-80.
938. Mallet, M. and G. Quéguiner, *Nouvelles réactions d'halogenopyridines avec le n-butyllithium. proposition d'un mécanisme par métallation et migration du brome.* Tetrahedron, 1979. **35**(13): p. 1625-1631.
939. Miller, R.E., et al., *Combined Directed ortho Metalation−Halogen Dance (HD) Synthetic Strategies. HD−Anionic ortho Fries Rearrangement and Double HD Sequences.* Organic Letters, 2010. **12**(10): p. 2198-2201.
940. Schnürch, M., et al., *Halogen dance reactions—A review.* Chemical Society Reviews, 2007. **36**(7): p. 1046-1057.
941. Schlosser, M., *The 2×3 Toolbox of Organometallic Methods for Regiochemically Exhaustive Functionalization.* Angewandte Chemie International Edition, 2005. **44**(3): p. 376-393.
942. Erb, W. and F. Mongin, *Halogen 'dance': a way to extend the boundaries of arene deprotolithiation.* Tetrahedron, 2016. **72**(33): p. 4973-4988.
943. Matthias, J., et al., *Synthesis of a dihalogenated pyridinyl silicon rhodamine for mitochondrial imaging by a halogen dance rearrangement.* Beilstein Journal of Organic Chemistry, 2019. **15**: p. 2333-2343.
944. Fulmer, G.R., et al., *NMR Chemical Shifts of Trace Impurities: Common Laboratory Solvents, Organics, and Gases in Deuterated Solvents Relevant to the Organometallic Chemist.* Organometallics, 2010. **29**(9): p. 2176-2179.
945. Williams, A.T.R., S.A. Winfield, and J.N. Miller, *Relative fluorescence quantum yields using a computer-controlled luminescence spectrometer.* Analyst, 1983. **108**(1290): p. 1067-1071.
946. Würth, C., et al., *Relative and absolute determination of fluorescence quantum yields of transparent samples.* Nature Protocols, 2013. **8**: p. 1535.

947. Sens, R. and K.H. Drexhage, *Fluorescence quantum yield of oxazine and carbazine laser dyes.* Journal of Luminescence, 1981. **24-25**: p. 709-712.
948. Giedt, R.J., et al., *Computational imaging reveals mitochondrial morphology as a biomarker of cancer phenotype and drug response.* Scientific Reports, 2016. **6**: p. 32985.
949. Yang, X., et al., *Mitochondrial dynamics quantitatively revealed by STED nanoscopy with an enhanced squaraine variant probe.* bioRxiv, 2019: p. 646117.
950. Editorial, *Phototoxicity revisited.* Nat Methods, 2018. **15**(10): p. 751.
951. Icha, J., et al., *Phototoxicity in live fluorescence microscopy, and how to avoid it.* Bioessays, 2017. **39**(8).
952. Birch, D., et al., *Fluorophore labeling of a cell-penetrating peptide induces differential effects on its cellular distribution and affects cell viability.* Biochimica et Biophysica Acta (BBA) - Biomembranes, 2017. **1859**(12): p. 2483-2494.
953. Zanetti-Domingues, L.C., et al., *Hydrophobic fluorescent probes introduce artifacts into single molecule tracking experiments due to non-specific binding.* PLoS One, 2013. **8**(9): p. e74200.
954. Lukinavicius, G., et al., *Fluorescent dyes and probes for super-resolution microscopy of microtubules and tracheoles in living cells and tissues.* Chem Sci, 2018. **9**(13): p. 3324-3334.
955. Stoddart, M.J., *Cell Viability Assays: Introduction*, in *Mammalian Cell Viability: Methods and Protocols*, M.J. Stoddart, Editor. 2011, Humana Press: Totowa, NJ. p. 1-6.
956. Bell, S.P. and A. Dutta, *DNA Replication in Eukaryotic Cells.* Annual Review of Biochemistry, 2002. **71**(1): p. 333-374.
957. Mölder, A., et al., *Non-invasive, label-free cell counting and quantitative analysis of adherent cells using digital holography.* Journal of Microscopy, 2008. **232**(2): p. 240-247.
958. Fulda, S., et al., *Cellular stress responses: cell survival and cell death.* Int J Cell Biol, 2010. **2010**: p. 214074.
959. Boonstra, J. and J.A. Post, *Molecular events associated with reactive oxygen species and cell cycle progression in mammalian cells.* Gene, 2004. **337**: p. 1-13.
960. Arigovindan, M., et al., *High-resolution restoration of 3D structures from widefield images with extreme low signal-to-noise-ratio.* Proc Natl Acad Sci U S A, 2013. **110**(43): p. 17344-9.
961. Preibisch, S., et al., *Efficient Bayesian-based multiview deconvolution.* Nat Methods, 2014. **11**(6): p. 645-8.
962. Richardson, W.H., *Bayesian-Based Iterative Method of Image Restoration*.* Journal of the Optical Society of America, 1972. **62**(1): p. 55.
963. Blasse, C., et al., *PreMosa: extracting 2D surfaces from 3D microscopy mosaics.* Bioinformatics, 2017. **33**(16): p. 2563-2569.
964. Shihavuddin, A., et al., *Smooth 2D manifold extraction from 3D image stack.* Nat Commun, 2017. **8**: p. 15554.
965. Dabov, K., et al., *Image denoising by sparse 3-D transform-domain collaborative filtering.* IEEE Trans Image Process, 2007. **16**(8): p. 2080-95.
966. Morales-Navarrete, H., et al., *A versatile pipeline for the multi-scale digital reconstruction and quantitative analysis of 3D tissue architecture.* Elife, 2015. **4**.
967. Buades, A., B. Coll, and J. Morel. *A non-local algorithm for image denoising.* in *2005 IEEE Computer Society Conference on Computer Vision and Pattern Recognition (CVPR'05)*. 2005.
968. Trussell, H.J., *Chapter 1 - Digital Imaging: Capture, Display, Restoration, and Enhancement*, in *Academic Press Library in Signal Processing*, J. Trussell, et al., Editors. 2014, Elsevier. p. 3-9.
969. Luisier, F., T. Blu, and M. Unser, *Image denoising in mixed Poisson-Gaussian noise.* IEEE Trans Image Process, 2011. **20**(3): p. 696-708.
970. Makitalo, M. and A. Foi, *Optimal inversion of the generalized Anscombe transformation for Poisson-Gaussian noise.* IEEE Trans Image Process, 2013. **22**(1): p. 91-103.
971. Haider, S.A., et al., *Fluorescence microscopy image noise reduction using a stochastically-connected random field model.* Scientific Reports, 2016. **6**: p. 20640.
972. Li, J., F. Luisier, and T. Blu, *PURE-LET Image Deconvolution.* IEEE Trans Image Process, 2018. **27**(1): p. 92-105.

973. Jezierska, A., et al. *A primal-dual proximal splitting approach for restoring data corrupted with poisson-gaussian noise*. in *2012 IEEE International Conference on Acoustics, Speech and Signal Processing (ICASSP)*. 2012.
974. Chouzenoux, E., et al., *A Convex Approach for Image Restoration with Exact Poisson--Gaussian Likelihood.* SIAM Journal on Imaging Sciences, 2015. **8**(4): p. 2662-2682.
975. Jia, L., et al., *A reweighted L2 method for image restoration with Poisson and mixed Poisson-Gaussian noise.* Inverse Problems & Imaging, 2015. **9**(3): p. 875-894.
976. Gazagnes, S., E. Soubies, and L. Blanc-Féraud. *High density molecule localization for super-resolution microscopy using CEL0 based sparse approximation*. in *2017 IEEE 14th International Symposium on Biomedical Imaging (ISBI 2017)*. 2017.
977. Marnissi, Y., et al., *A Variational Bayesian Approach for Image Restoration—Application to Image Deblurring With Poisson–Gaussian Noise.* IEEE Transactions on Computational Imaging, 2017. **3**(4): p. 722-737.
978. Bayes, T. and R. Price, *An Essay towards Solving a Problem in the Doctrine of Chances. By the Late Rev. Mr. Bayes, F. R. S. Communicated by Mr. Price, in a Letter to John Canton, A. M. F. R. S.* Philosophical Transactions (1683-1775), 1763. **53**: p. 370-418.
979. Schmidt, U., Q. Gao, and S. Roth. *A generative perspective on MRFs in low-level vision*. in *2010 IEEE Computer Society Conference on Computer Vision and Pattern Recognition*. 2010.
980. Schmidt, U., K. Schelten, and S. Roth. *Bayesian deblurring with integrated noise estimation*. in *CVPR 2011*. 2011.
981. Gao, Q., et al., *Bayesian Joint Super-Resolution, Deconvolution, and Denoising of Images with Poisson-Gaussian Noise.* 2018 IEEE 15th International Symposium on Biomedical Imaging (ISBI 2018), 2018: p. 938-942.
982. Gao, Q. and S. Roth. *How Well Do Filter-Based MRFs Model Natural Images?* 2012. Berlin, Heidelberg: Springer Berlin Heidelberg.
983. Chen, D.-Q., *Regularized Generalized Inverse Accelerating Linearized Alternating Minimization Algorithm for Frame-Based Poissonian Image Deblurring.* SIAM Journal on Imaging Sciences, 2014. **7**(2): p. 716-739.
984. Jezierska, A., et al. *Iterative poisson-Gaussian noise parametric estimation for blind image denoising*. in *2014 IEEE International Conference on Image Processing (ICIP)*. 2014.
985. Mäkitalo, M. and A. Foi, *Noise Parameter Mismatch in Variance Stabilization, With an Application to Poisson–Gaussian Noise Estimation.* IEEE Transactions on Image Processing, 2014. **23**(12): p. 5348-5359.
986. Eck, S., et al., *A spherical harmonics intensity model for 3D segmentation and 3D shape analysis of heterochromatin foci.* Medical Image Analysis, 2016. **32**: p. 18-31.
987. Daddysman, M.K., M.A. Tycon, and C.J. Fecko, *Photoinduced damage resulting from fluorescence imaging of live cells.* Methods Mol Biol, 2014. **1148**: p. 1-17.
988. Spielmann, H., et al., *The second ECVAM workshop on phototoxicity testing. The report and recommendations of ECVAM workshop 42.* Altern Lab Anim, 2000. **28**(6): p. 777-814.
989. Cole, R., *Live-cell imaging.* Cell Adh Migr, 2014. **8**(5): p. 452-9.
990. Mora-Bermudez, F. and J. Ellenberg, *Measuring structural dynamics of chromosomes in living cells by fluorescence microscopy.* Methods, 2007. **41**(2): p. 158-67.
991. Wu, Y., et al., *Inverted selective plane illumination microscopy (iSPIM) enables coupled cell identity lineaging and neurodevelopmental imaging in Caenorhabditis elegans.* Proc Natl Acad Sci U S A, 2011. **108**(43): p. 17708-13.
992. Tomer, R., et al., *Quantitative high-speed imaging of entire developing embryos with simultaneous multiview light-sheet microscopy.* Nat Methods, 2012. **9**(7): p. 755-63.
993. Icha, J., et al., *Independent modes of ganglion cell translocation ensure correct lamination of the zebrafish retina.* J Cell Biol, 2016. **215**(2): p. 259-275.
994. Strnad, P., et al., *Inverted light-sheet microscope for imaging mouse pre-implantation development.* Nat Methods, 2016. **13**(2): p. 139-42.

995. Strobl, F. and E.H. Stelzer, *Non-invasive long-term fluorescence live imaging of Tribolium castaneum embryos.* Development, 2014. **141**(11): p. 2331-8.
996. Knoll, S.G., W.W. Ahmed, and T.A. Saif, *Contractile dynamics change before morphological cues during fluorescence [corrected] illumination.* Sci Rep, 2015. **5**: p. 18513.
997. Roehlecke, C., et al., *The influence of sublethal blue light exposure on human RPE cells.* Mol Vis, 2009. **15**: p. 1929-38.
998. McDonald, A., et al., *Light-induced Ca(2+) transients observed in widefield epi-fluorescence microscopy of excitable cells.* Biomed Opt Express, 2012. **3**(6): p. 1266-73.
999. Cha, S.-H., *Taxonomy of nominal type histogram distance measures*, in *Proceedings of the American Conference on Applied Mathematics*. 2008, World Scientific and Engineering Academy and Society (WSEAS): Cambridge, Massachusetts. p. 325-330.

LIST OF FIGURES

LIST OF TABLES

DEFINITION OF ABBREVIATIONS

abbreviation	meaning
%IA	percent of applied radioactivity
%ID/g	percent injected dose per gram of tissue
(f)BALM	(fluctuation-assisted) binding-activated localization microscopy
(F)PALM	(fluorescence) photoactivated localization microscopy
(m)PH	(motorized) pinhole
[^{18}F]FDG	2-[^{18}F]fluoro-2-deoxy-D-glucose
[^{68}Ga]Ga-PSMA-11	Glu-NH-CO-NH-Lys(Ahx)-[[^{68}Ga]Ga(HBED-CC)]
2D	two dimensions, two-dimensional
2PE	two-photon excitation
2-PMPA	2-(phosphonomethyl)-pentanedioic acid
3D	three dimensions, three-dimensional
4D	four dimensions, four-dimensional
abs	absorption
AEG	N-(2-aminoethyl)glycine
AF594	Alexa Fluor 594
AFM	atomic force microscopy
AI (computer science)	artificial intelligence
AI (optics)	adaptive illumination
ALT	alternative lengthening of telomeres
AOTF	acousto-optical tunable filter
APB	ALT-associated promyelocytic leukemia nuclear bodies
APD	avalanche photodiode

abbreviation	meaning
ATM	ataxia-telangiectasia mutated
ATP	adenosine triphosphate
ATRX	alpha thalassemia/mental retardation syndrome X-linked
BC	benzylcytosine
BG	benzylguanine
BLAST	biophotonic laser-assisted surgery tool
BNID	BioNumbers ID
BP	bandpass filter
BSA	bovine serum albumin
CCV	clathrin-coated vesicle
CLC	clathrin light chain
CNN	convolutional NN
COD	coefficient of determination
CP	carbopyronine
CRISPR	clustered, regularly interspaced, short palindromic repeats
CRPCa	castration-resistant prostate cancer
CT	computed tomography
CTCF	CCCTC-binding factor
ctrl	control
CW	continuous wave
DARPin	designed ankyrin repeat protein
DBS	directional beam splitter
DCM	dichloromethane

abbreviation	meaning
DDR	DNA damage response
DEPT	distortionless enhancement by polarization transfer
det	detection
DFT	density functional theory
DIPEA	*N,N*-diisopropylethylamine
DKFZ	Deutsches Krebsforschungszentrum (German Cancer Research Center)
DL	deep learning
DMEM	Dulbecco's modified Eagle medium
DMF	*N,N*-dimethylformamide
DMSO	dimethyl sulfoxide
DNA	deoxyribonucleic acid
DOTA	1,4,7,10-tetraazacyclododecane-1,4,7,10-tetraacetic acid
DOTAGA	1,4,7,10-tetraazacyclododececane,1-(glutaric acid)−4,7,10-triacetic acid
DRE	digital rectal exam
D-Rex	dark state relaxation
dsDNA	double-stranded DNA
dSTORM	direct stochastic optical reconstruction microscopy
DyMIN	dynamic intensity minimum
EC	electron capture
EC_{50}	half maximal effective concentration
ECTR	extrachromosomal telomeric repeat
eDHFR	*Escherichia coli* dihydrofolate reductase
EDTA	ethylenediaminetetraacetic acid

abbreviation	meaning
EM	electron microscopy
em	emission
ER	endoplasmatic reticulum
ESI	electrospray ionization
EtOH	ethanol
exc	excitation
ExSTED	expansion stimulated emission depletion microscopy
Fab	antibody fragment
FAP	fluorogen activating protein
FbFP	flavin-based fluorescent protein
FBS	fetal bovine serum
FCol	fiber collimator
FCp	fiber coupler
FDA	Food and Drug Administration
FISH	fluorescence in situ hybridization
FlAsH	fluorescein arsenical hairpin binder
FN	false negative
FN3	fibronectin type III domain
FOLH1	folate hydrolase I
FOV	field of view
FP (biology)	fluorescent protein
FP (image processing)	false positive
FPGA	field-programmable gate array

abbreviation	meaning
fpm	frames per minute
FR	Faraday rotator
FSC	forward scatter
FWHM	full width half maximum
G1	growth phase 1
G2	growth phase 2
G4	quadruplex
GCP II	glutamate carboxypeptidase II
GFP	green fluorescent protein
GS	goat serum
GSD	ground state depletion
GSDIM	ground state depletion with individual molecular return
GSH	glutathione
GSSG	glutathione disulfide
HBED-CC	*N,N'*-bis-[2-hydroxy-5-(carboxyethyl)benzyl]ethylenediamine-*N,N'*-diacetic acid
HD	halogen dance
HEPES	4-(2-hydroxyethyl)piperazine-1-ethanesulfonic acid
HILO	highly inclined and laminated optical sheet
HOMO	highest occupied molecular orbital
HP1	heterochromatin protein 1
HPLC	high performance liquid chromatography
HRMS	high-resolution mass spectrometry
HSQC	heteronuclear single quantum correlation

abbreviation	meaning
I&F	imaging and fluorescence
I&S	imaging and surgery
I&T	imaging and therapy
IC_{50}	half maximal inhibitory concentration
ICG	indocyanine green
IF	indirect immunofluorescence
IFP1.4	infrared fluorescent protein 1.4
iLOV	improved light, oxygen or voltage-sensing
IRF	instrument response function
iRFP	near-infrared fluorescent protein
ITL	interstitial telomere loop
ITS	interstitial telomere sequences
JF	Janelia Fluor
L	lens
LLSM	lattice light sheet microscopy
LOR	line of response
LP	longpass filter
LSFM	light sheet fluorescence microscopy
LT	long telomeres
M (biology)	mitosis
M (optics)	mirror
m/z	mass-to-charge
MALDI-MS	matrix-assisted laser desorption/ionization mass spectrometry

abbreviation	meaning
MAP	maximum *a posteriori*
mbFISH	molecular beacon FISH
mCRPCa	metastatic castration-resistant prostate cancer
MeCN	acetonitrile
MINFIELD	minimized FOV and minimized fluorophore exposure to the STED beam
MINFLUX	single molecule localization with minimal emission fluxes
miniSOG	mini singlet oxygen generator
ML	machine learning
MMS21	methyl methanesulfonate-sensitivity protein 21
MMSE	minimum mean square error
MOST	molecular states for multiple off-state transitions
MRF	Markov random field
MRI	magnetic resonance imaging
MS	mass spectrometry
Mw	molecular weight
NaAc	sodium acetate
NAALADase	*N*-acetyl-L-aspartyl-L-glutamate peptidase I
NAD(P)H	nicotinamide adenine dinucleotide (phosphate)
n-BuLi	butyllithium
NHEJ	non-homologous end joining
NIR	near-infrared
NMR	nuclear magnetic resonance
NN	neural network

abbreviation	meaning
NSOM	near-field scanning optical microscopy
NT	normal telomeres
NV	nitrogen vacancy
OCT	optical coherence tomography
OF	optical fiber
OI	optical imaging
OTF	optical transfer function
p.i.	post injection
PA NL-SIM	patterned-activation nonlinear SIM
paFP	photoactivatable fluorescent protein
PAINT	point accumulation for imaging in nanoscale topography
PBL	peripheral blood leukocyte
PBS (biochemistry)	phosphate-buffered saline
PBS (optics)	polarizing beam splitter cube
PCa	prostate cancer
PCC	Pearson correlation coefficient
pcFP	photoconvertible fluorescent protein
PDB	Protein Data Bank
PET	positron emission tomography
PFA	paraformaldehyde
PI	propidium iodide
PIE	pulse-interleaved excitation
PIP1	POT1-interacting protein 1

abbreviation	meaning
PML	promyelocytic leukemia
PML-NB	PML nuclear bodies
PMT	photomultiplier tube
PNA	peptide nucleic acid
POI	protein of interest
POT1	protection of telomeres 1
PRR	pulse repetition rate
PSA	prostate-specific antigen
PSF	point spread function
psFP	photoswitchable fluorescent protein
PSMA	prostate-specific membrane antigen
PSMA-10	$[Glu\text{-}urea\text{-}Lys(Ahx)]_2$-HBED-CC
PTOP1	POT1 and TIN2 organizing protein 1
QD	quantum dot
Q-FISH	quantitative FISH
qPCR	quantitative polymerase chain reaction
QS	Quadscanner
Rap1	repressor/activator protein 1
RCY	radiochemical yield
ReAsH	resorufin arsenical hairpin binder
ReLU	rectified linear unit
RESCue	reduction of state transition cycles
RESOLFT	reversible saturable/switchable optical linear (fluorescence) transitions

abbreviation	meaning
RhoBo	rhodamine-derived bis-boronic acid
RIBE	radiation-induced bystander effect
RNA	ribonucleic acid
ROI	region of interest
ROS	reactive oxygen species
ROSE	repetitive optical selective exposure
ROXS	reducing and oxidizing systems
RP-HPLC	reversed-phase high performance liquid chromatography
rpm	rounds per minute
RPMI	Roswell Park Memorial Institute
RT	room temperature
S	DNA synthesis phase
SC	supercontinuum laser
scFv	single-chain variable fragment
SD	standard deviation
sgRNA	single guide RNA
SIM (biology)	SUMO interacting motif
SIM (optics)	structured illumination microscopy
SiR	silicone rhodamine
SLM	spatial light modulator
SMLM	single molecule localization microscopy
SNR	signal-to-noise ratio
SOFI	super-resolution optical fluctuation imaging

abbreviation	meaning
SP	shortpass filter
SP100	Speckled 100 kDa
SPEM	saturated patterned excitation microscopy
SPIM	selective plane illumination microscopy
SPM	scanning probe microscopy
SPT	single particle tracking
SRRF	super-resolution radial fluctuation
SS	safety shutter
SSC (biochemistry)	saline sodium citrate
SSC (flow cytometry)	side scatter
SSIM	saturated structured illumination microscopy
STED	stimulated emission depletion
STM	scanning tunneling microscopy
STORM	stochastic optical reconstruction microscopy
STR	subtelomeric region
SUMO	small ubiquitin-like modifier
SUV	standardized uptake value
TAC	thesis advisory committee
TAE	tris-acetate-ethylenediaminetetraacetic acid
TALE	transcription activator-like effector
TALEN	transcription activator-like effector-based nuclease
t-BuLi	*tert*-butyllithium
TCSPC	time-correlated single photon counting

abbreviation	meaning
TERC	telomerase RNA component
TERT	telomerase reverse transcriptase
TeSLA	telomere shortest-length assay
TFA	trifluoroacetic acid
TFP	tetrafluorophenyl
THF	tetrahydrofuran
TIN2	TRF1-interaction nuclear factor 2
TINT1	TIN2-interacting protein 1
TIRF	total internal reflection fluorescence
TLC	thin-layer chromatography
TMM	telomere maintenance mechanism
TP	true positive
TPE	telomere position effect
TPE-OLD	telomere position effect over long distances
TPP1	TINT1/PIP1/PTOP1
T-Rex	triplet state relaxation
TRF	terminal restriction fragment
TRF1/2	telomeric repeat binding factor 1/2
T-SCE	telomere sister chromatid exchange
UICC	Union for International Cancer Control
UnaG	Unagi green fluorescent protein
U-STELA	universal single-telomere length analysis
UV	ultraviolet

abbreviation	meaning
VHH	camelid heavy-chain variable fragments
VST	very short telomeres
WYSIWYG	what you see is what you get
XRF	X-ray fluorescence
Y-FAST	yellow fluorescence-activating and absorption-shifting tag
ZFN	zinc finger nuclease
ZFP	zinc finger protein
α-NAAG	*N*-acetyl-L-aspartyl-L-glutamate
λ/2	λ/2 plate
λ/4	λ/4 plate

PUBLICATIONS

Journal Articles

Matthias, J., Spilger, R., Chung, I., Vlijm, R., Engelhardt, J., Rohr, K., Hell, S.W., Rippe, K., *Human telomere structure at the nanoscale in intact cells visualized by STED microscopy*. (to be submitted).

Matthias, J., Engelhardt, J., Schäfer, M., Bauder-Wüst, U., Meyer, P.T., Haberkorn, U., Eder, M., Kopka, K., Hell, S.W., Eder, A.C., *The intracellular fate of PSMA inhibitors as revealed by STED nanoscopy*. (submitted, September 2019).

Matthias, J., Kanagasundaram, T., Kopka, K., Kramer, C. S., *Synthesis of a di-halogenated pyridinyl silicon rhodamine for mitochondrial imaging by a halogen dance rearrangement*. Beilstein Journal of Organic Chemistry, 2019. **15**: p. 2333-2343.

Gao, Q., Eck, S., Matthias, J., Chung, I., Engelhardt, J., Rippe, K., Rohr, K., *Bayesian Joint Super-Resolution, Deconvolution, and Denoising of Images with Poisson-Gaussian Noise.* 2018 IEEE 15th International Symposium on Biomedical Imaging (ISBI 2018), 2018: p. 938-942.

Butkevich, A.N., Belov, V. N., Kolmakov, K., Sokolov, V. V., Shojaei, H., Sidenstein, S. C., Kamin, D., Matthias, J., Vlijm, R., Engelhardt, J., Hell, S. W., *Hydroxylated Fluorescent Dyes for Live-Cell Labeling: Synthesis, Spectra and Super-Resolution STED*. Chemistry, 2017. **23**(50): p. 12114-12119.

Selected Talks and Conference Posters

Matthias, J., Spilger, R., Chung, I., Vlijm, R., Engelhardt, J., Rohr, K., Hell, S.W., Rippe, K., *The Human Telomere Structure at the Nanoscale*. 1st NOTCH Meeting, 10/2019, Heidelberg, Germany (talk).

Matthias, J., Chung, I., Engelhardt, J., Rippe, K., Hell, S.W., *Investigating the Nanoscale Structural Organization of ALT-Associated Promyelocytic Nuclear Bodies in Living Cells*. Annual DKFZ PhD Poster Presentation, 11/2017, Heidelberg, Germany (poster).

Matthias, J., Chung, I., Engelhardt, J., Rippe, K., Hell, S.W., *STED Nanoscopy of Telomeres and APBs.* 5th CancerTelSys Consortium, 11/2016, Heidelberg, Germany (talk).

Matthias, J., Chung, I., Engelhardt, J., Rippe, K., Hell, S.W., *Investigating the Nanoscale Structural Organization of ALT-Associated Promyelocytic Nuclear Bodies in Living Cells*. Labeling & Nanoscopy, 10-11/2016, Heidelberg, Germany (poster).

Matthias, J., Chung, I., Engelhardt, J., Rippe, K., Hell, S.W., *Investigating the Nanoscale Structural Organization of ALT-Associated Promyelocytic Nuclear Bodies in Living Cells*. 12th EMBL Conference: Transcription and Chromatin, 08/2016, Heidelberg, Germany (poster).

Matthias, J., Chung, I., Engelhardt, J., Rippe, K., Hell, S.W., *Investigating the Nanoscale Structural Organization of ALT-Associated Promyelocytic Nuclear Bodies in Living Cells*. 21st Annual DKFZ PhD Retreat, 07/2016, Weil der Stadt, Germany (talk).

EIDESSTATTLICHE VERSICHERUNG

Eidesstattliche Versicherung gemäß §8 der Promotionsordnung für die Naturwissenschaftlich-Mathematische Gesamtfakultät der Universität Heidelberg

1. Bei der eingereichten Dissertation zu dem Thema *STED Nanoscopy to Illuminate New Avenues in Cancer Research – From Live Cell Staining and Direct Imaging to Decisive Preclinical Insights for Diagnosis and Therapy* handelt es sich um meine eigenständig erbrachte Leistung.

2. Ich habe nur die angegebenen Quellen und Hilfsmittel benutzt und mich keiner unzulässigen Hilfe Dritter bedient. Insbesondere habe ich wörtlich oder sinngemäß aus anderen Werken übernommene Inhalte als solche kenntlich gemacht.

3. Die Arbeit oder Teile davon habe ich bislang nicht an einer Hochschule des In- oder Auslands als Bestandteil einer Prüfungs- oder Qualifikationsleistung vorgelegt.

4. Die Richtigkeit der vorstehenden Erklärungen bestätige ich.

5. Die Bedeutung der eidesstattlichen Versicherung und die strafrechtlichen Folgen einer unrichtigen oder unvollständigen eidesstattlichen Versicherung sind mir bekannt.

Ich versichere an Eides statt, dass ich nach bestem Wissen die reine Wahrheit erklärt und nichts verschwiegen habe.

Heidelberg, 31. Oktober 2019 Jessica Matthias